TECTONIC AND ENVIRONMENTAL RECONSTRUCTIONS: PERSPECTIVES FROM GEOCHEMISTRY AND ISOTOPES OF SEDIMENTARY ROCKS

EDITED BY: Kai-Jun Zhang, Qiangtai Huang, Jiangong Wei, I. Tonguç Uysal and Lu Lu

PUBLISHED IN: Frontiers in Earth Science

frontiers Research Topics

ISSN 1664-8714
ISBN 978-2-88976-309-2
DOI 10.3389/978-2-88976-309-2

About Frontiers

Frontiers is more than just an open-access publisher of scholarly articles: it is a pioneering approach to the world of academia, radically improving the way scholarly research is managed. The grand vision of Frontiers is a world where all people have an equal opportunity to seek, share and generate knowledge. Frontiers provides immediate and permanent online open access to all its publications, but this alone is not enough to realize our grand goals.

Frontiers Journal Series

The Frontiers Journal Series is a multi-tier and interdisciplinary set of open-access, online journals, promising a paradigm shift from the current review, selection and dissemination processes in academic publishing. All Frontiers journals are driven by researchers for researchers; therefore, they constitute a service to the scholarly community. At the same time, the Frontiers Journal Series operates on a revolutionary invention, the tiered publishing system, initially addressing specific communities of scholars, and gradually climbing up to broader public understanding, thus serving the interests of the lay society, too.

Dedication to Quality

Each Frontiers article is a landmark of the highest quality, thanks to genuinely collaborative interactions between authors and review editors, who include some of the world's best academicians. Research must be certified by peers before entering a stream of knowledge that may eventually reach the public - and shape society; therefore, Frontiers only applies the most rigorous and unbiased reviews.
Frontiers revolutionizes research publishing by freely delivering the most outstanding research, evaluated with no bias from both the academic and social point of view. By applying the most advanced information technologies, Frontiers is catapulting scholarly publishing into a new generation.

What are Frontiers Research Topics?

Frontiers Research Topics are very popular trademarks of the Frontiers Journals Series: they are collections of at least ten articles, all centered on a particular subject. With their unique mix of varied contributions from Original Research to Review Articles, Frontiers Research Topics unify the most influential researchers, the latest key findings and historical advances in a hot research area! Find out more on how to host your own Frontiers Research Topic or contribute to one as an author by contacting the Frontiers Editorial Office: frontiersin.org/about/contact

TECTONIC AND ENVIRONMENTAL RECONSTRUCTIONS: PERSPECTIVES FROM GEOCHEMISTRY AND ISOTOPES OF SEDIMENTARY ROCKS

Topic Editors:
Kai-Jun Zhang, University of Chinese Academy of Sciences, China
Qiangtai Huang, Sun Yat-sen University, China
Jiangong Wei, Guangzhou Marine Geological Survey, China
I. Tonguç Uysal, Istanbul University-Cerrahpasa, Turkey
Lu Lu, China University of Mining and Technology, China

Citation: Zhang, K.-J., Huang, Q., Wei, J., Uysal, I. T., Lu, L., eds. (2022). Tectonic and Environmental Reconstructions: Perspectives From Geochemistry and Isotopes of Sedimentary Rocks. Lausanne: Frontiers Media SA.
doi: 10.3389/978-2-88976-309-2

Table of Contents

frontiers | Frontiers in Earth Science

EDITORIAL
published: 12 May 2022
doi: 10.3389/feart.2022.914962

Editorial: Tectonic and Environmental Reconstructions: Perspectives From Geochemistry and Isotopes of Sedimentary Rocks

Kai-Jun Zhang[1]*, *Qiang-Tai Huang*[2], *Jiangong Wei*[3], *Tonguc Uysal*[4] and *Lu Lu*[5]

[1]Asian Tectonics Research Group, College of Earth and Planetary Sciences, University of Chinese Academy of Sciences, Beijing, China, [2]School of Marine Sciences, Sun Yat-sen University, Guangzhou, China, [3]Guangzhou Marine Geological Survey, Guangzhou, China, [4]Department of Earth Sciences, Ankara University, Ankara, Turkey, [5]School of Resources and Earth Sciences, China University of Mining and Technology, Xuzhou, China

Keywords: sedimentary rocks, geochemistry, Isotopes, Tectonics, environment 14 15

Editorial on the Research Topic

Tectonic and Environmental Reconstructions: Perspectives From Geochemistry and Isotopes of Sedimentary Rocks

Sedimentary sequences hold the remarkable advantage that they comprise a vertically accumulated and relatively undistorted record of erosion, sedimentation, and climatic-tectonic environments and, therefore, obviate many of the difficulties intrinsic in disentangling complex structural overprints (McLennan et al., 2001; Zhang, 2004; Pietranik et al., 2008; Zhang et al., 2007; 2012, 2017). The geochemical and isotopic studies of sedimentary rocks and minerals therein form a vital approach to tectonic and environmental reconstructions. Latest decades have witnessed significant progress in geochemistry and isotopes of sedimentary rocks and minerals and their applications to fundamental geological issues. For example, advances in dating on calcite using U–Pb isotopic system (e.g., Roberts et al., 2017; Godeau et al., 2018) and dating on illite using K–Ar isotopic system (e.g., Hamilton et al., 1989; Pevear, 1999) provide additional methods to define the ages of sedimentation/strata besides the conventional paleontological method; documentation of U–Pb–Lu–Hf isotope systematics of detrital zircons from siliciclastic rocks makes it possible to examine the nature of major crustal growth events (e.g., McLennan et al., 2001; Pietranik et al., 2008), both regional and global; work on the geochemistry of limestones deposited in various plate tectonic settings permits the development of proxies for the discrimination of depositional regimes (Zhang et al., 2017). Therefore, the collection of works regarding this topic is timely and essential to exchange new ideas in the international community and provoke and promote studies in this field.

In the collection of this Research Topic, 11 contributions were published, with a focus on the recent advances in sedimentary geochemistry and isotopes at whole-rock and/or single mineral scale and their applications to tectonic and environmental reconstructions. Besides, this topic collected provocative ideas regarding the methodology and give summaries of its recent development. Importantly, this Research Topic presented new datasets or summaries on the geochemistry and isotopes of specific sedimentary rock or mineral on key regimes. Moreover, this Research Topic published practice examples on a regional scale that can be tracked and referred to by researchers in the same field.

The collection covers the following several major themes.

OPEN ACCESS

Edited and reviewed by:
Martyn Tranter,
Aarhus University, Denmark

***Correspondence:**
Kai-Jun Zhang
kaijun@ucas.ac.cn

Specialty section:
This article was submitted to Geochemistry, a section of the journal Frontiers in Earth Science

Received: *07 April 2022*
Accepted: *14 April 2022*
Published: *12 May 2022*

Citation:
Zhang K-J, Huang Q-T, Wei J, Uysal T and Lu L (2022) Editorial: Tectonic and Environmental Reconstructions: Perspectives From Geochemistry and Isotopes of Sedimentary Rocks. Front. Earth Sci. 10:914962. doi: 10.3389/feart.2022.914962

1) Sedimentary geochemistry and isotopes and their applications to unraveling the paleogeographic, paleoclimatic, and sedimentary evolution of the maritime space in the western Pacific.

For example, Li et al. and Liu et al. explored the sources of organic carbon in the Mariana Trench, the deepest part of the earth, and the paleoclimate of the middle Okinawa Trough Since the Middle Holocene, respectively, both based on analysis of glycerol dialkyl glycerol tetraether (GDGT). Wang et al. documented the hydrocarbon geochemistry of core sediments from the SW Basin of the South China Sea and probe the implications for sedimentary environment. Xu et al. envisaged topographic and climatic control on chemical weathering of mountainous riverine sediments of Hainan Island, South China Sea, based on investigation of sedimentary geochemistry.

2) New ideas on the methodology regarding sedimentary geochemistry and isotopes as well as their applications to geological issues.

Liu et al. analyzed Mesozoic tectono-thermal events of the Qinshui Basin in central North China Craton, based on measurements on illite crystallinity and vitrinite reflectance. Li et al. reconstructed the maximum burial temperature of the Sichuan Basin, southern China in use of clumped isotopes. Shaogong et al. dated the paragneiss in the Dabie–Sulu UHP orogen of eastern China by means of zircon U-Pb isotope systematics.

3) Geochemistry and isotopes of specific sedimentary rock or mineral on important regimes.

Yang et al. investigated the whole-rock and *in situ* geochemistry of siderites in the Lopingian coal-bearing series, western Guizhou of southern China to reveal their genetic mechanism and environment implications. Chenrai et al. reported the occurrence and genesis of bedding-parallel fibrous calcite veins in Permian siliciclastic and carbonate rocks in central Thailand.

4) Applications of sedimentary geochemistry to petroleum industry

This is the most characteristic brightness of this collection. For example, Yingjie et al. reported the variation of clay minerals during alkaline surfactant polymer flooding in the oilfields in the Songliao Basin of eastern China. Fan et al. carried out pyrolysis experiment on water-saturated shale plunger samples to shed insight to oil generation and expulsion of shales.

AUTHOR CONTRIBUTIONS

K-JZ contributed to conception and wrote and reviewed the manuscript. K-JZ, Q-TH, JW, TU, and LL contributed to manuscript revision, read, and approved the submitted version.

REFERENCES

Godeau, N., Deschamps, P., Guihou, A., Leonide, P., Tendil, A., Gerdes, A., et al. (2018). U-pb Dating of Calcite Cement and Diagenetic History in Microporous Carbonate Reservoirs: Case of the Urgonian Limestone, France. *Geology* 46, 247–250. doi:10.1130/g39905.1

Hamilton, P. J., Kelley, S., and Fallick, A. E. (1989). K-ar Dating of Illite in Hydrocarbon Reservoirs. *Clay Miner.* 24, 215–231. doi:10.1180/claymin.1989.024.2.08

McLennan, S. M., Bock, B., Compston, W., Hemming, S. R., and McDaniel, D. K. (2001). Detrital Zircon Geochronology of Taconian and Acadian Foreland Sedimentary Rocks in New England. *J. Sediment. Res.* 71, 305–317. doi:10.1306/072600710305

Pevear, D. R. (1999). Illite and Hydrocarbon Exploration. *Proc. Natl. Acad. Sci. U.S.A.* 96 (7), 3440–3446. doi:10.1073/pnas.96.7.3440

Pietranik, A. B., Hawkesworth, C. J., Storey, C. D., Kemp, A. I. S., Sircombe, K. N., Whitehouse, M. J., et al. (2008). Episodic, Mafic Crust Formation from 4.5 to 2.8 Ga: New Evidence from Detrital Zircons, Slave Craton, Canada. *Geol* 36, 875–878. doi:10.1130/g24861a.1

Roberts, N. M. W., Rasbury, E. T., Parrish, R. R., Smith, C. J., Horstwood, M. S. A., and Condon, D. J. (2017). A Calcite Reference Material for LA-ICP-MS U-Pb Geochronology. *Geochem. Geophys. Geosyst.* 18, 2807–2814. doi:10.1002/2016gc006784

Zhang, K.-J., Li, Q.-H., Yan, L.-L., Zeng, L., Lu, L., Zhang, Y.-X., et al. (2017). Geochemistry of Limestones Deposited in Various Plate Tectonic Settings. *Earth-Science Rev.* 167, 27–46. doi:10.1016/j.earscirev.2017.02.003

Zhang, K.-J. (2004). Secular Geochemical Variations of the Lower Cretaceous Siliciclastic Rocks from Central Tibet (China) Indicate a Tectonic Transition from Continental Collision to Back-Arc Rifting. *Earth Planet. Sci. Lett.* 229, 73–89. doi:10.1016/j.epsl.2004.10.030

Zhang, K.-J., Zhang, Y.-X., Li, B., and Zhong, L.-F. (2007). Nd Isotopes of Siliciclastic Rocks from Tibet, Western China: Constraints on Provenance and Pre-cenozoic Tectonic Evolution. *Earth Planet. Sci. Lett.* 256, 604–616. doi:10.1016/j.epsl.2007.02.014

Zhang, K. J., Li, B., and Wei, Q. G. (2012). Geochemistry and Nd Isotopes of the Songpan-Ganzi Triassic Turbidites, Central China: Diversified Provenances and Tectonic Implications. *J. Geol.* 120, 68–82. doi:10.1086/662716

Conflict of Interest: The authors declare that the research was conducted in the absence of any commercial or financial relationships that could be construed as a potential conflict of interest.

frontiers in Earth Science

ORIGINAL RESEARCH
published: 13 April 2021
doi: 10.3389/feart.2021.653742

The Sources of Organic Carbon in the Deepest Ocean: Implication From Bacterial Membrane Lipids in the Mariana Trench Zone

*Jiwei Li[1,2†], Zhiyan Chen[1,3,4†], Xinxin Li[4,5], Shun Chen[1], Hengchao Xu[1], Kaiwen Ta[1], Shamik Dasgupta[1], Shijie Bai[1], Mengran Du[1], Shuangquan Liu[1] and Xiaotong Peng[1]**

[1] Institute of Deep-Sea Science and Engineering, Chinese Academy of Sciences, Beijing, China, [2] Southern Marine Science and Engineering Guangdong Laboratory (Zhuhai), Sun Yat-sen University, Zhuhai, China, [3] School of Environment, Harbin Institute of Technology, Harbin, China, [4] Shenzhen Key Laboratory of Marine Archaea Geo-Omics, Department of Ocean Science and Engineering, Southern University of Science and Technology, Shenzhen, China, [5] Southern Marine Science and Engineering Guangdong Laboratory (Guangzhou), Guangzhou, China

OPEN ACCESS

Edited by:
Jiangong Wei, Guangzhou Marine Geological Survey, China

Reviewed by:
Wei Xie, Sun Yat-sen University, Zhuhai Campus, China
Hongxiang Guan, Guangzhou Institute of Energy Conversion (CAS), China

***Correspondence:**
Xiaotong Peng
xtpeng1973@163.com

[†] These authors have contributed equally to this work

Specialty section:
This article was submitted to Geochemistry, a section of the journal Frontiers in Earth Science

Received: *15 January 2021*
Accepted: *23 March 2021*
Published: *13 April 2021*

Citation:
Li J, Chen Z, Li X, Chen S, Xu H, Ta K, Dasgupta S, Bai S, Du M, Liu S and Peng X (2021) The Sources of Organic Carbon in the Deepest Ocean: Implication From Bacterial Membrane Lipids in the Mariana Trench Zone. Front. Earth Sci. 9:653742. doi: 10.3389/feart.2021.653742

Hadal trenches have higher microbial carbon turnover rates as compared to adjacent abyssal plains. However, the source of organic carbon in the trench remains enigmatic. In this study, we show that a fraction of organic carbon is possibly derived *in situ* and correlated with chemoautotrophic communities supported by the fluid discharge of water-rock interaction in the trench wall, based on analysis of glycerol dialkyl glycerol tetraether (GDGT) membrane lipids, including archaeal isoprenoid GDGTs (IsoGDGTs) and bacterial branched GDGTs (BrGDGTs), in sediments and rocks of the Mariana and Yap Trenches, northwest Pacific Ocean. These trench sediments contained relative higher BrGDGTs ratios, which was a rare observation in the open ocean. The BrGDGT-to-IsoGDGT ratios ranged in 0.02–0.88 (mean = 0.10 ± 0.11) in sediments and 0.09–0.38 (mean = 0.17 ± 0.13) in altered rocks. The calculated values of branched and isoprenoid tetraether (BIT) index ranged from 0.02–0.73 (mean = 0.18 ± 0.11) in sediments and from 0.16–0.9 in altered rocks (mean = 0.37 ± 0.27). Moreover, these GDGTs exhibited similar characteristics to those of altered basalt rocks, indicating inputs of organic carbon from the trench subsurface environment. Thus, in addition to organic-rich material settling, we propose chemoautotrophic activity in oceanic crust could be an additional source of organic carbon in the deepest part of the ocean, with an important role in deep-sea carbon cycles.

Keywords: hadal trenches, organic carbon, water-rock interaction, membrane lipids, deep-sea carbon cycles, chemoautotrophic activity

INTRODUCTION

Hadal trenches, which are located on the axis of subduction zones, are covered by water depths ranging from 6,500 m to 11,000 m and represent some of the most remote and least-explored regions on Earth (Jamieson et al., 2010; Jamieson et al., 2017, 2018). It has recently been revealed that there is a significantly higher microbial carbon turnover rate in hadal sediment than that in adjacent abyssal plain (Glud et al., 2013; Luo et al., 2018). This environment is also known to

sustain a diverse array of metazoan organisms (Jamieson et al., 2010) and heterotrophic microbial populations (Nunoura et al., 2015). It has been speculated that the supply of nutritious food at such great depths largely relied on the flux of fresh organic-rich particulate matter (Glud et al., 2013; Nunoura et al., 2015) and input of the decaying biota and carcasses from the upper ocean (Oguri et al., 2013). Moreover, low temperature water-rock interaction between bedrock and seawater, such as serpentinization and basalt rock alteration, is a common phenomenon at the bottom of trenches (Fryer et al., 1999; Stern et al., 2006; Du et al., 2019) and chemosynthetic microbial communities utilizing crustal fluid are also known to occur in trenches (Fujikura et al., 1999; Hand et al., 2012; Ohara et al., 2012). For example, the existence of fluid discharge features, including fluid discharge points and associated pockmarks, as well as chemosynthetic microorganisms, in the outer rise region was directly observed by submersible investigations in the southern Mariana trench (Du et al., 2019). Around these fluid discharge features, iddingsite-rich muds with high hydrogen and methane concentration were close association with augite, indicating the occurrence of iddingsitisation in these altered basalts (Du et al., 2019). However, the potential contribution of carbon fixation by these chemosynthetic microbial communities, which related to water-rock interaction, in the trench bottom remains enigmatic.

The membrane lipid GDGTs of prokaryotes, including IsoGDGTs and BrGDGTs (for structures see **Supplementary Figure 1**), in marine sediments are important biomarkers for tracing organic matter sources (Hopmans et al., 2004; Schouten et al., 2013; Weijers et al., 2014). BrGDGTs have been predominantly found in terrestrial settings such as soils and peat deposits. Although BrGDGTs may also be *in situ* formed in normal marine environments, the abundance of marine BrGDGTs differs from that of terrestrial soil by orders of magnitude (Peterse et al., 2009; Schouten et al., 2013; Weijers et al., 2014). The BIT index was proposed based on BrGDGTs and Crenarchaeol (representative of marine IsoGDGTs) contents (see **Supplementary Equations**) (Hopmans et al., 2004). In terrestrial soils, the BIT value is approximately 0.90 ± 0.14, whereas that of open marine sediments is 0.04 ± 0.03 (Schouten et al., 2013). Therefore, this index is previously used to characterize the contribution of terrestrial soil inputs in marine environments (Schouten et al., 2013). However, several previous studies have found that relatively high BrGDGT content also presented in some chemoautotrophic systems, such as cold seep (Zhang et al., 2020), hydrothermal fields (Hu et al., 2012; Lincoln et al., 2013; Pan et al., 2016), and serpentinite-hosted ecosystems (Newman et al., 2020). These findings indicated that the high relative abundance of BrGDGT in the sedimentary environment of Open Ocean may be an indicator of the chemoautotrophic ecosystem.

To elucidate the source of organic matter at the bottom of trenches, we examined the GDGT lipid profiles of the sediments and rock samples retrieved from the southern Mariana Trench and northern Yap Trench, northwest Pacific Ocean. Our results demonstrated relatively high BrGDGT ratios within trench sediments, with similar composition to those of altered basaltic rocks rather than of sediments in open oceans, suggesting chemoautotrophic carbon fixation in the subduction zone could be an effective source of organic carbon in the deepest parts of the ocean.

MATERIALS AND METHODS

Sample Collection

Sediment and rock samples were collected from the Yap and Mariana Trenches during cruises that were conducted in 2016 and 2017 (**Figure 1** and **Supplementary Table 1**). The multiple sediment core sample, S01, was collected from the northern Yap Trench at a water depth of 5,058 m using a sediment multi-core sampler on the R/V XIANG-YANG-HONG-09, during cruise DY-37 conducted by the China Ocean Mineral Resource R&D Association in 2016.

Nine dives (Dive 114-112) were also performed at the "Challenger deep" of Mariana trench by the "Jiaolong" Human Occupied Vehicle during cruise DY-37. On the two sides of the trench walls, a large number of rock fragments were scattered on the seafloor which is covered with thin sediments (**Supplementary Figures 2A-C**). These rock samples have undergone varying degrees of alteration. During dive 114 and 115, a few fluid discharging points (1 m in height and 2–5 m diameter) and small pockmarks (3–6 m in diameter) were observed at the southern wall with water depths ranging from 5,448 m to 6,669 m (Du et al., 2019). During dive 121, high altered basement rocks were observed at the Northern trench wall (**Supplementary Figure 2D**). A total of six rock samples (7 subsamples) were used in this study (**Supplementary Figure 3**). They were collected from the two sides of the "Challenger Deep". Three samples, including JL118-G01, JL119-G01, and JL121-G04, were collected from northern wall with water depth ranging from 5,552 m to 6,697 m; while the other three samples JL115-G03, JL120-G01, and JL120-G02, were collected from its southern wall with water depths from 5,544 m to 6,296 m.

Four sediment box cores (B01, B06, B09, and B10) were collected from the southern Marianna Trench with a water depth from 5,525 m to 8,638 m using the box sediment sampler onboard the R/V TAN-SUO-YI-HAO, during cruise TS01 conducted by the Chinese Academy of Sciences in 2016. After the sediment boxes were collected on deck, short sediment cores were obtained by inserting PVC plastic pipes into the sediments. LR01 was a 23 cm long sediment core, and was sampled at the deepest site of the "Challenger Deep" onboard the R/V TAN-SUO-YI-HAO, during cruise TS03 conducted by the Chinese Academy of Sciences in 2017. It was collected by using the "Tianya" deep-sea Lander system, designed by the Institute of Deep-sea Science and Engineering, Chinese Academy of Sciences, with the features of sediment sampling, capturing macroorganisms and recording HD videos below 11,000 m water depth (**Supplementary Figure 4**). The sediment sampler of "Tianya" Lander, a cuboid cavity made of aluminum alloy, was installed at the foot of the lander frame, and inserted into the sediments by the dive gravity to complete the sampling process. The cores in each recovery were immediately sectioned into slices of 2 cm in thickness onboard, using an aseptic scalpel.

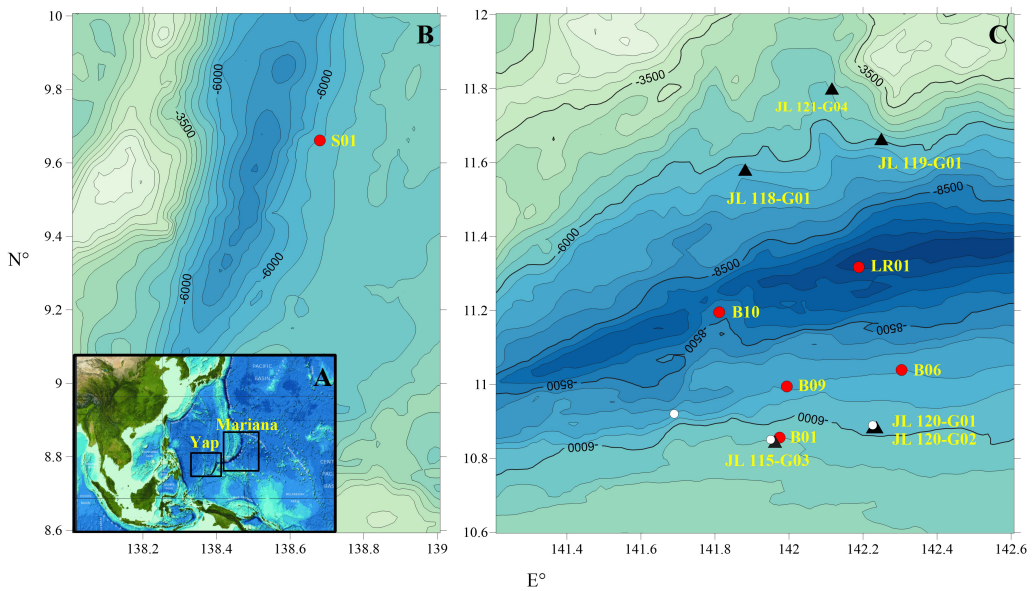

FIGURE 1 | (A) The locations of Yap and Mariana trenches at the northwest Pacific Ocean. **(B)** Regional bathymetric map and the S01 sampling site at the northern Yap trench. **(C)** Regional bathymetric map and the sampling sites at the Mariana Trench. The black triangles represent the rock samples and red circles represent the sediment cores. The lately discovered fluid discharge field and pockmarks on the incoming plate of Mariana trench are marked in white circles (Du et al., 2019).

The LR01 sample was stored at −80°C, whereas the remaining sediment and altered rock samples were stored at −20°C. To avoid pollution, we removed the surface of rock sample using sterile hammer, cleaned with ethanol (70% v) and milliQ water after returning to the laboratory, and extracted the lipids from the interior part.

Lipids Analysis

In the laboratory, the selected sediments and rocks were ground into powders using an agate pestle and mortar after freeze-drying. An aliquot of each sample (5–10 g) was extracted (× 5) ultrasonically with a mixture of dichloromethane and methanol (9:1, V/V) to obtain the total lipid extract. After condensation via a rotary evaporator, the extracted total lipids were further separated into alkanes and polar lipids using silica gel (60–100 mesh) flash column chromatography with *n*-hexane and methanol eluents, respectively. The polar fractions were then passed through 0.45-μm PTFE syringe filters and dried under a stream of nitrogen gas.

The *n*-alkanes and GDGTs were measured at the State Key Laboratory of Biogeology and Environmental Geology, China University of Geosciences (Wuhan), China. The aliphatic fraction containing *n*-alkanes was analyzed in an Agilent 6890 gas chromatography and 5,973 mass spectrometer (GC-MS), equipped with a silica capillary column (DB-5MS; 60 m × 0.25 mm × 0.25 μm). The GC oven temperature program for *n*-alkanes ramped from 50°C to 120°C at 8°C/min, and then from 120°C to 300°C at 5°C/min, held at 300°C for 20 min with helium as the carrier gas. The ionization energy was 70 eV and the temperature of interface between GC and MS was set as 280°C.

With respect to GDGTs analysis, the dried polar fraction was redissolved in *n*-hexane/isopropanol (99:1, v/v) for further analysis. Synthesized C_{46} GDGT was added as an internal standard in each redissolved sample. The GDGTs were analyzed using an Agilent 1200 series liquid chromatography tandem mass spectrometer, with ChemStation management software. Following injection by an autosampler, the GDGT compounds were separated using an Alltech Prevail Cyano column (150 mm × 2.1 mm, 3 μm). Archaeal IsoGDGTs and bacterial BrGDGTs were then analyzed using single ion monitoring at m/z 1302, 1300, 1298, 1296, 1292, 1050, 1048, 1046, 1036, 1034, 1032, 1022, 1020, and 1018. A few GDGT isomers, including 5- and 6- methyl GDGTs could not be separated by using the single ion monitoring method of this study.

TOC, TN, and Carbon Stable Isotope Analysis

The total organic carbon (TOC), total nitrogen (TN), and carbon isotopic ($\delta^{13}C$) compositions of the sediments were measured at the State Key Laboratory of Biogeology and Environmental Geology, China University of Geosciences (Wuhan), China. The freeze-dried sediment samples were rapidly homogenized by grinding and weighed aliquots of the sample were acidified by adding 2 mL of 1 M HCl to every 100 mg of sample. The acidified samples were dried at >60°C under a stream of filtered air, then mixed with 1 mL of Milli-Q water and freeze-dried again. The samples were weighed again to account for the change in weight during the acid treatment. Aliquots of approximately 20 mg were added into 5 × 8 mm tin capsules for the measurement of TOC, TN, and carbon isotopes ($\delta^{13}C$) using a continuous-flow isotope-ratio mass spectrometer (Delta V Advantage, Thermo

Scientific, Germany) coupled to an elemental analyzer (Flash EA 1112 Thermo Scientific, Italy) in the laboratory. The $\delta^{13}C$ results are expressed relative to Vienna PeeDee Belemnite. Replicates of an acetanilide standard (Thermo Scientific) were analyzed along with samples, which indicated that the analytical errors were <0.1‰ for $\delta^{13}C$. The C/N ratios were determined as mol/mol ratios, which were transformed from the %TOC and %TN weight data that were obtained as a part of the stable isotope analyses.

X-Ray Diffraction Analysis

After freeze-drying, the selected sediment and rock samples were thoroughly ground using a mortar and pestle before passing through a 200-mesh sieve. X-ray diffraction analyses were performed on the powdered sub-samples. Sample mounts were step scanned from 2.5° to 65° 2θ with a step size of 0.02° and 50 s counting time. The samples were run on a D/max2550VB3 + /PC X-ray diffractometer at 20 kV and 30 mA with CuK-alpha radiation (1.54061 Å) and a graphite monochromator. Phase analyses were performed on a PDF2 (2004) computer with Jada 5.0 software.

RESULTS

Bulk Organic Geochemical Parameters

In this study, the abundance of TOC ranged from 0.12 to 0.42% in all sediment samples, with highest abundance at the core top sediment in B06 (1,0911 m) and lowest abundance at 33–34 cm of core B01 (5,525 m) (**Figure 2** and **Supplementary Table 2**). The $\delta^{13}C$ and C/N molar ratio of the bulk TOC of the sediment samples ranged between −21.72‰ and −16.70‰ (mean = −19.02 ± 1.05‰, n = 67) and between 3.00 and 8.21 (mean = 4.96 ± 1.12, n = 67), respectively, with no obvious trend with the increasing water depth or core depth (**Supplementary Table 2** and **Figure 3**). As for reference site of 5,000 m water depth, mean TOC of S01 (5,058 m) in Yap Trench was a bit higher than that of B01 in Mariana Trench but still lower than other deeper sites. Therefore, the mean TOC of sediment cores of were generally increased with the increasing water depth in Mariana Trench. Regarding to each sediment core, TOC showed peak abundance at the surface (0–5 cm) of sediment core and fluctuatingly decreased with the sediment core depth (**Figure 2**).

GDGTs in Trench Sediments and Altered Rocks

The sum abundance of BrGDGT and IsoGDGT (Chen et al., 2020) in sediment was generally increased with increased water depth as TOC (**Figure 2**), varied from 0.02 to 7.48 ng/g dw and 0.16 to 363.85 ng/g dw, respectively. The distribution of the BrGDGTs was dominated by hexamethylated BrGDGTs (16-74%), followed by tetramethylated BrGDGTs (13-57%) and pentamethylated BrGDGTs (13-64%) (**Supplementary Table 2**). The domination of hexamethylated groups was coherent with another investigation of the sedimentary BrGDGTs in the bottom of Mariana trench (Xiao et al., 2019). The BrGDGT-to-IsoGDGT (Br/Iso) ratios ranged in 0.02-0.88 (mean = 0.10, n = 67) and 0.09–0.38 (mean = 0.17, n = 7). The calculated BIT values ranged in 0.02-0.73 (mean = 0.18, n = 67) (**Supplementary Table 2**). Approximately 58% of the sediment samples had BIT values over 0.15.

BrGDGTs of altered rock samples had also been identified. The sum abundance of BrGDGTs in these altered rock samples ranged from 0.03 to 0.41 ng/g dw. Similar distribution of BrGDGT composition was found in altered rock as in sediments. Dominated hexamethylated BrGDGTs were ranged from 44 to 72%, tetramethylated and pentamethylated groups contributed

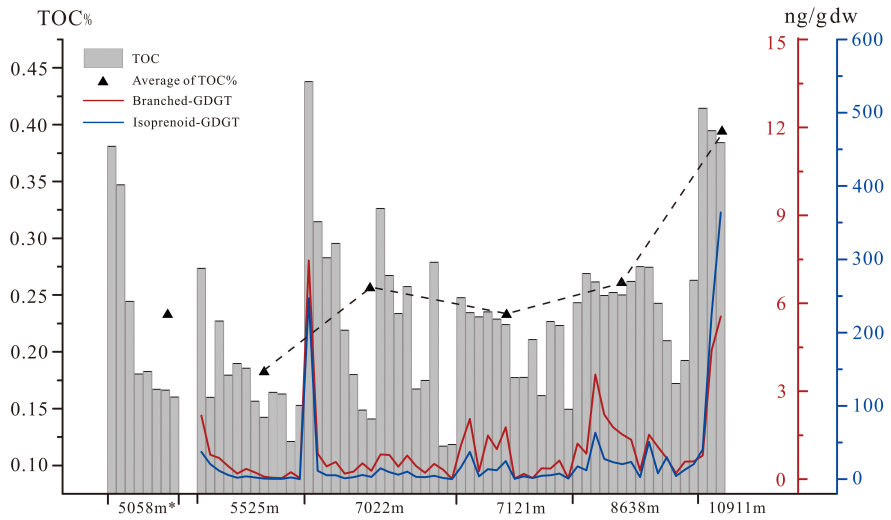

FIGURE 2 | Abundance of TOC and GDGTs from 5000-11000 m in Mariana/Yap Trenches. The distribution of TOC, BrGDGTs and IsoGDGTs (normalized to dry weight of sediment) in the trench sediments from Mariana and Yap Trench. (The asterisk represents the Yap sediment core S01; The mean value of TOC calculates from the subsamples of the first 20 cm of each sediment column). The concentration of IsoGDGT has been published on Chen et al., 2020.

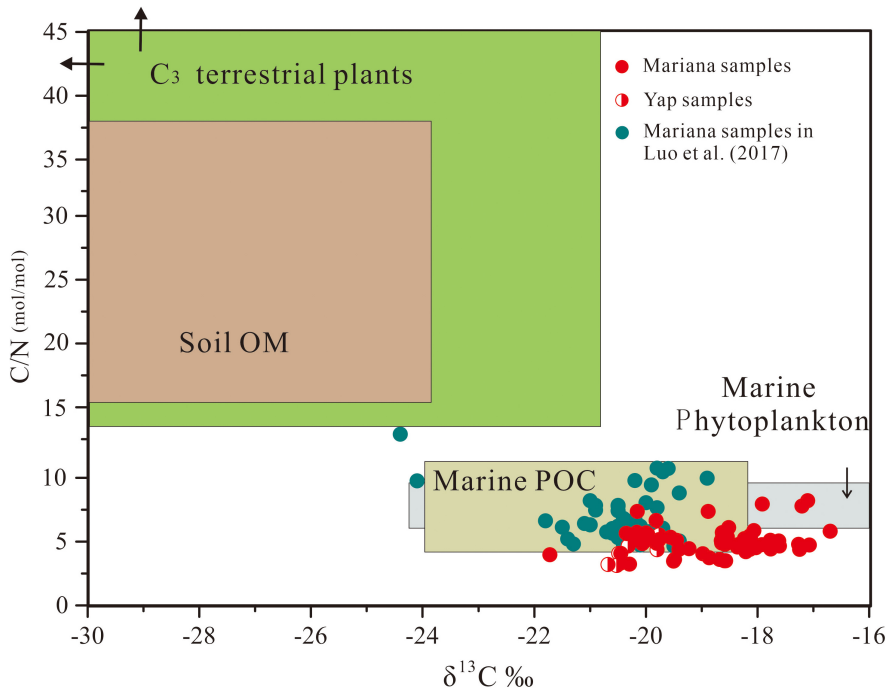

FIGURE 3 | Relationship between $\delta^{13}C$ of TOC and molar C/N ratios of organic matter. The domains of marine particle organic matter (Marine POC), marine phytoplankton, soil organic matter (Soil OM), and C3 vascular plant are based on Goni et al., 2008; Khan et al., 2015 and references therein. The data of blue-green points in this figure are derived from Luo et al., 2017.

10–28% and 15–29%, respectively. Br/Iso ratio in altered rocks was ranged from 0.03 to 0.38 (mean = 0.17, n = 7). The calculated BIT values ranged in 0.16-0.90 (mean = 0.37, n = 7) (**Supplementary Table 2**).

n-Alkane and Related Index in Sediments

n-Alkanes in the range of C_{16} – C_{29} were mainly discovered in the trench sediments. The *n*-alkanes presented unimodal distribution pattern centered at C_{21} – C_{23} for S01 (5,058 m) and B01 (5,525 m), while cantered at C_{16} – C_{18} for the sediment cores below 7,000 m without odd/even predominance (**Figure 4**). Inhomogeneous distribution of *n*-alkanes was found in both abundance and composition in trench sediments. The total *n*-alkanes concentrations ranged from 0.003 to 119.4 mg/g dw. The *n*-alkane of C_{16} – C_{18} were the major components that led to the increase in abundance of the total *n*-alkane below 7,000 m (**Figure 4** and **Supplementary Table 3**). The average chain length (ACL) is the weight-averaged number of carbon atoms. The majority value ACL ranged from 17.0 to 22.7 (only one sample in B06 reached singularly high as 36.4). The carbon preference index (CPI) of C_{15} – C_{25} ranged from 0.37 to 3.82, with majority samples (65%) less than one (CP1 < 1). Uunresolved Complex Mixture (UCM) was obviously observed in most of the samples from trench slope (7,000-8,000 m) and several samples at 5,000 m sites in this study, accompanying with substantial branched alkanes and cycloalkanes indicated by Mass Spectrum (**Supplementary Figure 5**). UCM was presented for 73, 46, and 80% of the samples in B06 (7,022 m), B09 (7,121 m) and B10 (8,638 m), respectively.

Mineral Composition of the Sediments and Altered Rocks

We analyzed the mineral composition of selected sedimentary layers and all altered rocks samples. The X-ray diffraction results showed that quartz, feldspar, zeolite, montmorillonite, chlorite and halite were commonly detected in these sediment samples. While in these altered rocks, quartz, feldspar, chlorite, sepiolite, daubreelite, and talc were detected. Among them, it should be noted that zeolite presented in all of these altered rock samples (**Supplementary Table 4**).

DISCUSSION

Unusually High Proportions of BrGDGTs in Oceanic Trench Sediments and Altered –Rocks

BrGDGTs have been reported in the trench sedimentary environments, such as the Mariana Trench (Ta et al., 2019; Xu et al., 2020), the Kermadec Trench (Xu et al., 2020), and Atacama Trench (Xu et al., 2020). One notable observation was that relative high abundance of BrGDGTs was examined at two sites with water depths shallower than 6,000 m in the Mariana trench (Ta et al., 2019). In consistent to result of Ta et al. (2019), our data further shows that approximately 58% of the sediment samples

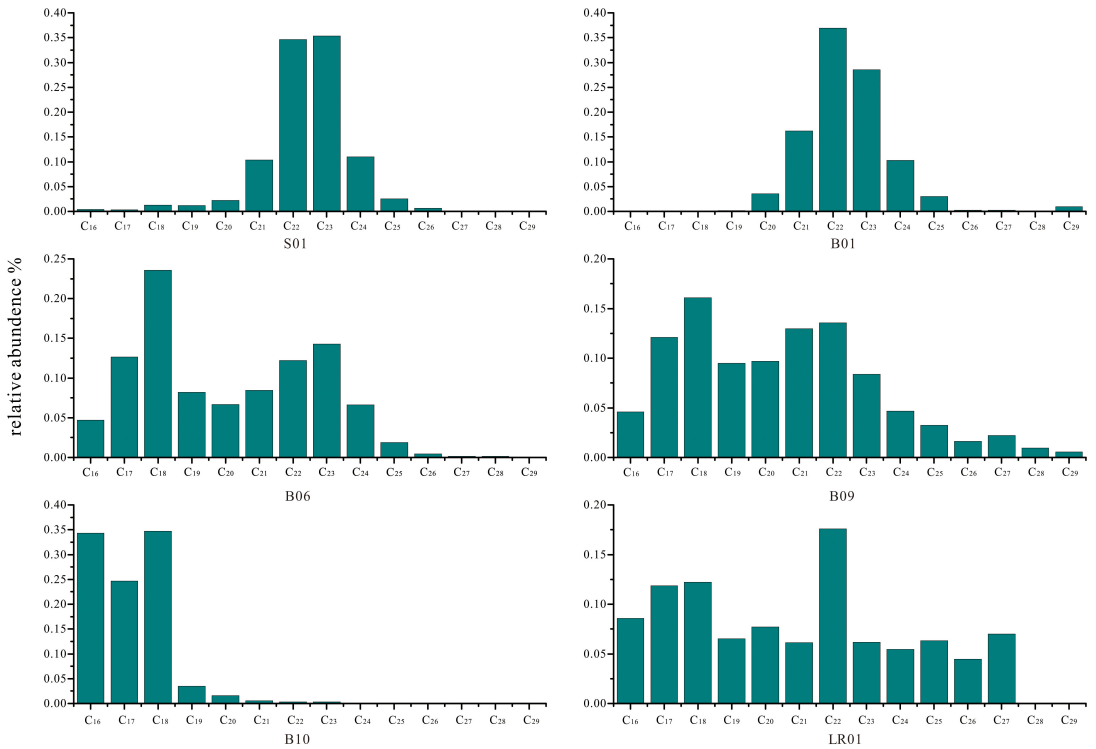

FIGURE 4 | The mean relative concentration of *n*-alkanes in the trench sediment cores.

had BIT values over 0.15. Although the BIT values of these trench sediments were lower than those observed in terrestrial soils, they were on average far greater than those previously reported for open marine sediments, and approached those of river mouth sediments (Weijers et al., 2014). However, the Mariana and Yap Trench are more than 2,000 km away from large landmasses, and marine production of IsoGDGTs rapidly dilutes the terrestrial BrGDGTs from river flows and dust inputs.

These BrGDGTs were possibly produced *in situ* in the ocean. The abundance ratio of hexamethylated to pentamethylated (IIIa/IIa) was inferred to be an indicator for BrGDGT source with higher values in deep sea sediments (2.6-5.1) than in soil (<0.59) (Xiao et al., 2016). BrGDGT was 3.87 ± 1.38 (n = 67) in the trench sediments (**Supplementary Table 2**), indicating little contribution of terrestrial soil inputs (Xiao et al., 2016). This conclusion was consistent with two recent studies, which reported that BrGDGTs in the Mariana trench were characterized by high cyclopentyl rings (Ta et al., 2019) and predominance of hexamethylated 6-methyl BrGDGT (Xiao et al., 2019). Furthermore, other organic geochemical indices also did not support its terrestrial origin. Typically, TOC/TN molar ratio of aquatic organic matter is restricted within values from ∼4 to ∼10, and $\delta^{13}C$ from −34‰ to −12‰ (Lamb et al., 2006). Based on the bulk TOC/TN molar ratios (4.2-11) and $\delta^{13}C$ values of TOC (−21.8‰ – −18.9‰), Luo et al. (2017) suggested that the organic matter in the Mariana sediments was primarily marine origin. In this study, the TOC/TN molar ratio and $\delta^{13}C$ of the bulk organic matter of the sediment samples, which ranged between 3.00 and 8.21 (mean = 4.96 ± 1.12, n = 67) and between −21.72‰ and −16.70‰ (mean = −19.02 ± 1.05‰, n = 67), respectively (**Supplementary Table 2** and **Figure 3**), confirmed they were of marine sources (Lamb et al., 2006; Khan et al., 2015). This conclusion was also supported by the characteristics and distributions of *n*-alkanes in the trench sediments (n < 27, **Figure 4** and **Supplementary Table 3**), with a dominance of short chain *n*-alkane and absence of odd-even preference (Nelson, 1978; Serrazanetti et al., 1995). Therefore, it seems likely that the measured BrGDGTs have formed by *in situ* production in the marine environment. Additionally, since the surface ocean and deep seawater column in this region have constant aerobic conditon (Nunoura et al., 2015) and very low BrGDGT ratios (Schouten et al., 2013; Yamamoto et al., 2016), the relative abundance of BrGDGTs in trench sediments cannot be explained by funnelled inputs from the upper layers of the ocean. Therefore, the relative abundance of BrGDGTs in trench sediments might therefore be *in situ* production of the trench bottom (trench sediments or altered rocks).

Comparative analysis of trench sediment BrGDGT distributions with trench altered rocks and those from other sources suggests BrGDGTs in trench sediments were primarily derived from altered trench wall rocks. A ternary diagram of BrGDGT-Crenarchaeol-GDGT-0 abundance (**Figure 5A**) revealed significant differences between the GDGT characteristics of trench samples (both of sediments and altered rocks) and of terrestrial soil samples. Trench samples also showed higher levels of BrGDGTs and GDGT-0, on average,

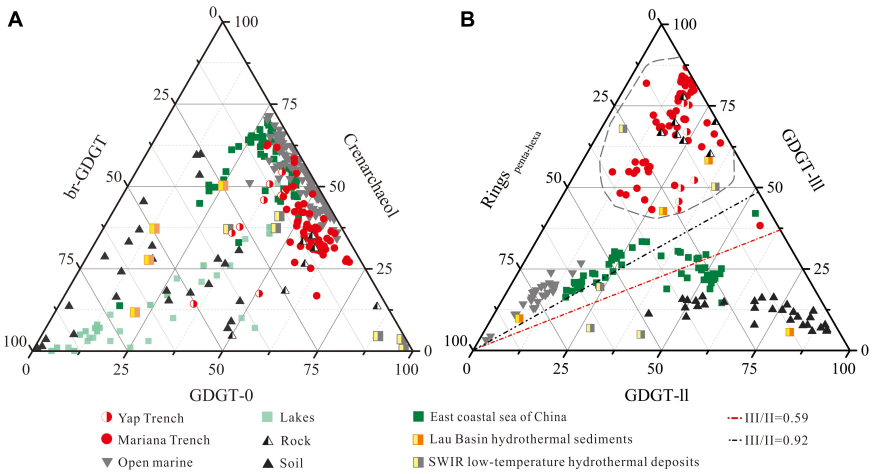

FIGURE 5 | Ternary diagram revealing the source of the GDGTs in the trench sediment. **(A)** GDGT-0, Crenarchaeol and sum of BrGDGTs; **(B)** GDGT-II, GDGT-III and rings of penta-hexa. In this figure, III/II refers to the ratio between GDGT-IIIa and GDGT-IIa (Xiao et al., 2016), whereas rings$_{penta-hexa}$ is the sum of the abundances of ring-shaped GDGT-II and GDGT-III. Br-GDGT refers to bacterial branched GDGT. The sources of data used in this Figure are as follows: open marine data containing particles and surface sediments from NW Pacific (Yamamoto et al., 2016) and surface sediments from SE Pacific (Kaiser et al., 2015); lake data containing particulates and surface sediments from 47 European lakes (Blaga et al., 2009); coastal sediment data containing surface sediments from Gulf of Lions (Kim et al., 2010) and the east coastal sea of China (Lü et al., 2014); soil data containing soil samples from 6 provinces in eastern China (Wu, 2014); data on hydrothermal sediments (Hu et al., 2012); data on low-temperature hydrothermal deposits (Pan et al., 2016). For structures see **Supplementary Figure 1**.

when compared to open marine sediments. When BrGDGTs alone were taken into consideration, a ternary diagram was drawn by plotting the composition of GDGT-II, GDGT-III, and Rings$_{penta-hexa}$ (the sum of GDGT-IIb, GDGT-IIc, GDGT-IIIb, and GDGT-IIIc) (**Figure 5B**). This result shows that the lipids of microbes in trench sediments differ significantly from those of waters nearby this region (Yamamoto et al., 2016) yet shared similar characteristics with lipids of microbes associated with altered rocks from this study and some previous reported hydrothermal sediment and deposits (Hu et al., 2012; Pan et al., 2016). This conclusion is further supported by comparative analysis of the interrelation between the BIT and two other parameters calculated from BrGDGTs, the methylation of branched tetraethers (MBT) and cyclization of branched tetraether (CBT) ratio (Weijers et al., 2007) [see the **Equation** (2) and (3)]. Again, the trench sediments cluster together with the altered trench wall rocks as well as some of the hydrothermal samples (**Figure 6**; Hu et al., 2012; Pan et al., 2016), characterized by higher CBT values and lower MBT values when compared to those of open ocean, soil and coastal sediments. Therefore, these results indicated that most part of BrGDGTs in the trench sediments might be sourced from the altered trench rocks.

Meanwhile, relatively high levels of BrGDGTs have also been reported in studies on chemoautotrophic systems, such as seafloor cold seep (Zhang et al., 2020), hydrothermal fields (Hu et al., 2012; Lincoln et al., 2013; Pan et al., 2016), and serpentinite-hosted ecosystems (Newman et al., 2020). For example, the BIT of hydrothermal sediments of the Lau Basin (Hu et al., 2012), and the low temperature hydrothermal deposits from the Southwest Indian Ridge (Pan et al., 2016) ranged in 0.1–0.76 and 0.24–0.69, respectively. Although they might not be directly sourced from these chemoautotrophic microorganisms (Pan et al., 2016), they were likely derived from heterotrophic BrGDGT-producing bacteria which were fueled by the organic production from the chemoautotrophic communities (Pan et al., 2016). This inference was consistent with the recent findings by Weber et al. (2018), which reported that some BrGDGTs were indeed closely related to chemoautotrophic microorganisms under methanotrophic conditions. Having similar microbial composition is a sound explanation for the close BrGDGTs characteristics between trench sediments, altered rocks, and hydrothermal sediments and deposits. Additionally, wildly distributed UCM in range of short carbon chain of hydrocarbon fractions in slope sediments may further indicated similar synthesis that found in petroleum contaminated or thermal reaction influenced sediments (Frysinger et al., 2003; McCollom et al., 2015), suggesting strongly biodegradation or weathering (Wenger and Isaksen, 2002; Hasinger et al., 2012). UCM in sediment of Mariana (4,000–7,000 m) was previously reported in Guan et al. (2019) which suggested UCM source from biodegraded oils with marine source and likely transported by normal faults and strike-slip faults on the seafloor (Tao et al., 2015; Guan et al., 2019).

In the hydrothermal microbial communities, one of the most conspicuous manifestations is the dominance of chemoautotrophic microorganisms. With regard to the marine trenches, chemoautotrophic communities are far from uncommon (Fujikura et al., 1999; Hand et al., 2012; Ohara et al., 2012). On one hand, the geological settings of the trench bottom can provide habitat niches (e.g., methanotrophic and ammonia oxidizing conditions) for chemolithoautotrophic life (Spang et al., 2010, Nunoura et al., 2015, 2018). The distribution of IsoGDGT in Mariana Trench revealed increasing presence of deep deweling ammonia oxidizing archaeal group

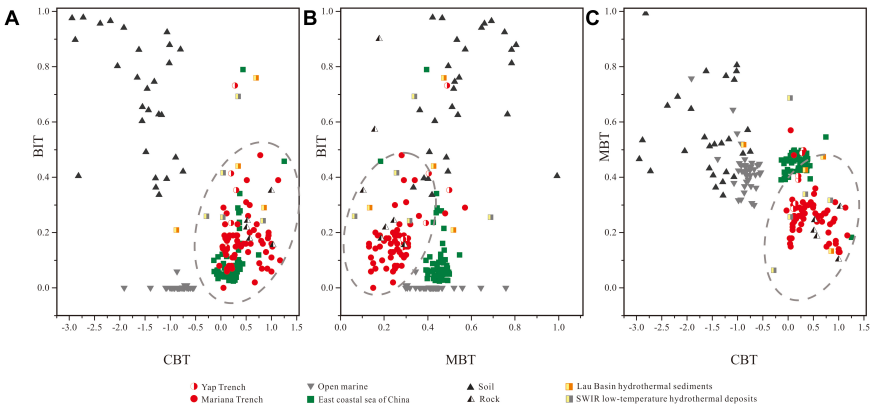

FIGURE 6 | The interrelation between the BIT, MBT and CBT in sediments. **(A)** BIT and CBT. **(B)** BIT and MBT. **(C)** MBT and CBT. The sources of data used in the Figure are as follows: open marine data containing particles and surface sediments from NW Pacific (Yamamoto et al., 2016); lake data containing particulates and surface sediments from 47 European lakes (Blaga et al., 2009); coastal sediment data containing surface sediments from Gulf of Lions (Kim et al., 2010) and the east coastal sea of China (Lü et al., 2014); soil data containing soil samples from 6 province in eastern China (Wu, 2014); data on hydrothermal sediments (Hu et al., 2012); data on low-temperature hydrothermal deposits (Pan et al., 2016).

(*Thaumarchaeota*) in the sediments (Chen et al., 2020). On the other hand, chemolithoautotrophic group of CH_4 and H_2 utilizing in sediment may raise its attention based on conspicuous abundance of dissolved H_2 and H_2-utilizing chemolithotrophs that were recently identified in the altered rocks and muds of the fluid discharge field at the incoming plate of the southern Mariana trench (Du et al., 2019). Meanwhile, the process of serpentinization, which can generate substantial amounts of crustal fluids for microbial CH_4 and H_2 utilization, has been reported to widely occur at the southern Mariana forearc (Ohara et al., 2012; Plümper et al., 2017). Moreover, Tarn et al. (2016) suggested that the microbial communities of Mariana Trench bottom water indeed characteristically display a degree of overlap with microbial communities from low-temperature diffuse flow hydrothermal vents and deep-subsurface locations. Specifically, taxa frequently encountered in vent datasets, such as *Gammaproteobacteria*, *Epsilonproteobacteria, SAR324*, *Thiovulgaceae*, and *SUP05*, were also detected in the trench sediments (Tarn et al., 2016). In addition, abundant of hydrocarbon-degrading bacteria and unknown sources of alkanes were also unexpectedly detected in the sediment of the Mariana trench (Li et al., 2019; Liu et al., 2019). This phenomenon may also be related to the activity of water-rock interaction in the trench bottom (Li et al., 2019). Overall, high similarity in GDGTs between the trench sediments and altered rocks together with these previous microbial and geochemical evidence might imply the wide distribution of chemoautotrophically-based microbial communities in the trench walls, supported by active geological fluid discharge from water-rock interaction.

The Schematic Model of Chemoautotrophic Organic Carbon Production in the Trench Zone

We proposed a schematic model to explore this relationship between water-rock interaction and chemoautotrophic organic carbon in the trench zone (**Figure 7**). On one hand, fluid discharge and mud volcanoes induced by large-scale serpentinization were widely distributed along the forearc of the Mariana Trench (Fryer et al., 1999; Stern et al., 2006). The chemoautotrophic communities fed by these fluids have been reported in the literature. For example, the serpentinization-formed "Shinkai Seep Field" was discovered at the Southern Mariana Forearc (Ohara et al., 2012). Based on this discovery, they proposed that fluid discharge from serpentinization could be widespread in oceanic trenches. Moreover, Plümper et al. (2017) found organic matter encapsulated in rock clasts from an oceanic serpentinite mud volcano above the Izu–Bonin–Mariana subduction zone. Because of this result, they predicted that the serpentinization-fueled systems in the hydrated forearc mantle of Mariana subduction zone may represent one of Earth's largest hidden microbial ecosystems. On the other hand, low-temperature alteration reactions between basaltic rocks and seawater also would be a pervasive phenomenon in the trench environments. This conclusion is supported by the common detection of zeolite in the trench sediments and altered rocks (**Supplementary Table 4**). Zeolite is possibly formed by the low-temperature hydrothermal alteration of basalt (Liou, 1979). This process can also fuel the chemoautotrophic communities, which constitute a trophic base of the basalt habitat in the oceanic crust (Cowen et al., 2003; Santelli et al., 2008). At present, chemoautotrophic carbon fixation associated with carbon and sulfur cycling in seafloor basalts has been proved by multiple lines of indirect evidence, such as depletions in δ^{34}S-pyrite (Rouxel et al., 2008) and DNA sequences (Cowen et al., 2003; Orcutt et al., 2011; Lever et al., 2013). Additionally, the occurrence of fluids discharge feature and H_2-utilizing chemolithotrophs (Du et al., 2019) in the outer rise zone of the incoming plate at the southern Mariana trench further supported this conclusion.

In our schematic model, the plate bending caused by subduction processes has generated numerous faults, fractures and microfissures, both within the outer rise zone of the

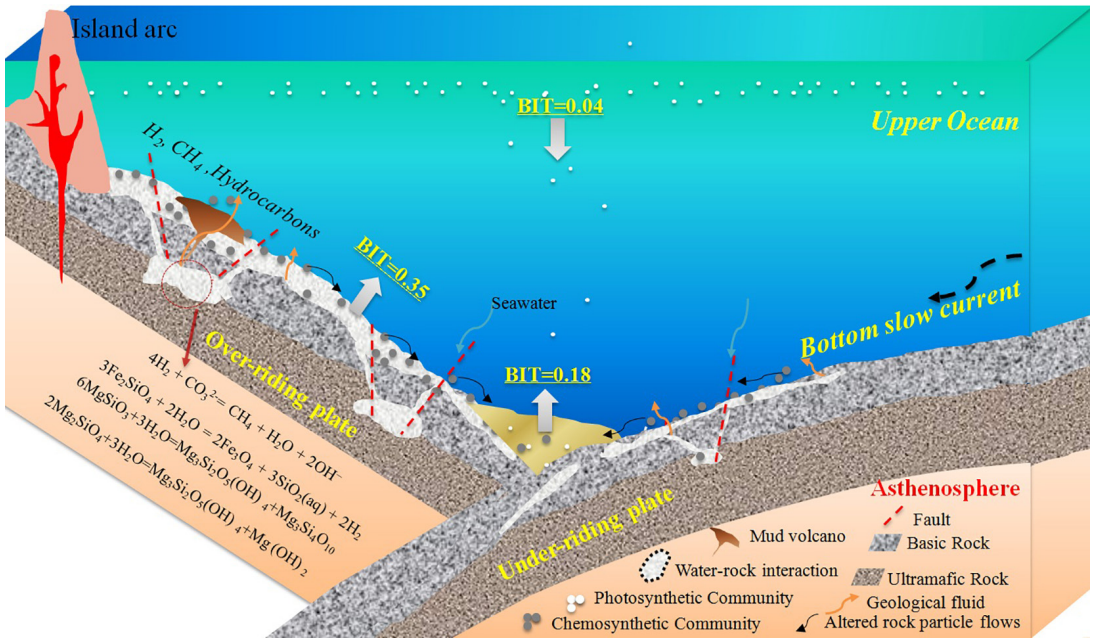

FIGURE 7 | A schematic model of the sources, production and transport of GDGTs in the trenches. Plate bending caused by subduction processes has generated numerous fractures, faults and microfissures both within the subduction slab and overriding plate, triggering water-rock interactions in the oceanic crust. These water-rock interactions facilitate the widespread growth of chemoautotrophic communities across the trench zone.

subduction slab and the forearc of the overriding plate, which provides channels for the influx of water into the oceanic crust, thereby triggering water-rock interactions on a large scale. The geological fluids generated by these interactions are then released in the same channels from the oceanic crust. The fluids are rich in hydrogen, methane, hydrocarbons, and other reduced inorganic matter (e.g., Fe, Mn, and S), making them excellent substrates for chemoautotrophic microorganisms. These water-rock interactions facilitate the widespread growth of chemoautotrophic communities across the trench. As shown in **Supplementary Figure 6**, an increasing trend of BIT was observed in S01, B01 and B06, that corresponds to results in Ta et al. (2019), where an identical trend from surface to bottom was reported in a meter-long sediment core recovered from the Mariana Trench subduction zone (∼5000 m). Higher BIT values in the core bottom at water depths of 5,000–7,000 m, underlain by subducted oceanic crust, suggested abnormal distribution of BrGDGT, compared to those recorded from open oceans with low BIT values. However, such distribution pattern was weak or even reversed at deeper water sites (see B09 and B10). Previously, low BIT values were reported in the sediment cores at the bottom of the Trench (∼11,000 m) by Xiao et al. (2019), which is in line with our findings in core LR01. We speculate that with weakening tectonic distortion of the subducted plate at deeper water depths, increasing BIT values are rarely observed at surface and subsurface sediment (at least 40 cm in this study).

Finally, in the schematic model, the excess labile organic matter produced by these communities are transported laterally to the deeper parts of the trenches through gravity flows, leading to relatively higher microbial carbon turnover rate. No direct evidence of synthesis of BrGDGTs by the chemoautotrophic group is evident yet. However, increasing trend of BIT values from surface to bottom core at subduction zones, and similar composition of BrGDGTs with altered rocks and minerals implies a strong connection between the ecology shaped by chemical fluids in deep sediments and microbial synthesizers of BrGDGT. Overall, we propose that chemoautotrophy driven by geological activity could be an effective supplement to the trench organic carbon pool in addition to photosynthetic products sourced from the upper ocean.

CONCLUSION

In this study, mineralogical compositions, bulk organic geochemical parameters and membrane lipids compositions were examined in sediments and rocks of the Mariana and Yap Trenches, northwest Pacific Ocean. The results shown that these trench sediments and altered rocks contained relative higher BrGDGTs contents, with the BrGDGT-to-IsoGDGT ratios ranged in 0.02–0.88 (mean = 0.10 ± 0.11) and 0.09–0.38 (mean = 0.17 ± 0.13), respectively. Meanwhile, the BIT index ranged in 0.02–0.73 (mean = 0.18 ± 0.11) in sediments and from 0.16–0.9 in altered rocks (mean = 0.37 ± 0.27), which are much higher than those of open ocean. Together with bulk TOC, TN and *n*-alkanes data, we suggested that these BrGDGTs were *in situ* production in the trench zone. Furthermore, these GDGTs exhibited similar characteristics to those of altered basalt rocks, indicating a fraction of organic carbon was possibly derived from chemoautotrophic communities supported by the fluid discharge

of water-rock interaction in the trench walls. This was further supported by the common detection of zeolite, indicative of water-rock alteration, in both altered rocks and trench sediments. Thus, we propose chemoautotrophic activity in oceanic crust could be an additional source of organic carbon in the trench sedimentary environments.

DATA AVAILABILITY STATEMENT

The datasets presented in this study can be found in online repositories. The names of the repository/repositories and accession number(s) can be found below: https://doi.org/10.5281/zenodo.3551342.

AUTHOR CONTRIBUTIONS

XP devised the project. JL provided the main conceptual ideas and wrote the manuscript. ZC worked out almost all of the experiments and performed the numerical calculations. XL and SD worked with the analysis of membrane lipid data. SC, HX, and KT helped with the sampling in voyages. SB, MD, and SL worked in technical details and part of mineral data analysis. All authors contributed to the article and approved the submitted version.

FUNDING

This study was financially supported by the National Key Research and Development Project of China (No. 2017YFC0306604), the National Key Basic Research Program of China (No. 2015CB755905), the National Natural Science Foundation of China (Nos. 41576038 and 41876050), and the Youth Innovation Promotion Association CAS to JL, Shenzhen international collaborative research project (No. GJHZ20180928155004783), and Shenzhen Key Laboratory of Marine Archaea Geo-Omics, Southern University of Science and Technology (No. ZDSYS20180208184349083) to XL.

SUPPLEMENTARY MATERIAL

The Supplementary Material for this article can be found online at: https://www.frontiersin.org/articles/10.3389/feart.2021.653742/full#supplementary-material

REFERENCES

Blaga, C. I., Reichart, G.-J., Heiri, O., and Sinninghe Damsté, J. S. (2009). Tetraether membrane lipid distributions in water-column particulate matter and sediments: a study of 47 European lakes along a north–south transect. *J. Paleolimnol.* 41, 523–540. doi: 10.1007/s10933-008-9242-2

Chen, Z., Li, J., Li, X., Chen, S., Dasgupta, S., Bai, S., et al. (2020). Characteristics and implications of isoprenoid and hydroxy tetraether lipids in hadal sediments of Mariana and Yap Trenches. *Chem. Geol.* 551:119742. doi: 10.1016/j.chemgeo.2020.119742

Cowen, J. P., Giovannoni, S. J., Kenig, F., Johnson, H. P., Butterfield, D., Rappé, M.S., et al. (2003). Fluids from Aging Ocean Crust That Support Microbial Life. *Science* 299, 120–123. doi: 10.1126/science.1075653

Du, M., Peng, X., Seyfried, W. E. Jr., Ka, T., Guo, Z., Chen, S., et al. (2019). Fluid discharge linked to bending of the incoming plate at the Mariana subduction zone. *Geochem. Perspect. Lett.* 11, 1–5. doi: 10.7185/geochemlet.1916

Fryer, P., Wheat, C. G., and Mottl, M. J. (1999). Mariana blueschist mud volcanism: implications for conditions within the subduction zone. *Geology* 27, 103–106. doi: 10.1130/0091-76131999027<0103:MBMVIF<2.3.CO;2

Frysinger, G. S., Gaines, R. B., Xu, L., and Reddy, C. M. (2003). Resolving the Unresolved Complex Mixture in Petroleum-Contaminated Sediments. *Environ. Sci. Technol.* 37, 1653–1662. doi: 10.1021/es020742n

Fujikura, K., Kojima, S., Tamaki, K., Maki, Y., Hunt, J., and Okutani, T. (1999). The deepest chemosynthesis-based community yet discovered from the hadal zone, 7326 m deep, in the Japan Trench. *Mar. Ecol. Prog. Ser.* 190, 17–26. doi: 10.3354/meps190017

Glud, R. N., Wenzhöfer, F., Middelboe, M., Oguri, K., Turnewitsch, R., Canfield, D. E., et al. (2013). High rates of microbial carbon turnover in sediments in the deepest oceanic trench on Earth. *Nat. Geosci.* 6, 284–288. doi: 10.1038/ngeo1773

Goni, M. A., Monacci, N., Gisewhite, R., Crockett, J., Nittrouer, C., Ogston, A., et al. (2008). Terrigenous organic matter in sediments from the Fly River delta-clinoform system (Papua New Guinea). *J. Geophys. Res.* 113:F01S10. doi: 10.1029/2006JF000653

Guan, H., Chen, L., Luo, M., Liu, L., Mao, S., Ge, H., et al. (2019). Composition and origin of lipid biomarkers in the surface sediments from the southern Challenger Deep. Mariana Trench. *Geosci. Front.* 10, 351–360. doi: 10.1016/j.gsf.2018.01.004

Hand, K. P., Bartlett, D. H., Fryer, P., et al. (2012). *Analyses Of Outcrop And Sediment Grains Observed And Collected From The Sirena Deep And Middle Pond Of The Mariana Trench*. Washington, DC: AGU Fall Meeting.

Hasinger, M., Scherr, K. E., Lundaa, T., Bräuer, L., Zach, C., and Loibner, A. P. (2012). Changes in iso- and n-alkane distribution during biodegradation of crude oil under nitrate and sulphate reducing conditions. *J. Biotechnol.* 157, 490–498. doi: 10.1016/j.jbiotec.2011.09.027

Hopmans, E. C., Weijers, J. W. H., Schefuß, E., Herfort, L., Sinninghe Damsté, J. S., and Schouten, S. (2004). A novel proxy for terrestrial organic matter in sediments based on branched and isoprenoid tetraether lipids. *Earth Planet. Sci. Lett.* 224, 107–116. doi: 10.1016/j.epsl.2004.05.012

Hu, J., Meyers, P. A., Chen, G., Peng, P., and Yang, Q. (2012). Archaeal and bacterial glycerol dialkyl glycerol tetraethers in sediments from the Eastern Lau Spreading Center, South Pacific Ocean. *Org. Geochem.* 43, 162–167. doi: 10.1016/j.orggeochem.2011.10.012

Jamieson, A. J., Fang, J., and Cui, W. (2018). Exploring the Hadal Zone: recent Advances in Hadal Science and Technology. *Deep Sea Res. II Top. Stud. Oceanogr.* 155, 1–3. doi: 10.1016/j.dsr2.2018.11.007

Jamieson, A. J., Fujii, T., Mayor, D. J., Solan, M., and Priede, I. G. (2010). Hadal trenches: the ecology of the deepest places on Earth. *Trends Ecol. Evol.* 25, 190–197. doi: 10.1016/j.tree.2009.09.009

Jamieson, A. J., Malkocs, T., Piertney, S. B., Fujii, T., and Zhang, Z. (2017). Bioaccumulation of persistent organic pollutants in the deepest ocean fauna. *Nat. Ecol. Evol.* 1:51. doi: 10.1038/s41559-016-0051

Kaiser, J., Schouten, S., Kilian, R., Arz, H. W., Lamy, F., and Sinninghe Damsté, J. S. (2015). Isoprenoid and branched GDGT-based proxies for surface sediments from marine, fjord and lake environments in Chile. *Org. Geochem.* 8, 117–127. doi: 10.1016/j.orggeochem.2015.10.007

Khan, N. S., Vane, C. H., and Horton, B. P. (2015). "Stable carbon isotope and C/N geochemistry of coastal wetland sediments as a sea-level indicator," in *Handbook of Sea-Level Research*, eds I. Shennan, A. J. Long, and B. P. Horton (Chichester, UK: John Wiley & Sons Ltd), 295–311. doi: 10.1002/9781118452547.ch20

Kim, J.-H., Zarzycka, B., Buscail, R., Peterse, F., Bonnin, J., Ludwig, W., et al. (2010). Contribution of river-borne soil organic carbon to the Gulf of Lions (NW Mediterranean). *Limnol. Oceanogr.* 55, 507–518. doi: 10.4319/lo.2010.55.2.0507

Lamb, A. L., Wilson, G. P., and Leng, M. J. (2006). A review of coastal palaeoclimate and relative sea-level reconstructions using δ13C and C/N ratios in organic material. *Earth Sci. Rev.* 75, 29–57. doi: 10.1016/j.earscirev.2005.10.003

Lever, M. A., Rouxel, O., Alt, J. C., Shimizu, N., Ono, S., Coggon, R. M., et al. (2013). Evidence for microbial carbon and sulfur cycling in deeply buried ridge flank basalt. *Science* 339, 1305–1308. doi: 10.1126/science.1229240

Li, W.-L., Huang, J.-M., Zhang, P.-W., Cui, G.-J., Wei, Z.-F., Wu, Y.-Z., et al. (2019). Periodic and Spatial Spreading of Alkanes and *Alcanivorax* Bacteria in Deep Waters of the Mariana Trench. *Appl. Environ. Microbiol.* 85, e02089–18. doi: 10.1128/AEM.02089-18

Lincoln, S. A., Bradley, A. S., Newman, S. A., and Summons, R. E. (2013). Archaeal and bacterial glycerol dialkyl glycerol tetraether lipids in chimneys of the Lost City Hydrothermal Field. *Org. Geochem.* 60, 45–53. doi: 10.1016/j.orggeochem.2013.04.010

Liou, J. G. (1979). Zeolite facies metamorphism of basaltic rocks from the East Taiwan ophiolite. *Am. Mineral.* 64, 1–14.

Liu, J., Zheng, Y., Lin, H., Wang, X., Li, M., Liu, Y., et al. (2019). Proliferation of hydrocarbon-degrading microbes at the bottom of the Mariana Trench. *Microbiome* 7:47. doi: 10.1186/s40168-019-0652-3

Lü, X., Yang, H., Song, J., Versteegh, G. J. M., Li, X., Yuan, H., et al. (2014). Sources and distribution of isoprenoid glycerol dialkyl glycerol tetraethers (GDGTs) in sediments from the east coastal sea of China: application of GDGT-based paleothermometry to a shallow marginal sea. *Org. Geochem.* 75, 24–35. doi: 10.1016/j.orggeochem.2014.06.007

Luo, M., Gieskes, J., Chen, L., Shi, X., and Chen, D. (2017). Provenances, distribution, and accumulation of organic matter in the southern Mariana Trench rim and slope: implication for carbon cycle and burial in hadal trenches. *Mar. Geol.* 386, 98–106. doi: 10.1016/j.margeo.2017.02.012

Luo, M., Glud, R. N., Pan, B., Wenzhöfer, F., Xu, Y., Lin, G., et al. (2018). Benthic Carbon Mineralization in Hadal Trenches: insights From In Situ Determination of Benthic Oxygen Consumption. *Geophys. Res. Lett.* 45, 2752–2760. doi: 10.1002/2017GL076232

McCollom, T. M., Seewald, J. S., and German, C. R. (2015). Investigation of extractable organic compounds in deep-sea hydrothermal vent fluids along the Mid-Atlantic Ridge. *Geochim. Cosmochim. Acta* 156, 122–144. doi: 10.1016/j.gca.2015.02.022

Nelson, D. R. (1978). Long-Chain Methyl-Branched Hydrocarbons: occurrence, Biosynthesis, and Function. *Adv. Insect Physiol.* 13, 1–33. doi: 10.1016/S0065-2806(08)60263-5

Newman, S. A., Lincoln, S. A., O'Reilly, S., Liu, X., Shock, E. L., Kelemen, P. B., et al. (2020). Lipid Biomarker Record of the Serpentinite-Hosted Ecosystem of the Samail Ophiolite, Oman and Implications for the Search for Biosignatures on Mars. *Astrobiology* 20, 830–845. doi: 10.1089/ast.2019.2066

Nunoura, T., Nishizawa, M., Hirai, M., Shimamura, S., Harnvoravongchai, P., Koide, O., et al. (2018). Microbial Diversity in Sediments from the Bottom of the Challenger Deep, the Mariana Trench. *Microbes Environ.* 33, 186–194. doi: 10.1264/jsme2.ME17194

Nunoura, T., Takaki, Y., Hirai, M., Shimamura, S., Makabe, A., Koide, O., et al. (2015). Hadal biosphere: insight into the microbial ecosystem in the deepest ocean on Earth. *Proc. Natl. Acad. Sci. U. S. A.* 112, E1230–6. doi: 10.1073/pnas.1421816112

Oguri, K., Kawamura, K., Sakaguchi, A., Toyofuku, T., Kasaya, T., Murayama, M., et al. (2013). Hadal disturbance in the Japan Trench induced by the 2011 Tohoku–Oki Earthquake. *Sci. Rep.* 3:1915. doi: 10.1038/srep01915

Ohara, Y., Reagan, M. K., Fujikura, K., Watanabe, H., Michibayashi, K., Ishii, T., et al. (2012). A serpentinite-hosted ecosystem in the Southern Mariana Forearc. *Proc. Natl. Acad. Sci.U. S. A.* 109, 2831–2835. doi: 10.1073/pnas.1112005109

Orcutt, B. N., Bach, W., Becker, K., Fisher, A. T., Hentscher, M., Toner, B. M., et al. (2011). Colonization of subsurface microbial observatories deployed in young ocean crust. *ISME J.* 5, 692–703. doi: 10.1038/ismej.2010.157

Pan, A., Yang, Q., Zhou, H., Ji, F., Wang, H., and Pancost, R. D. (2016). A diagnostic GDGT signature for the impact of hydrothermal activity on surface deposits at the Southwest Indian Ridge. *Org. Geochem.* 99, 90–101. doi: 10.1016/j.orggeochem.2016.07.001

Peterse, F., Kim, J.-H., Schouten, S., Kristensen, D. K., Koç, N., and Sinninghe Damsté, J. S. (2009). Constraints on the application of the MBT/CBT palaeothermometer at high latitude environments (Svalbard, Norway). *Org. Geochem.* 40, 692–699. doi: 10.1016/j.orggeochem.2009.03.004

Plümper, O., King, H. E., Geisler, T., Liu, Y., Pabst, S., Savov, I. P., et al. (2017). Subduction zone forearc serpentinites as incubators for deep microbial life. *Proc. Natl. Acad. Sci. U. S. A.* 114, 4324–4329. doi: 10.1073/pnas.1612147114

Rouxel, O., Ono, S., Alt, J., Rumble, D., and Ludden, J. (2008). Sulfur isotope evidence for microbial sulfate reduction in altered oceanic basalts at ODP Site 801. *Earth Planet. Sci. Lett.* 268, 110–123. doi: 10.1016/j.epsl.2008.01.010

Santelli, C. M., Orcutt, B. N., Banning, E., Bach, W., Moyer, C. L., Sogin, M. L., et al. (2008). Abundance and diversity of microbial life in ocean crust. *Nature* 453, 653–657.

Schouten, S., Hopmans, E. C., and Sinninghe Damsté, J. S. (2013). The organic geochemistry of glycerol dialkyl glycerol tetraether lipids: a review. *Org. Geochem.* 54, 19–61. doi: 10.1016/j.orggeochem.2012.09.006

Serrazanetti, G. P., Pagnucco, C., Conte, L. S., and Cattani, O. (1995). Hydrocarbons, sterols and fatty acids in sea urchin (*Paracentrotus lividus*) of the adriatic sea. *Chemosphere* 30, 1453–1461. doi: 10.1016/0045-6535(95)00039-B

Spang, A., Hatzenpichler, R., Brochier-Armanet, C., Rattei, T., Tischler, P., Spieck, E., et al. (2010). Distinct gene set in two different lineages of ammonia-oxidizing archaea supports the phylum Thaumarchaeota. *Trends Microbiol.* 18, 331–340. doi: 10.1016/j.tim.2010.06.003

Stern, R. J., Kohut, E., Bloomer, S. H., Leybourne, M., Fouch, M., and Vervoort, J. (2006). Subduction factory processes beneath the Guguan cross-chain, Mariana Arc: no role for sediments, are serpentinites important?. *Contrib. Mineral. Petrol.* 151, 202–221. doi: 10.1007/s00410-005-0055-2

Ta, K., Peng, X., Xu, H., Du, M., Chen, S., Li, J., et al. (2019). Distributions and Sources of Glycerol Dialkyl Glycerol Tetraethers in Sediment Cores From the Mariana Subduction Zone. *J. Geophys. Res. Biogeosci.* 124, 857–869. doi: 10.1029/2018JG004748

Tao, S., Wang, C., Du, J., Liu, L., and Chen, Z. (2015). Geochemical application of tricyclic and tetracyclic terpanes biomarkers in crude oils of NW China. *Mar. Pet. Geol.* 67, 460–467. doi: 10.1016/j.marpetgeo.2015.05.030

Tarn, J., Peoples, L. M., Hardy, K., Cameron, J., and Bartlett, D. H. (2016). Identification of Free-Living and Particle-Associated Microbial Communities Present in Hadal Regions of the Mariana Trench. *Front. Microbiol.* 7:665. doi: 10.3389/fmicb.2016.00665

Weber, Y., Sinninghe Damsté, J. S., Zopfi, J., De Jonge, C., Gilli, A., Schubert, C. J., et al. (2018). Redox-dependent niche differentiation provides evidence for multiple bacterial sources of glycerol tetraether lipids in lakes. *Proc. Natl. Acad. Sci. U. S. A.* 115, 10926–10931. doi: 10.1073/pnas.1805186115

Weijers, J. W. H., Schefuß, E., Kim, J.-H., Sinninghe Damsté, J. S., and Schouten, S. (2014). Constraints on the sources of branched tetraether membrane lipids in distal marine sediments. *Org. Geochem.* 72, 14–22. doi: 10.1016/j.orggeochem.2014.04.011

Weijers, J. W. H., Schouten, S., van den Donker, J. C., Hopmans, E. C., and Sinninghe Damsté, J. S. (2007). Environmental controls on bacterial tetraether membrane lipid distribution in soils. *Geochim. Cosmochim. Acta* 71, 703–713. doi: 10.1016/j.gca.2006.10.003

Wenger, L. M., and Isaksen, G. H. (2002). Control of hydrocarbon seepage intensity on level of biodegradation in sea bottom sediments. *Org. Geochem.* 33, 1277–1292. doi: 10.1016/S0146-6380(02)00116-X

Wu, X. (2014). *The Application Of Glycerol Dialkyl Glycerol Tetraether In Reconstruction Of Kusai Lake Paleo-Environment On The Qinghai-Tibetan Plateau. (in chinese)*. Ph.D. thesis, Beijing: University of Chinese Geosciences.

Xiao, W., Wang, Y., Liu, Y., Zhang, X., Shi, L., and Xu, Y. (2019). Predominance of hexamethylated 6-methyl branched glycerol dialkyl glycerol tetraethers in the Mariana Trench: source and environmental implication. *Biogeosciences* 17, 2135–2148. doi: 10.5194/bg-17-2135-2020

Xiao, W., Wang, Y., Zhou, S., Hu, L., Yang, H., and Xu, Y. (2016). Ubiquitous production of branched glycerol dialkyl glycerol tetraethers(brGDGTs) in global marine environments: a new source indicator for brGDGTs. *Biogeosciences* 13, 5883–5894. doi: 10.5194/bg-13-5883-2016

Xu, Y., Jia, Z., Xiao, W., Fang, J., Wang, Y., Luo, M., et al. (2020). Glycerol dialkyl glycerol tetraethers in surface sediments from three Pacific trenches: distribution, source and environmental implications. *Org. Geochem.* 147:104079. doi: 10.1016/j.orggeochem.2020.104079

Yamamoto, M., Shimamoto, A., Fukuhara, T., and Tanaka, Y. (2016). Source, settling and degradation of branched glycerol dialkyl glycerol tetraethers in the

marine water column. *Geochim. Cosmochim. Acta* 191, 239–254. doi: 10.1016/j.gca.2016.07.014

Zhang, Z.-X., Li, J., Chen, Z., Sun, Z., Yang, H., Fu, M., et al. (2020). The effect of methane seeps on the bacterial tetraether lipid distributions at the Okinawa Trough. *Mar. Chem.* 225:103845. doi: 10.1016/j.marchem.2020.103845

Conflict of Interest: The authors declare that the research was conducted in the absence of any commercial or financial relationships that could be construed as a potential conflict of interest.

The handling editor declared a past collaboration with several of the authors JL and HX.

frontiers in Earth Science

ORIGINAL RESEARCH
published: 30 April 2021
doi: 10.3389/feart.2021.664959

Geochemical Characteristics of Hydrocarbons in Core Sediments From the Southwest Sub-Basin of the South China Sea and Its Implications for the Sedimentary Environment

Xianqing Wang[1], Zhifeng Wan[2], Chongmin Chen[2] and Sheng Chen[2]*

[1] Guangzhou Marine Geological Survey, China Geological Survey, Guangzhou, China, [2] School of Marine Sciences, Sun Yat-sen University, Guangzhou, China

OPEN ACCESS

Edited by:
Lu Lu,
China University of Mining and Technology, China

Reviewed by:
Peng Cheng,
Guangzhou Institute of Geochemistry, Chinese Academy of Sciences, China
Qing Li,
Qingdao Institute of Marine Geology (QIMG), China
Min Luo,
Shanghai Ocean University, China

***Correspondence:**
Zhifeng Wan
wanzhif@mail.sysu.edu.cn

Specialty section:
This article was submitted to Geochemistry, a section of the journal Frontiers in Earth Science

Received: *06 February 2021*
Accepted: *12 April 2021*
Published: *30 April 2021*

Citation:
Wang X, Wan Z, Chen C and Chen S (2021) Geochemical Characteristics of Hydrocarbons in Core Sediments From the Southwest Sub-Basin of the South China Sea and Its Implications for the Sedimentary Environment. Front. Earth Sci. 9:664959. doi: 10.3389/feart.2021.664959

Marine sediments are found to record various information for example the evolution of ocean and the exchange of matter and energy between the surrounding continents and oceans. The Southwest Sub-basin is one of the most important tectonic unit in the South China Sea Basin. The geochemical information of the sediments provides potential to understand the sedimentary history of the Southwest Sub-basin of South China Sea. In this paper, the aliphatic hydrocarbon compounds in two core sediments from the Southwest sub-basin were analyzed using lipid biomarker analysis. The average concentration of the total organic carbon (TOC) and the total nitrogen (TN) for both core sediment A and sediment B are similar, falling in the range of 0.64% ± 0.18 and 0.10% ± 0.02%, respectively. The C/N ratios vary from 3.2 to 11.1, reflecting that the organic carbon was a mixture of terrestrial and marine sources with more contributions from marine sources in core sediment B than sediment A. The long-chain *n*-alkanes of both core sediments show an even-odd predominance, reflecting the contributions of terrestrial higher plants and short-chain *n*-alkanes from marine plankton or bacteria. The Pr/Ph of core sediments A and B are 0.3–0.5 and 0.2–0.4, respectively, both of which are far less than 1, indicating that the sedimentary environment was dominated by strong reduction and long-term stability. The odd-even distribution of medium-chain *n*-alkanes (n-C_{14-20}) in the core sediments A and B is due to the reduction of *n*-fatty acids with an odd carbon dominance in a strongly reductive depositional environment.

Keywords: core sediments, organic matter, aliphatic hydrocarbons, Southwest sub-basin of South China Sea, sedimentary environment

INTRODUCTION

The South China Sea, one of the marginal sea of the Pacific Northwest Sea. According to water depth, topography and geology, and geophysical data, the South China Sea Basin was divided into the Northwest sub-basin, Southwest sub-basin and Eastern sub-basin (Briais et al., 1993; Sun et al., 2009). The Southwest sub-basin is located among the Xisha Islands, Zhongsha Islands and Nansha

Islands. It is a NE-trending triangular basin with a northeast direction of approximately 600 km and a northeast margin of approximately 400 km with a water depth of 3,000–4,000 m (Li, 2011). It is the lowest depression in the South China Sea basin (**Figure 1**). As the interaction zone between the continent and the ocean, the South China Sea's unique geographical location, complex tectonic environment and special ocean currents have formed its complex sedimentary environment, and its sedimentary material sources are various and diverse (Hamilton, 1979; Tapponnier et al., 1982).

Due to bordering on many countries, the Southwest Sub-basin of South China Sea is lack of comprehensive and systematic investigations over decades. Most of the research was concentrated on the northern South China Sea. For the southern South China Sea, organic geochemistry research has also been done (Duan, 2000; Hu et al., 2009; Tahir et al., 2015; Kerimov et al., 2019). However, compared with other sea areas, the geochemical studies in the southern South China Sea also appear to be lagging and weak. There are few reports on the geochemical characteristics, influencing factors and environmental records of hydrocarbon compounds in the core sediments in this area.

Molecular fossils could maintain the carbon skeleton of original biochemical components during the evolution processes of organic matter, recording information about original organisms and thus can be used to reveal information of biological input, sedimentary environment and diagenetic changes (Meyers and Lallier-Vergés, 1999; Meyers, 2003). In this paper, two core sediments collected from the Southwest sub-basin as the research object, analyzed the organic geochemical index of *n*-alkanes and their carbon molecular assemblages, the aim of this study was to trace the source of organic matter and understand the sea-land interaction during modern marine sedimentation in the southwest sub-basin, and to provide a scientific basis for the indication of climate and environment.

SAMPLE AND ANALYSIS METHODS

Sample Collection

The sampling sites were located in the southwest sub-basin of the South China Sea (**Figure 1**). Sediment cores were collected by the "Haiyang 4" ship of the Guangzhou Marine Geological Survey in September 2015, using a large gravity sampler. The sediment cores were collected from water depths of 4,050–4,030 m with their lengths of 4.75 and 5 m, respectively. Man-made damages and obvious biological disturbances were not observed during collection and sampling processes, therefore, the geochemical information can be used as indicators for original sedimentary characteristics. Core sediments were subsampled immediately and stored at −20°C for the further analyses.

Experimental Analysis

Total Organic Carbon (TOC)

Sediments were freeze-dried at −50°C and ground into powder about 200 mesh. Approximately120 mg of powder was put into a crucible, and excess HCl at a concentration of 6 mol/l was added. The samples were laid over night, followed by being heated at 80°C for 2 h to remove the carbonate and rinsed with deionized water until neutral. The cleaned samples were dried at 110°C and measured with LecoC230.

Sample Extraction and Separation of Soluble Organic Matter

The organic matters were extracted by Soxhlet for 72 h with a mixed solvent of dichloromethane/methanol (9:1, volume ratio). Before extraction, the appropriate amount of activated copper sheet was added to the receiving bottle of the extraction liquid to remove the elemental sulfur. The internal standard $C_{20}D_{42}$ was added to the receiving bottle of extraction liquid. After extraction, the extracts were concentrated by rotary evaporation and transferred to a suitable bottle, which was then blown to dryness with nitrogen and get soluble organic matter. The soluble organic matter was saponified with KOH/CH_3OH (1 mol/l) (i.e., 70°C heating reflux 2 h), then neutral components were extracted by adding *n*-hexane. After the organic matter was transferred to a silica gel column, the organic matter was washed with 3 volumes of *n*-hexane to obtain hydrocarbon components.

Gas Chromatography—Mass Spectrometry (GC-MS)

Instrument Model: Thermo Trace GC Ultra-AL/AS3000 GC–MS; ion source for the electron bombardment source (70 eV); ion source temperature: 230°C; inlet temperature: 290°C; number of scans: 0.7911/s; scanning rate: 500 amu/s, 30–750 amu. The carrier gas was high-purity helium.

Hydrocarbon Detection: The column model was a HP-1 capillary column (60 m *0.32 mm, i.d., *0.25 μm coating). The temperature program was as follows. The initial temperature was 80°C, the temperature was maintained for 3 min, and the temperature was raised to 315°C at 3°C/min for 30 min. Using a splitless injection mode, the carrier gas was high-purity helium with a flow rate of 1.1 ml/min.

RESULTS

The Results of the TOC and Total Nitrogen (TN)

The TOC, total TN and TOC/TN of the two core A and B in the southwest sub-basin are listed in **Table 1**. The mean TOC of core sediment A was 0.64% ± 0.18% (0.29–0.88%). The average concentration of TN was 0.10% ± 0.02% (0.04–0.12%), and the average C/N was 6.91 ± 2.03 (3.22–11.15). The mean TOC of core sediment B was 0.64% ± 0.12% (0.43–0.86%). The average concentration of TN was 0.10% ± 0.01% (0.08–0.11%), and the average C/N was 6.38 ± 1.33 (4.8–9.3). The average TOC of cores A and B were equivalent to 0.7 and 0.53% of the two cores measured by Duan (2000) in the Nansha Sea.

Hydrocarbon Compounds

The hydrocarbons detected in the two cores sediments A and B ranged from C_{14} to C_{33}, mainly including *n*-alkanes and acyclic diolefins (pristane and phytane) (**Table 2**). The concentrations of total *n*-alkanes of core A varied from 716.7 to 2799.8 ng/g (**Table 2**), and the concentration of total *n*-alkanes of core

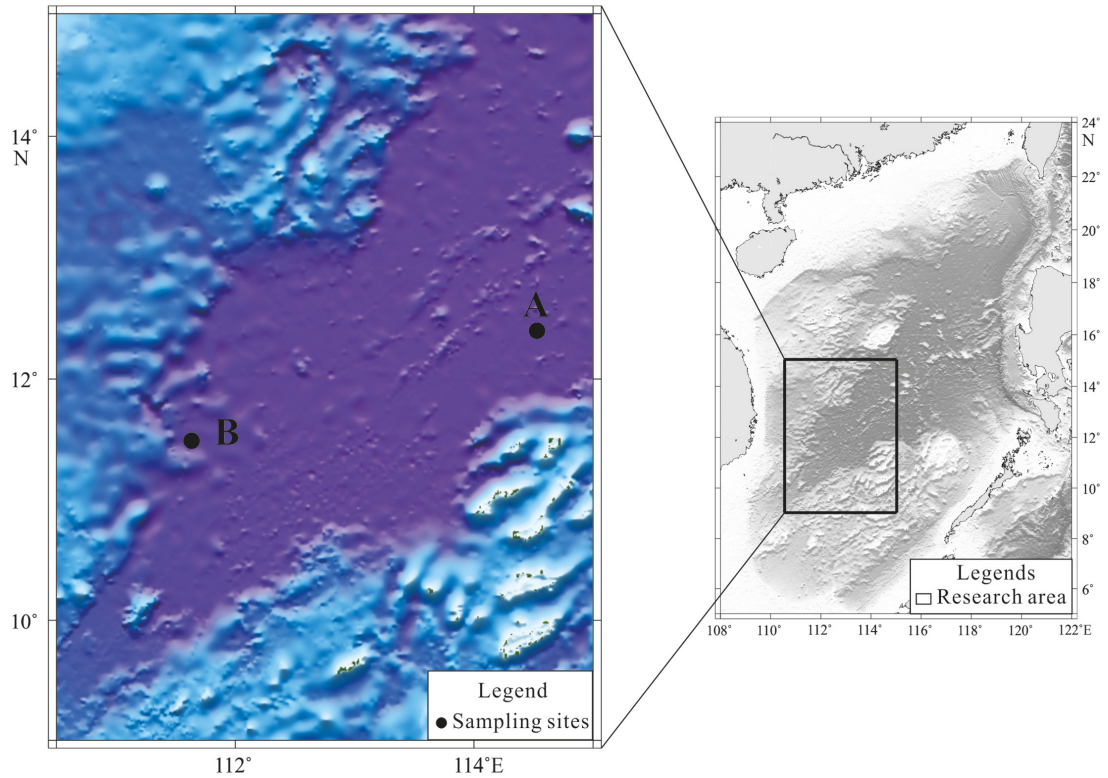

FIGURE 1 | The distribution of sampling sites and the tectonic location of the Southwest Sub-basin.

sediment B were 1008.3–2109.9 ng/g (**Table 3**). In the two core A and B, *n*-C_{27}, *n*-C_{29}, and *n*-C_{31} were the main peak carbons, and the values of CPI_{24-35} of long-chain *n*-alkanes were 3.6 (2.1–5.0) and 2.9 (1.8–3.6). The sum of the most abundant *n*-alkanes related to terrestrial origins (*n*-C_{27}, *n*-C_{29}, and *n*-C_{31}) were defined as ΣTer-alkanes, which were 211.4–1004.0 ng/g, accounting for 18.8–48.9% of the total *n*-alkanes (averaging 31.1%) at station A. The ΣTer-alkanes for B ranged from 224.4 to 670.6 ng/g, representing 14.5–34.0% of the total *n*-alkanes (averaging 23.4%).

Short-chain *n*-alkanes are attributed to be derived from marine algae and bacteria (Blumer et al., 1971). Low-carbon alkanes show a significant advantage of even carbon number, and the maximum relative abundances are *n*-C_{16}, *n*-C_{18}, and *n*-C_{20}. For core sediment A, the ΣMar-alkanes, defined as the sum of *n*-C_{15}, *n*-C_{17}, and *n*-C_{19}, were 52.2–325.4 ng/g, accounting for 2.7–13.2% (averaging 8.9%) of the total *n*-alkanes. The ΣMar-alkanes at B were 64.5–266.5 ng/g, accounting for 5.2–12.6% (averaging 8.4%) of the total *n*-alkanes.

The concentrations of pristane in cores A and B were 10.2–95.9 and 12.3–78.7 ng/g, respectively, and the concentrations of phytane were 32.8–212.5 and 51.9–184.1 ng/g, respectively.

TABLE 1 | The total organic carbon (TOC), total nitrogen (TN), carbon to nitrogen ratio (C/N).

A				B			
Depth	**C (%)**	**N (%)**	**C/N**	**Depth**	**C (%)**	**N (%)**	**C/N**
20 cm	0.76	0.12	6.5	20 cm	0.75	0.11	6.7
60 cm	0.88	0.12	7.3	60 cm	0.65	0.11	5.9
100 cm	0.82	0.12	7.1	100 cm	0.56	0.10	5.7
140 cm	0.55	0.11	5.1	140 cm	0.76	0.09	8.7
180 cm	0.65	0.10	6.3	180 cm	0.43	0.08	5.2
220 cm	0.80	0.10	8.0	220 cm	0.59	0.11	5.4
260 cm	0.37	0.04	9.6	260 cm	0.70	0.10	6.9
300 cm	0.50	0.10	5.1	300 cm	0.86	0.09	9.3
340 cm	0.66	0.10	6.4	340 cm	0.69	0.11	6.2
380 cm	0.60	0.10	6.1	380 cm	0.61	0.11	5.5
420 cm	0.29	0.09	3.2	420 cm	0.69	0.10	6.8
460 cm	0.76	0.09	8.1	460 cm	0.62	0.10	6.0
470 cm	0.67	0.06	11.1	495 cm	0.45	0.09	4.8

DISCUSSION

Downcore Profiles of TOC and TN in Sediments and Their Source Indication

Carbon and nitrogen form the basis of life and play important roles in many terrestrial and aquatic biogeochemical cycles (Likens et al., 1981). Carbon in marine sediments is an important part of the carbon cycle. Nitrogen is the most basic bioactive element that limits the growth of phytoplankton in the ocean.

TABLE 2 | Concentration (ng/g sed.dry weight) of hydrocarbon in A station of the Southwest Sub-basin.

Depth	20 cm	60 cm	100 cm	140 cm	180 cm	220 cm	260 cm	300 cm	340 cm	380 cm	420 cm	460 cm	470 cm
Compounds													
n-C_{14}	36.2	3.1	4.5	3.6	0.6	1.0	0.1	8.3	4.0	2.9	0.7	0.5	3.1
n-C_{15}	43.7	9.6	21.5	20.2	6.0	8.3	1.9	14.9	11.9	8.4	5.3	5.1	7.2
n-C_{16}	306.4	133.5	157.1	153.8	101.3	115.5	56.1	138.9	120.5	88.5	87.9	59.7	64.8
n-C_{17}	187.7	84.6	114.3	110.9	86.4	89.4	59.3	92.0	114.3	34.2	31.0	28.4	25.5
Pr	95.9	40.0	53.4	68.9	45.9	45.6	35.9	47.7	75.3	13.7	11.9	10.7	10.2
n-C_{18}	371.1	197.8	203.0	177.4	147.3	156.9	95.3	159.9	180.8	115.1	129.3	100.6	85.9
Phy	212.5	97.3	118.6	140.5	95.4	107.8	69.1	101.4	198.0	44.6	45.2	32.8	32.2
n-C_{19}	94.1	40.8	90.7	52.7	37.0	50.5	19.0	36.3	62.0	27.1	25.5	21.9	19.5
n-C_{20}	286.1	157.7	153.2	132.2	103.8	113.9	59.3	102.6	100.5	80.2	93.8	74.8	65.3
n-C_{21}	97.1	47.6	69.2	54.0	42.3	54.8	21.2	40.6	40.3	33.5	33.8	37.1	32.2
n-C_{22}	199.7	99.0	87.0	83.5	67.5	69.5	34.3	62.9	60.1	46.5	61.1	54.5	45.6
n-C_{23}	102.7	59.3	56.8	59.4	51.1	58.8	23.4	48.3	45.3	40.3	53.0	74.5	57.5
n-C_{24}	132.0	61.4	55.2	59.2	46.7	49.5	21.8	49.1	43.2	35.0	48.0	50.3	41.6
n-C_{25}	55.0	69.7	67.1	65.4	61.1	66.7	27.9	55.7	54.0	51.4	69.6	116.5	85.9
n-C_{26}	107.5	51.6	77.1	48.5	45.8	48.4	18.5	38.7	38.4	32.4	43.8	51.1	41.7
n-C_{27}	91.6	84.6	77.1	81.2	76.7	82.0	37.7	59.3	74.2	75.9	105.6	197.9	157.3
n-C_{28}	82.0	55.3	42.6	53.5	43.9	42.8	18.7	33.5	39.8	37.2	44.2	72.5	55.7
n-C_{29}	213.1	176.7	147.6	169.7	157.3	157.8	86.1	109.1	150.1	160.8	243.6	382.1	286.1
n-C_{30}	53.4	36.8	34.4	39.8	36.2	37.4	13.4	23.0	30.5	28.4	36.5	73.3	58.5
n-C_{31}	220.7	193.3	167.4	172.3	172.8	173.4	87.6	119.8	158.8	161.9	244.0	424.0	315.2
n-C_{32}	27.5	17.3	18.5	22.2	20.0	20.8	6.5	10.6	14.6	14.3	18.8	41.2	33.0
n-C_{33}	92.2	72.1	69.1	79.7	74.5	87.3	28.5	41.5	61.4	59.2	75.9	187.5	133.4
Total *n*-alkanes	2799.8	1651.8	1713.4	1639.1	1378.3	1484.5	716.7	1245.0	1404.7	1133.2	1451.5	2053.5	1615.0
ΣTer-alkanes	525.3	454.6	392.1	423.2	406.7	413.1	211.4	288.2	383.1	398.6	593.1	1004.0	758.6
ΣMar-alkanes	325.4	135.0	226.6	183.7	129.4	148.2	80.3	143.2	188.2	69.6	61.8	55.3	52.2
TAR	1.6	3.4	1.7	2.3	3.1	2.8	2.6	2.0	2.0	5.7	9.6	18.2	14.5
CPI_{24-33}	2.1	3.2	2.7	3.0	3.3	3.3	4.0	3.1	3.5	4.0	4.5	5.0	4.7
Pr/Ph	0.5	0.4	0.5	0.5	0.5	0.4	0.5	0.5	0.4	0.3	0.3	0.3	0.3

Pr, pristane; Phy, phytane; CPI, carbon preference index; Σ*Ter-alkanes,* $\Sigma C_{27+29+31}$*;* Σ*Mar-alkanes,* $\Sigma C_{15+17+19}$*; TAR,* Σ*Ter-alkanes/*Σ*Mar-alkanes; N.D., not detected.*

Therefore, it is very important to study the distribution of carbon and nitrogen in core sediments.

The downcore profiles of TOC, TN and TOC/TN with depth of core sediment A are shown in **Figure 2**. From bottom to top, according to the vertical concentration changes of TOC and TN, 4 stages were identified: (1) Under the layer below a depth of 380 cm, the concentration of TOC was low and varied significantly. The concentration first increased from the bottom, dropped to the lowest value (0.29%) at 420 cm, and then increased again. The concentration of TN had a similar trend but did not change as strong as TOC; (2) At depths between 380cm and 340 cm, the concentration of TOC was low and consistent; the concentration of TN was also relatively uniform; (3) The concentration of TOC varied greatly at depths between 340m and 220 cm, and the lowest TN value were found at a depth of 260 cm (0.04%); (4) Above the depth of 220 cm, the concentration of TOC showed a high, rising, but fluctuating trend; however, the change was small; the concentration of TN generally rose, with the highest value (0.04%) appearing at the depth of 60 cm. Overall, the vertical concentration variation trends of TOC and TN in core sediment A was generally the same, with differences in individual locations.

The curves of TOC, TN and TOC/TN with depth for core sediment B are shown in **Figure 3**. From bottom to top, 3 stages were identified. (1) In the layer below 300 cm, the TOC of core sediment B changed slightly, showing an upward trend overall, with a high value (0.86%) at a depth of 300 cm and a low value of TN (0.09%). (2) At a depth of 300–180 cm, the concentration of TOC showed a downward trend, and the concentration of TN fluctuated greatly. (3) At a depth above 180 cm, the TOC showed an upward trend but fluctuated while the concentration of TN increased gently. According to the change of TOC, we can find that the trend of TOC and TN are the same at a depth of 340 cm and below, while TOC and TN have an opposite trend at a depth of 340 cm and above.

The C/N of organic matter in marine sediments can be used to determine the source of organic matter. Organic matter is usually thought to originate from marine organisms at a C/N of 5-7 (Redfield et al., 1963), while the C/N of organic matter in higher plants from terrestrial sources is generally greater than 15 (Meyers, 1997). As seen from **Figures 2**, **3**, the C/N of the core A and B vary greatly with depth, and the average C/N of core sediment A is 6.91 ± 2.03, ranging from 3.22 to 11.15 and indicating that organic carbon in sediments is a mixed source

TABLE 3 | Concentration (ng/g sed.dry weight) of hydrocarbon in B station of the Southwest Sub-basin.

Depth	20 cm	60 cm	100 cm	140 cm	180 cm	220 cm	260 cm	300 cm	340 cm	380 cm	420 cm	460 cm	495 cm
Compounds													
n-C_{14}	18.6	8.7	42.2	0.9	4.7	1.9	0.4	0.3	0.7	19.6	24.4	6.9	30.7
n-C_{15}	26.5	25.8	31.1	11.2	15.2	11.2	5.0	4.1	8.5	22.5	31.2	26.9	66.9
n-C_{16}	235.9	166.8	204.3	104.8	181.4	148.1	98.9	86.5	142.0	175.2	183.2	226.8	296.7
n-C_{17}	78.4	70.1	80.1	54.2	58.2	52.8	41.0	32.0	61.6	55.6	56.1	88.2	124.4
Pr	32.1	26.2	24.1	26.9	21.6	20.9	18.9	12.3	26.7	22.4	22.4	39.4	78.7
n-C_{18}	245.4	206.4	228.5	143.6	218.6	195.9	199.1	135.0	224.4	190.5	176.1	227.1	282.4
Phy	113.8	101.9	98.5	78.4	90.2	80.7	75.1	51.9	92.0	77.7	80.8	124.1	184.1
n-C_{19}	60.4	44.5	60.1	36.9	55.8	41.1	38.9	28.5	50.1	43.8	41.4	62.1	75.3
n-C_{20}	165.4	109.2	164.3	75.7	163.3	139.1	133.5	98.6	171.0	129.7	118.8	155.9	185.3
n-C_{21}	71.8	47.1	68.1	40.4	63.6	50.1	38.8	36.5	65.8	55.1	52.3	68.9	88.0
n-C_{22}	88.5	91.9	94.9	58.2	93.1	74.4	65.5	60.8	102.5	76.4	69.8	87.7	109.8
n-C_{23}	71.6	85.7	71.3	81.4	71.1	59.4	55.5	42.8	77.3	65.3	55.8	71.8	92.5
n-C_{24}	59.8	86.4	60.2	70.0	56.8	46.8	42.2	38.0	78.6	58.5	52.2	60.2	69.0
n-C_{25}	62.0	96.8	70.9	114.4	76.3	65.2	54.7	47.4	72.7	67.1	61.8	67.4	63.1
n-C_{26}	43.4	91.8	51.6	78.7	53.6	41.4	40.4	35.9	64.4	48.3	41.1	46.6	59.3
n-C_{27}	40.5	80.8	52.7	153.0	75.4	71.5	62.7	50.7	69.1	70.1	63.7	56.4	68.9
n-C_{28}	28.7	64.4	38.0	89.2	52.6	41.1	30.8	28.1	51.2	38.5	42.2	45.3	51.0
n-C_{29}	94.1	164.2	113.1	265.0	184.3	166.4	127.7	101.8	149.1	151.7	136.5	136.9	169.0
n-C_{30}	20.8	47.8	25.2	85.7	33.3	26.0	23.6	21.3	33.0	29.3	30.1	24.1	32.0
n-C_{31}	89.7	196.0	115.5	252.6	174.4	147.6	129.7	108.9	151.3	157.8	146.3	136.2	170.6
n-C_{32}	10.8	36.0	12.7	64.5	15.4	11.3	10.6	10.5	14.1	12.8	14.1	12.4	14.5
n-C_{33}	30.7	98.5	42.9	190.8	69.2	52.2	39.8	40.6	54.6	54.5	54.3	48.8	60.5
Total *n*-alkanes	1542.7	1818.9	1627.6	1971.3	1716.4	1443.5	1238.8	1008.3	1642.0	1522.2	1451.4	1656.7	2109.9
ΣTer-alkanes	224.4	441.0	281.3	670.6	434.2	385.5	320.2	261.4	369.5	379.6	346.5	329.4	408.5
ΣMar-alkanes	165.2	140.4	171.4	102.3	129.2	105.1	84.8	64.5	120.2	121.9	128.7	177.2	266.5
TAR	1.4	3.1	1.6	6.6	3.4	3.7	3.8	4.1	3.1	3.1	2.7	1.9	1.5
CPI_{24-33}	2.5	2.3	2.6	2.8	3.2	3.6	3.4	3.1	2.6	3.3	3.1	1.8	2.9
Pr/Ph	0.3	0.3	0.2	0.3	0.2	0.3	0.3	0.2	0.3	0.3	0.3	0.3	0.4

Pr, pristane; Phy, phytane; CPI, carbon preference index; Σ*Ter-alkanes,* $\Sigma C_{27+29+31}$*;* Σ*Mar-alkanes,* $\Sigma C_{15+17+19}$*; TAR,* Σ*Ter-alkanes/*Σ*Mar-alkanes; N.D., not detected.*

of terrigenous and marine. Meanwhile, the average C/N of core sediment B is 6.38 ± 1.33 (4.79–9.34), which also reflects the input of both terrigenous and marine organic matter. The C/N of A and B are both lower, indicating that the organic carbon is mainly from a marine source, while the lower C/N value of B indicates that the contribution of marine sources to organic carbon in core sediment B are larger than that of A.

In the two cores, the TOC and TN have a positive correlation (**Figure 4**), the positive relationship of TOC and TN suggests that TN measured in the sediments mostly exists in the form of organic nitrogen (Goñi et al., 1998). In addition, Qian et al. (1997) also proposed a method to quantitatively estimate the concentration of aquatic organic carbon (Ca), terrestrial organic carbon (Ct), aquatic nitrogen (Na) and terrestrial nitrogen (Nt). According to this method, assuming that the TOC/TN ratios of aquatic and terrestrial organic matter are 5 and 20, respectively (as a zero-order approximation) (Jia et al., 2002), the above parameters have the following relationship:

$$TOC = Ca + Ct$$

$$TN = Na + Nt$$

$$Ca/Na = 5$$

$$Ct/Nt = 20$$

Among them, TOC and TN represent the measured values. The solution of this equation formed by the above relationship calculates the available aquatic organic carbon and terrestrial organic carbon as follows:

$$Ca = (20TN - TOC)/3$$

$$Ct = 4(TOC - 5TN)/3$$

The concentrations of aquatic organic carbon (Ca) and terrestrial organic carbon (Ct) in the core sediment A are 72.2 and 27.8% of the TOC, as calculated by the above formula; aquatic nitrogen (Na) and terrigenous nitrogen (Nt) account for 87.2 and 22.8% of the TN, respectively. Therefore, TOC and TN in the core sediment A are mainly marine sources. The concentration of aquatic organic carbon (Ca) and terrestrial organic carbon (Ct) in core sediment B account for 74.9 and 25.1% of the total organic carbon, and aquatic N and Nt account for 90.8 and 9.2% of the total nitrogen, respectively. Therefore, organic carbon and

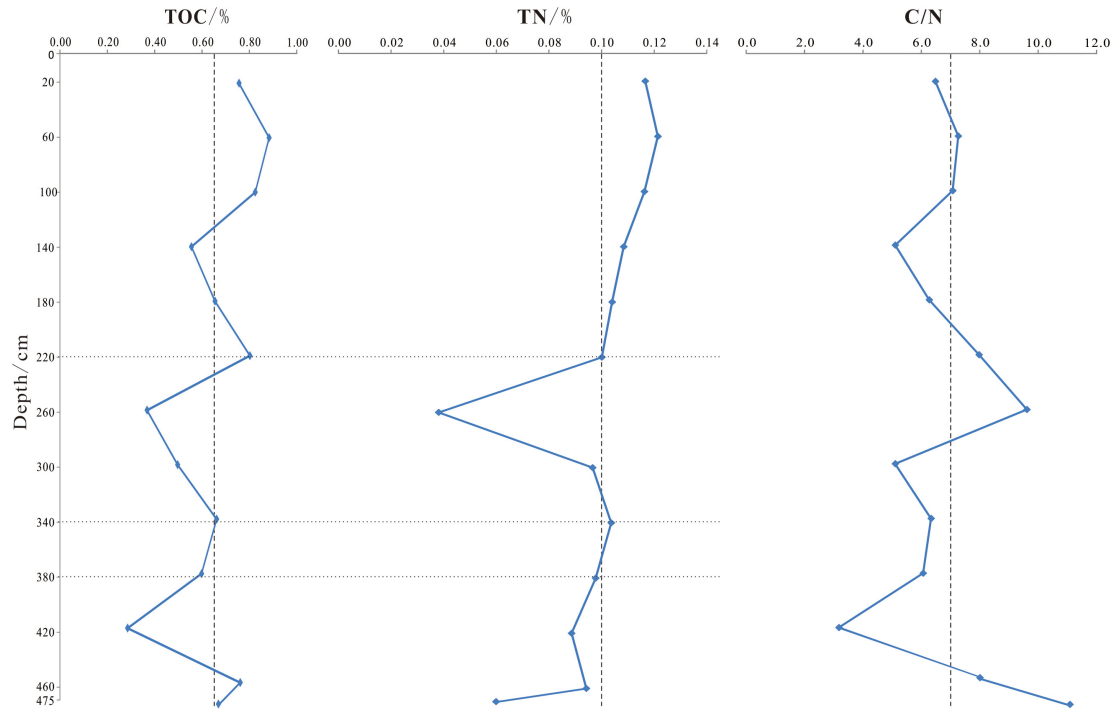

FIGURE 2 | Vertical profiles of TOC, TN, and CN in core sediment A.

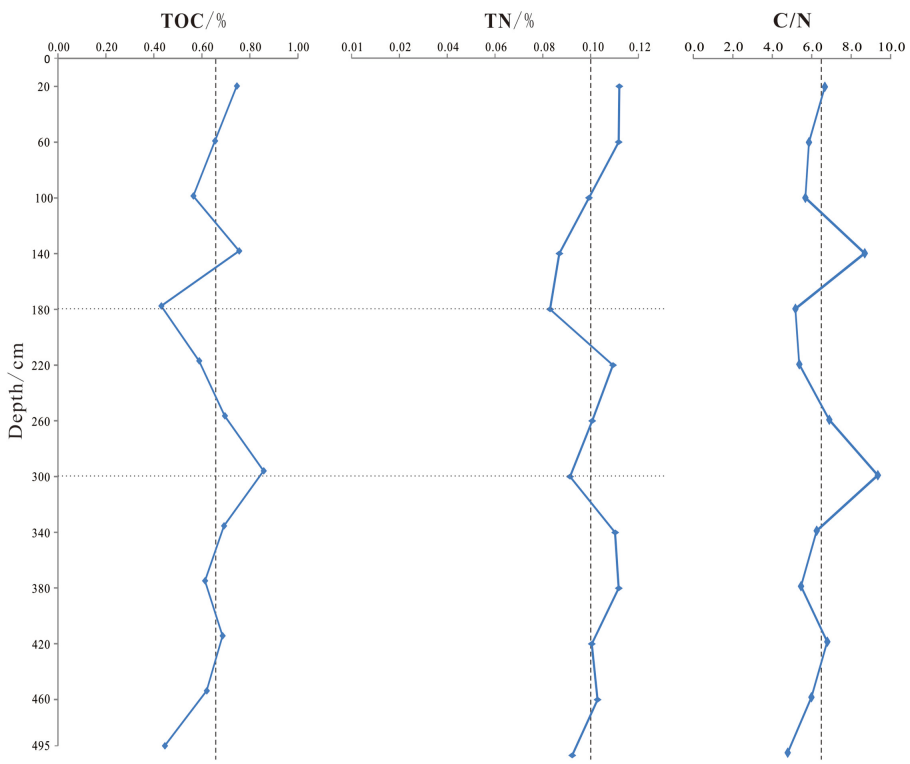

FIGURE 3 | Vertical profiles of TOC, TN, and C/N in core sediment B.

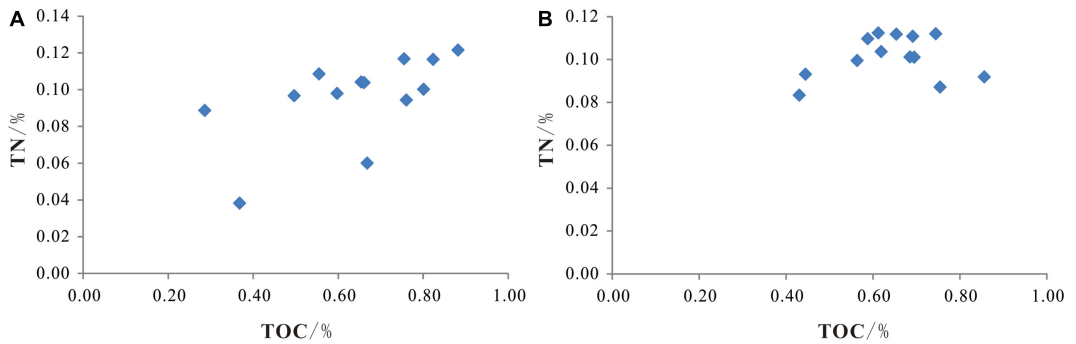

FIGURE 4 | The correlation of TOC and TN in core sediments **(A,B)**.

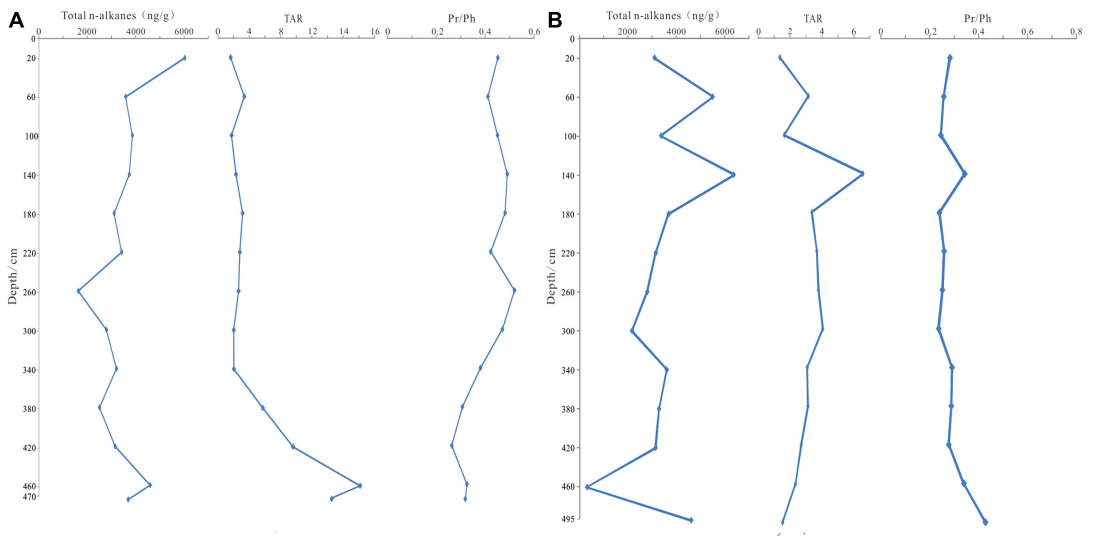

FIGURE 5 | Vertical profiles of the typical molecular compositional patterns of core **(A,B)**.

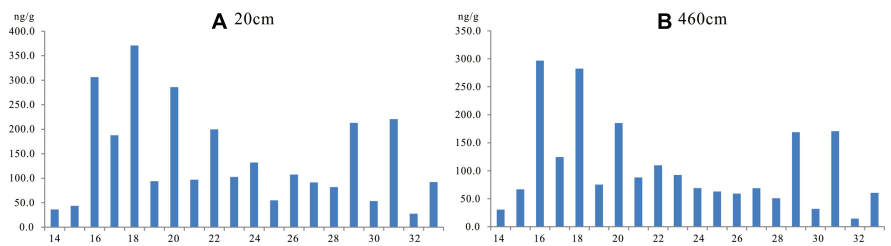

FIGURE 6 | Distribution of *n*-alkanes in the representative horizon in the core sediments **(A,B)**.

nitrogen in the core sediment B are also mostly marine sources, which is consistent with the result of the C/N.

Molecular Composition of Hydrocarbons and Indication Sedimentary Environment

n-alkanes are widely distributed in organisms such as bacteria, algae and higher plants. The *n*-alkanes derived from specific organisms usually with distinct distribution patterns and compositions (Parker et al., 1967; Han and Calvin, 1969; Winters et al., 1969). The distribution of *n*-alkanes detected in sediment samples was C_{14} − C_{33}, with an average CPI_{24-33} of long-chain *n*-alkanes for A and B stations being 3.6 and 2.9, respectively, while the CPI was 2–10, which is a hallmark of terrestrial organic matter inputs in typical marine sediment (Clark and Blumer, 1967). Short-chain *n*-alkanes are derived from marine plankton or bacteria (Blumer et al., 1971). In addition, *n*-C_{29}, *n*-C_{31} and *n*-C_{33} are the main peak carbons of long-chain *n*-alkanes

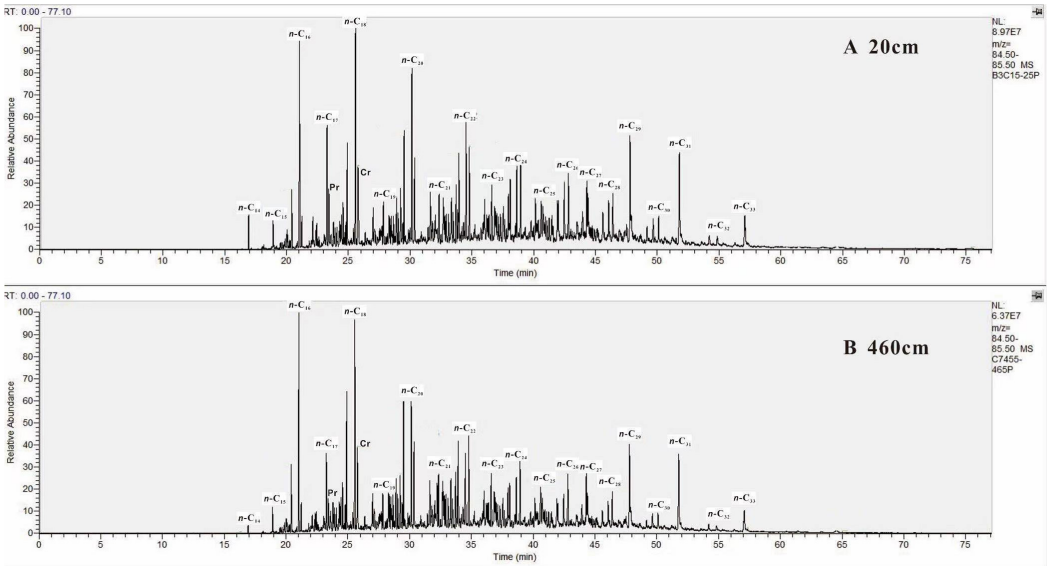

FIGURE 7 | The chromatogram of the typical samples in core sediments **(A,B)**.

in all layers of sediments, reflecting the organic characteristics of typical modern sediments (Bray and Evans, 1961; Eglinton et al., 1962; Eglinton and Hamilton, 1963; Clark and Blumer, 1967; Cranwell, 1973; Weete, 1976; Meyers, 2003), in which the n-C_{27} and n-C_{29} represent the input of woody plants and n-C_{31} and n-C_{33} represent the inputs of herbs (Meyers, 2003; Cranwell, 2010); pristane and phytane are mainly produced from degradation products of chlorophyllophyton-based side chains from photosynthetic plants (Powell and McKirdy, 1973). There are isotope data on the surface sediments of the Southwest Sub-basin. Most of the hydrocarbons cannot be detected due to their low concentration. The carbon isotope composition detected is between −25.41∼−32.41‰ (Wan et al., 2019).

The concentration of total n-alkanes in core A was ranging from 716.7 to 2799.8 ng/g (**Table 2**), with the lowest content was found in the middle layer and higher contents were observed in the top and bottom layers. The concentration of total n-alkanes in core B was varying from 1008.3 to 2109.9 ng/g (**Table 3**), and the vertical variation was quite fluctuant. TAR(TAR $= \Sigma C_{27} + C_{29} + C_{31}/\Sigma C_{15} + C_{17} + C_{19}$) was used to evaluate the relative contributions of ternary alkanes from terrestrial and marine sources (Meyers, 1997). The TAR in the core sediment A range from 1.6 to 18.2 with an average of 5.4 (**Table 2**). The TAR ranged from 1.4 to 6.6 in the core sediment B with an average of 3.1 (**Table 3**), it shows that the contribution of terrestrial organic matter to n-alkanes is dominant in the two core sediments. The vertical features of TAR in the core sediment A can be divided into two sections: TAR values were bigger below the depth of 340 cm in the core sediment A, while those above the depth of 340 cm remained stable, indicating that the terrigenous organic matter had a greater contribution to n-alkanes at the bottom of the core sediment A.

Pr/Ph is usually used as a parameter for the degree of oxidation-reduction of sedimentary environments and reconstruction of paleoenvironment (Powell and McKirdy, 1973; Didyk et al., 1978). Both pristane and phytane are derived from phytol, which is favorable for the formation of Pr under oxidative conditions during the evolution process, whereas production of Ph is favored in reducing conditions (Didyk et al., 1978). Therefore, it is generally believed that Pr/Ph < 1.0 indicates a depositional environment of anoxia reduction, whereas Pr/Ph > 1.0 reveals an oxidized depositional environment (Peters and Moldowan, 1993). The Pr/Ph value of core sediment A was 0.3–0.5, with an average of 0.4, and was slightly increased downward the vertical direction. The Pr/Ph value of the core sediment B was 0.2–0.4 with an average of 0.3, and it vertically decreased. The Pr/Ph values of the both cores are far less than 1, similar to the Pr/Ph values of 0.44–0.73 in the four samples measured by Duan et al. (1996) in the Nansha Sea area. The Pr/Ph values of the core sediments remain the same with depth (**Figure 5**), which shows that the depositional environment was strongly reduced and stable over long term, which is beneficial for the preservation of marine organic matter. These conclusions thus highlight the contribution of marine organic matter (Meyers, 1997; Hu et al., 2013) and are consistent with the conclusion of the C/N ratio of both core sediments.

Indication of Medium-Chain *n*-Alkanes Distribution

The even/odd predominance patterns in the n-alkane (n-C_{14-20}) of core A and B (**Figures 6**, **7**) show an anomalous sedimentary environment (Kuhn et al., 2010). It is generally believed that this phenomenon may be caused by (1) high-salt carbonate environments (Dembicki et al., 1976; Guoying et al., 1980; Ten Haven et al., 1985); (2) anthropogenic fossil fuel contamination or hydrocarbon leaks in the underlying high-maturity formations (Lichtfouse et al., 1997); (3) the strong

reduction of the environment and the reduction in the *n*-fatty acids with an odd carbon dominance (Welte and Ebhardt, 1968; Welte and Waples, 1973).

Both cores were predominantly comprised of medium-fine sand and clay silt, suggesting that the presence of high-salt carbonate environments is impossible. The distribution of *n*-alkanes (CPI = 1.8–5.0) of both cores shows the characteristics of modern sedimentation. Therefore, it is also impossible for the even/odd predominance patterns in the medium-chain *n*-alkane in sediments to be dominated by the fossilization of modern fossil fuels or the leakage of hydrocarbons from deeper strata to lower strata (CPI $\approx$ 1) (Nishimura and Baker, 1986; Freeman and Colarusso, 2001). The ratio of Pr/Ph in the sediment ranged from 0.2 to 0.5, indicating a strong reduction depositional environment, and strong reduction makes the odd-carbon *n*-fatty acids reduce to even-carbon *n*-alkanes. Therefore, we speculate that the even/odd predominance patterns in the *n*-alkane (n-C_{14-20}) of core A and B are results from the intense reduction environment during deposition.

CONCLUSION

(1) The mean TOC of core sediment A is 0.64% $\pm$ 0.18%, and the average concentration of TN is 0.10% $\pm$ 0.02% (0.04–0.12%). The average concentration of TOC of core sediment B is 0.64% $\pm$ 0.12%, and the average concentration of TN is 0.10% $\pm$ 0.01%. The C/N ratio reflects that the organic carbon in the sediments is a mixture of terrestrial and marine sources, the contribution of marine sources to organic carbon in core sediment B is bigger than that of A.

(2) The long-chain *n*-alkanes in all layers of the both core sediments show an odd-even predominance, with n-C_{29}, n-C_{31} and n-C_{33} being the main carbons, which reflect the contribution of terrigenous higher plants and short-chain *n*-alkanes from marine plankton or bacteria. The Pr/Ph of core A and B were 0.3–0.5 and 0.2–0.4, respectively, which are both far less than 1, and the Pr/Ph values remained the same with depth changes, indicating that the sedimentary environment was dominated by strong reduction and long-term stability.

(3) The even-odd distribution patterns of medium-chain *n*-alkanes (n-C_{14-20}) in the core A and B possibly caused by the strong reductive depositional environment. The strong reduction allowed the conversion of odd-carbon *n*-fatty acids to even-carbon *n*-alkanes.

DATA AVAILABILITY STATEMENT

The original contributions presented in the study are included in the article/supplementary material, further inquiries can be directed to the corresponding author/s.

AUTHOR CONTRIBUTIONS

XW: writing-original draft, experimental analysis, and data analysis. ZW: main idea, methodology, writing—review and editing, project administration, and funding acquisition. CC: data analysis and writing—review and editing. SC: experimental analysis. All authors contributed to the article and approved the submitted version.

REFERENCES

Blumer, M., Guillard, R. R. L., and Chase, T. (1971). Hydrocarbons of marine phytoplankton. *Mar. Biol.* 8, 183–189. doi: 10.1007/bf00355214

Bray, E. E., and Evans, E. D. (1961). Distribution of n-paraffins as a clue to recognition of source beds. *Geochim. Cosmochim. Acta* 22, 2–15. doi: 10.1016/0016-7037(61)90069-2

Briais, A., Patriat, P., and Tapponnier, P. (1993). Updated interpretation of magnetic anomaliesand seafloor spreading in the South China Sea: implications for the tertiary tectonics of Southeast Asia. *J. Geophys. Res.* 98, 6299–6328. doi: 10.1029/92jb02280

Clark, R. C., and Blumer, M. (1967). Distribution of n-paraffins in marine organisms and sediment. *Limnol. Oceanogr.* 12, 79–87. doi: 10.4319/lo.1967.12.1.0079

Cranwell, P. A. (1973). Chain-length distribution of *n*-alkanes from lake sediments in relation to post glacial environmental change. *Freshwater Biol.* 3, 259–265. doi: 10.1111/j.1365-2427.1973.tb00921.x

Cranwell, P. A. (2010). Chain-length distribution of *n*-alkanes from lake sediments in relation to post-glacial environmental change. *Freshwater Biol.* 3, 259–265.

Dembicki, H. Jr., Meinschein, W. G., and Hattin, D. E. (1976). Possible ecological and environmental significance of the predominance of even-carbon number C20–C30 *n*-alkanes. *Geochim. Cosmochim. Acta.* 40, 203–208. doi: 10.1016/0016-7037(76)90177-0

Didyk, B. M., Simoneit, B. R. T., Brassell, S. C., and Eglinton, G. (1978). Organic geochemical indicators of palaeoenvironmental conditions of sedimentation. *Nature* 272, 216–222. doi: 10.1038/272216a0

Duan, Y. (2000). Organic geochemistry of recent marine sediments from the nansha sea, china. *Org. Geochem.* 31, 159–167. doi: 10.1016/s0146-6380(99)00135-7

Duan, Y., Song, Z. G., and Luo, B. J. (1996). Study on organic geochemistry of marine core sediments from Chinese Nansha sea areas. *Mar. Sci. Bull.* 15, 42–48.

Eglinton, G., and Hamilton, R. J. (1963). "Chapter 8 – the distribution of alkanes," in *Chemical Plant Taxonomy*, ed. T. Swain (London: Academic Press), 187–217. doi: 10.1016/b978-0-12-395540-1.50012-9

Eglinton, G., Hamilton, R. J., Raphael, R. A., and Gonzalez, A. G. (1962). Hydrocarbon constituents of the wax coatings of plant leaves: a taxonomic survey. *Nature* 193:739. doi: 10.1038/193739a0

Freeman, K. H., and Colarusso, L. A. (2001). Molecular and isotopic records of c 4, grassland expansion in the late miocene. *Geochim. Cosmochim. Acta* 65, 1439–1454. doi: 10.1016/s0016-7037(00)00573-1

Goñi, M. A., Ruttenberg, K. C., and Eglinton, T. I. (1998). A reassessment of the sources and importance of land-derived organic matter in surface sediments from the Gulf of Mexico. *Geochim. Cosmochim. Acta* 62, 3055–3075. doi: 10.1016/s0016-7037(98)00217-8

Guoying, S., Shanfa, F., Dehan, L., Nengxian, S., and Hongming, Z. (1980). The geochemistry of *n*-alkanes with an even–odd predominance in the Tertiary Shahejie formation of northern China. *Phys. Chem. Earth.* 12, 115–121. doi: 10.1016/0079-1946(79)90093-4

Hamilton, W. B. (1979). *Tectonics of the Indonesia region*. Us Geological Survey Professional Paper, 1078. Reston: USGS.

Han, J., and Calvin, M. (1969). Hydrocarbon distribution of algae and bacteria, and microbiological activity in sediments. *Proc. Natl. Acad. Sci. U.S.A.* 64, 436–443. doi: 10.1073/pnas.64.2.436

Hu, J. F., Peng, P., and Chivas, A. R. (2009). Molecular biomarker evidence of origins and transport of organic matter in sediments of the pearl river estuary and adjacent south china sea. *Appl. Geochem.* 24, 1666–1676. doi: 10.1016/j.apgeochem.2009.04.035

Hu, L. M., Shi, X. F., Guo, Z. G., Liu, Y. G., and Ma, D. Y. (2013). Geochemical characteristics of hydrocarbons in the core sediments from the south yellow sea and its implication for the sedimentary environment. *Acta Sedimentol. Sin.* 31, 108–119.

Jia, G. D., Peng, P. A., and Fu, J. M. (2002). Sedimentation records of accelerated eutrophication for the last 100 years at the Pearl River estuary. *Quat. Sciences* 22, 158–165.

Kerimov, V. Y., Leonov, M. G., Osipov, A. V., Mustaev, R. N., and Hai, V. N. (2019). Hydrocarbons in the basement of the south china sea (vietnam) shelf and structural–tectonic model of their formation. *Geotectonics* 53, 42–59. doi: 10.1134/s0016852119010035

Kuhn, T. K., Krull, E. S., Bowater, A., Grice, K., and Gleixner, G. (2010). The occurrence of short chain *n*-alkanes with an even over odd predominance in higher plants and soils. *Org. Geochem.* 41, 88–95. doi: 10.1016/j.orggeochem.2009.08.003

Li, J. B. (2011). Dynamics of the continental margins in south china sea: scientific experiments and research progresses. *Chin. J. Geophys.* 54, 883–893. doi: 10.1002/cjg2.1671

Lichtfouse, E., Bardoux, G., Mariotti, A., Balesdent, J., Ballentine, D. C., and Macko, S. A. (1997). Molecular, ^{13}C, and ^{14}C evidence for the allochthonous and ancient origin of C_{16}–C_{18} *n*-alkanes in modern soils. *Geochim. Cosmochim. Acta* 61, 1891–1898. doi: 10.1016/s0016-7037(97)00021-5

Likens, G. E., Bormann, F. H., and Johnson, N. M. (1981). *Interactions Between Major Biogeochemical Cycles in Terrestrial Ecosystems[M]. Some Perspectives of the Major Biogeochemical Cycles*. New York, NY: John Wiley & Sons Ltd, 93–112.

Meyers, P. A. (1997). Organic geochemical proxies of paleoceanographic, paleolimnologic, and paleoclimatic processes. *Org. Geochem.* 27, 213–250. doi: 10.1016/s0146-6380(97)00049-1

Meyers, P. A. (2003). Applications of organic geochemistry to paleolimnological reconstructions: a summary of examples from the laurentian great lakes. *Org. Geochem.* 34, 261–289. doi: 10.1016/s0146-6380(02)00168-7

Meyers, P. A., and Lallier-Vergés, E. (1999). Lacustrine sedimentary organic matter records of late quaternary paleoclimates. *J. Paleolimnol.* 21, 345–372.

Nishimura, M., and Baker, E. W. (1986). Possible origin of *n*-alkanes with a remarkable even-to-odd predominance in recent marine sediments. *Geochim. Cosmochim. Acta* 50, 299–305. doi: 10.1016/0016-7037(86)90178-x

Parker, P. L., Van Baalen, B. C., and Maurer, L. (1967). Fatty acids in eleven species of blue-green algae: geochemical significance. *Science* 155, 707–708. doi: 10.1126/science.155.3763.707

Peters, K. E., and Moldowan, J. M. (1993). *The Biomarker Guide: Interpreting Molecular Fossils in Petroleum and Ancient Sediments*. New Jersey, NJ: Prentice Hall, Inc.

Powell, T. G., and McKirdy, D. M. (1973). Relationship between ratio of pristane to phytane, crude oil composition and geological environment in australia. *Nature* 243, 37–39. doi: 10.1038/physci243037a0

Qian, L. J., Wang, S. M., Xue, B., Chen, R. S., and Ke, S. Z. (1997). A method of quantitative estimating terrestrial organic carbon in lake sedimentation research. *Chin. Sci. Bull.* 42, 1655–1657.

Redfield, A. C., Ketchum, B. H., and Richards, F. A. (1963). "The influence of organisms on the composition of sea water," in *The Sea*, ed. M. N. Hill (New York, NY: Wiley), 26–77.

Sun, Z., Zhong, Z., Keep, M., Zhou, D., Cai, D., Li, X., et al. (2009). 3D analogue modeling of the South China Sea: a discussion on breakup pattern. *J. Asian Earth Sci.* 34, 544–556. doi: 10.1016/j.jseaes.2008.09.002

Tahir, N. M., Pang, S. Y., and Simoneit, B. R. T. (2015). Distribution and sources of lipid compound series in sediment cores of the southern South China Sea. *Environ. Sci. Pollut. Res.* 22, 7557–7568. doi: 10.1007/s11356-015-4184-5

Tapponnier, P., Peltzer, G., Le Dain, A. Y., Armijo, R., and Cobbold, P. (1982). Propagating extrusion tectonics in asia: new insights from simple experiments with plasticine. *Geology* 10:611. doi: 10.1130/0091-7613(1982)10<611:petian>2.0.co;2

Ten Haven, H. L., de Leeuw, J. W., and Schenck, P. A. (1985). Organic geochemical studies of a Messinian evaporitic basin, northern Apennines (Italy) I: hydrocarbon biological markers for a hypersaline environment. *Geochim. Cosmochim. Acta* 49, 2181–2191. doi: 10.1016/0016-7037(85)90075-4

Wan, Z. F., Wang, X. Q., Li, Y. F., Xu, X., Sun, Y. F., Yin, Z. X., et al. (2019). The composition and geochemical significance of organic matters in surface sediments from the southwest sub-basin of the south china sea. *J. Asian Earth Sci.* 171, 103–117. doi: 10.1016/j.jseaes.2018.07.012

Weete, J. D. (1976). "Algal and fungal waxes," in *Chemistry and Biochemistry of Natural Waxes*, ed. P. E. Kolattukudy (New York, NY: Elsevier), 349–417.

Welte, D. H., and Ebhardt, G. (1968). Distribution of long chain n-paraffins and n-fatty acids in sediments from the Persian Gulf. *Geochim. Cosmochim. Acta* 32, 465–466. doi: 10.1016/0016-7037(68)90080-x

Welte, D. H., and Waples, D. W. (1973). Über die Bevorzugung geradzahliger n-Alkane in Sedimentgesteinen. *Sci. Nat.* 60, 516–517. doi: 10.1007/bf00603253

Winters, K., Parker, P. L., and Baalen, C. V. (1969). Hydrocarbons of blue-green algae: geochemical significance. *Science* 163, 467–468. doi: 10.1126/science.163.3866.467

Conflict of Interest: The authors declare that the research was conducted in the absence of any commercial or financial relationships that could be construed as a potential conflict of interest.

frontiers in Earth Science

ORIGINAL RESEARCH
published: 22 September 2021
doi: 10.3389/feart.2021.759372

Using Clumped Isotopes to Reconstruct the Maximum Burial Temperature: A Case Study in the Sichuan Basin

Pingping Li[1,2]*, *Jinbao Duan*[3], *Zhongzhen Cheng*[2] *and Huayao Zou*[1,2]

[1]State Key Laboratory of Petroleum Resources and Prospecting, China University of Petroleum, Beijing, China, [2]College of Geosciences, China University of Petroleum, Beijing, China, [3]SINOPEC Exploration Company, Chengdu, China

OPEN ACCESS

Edited by:
Qiangtai Huang,
Sun Yat-sen University, China

Reviewed by:
Jibao Dong,
Institute of Earth Environment (CAS), China
Fuyun Cong,
China University of Geosciences Wuhan, China

***Correspondence:**
Pingping Li
lpp@cup.edu.cn

Specialty section:
This article was submitted to Geochemistry, a section of the journal Frontiers in Earth Science

Received: 16 August 2021
Accepted: 03 September 2021
Published: 22 September 2021

Citation:
Li P, Duan J, Cheng Z and Zou H (2021) Using Clumped Isotopes to Reconstruct the Maximum Burial Temperature: A Case Study in the Sichuan Basin. Front. Earth Sci. 9:759372. doi: 10.3389/feart.2021.759372

For strata that have experienced continual burial in the early stage and uplift in the late stage, the present-day temperature is lower than the maximum burial temperature (MBT), which is a key parameter for studying the hydrocarbon generation history of source rocks in petroliferous basins. In this paper, a new method for reconstructing the MBT is proposed based on the solid-state reordering model of carbonate clumped isotopes (Δ_{47}). The MBT reconstructed using the Δ_{47} was compared with the MBT constrained using the traditional Easy%R_o model. The clumped isotope temperature ($T_{\Delta47}$) of the Permian micritic limestone from the Xibeixiang outcrop (about 62°C) is much higher than its initial formation temperature (20–25°C), suggesting that the limestone experienced partial solid-state reordering during the late burial process. The MBT of the calcite obtained from the solid-state reordering model is 139–147°C, which is quite similar to the MBT determined using the Easy%R_o model (139.5–147.5°C). $T_{\Delta47}$ of the Permian and Triassic limestone and calcite cements in the Puguang gas field are 150–180°C, while $T_{\Delta47}$ of the micritic dolostone is about 70°C, suggesting that the Δ_{47} of the limestone and calcite cements experienced complete solid-state reordering and the dolostone only experienced partial solid-state reordering. The MBT of the dolomite determined using the solid-state reordering model is 200–220°C, which is also similar to the MBT determined using the Easy %R_o model (202–227°C). Therefore, the case studies from the Sichuan Basin suggest that Δ_{47} can be used to reconstruct the MBT of ancient carbonate strata lacking vitrinite and detrital zircon data. However, different types of carbonate samples should be used to reconstruct the MBT for strata that have experienced different temperature histories. Micritic limestone and very finely crystallized dolostone can be used to reconstruct the MBT of strata that have experienced MBTs of <150–200°C and >200–250°C, respectively.

Keywords: clumped isotopes, maximum burial temperature, carbonate, solid-state reordering, Sichuan Basin, vitrinite reflectance

INTRODUCTION

The burial temperature (especially the maximum burial temperature, MBT) of certain strata in a particular sedimentary basin is closely related to the maturity of the organic matter and the hydrocarbon generation of the source rocks (Hunt, 1996; Helgeson et al., 2009; Qiu et al., 2012), and it can also affect the phases in oil and gas reservoirs (Barker, 1990; Hill et al., 2003; Zhu et al., 2018). As a result, the MBT is one of the key parameters for basin modeling and the evaluation of oil and gas resources (Kinley et al., 2008; Qiu et al., 2012; Wood, 2018). For sedimentary basins that have experienced continuous subsidence and burial, the burial depth of certain strata was the largest during the burial process, and its present-day burial temperature is the MBT, which can be determined using current heat flow or geothermal gradient models (Zuo et al., 2011). However, for sedimentary basins that subsided in the early stage and were uplifted and exhumed in the late stage, the present-day burial temperature of certain strata is usually lower than the MBT (Hao et al., 2008; English et al., 2016; Dou et al., 2021), which cannot be directly determined using current heat flow or geothermal gradient models. As a result, reconstructing the MBT of certain strata in a basin that experienced late uplift and exhumation is key to the evaluation of the oil and gas exploration potential, and it is also a research focus in basin modeling.

Common methods of MBT reconstruction include the maturity index of the organic matter (Héroux et al., 1979; Hackley et al., 2015; Luo et al., 2020b) and low temperature thermochronology (Carlson, 1990; Craddock and Houseknecht, 2016; Ehlers and Farley, 2003; Yamada et al., 2007). The maturity index of the organic matter is commonly characterized by the vitrinite reflectance (Mukhopadhyay, 1994; Katz and Lin, 2021), which is mainly controlled by the temperature (Hunt, 1996). Therefore, the current vitrinite reflectance (R_o), combined with an organic matter maturation model (such as the Easy%R_o model; Sweeney and Burnham, 1990), can be used to determine the MBT. For strata without vitrinite data, the bitumen reflectance and graptolite reflectance can be used to calculate the equivalent R_o (Jacob, 1989; Luo et al., 2020b), but different conversion methods exist, and they have different application scopes (Schmidt et al., 2019; Katz and Lin, 2021). Low temperature thermochronology mainly uses annealing kinetic models of fission tracks in minerals (such as apatite and zircon) and (U-Th)/He thermochronology to determine the temperature evolution (Carlson, 1990; Craddock and Houseknecht, 2016; Ehlers and Farley, 2003; Yamada et al., 2007). The annealing kinetic model of apatite fission tracks is only applicable at relatively low temperatures (below 125°C; Carlson, 1990). For strata that have experienced temperatures of >150°C, only the annealing of zircon fission tracks can be used (Yamada et al., 2007), but a unified annealing kinetic model of zircon has not yet been established. The (U-Th)/He thermochronology of zircon can be used to determine the corresponding MBT and time (Reiners, 2005), but for ancient marine strata, detrital zircons are often not easy to obtain, which limits the use of this method. Therefore, for ancient marine strata, both the maturity index of the organic matter and low temperature thermochronology have certain limitations in MBT reconstruction.

Carbonate minerals (such as calcite and dolomite) are commonly present in ancient marine strata. Carbonate clumped isotopes (Δ_{47}), developed in recent years, can be used to determine the formation temperature of carbonate minerals ($T_{\Delta47}$), which have been called clumped isotope thermometers (Ghosh et al., 2006; Eiler, 2007). Unlike traditional oxygen isotope ($\delta^{18}O$) thermometers, clumped isotopes can be used to directly determine the formation temperature of carbonate minerals using the abundance of ^{13}C-^{18}O in the carbonate minerals, without relying on the $\delta^{18}O$ of the fluid from which the carbonate minerals grew (Eiler, 2007). However, $T_{\Delta47}$ determined from the clumped isotopes can differ from the original formation temperature due to solid-state reordering. If the carbonate minerals experienced high temperatures during late burial, the ^{13}C and ^{18}O underwent solid-state diffusion, resulting in changes in the abundance of ^{13}C-^{18}O in the minerals and $T_{\Delta47}$ of the minerals (Passey and Henkes, 2012; Stolper and Eiler, 2015). Kinetic models of the solid-state reordering of carbonate minerals have been developed in recent years (Passey and Henkes, 2012; Stolper and Eiler, 2015; Lloyd et al., 2018; Hemingway and Henkes, 2021). The carbonate minerals in ancient carbonate strata have usually experienced high temperatures and solid-state reordering of ^{13}C and ^{18}O. Therefore, the solid-state reordering of calcite and dolomite in ancient carbonate strata can be used to reconstruct the MBT according to the established solid-state reordering models for calcite and dolomite (Passey and Henkes, 2012; Stolper and Eiler, 2015; Lloyd et al., 2018). This provides a potential new method for reconstructing the MBT of ancient marine carbonate strata lacking vitrinite and detrital zircon data.

The purpose of this study was to reconstruct the MBT using the clumped isotopes of the Permian and Triassic limestone and dolostone samples from the Sichuan Basin and to compare the MBT determined using carbonate clumped isotopes and the Easy %R_o model in order to verify the reliability of using the carbonate clumped isotope method to reconstruct the MBT and to provide a good case study for MBT reconstruction of ancient marine carbonate strata.

GEOLOGIC SETTING

The Sichuan Basin is a multi-cycle basin located in southwestern China (**Figure 1**), with the Ediacaran to Quaternary sediments. It experienced six main tectonic cycles: the Yangtze (before 630 Ma), Caledonian (630–320 Ma), Hercynian (320–252 Ma), Indosinian (252–195 Ma), Yanshanian (195–65 Ma), and Himalayan (65–0 Ma) movements (Zhai, 1989). Among them, the marine deposits were mainly developed from the Yangtze to the Early Indosinian, while the continental deposits were mainly developed from the Late Indosinian to the Himalayan.

The Sichuan Basin experienced early extension and late compression and uplift (Zhai, 1989). From the Yangtze to the Early Indosinian, two weak extension events resulted in the development of two intracratonic sags in the Sichuan Basin (the Early Cambrian Mianyang-Changning sag and the Late Permian Kaijiang-Liangping sag) (Liu et al., 2021). Strong

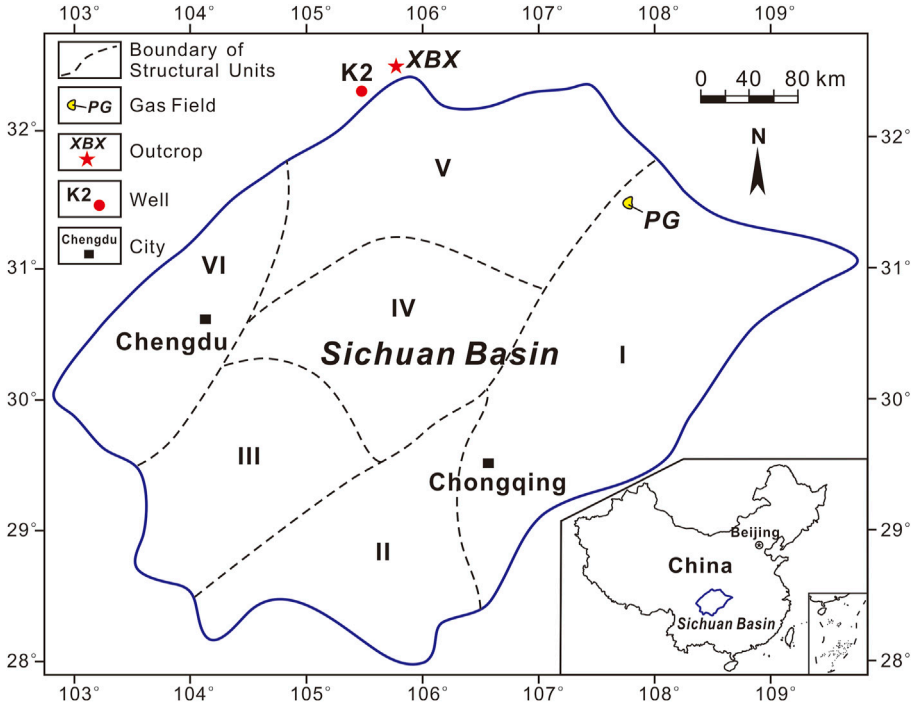

FIGURE 1 | Locations of the Puguang (PG) gas field, well-K2, and the Xibeixiang (XBX) outcrop in the Sichuan Basin. I = eastern complete fault-fold zone, II = southern gentle fault-fold zone, III = southwestern gentle fault-fold zone, IV = central flat zone, V = northern gentle fault-fold zone, VI = western gentle fault-fold zone.

compression and uplift have occurred since the Late Indosinian, and the Sichuan Basin has evolved into a foreland basin. In particular, the Longmanshan, located in the western boundary of the Sichuan Basin, uplifted gradually from the northeast to the southwest (Burchfiel et al., 1995). During the Yanshanian, many large northeast-southwest striking folds and faults were formed in the eastern Sichuan Basin due to regional northwest-southeast compression (Zhai, 1989). Then, rapid uplift and exhumation occurred during the Late Yanshanian and Himalayan (Deng et al., 2013). It is a typical basin that has experienced early subsidence and late uplift and exhumation in western China.

Marine carbonates and shales were deposited during the Permian and Early Triassic. From the bottom to top, the Permian can be divided into the Liangshan (P_1l), Qixia (P_1q), Maokou (P_1m), Longtan (P_2l)/Wujiaping (P_2w), and Changxing (P_2c)/Dalong (P_2d) formations, and the Lower Triassic can be divided into the Feixianguan (T_1f) and Jialingjiang (T_1j) formations (Zhai, 1989). The P_2l/P_2w and P_2d mainly consist of shales, which are the main source rocks of the P_2c and T_1f gas reservoirs (Li et al., 2005; Yu et al., 2021), while the P_2c and T_1f mainly consist of dolostone and limestone, which are the main reservoirs rocks of the main large gas fields (such as the Puguang, Yuanba, and Longgang gas fields) discovered in recent years (Ma et al., 2007; Du et al., 2010; Guo et al., 2018). The dolostone in the P_2c and T_1f was mainly developed on the platform margins of the Kaijiang-liangping trough, and it was formed in a near surface to quite shallow burial environment. The dolomitization fluids were sourced from the T_1f evaporated sea water (Jiang et al., 2014; Li et al., 2021).

SAMPLING AND ANALYTICAL METHODS

Three P_1q limestone samples (D1, D4, and D6) and two P_2d shale samples were collected from the XBX outcrop (**Figure 1**), and three P_2c-T_1f limestone samples (L56, L61, and L62), four P_2c-T_1f dolostone samples (D83, D89, D90, and D99), three P_2c-T_1f calcite cement samples (Cem5, Cem8, and Cem25), and thirteen P_2w shale samples were collected from the Puguang (PG) gas field (**Figure 1**).

All of the shale samples were analyzed for R_o using conventional microphotometric methods (Stach et al., 1982) at the State Key Laboratory of Petroleum Resources and Prospecting, China University of Petroleum (Beijing). The number of readings was generally >20 for the random reflectance, and the error of each sample was within 0.2%.

Thin sections of all of the limestone and dolostone samples were prepared for petrographic observations. Then, all of the limestone and dolostone samples and calcite cement samples were powdered to less than 0.15 mm (100 mesh) for $\delta^{13}C$, $\delta^{18}O$, and clumped isotope (Δ_{47}) analyses at the California Institute of Technology (Caltech). The detailed analytical procedures have been described in previously published papers (Ghosh et al., 2006; Huntington et al., 2009; Ryb and Eiler, 2018; Li et al., 2020). First, about 10 mg of carbonate sample was reacted with 103% phosphoric acid at 90°C, and the CO_2 produced was purified using a gas-chromatography column. Then, the 44–49 masses of the CO_2 were measured using a Thermo MAT253 isotope ratio mass spectrometer. Then, the $\delta^{13}C$, $\delta^{18}O$, and Δ_{47} values were calculated using the methods described by Huntington et al. (2009). Finally, the Δ_{47} values were converted into the absolute reference frame (Dennis et al., 2011), and the

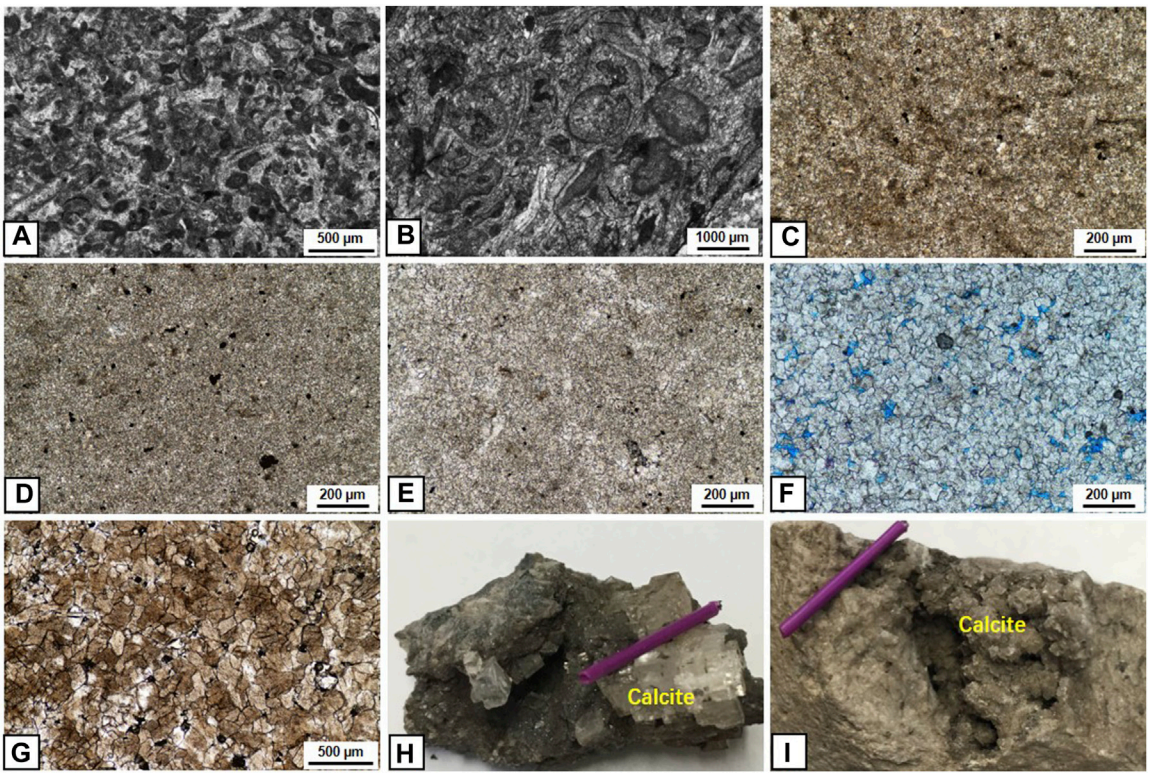

FIGURE 2 | (A–G) Thin-section photomicrographs of limestone and dolostone samples, and **(H,I)** photographs of calcite cements. **(A)** Sample D1, XBX outcrop, bioclastic limestone. **(B)** Sample L56, well PG6, 5383.1 m, P_2c, bioclastic limestone. **(C)** Sample L62, well MB3, 4014.0 m, T_1f, micritic limestone. **(D)** Sample D83, well MB4, 3892.5 m, T_1f, micritic dolostone. **(E)** Sample D90, well PG2, 4878.0 m, T_1f, micritic dolostone. **(F)** Sample D89, well PG12, 6007.0 m, T_1f, fine crystallized dolostone. **(G)** Sample D99, well PG6, 5339.0 m, P_2c, medium crystallized dolostone. **(H)** Sample Cem8, well MB3, P_2c, 4394.6 m, coarse calcite cements (the length of the small purple stick is 2.0 cm). **(I)** Sample Cem5, well DW102, 4825.0 m, T_1f, coarse calcite cements in vugs in dolostone. Note: the wells MB3, MB4, DW102, PG2, PG6 and PG12 are all located in the Puguang gas field.

clumped isotopes temperature ($T_{\Delta47}$) of each sample was calculated using the temperature calibrations developed by Bonifacie et al. (2017). Most of the samples were measured two or three times. The standard deviation of the $\delta^{13}C$ and $\delta^{18}O$ measurement is <0.01‰, and that of the Δ_{47} measurements is <0.02‰. The standard errors of the in-house standard (CIT Carrara and TV04) were <0.01‰. The raw data of d45-d79, D47 of samples, standards, equilibrated gases and heated gases were listed in the **Supplementary Table 1**.

RESULTS

Petrography

The crystal size of the carbonate minerals can be divided into micritic (<50 μm), very fine (50–100 μm), fine (100–250 μm), medium (250–500 μm), and coarse (>500 μm) (Bissell and Chilingar, 1967). All of the limestone samples collected from the XBX outcrop are bioclastic limestone, the cement between the bioclastics is micritic calcite with crystal sizes of <10 μm, and no obvious crystallization was observed in the bioclastics and calcite cement (**Figure 2A**). The limestone samples collected from the Puguang gas field include bioclastic limestone (**Figure 2B**) and micritic limestone (**Figure 2C**). The crystal sizes of the calcite are <10 μm, and no obvious crystallization occurred in these limestone samples. The dolostone samples collected from the Puguang gas field include micritic dolostone (**Figures 2D,E**), very fine crystallized dolostone (**Figure 2F**), and fine crystallized dolostone (**Figure 2G**). The crystal size of the two micritic dolostone samples is about 10 μm (average of 12 μm for D87 and 10 μm for D90), and intercrystal pores were hardly observed in the two micritic dolostone samples. The average crystal size of the very fine crystallized dolostone (D89) is about 70 μm, with very limited dolomite recrystallization, and some pores are developed between the subhedral dolomite crystals (**Figure 2F**). The crystal sizes of the fine crystallized dolostone (D99) are 150–200 μm (average of 194 μm), with obvious dolomite recrystallization, and black solid bitumen was observed in the pores between the subhedral dolomite crystals (**Figure 2G**). The calcite cement samples (crystal sizes of 0.3–1.0 cm) collected from the Puguang gas field are mainly developed in vugs in dolostone, and it is generally associated with black solid bitumen (**Figures 2H,I**).

$\delta^{13}C$, $\delta^{18}O$, Δ_{47}, and Clumped Isotope Temperature ($T_{\Delta47}$)

The $\delta^{13}C$, $\delta^{18}O$, Δ_{47}, and $T_{\Delta47}$ values of all of the carbonate samples collected from the XBX outcrop and the Puguang gas field are

TABLE 1 | The $\delta^{13}C$, $\delta^{18}O$, Δ_{47}, and $T_{\Delta47}$ values of the carbonate samples from the XBX outcrop and the PG gas field in the Sichuan Basin.

Area	Sample ID	Sample Type	Strata	Depth (m)	BT (°C)	N	$\delta^{13}C$ ‰VPDB	$\delta^{18}O$ ‰VPDB	Δ_{47} CDES, ‰	$T_{\Delta47}$(°C)
XBX	D1*	L	P_2q	—	17	3	3.878 ± 0.027	−6.336 ± 0.109	0.494 ± 0.008	65.6 ± 3.6
XBX	D4*	L	P_2q	—	17	3	3.451 ± 0.036	−5.296 ± 0.108	0.514 ± 0.017	56.7 ± 7.0
XBX	D6*	L	P_2q	—	17	3	3.479 ± 0.008	−4.793 ± 0.038	0.499 ± 0.004	63.3 ± 1.8
PG	Cem5	C	T_1f	4,825	115	2	−0.840 ± 0.003	−7.732 ± 0.036	0.355 ± 0.008	156.5 ± 7.9
PG	Cem8	C	P_2c	4,395	108	1	−1.108 ± 0.003	−4.722 ± 0.007	0.368 ± 0.010	145.0 ± 8.9
PG	Cem25	C	P_2c	4,360	108	2	−0.227 ± 0.004	−6.535 ± 0.005	0.359 ± 0.007	152.7 ± 6.1
PG	L56	L	P_2c	5,383	133	1	2.505 ± 0.010	−6.943 ± 0.007	0.333 ± 0.013	178.4 ± 14.9
PG	L61	L	T_1f	5,350	133	1	4.014 ± 0.006	−6.868 ± 0.004	0.347 ± 0.015	163.9 ± 15.6
PG	L62	L	T_1f	4,014	101	1	3.701 ± 0.004	−6.366 ± 0.005	0.333 ± 0.014	179.1 ± 16.2
PG	D83	MD	T_1f	3,892	100	3	2.478 ± 0.007	−4.257 ± 0.010	0.479 ± 0.009	72.5 ± 4.5
PG	D90	MD	T_1f	4,878	123	2	2.748 ± 0.001	−4.044 ± 0.005	0.481 ± 0.019	71.7 ± 8.9
PG	D89	VFCD	T_1f	6,007	137	2	2.765 ± 0.005	−4.209 ± 0.005	0.449 ± 0.009	88.5 ± 5.4
PG	D99	FCD	P_2c	5,339	128	2	3.903 ± 0.005	−6.300 ± 0.008	0.391 ± 0.010	126.3 ± 7.6

*Note: L = limestone, C = calcite, MD = micritic dolostone, VFCD = very fine crystallized dolostone, FCD = fine crystallized dolostone, BT = burial temperature. N is the number of sample tests, the $\delta^{13}C$, $\delta^{18}O$, and Δ_{47} values are the average values of each measurement, the errors of the $\delta^{13}C$, $\delta^{18}O$, and Δ_{47} values are average standard deviations. $T_{\Delta47}$ was calculated using the following equation: $\Delta_{47\ CDES90} = 0.0422 \times 10^6 \times T^{-2} + 0.1262$ (Bonifacie et al., 2017). * denotes from Li et al. (2020).*

TABLE 2 | The vitrinite reflectance (R_o) of the shale samples from the XBX outcrop and PG gas field in the Sichuan Basin.

Area	Well	Depth (m)	Strata	Number of measuring points	R_o (%)
XBX	—	—	P_2d	20	0.92
XBX	—	—	P_2d	20	0.96
PG	MB3	4,891–4,892	P_2w	34	2.39
PG	MB3	4,930–4,933	P_2w	27	2.43
PG	MB3	4,952–4,954	P_2w	33	2.67
PG	MB3	4,952–4,954	P_2w	25	2.60
PG	MB3	5,153–5,157	P_2w	34	2.71
PG	MB3	5,185–5,186	P_2w	20	2.79
PG	MB3	5,185–5,186	P_2w	21	2.76
PG	PG5	5,586–5,591	P_2w	25	3.05
PG	PG5	5,596–5,602	P_2w	25	2.95
PG	PG5	5,674–5,678	P_2w	25	3.19
PG	PG5	5,681–5,687	P_2w	30	2.68
PG	PG5	5,732–5,734	P_2w	24	3.10
PG	PG5	5,744–5,747	P_2w	36	3.11

presented in **Table 1**. The $\delta^{13}C$, $\delta^{18}O$, and Δ_{47} values of the three limestone samples from the XBX outcrop range from 3.451 to 3.788‰, −6.336‰ to −4.793‰, and 0.499–0.514‰. For the limestone, dolostone, and calcite cement samples collected from then Puguang gas field, the $\delta^{13}C$ values range from 2.505 to 4.014‰, 2.478–3.903‰, and −1.108‰ to −0.227‰, respectively; the $\delta^{18}O$ values range from −6.943‰ to −6.366‰, −6.300‰ to −4.044‰, and −7.732‰ to −4.722‰, respectively; and the Δ_{47} values range from 0.333 to 0.347‰, 0.391–0.481‰, and 0.355–0.368‰, respectively. The $\delta^{13}C$ values of the limestone and dolostone samples from the Puguang gas field are basically similar (2.505–4.014‰), while the $\delta^{13}C$ values of the calcite cement (−1.108‰ to −0.227‰) are significantly lower than those of the limestone and dolostone samples.

$T_{\Delta47}$ of all of the carbonate samples exhibit a relatively large variation (**Table 1**). $T_{\Delta47}$ of the limestone from the XBX outcrop are 57.6–65.6°C (average of 61.9°C); while $T_{\Delta47}$ of the calcite cement and limestone samples from the Puguang gas field are 145–156.5°C (average of 151.4°C) and 163.9–179.1°C (average of 173.8°C), respectively. There is a large difference in $T_{\Delta47}$ of the four dolostone samples from the Puguang gas field. $T_{\Delta47}$ of the two micritic dolostone samples are 71.7 ± 8.9°C (D90) and 72.5 ± 4.5°C (D83), that of the very fine crystallized dolostone is 88.5 ± 5.4°C, and that of the fine crystallized dolostone is 126.3 ± 7.6°C (D99).

Vitrinite Reflectance (R_o)

The R_o values of the Permian shales from the XBX outcrop and the Puguang gas field are presented in **Table 2**. The R_o values of the two P_2d shale samples from the XBX outcrop are 0.92 and 0.96%, while the R_o values of the P_2w shales from the Puguang gas field are 2.39–3.11% (average of 2.80%).

DISCUSSION

EASY%R_o Model and Maximum Burial Temperature Reconstruction for the Xibeixiang Outcrop and Puguang Gas Field

The maturity of organic matter, which is usually characterized by R_o and/or equivalent R_o (such as the solid bitumen reflectance or graptolite reflectance), is a commonly used method for paleotemperature reconstruction (Mukhopadhyay, 1994; Hackley et al., 2015; Luo et al., 2020b). The maturity evolution of organic matter is an irreversible process and can be characterized by a first-order chemical kinetics reaction. According to the Arrhenius equation, the maturity of organic matter has an exponential relationship with temperature and a linear relationship with time. As a result, temperature is the most important parameter affecting the maturity evolution of organic matter (Hunt, 1996). Theoretically, the MBT can be obtained based on a model of the evolution of the organic matter's maturity with temperature (such as the EASY%R_o model; Sweeney and Burnham, 1990).

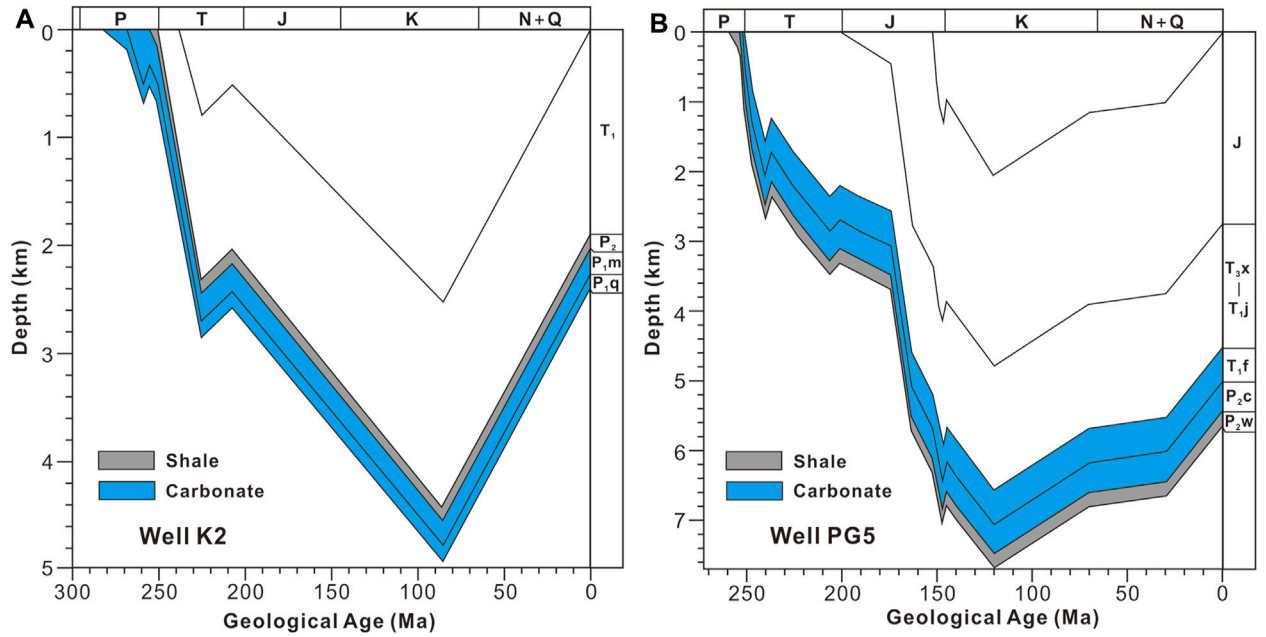

FIGURE 3 | The general burial history of **(A)** well K2 near the Xibeixiang outcrop (modified from Luo et al., 2020a) and **(B)** well PG5 in the Puguang gas field (modified from Hao et al., 2008). P=Permian, T=Triassic, J=Jurassic, K=Cretaceous, N=Neogene, Q=Quaternary.

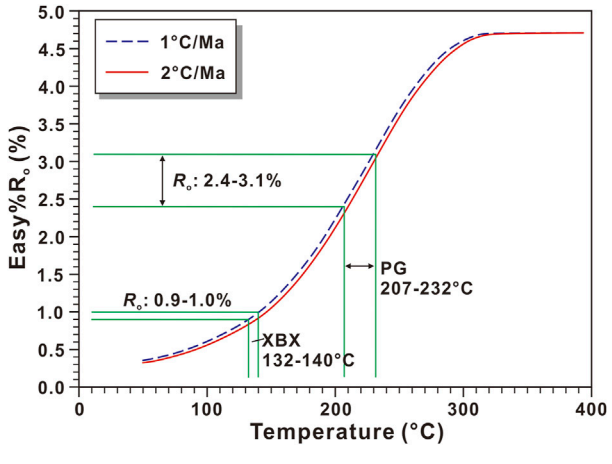

FIGURE 4 | The evolution of the vitrinite reflectance (R_o) vs. temperature based on the Easy%R_o model (Sweeney and Burnham, 1990). Note the maximum burial temperatures of the Permian shale in the Xibeixiang (XBX) outcrop and the Puguang (PG) gas field are 132–140 and 207–232°C, respectively.

The EASY%R_o model is a widely accepted model for the evolution of the maturity of organic matter, and the organic matter maturity (R_o) can be calculated for a given heating rate (Sweeney and Burnham, 1990). According to apatite fission track analysis (Deng et al., 2013), the Permian and Triassic strata in the XBX outcrop and the Puguang gas field reached their maximum burial depths at about 80 and 120 Ma, respectively (**Figure 3**). The area of the XBX outcrop was uplifted in the Late Indosinian (Burchfiel et al., 1995), and the R_o of the Permian shale near the XBX outcrop in the NW Sichuan Basin is <1.3% (Fu et al., 2010), so the MBT of the Permian shale should be less than 160°C (**Figure 4**). A lot of solid bitumen with a relatively high maturity (R_o>1.7%) is commonly present in the Permian and Triassic gas reservoir in the Puguang gas field, suggesting that large scale oil-cracking occurred in this gas field, and the maximum burial temperature may have exceeded 200°C (Hao et al., 2008). In addition, the heat flow has decreased gradually since the Late Permian (Zhu et al., 2016). Thus, the burial temperature of the Permian and Triassic strata in the XBX outcrop and the Puguang gas field should have reached the maximum values when the burial depths reached the maximum values at about 80 and 120 Ma (**Figure 3**), respectively. As a result, the heating rates should be about 1.0°C/Ma (150°C/(260–80 Ma) = 0.83°C/Ma) and 2.0°C/Ma (220°C/(250–120 Ma) = 1.7°C/Ma) for the XBX outcrop and the Puguang gas field, respectively.

The evolution of R_o with temperature based on the EASY%R_o model for heating rates of 1.0 and 2.0°C/Ma is shown in **Figure 4**. According to this model, R_o of the P_2d shale in the XBX outcrop is 0.92–0.96%, so the MBT of the P_2d should be 132–140°C, while R_o of the P_2w shale in the Puguang gas field is 2.39–3.11%, so the MBT of the P_2w should be 207–232°C (**Figure 4**). The thicknesses of the intervals between the P_1q limestone and the P_2d shale in the XBX outcrop and between the P_2c-T_1f dolostone and the P_2w shale in the Puguang gas field are about 300 and 200 m (**Figure 3**), respectively. In addition, the paleotemperature gradient in the Late Cretaceous was about 25°C/km (Zhu et al., 2016). As a result, the MBTs of the P_1q limestone in the XBX outcrop and the P_2c-T_1f dolostone in the Puguang gas field should be 139.5–147.5 and 202–227°C, respectively. The MBT determined using the

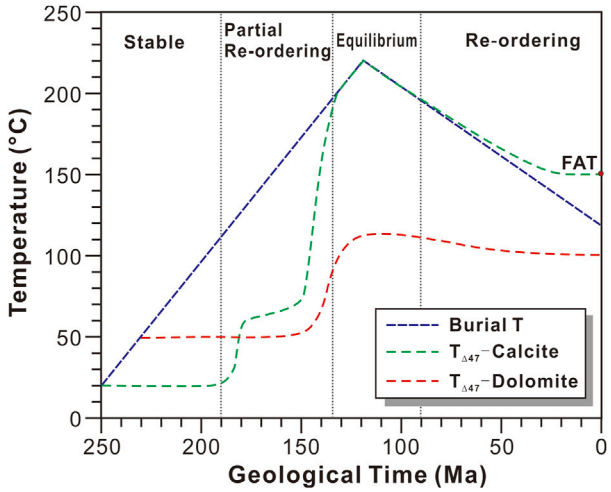

FIGURE 5 | The general clumped isotope temperature ($T_{\Delta47}$) evolution of the P_2c-T_1f dolomite and calcite from the Puguang gas field in the Sichuan Basin, assuming that the maximum burial temperature reached 220°C and then decreased to 110°C during the late uplift event. The solid-state reordering models for calcite and dolomite are from Stolper and Eiler (2015) and Lloyd et al. (2018), respectively. FAT = Final apparent temperature.

EASY%R_o model supplies a basic constraint on the MBT determined using the solid-state reordering model of carbonate clumped isotopes.

Solid-State Reordering of Calcite and Maximum Burial Temperature of P_1q in the Xibeixiang Outcrop

Carbonate clumped isotopes (Δ_{47}) can be used to directly determine the formation temperature or the equilibrium temperature of carbonate minerals, and they are independent of the $\delta^{18}O$ of the fluid from which the carbonate minerals were deposited. This is called the clumped isotope thermometer (Ghosh et al., 2006; Eiler, 2007). The clumped isotope thermometer is mainly based on the exchange reactions of the ^{13}C and ^{18}O in carbonate minerals, and the abundance of ^{13}C-^{18}O in carbonate minerals is a function of temperature (Eiler, 2007). However, the clumped isotope temperature ($T_{\Delta47}$) may be altered by high temperatures and/or recrystallization during the late burial process and can be completely different from the original formation temperature (Passey and Henkes, 2012). Ancient carbonate minerals have usually experienced relatively high temperatures during late burial, which resulted in solid-state exchange (reordering) of the ^{13}C-^{18}O in the carbonate minerals. Consequently, the abundances of ^{13}C-^{18}O in carbonate minerals will differ from the original abundances when the carbonate minerals were formed, and the $T_{\Delta47}$ values should also be different from the original formation temperature of the carbonate minerals. In addition, recrystallization after mineral formation can also change the abundance of ^{13}C-^{18}O and $T_{\Delta47}$ of the carbonate minerals (Ryb and Eiler, 2018). Therefore, for ancient carbonate minerals, the present-day $T_{\Delta47}$ is often the result of the combined effect of recrystallization and solid-state reordering. The solid-state reordering of Δ_{47} can be characterized using a kinetic model, and the MBT of the carbonate minerals can be reconstructed if the carbonate minerals experienced no or limited recrystallization.

There are two main kinetic models for characterizing the solid-state reordering of carbonate minerals: the transient defect/equilibrium defect model (Henkes et al., 2014) and the exchange-diffusion model (Stolper and Eiler, 2015). The best agreement between model predictions and natural dolomite marbles was found when using the exchange-diffusion model (Lloyd et al., 2018). Therefore, the exchange-diffusion model was used to in this study. According to the exchange-diffusion model, the variation of $T_{\Delta47}$ was shown in **Figure 5**, if the Permian-Triassic limestone was formed at about 30°C and reached a maximum temperature of about 220°C at 120 Ma. When the burial temperature was <100°C, no solid-state reordering occurred and $T_{\Delta47}$ of the calcite would be stable. When the burial temperature was between 100 and 200°C, partial solid-state reordering occurred and $T_{\Delta47}$ of the calcite increased as the burial temperature increased. When the burial temperature was >200°C, full solid-state reordering occurred and $T_{\Delta47}$ of the calcite reached equilibrium with the burial temperature. When the burial temperature was <200°C during the late uplift and exhumation, partial solid-state reordering occurred again and $T_{\Delta47}$ of the calcite decreased as the burial temperature decreased. If the burial temperature was decreased from above 200°C to below 150°C during the uplift, $T_{\Delta47}$ of the calcite would have decreased to a blocking temperature (final apparent temperature) of about 175–200°C (Henkes et al., 2014), and it did not decrease as the burial temperature decreased (**Figure 5**). The solid-state reordering of dolomite is similar to that of calcite, but $T_{\Delta47}$ of dolomite is stable when the burial temperature is <150°C, and it does not reach equilibrium with the burial temperature when the burial temperature is <250–300°C (Lloyd et al., 2018).

$T_{\Delta47}$ of the limestone from the XBX outcrop is 62°C on average, which is significantly higher than the seawater temperature (20–30°C) during the deposition of P_1q (Henkes et al., 2018), but is far lower than the blocking temperature after reaching the equilibrium temperature. According to the kinetic model of the solid-state reordering of calcite, it can be inferred that the limestone only underwent partial solid-state reordering, and it did not reach equilibrium. The petrological characteristics of the three bioclastic limestone samples (D1–D3) from the XBX outcrop show that the bioclastics were cemented with micritic calcite, and no obvious recrystallization was observed. Therefore, the $T_{\Delta47}$ values of the present-day limestone samples were mainly affected by the solid-state reordering process. As a result, the solid-state reordering model can be used to reconstruct the MBT of these limestone samples. Based on the solid-state reordering model for the calcite in the XBX outcrop, the relationship between $T_{\Delta47}$ and MBT is shown in **Figure 6**. $T_{\Delta47}$ of the present-day limestone is 62°C, and the corresponding MBT of the XBX limestone is about 139–147°C (**Figure 6**), which is basically consistent with the MBT constrained by the EASY% R_o model (139.5–147.5°C).

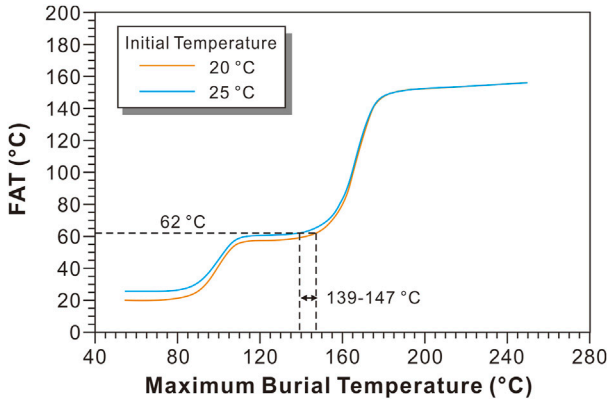

FIGURE 6 | Relationship between the final apparent temperature (FAT) and the maximum burial temperature of the limestone from the Xibeixiang (XBX) outcrop, assuming that the calcite crystalized at 20 and 25°C at 270 Ma using Stolper and Eiler (2015) solid-state reordering model for calcite.

Solid-State Reordering of Dolomite and the Maximum Burial Temperature of the P_2c-T_1f in the Puguang Gas Field

The MBT determined using the EASY%R_o model is >200°C (202–227°C; **Figure 4**), which supports the fact that widespread oil cracking occurred in the Puguang gas field (Hao et al., 2008), while the present-day burial temperature of the P_2c-T_1f is 100–135°C. According to the solid-state reordering model of calcite (**Figure 5**) and the temperature history of the Puguang gas field, the limestone or early-formed calcite cements should have experienced complete solid-state reordering, and the final apparent temperature of the limestone and calcite cement should be similar to the blocking temperature (150–160°C) because the present-day burial temperature is 100–135°C due to the late uplift and exhumation. $T_{\Delta47}$ of the micritic limestone and bioclastic limestone is 150–170°C, which is consistent with the blocking temperature predicted by the solid-state reordering model for calcite. The coarse calcite cements, associated with the solid bitumen and having more negative $\delta^{13}C$ values (−1.108‰ to −0.227‰) than that of its bulk rock (dolostone), are considered to be the product of oil cracking and thermochemical sulfate reduction (TSR) processes (Hao et al., 2008), and they were deposited during the early burial process not during the late uplift and exhumation. $T_{\Delta47}$ of the calcite cements in the Puguang gas field are 145–156.5°C (average of 151.4°C), which is also very close to the blocking temperature of calcite predicted by the model. The small differences in the final apparent temperatures of the limestone and the coarse calcite cements in the Puguang gas field according to the uniform solid-state reordering model may be due to the different kinetic parameters used in the solid-state reordering models of the coarse calcite and micritic limestone, especially during the cooling process. However, no published paper has discussed this problem, and it is not discussed in detail in this paper. However, it is certain that the relatively high temperature (>200°C) in the Puguang gas field resulted in the complete solid-state reordering of the micritic limestone and the coarse calcite cements. Therefore, the micritic limestone and coarse calcite cements cannot be used to reconstruct the MBT in the Puguang gas field.

However, the temperature of the onset of the partial reordering of dolomite is much higher than that of calcite, and the complete solid-state reordering temperature of dolomite can be as high as 250–300°C (Lloyd et al., 2018). As a result, the solid-state reordering of the dolostone samples can be used to reconstruct the MBT in the Puguang gas field. The $T_{\Delta47}$ values of the dolostone with different dolomite crystal sizes from the Puguang gas field are significantly different (**Table 1**). $T_{\Delta47}$ of the micritic dolostone (71.7–72.5°C) is the lowest, followed by $T_{\Delta47}$ of the very finely crystallized dolostone (88.5 ± 5.4°C), but $T_{\Delta47}$ of the two types of dolostone are very close to each other. $T_{\Delta47}$ of the finely crystallized dolostone (126.3 ± 7.6°C) is significantly higher than that of the micritic dolostone and the very finely crystallized dolostone, suggesting that $T_{\Delta47}$ of the finely crystallized dolostone was also affected by relatively strong recrystallization, while the very finely crystallized dolostone only experienced very limited recrystallization.

It is widely accepted that the micritic and very finely crystallized dolostones were caused by penecontemporaneous dolomitization, which occurred under near surface conditions or quite shallow burial conditions. As a result, the initial formation temperatures of the micritic and very finely crystallized dolostones should be similar to the temperature of the coeval seawater. The temperature (30–40°C) in Southern China was lethally hot during the Late Permian-Early Triassic (Sun et al., 2012), so the initial formation temperature of the micritic and very finely crystallized dolostones can be assumed to be 30–40°C. Assuming that the MBT reached 180°C, 200°C, 220°C, and 240°C, the corresponding $T_{\Delta47}$ evolution of the dolostone can be predicted using the solid-state reordering model for dolomite (**Figure 7**). If the MBT reached 180°C, only $T_{\Delta47}$ of the micritic dolostone (D83) and the very finely crystallized dolostone (D89) are within the predicted range (1.0 σ error included; **Figure 7A**), while $T_{\Delta47}$ of the finely crystallized dolostone (D99) is significantly higher than the predicted range. If the MBT reached 200°C or 220°C, only $T_{\Delta47}$ of the very finely crystallized dolostone (D89) is within the predicted range, and $T_{\Delta47}$ of the micritic dolostone and the finely crystallized dolostone (D99) are slightly lower and significantly higher than the predicted range, respectively (**Figures 7B,C**). If the MBT reached 240°C, only $T_{\Delta47}$ of the finely crystallized dolostone (D99) is within the predicted range, and $T_{\Delta47}$ of the micritic dolostone and the very finely crystallized dolostone are lower than the predicted range (**Figure 7D**). As was discussed above, $T_{\Delta47}$ of the limestone and calcite cements were similar to the blocking temperature during the late cooling process, suggesting that the calcite experienced complete solid-state reordering, and the MBT should be >200°C. Combined with the $T_{\Delta47}$ evolution shown in **Figure 6**, the MBT of the P_2c-T_1f in the PG gas field should be 200–220°C, which is similar to the MBT determined using the EASY%R_o model (202–227°C).

Based on the model of the relationship between the final apparent temperature (present-day $T_{\Delta47}$) and the MBT (**Figure 8**), the MBTs determined using the present-day $T_{\Delta47}$ of the micritic dolostone (D83 and D90), the very finely crystallized dolostone (D89), and the finely

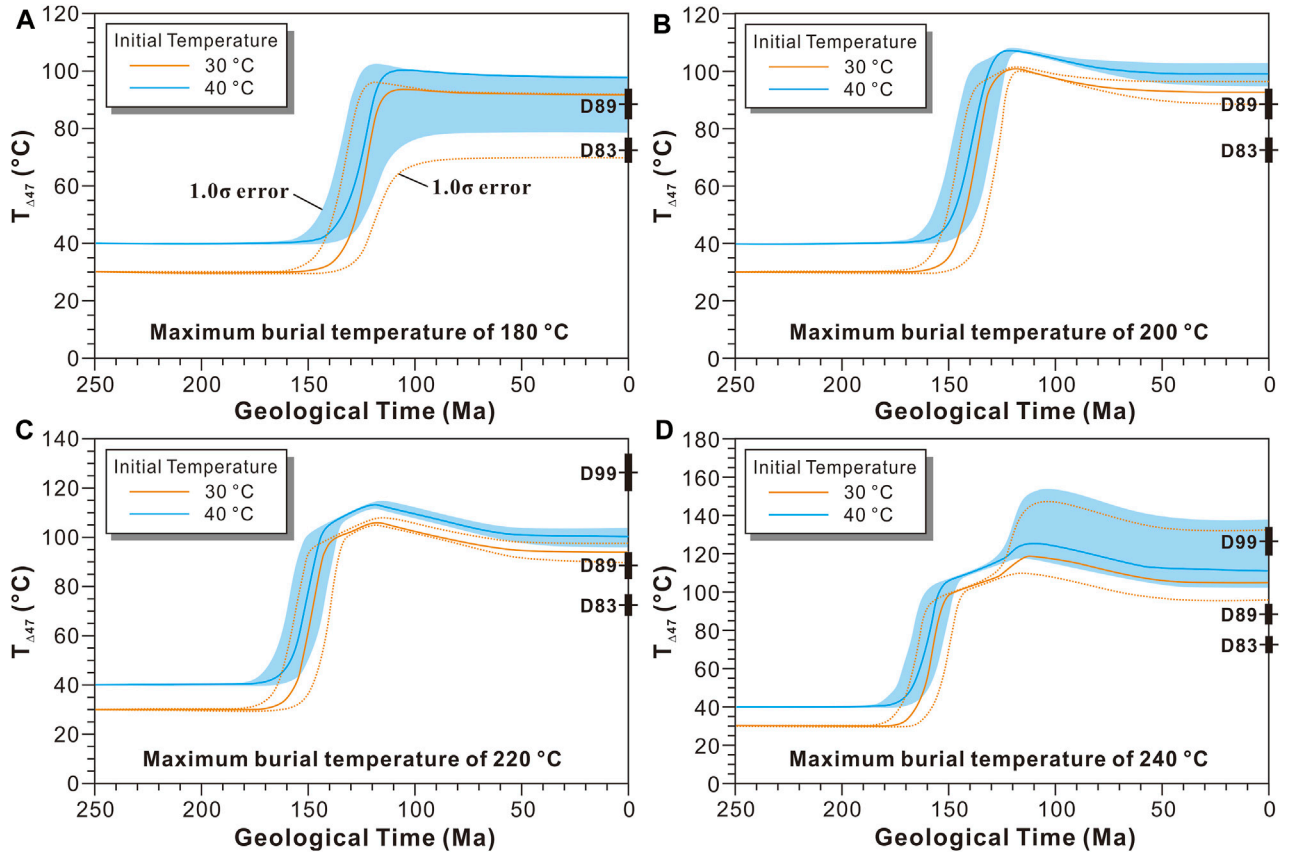

FIGURE 7 | The general clumped isotope temperature ($T_{\Delta47}$) evolution of the dolostone from the Puguang gas field, assuming that the dolomite crystalized at 30 and 40°C at 250 Ma, and the maximum burial temperature reached 180, 200, 220, or 240°C and then decreased to 110°C during the late uplift event. The solid-state reordering model for dolomite is from Lloyd et al. (2018). Note: the D83, D89, and D99 represent dolostone samples, the black horizontal lines and columns in the right side represent the $T_{\Delta47}$ and error bar of the samples D83, D89, and D99.

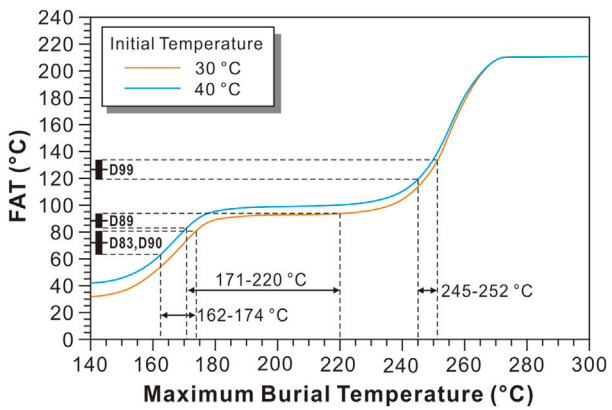

FIGURE 8 | Relationship between the final apparent temperature (FAT) and the maximum burial temperature of the dolostone from the Puguang gas field, assuming that the dolomite crystalized at 30 and 40°C at 250 Ma. The solid-state reordering model for dolomite is from Lloyd et al. (2018).

crystallized dolostone (D99) are 162–174, 171–220, and 245–252°C, respectively. Only the MBT determined using the finely crystallized dolostone falls within the temperature range determined using the EASY%R_o model. The MBT determined using the micritic dolostone is slightly lower than the temperature range determined using the EASY%R_o model. This may be due to the kinetic parameter of the solid-state reordering model for dolomite was constructed based on dolomite with some recrystallization. While the MBT determined using the finely crystallized dolostone is significantly higher than the temperature range determined using the EASY%R_o model, which is most likely due to the occurrence of significant recrystallization. However, the time and temperature at which the recrystallization reached final equilibrium is unknown. Consequently, the present-day $T_{\Delta47}$ of the finely crystallized dolostone cannot be used to determine the MBT. Perhaps U-Pb dating of carbonate can be used to accurately determine the final equilibrium age of the dolostone (Pan et al., 2020), and combined with the general burial and thermal gradient information, it can be used to reconstruct the MBT based on the solid-state reordering model, which is a valuable research direction for future studies.

CONCLUSION

The maximum burial temperature (MBT) of the XBX outcrop and the Puguang gas field was reconstructed using the solid-state

reordering models for calcite and dolomite. The MBTs of the P_1q limestone in the XBX outcrop and the P_2c-T_1f dolostone in the Puguang gas field determined using the solid-state reordering models for calcite and dolomite are 139–147 and 200–220°C, respectively, which are similar to the ranges determined using the EASY%R_o model (139.5–147.5 and 202–227°C, respectively). Based on this study in the Sichuan Basin, the solid-state reordering models for calcite and dolomite provide a new potential method for reconstructing the MBT of ancient carbonate strata with MBTs of <150–200 and 250–300°C, respectively. In particular, the MBT determined using the solid-state reordering model for dolostone with limited crystallization is acceptable, while that of dolostone with obvious crystallization is significantly higher than the actual MBT. In addition, the solid-state reordering kinetic model for micritic dolostone also needs to be further optimized in future research.

DATA AVAILABILITY STATEMENT

The original contributions presented in the study are included in the article/**Supplementary Materials**, further inquiries can be directed to the corresponding author.

AUTHOR CONTRIBUTIONS

PL, Conceptualization, Methodology, Writing-Original Draft; JD, Resources; ZC, Investigation; HZ, Supervision, Funding acquisition.

FUNDING

This study was supported by the Strategic Priority Research Program of the Chinese Academy of Sciences (No. XDA14010306), NSFC Basic Research Program on Deep Petroleum Resource Accumulation and Key Engineering Technologies (U19B6003).

ACKNOWLEDGMENTS

We thank Uri Ryb and Nami Kitchen at Caltech for clumped isotopes measurement.

SUPPLEMENTARY MATERIAL

The Supplementary Material for this article can be found online at: https://www.frontiersin.org/articles/10.3389/feart.2021.759372/full#supplementary-material

REFERENCES

Barker, C. (1990). Calculated Volume and Pressure Changes during the thermal Cracking of Oil to Gas in Reservoirs. *AAPG Bull.* 74, 1254–1261. doi:10.1306/0c9b247f-1710-11d7-8645000102c1865d

Bissell, H. J., and Chilingar, G. V. (1967). "Chapter 4 Classification of Sedimentary Carbonate Rocks," in *Carbonate rocks: Origin, occurrence and classification–Development in sedimentology 9A*. Editors G. V. Chilingar, H. J. Bissell, and R. W. Fairbridge (Amsterdam: Elsevier), 87–168. doi:10.1016/s0070-4571(08)71112-9

Bonifacie, M., Calmels, D., Eiler, J. M., Horita, J., Chaduteau, C., Vasconcelos, C., et al. (2017). Calibration of the Dolomite Clumped Isotope Thermometer from 25 to 350 °C, and Implications for a Universal Calibration for All (Ca, Mg, Fe) CO3 Carbonates. *Geochimica et Cosmochimica Acta* 200, 255–279. doi:10.1016/j.gca.2016.11.028

Burchfiel, B. C., Zhiliang, C., Yupinc, L., and Royden, L. H. (1995). Tectonics of the Longmen Shan and Adjacent Regions, central China. *Int. Geology. Rev.* 37, 661–735. doi:10.1080/00206819509465424

Carlson, W. D. (1990). Mechanisms and Kinetics of Apatite Fission-Track Annealing. *Am. Mineral.* 75, 1120–1139.

Craddock, W. H., and Houseknecht, D. W. (2016). Cretaceous-Cenozoic Burial and Exhumation History of the Chukchi Shelf, Offshore Arctic Alaska. *Bulletin* 100, 63–100. doi:10.1306/09291515010

Deng, B., Liu, S.-g., Li, Z.-w., Jansa, L. F., Liu, S., Wang, G.-z., et al. (2013). Differential Exhumation at Eastern Margin of the Tibetan Plateau, from Apatite Fission-Track Thermochronology. *Tectonophysics* 591, 98–115. doi:10.1016/j.tecto.2012.11.012

Dennis, K. J., Affek, H. P., Passey, B. H., Schrag, D. P., and Eiler, J. M. (2011). Defining an Absolute Reference Frame for 'clumped' Isotope Studies of CO2. *Geochimica et Cosmochimica Acta* 75, 7117–7131. doi:10.1016/j.gca.2011.09.025

Dou, L., Wang, R., Wang, J., Cheng, D., Green, P. F., and Wei, X. (2021). Thermal History Reconstruction from Apatite Fission-Track Analysis and Vitrinite Reflectance Data of the Bongor Basin, the Republic of Chad. *Bulletin* 105, 919–944. doi:10.1306/11182019167

Du, J. H., Xu, C. C., Wang, Z. C., Shen, P., He, H. Q., Yang, Y., et al. (2010). *Natural gas exploration of Permian-Triassic reef & oolite in Sichuan Basin*. Beijing: Petroleum Industry Press, 1–160. (in Chinese).

Ehlers, T. A., and Farley, K. A. (2003). Apatite (U-Th)/He Thermochronometry: Methods and Applications to Problems in Tectonic and Surface Processes. *Earth Planet. Sci. Lett.* 206, 1–14. doi:10.1016/s0012-821x(02)01069-5

Eiler, J. M. (2007). "Clumped-isotope" Geochemistry-The Study of Naturally-Occurring, Multiply-Substituted Isotopologues. *Earth Planet. Sci. Lett.* 262, 309–327. doi:10.1016/j.epsl.2007.08.020

English, K. L., Redfern, J., Corcoran, D. V., English, J. M., and Cherif, R. Y. (2016). Constraining Burial History and Petroleum Charge in Exhumed Basins: New Insights from the Illizi Basin, Algeria. *Bulletin* 100, 623–655. doi:10.1306/12171515067

Fu, X. D., Qin, J. Z., Tenger, and Wang, X. F. (2010). Evaluation on Dalong Formation Source Rock in the north Sichuan Basin. *Pet. Geology. Exp.* 32, 566–571. (in Chinese with English abstract).

Ghosh, P., Adkins, J., Affek, H., Balta, B., Guo, W., Schauble, E. A., et al. (2006). 13C-18O Bonds in Carbonate Minerals: A New Kind of Paleothermometer. *Geochimica et Cosmochimica Acta* 70, 1439–1456. doi:10.1016/j.gca.2005.11.014

Guo, X., Hu, D., Li, Y., Duan, J., Ji, C., and Duan, H. (2018). Discovery and Theoretical and Technical Innovations of Yuanba Gas Field in Sichuan Basin, SW China. *Pet. Exploration Dev.* 45, 15–28. doi:10.1016/s1876-3804(18)30002-8

Hackley, P. C., Araujo, C. V., Borrego, A. G., Bouzinos, A., Cardott, B. J., Cook, A. C., et al. (2015). Standardization of Reflectance Measurements in Dispersed Organic Matter: Results of an Exercise to Improve Interlaboratory Agreement. *Mar. Pet. Geology.* 59, 22–34. doi:10.1016/j.marpetgeo.2014.07.015

Hao, F., Guo, T., Zhu, Y., Cai, X., Zou, H., and Li, P. (2008). Evidence for Multiple Stages of Oil Cracking and Thermochemical Sulfate Reduction in the Puguang Gas Field, Sichuan Basin, China. *Bulletin* 92, 611–637. doi:10.1306/01210807090

Helgeson, H. C., Richard, L., McKenzie, W. F., Norton, D. L., and Schmitt, A. (2009). A Chemical and Thermodynamic Model of Oil Generation in Hydrocarbon Source Rocks. *Geochimica et Cosmochimica Acta* 73, 594–695. doi:10.1016/j.gca.2008.03.004

Hemingway, J. D., and Henkes, G. A. (2021). A Disordered Kinetic Model for Clumped Isotope Bond Reordering in Carbonates. *Earth Planet. Sci. Lett.* 566, 116962. doi:10.1016/j.epsl.2021.116962

Henkes, G. A., Passey, B. H., Grossman, E. L., Shenton, B. J., Pérez-Huerta, A., and Yancey, T. E. (2014). Temperature Limits for Preservation of Primary Calcite Clumped Isotope Paleotemperatures. *Geochimica et Cosmochimica Acta* 139, 362–382. doi:10.1016/j.gca.2014.04.040

Henkes, G. A., Passey, B. H., Grossman, E. L., Shenton, B. J., Yancey, T. E., and Pérez-Huerta, A. (2018). Temperature Evolution and the Oxygen Isotope Composition of Phanerozoic Oceans from Carbonate Clumped Isotope Thermometry. *Earth Planet. Sci. Lett.* 490, 40–50. doi:10.1016/j.epsl.2018.02.001

Héroux, Y., Chagnon, A., and Bertrand, R. (1979). Compilation and Correlation of Major thermal Maturation Indicators. *AAPG Bull.* 63, 2128–2144. doi:10.1306/2f9188f1-16ce-11d7-8645000102c1865d

Hill, R. J., Tang, Y., and Kaplan, I. R. (2003). Insights into Oil Cracking Based on Laboratory Experiments. *Org. Geochem.* 34, 1651–1672. doi:10.1016/s0146-6380(03)00173-6

Hunt, J. M. (1996). *Petroleum Geology and Geochemistry*. 2nd edition. New York: Freeman and Company, 144p.

Huntington, K. W., Eiler, J. M., Affek, H. P., Guo, W., Bonifacie, M., Yeung, L. Y., et al. (2009). Methods and Limitations of 'clumped' CO2isotope (Δ47) Analysis by Gas-Source Isotope Ratio Mass Spectrometry. *J. Mass. Spectrom.* 44 (9), 1318–1329. doi:10.1002/jms.1614

Jacob, H. (1989). Classification, Structure, Genesis and Practical Importance of Natural Solid Oil Bitumen ("migrabitumen"). *Int. J. Coal Geology.* 11, 65–79. doi:10.1016/0166-5162(89)90113-4

Jiang, L., Worden, R. H., Cai, C., Li, K., Xiang, L., Cai, L., et al. (2014). Dolomitization of Gas Reservoirs: The Upper Permian Changxing and Lower Triassic Feixianguan Formations, Northeast Sichuan Basin, China. *J. Sediment. Res.* 84, 792–815. doi:10.2110/jsr.2014.65

Katz, B. J., and Lin, F. (2021). Consideration of the Limitations of thermal Maturity with Respect to Vitrinite Reflectance, Tmax, and Other Proxies. *Bulletin* 105, 695–720. doi:10.1306/09242019261

Kinley, T. J., Cook, L. W., Breyer, J. A., Jarvie, D. M., and Busbey, A. B. (2008). Hydrocarbon Potential of the Barnett Shale (Mississippian), Delaware Basin, West Texas and southeastern New Mexico. *Bulletin* 92, 967–991. doi:10.1306/03240807121

Li, J., Xie, Z., Dai, J., Zhang, S., Zhu, G., and Liu, Z. (2005). Geochemistry and Origin of Sour Gas Accumulations in the Northeastern Sichuan Basin, SW China. *Org. Geochem.* 36, 1703–1716. doi:10.1016/j.orggeochem.2005.08.006

Li, P., Zou, H., Hao, F., Yu, X., Wang, G., and Eiler, J. M. (2020). Using Clumped Isotopes to Determine the Origin of the Middle Permian Qixia Formation Dolostone, NW Sichuan Basin, China. *Mar. Pet. Geology.* 122, 104660. doi:10.1016/j.marpetgeo.2020.104660

Li, P., Zou, H., Yu, X., Hao, F., and Wang, G. (2021). Source of Dolomitizing Fluids and Dolomitization Model of the Upper Permian Changxing and Lower Triassic Feixianguan Formations, NE Sichuan Basin, China. *Mar. Pet. Geology.* 125, 104834. doi:10.1016/j.marpetgeo.2020.104834

Liu, S., Yang, Y., Deng, B., Zhong, Y., Wen, L., Sun, W., et al. (2021). Tectonic Evolution of the Sichuan Basin, Southwest China. *Earth-Science Rev.* 213, 103470. doi:10.1016/j.earscirev.2020.103470

Lloyd, M. K., Ryb, U., and Eiler, J. M. (2018). Experimental Calibration of Clumped Isotope Reordering in Dolomite. *Geochimica et Cosmochimica Acta* 242, 1–20. doi:10.1016/j.gca.2018.08.036

Luo, B., Wen, L., Zhang, Y., Xie, C., Cao, J., Xiao, D., et al. (2020b). Differential Gas Accumulation Process of the Middle Permian Qixia Formation, Northwestern Sichuan Basin. *Oil Gas Geology.* 41, 393–406. (in Chinese with English abstract).

Luo, Q., Fariborz, G., Zhong, N., Wang, Y., Qiu, N., Skovsted, C. B., et al. (2020a). Graptolites as Fossil Geo-Thermometers and Source Material of Hydrocarbons: An Overview of Four Decades of Progress. *Earth-Science Rev.* 200, 103000. doi:10.1016/j.earscirev.2019.103000

Ma, Y., Guo, X., Guo, T., Huang, R., Cai, X., and Li, G. (2007). The Puguang Gas Field: New Giant Discovery in the Mature Sichuan Basin, Southwest China. *Bulletin* 91, 627–643. doi:10.1306/11030606062

Mukhopadhyay, P. K. (1994). "Vitrinite Reflectance as Maturity Parameter," in *Vitrinite reflectance as a maturity parameter: Applications and limitations.* Editors P. K. Mukhopadhyay and W. G. Dow (Washington, DC: American Chemical Society Symposium Series), 570, 1–24. doi:10.1021/bk-1994-0570.ch001

Pan, L., Shen, A., Zhao, J.-x., Hu, A., Hao, Y., Liang, F., et al. (2020). LA-ICP-MS U-Pb Geochronology and Clumped Isotope Constraints on the Formation and Evolution of an Ancient Dolomite Reservoir: The Middle Permian of Northwest Sichuan Basin (SW China). *Sediment. Geology.* 407, 105728. doi:10.1016/j.sedgeo.2020.105728

Passey, B. H., and Henkes, G. A. (2012). Carbonate Clumped Isotope Bond Reordering and Geospeedometry. *Earth Planet. Sci. Lett.* 351-352, 223–236. doi:10.1016/j.epsl.2012.07.021

Qiu, N., Chang, J., Zuo, Y., Wang, J., and Li, H. (2012). Thermal Evolution and Maturation of Lower Paleozoic Source Rocks in the Tarim Basin, Northwest China. *Bulletin* 96, 789–821. doi:10.1306/09071111029

Reiners, P. W. (2005). Zircon (U-Th)/He Thermochronometry. *Rev. Mineralogy Geochem.* 58, 151–179. doi:10.2138/rmg.2005.58.6

Ryb, U., and Eiler, J. M. (2018). Oxygen isotope composition of the Phanerozoic ocean and a possible solution to the dolomite problem. *Proc. Natl. Acad. Sci. USA*, 115, 6602–6607. doi:10.1073/pnas.1719681115

Schmidt, J. S., Menezes, T. R., Souza, I. V. A. F., Spigolon, A. L. D., Pestilho, A. L. S., and Coutinho, L. F. C. (2019). Comments on Empirical Conversion of Solid Bitumen Reflectance for thermal Maturity Evaluation. *Int. J. Coal Geology.* 201, 44–50. doi:10.1016/j.coal.2018.11.012

Stach, E., Mackowsky, M. T., Taylor, G. H., Chandra, D., Teichmuller, M., and Teichmuller, R. (1982). *Stach's text book of coal petrology.* 3rd ed. Stuttgart: Borntraeger, 535.

Stolper, D. A., and Eiler, J. M. (2015). The Kinetics of Solid-State Isotope-Exchange Reactions for Clumped Isotopes: a Study of Inorganic Calcites and Apatites from Natural and Experimental Samples. *Am. J. Sci.* 315, 363–411. doi:10.2475/05.2015.01

Sun, Y., Joachimski, M. M., Wignall, P. B., Yan, C., Chen, Y., Jiang, H., et al. (2012). Lethally Hot Temperatures during the Early Triassic Greenhouse. *Science* 338, 366–370. doi:10.1126/science.1224126

Sweeney, J. J., and Burnham, A. K. (1990). Evaluation of a Simple Model of Vitrinite Reflectance Based on Chemical Kinetics. *Aapg Bull.* 74, 1559–1570.

Wood, D. A. (2018). Kerogen Conversion and thermal Maturity Modelling of Petroleum Generation: Integrated Analysis Applying Relevant Kerogen Kinetics. *Mar. Pet. Geology.* 89, 313–329. doi:10.1016/j.marpetgeo.2017.10.003

Yamada, R., Murakami, M., and Tagami, T. (2007). Statistical Modelling of Annealing Kinetics of Fission Tracks in Zircon; Reassessment of Laboratory Experiments. *Chem. Geology.* 236, 75–91. doi:10.1016/j.chemgeo.2006.09.002

Yu, Y., Li, P., Guo, R., Zhao, Y., Li, S., and Zou, H. (2021). Upwelling-induced Organic Matter Enrichment of the Upper Permian Dalong Formation in the Sichuan Basin, SW China and its Paleoenvironmental Implications. *Palaeogeogr. Palaeoclimatol. Palaeoecol.* 576, 110510. doi:10.1016/j.palaeo.2021.110510

Zhai, G. M. (1989). *Petroleum Geology of China*, Vol. 10. Beijing: Petroleum Industry Press. (in Chinese).

Zhu, C., Hu, S., Qiu, N., Rao, S., and Yuan, Y. (2016). The thermal History of the Sichuan Basin, SW China: Evidence from the Deep Boreholes. *Sci. China Earth Sci.* 59, 70–82. doi:10.1007/s11430-015-5116-4

Zhu, G., Milkov, A. V., Chen, F., Weng, N., Zhang, Z., Yang, H., et al. (2018). Non-cracked Oil in Ultra-deep High-Temperature Reservoirs in the Tarim basin, China. *Mar. Pet. Geology.* 89, 252–262. doi:10.1016/j.marpetgeo.2017.07.019

Zuo, Y., Qiu, N., Zhang, Y., Li, C., Li, J., Guo, Y., et al. (2011). Geothermal Regime and Hydrocarbon Kitchen Evolution of the Offshore Bohai Bay Basin, North China. *Bulletin* 95, 749–769. doi:10.1306/09271010079

Conflict of Interest: JD was employed by SINOPEC Exploration Company.

The remaining authors declare that the research was conducted in the absence of any commercial or financial relationships that could be construed as a potential conflict of interest.

Publisher's Note: All claims expressed in this article are solely those of the authors and do not necessarily represent those of their affiliated organizations, or those of the publisher, the editors and the reviewers. Any product that may be evaluated in this article, or claim that may be made by its manufacturer, is not guaranteed or endorsed by the publisher.

frontiers in Earth Science

ORIGINAL RESEARCH
published: 25 October 2021
doi: 10.3389/feart.2021.765497

Mesozoic Tectono-Thermal Event of the Qinshui Basin, Central North China Craton: Insights From Illite Crystallinity and Vitrinite Reflectance

Runchuan Liu[1,2,3,4], Zhanli Ren[2], Peng Yang[2]*, Huaiyu He[1,3,4], Thomas M. Smith[1,3,4], Wei Guo[1,3,4] and Lin Wu[1,3,4]*

[1]State Key Laboratory of Lithospheric Evolution, Institute of Geology and Geophysics, Chinese Academy of Sciences, Beijing, China, [2]State Key Laboratory of Continental Dynamics, Department of Geology, Northwest University, Xi'an, China, [3]Institutes of Earth Science, Chinese Academy of Sciences, Beijing, China, [4]College of Earth and Planetary Sciences, University of Chinese Academy of Sciences, Beijing, China

The Qinshui Basin is in the Central Orogenic Belt of the North China Craton (NCC), and the production of coalbed methane accounts for 70% of China's total coalbed methane output. Aiming at the unclear dynamic causes of large-scale coalbed methane accumulation in the basin and the unclear response relationship with the destruction of the NCC, we present joint illite crystallinity and vitrinite reflectance study across the Zijin Mountain and Qincan 1 wells of the Qinshui Basin, respectively. Inverse modeling suggested that tectono-thermal events occurred during the Early Cretaceous, associated with the maximum burial depth and heat flow. The maximum paleo-geothermal temperature and gradient reconstruction results recorded at the Carboniferous strata are 180–190°C and 6.5°C/100 m. The denudation thicknesses recorded by illite crystallinity of Zijinshan and the vitrinite reflectance of the Qincan 1 Well are 3,180.63 m and 3,269.32 m, respectively. We propose that the Qinshui Basin was affected by the extensional environment of the NCC, which caused deep lithospheric thinning and magma upwelling, and a tectono-thermal event occurred during the Early Cretaceous in Qinshui Basin. In addition, the accumulation of coalbed methane, triggered by a tectono-thermal event during the Early Cretaceous, is consistent with the early Cretaceous accumulation and mineralization events in the NCC. Overall, our results reflect the subduction event influence of the western Pacific plate into the East Asian continental plate on the tectono-thermal history of the Central Orogenic Belt of the NCC, which is theoretically significant for clarifying the thermal lithospheric thickness and rheological structure of the basin, as well as the evolutionary history of coalbed methane, and the basin response relationship to the destruction of the NCC.

Keywords: Qinshui Basin, North China Craton, Tectono-thermal event, Illite, Basin modeling

OPEN ACCESS

Edited by:
Kai-Jun Zhang,
University of Chinese Academy of Sciences, China

Reviewed by:
Kun Yu,
Chinese Academy of Sciences (CAS), China
Hongjian Zhu,
Yanshan University, China

****Correspondence:***
Zhanli Ren
Renzhanl@nwu.edu.cn
Peng Yang
p.yang@nwu.edu.cn

Specialty section:
This article was submitted to Geochemistry, a section of the journal Frontiers in Earth Science

Received: *27 August 2021*
Accepted: *27 September 2021*
Published: *25 October 2021*

Citation:
Liu R, Ren Z, Yang P, He H, Smith TM, Guo W and Wu L (2021) Mesozoic Tectono-Thermal Event of the Qinshui Basin, Central North China Craton: Insights From Illite Crystallinity and Vitrinite Reflectance. Front. Earth Sci. 9:765497. doi: 10.3389/feart.2021.765497

INTRODUCTION

Structurally, the Qinshui Basin belongs to the Shanxi block in the center of the North China Craton (NCC) (He, 2015; Zhu et al., 2015). It is one of the areas with the most abundant coal resources within the NCC, and the production of coalbed methane ranks first in China. At present, there are about 11,000 coalbed methane wells in the basin, accounting for more than 70% of the total number

of coalbed methane drilling wells in China, making it one of China's most important energy sources (Zhao et al., 2016; Li Z. et al., 2018, Li et al., 2018 R.).

During the late Mesozoic, the NCC has experienced intense transformation and destruction, and the early Cretaceous was a critical period of lithospheric thinning and destruction for the eastern NCC (Li et al., 2012b). Numerous studies, therefore, focused on the spatial distribution of the transformation and of the destruction of the NCC (Zhang et al., 2006; Zhang, 2012; Zhu et al., 2015; Meng et al., 2019; Liu, 2020). Up to now, the timing, the spatial range, the specific process, and the dynamic mechanism of lithospheric thinning and destruction have been investigated (Ying et al., 2011; Zhu et al., 2012, 2014, 2017; Zhu and Xu, 2019; Zhai et al., 2020, 2021a, 2021b). The range of destruction of the NCC is thought to be limited to only the eastern region. However, additional evidence shows that the lithospheric thickness in the central and western parts of the NCC varies greatly (Chen, 2009; Chang et al., 2011; Ling et al., 2017), indicating that the thinning and reformation of the lithospheric mantle also occurred in the central and western NCC, but the influence of destruction event on the Qinshui Basin remains unclear.

Due to the limited spatial distribution of mantle xenoliths and magmatic rocks, the research on lithospheric thinning and the evolution history of the Ordos Basin in the western part of the NCC is limited, and the research on whole strata of the Qinshui Basin in the central part is even weaker. It is still under debate whether there is excessive thinning of lithosphere and cratonic destruction in the central (Qinshui Basin) and western (Ordos Basin) parts of the NCC (SongLin et al., 2011; Zhu et al., 2012; Ling et al., 2017; Xinhui et al., 2017; Liu, 2020). In addition to abnormal changes in the geothermal field, which can to a certain extent reveal the process of deep lithospheric activity, the tectono-thermal history during the Mesozoic and Cenozoic in the basin and the restoration of the paleotemperature field are the keys to recovering the thermal structure of the lithosphere in different periods. In other words, the tectono-thermal history of different parts of the Qinshui Basin needs to be accurately described and compared to improve the understanding of its tectono-thermal history, which is directly related to the generation, migration, and accumulation processes of coal/gas and the evaluation of the mature evolution of the organic matter.

To date, many petroleum geologists have focused on the tectonic uplift history, thermal evolution history, and coalbed methane of the Qinshui basin, suggesting that the Qinshui Basin was affected by the destruction of the NCC, which caused a tectonic thermal event in the basin during the Early Cretaceous, prompting the rapid over-maturation of source rocks and the production of coalbed methane (Ren et al., 2005; Sun et al., 2005; Ren et al., 2006; Sun et al., 2006; Wei et al., 2007; Meng et al., 2015a, 2015b; Sun et al., 2018; Meng et al., 2019; Yu et al., 2020a; Ren et al., 2020). It has been demonstrated by hydrocarbon explorations that a large amount of coalbed methane was preserved in the north and south parts of the basin. All of these past works provide a very important foundation for our research. In addition, the study of both the geothermal field and the thermal structure of the lithosphere is an effective way to examine the deep geodynamics and the evolution of the craton. Strengthening the study of geothermal events in The Qinshui Basin in the Early Cretaceous is not only of great theoretical significance to improve the understanding of the dynamic evolution mechanism of the lithosphere in NCC, but it is also of great practical significance to mineralization research, reservoir-forming, and the exploration of coal, coalbed methane and other mineral resources in the Qinshui Basin of the central NCC. Recently, geologists and industry paid close attention to the dynamic evolution of the lithosphere and its relationship with mineral accumulation (mineralization) in the central and western parts of the NCC.

The purpose of this study is to reveal the tectonic thermal evolution history and its deep mechanism of different strata, and to discuss the response relationship with basin hydrocarbon source generation and the NCC craton destruction, using the paleotemperature scale and a standard basin modeling procedure. Therefore, in this work, an integrated method combining the illite crystallinity, vitrinite reflectivity, and Basin Mod 1D is proposed to improve the understanding of the thermal history of the formation in the central Qinshui basin. For such a purpose, we systematically collected, tested, and analyzed samples from different layers in the central basin, combined with vitrinite reflectance (R_o) data from different layers in Well Qincan 1. Based on our data, we obtained a comprehensive reconstruction of the thermal history of different stratum in the central basin, which is of theoretical significance for clarifying the thermal lithospheric thickness and rheological structure of the basin, as well as the evolution history of coalbed methane, and the basin response relationship to the destruction of the NCC.

GEOLOGICAL SETTING

The intracratonic NCC is located between the Central Asian Orogen Belt (CAOB) and the Central China Orogenic Belt (CCOB), and by convention, the NCC has been subdivided into the West Block, Eastern Block, and the Trans-North China Orogen (Zhao et al., 2009, 2001) (**Figure 1**). Variably exposed Archean to Paleoproterozoic rocks compose the basement of the NCC, it is unconformably overlaid on the Mesoproterozoic unmodified volcano-sedimentary sequence and Phanerozoic caprock (Shanxi, 1989). Archean stratigraphy is represented by strata of the Wutai Group and Huping Group, dominated by Tiebao movement and forms a lithology represented by schist, gneiss, marble, and migmatite, whereas Proterozoic stratigraphy consists of schist, gneiss, sandstone, powder sandstone, and mud shale, from bottom to top. The early Paleozoic strata in the Qinshui Basin are mainly represented by the Cambrian-Middle Ordovician thick carbonate rocks, including argillaceous limestone, oolitic limestone, dolomite, and other huge thick deposits, and a large-scale unconformity denudation event was experienced between the Middle Ordovician and the Early Carboniferous, leading to the absence of the Silurian, Devonian, and part of the Early Carboniferous strata. Late Carboniferous to Early Permian alternate marine and terrestrial sequences, and is

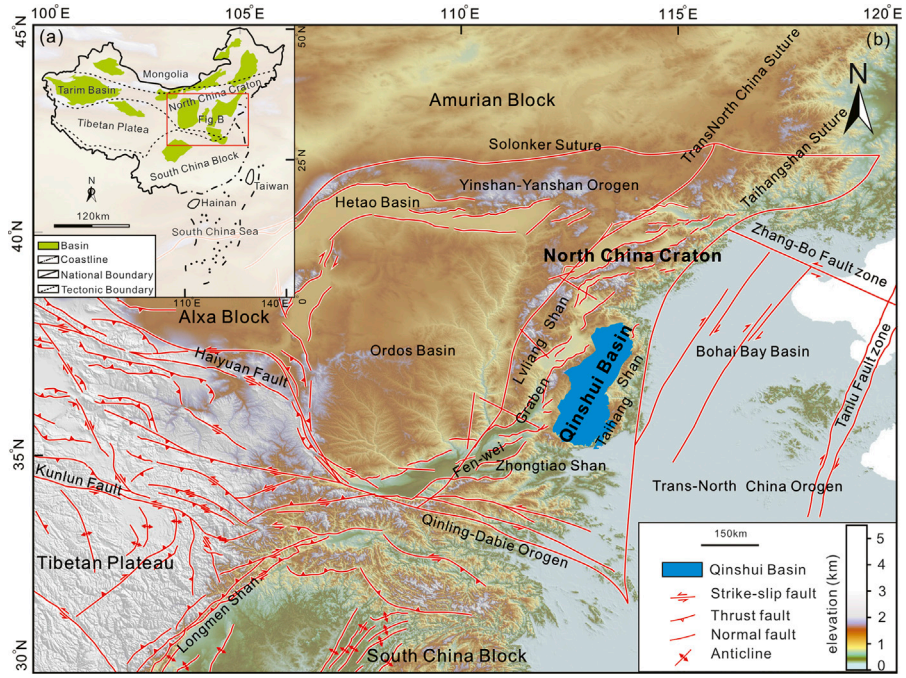

FIGURE 1 | Geological Setting of Qinshui Basin **(A)** Tectonic and basin map of China. Structures are modified from (Yang et al., 2018, 2021a) **(B)** Regional topographic and neotectonic map of North China. Structures are modified from Ye et al. (1987); Deng et al. (1987); Qi and Yang, (2010), Zhang et al. (2019), and Su et al. (2021). Red boxes show the location of the study areas. **(B)** Distribution map of North China Craton and Qinshui Basin.

characterized by coal-bearing strata, overlaid by the Late Permian to Triassic red beds and conglomerates (Shanxi, 1989; Zhu et al., 2014).

The Qinshui Basin is located in the south-central part of the Trans-North China Orogen, surrounded by the Taihang Mountains in the east, the Huo Mountains in the west, the Zhongtiao Mountains in the south, and the Wutai Mountains in the north (Cai et al., 2011) (**Figure 2**). The crust of the study area is relatively thin, and the strata of Paleozoic are widely exposed around the basin while the Mesozoic strata are exposed in the center part of the basin. Besides, the provenance of the strata is extensive, the tectono-thermal history of the Qinshui Basin is complex, and the stratigraphic denudation discontinuity is obvious and its development experienced multi-cyclic tectonic-sedimentary evolution (Cai et al., 2011; Li et al., 2012a; Zhu et al., 2014; Chen et al., 2018). It is an ideal place to study the tectono-thermal history of the south-central NCC during the Paleozoic and Mesozoic (**Figure 1**; **Figure 2**).

SAMPLING AND METHODOLOGY

Sample Collection and Preparation

To investigate the tectono-thermal history and denudation thickness of the Qinshui Basin, we collected the vitrinite reflectance data of the Qincan 1 well from PetroChina Huabei Oilfield Company, the vitrinite reflectance was tested with the same methods as described in Yu et al. (2020a) (Table 3); note that the abnormal high reflectance of vitrinite near the unconformity of the Carboniferous and Ordovician strata has been eliminated.

We also collected mudstones and shale stones from the western edge of the basin to the center of the basin to purify illite (**Figures 2**, **3**). We sampled unaltered outcrops of fresh rocks in the elevated area to maximize the relief wherever lithology and access were permitted. All samples collected in this work are Permian–Jurassic mudstones at an elevation ranging from 956 to 1,680 m (**Supplementary Table S1**; **Figure 2**). All the samples were analyzed for XRF to calculate the illite crystallinity and relative content of clay minerals and analyzed at the Exploration and Development Research Institute of Daqing Oilfield (China National Petroleum Corporation), China.

Scanning Electron Microscopy Analysis

Polished thin sections were made from representative samples for microscopic observation. To further identify the clay minerals and composition of the illite structure, scanning electron microscopy (SEM) observations and energy dispersive spectrometry (EDS) analyses were carried out with an acceleration voltage of 15 kV and a working distance of 10 cm at the Electron Microprobe Analysis and Scanning Electron Microscope Laboratory of the Institute of Geology and Geophysics, Chinese Academy of Sciences (IGGCAS). To obtain high-quality images, the polished samples were coated with 8 nm carbon before analysis.

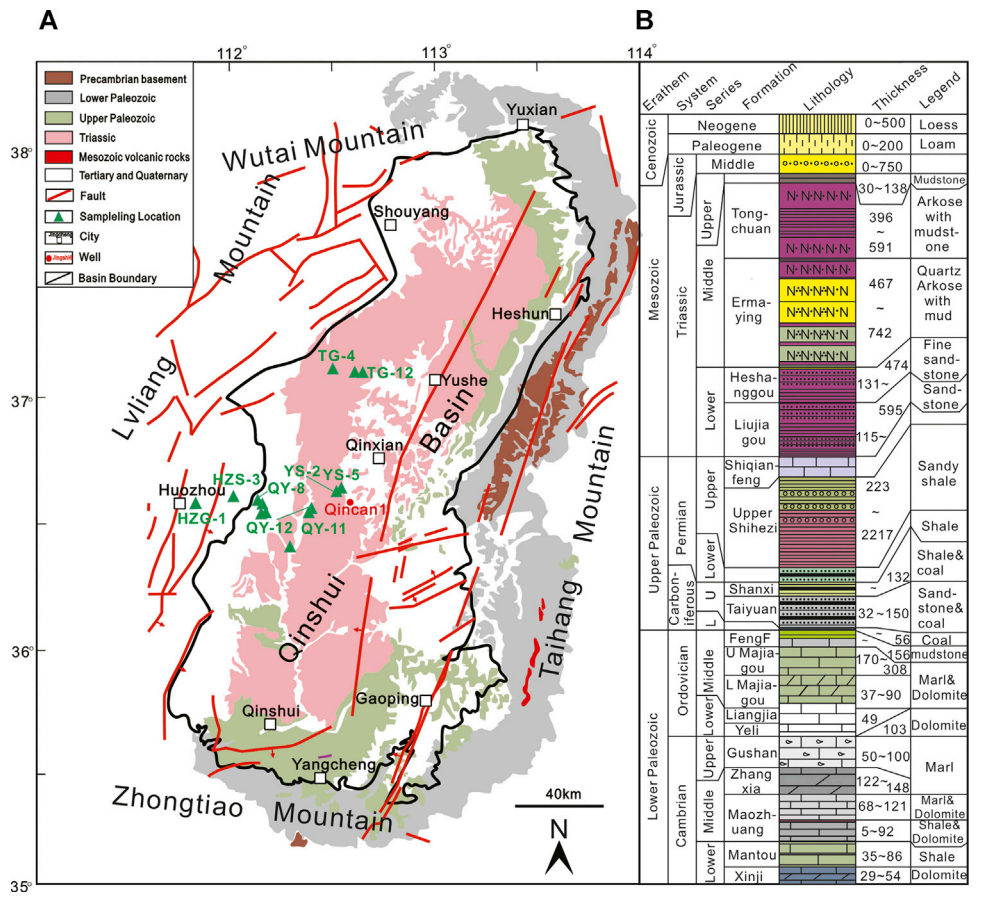

FIGURE 2 | (A) Sample location in Qinshui Basin, includes crack, well location, and city location. Structures modified from Meng et al. (2015), Zhu et al. (2014). **(B)** Regional stratigraphy column of the Cambrian-Cenozoic strata in the Qinshui Basin (Shanxi, 1989; Zhu, 2013; Zhu et al., 2014; Li Z. et al., 2018; Liu, 2020).

XRD Analysis

To achieve illite XRD analysis tests, the mudstone, siltstone, and calcareous mudstone samples needed to be ~150 g with more than 40% clay content. We chose clay-rich samples (argillaceous siltstone, silty mudstone, mudstone, etc.,.) and crushed them to the diameter of 0.5–1 cm with a hammer; we subsequently used a DF-4 hammer crusher to crush the samples for less than 30 s. We used the Stock method to collect 40 mg of particles having diameter <2 μm and removed the liquid in suspension using an LXJ-64-1 centrifuge (Kisch, 1987; H.J.; Kisch, 1990).

We prepared the Oriented Clay Tablets by Precipitation Method with density >3 mg/cm^2 and dried the tablets naturally at room temperature (Kisch, 1987; H.J.; Kisch, 1990). We carried out the ethylene glycol expansion experiment at 50°C, then according to the clay minerals contained in the sample, we heated the sample at 500°C, the precision on the temperature of the muffle furnace used for heating is ±2°C. The experimental instrument is the Rigaku D/max-2200X diffractometer, with the following measurement parameters: 40 kV voltage, 40 mA current, Cu target, 1/2° emitting slit, 5.5 mm receiving slit, 0.04° Soller slit, scanning step length of 0.017°Δ2θ, and scan time of the 20 s by X' Celerator detector. The scanning range for mineral phase and polytype identification is 4–60°Δ2θ. The test range of crystallinity of illite and chlorite for oriented flake is 2.6–15°Δ2θ.

RESULTS

Clay Mineral Assemblage

Through the X-ray diffraction analysis of the sample, we can determine the dominant authigenic clay mineral assemblages in each stratigraphic unit (**Supplementary Table S2**). The clay minerals in the Triassic, Jurassic, Permian, and Cambrian strata in the central area of the Qinshui Basin are dominated by illite, and the combination of clay minerals is I + C + K. The interlayer ratio of I/S disorder is high, and illite accounts for 70–90%. The clay mineral assemblage in the Carboniferous strata is dominated by kaolinite, and the clay mineral assemblage is I + C + K with the high interlayer ratio of I/S disorder, and illite accounts for 80–90% (**Figure 4**; **Figure 5A**).

According to **Figure 5**, there is a high illite content in each layer, most samples account for 50–80% of the total content of clay minerals (**Figure 5A**), and the illite proportion in the shallow layer is higher than that the deep layer (**Figure 5B**), which may be caused by the sample difference. Kaolinite and the I/S mixed layer account for less than 30% of clay minerals. As the burial depth increases, kaolinite will turn into chlorite when the medium changes from acidic to alkaline (Gao et al., 2020; Zhu et al., 2021). The I/S trend of different layers stays stable, but the proportion of illite is high, indicating the high TTI (Time-Temperature Indicator) of the

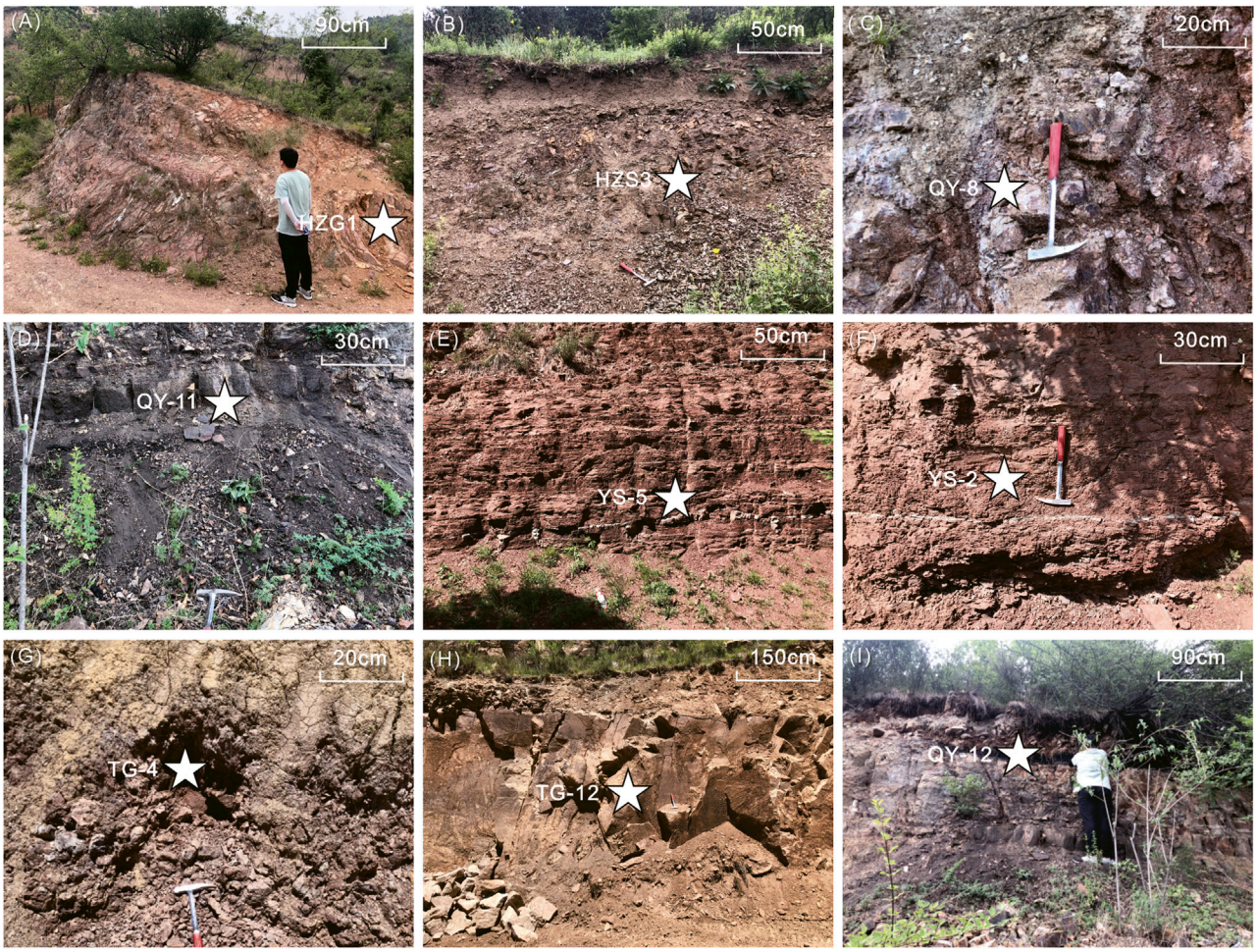

FIGURE 3 | Geological profile of the Qinshui Basin. **(A)** Dark purple red shale of Guanjiashan, Guanjialiang village, Huozhou **(B)** Cambrian Mantou formation shale in East Qiliyu village, Huozhou **(C)** Maroon ferruginous claystone of the Carboniferous Hutian section, Huozhou **(D)** Gray black mud shale of the Shihezi Formation in Donggou, Qinyuan **(E)** Purple-red mudstone in the Triassic Heshanggou formation, Qinyuan **(F)** Sandy mudstone in the Triassic Liujiagou formation, Qinyuan **(G)** Fuchsia mudstone of the Jurassic Ruqu formation, Zijinshan **(H)** Hujiacun Stage of Yanchang Formation, Zijinshan **(I)** Gray-black silty mudstone of the Permian Shihezi 1-2 Formation, Qinyuan.

study area (**Figure 5B**) (Ramseyer and Boles, 1986). The distribution of clay mineral content shows that the basin has experienced a high paleogeothermal evolution process.

Through SEM observation (**Figure 6** and Supplementary Material), except for the upper Paleozoic Carboniferous Hutian section, the interlayer illite of mudstone and sandy mudstone in other layers is the main clay mineral of most samples. Illite associated with illite/smectite (I/S) and illite without I/S can be observed in different horizons, we can identify illite in four forms according to microstructure: ①. Strip illite associated with I/S (**Figure 6A**). ②. Feather and filamentous illite associated with I/S (**Figure 6D**). ③. Feather and Bridge illite (**Figure 6E**). ④. Rosette illite (**Figure 6I**).

The illite energy spectrum is characterized by Al/Si ratio is close to 0.8 and high K content, and the main elements are O, Al, Si, and K, and the K/Al ratio is close to 0.4 (Uysal, 2000; Uysal et al., 2000, 2001, 2006; Zhu et al., 2021). I/S (R = 3) mainly appears in the form of cotton floc (**Figures 6A,G**), and its energy spectrum is characterized by K/Ca content close to 0.5 and Al/Si ratio close to 0.5 (More details in the Supplementary material). Chlorite mainly occurs in the Shihezi Formation of Upper Paleozoic and Heshanggou formation of Lower Triassic of Mesozoic. Leaf-like (**Figure 6C**) and needle/layered liked chlorite can be observed, and its energy spectrum is characterized by high Fe content, and the Fe/Si ratio is greater than 0.5 (**Figure 6F**). Kaolinite is mainly observed in the maroon iron clay rock of the upper series of the Hutian section of the Carboniferous in the upper Paleozoic, and it is hard to find kaolinite in the other horizons, which is in the form of vermicular porous (**Figure 6B**), and its energy spectrum characteristics show that the elements only contain O, Al, and Si, with Si/O ~1, the Si/Al ~0.8 (More details in the Supplementary material). It can be observed that kaolinite rarely contains other clay mineral components (Uysal, 2000; Uysal et al., 2000, 2001, 2006; Zhu et al., 2021).

In the SEM experimental observation, it is obvious that illite is the main component of sandstone interlayer clay minerals, and the other clay mineral components are relatively rare, indicating that the higher paleogeothermal temperature is conducive to the formation of illite in the process of basin evolution. Illite associated with I/S

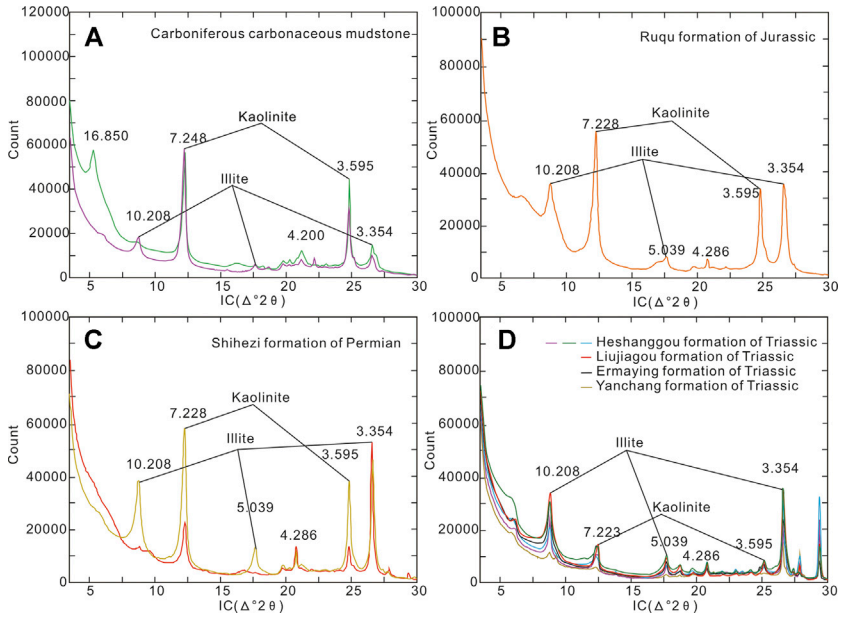

FIGURE 4 | X-ray diffraction of illite in central Qinshui Basin. **(A)** Carboniferous carbonaceous mudstone. **(B)** Ruqu formation of Jurassic sample. **(C)** Shihezi formation of Permian sample. **(D)** Triassic formation sample.

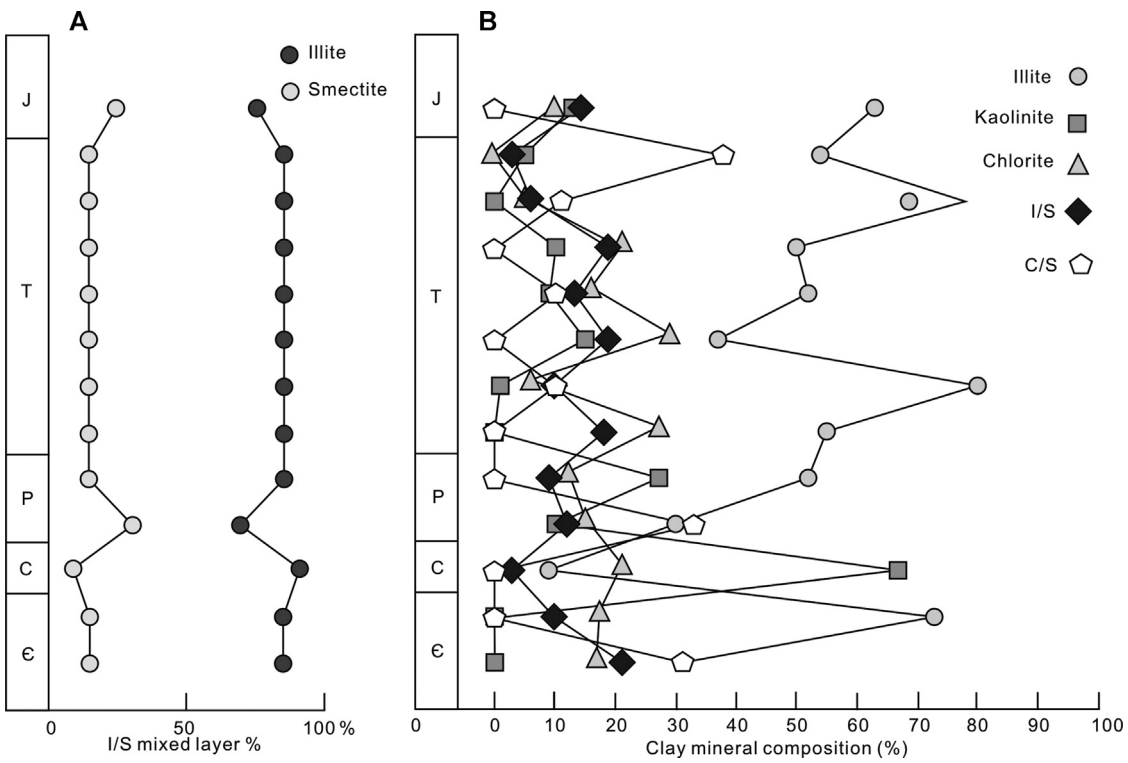

FIGURE 5 | Distribution of crystallinity and clay minerals map **(A)** Illite content and stratum change diagram in I/S layer **(B)** Clay mineral and stratum distribution diagram.

may be authigenic illite, but it may be affected by grinding flakes resulting in the formation of imperfect plates. However, it can be seen that many illite crystals growing alone have good crystal forms, showing rose and feather crystal forms (**Figure 6I**). Generally, illite with good crystal form represents the authigenic illite, but the crystalline morphology of terrigenous clastic illite is generally poor and is easy to be damaged in the process of long-distance transportation.

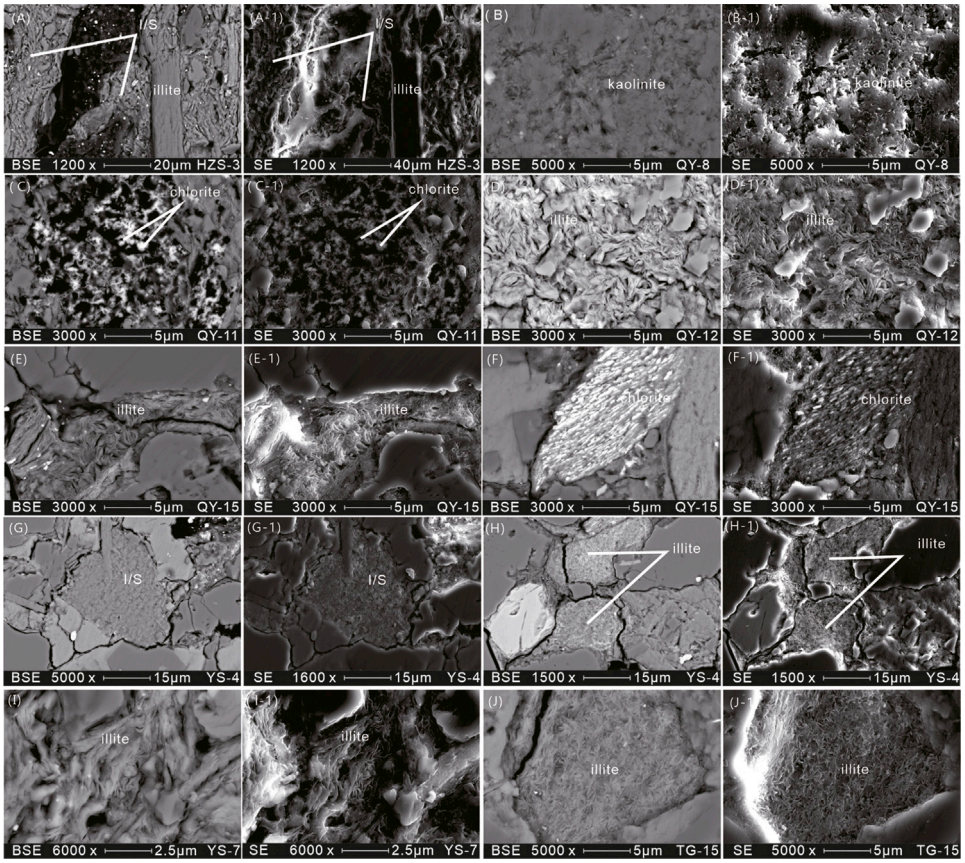

FIGURE 6 | The "**(A)**" represents BSE section photomicrographs and "(**A**-1)" represents SE section photomicrographs, which are the same structure, and so are other pictures. **(A)** and (**A**-1) illustrating textural features of cotton wadded I-S (R = 3) and strip illite in Cambrian mudstone (HZS-3). **(B)** and (**B**-1) illustrating textural features of vermicular porous kaolinite in maroon iron clay rock of the Carboniferous Hutian section (QY-8). **(C)** and (**C**-1) illustrating textural features of blade chlorite in Grayish black mud shale of the upper Paleozoic Shihezi Formation (QY-11). **(D)** and (-1) illustrating textural features of feathery and filamentous illite in Grayish black silty mudstone of the upper Paleozoic Shihezi Formation (QY-12). **(E)** and (-1) illustrating textural features of feathery and bridged illite in the purple-red mudstone of Lower Triassic Heshanggou Formation of Mesozoic (QY-15). **(F)** and (-1) illustrating textural features of needle-shaped and laminated chlorite in the purple-red mudstone of Lower Triassic Heshanggou Formation of Mesozoic (QY-15). **(G)** and (-1) illustrating textural features of cotton wadded I/S (R = 3) in mudstone of the Lower Triassic Heshanggou Formation of Mesozoic (YS-4). **(H)** and (-1) illustrating textural features of ribbon-packed, strip-shaped illite in mudstone of the Lower Triassic Heshanggou Formation of Mesozoic (YS-4). **(I)** and (-1) illustrating textural features of roseate illite in purple mudstone of the Middle Triassic Ermaying Formation of Mesozoic (YS-7). **(J)** and (-1) illustrating textural features of filamentous and feathery illite in purple mudstone of the Upper Triassic Yanchang Formation of Mesozoic (TG-15).

Paleotemperature Restoration

Paleotemperature Restored by Vitrinite Reflectance

The vitrinite reflectance of the Qincan 1 well is between 1.0 and 2.5% at the range of 500–1,000 m depth (**Supplementary Table S3**). The evolution degree of organic matter belongs to high maturity or over-maturity, combined with low current geothermal gradient, indicating that the basin has experienced high paleotemperature.

Based on the strong correlation between vitrinite reflectance and maximum paleotemperature, the maximum paleotemperature that the stratum experienced can be calculated (Barker et al., 2016; Yang et al., 2017a, 2020). According to the relationship between the maximum paleotemperature and the burial depth, we can determine the paleo-gradient, the relationship between ln (R_o) and T_{max}/°C is calculated as follows:

$$\ln(Ro) = 0.0096T_{max} - 1.4$$

According to this formula, the relationship between the maximum paleotemperature and depth of the Qincan 1 well in the central part of the Qinshui Basin can be obtained (**Supplementary Table S3**; **Figure 7**).

According to Vitrinite reflectance data from the Qincan 1 well, we calculated the maximum paleotemperature gradient to be 6.5°C/100 m, however, the current geothermal gradient of the Qincan 1 well is 2.4°C/100 m, which means the paleotemperature gradient is significantly higher than the current geothermal gradient (**Figure 7**).

Paleotemperature Restored by Illite Crystallinity

We tested the illite crystallinity of mudstone samples from Permian to Triassic, which we also calibrated with international standard samples.

According to **Supplementary Table S1**, we observed a correlation between the age of the stratum and the altitude; when altitude decreases and formation ages get older, the illite crystallinity of outcropping samples in the field gradually decreases, implying that the paleotemperature gradually increases. Therefore, there is a strong correlation between the

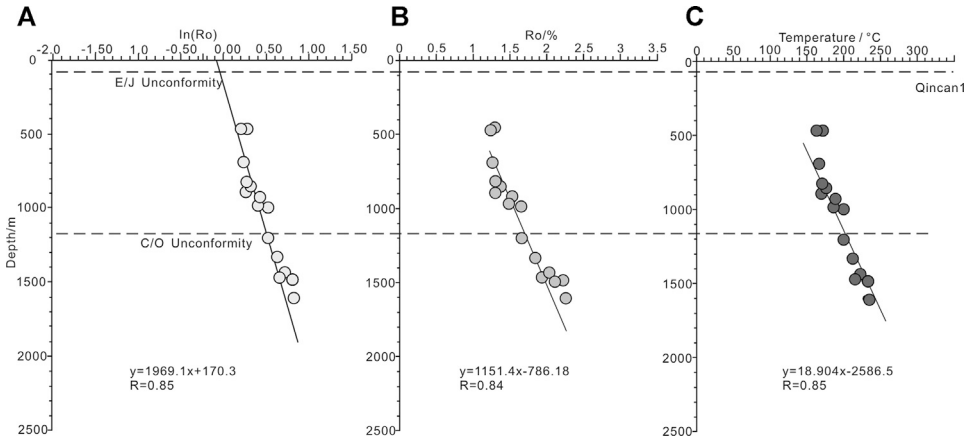

FIGURE 7 | Vitrinite reflectance (R_o) and depth map. **(A)**The relationship between ln (R_o) and depth of Qincan 1. **(B)** The relationship between Ro and depth of Qincan 1. **(C)** Maximum palegeotemperature of Qincan 1 well in central basin reverted by Ro.

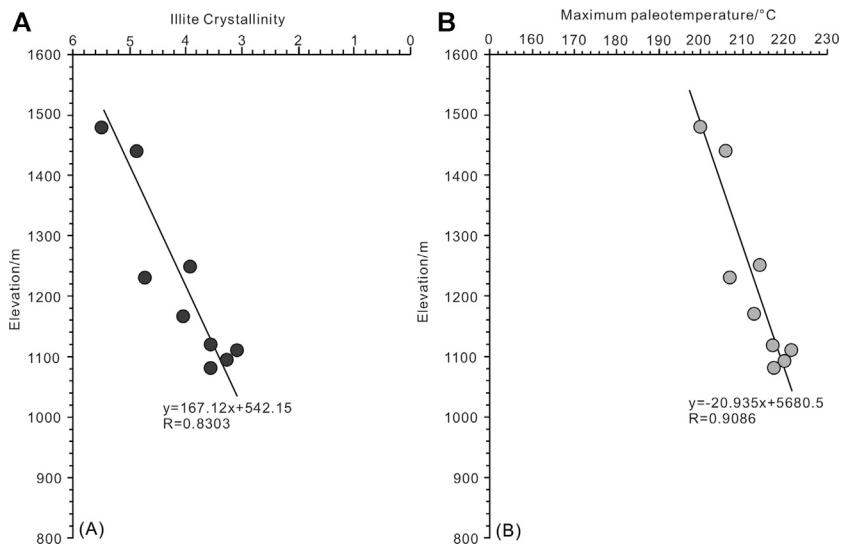

FIGURE 8 | Illite crystallinity, Illite crystallinity inversion of maximum paleotemperature and elevation map **(A)** Illite crystallinity and elevation map in central Qinshui Basin. **(B)** Maximum paleotemperature inverted by Illite crystallinity in central Qinshui Basin.

sampling altitude and the maximum paleotemperature calculated by illite crystallinity (**Figure 8**).

The characteristics of illite crystallinity of mudstone in the central Qinshui Basin decrease from top to bottom, indicating that the basin and surrounding orogenic belt were continuously uplifted and denuded to deeper and higher metamorphic degrees after the Late Triassic. For some of the samples, illite crystallinity is between 0.25 and 0.42°, it belongs to low-grade metamorphism, reflecting the characteristics of illite of denuded Precambrian metamorphic around the basin. Combined with the high content of illite in the I/S mixed layer (**Figure 5A**) and moderate contents of kaolinite in the clay minerals (**Figure 5B**), this indicated that the clay minerals in the mudstone were affected by a high-temperature geothermal field.

Illite/smectite (I/S) mixed-layer minerals are the most widely distributed mixed-layer clay minerals in sedimentary rocks. It is produced due to the mixing of the two terminal elements of illite and smectite in different proportions. Experimental studies have confirmed that when the temperature or depth increases, the proportion of the illite layer in the I/S layer gradually increases (Ramseyer and Boles, 1986). This is associated with the gradual transformation of the mixed layer from a disordered to an ordered structure. The degree of order of various types of I/S layer mineral structure and its existence temperature ranges are respectively (Harvey and Browne, 1991; M, 1993):

R = 0 type, R_0 I/S, illite content <60%, stable temperature <140°C; R = 1 type, R_1 I/S, illite content 60–85%, stable temperature 100–180°C; R = 3 type, R_3 I/S, illite content >85%, stable temperature >190°C; The relationship between

the crystallinity of illite and its formation temperature has already been established in previous studies from Ji (2000). Our work relies on these results to calculate the formation temperature of authigenic illite. The relationship between the crystallinity of authigenic illite (IC/°) and its formation temperature (T/°C) is as follows:

$$T = 384.98e - 0.6219 \times IC$$

To use crystallinity of illite minerals (including I/S minerals), recovery paleotemperatures, and stratum denudation depths, we considered the distribution of outcrop strata and studied two sections, the paleo-geothermal temperature of illite crystallinity recovery is between 200 and 220 °C (**Supplementary Table S1**); overall, the temperature increases with the age of the stratum, and decreases with the sample elevation.

Erosion Thickness Restoration

Erosion Thickness Restored by Vitrinite Reflectance

With the increase of burial temperature, the degree of the thermal evolution of organic matter gradually increases, and the value of vitrinite reflectance (R_o) increases. However, the thermal evolution process of vitrinite reflectance is irreversible; in other words, when a formation is uplifted and cooled, the Vitrinite reflectance value will not decrease as the temperature decreases. Therefore, through a certain conversion relationship (Barker and Pawlewicz, 1986), it is possible to restore the highest ancient geothermal temperature reached in the geological period recorded by vitrinite reflectance. Based on the vitrinite reflectance distributed in the upper and lower structural layers of the unconformity, Dow (1977) used a different method to estimate the denudation thickness of a certain period for a formation. The application of the vitrinite reflectance difference method in the research fields of basin subsidence history, tectonic evolution history, or tectono-thermal evolution history, has shortcomings, as explained by several authors (Chen et al., 1999; Hu et al., 1999; Tong et al., 2005; Tong and Zhu, 2006), who made reasonable improvements, which we as describe below.

Hu et al. (1999) pointed out that the method proposed by Dow (1977) to directly estimate the uplift scale and denudation amount of strata by using the Vitrinite reflectance data above and below the unconformity surface lacks theoretical basis, and the results obtained by this method does not correspond to the represented denudation thickness but is equivalent to the loss amount of strata caused by normal fault dislocation. Chen et al. (1999) considered that the effect of reburial on the vitrinite reflectance distributed above and below the unconformity surface is different, and considered that in the early stage of reburial, the vitrinite reflectance in the upper part of the unconformity surface changes greatly, while that in the lower part of the unconformity surface it changes less. When the reburial process reaches a certain extent, the difference between the vitrinite reflectance above and below the unconformity surface will become smaller and smaller, even unable to be distinguished, which brings some difficulties to estimating the denudation thickness by using the alternate method by Dow (1977). Therefore, Chen et al. (1999) proposed a vitrinite reflectance method based on the Dow (1977) method to restore the denudation thickness. Based on the theory of Dow (1977), Chen et al. (1999), Tong et al. (2005), and Tong and Zhu. (2006) further developed the maximum paleotemperature method which links the denudation thickness and Vitrinite reflectance value. First, this new method has the advantage of being similar in the determination of the highest paleotemperature, and second, it has a simple calculation process. We reconstructed the denudation thickness by using the vitrinite reflectance distributed in the underlying stratum of the unconformity. Based on vitrinite reflectance, we also established a linear regression relationship between Vitrinite reflectance and the depth, and by extrapolating it to ln (0.2) = 1.61, we obtained the approximate paleo-surface elevation. The elevation difference between the paleo-surface and unconformity is the denudation thickness of the formation. Through this method, we estimated the denudation thickness of Jurassic formation in the Qincan 1 well to be ~3,269 m (**Figure 9**).

Erosion Thickness Restored by Illite Crystallinity

The principle of using paleogeotemperature and paleotemperature gradient to estimate the denudation thickness of the formation is similar to the calculation of the denudation thickness by vitrinite reflectance, both being based on the difference between paleo-surface and current surface. Additionally, we can use the diversity of the paleotemperature and the current temperature for a similar depth to reconstruct the denudation thickness (**Figure 9**). Firstly, we should calculate the paleo-gradient using both paleotemperature and depth data (**Supplementary Table S1**; **Figure 9**). Concerning heat balance basin (the paleo-gradient is similar to the current gradient), we use the difference between paleogeotemperature and the current temperature at denudation surface or stratum interface to calculate the denudation thickness by the relationship between geotemperature and depth (Dow, 1977). For our purposes, we should first apply heat balance correction for the heat imbalance basin, in other words, we should subtract the temperature drop caused by the nature of the basin, cooling from paleogeotemperature to the current geotemperature, and then calculate the ablation thickness based on geotemperature difference between paleogeotemperature and current geotemperature at the denudation surface (Dow, 1977). Here, the ablation thickness represents the height difference between ancient and present surfaces (**Figure 9**).

Such corrections, as described above, must be applied in the case of the Qinshui Basin, an imbalance basin, since the paleotemperature gradient is much higher than the present gradient. Therefore, we use the paleotemperature data (**Supplementary Table S1**) which was calculated by illite crystallinity from mudstone in the Zijinshan mountain section, and by extrapolation on the graph of temperature vs depth, we obtain the trend line of paleotemperature gradient (**Figure 8**). By comparing the current geotemperature gradient with heat balance correction, we calculate an erosion thickness of ~3181 m (**Figure 9**).

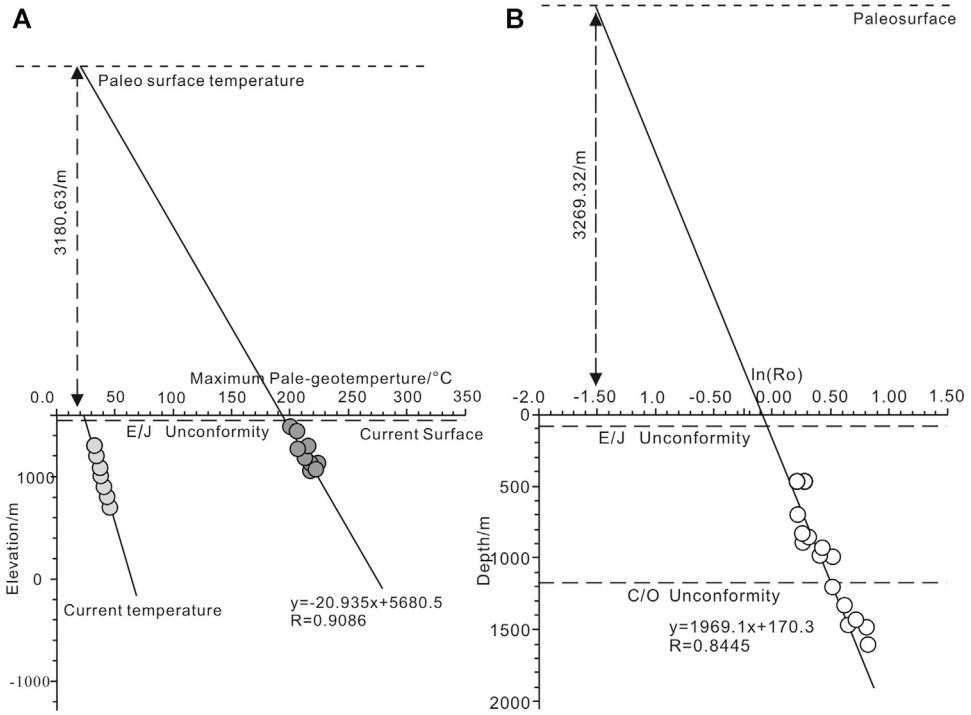

FIGURE 9 | Denudation thickness of central Qinshui Basin **(A)** Denudation thickness restored by illite crystallinity. **(B)** Denudation thickness of Qincan 1 well restored by ln (R_o).

Burial History and Tectono-Thermal History Restoration

Based on the reconstruction of the maximum paleotemperature of the basin, the tectono-thermal history of well Qincan 1 was simulated by the software Basin Mod 1D (**Figure 10**). The software includes several models, such as burial history, tectono-thermal history, hydrocarbon generation history, migration, and accumulation history. In this study, we mainly use the Basin Mod 1D module to simulate the burial history and tectono-thermal history of the Qinshui basin.

Firstly, the relationship between vitrinite reflectance and depth is used to calculate the denudation thickness since the Early Cretaceous thermal event (**Figure 9**), estimated at 3,269.32 m. Secondly, combined with geological parameters such as stratum stratification data of the Qincan 1 well and the geological background in the middle of Qinshui Basin, the burial history curve of the Qincan 1 well is established. According to the apatite fission-track (AFT) study results (Zhu et al., 2014), the AFT data (Zhu, 2013) reflect the uplift process since the Early Cretaceous. Finally, by adjusting the amount of strata denudation and geothermal gradient, the simulated Vitrinite reflectance should be consistent with the measured Vitrinite reflectance, and the accurate tectono-thermal history evolution path can be obtained.

From **Figure 10**, it appears clear that the change of geothermal flow can be divided into two stages. The first stage is characterized by a large geothermal flow of ~68 Mw/m^2, in the Early Carboniferous, and slowly decreasing to 60 mW/m^2 in the Late Triassic; the second stage corresponds to a geothermal flow gradually rising, reaching a peak value of 84.8 mW/m^2 in the Early Cretaceous, and then decreasing to 61.69 mW/m^2 at the present-day.

According to simulations, the evolution of the paleogeotemperature gradient is also divided into two stages. The first stage, from the Early Carboniferous to the Late Triassic, is relatively stable at 2.9°C/100 m, and a second stage, taking place after the Late Triassic, where the paleogeotemperature gradient increased to a maximum value of 6.51°C/100 m during the Early Cretaceous (**Figure 10**). According to the burial history (**Figure 10**), the basin reached its maximum depth at the Early-Middle Cretaceous, and gradually uplifted from the Middle-Late Cretaceous. The relationship between the simulated vitrinite reflectance curve and the measured vitrinite reflectance curve fit well, indicating that the tectono-thermal history recovery is reliable.

DISCUSSION

Separation of Illite

If the separation of illite is not so pure, the determined value of the crystallinity of illite may include some bias due to the presence of detrital illite. Detrital illite refers here to terrigenous illite detritus deposited concomitantly with sediments, mainly from metamorphic illite originating from the study area. Consequently, the paleo-geotemperature reflected by the crystallinity of illite may not reflect the paleo-geotemperature of the source strata, but the provenance. Therefore, the separation and

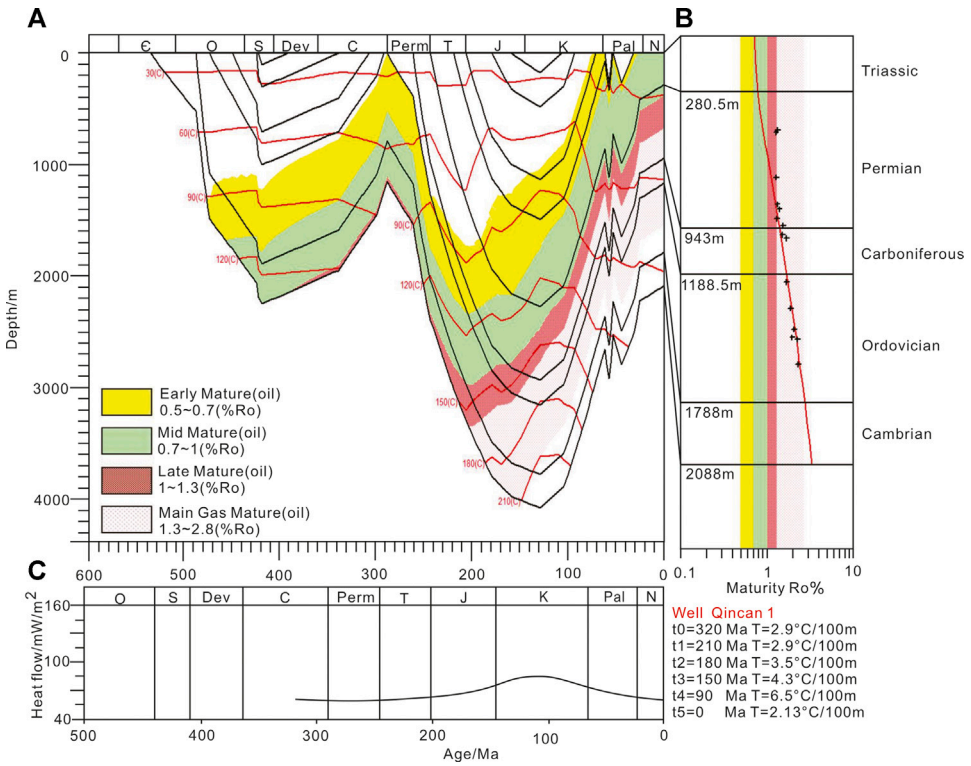

FIGURE 10 | Recovery of burial history and tectono-thermal history of Qincan 1 well in central Qinshui Basin. **(A)** Burial history and tectono-thermal history of Qincan 1 well. **(B)** Fitting relationship between measured Ro and simulated Ro. **(C)** Geothermal flow evolution in different periods of Qincan 1 well.

purification of authigenic illite is an important step to avoid the presence of detrital illite. To determine the crystallinity of authigenic illite, we must separate the authigenic illite from sandstone, mudstone, fault gouge, and other types of rock samples first, then remove the non-authigenic illite components from the rock samples and finally extract the authigenic illite.

As explained, the separation of authigenic illite will have a direct influence on the quality of the testing results; separation and purification of illite are essential to maximize the complete removal of detrital K-bearing minerals such as detrital K-feldspar and detrital illite. Moreover, the authigenic illite should also be enriched to the greatest extent, whereas the content of kaolinite, chlorite, smectite, and other non-authigenic illite components should be reduced to the greatest extent. Judging from the current situation, the only effective way to achieve this goal is to extract more fine-grained clay components.

The separation of illite is quite challenging for two reasons. Firstly, the separation of authigenic illite requires a fine particle size. Conventional clay separation generally requires the extraction of <2 μm components, while the separation of authigenic illite requires at least particle size of <0.3 μm; Secondly, the separation of authigenic illite requires successive separation steps to extract different continuous fractions simultaneously, e.g., 1–0.5 μm, 0.5–0.3 μm, 0.3–0.15 μm, and <0.15 μm. The separation and purification of illite are generally limited by instruments and equipment, and the separation was carried out to fraction sizes of 0.5 μm. Therefore, the clay minerals finally separated and purified may contain some detrital illite, chlorite, kaolinite, and other clay minerals, which might affect the test results. According to the XRD patterns (**Figure 6** and **Figure 4**), we can observe diffraction patterns characteristics of chlorite and kaolinite, which therefore indicate that the separation of early authigenic illite is not completely pure. Consequently, the calculated illite crystallinity might include detrital illite crystallinity, which might have an impact on the paleotemperature inversion calculation. But through the SEM (Supplementary Material, **Figure 6**), Most of the clay minerals in the sandstone interlayer are illite with a good crystal shape (**Figure 6**), and some illites are associated with I/S (**Figure 6A**), indicating that there are many authigenic illites to some extent.

Tectono-Thermal Event Time and Coalbed Methane Accumulation Period

According to the calculation results of the illite crystallinity and the vitrinite reflectance of well Qincan 1, a strong tectono-thermal event occurred in the basin. As a result, the maximum ancient geothermal gradient is 6.5°C/100 m, which is larger than the current geothermal gradient of 2.4°C/100 m, and the maximum paleo-geotemperature was around 180–190°C as recorded at the Carboniferous strata.

Previous studies have attempted to determine the occurrence time of tectono-thermal events in Qinshui Basin; the fission-track age of apatite, for example, is estimated at ~20–40 Ma, and the

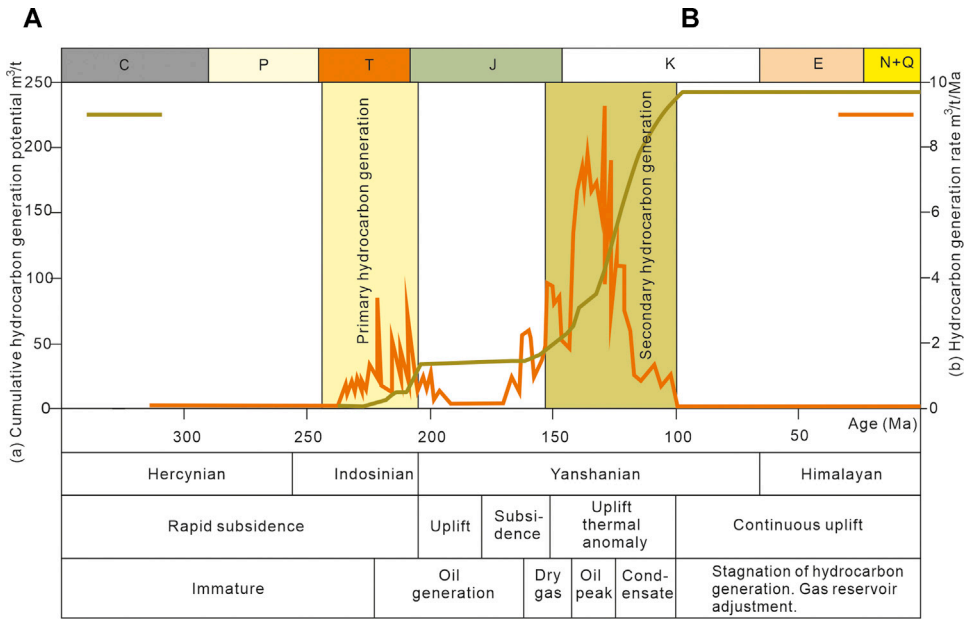

FIGURE 11 | Evolution of hydrocarbon generation potential and rate of source rocks in Qinshui Basin, modified from Hou, (2020).

zircon fission-track age is ~100–150 Ma (Ren et al., 2005; Zhu et al., 2014). If the fission-track age of zircon happened to be smaller than the age of the formation, it would indicate that the formation temperature was once greater than 250 °C and that the zircon has undergone annealing (Hurford, 1986; Fitzgerald and Gleadow, 1988; Yan et al., 2010; Malusà and Fitzgerald, 2019). Secondly, the isotope age determination results of the igneous rocks around the Qinshui Basin indicate that the time of magma intrusion and eruption is between the Late Jurassic and Early Cretaceous. For example, the Taershan-Erfengshan alkaline complex, which is in the southwest of the Qinshui Basin, has an Ar-Ar age of about 124 ± 0.3 Ma. In addition, the U-Pb age of the Wanrong-Gufeng Mountain in the southern Qinshui Basin ranges between 127 ± 1 Ma~140.5 ± 5.3 Ma (Yan et al., 1988; Shanxi, 1989; Wu et al., 1996, 2008; Ying et al., 2011; Si, 2015; Huo, 2016; Yang, 2016; Chang et al., 2017; Yang et al., 2017). It shows that the tectono-thermal events mainly occurred in the Late Jurassic to the Early Cretaceous period (More details in **Supplementary Table S4** and **Supplementary Figure S1**).

Among the geological factors, thermal field, tectonic stress field, hydrodynamic field, and formation conditions have an important influence on the formation of coalbed methane (Wu et al., 2014). The coal deposits in the Qinshui Basin began to form in the Late Carboniferous and gradually ceased when the delta deposits were formed in the early Permian (Sun et al., 2005; Ma et al., 2016; Chen et al., 2019; Yu et al., 2020a). The subsidence of the basin lasted until the Late Triassic when the temperature of the coal seam reached 135°C (the burial depth was up to 4 km). Influenced by the increase of temperature, the first stage of methane generation began, and the vitrinite reflectance maturity of the coal seam reached a medium level (R_o ≈ 1.2%) (Zeng et al., 1999; Cai et al., 2011). Then, the subsequent Indosinian orogenic movement caused the uplift and inversion of the basin during the Early Jurassic, and it remained in a state of slow deposition until the Late Jurassic (Zeng et al., 1999; Ma et al., 2016). At the same time, the exposed rocks around the Qinshui Basin, which include Taershan, Huyanshan, Zijinshan, Erfengshan, Gufengshan, etc, started to form (Yan et al., 1988; Shanxi, 1989; Wu et al., 1996, 2008; Ying et al., 2011; Si, 2015; Huo, 2016; Yang, 2016; Chang et al., 2017; Yang et al., 2017). It can be seen that there was a tectono-thermal event represented by intense magmatic activity in the Late Jurassic to Early Cretaceous, which is generally considered to be closely related to the secondary gas peak of coal seams in the basin at the same time (**Figure 11**) (Zeng et al., 1999; Xu et al., 2004; Jiang et al., 2005; Ren et al., 2005; Sun et al., 2005; Duan et al., 2011; Chen et al., 2019, 2019; Yu et al., 2020a; Gao et al., 2021).

From Late Jurassic to Early Cretaceous, magmatic thermal events caused rapid temperature increase of coal measures. A large amount of hydrocarbon was generated by coal measures, with coal rock as the main source of hydrocarbon generation. The rapid increase of gas led to hydrocarbon generation pressurization in the coal body (Ju et al., 2018); furthermore, the increase of temperature led to the expansion of gas to form abnormal high pressure (**Figure 11**).

Response of Thermal Events in Qinshui Basin to Destruction of NCC

The tectono-thermal event in Qinshui Basin between the Late Jurassic to Early Cretaceous was associated with the large-scale magmatic eruption and the formation of the Ultra-High-Pressure metamorphic belt (Yan et al., 1988; Shanxi, 1989; Wu et al., 1996; Zhang, 1997, 2002; Wu et al., 2008; Ying et al., 2011; Chen and Ding, 2012; Si, 2015; Huo, 2016; Yang,

2016; Chang et al., 2017; Yang et al., 2017; Yu et al., 2020a). Combined with the estimation of the maximum paleotemperature and paleotemperature gradient of illite crystallinity and vitrinite reflectance, the deep mantle of the basin was active during the Late Jurassic—Early Cretaceous with the lithosphere thinned and led to the formation of a high geothermal background value of mantle upwelling, which was the main reason for the tectono-thermal event and uplift denudation event of the basin in this period.

Previous studies have shown that the thickness of the thermal lithosphere of the present orogenic belt in the central part of the NCC is about 76–90 km (He et al., 2001; Wang et al., 2001; Zhang et al., 2006; Zhang, 2012). Based on their data, these authors estimated that the thickness of the thermal lithosphere of the Qinshui Basin in the Early Cretaceous was about 50–60 km, indicating that the lithosphere of the basin was thinned during the Early Cretaceous. At the same time, previous studies suggest that the NCC experienced strong lithospheric thinning and lithospheric mantle property transformation during the Mesozoic (Menzies et al., 1993; Griffin et al., 1998; Xu, 2001; Wu et al., 2008), accompanied by strong magmatism (F. Wu et al., 2005a; F.-Y. Wu et al., 2005b; Yang et al., 2008). Combined with the magmatism around the Qinshui Basin, we suggest that the lithospheric thinning in the Qinshui Basin is controlled by the thinning and destruction of the NCC.

Previous investigations have been conducted on the destruction of the NCC (Zhu et al., 2012, 2017; Yang et al., 2021b). According to Zhu et al. (2017), at 165 Ma, from the beginning of the Middle Jurassic Yanshanian movement episode A, the West Pacific plate subducted to the East Asian continental margin with a high speed and low angle, the tectonic environment in Qinshui Basin, therefore, corresponds to a compression environment, and angular unconformity events were generally developed. Starting from the Late Jurassic at 155 Ma, the western Pacific plate subducted from a low angle to a high angle subduction toward the edge of the East Asian continent (Zheng et al., 2018). With the rotation and retreat of the subducted plate, the corresponding tectonic environment of the Qinshui Basin became extensional, and magmatic activity began to appear; during this period, the Taihang Mountains began to uplift, and the eastern part of the Qinshui Basin as the western wing of the Taihang Mountains began to fold and uplift (Zhu, 2013). Accompanied by strong magmatism, the Late Paleozoic coal-measure strata experienced a high-temperature heating process. The regional tectonic stress field of the basin during the Middle-Late Jurassic is consistent with that of the whole of eastern China. The NNE trending folds are the most developed in the basin, covering the whole area on a large scale, reflecting the horizontal compressive stress field in the direction of NWW-SEE in the Yanshanian period. Under the action of this stress field, a wide and gently deformed syncline, Qinshui Basin, is formed (Zhu et al., 2015). At 140 Ma, the Yanshanian movement episode B began in the early Cretaceous, and the subduction angle of the Western Pacific plate to the East Asian continental margin began to decrease again. The tectonic environment corresponding to the Qinshui Basin was compressional, and crustal shortening, folding and stratigraphic angular unconformity events were widely developed (Zheng et al., 2018). From 125 Ma in the Early Cretaceous, the subduction angle of the Western Pacific plate to the East Asian continental margin changed to a high angle again, and the rate of subduction, rotation, and retreat reached the maximum, and finally left a retentive body in the mantle transition zone (Zhu et al., 2015). The corresponding area of Qinshui Basin, which was subjected to compression, thrust, and folds uplifting, began to develop structural inversion and normal faults. Since the late Cretaceous, the young and buoyant paleo Western Pacific plate gradually entered the subduction zone, and magmatic activity in the corresponding area of the Qinshui Basin gradually ceased, and the extensional tectonic activity was much weaker than that of the early Cretaceous (Shanxi, 1989). Throughout the Cretaceous period, there was a major structural system transition in eastern China, that is, the early continental collision and compression thrust structures were transformed into extensional structures, and the eastern NCC and Ordos basin became active with the lithosphere thinned (Ren et al., 2002; Chen and Ding, 2012; Yu et al., 2020b).

The Qinshui Basin is a transitional zone between rift basins in the east of the NCC and the Ordos Basin in the West, the thinning of the lithosphere and crustal extension also affected this area, forming a small amount of magmatic activity. The basin was subjected to weak NW-SE extensional tectonism and formed a series of small to normal faults based on the Yanshanian conjugate joints. Previous studies have shown that the deep cause of the early Cretaceous tectono-thermal events and the uplift and denudation events in the Qinshui Basin is mainly due to the subduction of the western Pacific plate into the deep part of the NCC, and the current low geothermal gradient in the Qinshui Basin is also affected by the withdrawal of the West Pacific Plate. Combined with the results of previous studies (Ren et al., 2020), our work suggests that the Qinshui Basin experienced a tectono-thermal event during the Late Jurassic to Early Cretaceous which is in response to deep lithospheric thinning of the NCC.

CONCLUSION

Paleotemperature and denudation restoration by vitrinite reflectance and illite crystallinity shed new light on the tectono-thermal history and mechanisms for the evolution of the Qinshui Basin of the NCC, which also expounded the generation mechanism of coalbed methane and its response to the destruction of the NCC from the tectono-thermal history perspective. The Qinshui basin experienced a tectono-thermal event during the Late Jurassic-Early Cretaceous. The deep reason for this thermal event may be that relate to the subduction of the Western Pacific Plate to the East Asian Continent resulting in the upwelling of deep asthenosphere material and the thinning of lithosphere thickness in the Qingshui area. During the Late Jurassic-Early Cretaceous, the maximum pale-geotemoerature and the highest pale-geotemperature gradient are 200°C, and

6.5°C/100 m, respectively, which is the main control on the scale of hydrocarbon generation.

DATA AVAILABILITY STATEMENT

The original contributions presented in the study are included in the article/**Supplementary Material**, further inquiries can be directed to the corresponding authors.

AUTHOR CONTRIBUTIONS

RL: Conceptualization, Methodology, Software, Experiment, Writing—original draft, Writing—review and editing. ZR: Modeling, Supervision, Funding acquisition. PY: Supervision, Conceptualization, Writing—original draft, review and editing. HH: Supervision, Funding acquisition. TS: Writing—review and editing. WG: Writing—original draft, Writing—editing. WL: Software, Experiment.

FUNDING

This work was supported by the National Natural Science Foundation of China (Grant Nos. 41630312, 41688103, 42102164).

ACKNOWLEDGMENTS

We sincerely thank Topic Science Editor Kai-jun Zhang for kind editorial handling and constructive work. We also thank two reviewers for their constructive and thoughtful comments, which significantly improved the manuscript. The authors are grateful to PetroChina Huabei Oilfield Company for supporting this study.

SUPPLEMENTARY MATERIAL

The Supplementary Material for this article can be found online at: https://www.frontiersin.org/articles/10.3389/feart.2021.765497/full#supplementary-material

REFERENCES

Barker, C. E., and Pawlewicz, M. J. (1986). "The Correlation of Vitrinite Reflectance with Maximum Temperature in Humic Organic Matter," in *In* Paleogeothermics: Evaluation of Geothermal Conditions In the Geological Past *Lecture Notes in Earth Sciences*. Editors G. Buntebarth and L. Stegena (Berlin, Heidelberg: Springer), 79–93. doi:10.1007/BFb0012103

Barker, M. K., Mazarico, E., Neumann, G. A., Zuber, M. T., Haruyama, J., and Smith, D. E. (2016). A New Lunar Digital Elevation Model from the Lunar Orbiter Laser Altimeter and SELENE Terrain Camera. *Icarus* 273, 346–355. doi:10.1016/j.icarus.2015.07.039

Cai, Y., Liu, D., Yao, Y., Li, J., and Qiu, Y. (2011). Geological Controls on Prediction of Coalbed Methane of No. 3 Coal Seam in Southern Qinshui Basin, North China. *Int. J. Coal Geology.* 88, 101–112. doi:10.1016/j.coal.2011.08.009

Chang, L., Wang, C., and Ding, Z. (2011). Upper Mantle Anisotropy in the Ordos Block and its Margins. *Sci. China Earth Sci.* 54, 888–900. doi:10.1007/s11430-010-4137-2

Chang, Z., Yang, H., and Zhou, A. (2017). LA-1CP-MS Zircon L-Pb Geochronology of the 1uyanshan Alkaline Intrusive Complex in the Luliang Mountain of North China Craton and its Geological Significance. *Geol. Bull. China* 36, 372–380. doi:10.1016/j.dib.2018.05.013

Chen, B., Stuart, F. M., Xu, S., Györe, D., and Liu, C. (2019). Evolution of Coal-Bed Methane in Southeast Qinshui Basin, China: Insights from Stable and noble Gas Isotopes. *Chem. Geology.* 529, 119298. doi:10.1016/j.chemgeo.2019.119298

Chen, G., and Ding, C. (2012). Analysis on the thermal History and Uplift Process of Zijinshan Intrusive Complex in the Eastern Ordos basin. *Chin. J. Geophys.* 55, 3731–3741. doi:10.6038/j.issn.0001-5733.2012.11.020

Chen, L. (2009). Lithospheric Structure Variations between the Eastern and central North China Craton from S- and P-Receiver Function Migration. *Phys. Earth Planet. Interiors* 173, 216–227. doi:10.1016/j.pepi.2008.11.011

Chen, S., Tang, D., Tao, S., Xu, H., Li, S., Zhao, J., et al. (2018). Characteristics of *In-Situ* Stress Distribution and its Significance on the Coalbed Methane (CBM) Development in Fanzhuang-Zhengzhuang Block, Southern Qinshui Basin, China. *J. Pet. Sci. Eng.* 161, 108–120. doi:10.1016/j.petrol.2017.11.042

Chen, Z., Liu, G., and Hao, S. (1999). A Corrected Method of Using Vitrinite Reflectance Data to Estimate the Thickness of Sediment Removed at an Unconformity. *Acta Sedimentologica Sinica* 17, 141–144.

Dow, W. G. (1977). Kerogen Studies and Geological Interpretations. *J. Geochemical Exploration* 7, 79–99. doi:10.1016/0375-6742(77)90078-4

Duan, Y., Zhang, X., Sun, T., Wu, B., He, J., and Xu, L. (2011). Carbon and Hydrogen Isotopic Compositions and Their Evolutions of Gases Generated by Herbaceous Swamp Peat at Different thermal Maturity Stages. *Chin. Sci. Bull.* 56, 1383–1389. doi:10.1007/s11434-011-4356-8

Fitzgerald, P. G., and Gleadow, A. J. W. (1988). Fission-track Geochronology, Tectonics and Structure of the Transantarctic Mountains in Northern Victoria Land, Antarctica. *Chem. Geology. Isotope Geosci. section* 73, 169–198. doi:10.1016/0168-9622(88)90014-0

Gao, H.-T., Zhu, Y.-M., Shang, F.-H., and Chen, C.-Y. (2021). Study on the Shale Gas Reservoir-Forming Characteristics of the Taiyuan Formation in the Eastern Qinshui Basin, China. *j nanosci nanotechnol* 21, 72–84. doi:10.1166/jnn.2021.18465

Gao, Z., Fan, Y., Xuan, Q., and Zheng, G. (2020). A Review of Shale Pore Structure Evolution Characteristics with Increasing thermal Maturities. *Adv. Geo-energy Res.* 4, 247–259. doi:10.46690/ager.2020.03.03

Griffin, W. L., Andi, Z., O'Reilly, S. Y., and Ryan, C. G. (1998). "Phanerozoic Evolution of the Lithosphere beneath the Sino-Korean Craton," in *"Phanerozoic Evolution of the Lithosphere beneath the Sino-Korean Craton," in* Geodynamics Series. Editors M. F. J. Flower, S. Chung, C. Lo, and T. Lee (Washington, D. C.: American Geophysical Union), 107–126. doi:10.1029/GD027p0107

Harvey, C. C., and Browne, P. R. L. (1991). Mixed-lay Er clay Geothermometry in the Wairakei Geothermal Field. 39, 614–621.doi:10.1346/ccmn.1991.0390607

He, L., Hu, S., and Wang, J. (2001). Characteristics of thermal Structure of Rock and Lithosphere in the Land Area of eastern China. *Prog. Nat. Sci.* 11.

He, L. (2015). Thermal Regime of the North China Craton: Implications for Craton Destruction. *Earth-Science Rev.* 140, 14–26. doi:10.1016/j.earscirev.2014.10.011

Hu, S., Wang, J., and Zhang, R. (1999). Using Vitrinite Reflectance Data to Estimate the Thickness of Stratum Denudation. *Pet. exploration Dev.* 26, 42–45+6.

Huo, T. (2016). Petrogenesis of Early Cretaceous Alkaline Intrusive Rocks in central North China Block: Constraints of Chronology and Sr-Nd-Hf Isotopes. *Lithos* 380-381, 105887. doi:10.1016/j.lithos.2020.105887

Hurford, A. J. (1986). Cooling and Uplift Patterns in the Lepontine Alps South Central Switzerland and an Age of Vertical Movement on the Insubric Fault Line. *Contrib. Mineral. Petrol.* 92, 413–427. doi:10.1007/BF00374424

Ji, J. (2000). Relationship between Illite Crystallinity and Temperature in Active Geothermal Systems of New Zealand. *Clays and Clay Minerals* 48, 139–144. doi:10.1346/ccmn.2000.0480117

Jiang, B., Qin, Y., Ju, Y., and Wang, J. (2005). Research on Tectonic Stress Field of Generate. *J. China Univ. Mining &Technology* 34, 564–569.

Ju, Y., Sun, Y., Tan, J., Bu, H., Han, K., Li, X., et al. (2018). The Composition, Pore Structure Characterization and Deformation Mechanism of Coal-Bearing Shales from Tectonically Altered Coalfields in Eastern China. *Fuel* 234, 626–642. doi:10.1016/j.fuel.2018.06.116

Kisch, H. J. (1990). Calibration of the Anchizone: a Critical Comparison of Illite "Crystallinity" Scales Used for Definition. *J.metamorphic Geol.* doi:10.1111/j.1525-1314.1990.tb00455.x

Kisch, H. J. (1987). "Correlation between Indicators of Very Low Grade Metamorphism," in *In* Low Temperature Metamorphism. Editor M. Frey (Glasgow: Blackie.), 227–300.

Li, R., Wang, S., Lyu, S., Xiao, Y., Su, D., and Wang, J. (2018a). Dynamic Behaviours of Reservoir Pressure during Coalbed Methane Production in the Southern Qinshui Basin, North China. *Eng. Geology.* 238, 76–85. doi:10.1016/j.enggeo.2018.03.002

Li, S., Lai, X., Liu, B., Wang, Z., He, J., and Sun, Y. (2011). Differences in Lithospheric Structures between Two Sides of Taihang Mountain Obtained from the Zhucheng-Yichuan Deep Seismic Sounding Profile. *Sci. China Earth Sci.* 54, 871–880. doi:10.1007/s11430-011-4191-4

Li, S., Tang, D., Xu, H., and Yang, Z. (2012a). Advanced Characterization of Physical Properties of Coals with Different Coal Structures by Nuclear Magnetic Resonance and X-ray Computed Tomography. *Comput. Geosciences* 48, 220–227. doi:10.1016/j.cageo.2012.01.004

Li, S., Zhao, G., Dai, L., Liu, X., Zhou, L., Santosh, M., et al. (2012b). Mesozoic Basins in Eastern China and Their Bearing on the Deconstruction of the North China Craton. *J. Asian Earth Sci.* 47, 64–79. doi:10.1016/j.jseaes.2011.06.008

Li, Z., Liu, D., Ranjith, P. G., Cai, Y., and Wang, Y. (2018b). Geological Controls on Variable Gas Concentrations: A Case Study of the Northern Gujiao Block, Northwestern Qinshui Basin, China. *Mar. Pet. Geology.* 92, 582–596. doi:10.1016/j.marpetgeo.2017.11.022

Ling, Y., Chen, L., Wei, Z., Jiang, M., and Wang, X. (2017). Crustal S-Velocity Structure and Radial Anisotropy beneath the Southern Part of central and Western North China Craton and the Adjacent Qilian Orogenic Belt from Ambient Noise Tomography. *Sci. China Earth Sci.* 60, 1752–1768. doi:10.1007/s11430-017-9092-8

Liu, R. (2020). Meso-Cenozoic thermal Regime and Lithospheric Thinning in the Qin Shui Basin, Central North China Craton. Available at: https://kns.cnki.net/kcms/detail/detail.aspx?dbcode=CMFD&dbname=CMFD202101&filename=1020314237.nh&uniplatform=NZKPT&v=sLWw8HfJafeHh68xohfyB3rXgvSc3Z1v0uHTFqt5%25mmd2FsPSCIx6r%25mmd2Bs2wBFnfJthw4VC (Accessed September 23, 2021).

Ma, X., Song, Y., Liu, S., Jiang, L., and Hong, F. (2016). Experimental Study on History of Methane Adsorption Capacity of Carboniferous-Permian Coal in Ordos Basin, China. *Fuel* 184, 10–17. doi:10.1016/j.fuel.2016.06.119

Meng, Q.-R., Wu, G.-L., Fan, L.-G., and Wei, H.-H. (2019). Tectonic Evolution of Early Mesozoic Sedimentary Basins in the North China Block. *Earth-Science Rev.* 190, 416–438. doi:10.1016/j.earscirev.2018.12.003

Meng, Y., Wang, X., and Chen, J. (2015a). *Geological Evidence of the Cenozoic Tectonic Uplifting in Taihang Mountains —Apatite Fission Track Evidence from Well Qincan 1*, 35. doi:10.3969/j.ISSN.1674-9057.2015.01.003

Meng, Y., Wang, X., Li, B., and Cai, Z. (2015b). Thermal Evolution History of Qinshui Basin in central North China Craton and Lithospheric Tectonic Evolution in Mesozoic and Cenozoic of Shanxi Plateau. *Northwest. Geology.* 48, 159–168.

Menzies, M. A., Fan, W., and Zhang, M. (1993). Palaeozoic and Cenozoic Lithoprobes and the Loss of >120 Km of Archaean Lithosphere, Sino-Korean Craton, China. *Geol. Soc. Lond. Spec. Publications* 76, 71–81. doi:10.1144/GSL.SP.1993.076.01.04

M. G. Malusà and P. G. Fitzgerald (Editors) (2019). *Fission-Track Thermochronology and its Application to Geology* (Cham: Springer International Publishing). doi:10.1007/978-3-319-89421-8

MingGuo, Z., YanBin, Z., YanBin, Z., QiuLi, L., Yi, Z., HaiLong, H., et al. (2021a). Cratonization, Lower Crust and continental Lithosphere. *Acta Petrologica Sinica* 37, 1–23. doi:10.18654/1000-0569/2021.01.01

Pollastro, R. M. (1993). Considerations and Applications of the Illite/Smectite Geothermometer in Hydrocarbon-Bearing Rocks of Miocene to Mississippian Age. *Clay s and Clay Minerals* 41, 119–133. doi:10.1346/ccmn.1993.0410202

Ramseyer, K., and Boles, J. R. (1986). Mixed-Layer Illite/Smectite Minerals in Tertiary Sandstones and Shales, San Joaquin Basin, California. *Clays and Clay Minerals* 34, 115–124. doi:10.1346/CCMN.1986.0340202

Ren, J., Tamaki, K., Li, S., and Junxia, Z. (2002). Late Mesozoic and Cenozoic Rifting and its Dynamic Setting in Eastern China and Adjacent Areas. *Tectonophysics* 344, 175–205. doi:10.1016/S0040-1951(01)00271-2

Ren, Z., Xiao, H., Liu, L., Zhang, S., Qin, Y., and Wei, C. (2005). The Evidence of Fission-Track Data for the Study of Tectonic thermal History in Qinshui Basin. *Chin.Sci.Bull.* 50, 104–110. doi:10.1007/bf03184091

Ren, Z., Zhang, S., Gao, S., Cui, J., and Liu, X. (2006). Relationship between thermal History and Various Energy mineral Deposits in Dongsheng Area. Yimeng Uplift. *Oil &Gas Geology.* 27.

Shanxi, R. S. G. (1989). *Regional Geology of Shanxi Provenance (In Chinese)*. Taiyuan, China: Shanxi Bureau of Geology and Mineral Resources.

Si, D. (2015). *Petrology and Geochemistry of Mesozoic Ore-Bearing Dioritic Rocks in Talishan-Erfengshan Area, Southern Taihang Mountains*.

Sun, B. L., Zeng, F. G., Xia, P., Zhu, Y. R., and Liu, C. (2018). Late Triassic-Early Jurassic Abnormal thermal Event Constrained by Zircon Fission Track Dating and Vitrinite Reflectance in Xishan coalfield, Qinshui Basin, central North China. *Geol. J.* 53, 1039–1049. doi:10.1002/gj.2942

Sun, Z. X., Zhang, W., Hu, B. Q., and Pan, T. Y. (2006). Features of Heat Flow and the Geothermal Field of the Qinshui Basin. *Geophys* 49, 130–134. doi:10.1002/cjg2.819

Sun, Z., Zhang, W., Hu, B., Li, W., and Pan, T. (2005). Geothermal Field and its Relation with Coalbed Methane Distribution of the Qinshui Basin. *Chin.Sci.Bull.* 50, 111–117. doi:10.1007/BF03184092

Tong, Y., Song, L., Zeng, S., Cheng, T., and Wei, Y. (2005). A New Method by Vitrinite Reflectance to Estimate Thickness of Eroded Strata. *J. Palaeogeography(Chinese Edition)* 7, 417–424.

Tong, Y., and Zhu, G. (2006). Some Important Problems of Using Vitrinite Reflectance to Recover Denudation. *J. Oil Gas Technol.* 28, 197–199.

Uysal, I., Mutlu, H., Altunel, E., Karabacak, V., and Golding, S. (2006). Clay Mineralogical and Isotopic (K-Ar, δ18O, δD) Constraints on the Evolution of the North Anatolian Fault Zone, Turkey. *Earth Planet. Sci. Lett.* 243, 181–194. doi:10.1016/j.epsl.2005.12.025

Uysal, I. T. (2000). Clay-Mineral Authigenesis in the Late Permian Coal Measures, Bowen Basin, Queensland, Australia. *Clays and Clay Minerals* 48, 351–365. doi:10.1346/CCMN.2000.0480306

Uysal, I. T., Glikson, M., Golding, S. D., and Audsley, F. (2000). The thermal History of the Bowen Basin, Queensland, Australia: Vitrinite Reflectance and clay Mineralogy of Late Permian Coal Measures. *Tectonophysics* 323, 105–129. doi:10.1016/S0040-1951(00)00098-6

Uysal, I. T., Golding, S. D., and Thiede, D. S. (2001). K-ar and Rb-Sr Dating of Authigenic Illite-Smectite in Late Permian Coal Measures, Queensland, Australia: Implication for thermal History. *Chem. Geology.* 171, 195–211. doi:10.1016/S0009-2541(00)00247-3

Wang, Y., Deng, J., Wang, J., and Xiong, L. (2001). Terrestrial Heat Flow Pattern and Thermo-Tectonic Domains in the Continental Area of China. *J. Graduate Sch. Chin. Acad. Sci.* 18.

Wei, C., Qin, Y., Wang, G. G. X., Fu, X., Jiang, B., and Zhang, Z. (2007). Simulation Study on Evolution of Coalbed Methane Reservoir in Qinshui basin, China. *Int. J. Coal Geology.* 72, 53–69. doi:10.1016/j.coal.2006.12.001

Wu, C., Qin, Y., and Zhou, L. (2014). Effective Migration System of Coalbed Methane Reservoirs in the Southern Qinshui Basin. *Sci. China Earth Sci.* 57, 2978–2984. doi:10.1007/s11430-014-4988-z

Wu, F.-Y., Yang, J.-H., Wilde, S. A., and Zhang, X.-O. (2005b). Geochronology, Petrogenesis and Tectonic Implications of Jurassic Granites in the Liaodong Peninsula, NE China. *Chem. Geology.* 221, 127–156. doi:10.1016/j.chemgeo.2005.04.010

Wu, F., Lin, J., Wilde, S., Zhang, X., and Yang, J. (2005a). Nature and Significance of the Early Cretaceous Giant Igneous Event in Eastern China. *Earth Planet. Sci. Lett.* 233, 103–119. doi:10.1016/j.epsl.2005.02.019

Wu, F., Xu, Y., Gao, S., and Zeng, J. (2008). Lithospheric Thinning and Destruction of the North China Craton. *Acta Petrologica Sinica* 24, 1145–1174.

Wu, L., Zhang, Z., and Zhang, Y. (1996). *The Origin and Mineralization of Alkaline Rocks in the Shanxi Platform Anticline*. Beijing: Science Press.

Xinhui, L., Yinshuang, A., Yaoyang, Z., Yongshun, C., and Jieyuan, N. (2017). Study of Lithospheric Structure in the central and Western North China Craton. *Prog. Geophys.* 32, 1458–1464.

Xu, W., Wang, D., Wang, Q., Pei, F., and Lin, J. (2004). 40Ar/39Ar Dating of Hornblende and Biotite in 655 Mesozoic Intrusive Complexes from the North China Block: Constraints on the Time of 656 Lithospheric Thinning. *Geochimica* 33, 221–231.

Xu, Y.-G. (2001). Thermo-tectonic Destruction of the Archaean Lithospheric Keel beneath the Sino-Korean Craton in china: Evidence, Timing and Mechanism.

Phys. Chem. Earth, A: Solid Earth Geodesy 26, 747–757. doi:10.1016/S1464-1895(01)00124-7

Yan, G., Mu, B., and Zeng, Y. (1988). Characteristics of REE, Oxygen and Strontium Isotope Composition for the Zijinshan Alkaline Rocks-Carbonatite Complex in Shanxi Province. *Acta Petrologica Sinica* 4, 29–36. doi:10.1007/bf02018710

Yan, Y., Hu, X., Lin, G., Liu, W., and Song, Z. (2010). Detrital Zircon and Apatite Fission Track Data in the Liaoxi Basins: Implication to Meso-Cenozoic Thermo-Tectonic Evolution of the Northern Margin of the North China Craton. *J. Earth Syst. Sci.* 119, 541–551. doi:10.1007/s12040-010-0028-3

Yang, H. (2016). *Geochronology of the Huyanshan Alkaline-Alkaline Complex in the Middle Segment of the Lvliang Uplift belt and its Tectonic Characteristics*.

Yang, J.-H., Wu, F.-Y., Wilde, S. A., Belousova, E., and Griffin, W. L. (2008). Mesozoic Decratonization of the North China Block. *Geol* 36, 467. doi:10.1130/G24518A.1

Yang, P., Wu, G., Ren, Z., Zhou, R., Zhao, J., Zhang, L., et al. (2020). Tectono-Thermal Evolution of Cambrian-Ordovician Source Rocks and Implications for Hydrocarbon Generation in the Eastern Tarim Basin, NW China. *J. Asian Earth Sci.* doi:10.1016/j.jseaes.2020.104267

Yang, P., Wu, G., Nuriel, P., Nguyen, A. D., Chen, Y., Yang, S., et al. (2021a). In situ LA-ICPMS U Pb Dating and Geochemical Characterization of Fault-Zone Calcite in the Central Tarim Basin, Northwest China: Implications for Fluid Circulation and Fault Reactivation. *Chem. Geol.* 568, 120125. doi:10.1016/j.chemgeo.2021.120125

Yang, J.-H., Xu, L., Sun, J.-F., Zeng, Q., Zhao, Y.-N., Wang, H., et al. (2021b). Geodynamics of Decratonization and Related Magmatism and Mineralization in the North China Craton. *Sci. China Earth Sci.* 64, 1409–1427. doi:10.1007/s11430-020-9732-6

Yang, P., Ren, Z., Xia, B., Zhao, X., Tian, T., Huang, Q., et al. (2017a). The Lower Cretaceous Source Rocks Geochemical Characteristics and Thermal Evolution History in the HaRi Sag, Yin-E Basin. *Pet. Sci. Technol.* 35, 1304–1313. doi:10.1080/10916466.2017.1327969

Yang, Y., Zhao, J., Liu, C., Xue, R., and Yan, Z. (2017b). The Zircon LA-ICP-MS L-Pb Ages and Geochemical Characteristics of Ta ' Ershan Intrusions, Southern Shanxi Province, and Their Geological Implications. *Geol. Rev.* 63, 809–821. doi:10.16509/j.georeview.2017.03.019

Yang, P., Ren, Z., Xia, B., Tian, T., Zhang, Y., Qi, K., et al. (2018). Tectono-Thermal Evolution, Hydrocarbon Filling and Accumulation Phases of the Hari Sag, in the Yingen-Ejinaqi Basin, Inner Mongolia, Northern China. *Acta Geol. Sin. - Engl. Ed.* 92, 1157–1169. doi:10.1111/1755-6724.13597

Ying, J.-F., Zhang, H.-F., and Tang, Y.-J. (2011). Crust-mantle Interaction in the central North China Craton during the Mesozoic: Evidence from Zircon U-Pb Chronology, Hf Isotope and Geochemistry of Syenitic-Monzonitic Intrusions from Shanxi Province. *Lithos* 125, 449–462. doi:10.1016/j.lithos.2011.03.004

Yu, K., Ju, Y., and Zhang, B. (2020a). Modeling of Tectono-thermal Evolution of Permo-Carboniferous Source Rocks in the Southern Qinshui Basin, China: Consequences for Hydrocarbon Generation. *J. Pet. Sci. Eng.* 193, 107343. doi:10.1016/j.petrol.2020.107343

Yu, K., Ju, Y., and Zhang, B. (2020b). Modeling of Tectono-thermal Evolution of Permo-Carboniferous Source Rocks in the Southern Qinshui Basin, China: Consequences for Hydrocarbon Generation. *J. Pet. Sci. Eng.* 193, 107343. doi:10.1016/j.petrol.2020.107343

Zeng, Y., Fan, B., Liu, H., and Wang, C. (1999). An Analysis of the History of thermal Evolution Hydrocarbon- Generating and the Heat Source about Main Seam of Shanxi Formation in southeastern Shanxi Province. *Sci. Geol.Sinica* 34, 90–98.

Zhai, M., Zhao, L., Zhu, X., Zhou, Y., Peng, P., Guo, J., et al. (2021b). Late Neoarchean Magmatic - Metamorphic Event and Crustal Stabilization in the North China Craton. *Am. J. Sci.* 321, 206–234. doi:10.2475/01.2021.06

Zhai, M., Zhu, X., Zhou, Y., Zhao, L., and Zhou, L. (2020). Continental Crustal Evolution and Synchronous Metallogeny through Time in the North China Craton. *J. Asian Earth Sci.* 194, 104169. doi:10.1016/j.jseaes.2019.104169

Zhang, K.-J., Cai, J.-X., and Zhu, J.-X. (2006). North China and South China Collision: Insights from Analogue Modeling. *J. Geodynamics* 42, 38–51. doi:10.1016/j.jog.2006.04.004

Zhang, K.-J. (2012). Destruction of the North China Craton: Lithosphere Folding-Induced Removal of Lithospheric Mantle? *J. Geodynamics* 53, 8–17. doi:10.1016/j.jog.2011.07.005

Zhang, K.-J. (1997). North and South China Collision along the Eastern and Southern North China Margins. *Tectonophysics* 270, 145–156. doi:10.1016/S0040-1951(96)00208-9

Zhang, K. (2002). Escape Hypothesis for North and South China Collision and Tectonic Evolution of the Qinling Orogen, Eastern Asia. *Eclogae Geologicae Helv.* 95.

ZhanLi, R., Qi, K., Kai, Q., RunChuan, L., JunPing, C., ZhiPeng, C., et al. (2020). Dynamic Background of Early Cretaceous Tectonic thermal Events and its Control on Various mineral Accumulations Such as Oil and Gas in the Ordos Basin. *Acta Petrologica Sinica* 36, 1213–1234. doi:10.18654/1000-0569/2020.04.15

Zhao, G., He, Y., and Sun, M. (2009). The Xiong'er Volcanic belt at the Southern Margin of the North China Craton: Petrographic and Geochemical Evidence for its Outboard Position in the Paleo-Mesoproterozoic Columbia Supercontinent. *Gondwana Res.* 16, 170–181. doi:10.1016/j.gr.2009.02.004

Zhao, G., Wilde, S. A., Cawood, P. A., and Sun, M. (2001). Archean Blocks and Their Boundaries in the North China Craton: Lithological, Geochemical, Structural and P-T Path Constraints and Tectonic Evolution. *Precambrian Res.* 107, 45–73. doi:10.1016/S0301-9268(00)00154-6

Zhao, X., Yang, Y., Sun, F., Wang, B., Zuo, Y., Li, M., et al. (2016). Enrichment Mechanism and Exploration and Development Technologies of High-Rank Coalbed Methane in South Qinshui Basin, Shanxi Province. *Pet. Exploration Develop.* 43, 303–309. doi:10.11698/PED.2016.02.1910.1016/s1876-3804(16)30039-8

Zheng, Y., Xu, Z., Zhao, Z., and Dai, L. (2018). Mesozoic Mafic Magmatism in North China: Implications for Thinning and Destruction of Cratonic Lithosphere. *Sci. China Earth Sci.* 61, 353–385. doi:10.1007/s11430-017-9160-3

Zhu, H., Huang, C., Ju, Y., Bu, H., Li, X., Yang, M., et al. (2021). Multi-scale Multi-Dimensional Characterization of clay-hosted Pore Networks of Shale Using FIBSEM, TEM, and X-ray Micro-tomography: Implications for Methane Storage and Migration. *Appl. Clay Sci.* 213, 106239. doi:10.1016/j.clay.2021.106239

Zhu, R.-X., Yang, J.-H., and Wu, F.-Y. (2012). Timing of Destruction of the North China Craton. *Lithos* 149, 51–60. doi:10.1016/j.lithos.2012.05.013

Zhu, R., Fan, H., Li, J., Meng, Q., Li, S., and Zeng, Q. (2015). Decratonic Gold Deposits. *Sci. China Earth Sci.* 58, 1523–1537. doi:10.1007/s11430-015-5139-x

Zhu, R., and Xu, Y. (2019). The Subduction of the West Pacific Plate and the Destruction of the North China Craton. *Sci. China Earth Sci.* 62, 1340–1350. doi:10.1007/s11430-018-9356-y

Zhu, R., Zhang, H., Zhu, G., Meng, Q., Fan, H., Yang, J., et al. (2017). Craton Destruction and Related Resources. *Int. J. Earth Sci. (Geol Rundsch)* 106, 2233–2257. doi:10.1007/s00531-016-1441-x

Zhu, X.-Q. (2013). *Tectonic Evolution of the central North China Craton since the Late Paleozoic– A Case Study of the Qinshui Basin*.

Zhu, X.-Q., Zhu, W.-B., Ge, R.-F., and Wang, X. (2014). Late Paleozoic Provenance Shift in the South-central North China Craton: Implications for Tectonic Evolution and Crustal Growth. *Gondwana Res.* 25, 383–400. doi:10.1016/j.gr.2013.04.009

Conflict of Interest: The authors declare that the research was conducted in the absence of any commercial or financial relationships that could be construed as a potential conflict of interest.

frontiers in Earth Science

ORIGINAL RESEARCH
published: 26 November 2021
doi: 10.3389/feart.2021.779991

Genetic Mechanism and Environment Implications of Siderites in the Lopingian Coal-Bearing Series, Western Guizhou of China: Constrained by Whole-Rock and *In Situ* Geochemistry

Tianyang Yang[1,2], *Yulin Shen*[1,2]*, *Yong Qin*[1,2], *Yijie Zhang*[3], *Lu Lu*[1,2], *Jun Jin*[1,2,4], *Yong Zhao*[5], *Yulin Zhu*[1,2] *and Yunfei Zhang*[1,2]

[1]*Key Laboratory of Coalbed Methane Resources and Reservoir Formation Process, Ministry of Education, Xuzhou, China,* [2]*School of Resources and Geosciences, China University of Mining and Technology, Xuzhou, China,* [3]*Sinopec Shengli Oilfield Administration Bureau Co., Ltd., Dongying, China,* [4]*Guizhou Engineering Technology Research Center for Coalbed Methane and Shale Gas, Guiyang, China,* [5]*Sinopec Xinjiang Xinchun Petroleum Development Co., Ltd., Dongying, China*

OPEN ACCESS

Edited by:
Qiangtai Huang,
Sun Yat-sen University, China

Reviewed by:
Xia Guoqing,
Chengdu University of Technology, China
Yong Fu,
Guizhou University, China

***Correspondence:**
Yulin Shen
yulinsh@163.com

Specialty section:
This article was submitted to Geochemistry, a section of the journal Frontiers in Earth Science

Received: *20 September 2021*
Accepted: *29 October 2021*
Published: *26 November 2021*

Citation:
Yang T, Shen Y, Qin Y, Zhang Y, Lu L, Jin J, Zhao Y, Zhu Y and Zhang Y (2021) Genetic Mechanism and Environment Implications of Siderites in the Lopingian Coal-Bearing Series, Western Guizhou of China: Constrained by Whole-Rock and In Situ *Geochemistry. Front. Earth Sci. 9:779991. doi: 10.3389/feart.2021.779991*

A large number of siderites have been found in the Lopingian (Late Permian) coal-bearing series in western Guizhou, which occurs in various microscopic morphologies and has potential insights into the sedimentary and diagenetic environments. An integrated set of analyses, such as microscopic observation; X-ray diffraction; whole-rock major and trace element, carbon, and oxygen isotope; and *in situ* major and trace element, has been carried out to unravel the genetic mechanism of the siderites and their environmental implications. According to the microscopic morphology, the siderites can be generally divided into three types and six subtypes, including gelatinous siderites (I), microcrystal-silty siderite [II; microlite siderites (II_1), powder crystal siderites (II_2)], and spheroidal siderite [III, petal-like siderite (III_1), radiating fibrous siderite (III_2) and concentric siderite (III_3)]. Whole-rock geochemical results show that the iron source for the formation of the siderites was mainly from extensive weathering of the Emeishan high-titanium basalts in hot climate conditions. The carbon and oxygen isotopic results indicate that the origin of CO_2 in type I siderites is derived from the dehydroxylation of organic matter. The CO_2 in types II_1 and II_2 siderites is mainly derived from deposited organic matter and marine carbonate rocks, respectively. The CO_2 source of type III siderites is sedimentary organic matter and marine carbonate rocks and is affected by different fluids during diagenesis. The whole-rock and *in situ* geochemical characteristics further point to that type I siderites were formed in the synsedimentary period most strongly affected by seawater. Redox proxies, such as V/Sc, V/(V+Ni), and δ Ce, constrained their formation in a stable and weakly reduced condition. Type II siderites could have been developed in saltwater. Among them, type II_1 siderites were formed in the early diagenetic stage, whereas type II_2 siderites originated from recrystallization of type II_1 siderites and accompanied by metasomatism with calcites under diagenetic fluids of weak reduction to weak oxidation conditions. Type III siderites were formed under the influence of multistage diagenetic fluids. Among them, type III_1

siderites formed by the growth of powder crystal siderites (II_2) under diagenetic fluids with a weak reducing condition. Type III_2 siderites formed by growth around microlite siderites under weak reducing diagenetic fluids. Type III_3 siderites formed by concentric growth in diagenetic fluids with weak reduction to weak oxidation conditions and relatively active conditions.

Keywords: siderites, sedimentary environments, diagenetic environments, coal-bearing series, Lopingian, western Guizhou

1 INTRODUCTION

Siderite is a common carbonate mineral, and sedimentary siderite is formed by complex reactions of iron and organic matter precipitated during quasi-syngenesis (Sánchez-Román et al., 2014; Wittkop et al., 2014; Weibel et al., 2016). Siderite mostly forms in sediments with organic-rich, low Eh (oxidation–reduction potential), weak oxidation to weak reduction conditions, high alkalinity, and low sulfur concentrations (Berner, 1981; Mozley, 1989; Haese et al., 1997; Uysal et al., 2000; Passey, 2014; Phillips et al., 2018; Hiatt et al., 2020). The geochemical characteristics of siderite have been used to characterize the porewater during diagenetic phases (Curtis et al., 1986; Mozley, 1989; El Albani et al., 2001; Passey, 2014; Hiatt et al., 2020), and the combination with other minerals can be used to distinguish marine and freshwater environments (Mozley and Wersin, 1992; Ludvigson et al., 1998; Choi et al., 2003; Lim et al., 2004; Rodrigues et al., 2015). For example, siderites in marine mudstones usually point to a rapid transgression in early diagenetic phase (Laenen and Craen, 2004). Moreover, the siderite morphology has been widely studied, and it is generally believed that cryptocrystalline siderite is mostly occurring in the marine environment, and authigenic spheroidal siderite is common in freshwater and organic-rich environment (Mozley, 1989; Laenen and Craen, 2004; Passey and Jolley, 2009; Passey, 2014; Weibel et al., 2016).

The siderite-bearing strata are widely developed in coal measures in western Guizhou, and some studies have been conducted to determine its characteristics, as well as the genesis (Shen et al., 2017; Shen et al., 2019; Zhang et al., 2018; Zhang et al., 2020). For example, various forms of siderite have been recently identified by Zhang et al. (2020), and the suggested morphology of siderites is controlled by sedimentary sequence. However, how the sedimentary and diagenetic environments control the formation of siderites has always been an extensively debated topic. In this article, we identified multiple siderite-bearing strata with variable micromorphological types of siderite at Lopingian coal-bearing series in Panxian, western Guizhou, China, and performed an integrated analysis on the samples and obtained a set of new petrological, mineralogical, and geochemical data. Based on these data, we analyzed the formation model of siderite and their implications for the depositional and diagenetic environment.

2 GEOLOGICAL BACKGROUND

The study area is located in Panxian, western Guizhou, at the junction of Yunnan and Guizhou, on the margin of an epicontinental basin covering South China (**Figure 1A**). During the late Permian, this area was in the Liupanshui fault depression (Xu and He, 2003). The Lopingian is a representative Upper Permian coal-bearing sequence in the region, and there are various sedimentary environments including continental, delta, and marine facies from west to east (Wang et al., 2011; Shen et al., 2016; Shen et al., 2019; Qin et al., 2018). Lopingian can be divided into Wuchiapingian and Changhsingian from bottom to top. The Wuchiapingian is mainly composed of gray, dark gray, and gray–yellow mudstones, silty mudstones, siltstones, fine sandstones, carbonate rocks, and coal seams. Multiple layers of marine key beds and regionally stable coal seams as products of pulsating transgression events can be used as good correlation marker beds (Wang et al., 2011; Shen et al., 2016). Meanwhile, the Changhsingian is mainly composed of gray and dark gray argillaceous siltstone, mudstone, limestone, and fine sandstone, with 6 to 20 coal seams (Shen et al., 2016). According to the sequence stratigraphic framework established by previous studies (Shao et al., 2011; Shen et al., 2016; Shen et al., 2019), the study strata can be divided into four third-order sequences.

The Y2 and Y3 drillings are located between Tucheng and Panzhou; Y3 drilling is located west of Panzhou (**Figure 1A**). The study strata are interpreted as delta, lagoonal tidal flat facies (Xu and He, 2003). Note that the siderite-bearing strata are usually grayish black to grayish yellow, which is different from the surrounding rock (**Figures 2A–C**). The main lithologies are mainly mudstone, silty mudstone, and few siltstones.

3 SAMPLES AND ANALYTICAL METHODS

A total of 25 siderite samples were taken from three drilling wells in the study area, among which J3 well samples were evenly distributed in the Late Permian coal-bearing series. To investigate the formation model of siderite and their implications for the sedimentary and diagenetic environments the following analytical methods were performed (**Figure 1B**).

The petrographical and mineralogical characteristics of the samples were detected by an Olympus BX53M microscope in the School of Resources and Geosciences, China University of Mining and Technology.

The whole-rock X-ray diffraction (XRD) analysis by X′ Pert Pro X-ray powder diffractometer was conducted in Regional Geology and Mineral Resources Institute of Hebei. The test conditions were as follows: (1) working voltage 40 kV; (2) working current 40 mA; (3) Cu-Kα ray, wavelength 0.15416 nm, Ni filter; and (4) continuous step scanning with a

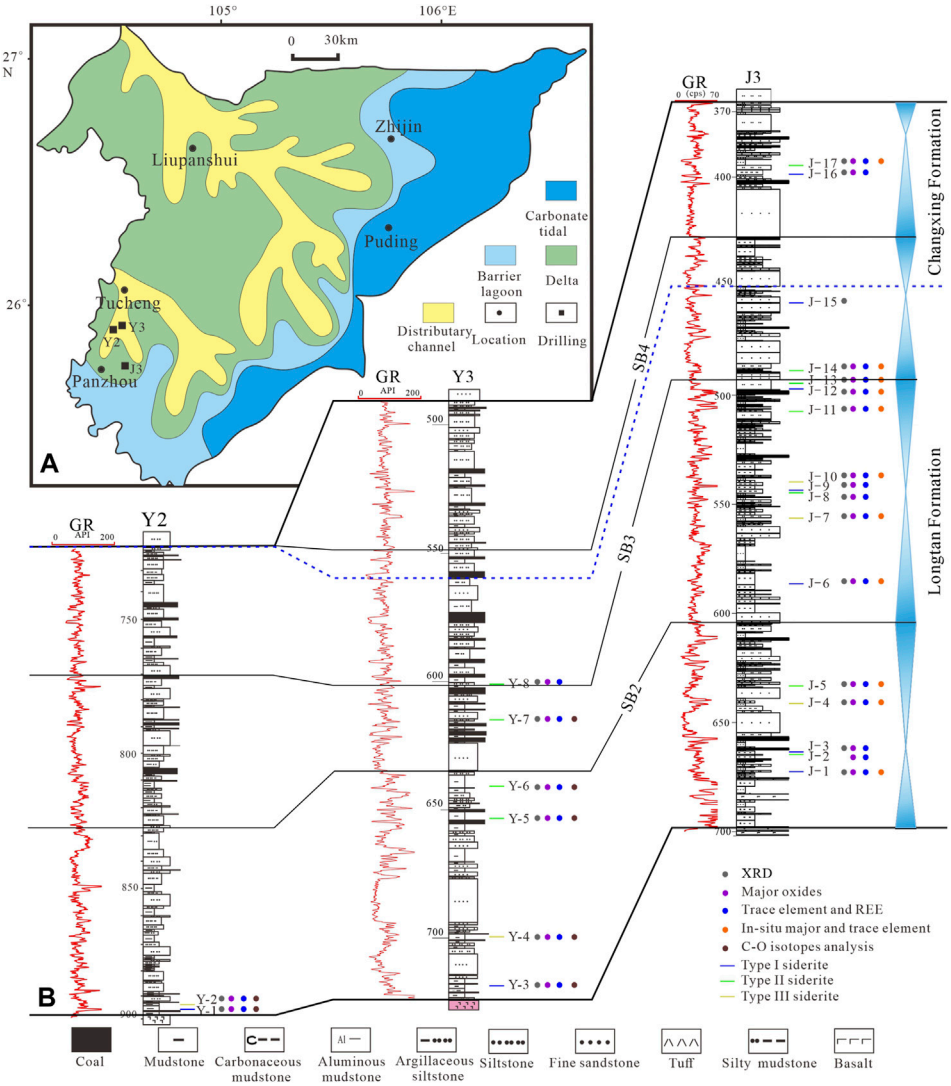

FIGURE 1 | (A): Lopingian sedimentary system and drillings location in western Guizhou (modified after Shen et al., 2016). **(B)**: Strata column, sampling positions, and analytical methods of J3, Y2, and Y3 wells.

step size of 0.017, the scanning speed is of 0.417782/s and the preset time is of 2′ 36″.

Whole-rock major element analyses were conducted on XRF (Primus II, Rigaku, Japan) at the Wuhan Sample solution Analytical Technology Co., Ltd., Wuhan, China. Detailed analysis procedure referred to "Methods for chemical analysis of silicate rocks-Part 28: Determination of 16 major and minor components" in the standard GB/T14506.28-2010.

Whole-rock trace element analyses were conducted on Agilent 7700e ICP-MS at the Wuhan Sample Solution Analytical Technology Co., Ltd., Wuhan, China. Detailed analysis procedure referred to "Methods for chemical analysis of silicate rocks-Part 30: Determination of 44 elements" in the standard GB/T14506.30-2010.

The samples for carbon and oxygen isotopic analysis were collected from Y2 and Y3 wells, and the analysis was conducted in the Geological and Environmental Institute of CUG (Wuhan). The siderite samples were first ground to less than 200-mesh and then reacted with phosphoric acid in a constant temperature tank at 72°C for 1 h. The collected CO_2 was transferred to the MAT-253 for the C-O isotopes analysis. The analysis precision better is than ±0.2‰.

In situ major and trace element analysis of siderite by LA-ICP-MS was conducted at the Wuhan Sample Solution Analytical Technology Co., Ltd., Wuhan, China. Laser sampling was performed using a GeolasPro laser ablation system that consists of a COMPexPro 102 ArF excimer laser (wavelength of 193 nm and maximum energy of 200 mJ) and a MicroLas optical system. Beam size of 32 μm and laser frequencies of 5 Hz were used during the analyses. An Agilent 7700e ICP-MS instrument was used to acquire ion-signal intensities. Each analysis incorporated a background acquisition of

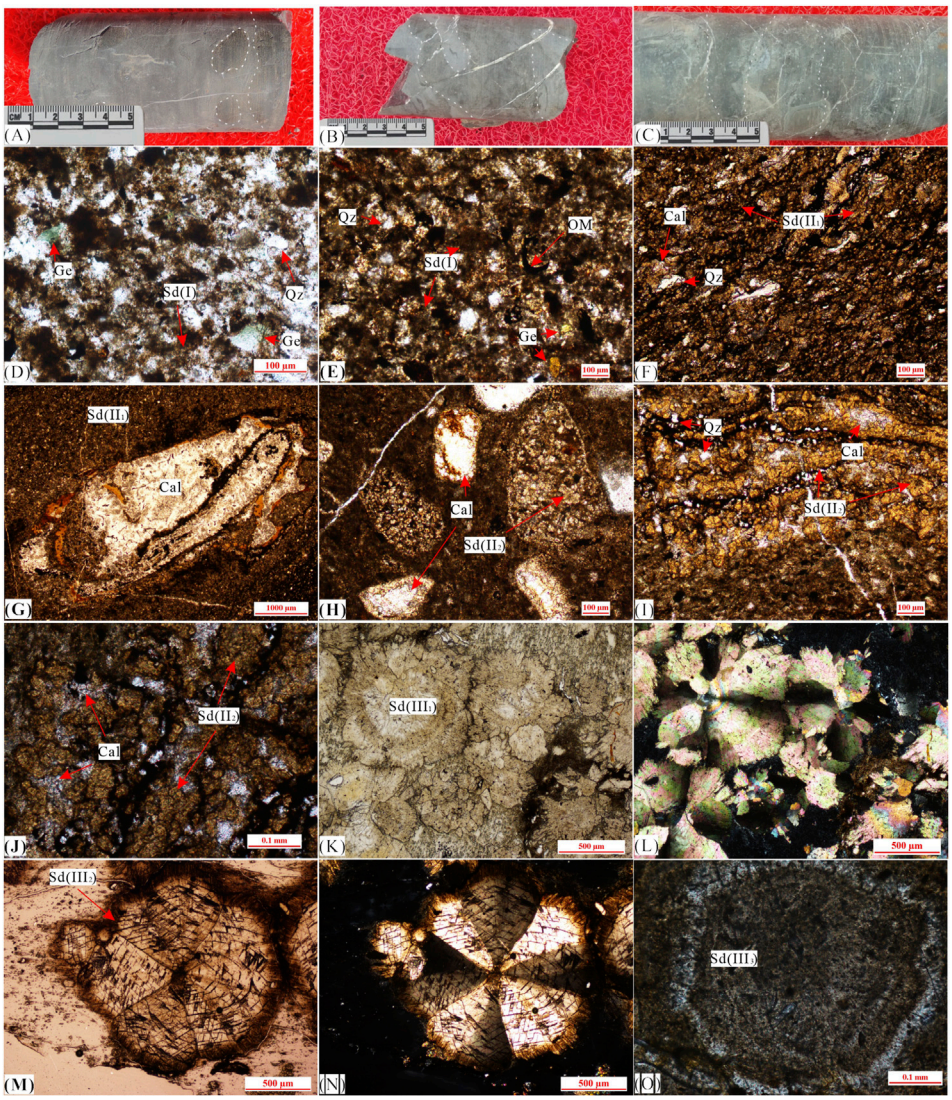

FIGURE 2 | Observation of drilling core and characteristics of siderites. **(A)** Siderite nodules and banded are discovered in the gray–black mudstone, J-3. **(B)** Siderite is lenticular and irregular agglomerated in the silty mudstone, J-7. **(C)** Irregular and banded siderite, J-11. **(D)** Gelatinous siderite mixed with clay minerals, showing angular glauconite, Y-3. **(E)** Gelatinous siderite is aggregated, and pyrite is locally developed, J-1. **(F)** Microlite siderite aggregate, evenly distributed, J-5. **(G)** Microlite siderite and powder crystal siderite are recrystallized around the shell of paleontology, J-13. **(H)** The paleontological shell is recrystallized into powder crystal siderite, J-14. **(I)** Powder crystal siderite, with large grains and developed to petal-like siderite, J-17. **(J)** Powder crystal siderite is recrystallized around calcite, and some are developed to petal-like siderite, Y-8. **(K)** Petal-like siderite, lane-polarized light, Y-2. **(L)** Cross-polarized light of "K." **(M)** Radiating fibrous siderite, lane-polarized light, Y-4. **(N)** Cross-polarized light of "M." **(O)** Concentric siderite, lane-polarized light, J-4. Sd, siderite; Qz, quartz; Ge, glauconite; OM, organic matter; Cal, calcite.

approximately 20 s followed by 50-s data acquisition from the sample.

4 RESULTS

4.1 Petrographic Characteristics

There are many siderite-bearing strata in western Guizhou, and the occurrence forms are diverse (**Figure 2**), mainly including nodular (**Figure 2A**), lenticular (**Figure 2B**), irregular (**Figures 2B,C**), and banded (**Figure 2C**). The banded siderite is usually surrounded by horizontal bedding and does not cut across the bedding (**Figure 2C**).

According to the microscopic morphology, the siderites can be generally divided into three types and six subtypes (**Figure 2**): gelatinous siderites (I), microlite siderites (II_1), powder crystal siderites (II_2), petal-like siderites (III_1), radiating fibrous siderites (III_2), and concentric siderites (III_3).

4.1.1 Gelatinous Siderite (I)

The gelatinous siderite is yellowish-brown under the polarizing microscope, and it is difficult to observe the grain boundary

TABLE 1 | Mineral compositions of the studied samples determined by XRD analysis (wt%).

Sample	Clays	Quartz	Siderite	Plagioclase	Calcite	Ankerite	Anatase	Pyrite	Hematite	Thenardite
J-1	17.0	20.6	49.4	—	5.3	—	5.2	—	—	2.4
J-3	9.0	38.6	37.4		6.3	—	8.7	—	—	—
J-4	77.6	13.0	3.06	3.4	—	—	2.9	—	—	—
J-5	16.6	18.0	62.8	—	—	—	2.6	—	—	—
J-6	13.5	37.4	28.2	—	1.9	16.8		—	2.3	—
J-7	19.4	11.2	66.7	1.7	1.0	—		—	—	—
J-8	11.0	52.0	23.6	1.3	5.1	—	6.8	—	—	—
J-9	21.0	39.1	31.1	1.4	—	—	7.4	—	—	—
J-10	20.0	23.6	48.2	2.8	—	—	5.4	—	—	—
J-11	16.4	39.6	23.9	3.0	1.3	—	6.0	—	—	9.7
J-12	42.8	26.3	21.7	4.7	—	4.5	—	—	—	—
J-13	14.9	8.2	72.3	—	1.6	—	—	3	—	—
J-14	23.4	13.3	50.8	—	—	—	—	2.4	—	—
J-15	19.4	23.2	12.0	—	—	42.8	—	—	2.6	—
J-16	9.0	39.1	10.9	4.5	11.2	11.5	12.0	1.8	—	—
J-17	16.5	26.1	42.6	1.7	12.1	1.0	—	—	—	—
Y-3	24.9	32.4	19.5	—	16.6	—	6.6	—	—	—
Y-4	3.6	4.4	90.7	—	1.4	—	—	—	—	—
Y-5	24.4	43.4	18.6	—	13.6	—	—	—	—	—
Y-6	16.3	12.4	57.9	—	13.4	—	—	—	—	—
Y-7	15.0	7.0	57.0	1.7	5.7	13.6	—	—	—	—
Y-8	3.0	9.4	77.7	—	9.9	—	—	—	—	—

(**Figures 2D,E**). Note that they were divided into two forms. One of which is evenly distributed in the pores between clastic particles, and the other is aggregated into blocks. Among them, uniform gelatinous siderite distributed in rocks is often filled in the pores between clastic particles in the form of cement and mixed with clay minerals (**Figure 2D**). The block-like gelatinous siderite is often surrounded by clastic particles, clay minerals, and organic matter (**Figure 2E**).

4.1.2 Microcrystal-Silty Siderite (II)

Crystal boundaries can be observed in microlite and powder crystal siderites under the microscope, which appear as hypidiomorphic or automorphic granular single crystal or aggregates with various shapes and sizes (**Figures 2F–J**). Among them, the microlite siderite often has color of light brown–yellow to light yellow, grain size between 0.004 and 0.03 mm, and mainly hypidiomorphic shapes. This kind of siderite is evenly distributed and mixed with clay minerals and organic matter or appears surrounding clastic particles (**Figure 2F**). The powder crystal siderite (II_2) is light yellow, and the grain size is between 0.015 and 0.09 mm with a good degree of crystallization. Siderite crystals are mainly automorphic and often develop at the edge of the cavity filled with calcite (**Figures 2G,H**) or in the area with high calcite content (**Figures 2I,J**).

4.1.3 Spheroidal Siderite (III)

This type of siderite has relatively large grain size, ranging from 0.1 to 1 mm, and appears light yellow to light yellowish brown under plane-polarized light (**Figure 2**). Although the petal-like siderite (III_1) has similar ring shapes, differences in morphology still exist. The fully developed siderite is spherical, and the incomplete siderite is bow-tie morphology (**Figure 2K**). Under cross-polarized light, the interference color is from pink to bright green (**Figure 2L**). Radiating fibrous siderite has a radiating texture, internal cleavage, and cross extinction under cross-polarized light (**Figures 2M,N**). Concentric siderite (III_3) has obvious concentric ring morphology (**Figure 2O**), and its distribution in the bedding is highly heterogeneous, usually concentrated in the form of aggregate.

XRD results show that the minerals in the samples include clay, quartz, siderite, plagioclase, calcite, ankerite, anatase, pyrite, hematite, and thenardite (**Table 1**). The siderite content ranges from 3.06 to 90.7 wt%. Other main components quartz, clay minerals, and calcite range from 4.4 to 52 wt%, 3 to 77.6 wt%, and 0 to 16.6 wt%, respectively. Other components are low, and some samples contain high ankerite. The content of type I siderite in rocks is relatively low. The XRD results show that the average content is only 26.3 wt%, with an exception of J-3 sample more than 40%. Type II siderite is common in rocks with high relative content (**Table 1**). The XRD analysis results showed that the average content in rocks reached up to 48.72% (**Table 1**). The distribution of spheroidal siderite in the rock is heterogeneous. The XRD analysis results show that the content varied largely among different samples (**Table 1**).

4.2 Whole Rock Geochemistry

4.2.1 Major Elements

The whole-rock major elements results are listed in **Table 2**. By normalizing the major elements results based on the upper crust (UC) (Taylor and McLennan, 1985), we find the concentration of main oxides in the studied samples is comparable to that in the UC, except the depletion of K_2O and the enrichment of TiO_2, *T*FeO (total iron), MnO, MgO, and CaO. The type I siderite-bearing samples have the highest content of SiO_2, and the samples containing the other two types of siderite are similar. All of

TABLE 2 | Statistics of major element oxide content (wt%), trace element, and rare earth element concentrations (μg/g) of the studied samples.

Sample	J-1	J-2	J-3	J-4	J-5	J-6	J-7	J-8	J-9	J-10	J-11	J-12	J-13	J-14	J-16	J-17	Y-1	Y-2	Y-3	Y-4	Y-5	Y-6	Y-7	Y-8
SiO_2	27.29	54.7	47.42	48.77	34.68	32.07	28.11	31.81	26.24	25.43	41.77	37.38	33.44	21.13	39.61	15.34	36.03	25.12	39.73	15.29	28.89	11.03	24.96	12
TiO_2	1.98	3.8	3.76	5.12	3.41	1.21	2.24	1.41	1.69	1.99	2.23	2.34	2.1	0.97	2.68	1.03	2.84	15.79	2.07	0.93	1.01	1.25	2.14	1.01
Al_2O_3	9.1	19	18.04	23.64	14.85	6.24	9.92	5.8	7.51	8.38	10.36	11.08	8.79	5.42	12.34	5.02	14.15	2.07	11.3	6.28	4.97	4.92	8.21	4.31
TFeO	33.74	9.46	14.36	7.98	22.6	26.91	34.42	34.27	35.43	35.4	23.87	25.71	27.72	35.15	21.18	43.57	26.77	32.19	17.25	47.13	27.68	38.72	25.05	39.17
MnO	0.72	0.03	0.18	0.03	0.26	0.66	0.86	0.69	0.65	0.6	0.4	0.27	0.38	0.5	0.36	1.21	0.27	0.17	0.56	0.3	1.24	1.04	0.42	0.59
MgO	1.51	1.09	1.18	1.5	1.56	3.88	2.16	3.68	3.76	3.91	3.32	4.3	4.42	5.64	3.96	3.2	1.05	0.52	0.9	1	1.81	3.16	3.54	2.96
CaO	4.04	0.96	1.74	0.39	1.06	6.06	1.81	2.46	3.16	2.39	2.23	3.02	3.38	5.23	4.94	3.24	5.93	0.72	9.18	1.48	7.04	5.93	7.05	5.54
Na_2O	0.34	0.6	0.58	1.04	0.67	0.49	0.63	0.14	0.32	0.47	0.74	0.81	0.74	0.26	0.68	0.29	0.08	0.17	0.22	0.09	0.15	0.23	0.47	0.16
K_2O	0.6	1.34	0.98	2.9	0.87	0.33	0.7	0.12	0.27	0.41	0.51	0.38	0.41	0.16	0.54	0.34	0.02	0.2	0.53	0.04	0.36	0.35	0.87	0.24
P_2O_5	0.36	0.43	0.42	0.11	0.28	0.64	0.3	0.35	0.38	0.42	0.21	0.48	0.53	0.64	0.91	0.38	0.35	0.3	0.28	0.22	0.77	0.97	0.42	0.5
LOI	20.05	8.3	11.02	7.46	19.75	20.88	19	19.7	20.66	20.97	14.3	14.29	17.49	24.05	12.39	26.63	11.73	22.21	17.49	26.52	25.77	31.67	26.59	31.16
SUM	99.73	99.69	99.69	98.96	99.98	99.37	100.14	100.42	100.06	100.36	99.93	100.06	99.41	99.15	99.58	100.24	99.22	99.44	99.5	99.29	99.68	99.27	99.71	97.64
CIA	83.69	84.77	85.84	81.68	82.49	76.07	77.72	90.79	84.7	80.69	77.61	78.2	75.28	84.18	81.33	79.11	97.92	95.38	89.68	94.95	84.92	81.16	76.82	84.38
Li	15.5	25.5	28	13.3	32	32.8	37	34.1	38.4	38.4	46.6	54.5	38.9	29.4	46.2	15	14.6	17	15.1	9.7	12.5	9.3	7.7	6.5
Be	2.6	3.4	3.4	5.5	3	1.9	2.7	2.2	2.5	3.3	2.5	1.9	2.3	2.1	2	2.8	1.4	3.8	2.9	2.9	2.8	2.9	2.4	3.4
Sc	16.2	27.8	24.8	32.3	22	11.9	18.6	15.9	20.5	20.4	17	21.6	14.6	10.8	19.1	13.2	23.5	14.3	15.4	11.2	9.4	13.3	14.7	17
V	169.4	325.1	297.8	357.1	260.6	109.6	206.1	151.2	199.5	220	194.5	213.2	166.3	153.4	221	126.1	391.1	147.8	153	93	137.9	86.9	158.8	118.9
Cr	72.5	105.3	123.2	227.3	72.7	62.3	73.8	37.9	55	75.9	105.1	157.2	108.1	79.2	89.5	38.6	63.9	41.7	62.5	17.1	33.5	60.1	143.7	37.2
Co.	49.2	30.4	36.9	22.2	39.5	15.4	57.7	22.2	26.5	28	33.2	21	26.4	20.1	31.6	67.3	84.5	45.2	38.7	51.6	11.2	31.6	22	76.1
Ni	53.3	71.9	81.2	67.7	53.1	31.5	81.6	61.9	67.8	65.8	97.2	89	71	46.8	118.3	47.7	44.1	42.1	49	47.4	11.3	30.8	33.6	57.1
Cu	92.3	193.5	187	212.6	146.9	35.6	99.3	63.9	71	83.1	85.5	79.7	85.3	30.9	113.3	51.1	105	60.5	101.5	38.1	40.1	51.5	70.7	45.7
Zn	81.5	133.4	168.2	158.9	130.8	61.3	150.3	71.7	76.6	88.3	96.8	120.4	89.9	54.3	111.9	115.2	197.8	130.5	173.8	302.1	49.6	81	105.6	221.1
Ga	18	35.3	34.2	41.8	27.1	11.3	20.6	13.4	15	16.7	19.6	21.6	16.3	11.1	23.6	9.9	31.7	32.4	21.2	19.6	9.3	9.4	15.6	6.4
Rb	22.7	46.7	36.2	88.5	28.2	11.4	22.7	4.6	9.5	13.7	17.5	14.3	14.4	5.5	20.1	12.2	1.8	9.6	25.3	3.7	14.6	13.7	33.3	8
Sr	180.2	276.8	248.8	441	229.5	224.2	243.3	102	241.5	150.9	198.2	195.9	155.8	159.5	365.1	138.5	190.9	199.1	140.1	64.2	148.8	145.1	234.2	181.3
Zr	250.7	574	492.3	592	361.8	159.7	238.2	157.3	185.7	222.6	271.9	251.6	235.7	130.7	358.8	137.5	196.1	463.2	359	124.9	147.1	163.8	193.9	194
Nb	41.3	87.5	77.6	75	51.1	22.4	32.8	18.9	24.3	29.5	41.6	38.7	36.9	18.7	39.3	17.7	25.5	48.7	46.2	15	17.5	21.4	28.5	14.3
Sn	2	4.1	3.8	4.5	3	1.2	2.2	1.3	1.5	1.8	2.3	2.2	1.8	1.2	2.7	1.1	1.7	4.9	2.7	1.1	1	0.9	1.5	
Cs	0.7	1.8	1.6	3.1	1.3	0.3	0.7	0.2	0.3	0.5	0.8	0.5	0.5	0.2	0.5	0.4	0	0.3	0.6	0.2	0.4	0.4	0.8	0.3
Ba	136.6	341	275.3	1,142.9	459.4	144.7	341	135.9	171.6	263.8	257.7	169.7	215.2	107.2	167.4	167.2	140.5	184.5	122.5	103	193.4	223.7	354.6	224.1
Hf	6.2	14	12.3	15.6	8.7	4	6	3.6	4.3	5.2	6.7	6.2	5.8	3.2	8.2	3.1	5.8	11.5	9	3.3	3.9	4.3	5.4	4.6
Ta	2.3	5.4	5	4.4	3.1	1.4	2	1.1	1.4	1.8	2.4	2.2	2.1	1.1	2.3	1.1	2.3	3.9	3.7	1.2	1.4	1.7	2.2	1
Tl	0.1	0.2	0.3	0.2	0.1	0	0	0	0	0	0.1	0	0.1	0	0.1	0	0	0	0	0	0	0	0.1	0
Pb	4.5	8.7	7.8	13.8	6.2	4.1	4.3	3.3	4.8	3.3	7.9	2.3	7.3	4.5	6.1	3.5	10.3	21	11.3	12.9	2.9	4.9	4.4	8.5
Th	6.2	16	13.6	16.7	8.4	3.9	5.7	3.3	4.2	5	7.1	6.1	6.1	3.6	8.5	3.2	5.3	13.7	10.1	3.3	4.6	4.6	5.2	3.8
U	1.4	3.7	3.2	3.7	1.9	1.8	1.2	0.8	1	1.1	1.4	1.4	1.4	1.5	1.6	0.8	1.5	2.5	2.3	1.1	1.9	1	1.2	0.8
La	44	93.4	82.5	118.3	50.9	39	43.5	25.1	30.9	37.7	43.6	38.6	40	32.2	61.7	21.6	35.8	54.3	68	18	38	40.8	32.9	31.4
Ce	86.5	201.1	176	228.9	110.8	79	89.7	52.4	63.4	74.8	87.8	83.7	84.4	69.2	139	47.1	102.4	125.6	144.9	39.8	78.4	90.5	68.5	66.3
Pr	10.6	24	21	26	14	9.4	10.9	6.4	7.8	9	10.2	10.4	10	8.4	17.4	5.6	13.5	15	15.3	5.5	11.5	12.3	9.1	8.5
Nd	42.3	91	82.9	95.1	55	39.6	45.1	27.9	33.6	38.8	39.5	44.2	42.1	36	76.8	24.3	57.9	59.9	68.5	23.9	53.1	54.4	38.4	35.5
Sm	8.9	15.8	15.5	13.8	11.3	8.4	8.2	6.9	7.9	9.2	7.6	10.7	9.6	8.5	18.6	6.1	15	14.6	12.6	6.3	16.1	12.4	8.6	7.9
Eu	3	3.7	4.2	2.9	3.2	2.7	2.3	2.4	2.6	2.9	2.4	3.7	3.2	3.5	6	1.7	4.9	3.7	3.3	2.1	5.7	4.2	2.8	2.4
Gd	7.9	12.4	14	9.4	10	7.2	7.4	7.9	8.5	8.7	7.5	10.8	9.2	8.9	16	6	15.5	15.2	12.8	7.1	17.6	11.3	8.7	6.9
Tb	1.1	2	2.1	1.7	1.6	1	1.2	1.1	1.2	1.2	1.2	1.3	1.3	1.2	1.9	0.9	2.6	2.6	1.8	1.2	2.3	1.4	1.3	1.1
Dy	6.6	11.2	11	10.8	8.8	5	7	5.8	5.9	6.6	6.5	6.7	6.2	6.4	9.4	5.1	13.6	15.5	9.4	7.3	10.8	6.3	6.6	6.2
Ho	1.1	2.2	2	2.2	1.7	0.8	1.4	1.1	1.1	1.1	1.2	1.1	1	1.1	1.5	0.9	2.3	2.9	1.6	1.4	1.8	1	1.2	1.2
Er	3.2	5.9	5.3	6.3	4.5	2.2	3.9	3	3	3.2	3.2	3	2.8	2.7	3.9	2.6	5.8	8.4	4.5	3.7	4.7	2.7	3.1	3.4
Tm	0.4	0.8	0.7	0.9	0.6	0.3	0.5	0.4	0.4	0.4	0.4	0.4	0.4	0.4	0.5	0.3	0.8	1.4	0.7	0.6	0.7	0.4	0.5	0.6
Yb	2.8	5.2	4.5	5.8	3.6	1.6	3.3	2.5	2.6	2.4	2.6	2.4	2.2	2.2	3.1	2.3	4.8	9	4.1	3.6	4.3	2.2	2.9	3.2
Lu	0.4	0.7	0.6	0.8	0.5	0.2	0.5	0.4	0.4	0.4	0.4	0.4	0.3	0.3	0.5	0.3	0.7	1.4	0.6	0.6	0.7	0.3	0.4	0.5
Sr/Ba	1.3	0.8	0.9	0.4	0.5	1.6	0.7	0.8	1.4	0.6	0.8	1.2	0.7	1.5	2.2	0.8	1.4	1.1	1.1	0.6	0.8	0.7	0.7	0.8
V/Cr	2.3	3.1	2.4	1.6	3.6	1.8	2.8	4	3.6	2.9	1.9	1.4	1.5	1.9	2.5	3.3	6.1	3.5	2.5	5.4	4.1	1.4	1.1	3.2
V/(V + Ni)	0.8	0.8	0.8	0.8	0.8	0.8	0.7	0.7	0.8	0.8	0.7	0.7	0.7	0.8	0.7	0.7	0.9	0.8	0.8	0.7	0.9	0.7	0.8	0.7
V/Sc	10.4	11.7	12	11.1	11.9	9.2	11.1	9.5	9.7	10.8	11.5	9.9	11.4	14.2	11.6	9.6	16.7	10.3	10	8.3	14.7	6.5	10.8	7
Sr/Cu	2	1.4	1.3	2.1	1.6	6.3	2.5	1.6	3.4	1.8	2.3	2.5	1.8	5.2	3.2	2.7	1.8	3.3	1.4	1.7	3.7	2.8	3.3	4
δ Ce	−0.05	−0.02	−0.03	−0.04	−0.03	−0.05	−0.04	−0.05	−0.05	−0.06	−0.04	−0.04	−0.04	−0.04	−0.03	−0.03	0.02	0	−0.03	−0.05	−0.09	−0.05	−0.06	−0.05
ΔEu	1.08	0.77	0.86	0.74	0.89	1.02	0.9	0.99	0.98	0.97	0.97	1.04	1.04	1.21	1.03	0.83	0.97	0.76	0.78	0.95	1.04	1.06	0.97	0.96

$\delta\ Ce = lg(3*Ce_N)/(2*La_N+Nd_N)$.

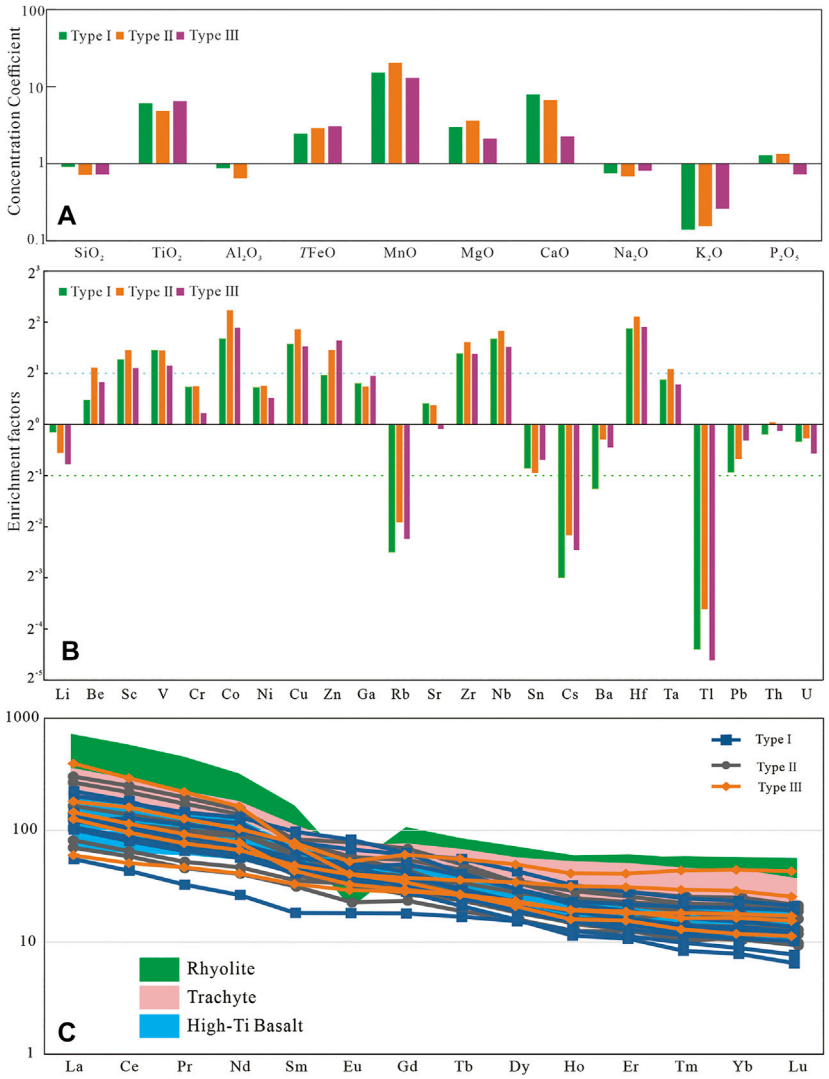

FIGURE 3 | (A) Major elements concentration coefficients (CC) of the studied samples, normalized by the UC. **(B)** Enrichment factors of trace elements of different types of siderite; **(C)** REE distribution pattern of different types of siderite. The pink and green areas are for trachyte and rhyolite (Xu et al., 2010), and the blue area is for high-Ti basalt (Xiao et al., 2004).

siderite-bearing samples have a high content of TiO_2, MgO, and MnO, which is likely related to the provenance. In addition, the *T*FeO content of samples containing type I siderite is the lowest, and the content of CaO gradually decreases from Samples containing type I to those containing type III.

4.2.2 Trace Elements

For most sedimentary deposits, some trace elements and aluminum can be well preserved and transported along with clastic materials and are usually immobile during diagenesis. These elements can be used for paleoenvironmental reconstruction only if their contents deviate greatly from average shale and have a good correlation with Al (Tribovillard et al., 2006). The enrichment factors of elements [$EF_{element\ X} = X/Al_{sample}/(X/Al_{average\ shale})$] are obtained by Al normalization, and the results are shown in **Figure 3B** (Tribovillard et al., 2006). Among them, the enrichment factors of Cr, Ni, Ga, Sr, Ba, Th, and U are between 0.5 and 2, close to the average shale. Th, Ga, and U have a good positive correlation with Al, whereas Sr, Ba, Ni, Cr, and Rb have a poor correlation (**Figure 4**).

4.2.3 Rare Earth Elements

The ΣREE values of the siderite-bearing samples are relatively high varying between 121 and 523 ppm. **Figure 3C** shows the distribution pattern of REE. The REE distribution pattern of all samples shows a significant enrichment of LREE. By comparing them with the values of the high-titanium basalts, trachytes, and rhyolites in the study area (Xiao et al., 2004; Xu et al., 2010) (**Figure 3C**), it was found that all samples are similar to the high-titanium basalts. The δ Ce values [$\delta\ Ce = lg\ (3 * Ce_N)/(2 * La_N + Nd_N)$] range from −0.09 to 0.02, whereas δ Eu

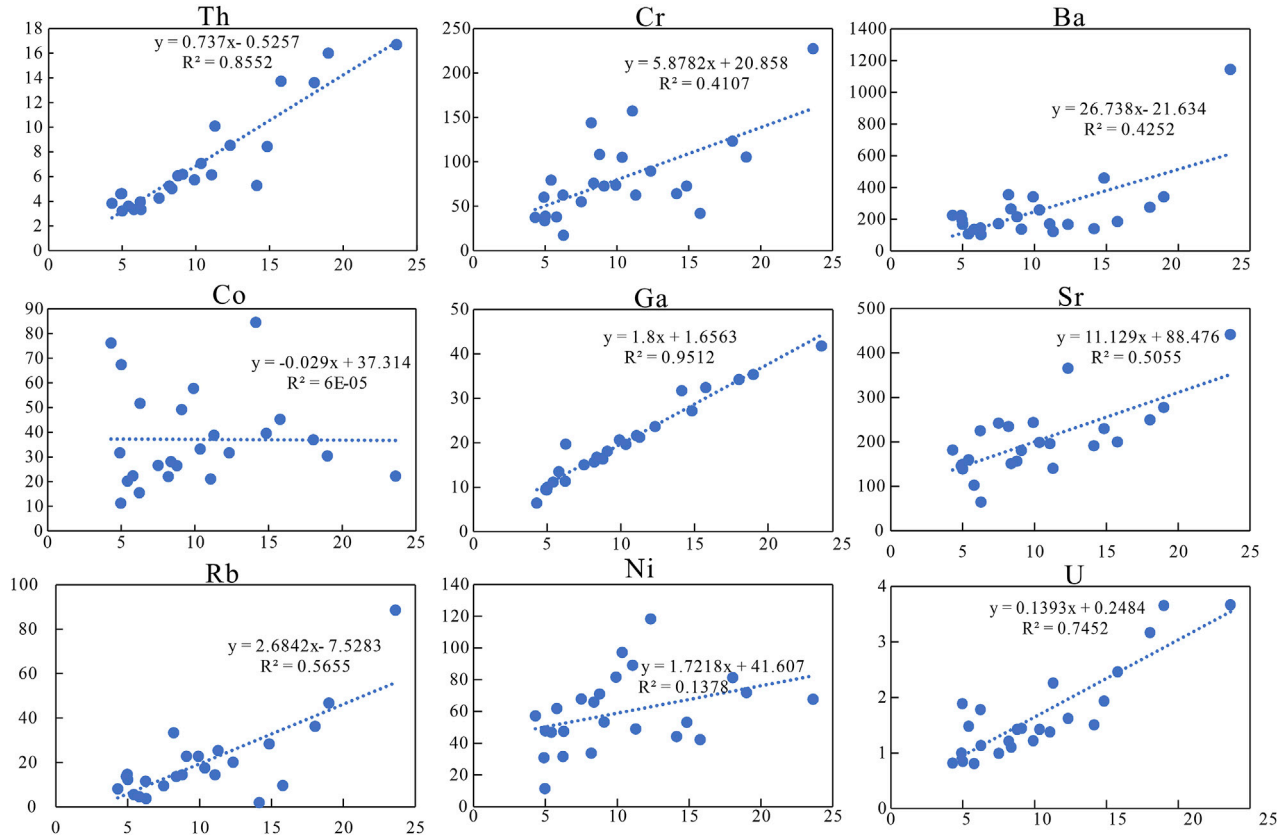

FIGURE 4 | Covariant relationship between Al and some trace elements, in which Th, Ga, and U are positively correlated with Al.

TABLE 3 | The results of carbon–oxygen isotope.

Sample	Siderite type	$\delta^{13}C‰$ (PDB)	$\delta^{18}O_{SMOW‰}$
Y-1	I	−10.06	17.34
Y-2	III	−6.33	28.38
Y-3	I	−9.20	20.65
Y-4	III	−11.94	25.78
Y-5	II	−10.58	23.23
Y-6	II	−2.80	24.64
Y-7	II	−4.01	23.31

values of samples with different types of siderite are different (**Table 2**). Most samples containing gelatinous siderite have δ Eu value larger than 1, whereas samples with type II siderite have δ Eu greatly variable from 0.77 to 1.04, (**Table 2**). The samples with type III siderite have δ Eu values ranging from 0.76 to 0.97, indicating slightly negative anomalies in element Eu.

4.3 Carbon–Oxygen Isotopic Compositions

The results of carbon–oxygen isotopes are shown in **Table 3**. The samples with type I siderite have uniform $\delta^{13}C_{PDB}$ and $\delta^{18}O_{SMOW}$ values of −9.20‰ to −10.06‰ and 17.34‰ to 20.65‰, respectively. The $\delta^{13}C_{PDB}$ values of samples with type II siderite range greatly from −2.80‰ to −10.58‰, which are dependent on the crystal types. The $\delta^{18}O_{SMOW}$ values are similar ranging from 23.23% to 24.64‰. The samples with type III siderite have $\delta^{13}C_{PDB}$ and $\delta^{18}O_{SMOW}$ of −6.33‰ to −11.94‰ and 25.78‰ to 28.38‰, respectively, with large fluctuation.

4.4 *In Situ* Geochemistry

The detailed results are shown in **Supplementary Appendix S1**, and the *in situ* spots are shown in **Figures 5**, **6**. Among them, the type I siderite has $FeCO_3$ (wt%) ranging from 26.62% to 51.64%, with an average of 36.63%, average $CaCO_3$ of 3.56%, and average $MgCO_3$ of 6.76%. For microlite siderite, the content of $FeCO_3$ (wt %) ranges from 47.34% to 86.8%, with an average of 72.67%. The contents of $CaCO_3$ and $MgCO_3$ vary greatly in different samples. The average content of $CaCO_3$ and $MgCO_3$ in J-5 is 4.43% and 2.79%, whereas that in J-11 is 7.64% and 7.99%, and that in J-13 is 8.58% and 10.27%, respectively. The environment formed by microlite siderite may be more extensive than that of gelatinous. The content of $FeCO_3$ (wt%) in powder crystal siderite ranges from 64.11% to 90.68%, with an average of 76.39%; the content of $CaCO_3$ ranges from 5.62% to 11.22%; and the content of $MgCO_3$ ranges from 2.76% to 16.76%, which are similar to the results of microcrystalline siderite samples. The content of $FeCO_3$ in type III siderite ranges from 71.26% to 91.87%, and the contents of $CaCO_3$ and $MgCO_3$ are lower than those in the other two types of siderite.

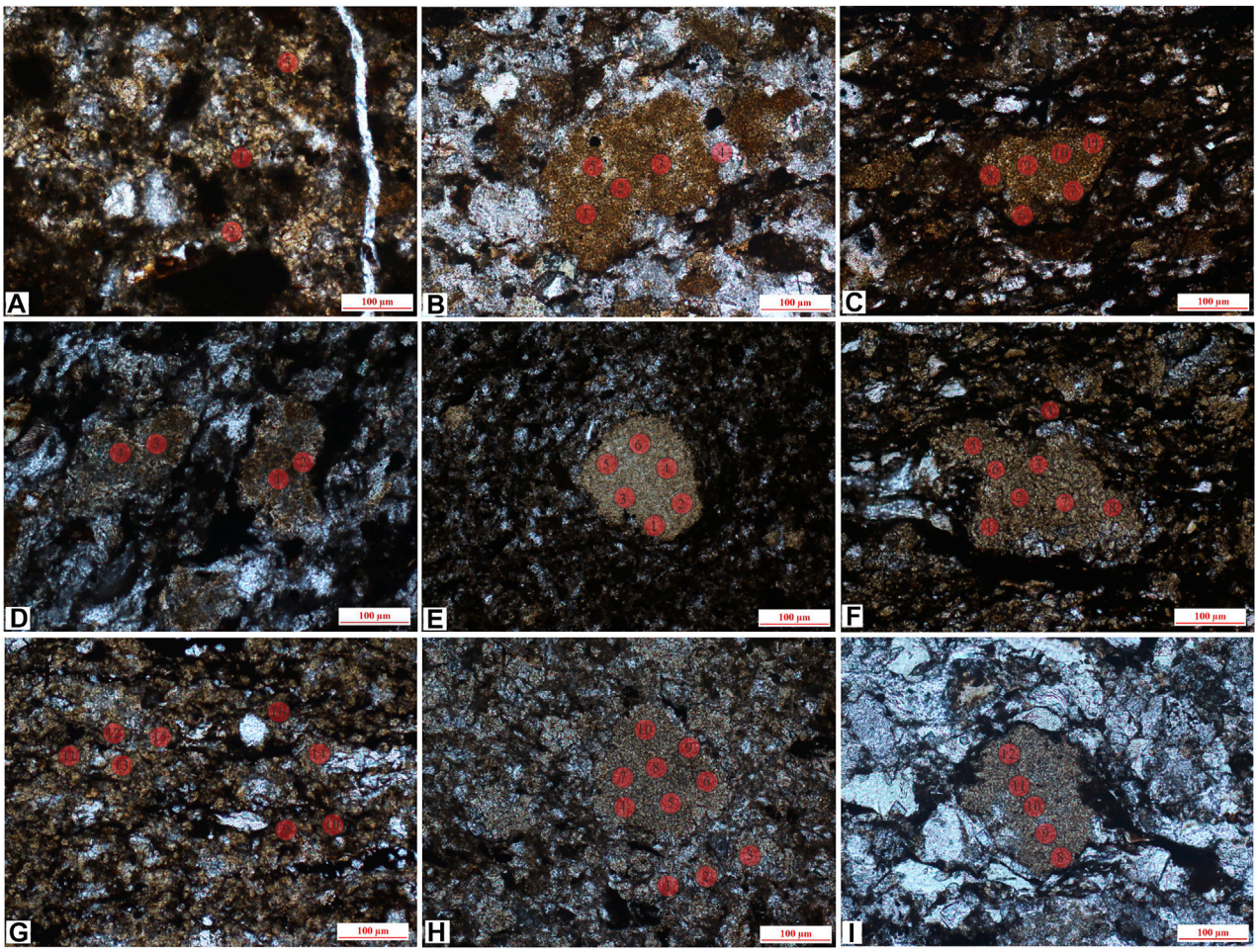

FIGURE 5 | *In situ* sites of gelatinous siderite and microlite siderite, **(A)** J-1, gelatinous siderite and partly recrystallized into powder crystal siderite (lane-polarized light); **(B,C)** J-6, mass aggregate, distributed among debris particles (lane-polarized light); **(D)** J-12, siderite is evenly distributed (lane-polarized light); **(E)** J-16, mass aggregate siderite and evenly distributed gelatinous siderite (lane-polarized light); **(F,G)** J-5, uniform distribution, microlite siderite (lane-polarized light); **(H)** J-11, microlite siderite is evenly distributed (lane-polarized light); **(I)** J-10 (1), mass microlite siderite is distributed between clastic particles (lane-polarized light).

The Sr/Ba value of type I siderite ranges from 0.79 to 3.75, with an average of 2.26, higher than that of the whole rock. δ Ce is between −0.08 and 0.06, with an average of 0.01; V/(V+Ni) is between 0.58 and 0.90, with an average of 0.73; and V/Cr is between 1.34 and 11.12, with an average of 2.36, which are also close to the whole rock. The V/Sc value is higher than the whole rock, with an average of 35.85. Different samples of type II_1 siderite are different in composition, although the *in situ* results are similar to that of the whole rock. The Sr/Ba value of type II_2 siderite ranges from 0.38 to 1.66, with an average of 0.58, which is quite different from the whole rock. There is little difference in Sr/Ba values of type III siderite, and the total average value is 0.50. The δ Ce value is between −0.19 and 0, and types III_1 and III_2 are different, reflecting the different diagenetic water where type III siderite formed. The V/(V+Ni), V/Cr, and V/Sc of III_1 and III_2 are also different.

5 DISCUSSION

5.1 Provenance Analysis of Siderite-Bearing Strata

The abundance of trace elements and the ratio of some immobile elements such as Al_2O_3/TiO_2, ΣREE, and La/Yb in mudstone can help to perform provenance analysis (Spears and Rice, 1973; McLennan et al., 1993; He et al., 2007; Dai et al., 2017; Xie et al., 2018; Liu et al., 2020). Rare earth elements are not easy to migrate during sedimentation and diagenesis, and the distribution pattern of REE can be used for provenance analysis (Boynton, 1984; Dai et al., 2017; Liu et al., 2019). **Figure 3C** shows that the REE distribution curves of all of siderite-bearing strata samples are relatively similar, which are characterized by enrichment in LREE and depletion in HREE. Eu has no obvious anomaly similar to Emeishan high-titanium basalt (Xiao et al., 2004). To study the provenance of the siderite-bearing strata, the discrimination

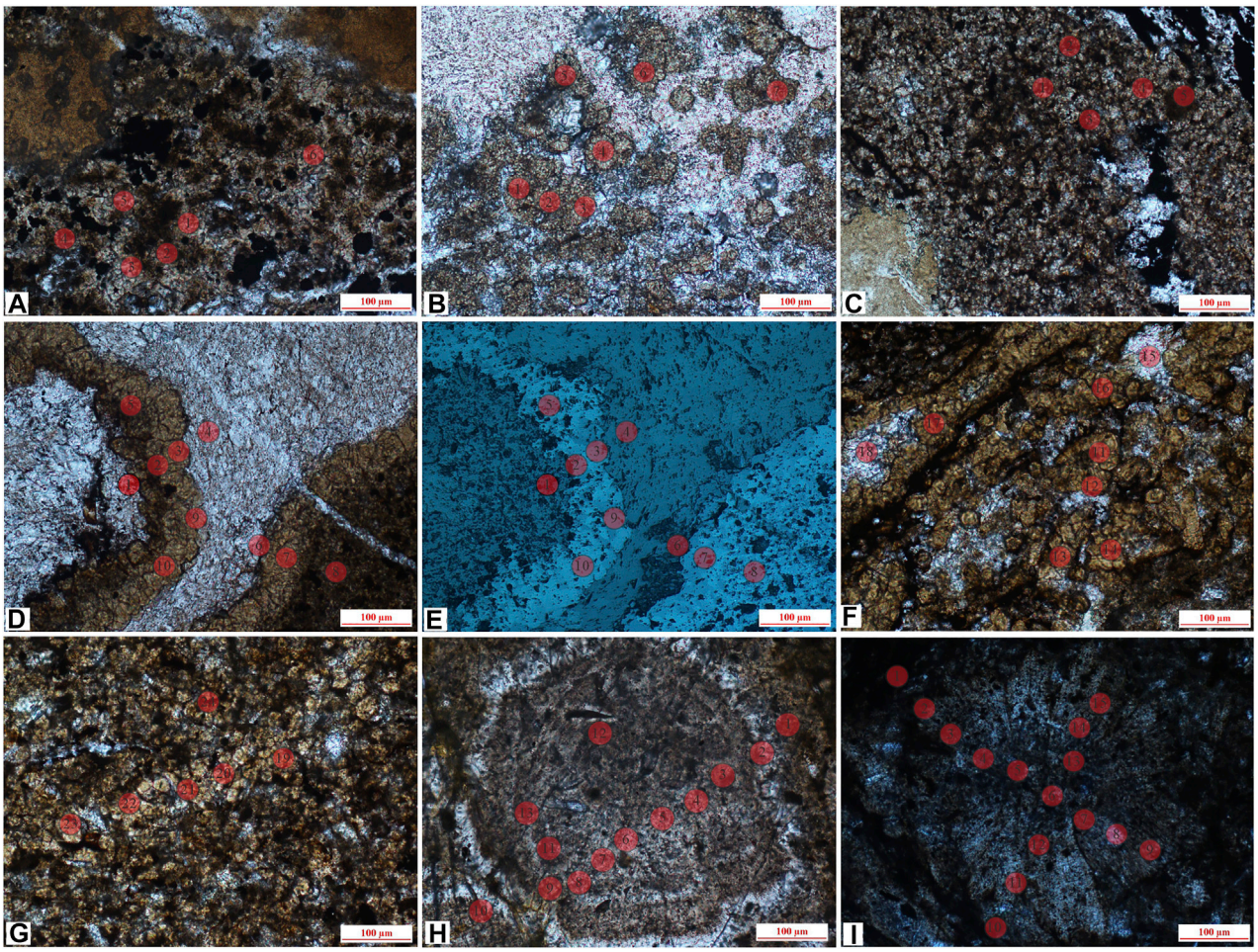

FIGURE 6 | *In situ* sites of microlite siderite, powder crystal siderite and sphaerosiderite, **(A)** J-13, microlite siderite, surrounded by clay minerals (lane-polarized light); **(B)** J-10 (2), powder crystal siderite, partially developed to petal-like siderite (lane-polarized light); **(C)** J-14, the powder crystal siderite is evenly distributed (lane-polarized light); **(D)** J-17 (1), powder crystal siderite and calcite (lane-polarized light); **(E)** reflecting light of **(D)**; **(F)** J-17 (2), powder crystal siderite, partially developed to petal-like siderite (lane-polarized light); **(G)** J-17 (3), powder crystal siderite (lane-polarized light); **(H)** J-4, concentric siderite (lane-polarized light); **(I)**. J-7, petal-like siderite (lane-polarized light).

diagram of ΣREE versus La/Yb was applied (Allègre and Michard, 1974; Xie et al., 2018) (**Figure 7A**). Apart from a small number of samples with gelatinous siderite that fall within the region of sedimentary rock, the others fall in the alkaline basalt (**Figure 7A**). Positive Eu anomalies indicate the existence of a large amount of mafic rock detritus, whereas strong negative Eu anomalies indicate the incorporation of felsic magmatic material (Dai et al., 2017; Liu et al., 2020). Al_2O_3/TiO_2 is also a reliable index used to discriminate the provenance of sedimentary rocks (Spears and Rice, 1973; He et al., 2003; He et al., 2007; Dai et al., 2017; Liu et al., 2020), and previous studies have suggested that Al_2O_3/TiO_2 <7 is characteristic of the Emeishan high-titanium basalt (He et al., 2007). **Figure 7B** shows that the δ Eu value of samples ranges from 0.74 to 1.21, and Al_2O_3/TiO_2 values are less than 7, falling in or similar to the field of Emeishan high-titanium basalt (Xiao et al., 2004; Dai et al., 2016; Liu et al., 2020). The high-titanium basalt in the east of Emeishan Large Igneous Province located in the Kangdian Upland is the most likely provenance area of the Late Permian coal-bearing strata in western Guizhou (Chung and Jahn, 1995; Xiao et al., 2004). During Late Permian, the South China was hot and humid (Bercovici et al., 2015; He et al., 2020; Zhang et al., 2020). In this case, the source rock suffered strong chemical weathering, and the iron was continuously leached under strong weathering and brought into the sedimentary basin after frequent regression and transgression, providing a sufficient iron source for the formation of siderite.

There are two major possible sources of carbon in sedimentary rocks: sedimentary organic matter and marine carbonate rocks (Ohmoto, 1972; Veizer et al., 1980; Liu et al., 2021). The CO_2 source was determined based on the discrimination diagram of $\delta^{13}C_{PDB}$ versus $\delta^{18}O_{SMOW}$ (**Figure 8**). The data of gelatinous siderite indicate that the source of CO_2 was derived from the dehydroxylation of organic matter, and its formation was affected by seawater and organic matter. The data distribution of microcrystal-silty siderite (II) is scattered, and its CO_2 source

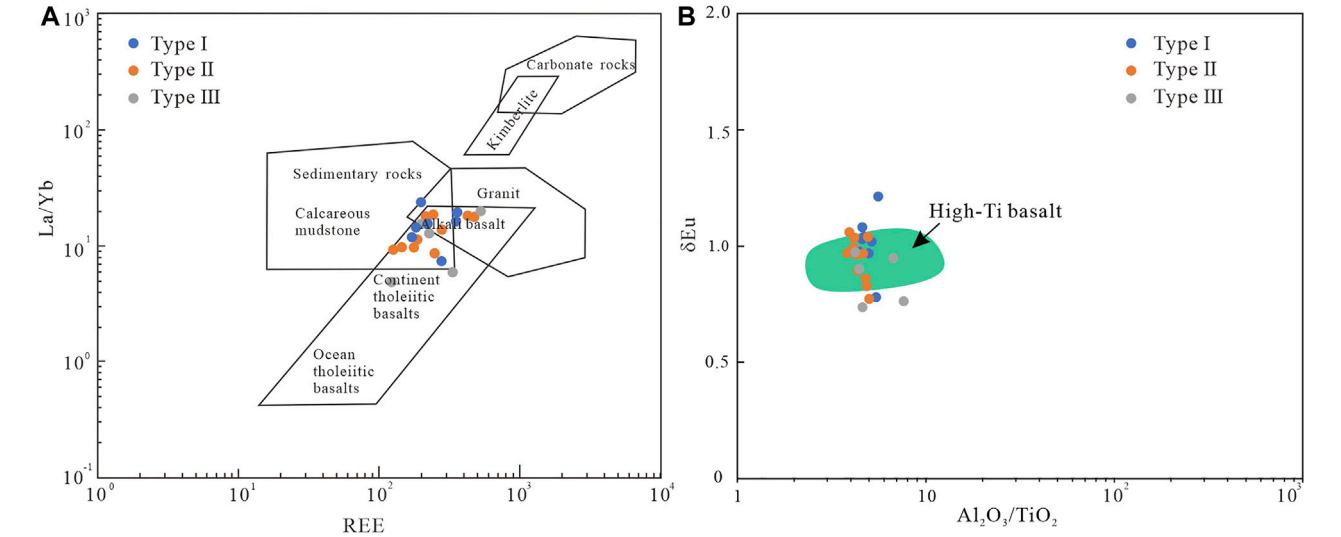

FIGURE 7 | Provenance analysis, **(A)** La/Yb vs. REE diagram; **(B)** δEu vs. Al_2O_3/TiO_2 diagram (data for high-Ti basalt are from Xiao et al., 2004).

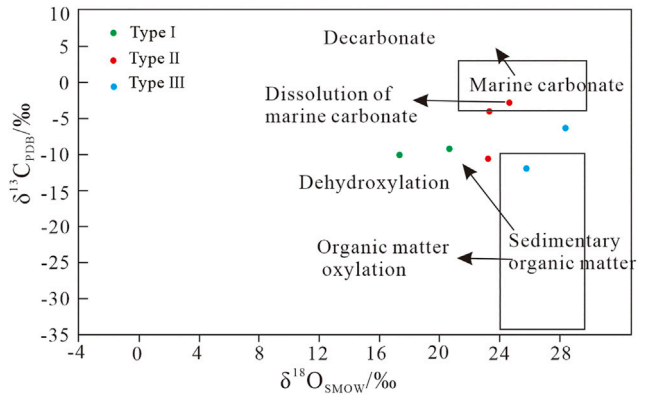

FIGURE 8 | Plot of $\delta^{13}C_{PDB}$ vs $\delta^{18}O_{SMOW}$ for the siderite samples (modified from Hoefs, 2009).

may be sedimentary organic matter and marine carbonate. Microlite siderite is evenly distributed in the strata (**Figure 2**), and its source is more likely sedimentary organic matter, whereas powder crystal siderite is formed by metasomatic calcite or paleontological shell. The CO_2 sources of spheroidal siderite are sedimentary organic matter and marine carbonate rocks, which are affected by different water during diagenesis. Moreover, the analysis results of spheroidal siderite may indicate the genesis of various spheroidal siderite.

5.2 Depositional Conditions of Siderite-Bearing Strata

Elemental concentration ratios such as Sr/Ba, Sr/Cu, V/(V+Ni) in clastic rocks can indicate the depositional conditions (Hatch and Leventhal, 1992; Mongenot et al., 1996; Rimmer et al., 2004; Akinlua et al., 2010; Zhao et al., 2016; Xu et al., 2017). Generally, Sr is enriched in the marine, and Ba is concentrated in the continental deposition. The Sr/Ba ratio reflects the influence degree by seawater and freshwater during the deposition period. The higher the value, the stronger the influence degree by seawater (Johnsson, 1993; Armstrong-Altrin et al., 2015). The whole-rock Sr/Ba value of samples with gelatinous siderite ranged from 1.14 to 2.18, with an average of 1.45 (**Figure 9A**). In addition, the gelatinous siderite-bearing strata contain glauconite (**Figure 2D**), indicating that the gelatinous siderite is strongly affected by seawater (Odin and Matter, 1981; Johnsson, 1993; Armstrong-Altrin et al., 2015; Banerjee et al., 2016). The whole-rock Sr/Ba value of samples with microlite-powder crystal siderite ranges from 0.5 to 0.9, with an average of 0.74, indicating that this kind of siderite was deposited under the joint action of seawater and freshwater (Johnsson, 1993; Armstrong-Altrin et al., 2015). The whole-rock Sr/Ba value of samples with sphaerosiderites ranged from 0.39 to 1.08, indicating that the paleosalinity of the water column during the sedimentary period of this type was relatively low, and the morphology was different under different paleosalinity.

The Sr/Cu ratio can indicate the paleoclimate (Roy and Roser, 2013; Sarki Yandoka et al., 2015). Under warm and humid climatic conditions, sediments usually show a low Sr/Cu ratio (Roy and Roser, 2013; Sarki Yandoka et al., 2015). **Figure 9B** shows that the whole-rock Sr/Cu of samples with gelatinous siderite ranges from 1.38 to 6.30 (mostly from 1 to 5), with an average of 3.21; that of the microlite-powder crystal siderite ranges from 1.33 to 3.97, with an average of 2.42. The spheroidal siderite has an Sr/Cu ranging from 1.69 to 3.29, and there is no significant difference in the value. The chemical index of alteration (CIA) indicates that the paleoclimate where types II and III siderite formed is warm and humid. The CIA of gelatinous siderite is greater than 80,

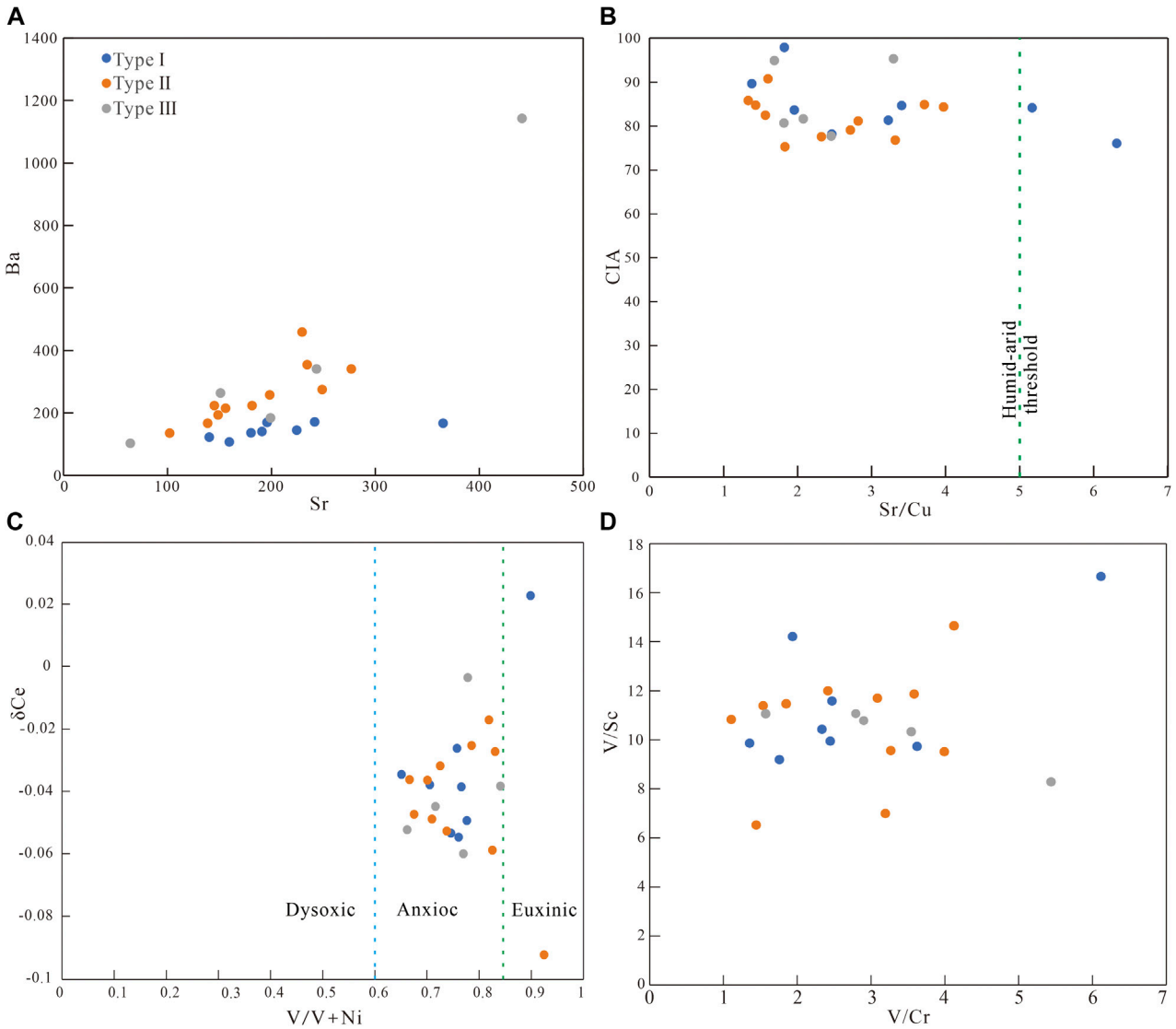

FIGURE 9 | Distribution diagrams of paleosalinity and redox proxies for siderite-bearing strata samples.

reflecting the hot and humid climate (Nesbitt and Young, 1982; McLennan, 1993).

The concentrations of V, Ni, and Ce in fine-grained sediments are sensitive to redox conditions and can help to characterize the depositional conditions (Wright et al., 1987; Jones and Manning, 1994; Holser, 1997; Chen et al., 2015). In general, the value of δ Ce > −0.1 indicates the anoxic condition, and less than −0.1 indicates the oxic condition (Wright et al., 1987; Holser, 1997; Chen et al., 2015). V/(V+Ni) ratios >0.84, 0.84–0.6, and <0.6 represent euxinic, anoxic, and dysoxic conditions, respectively (Hatch and Leventhal, 1992; Zhao et al., 2016; Xu et al., 2017). Moreover, V/Sc and V/Cr ratios can also provide information of depositional conditions (Jones and Manning, 1994; Rimmer et al., 2004). **Figure 9C** shows that the whole-rock δ Ce values of all samples are greater than −0.1, indicating that the water column in the sedimentary period was anoxic. The whole-rock V/(V+Ni) ratio of most samples is between 0.6 and 0.84, showing that they were formed under the weak reducing condition with weak stratification of the water column (Hatch and Leventhal, 1992; Zhao et al., 2016; Xu et al., 2017). The whole-rock V/Sc value of the samples varies little (**Figure 9D**). Among them, the type I siderite was 9.19 to 16.66, with a mean value of 11.45; the types II and III siderite ranges from 6.53 to 14.65 and 8.29 to 11.07, with an average value of 10.59 and 10.31, respectively. It shows that most siderite-bearing strata are formed in a weak reduction environment (Jones and Manning, 1994). The whole-rock V/Cr values of gelatinous siderite, microcrystal-silty siderite, and spheroidal siderites are 1.36 to 6.12, 1.11 to 4.12, 1.57 to 5.44, with an average value of 2.76, 2.69, and 3.25, respectively. Although the V/Cr values of some samples are low, the existing geochemical indicators show that most siderite-bearing strata

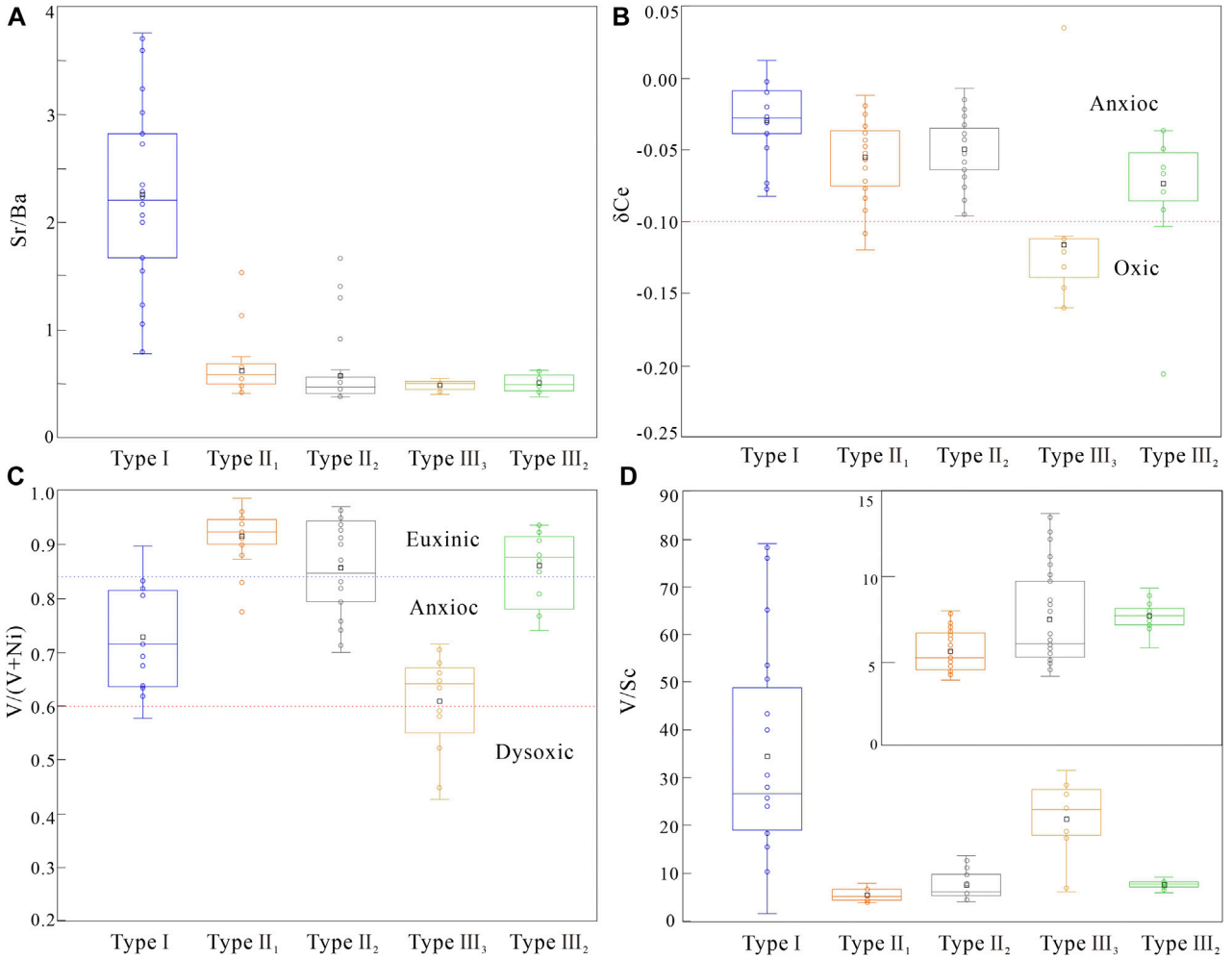

FIGURE 10 | *In situ* geochemical characteristics of different types of siderite.

samples are formed in a weak reduction to reduction environment (Jones and Manning, 1994; Rimmer et al., 2004).

5.3 Diagenetic Environment and Genesis of Siderite

Siderite is an authigenic mineral, and thus, different micro forms of siderite retain the information of diagenetic water during its formation.

According to the *in situ* test results, the $FeCO_3$ content of type I siderite is the lowest among the three types. The Al and Si contents are high, and the Al/Si ratio is almost the same, close to 0.9. The results show that gelatinous siderite is symbiotic with fine clay. The Sr/Ba value of each spot in type I siderite is between 0.79 and 3.75, with an average of 2.26 (**Figure 10A**), higher than that of the whole rock (**Figure 9A**). These characteristics indicate that the diagenetic fluid is mainly seawater with high paleosalinity, similar to sedimentary water (Johnsson, 1993; Armstrong-Altrin et al., 2015). The average value of δ Ce is −0.03 (**Figure 10B**), which is similar to the whole rock (**Table 2**). The mean value of V/(V+Ni) of the *in situ* mineral is 0.73. Compared with the whole-rock V/(V+Ni) of the corresponding samples, the V/(V+Ni) value of the *in situ* mineral is basically unchanged. The value of V/Sc of the *in situ* mineral is 10.25 to 79.02, with an average of 35.85, significantly higher than the whole rock (**Figure 10D**). These characters indicate that the type I siderite was formed in an early diagenetic environment, and the diagenetic water is mainly reduced and stagnant seawater (Hatch and Leventhal, 1992; Zhao et al., 2016). During the gelatinous siderite formation, the content of the clastic particles is low, and a large number of clay minerals are distributed in the sediments. During the syngenetic stage, the cryptic crystalline siderite precipitates from the seawater and filled in the limited space as cements.

The $FeCO_3$ content of type II_1 siderite is higher than that of type I siderite, whereas the content of Al and Si is lower, with average Al/Si value of 0.41. The type II_1 siderite appears hypidiomorphic granular aggregates, and the crystal morphology is not obvious, only with the boundary between crystal particles vaguely observed (**Figure 2F**). Moreover, the clay mineral content in the pores is relatively low, and the siderite is

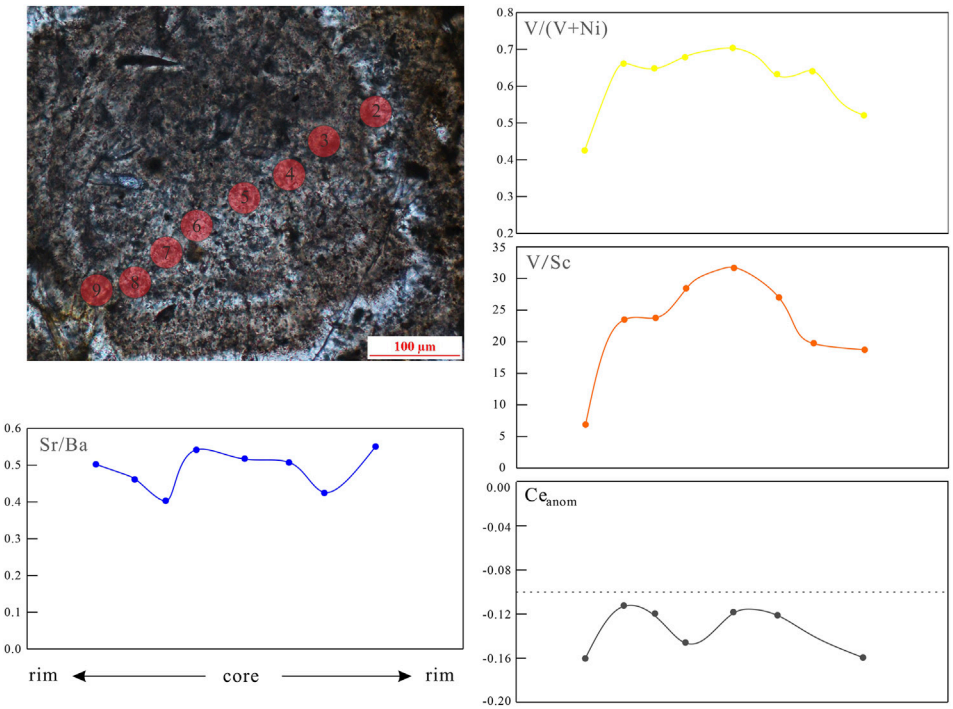

FIGURE 11 | Variation curves from center to edge of concentric siderite.

relatively pure. The above characteristics indicate that the microlite siderite is likely to be formed in the original intergranular pores. The average *in situ* Sr/Ba of type II_1 siderite is 0.64, and that of the whole rock is 0.66. There is almost no difference between them, meaning that the paleosalinity of the diagenetic water is similar to the sedimentary water body, that is, saltwater (Johnsson, 1993; Armstrong-Altrin et al., 2015). The average value of δ Ce in *in situ* mineral is −0.06, V/(V+Ni) is 0.93, and V/Sc is 4.80; δ Ce and V/(V+Ni) are similar to the average values of whole rock, whereas V/Sc is obviously lower than the average value of whole rock (**Figure 10D**; the average value of whole rock is 11.58). Therefore, the diagenetic water where type II_1 siderite formed is weakly reduced (Hatch and Leventhal, 1992; Jones and Manning, 1994; Rimmer et al., 2004; Zhao et al., 2016). The diagenetic environment of type II_1 siderite is similar to its sedimentary environment. It is a saltwater fluid with weak oxidation–reduction, and the diagenetic water is likely to be primary porewater. During the sedimentation of the strata with type II_1 siderite, the fluid washed the original pores, and the intergranular clay minerals decreased. The primary porewater through layers provides Fe-forming materials for the crystallization of siderite, which promotes the precipitation of siderite in intergranular pores and forms microlite siderite. However, because of the limited crystallization space, the siderite is filled in the pores and developed in the form of microlite siderite aggregate.

The type II_1 siderite appears as silty-sized crystal aggregates, and some develop into petal-like siderite (**Figures 2L,J**). The $FeCO_3$ content is approximately 80 wt%. The Sr/Ba ranges from 0.38 to 1.66, with an average value of 0.58 (**Figure 10A**), different from the average Sr/Ba of the whole rock of 0.96. The Sr/Ba value indicates that the type II_2 siderite was transformed by freshwater in the later diagenetic stage (Johnsson, 1993; Armstrong-Altrin et al., 2015). The *in situ* V/Sc values are 2.9 to 9.0, with an average of 5.24, which are lower than those of the whole rock (**Figure 9B**) (averagely 11.52). The V/(V+Ni) value is between 0.7 and 0.97 (**Figure 10C**), with an average of 0.85, which is higher than the whole rock (average 0.75). The δ Ce values range from −0.1 to −0.01 (**Figure 10B**), which is slightly lower than whole rock (from −0.03 to −0.06, average −0.04). These characteristics reveal the diagenetic water where type II_2 siderite formed is different from its sedimentary water; that is, the diagenetic water is not seawater sealed in sedimentary period or primary porewater, but relatively freshwater with weak oxidation to weak reduction (Hatch and Leventhal, 1992; Jones and Manning, 1994; Rimmer et al., 2004). During the burial period, the siderite had been transformed by the diagenetic fluid, which promoted the recrystallization of siderite crystals with smaller particles formed in the sedimentary period and formed powder crystal siderite with silty size and better crystal morphology.

The type III siderite can be divided into three subtypes based on microscopic morphology. According to the observed type III_1 siderite, the morphologies range from powder crystals through fan-shaped to petal-like morphologies (**Figures 2K,L**); it is likely to be formed by a single crystal, and the morphology is affected by pores and diagenetic fluid (Passey, 2014). According to the *in situ* results (**Figure 10**), the Sr/Ba ranges from 0.38 to 0.63, indicating

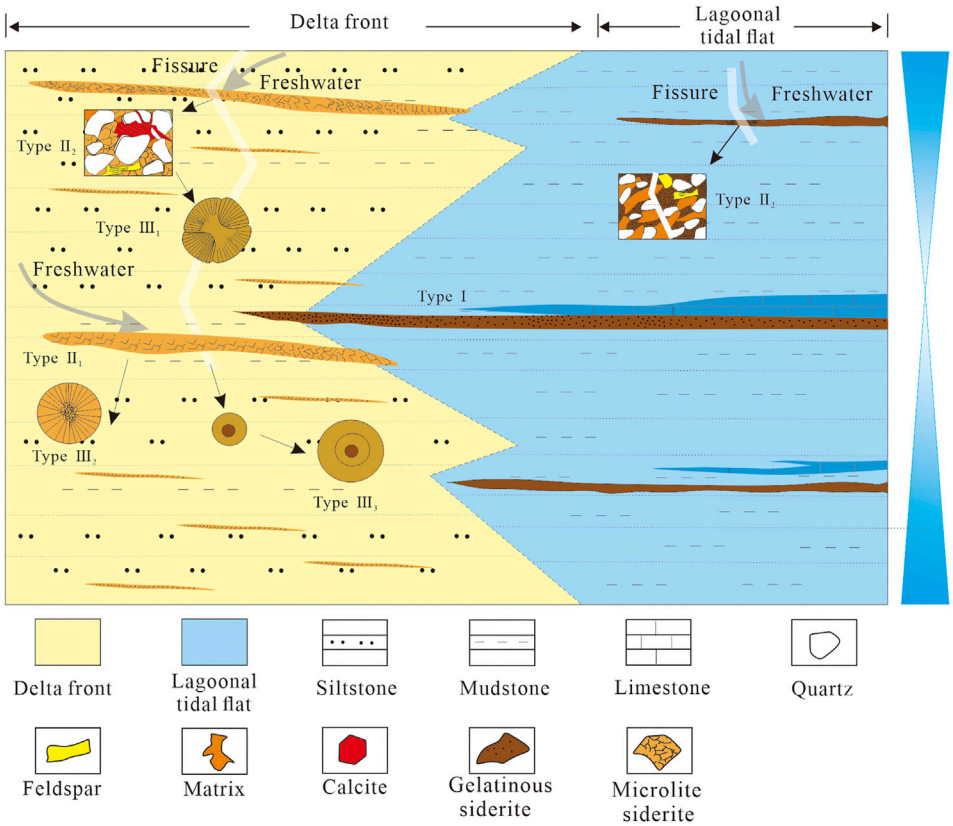

FIGURE 12 | Evolution model of different types of Siderite.

that the formation environment was affected by freshwater. The *in situ* V/Sc, V/(V+Ni), and δ Ce values are 5.6 to 9.3, 0.74 to 0.94, and −0.21 to −0.04, respectively. These characteristics indicate that the type III_2 siderite grows radially around the core with weak oxidation to weak reduction. The variation curves of many geochemical indexes from the core to the rim of type III_3 siderite show obvious symmetry (**Figure 11**), indicating that its growth is slow and continuous and carried out together with the diagenesis. Under the repeated action of diagenetic fluid, the type III_3 siderite grows in a circle around the cryptocrystalline core in a fluid with the weak oxidation–reduction property.

5.4 Evolution Model of Siderite and Geological Significance

Siderite in the study area shows various forms and has been affected by sedimentary environment and diagenetic environment. Regarding the sedimentary environment, the Upper Permian coal-bearing strata developed under carbonate tidal flat-barrier-lagoon-shallow delta conditions (Wang et al., 2011; Shen et al., 2016; Shen et al., 2019; Qin et al., 2018), and the climate was hot and humid. Such sedimentary condition was beneficial to the formation of siderite (Bercovici et al., 2015). The development and evolution model of siderite is shown in **Figure 12**. The formation of type I siderite is strongly affected by seawater during transgression, and the sedimentary water is stagnant seawater. During diagenesis, the diagenetic water along the fissures and beddings promoted the recrystallization of the gelatinous siderite to form the powder siderite (**Figure 12**). The sedimentary water of type II siderite gradually changed from seawater to brackish water in the transitional environment. During diagenesis, the diagenetic fluid of freshwater promoted the recrystallization of siderite along fissures and beddings or metasomatism with calcite to evolve into type II_2 siderite and sometimes into petal-like siderite (**Figure 12**). The type III_2 siderite grows radially around the core. The type III_3 siderite grows in a circle around the cryptocrystalline core in a relatively active fluid with weak oxidation–reduction under the repeated diagenetic fluid. Under the influence of multistage diagenetic fluid, the type III_3 siderite grows around the cryptocrystalline core.

The formation of siderite is obviously controlled by the different sedimentary and diagenetic environments. Among them, types I and II_1 siderite mainly formed in the syndiagenetic and early diagenetic stages, and their morphology is controlled by the sedimentary environment. Therefore, types I and II_1 siderite can indicate the sedimentary environments. Gelatinous siderite was most affected by seawater, mostly formed in the transgression or near the maximum flooding surface (Shen et al., 2019; Zhang et al., 2020).

Microlite siderite was influenced by freshwater during its formation and was most developed in the early stage of transgression or high-stand system tract.

6 CONCLUSION

Based on the morphology of siderite in coal-bearing series, it can be divided into three types and six subtypes. There is barely any difference in the sedimentary sources of various siderite-bearing strata, which are Emeishan high-titanium basalt developed in the west of the study area. Type I siderite CO_2 comes from sedimentary organic matter. Types II and III siderite CO_2 is mainly derived from sedimentary organic matter and marine carbonate.

The most significant difference in the sedimentary period of various siderite-bearing strata lies in the influence degree of seawater. Among them, type I siderite-bearing strata are strongly affected by seawater, whereas types II and III siderite-bearing strata are affected by seawater and freshwater. Different types of siderite bearing strata are formed in depositional conditions from weak oxidation to weak reduction.

The *in situ* results show that types I and II_1 siderites were formed in the early diagenetic stage. The diagenetic water of type I siderite is sedimentary seawater, and type II_1 siderite is mainly primary porewater. The diagenetic water of type II_2 siderite is freshwater, and type III is multistage fluid.

The siderite morphologies are controlled by the sedimentary environment and diagenetic environment. Among them, gelatinous siderite and microlite siderite are mainly formed in the syndiagenetic stage and early diagenetic stage, thus indicating the sedimentary environment. Gelatinous siderite is strongly influenced by seawater and is mainly formed in the carbonate tidal flat and barrier lagoon. Microlite siderite is formed in the shallow delta with relatively low sea level by the interaction of seawater and freshwater.

DATA AVAILABILITY STATEMENT

The raw data supporting the conclusion of this article will be made available by the authors, without undue reservation.

AUTHOR CONTRIBUTIONS

TY: Conceptualization, methodology, writing—original draft. YS: Conceptualization, supervision, project administration, funding acquisition. YQ: Writing—original draft, visualization,investigation. YiZ: Software, validation. JJ: Investigation, resources, supervision. YoZ: Writing-reviewing and Editing. YlZ: Writing-reviewing and Editing. YfZ: Data curation, validation.

FUNDING

Financial support for this work was provided by the National Natural Science Foundation of China (Nos. 42172186 and 41872168) and the Priority Academic Program Development of the Jiangsu Higher Education Institutions (PAPD).

SUPPLEMENTARY MATERIAL

The Supplementary Material for this article can be found online at: https://www.frontiersin.org/articles/10.3389/feart.2021.779991/full#supplementary-material

REFERENCES

Akinlua, A., Adekola, S. A., Swakamisa, O., Fadipe, O. A., and Akinyemi, S. A. (2010). Trace Element Characterisation of Cretaceous Orange Basin Hydrocarbon Source Rocks. *Appl. Geochem.* 25, 1587–1595. doi:10.1016/j.apgeochem.2010.08.008

Allègre, C. J., and Michard, G. (1974). *Introduction to Geochemistry 10 (Geophysics and Astrophysics Monographs)*. Boston, USA: D. Reidel Publishing Company.

Armstrong-Altrin, J. S., Machain-Castillo, M. L., Rosales-Hoz, L., Carranza-Edwards, A., Sanchez-Cabeza, J.-A., and Ruíz-Fernández, A. C. (2015). Provenance and Depositional History of continental Slope Sediments in the Southwestern Gulf of Mexico Unraveled by Geochemical Analysis. *Continental Shelf Res.* 95, 15–26. doi:10.1016/j.csr.2015.01.003

Banerjee, S., Bansal, U., Pande, K., and Meena, S. S. (2016). Compositional Variability of Glauconites within the Upper Cretaceous Karai Shale Formation, Cauvery Basin, India: Implications for Evaluation of Stratigraphic Condensation. *Sediment. Geology.* 331, 12–29. doi:10.1016/j.sedgeo.2015.10.012

Bercovici, A., Cui, Y., Forel, M.-B., Yu, J., and Vajda, V. (2015). Terrestrial Paleoenvironment Characterization across the Permian-Triassic Boundary in South China. *J. Asian Earth Sci.* 98, 225–246. doi:10.1016/j.jseaes.2014.11.016

Berner, R. A. (1981). A New Geochemical Classification of Sedimentary Environments. *Sepm Jsr* 51, 359–365. doi:10.1306/212F7C7F-2B24-11D7-8648000102C1865D

Boynton, W. V. (1984). Chapter 3 Cosmochemistry of the Rare Earth Elements: Meteorite Studies. *Dev. Geochem.* 2, 63–114. doi:10.1016/B978-0-444-42148-7.50008-3

Chen, J., Algeo, T. J., Zhao, L., Chen, Z.-Q., Cao, L., Zhang, L., et al. (2015). Diagenetic Uptake of Rare Earth Elements by Bioapatite, with an Example from Lower Triassic Conodonts of South China. *Earth-Science Rev.* 149, 181–202. doi:10.1016/j.earscirev.2015.01.013

Choi, K. S., Khim, B. K., and Woo, K. S. (2003). Spherulitic Siderites in the Holocene Coastal Deposits of Korea (Eastern Yellow Sea): Elemental and Isotopic Composition and Depositional Environment. *Mar. Geology.* 202, 17–31. doi:10.1016/s0025-3227(03)00258-5

Chung, S.-L., and Jahn, B.-M. (1995). Plume-lithosphere Interaction in Generation of the Emeishan Flood Basalts at the Permian-Triassic Boundary. *Geol* 23, 889–892. doi:10.1130/0091-7613(1995)023<0889:pliigo>2.3.co;2

Curtis, C. D., Coleman, M. L., and Love, L. G. (1986). Pore Water Evolution during Sediment Burial from Isotopic and mineral Chemistry of Calcite, Dolomite and Siderite Concretions. *Geochimica et Cosmochimica Acta.* 50, 2321–2334. doi:10.1016/0016-7037(86)90085-2

Dai, S., Chekryzhov, I. Y., Seredin, V. V., Nechaev, V. P., Graham, I. T., Hower, J. C., et al. (2016). Metalliferous Coal Deposits in East Asia (Primorye of Russia and South China): A Review of Geodynamic Controls and Styles of Mineralization. *Gondwana Res.* 29, 60–82. doi:10.1016/j.gr.2015.07.001

Dai, S., Ward, C. R., Graham, I. T., French, D., Hower, J. C., Zhao, L., et al. (2017). Altered Volcanic Ashes in Coal and Coal-Bearing Sequences: a Review of Their

Nature and Significance. *Earth-Science Rev.* 175, 44–74. doi:10.1016/j.earscirev.2017.10.005

El Albani, A., Vachard, D., Kuhnt, W., and Thurow, J. (2001). The Role of Diagenetic Carbonate Concretions in the Preservation of the Original Sedimentary Record. *Sedimentology* 48 (4), 875–886. doi:10.1046/j.1365-3091.2001.00398.x

Haese, R. R., Wallmann, K., Dahmke, A., Kretzmann, U., Müller, P. J., and Schulz, H. D. (1997). Iron Species Determination to Investigate Early Diagenetic Reactivity in marine Sediments. *Geochimica et Cosmochimica Acta* 61 (Issue 1), 63–72. doi:10.1016/S0016-7037(96)00312-2

Hatch, J. R., and Leventhal, J. S. (1992). Relationship between Inferred Redox Potential of the Depositional Environment and Geochemistry of the Upper Pennsylvanian (Missourian) Stark Shale Member of the Dennis Limestone, Wabaunsee County, Kansas, U.S.A. *Chem. Geology.* 99, 65–82. doi:10.1016/0009-2541(92)90031-Y

He, B., Xu, Y.-G., Chung, S.-L., Xiao, L., and Wang, Y. (2003). Sedimentary Evidence for a Rapid, Kilometer-Scale Crustal Doming Prior to the Eruption of the Emeishan Flood Basalts. *Earth Planet. Sci. Lett.* 213, 391–405. doi:10.1016/S0012-821X(03)00323-6

He, B., Xu, Y.-G., Huang, X.-L., Luo, Z.-Y., Shi, Y.-R., Yang, Q.-J., et al. (2007). Age and Duration of the Emeishan Flood Volcanism, SW China: Geochemistry and SHRIMP Zircon U-Pb Dating of Silicic Ignimbrites, post-volcanic Xuanwei Formation and clay Tuff at the Chaotian Section. *Earth Planet. Sci. Lett.* 255, 306–323. doi:10.1016/j.epsl.2006.12.021

He, Q., Dong, T., He, S., Zhai, G., Guo, X., Hou, Y., et al. (2020). Sedimentological and Geochemical Characterization of the Upper Permian Transitional Facies of the Longtan Formation, Northern Guizhou Province, Southwest China: Insights into Paleo-Environmental Conditions and Organic Matter Accumulation Mechanisms. *Mar. Pet. Geology.* 118, 104446. doi:10.1016/j.marpetgeo.2020.104446

Hiatt, E. E., Pufahl, P. K., and Guimarães da Silva, L. (2020). Iron and Phosphorus Biochemical Systems and the Cryogenian-Ediacaran Transition, Jacadigo basin, Brazil: Implications for the Neoproterozoic Oxygenation Event. *Precambrian Res.* 337, 105533. doi:10.1016/j.precamres.2019.105533

Hoefs, J. (2009). *Stable Isotope Geochemistry*. Berlin: Springer-Verlag.

Holser, W. (1997). Evaluation of the application of rare-earth elements to paleoceanography. *Palaeogeogr. Palaeocl.* 132, 309–323. doi:10.1016/S0031-0182(97)00069-2

Johnsson, M. J. (1993). *The System Controlling the Composition of Clastic Sediments*, 284. Pennsylvania: Geological Society of America, 1–20. doi:10.1130/SPE284-p1

Jones, B., and Manning, D. A. C. (1994). Comparison of Geochemical Indices Used for the Interpretation of Palaeoredox Conditions in Ancient Mudstones. *Chem. Geology.* 111, 111–129. doi:10.1016/0009-2541(94)90085-X

Laenen, B., and De Craen, M. (2004). Eogenetic Siderite as an Indicator for Fluctuations in Sedimentation Rate in the Oligocene Boom Clay Formation (Belgium). *Sediment. Geology.* 163, 165–174. doi:10.1016/S0037-0738(03)00177-5

Lim, D. I., Jung, H. S., Yang, S. Y., and Yoo, H. S. (2004). Sequential Growth of Early Diagenetic Freshwater Siderites in the Holocene Coastal Deposits, Korea. *Sediment. Geology.* 169, 107–120. doi:10.1016/j.sedgeo.2004.05.002

Liu, J., Nechaev, V. P., Dai, S., Song, H., Nechaeva, E. V., Jiang, Y., et al. (2020). Evidence for Multiple Sources for Inorganic Components in the Tucheng Coal deposit, Western Guizhou, China and the Lack of Critical-Elements. *Int. J. Coal Geology.* 223, 103468. doi:10.1016/j.coal.2020.103468

Liu, J., Song, H., Dai, S., Nechaev, V. P., Graham, I. T., French, D., et al. (2019). Mineralization of REE-Y-Nb-Ta-Zr-Hf in Wuchiapingian Coals from the Liupanshui Coalfield, Guizhou, Southwestern China: Geochemical Evidence for Terrigenous Input. *Ore Geology. Rev.* 115, 103190. doi:10.1016/j.oregeorev.2019.103190

Liu, Y.-F., Qi, H.-W., Bi, X.-W., Hu, R.-Z., Qi, L.-K., Yin, R.-S., et al. (2021). Two Types of Sediment-Hosted Pb-Zn Deposits in the Northern Margin of Lanping basin, SW China: Evidence from Sphalerite Trace Elements, Carbonate C-O Isotopes and Molybdenite Re-os Age. *Ore Geology. Rev.* 131, 104016. doi:10.1016/j.oregeorev.2021.104016

Ludvigson, G. A., González, L. A., Metzger, R. A., Witzke, B. J., Brenner, R. L., Murillo, A. P., et al. (1998). Meteoric Sphaerosiderite Lines and Their Use for Paleohydrology and Paleoclimatology. *Geol* 26, 1039–1042. doi:10.1130/0091-7613(1998)026<1039:mslatu>2.3.co;2

McLennan, S. M., Hemming, S., McDaniel, D. K., and Hanson, G. N. (1993). *Geochemical Approaches to Sedimentation, Provenance, and Tectonics*, 284. New York, NY: Special Paper of the Geological Society of America, 21–40. doi:10.1130/SPE284-p21

McLennan, S. M. (1993). Weathering and Global Denudation. *J. Geology.* 101, 295–303. doi:10.1086/648222

Mongenot, T., Tribovillard, N.-P., Desprairies, A., Lallier-Vergès, E., and Laggoun-Defarge, F. (1996). Trace Elements as Palaeoenvironmental Markers in Strongly Mature Hydrocarbon Source Rocks: the Cretaceous La Luna Formation of Venezuela. *Sediment. Geology.* 103, 23–37. doi:10.1016/0037-0738(95)00078-X

Mozley, P. S. (1989). Relation between Depositional Environment and the Elemental Composition of Early Diagenetic Siderite. *Geol* 17, 704–706. doi:10.1130/0091-7613(1989)017<0704:rbdeat>2.3.co;2

Mozley, P. S., and Wersin, P. (1992). Isotopic Composition of Siderite as an Indicator of Depositional Environment. *Geol* 20, 817–820. doi:10.1130/0091-7613(1992)020<0817:icosaa>2.3.co;2

Nesbitt, H. W., and Young, G. M. (1982). Early Proterozoic Climates and Plate Motions Inferred from Major Element Chemistry of Lutites. *Nature* 299, 715–717. doi:10.1038/299715a0

Odin, G. S., and Matter, A. (1981). De Glauconiarum Origine. *Sedimentology* 28, 611–641. doi:10.1111/j.1365-3091.1981.tb01925.x

Ohmoto, H. (1972). Systematics of Sulfur and Carbon Isotopes in Hydrothermal Ore Deposits. *Econ. Geol.* 67 (5), 551–578. doi:10.2113/gsecongeo.67.5.551

Passey, S. R. (2014). The Habit and Origin of Siderite Spherules in the Eocene Coal-Bearing Prestfjall Formation, Faroe Islands. *Int. J. Coal Geology.* 122, 76–90. doi:10.1016/j.coal.2013.12.009

Passey, S., and Jolley, D. (2009). A revised lithostratigraphic nomenclature for the Palaeogene Faroe Islands Basalt Group, NE Atlantic Ocean. *Earth Env. Sci. T. R. So.* 99, 127–158. doi:10.1017/S1755691009008044

Phillips, S. C., Hong, W.-L., Johnson, J. E., Fahnestock, M. F., and Bryce, J. G. (2018). Authigenic Carbonate Formation Influenced by Freshwater Inputs and Methanogenesis in Coal-Bearing Strata Offshore Shimokita, Japan (IODP Site C0020). *Mar. Pet. Geology.* 96, 288–303. doi:10.1016/j.marpetgeo.2018.06.007

Qin, Y., Moore, T. A., Shen, J., Yang, Z., Shen, Y., and Wang, G. (2018). Resources and Geology of Coalbed Methane in China: A Review. *Int. Geology. Rev.* 60, 777–812. doi:10.1080/00206814.2017.1408034

Rimmer, S., Thompson, J., Goodnight, S., and Robl, T. (2004). Multiple Controls on the Preservation of Organic Matter in Devonian-Mississippian marine Black Shales: Geochemical and Petrographic Evidence. *Palaeogeogr. Palaeoclimatol. Palaeoecol.* 215, 125–154. doi:10.1016/s0031-0182(04)00466-3

Rodrigues, A. G., De Ros, L. F., Neumann, R., and Borghi, L. (2015). Paleoenvironmental Implications of Early Diagenetic Siderites of the Paraíba Do Sul Deltaic Complex, Eastern Brazil. *Sediment. Geology.* 323, 15–30. doi:10.1016/j.sedgeo.2015.04.005

Roy, D., and Roser, B. (2013). Climatic Control on the Composition of Carboniferous-Permian Gondwana Sediments, Khalaspir basin, Bangladesh. *Gondwana Res.* 23, 1163–1171. doi:10.1016/j.gr.2012.07.006

Sánchez-Román, M., Fernández-Remolar, D., Amils, R., Sánchez-Navas, A., Schmid, T., Martin-Uriz, P. S., et al. (2014). Microbial Mediated Formation of Fe-Carbonate Minerals under Extreme Acidic Conditions. *Sci. Rep.* 4, 4767. doi:10.1038/srep04767

Sarki Yandoka, B., Abdullah, W., Abubakar, M., Hakimi, M., and Adegoke, A. (2015). Geochemical characterisation of Early Cretaceous lacustrine sediments of Bima Formation, Yola sub-basin, Northern Benue Trough, NE Nigeria: Organic matter input, preservation, Paleoenvironment and Palaeoclimatic conditions. *Mar. Petrol. Geol.* 61, 82–94. doi:10.1016/j.marpetgeo.2014.12.010

Shao, Y., Guo, Y., Qin, Y., Shen, Y., and Tian, L. (2011). Distribution Characteristic and Geological Significance of Rare Earth Elements in Lopingian Mudstone of Permian, Panxian County, Guizhou Province. *Mining Sci. Tech. (China)* 21 (4), 469–476. doi:10.1016/j.mstc.2011.06.002

Shen, Y. L., Qin, Y., Li, Z. F., Jin, J., Wei, Z. H., Zheng, J., et al. (2017). The Sedimentary Origin and Geological Significance of Siderite in the Longtan Formation of Western Guizhou Province. *Earth Sci. Front.* 24, 152–161. (in Chinese with English abstract). doi:10.13745/j.esf.yx.2016-11-51

Shen, Y., Qin, Y., Guo, Y., Yi, T., Yuan, X., and Shao, Y. (2016). Characteristics and Sedimentary Control of a Coalbed Methane-Bearing System in Lopingian (Late

Permian) Coal-Bearing Strata of Western Guizhou Province. *J. Nat. Gas Sci. Eng.* 33, 8–17. doi:10.1016/j.jngse.2016.04.047

Shen, Y., Qin, Y., Wang, G. G. X., Xiao, Q., Shen, J., Jin, J., et al. (2019). Sealing Capacity of Siderite-Bearing Strata: the Effect of Pore Dimension on Abundance and Micromorphology Type of Siderite in the Lopingian (Late Permian) Coal-Bearing Strata, Western Guizhou Province. *J. Pet. Sci. Eng.* 178, 180–192. doi:10.1016/j.petrol.2019.03.032

Spears, D. A., and Rice, C. M. (1973). An Upper Carboniferous Tonstein of Volcanic Origin. *Sedimentology* 20, 281–294. doi:10.1111/j.1365-3091.1973.tb02050.x

Taylor, S. R., and McLennan, S. M. (1985). *The Continental Crust: Its Composition and Evolution: An Examination of the Geochemical Record Preserved in Sedimentary Rocks*. Oxford: Blackwell Scientific, 312.

Tribovillard, N., Algeo, T. J., Lyons, T., and Riboulleau, A. (2006). Trace Metals as Paleoredox and Paleoproductivity Proxies: An Update. *Chem. Geology.* 232, 12–32. doi:10.1016/j.chemgeo.2006.02.012

Uysal, I. T., Golding, S. D., and Glikson, M. (2000). Petrographic and Isotope Constraints on the Origin of Authigenic Carbonate Minerals and the Associated Fluid Evolution in Late Permian Coal Measures, Bowen Basin (Queensland), Australia. *Sediment. Geology.* 136, 189–206. doi:10.1016/S0037-0738(00)00097-X

Veizer, J., Holser, W. T., and Wilgus, C. K. (1980). Correlation of and Secular Variations. *Geochimica et Cosmochimica Acta* 44, 579–587. doi:10.1016/0016-7037(80)90250-1

Wang, H., Shao, L., Hao, L., Zhang, P., Glasspool, I. J., Wheeley, J. R., et al. (2011). Sedimentology and Sequence Stratigraphy of the Lopingian (Late Permian) Coal Measures in Southwestern China. *Int. J. Coal Geology.* 85, 168–183. doi:10.1016/j.coal.2010.11.003

Weibel, R., Lindström, S., Pedersen, G. K., Johansson, L., Dybkjær, K., Whitehouse, M. J., et al. (2016). Groundwater Table Fluctuations Recorded in Zonation of Microbial Siderites from End-Triassic Strata. *Sediment. Geology.* 342, 47–65. doi:10.1016/j.sedgeo.2016.06.009

Wittkop, C., Teranes, J., Lubenow, B., and Dean, W. (2014). Carbon- and Oxygen-Stable Isotopic Signatures of Methanogenesis, Temperature, and Water Column Stratification in Holocene Siderite Varves. *Chem. Geol.* 389, 153–166. doi:10.1016/j.chemgeo.2014.09.016

Wright, J., Schrader, H., and Holser, W. T. (1987). Paleoredox Variations in Ancient Oceans Recorded by Rare Earth Elements in Fossil Apatite. *Geochimica et Cosmochimica Acta* 51, 631–644. doi:10.1016/0016-7037(87)90075-5

Xiao, L., Xu, Y. G., Mei, H. J., Zheng, Y. F., He, B., and Pirajno, F. (2004). Distinct Mantle Sources of Low-Ti and High-Ti Basalts from the Western Emeishan Large Igneous Province, SW China: Implications for Plume-Lithosphere Interaction. *Earth Planet. Sci. Lett.* 228, 525–546. doi:10.1016/j.epsl.2004.10.002

Xie, G., Shen, Y., Liu, S., and Hao, W. (2018). Trace and Rare Earth Element (REE) Characteristics of Mudstones from Eocene Pinghu Formation and Oligocene Huagang Formation in Xihu Sag, East China Sea Basin: Implications for Provenance, Depositional Conditions and Paleoclimate. *Mar. Pet. Geology.* 92, 20–36. doi:10.1016/j.marpetgeo.2018.02.019

Xu, B., and He, M. (2003). *Coal Geology of Guizhou Province*. Xuzhou, China: China University of Mining and Technology Press.

Xu, Q., Liu, B., Ma, Y., Song, X., Wang, Y., and Chen, Z. (2017). Geological and Geochemical Characterization of Lacustrine Shale: A Case Study of the Jurassic Da'anzhai Member Shale in the central Sichuan Basin, Southwest China. *J. Nat. Gas Sci. Eng.* 47, 124–139. doi:10.1016/j.jngse.2017.09.008

Xu, Y.-G., Chung, S.-L., Shao, H., and He, B. (2010). Silicic Magmas from the Emeishan Large Igneous Province, Southwest China: Petrogenesis and Their Link with the End-Guadalupian Biological Crisis. *Lithos* 119, 47–60. doi:10.1016/j.lithos.2010.04.013

Zhang, T., Shen, Y. L., Li, Z. F., Jin, J., Zong, Y., Liu, J. B., et al. (2018). Genesis of Siderite Precipitated in the Lopingian Coal Measures in Zhijin Mining Area, Western Guizhou. *Geol. J. China Universities* 24, 481–490. (in Chinese with English abstract). doi:10.16108/j.issn1006-7493.2017141

Zhang, Y. J., Shen, Y. L., Yang, T. Y., Zhao, Y., and Tong, G. C. (2020). Development Characteristics of Siderite in the Constraint of Sequence Frame: A Case Study of Late Permian Coal Measures in Panguan Area. *J. China Coal Soc.* 45 (S2), 976–985. (in Chinese with English abstract). doi:10.13225/j.cnki.jccs.2020.0200

Zhao, J., Jin, Z., Jin, Z., Geng, Y., Wen, X., and Yan, C. (2016). Applying Sedimentary Geochemical Proxies for Paleoenvironment Interpretation of Organic-Rich Shale Deposition in the Sichuan Basin, China. *Int. J. Coal Geology.* 163, 52–71. doi:10.1016/j.coal.2016.06.015

Conflict of Interest: YoZ was employed by the company Sinopec Shengli Oilfield Administration Bureau Co., Ltd. YiZ was employed by the company Sinopec Xinjiang Xinchun Petroleum Development Co., Ltd.

The remaining authors declare that the research was conducted in the absence of any commercial or financial relationships that could be construed as a potential conflict of interest.

frontiers in Earth Science

ORIGINAL RESEARCH
published: 22 December 2021
doi: 10.3389/feart.2021.764052

Response to the Variation of Clay Minerals During ASP Flooding in the Saertu Oilfield in the Songliao Basin

Liang Yingjie[1,2], *Liang Wenfu*[3]*, *He Wang*[1] and *Li Zian*[4]

[1]Key Lab of Mineral and Mineralization, Guangzhou Institute of Geochemistry, Chinese Academy of Sciences, Guangzhou, China, [2]Graduate Education, University of Chinese Academy of Sciences, Beijing, China, [3]Second Oil Production Plant, Daqing Oilfield Company Limited, Daqing, China, [4]School of Marine Sciences, Sun Yat-sen University, Guangzhou, China

In this paper, the variation of clay minerals and their influence on reservoir physical properties and residual oil before and after ASP flooding are analyzed. The results show that the total amount of clay minerals in reservoirs decreases after ASP flooding in the ultra-high-water-cut-stage reservoirs of the Naner Zone in the Saertu Oilfield, Songliao Basin. Therein, the illite content reduces, while the content of illite smectite mixed-layer and chlorite increases. The content of kaolinite varies greatly. The content of kaolinite decreases in some samples, while it increases in other samples. The clay minerals block the pore throat after ASP flooding. As a result, the pore structure coefficient and the seepage tortuosity increase, the primary intergranular pore throat shrinks, and the pore–throat coordination number decreases. Nevertheless, the dissolution of clay minerals reduces the pore–throat ratio and increases porosity and permeability. The variation of clay minerals after ASP flooding not only intensifies the reservoir heterogeneity but also affects the formation and distribution of residual oil. The residual oil of the oil–clay mixed adsorption state is a newly formed residual oil type related to clay, which accounts for 44.2% of the total residual oil reserves, so it is the main occurrence form of the oil in reservoirs after ASP flooding. Therefore, the exploitation of this type of residual oil has great significance to enhance the oil recovery in ultra-high-water-cut-stage reservoirs.

Keywords: ASP flooding, clay minerals, pore structure and physical properties, residual oil, ultra-high water cut stage, the Songliao basin

OPEN ACCESS

Edited by:
Qiangtai Huang,
Sun Yat-sen University, China

Reviewed by:
Pingping Li,
China University of Petroleum, China
Hongjian Zhu,
Yanshan University, China

****Correspondence:***
Liang Wenfu
liangwf2049@163.com

Specialty section:
This article was submitted to Geochemistry, a section of the journal Frontiers in Earth Science

Received: *24 August 2021*
Accepted: *13 October 2021*
Published: *22 December 2021*

Citation:
Yingjie L, Wenfu L, Wang H and Zian L (2021) Response to the Variation of Clay Minerals During ASP Flooding in the Saertu Oilfield in the Songliao Basin. Front. Earth Sci. 9:764052. doi: 10.3389/feart.2021.764052

INTRODUCTION

ASP flooding refers to a chemical flooding method that utilizes a composite system of alkali, surfactant, and polymer for petroleum exploitation. It is one of the enhanced oil recovery (EOR) technologies used in many ultra-high-water-cut-stage reservoirs (Zhang et al., 2009; Cheng et al., 2012; Cheng et al., 2014; Wu et al., 2015a; Xv et al., 2015). A large amount of studies indicates that the composition, distribution, and content of clay minerals in the reservoirs have a great influence on the pore structure and physical properties (e.g., porosity and permeability), which will directly affect the oil production efficiency (Chen et al., 2016; Zhao et al., 2017; Zhu et al., 2021). There are many physical and chemical reactions between pore fluids and rock components in the formation during ASP flooding (Song et al., 2011; Wu et al., 2015a; Song et al., 2015; Sheng., 2016), especially the strong water–rock reaction of clay minerals. Pore structure and physical properties in

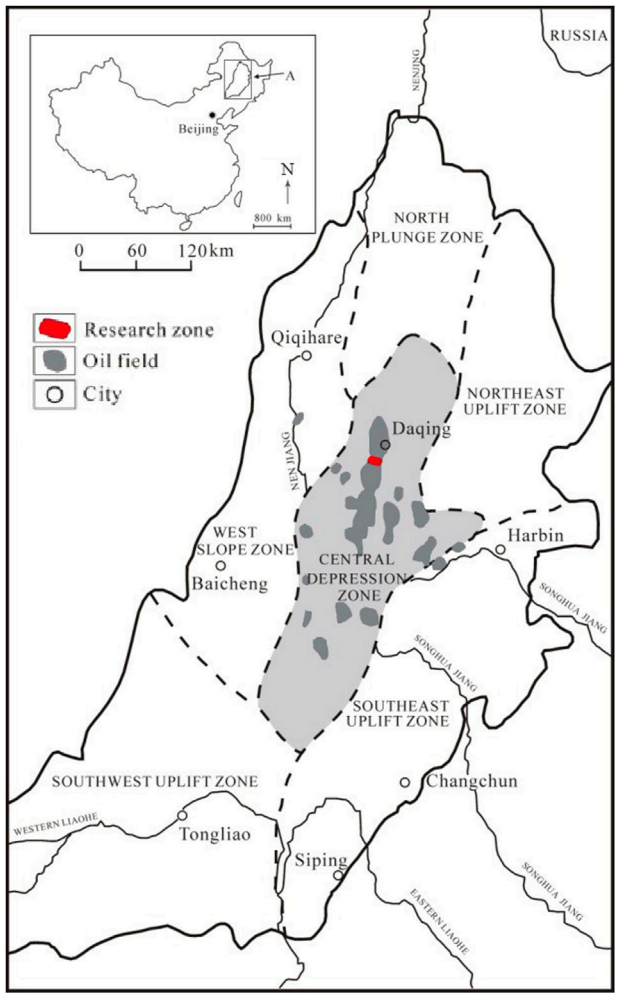

FIGURE 1 | Location of the Naner Zone in the Saertu Oilfield (A: Location of the Songliao Basin).

reservoirs change under the chemical dissolution of rock minerals and the precipitation and agglomeration of clay mineral particles in the pore fluid because of the adsorption-flocculation of the polymer (Kazempour et al., 2013; Huang et al., 2020). Ultimately, all these changes of the pore structure and physical properties of reservoirs will affect the formation and distribution of residual oil (Liu et al., 2013; Liu et al., 2014; Liu et al., 2015; Mansa et al., 2017; Wu et al., 2015b). Therefore, it is significant for the effective development of residual oil to investigate the variation of clay minerals after ASP flooding in ultra-high-water-cut-stage reservoirs. In the paper, the response to the variation of clay minerals in reservoirs during ASP flooding is studied for the ultra-high-water-cut-stage reservoirs of the Naner Zone in the Saertu Oilfield, Songliao Basin. Besides, the effect of these variations on pore structure, physical properties, and residual oil distribution are also investigated. The results of this study provide technical support for the effective development of residual oil after ASP flooding.

GEOLOGICAL SETTING

The Naner Zone (research zone) of the Saertu Oilfield is located in the northern part of Daqing Placanticline from the Songliao Basin (**Figure 1**) (Hu et al., 2005). Three sets of oil reservoirs (Saertu, Putaohua, and Gaotaizi) are developed in the Naner Zone (**Figure 2**). These reservoirs belong to the fluern part of the daqivial-delta deposition, and their burial depth is about 827–1,200 m (Sui et al., 2000; Zhao et al., 2000). In this study, the second segment of the Saertu reservoir (member Sa II) is selected as the target layer.

Member Sa II is a sandstone reservoir with good permeability, and its thickness is about 52–56 m. The sandstone type is arkose, and a small part is hard sandy arkose with a fine sand-like structure. The detrital minerals are mainly composed of feldspar and quartz. Feldspar accounts for 43%–54% of the total content, consisting of a large amount of orthoclase and a small amount of plagioclase and microcline. In addition, quartz accounts for 30%–43% of the total content. The cement is mainly composed of argilla, and the argillaceous content is more than 3%. The clay mineral composition of cement is mainly kaolinite, followed by chlorite, illite, and illite smectite mixed layers. The cementation type is pore-contact, and the intergranular pore is the main type of pores (Xing and Jiang, 1993; Gao, et al., 2015).

At present, ASP flooding has been conducted on the Sa II reservoir, that is, injection of an alkali (sodium hydroxide)–surfactant (petroleum sulfonate)–polymer (polyacrylamide) system to the Sa II reservoir for oil displacement. The injection concentrations of the ASP system of alkali, surfactant, and polymer are 1.2, 0.3, and 0.18 wt%, respectively. The molecular weight of the polymer is 25 million. The salinities of formation water before and after ASP flooding are 7,178 and 7,463 mg/L, respectively, and the type of formation water is sodium bicarbonate (NaHCO).

MATERIALS AND METHODS

Materials

The core samples required for this study were collected from the Sa II reservoir of the Saertu Formation in the Naner Zone of the Saertu Oilfield, and the core depth is 930–943 m. A total of 10 core samples were taken, including five ASP flooding samples with an average air permeability of 0.638 μm^2 and an average porosity of 27.9% and five water flooding samples (before ASP flooding) with an average air permeability of 0.443 μm^2 and an average porosity of 26.9%. The lithologies are all oil-bearing siltstones with good reservoir properties.

Methods

Scanning electron microscopy (SEM) and X-ray diffraction methods were applied to the surface morphology, and whole-rock mineral and clay mineral analysis of the core samples was conducted to determine the pore structure and mineral composition of the cores and to explore the characteristics of

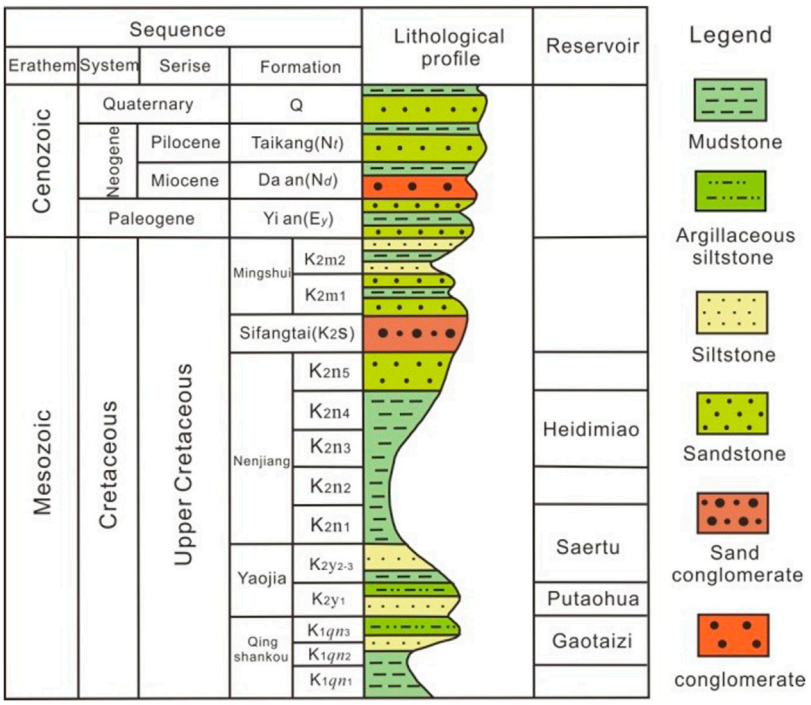

FIGURE 2 | Profile map of the different reservoirs in the Naner Zone.

changes in the pore structure and clay minerals of the cores before and after ASP flooding (Fang, et al., 2016; Zhu et al., 2021).

Scanning Electron Microscope Analysis Method

SEM was used to directly observe the morphology and pore structure of core samples, including the shape, size, and distribution characteristics of pores, inter-pore connectivity, and the distribution characteristics of solid particle skeleton and clay minerals (Houben et al., 2013; Zhu et al., 2018). A scanning electron microscope was used to observe the samples, which were then firstly dried by the critical point drying method, i.e., using the property that the surface tension of a substance is equal to zero at the critical state to completely vaporize the liquid of the sample and exhaust it as a gas to achieve the purpose of complete drying. Then the sample is treated with conductive treatment to make the sample surface conductive. In this paper, the metal coating method is used, which uses a special device to cover the sample surface with metals of low resistivity, such as gold, platinum, and palladium, after evaporation.

X-Ray Diffraction Analysis Method

X-ray diffraction is applied to the analysis of whole-rock minerals and clay minerals in core samples (Wang et al., 2019). To determine the core samples by X-ray diffraction, the natural orientation sheet (N) is firstly prepared by the extraction method; i.e., start the vacuum pump, put the soaked microporous filter membrane on the funnel, pour the suspension in several times, pump the suspension in 10 min each time, remove the filter membrane when the clay membrane reaches a thickness of 30–40 μm, put the membrane on the slide backward, and put it in the culture blood to dry. Then the naturally oriented slides were thermostated with ethylene glycol vapor at 45°C for 7 h and cooled to room temperature to make ethylene glycol-saturated slides (EG), and the ethylene glycol-saturated slides were thermostated at (550 + 10)°C for 2 h and cooled naturally to room temperature to make heated slides (550°C). And the ray diffraction spectra of the naturally oriented sheet (N), glycol-treated sheet (EG), and heated sheet (550°C) were completed under certain experimental conditions. Finally, for the specific characteristics of clay minerals in sedimentary rocks, the percentages of every single mineral in clay minerals were calculated by taking advantage of the phenomenon where swelling minerals in clay minerals are heated and dehydrated and their crystalline spacing shrinks to 1.0 nm, and the characteristic peaks of kaolinite and chlorite overlap at 0.7 nm in the diffractogram of natural orientation.

VARIATION CHARACTERISTICS OF RESERVOIR CLAY MINERALS BEFORE AND AFTER ASP FLOODING

Morphology and Distribution Characteristics of Clay Minerals

SEM images show that different types of clay minerals have different morphologies and distribution characteristics. Kaolinite is an alteration product of feldspar, and its

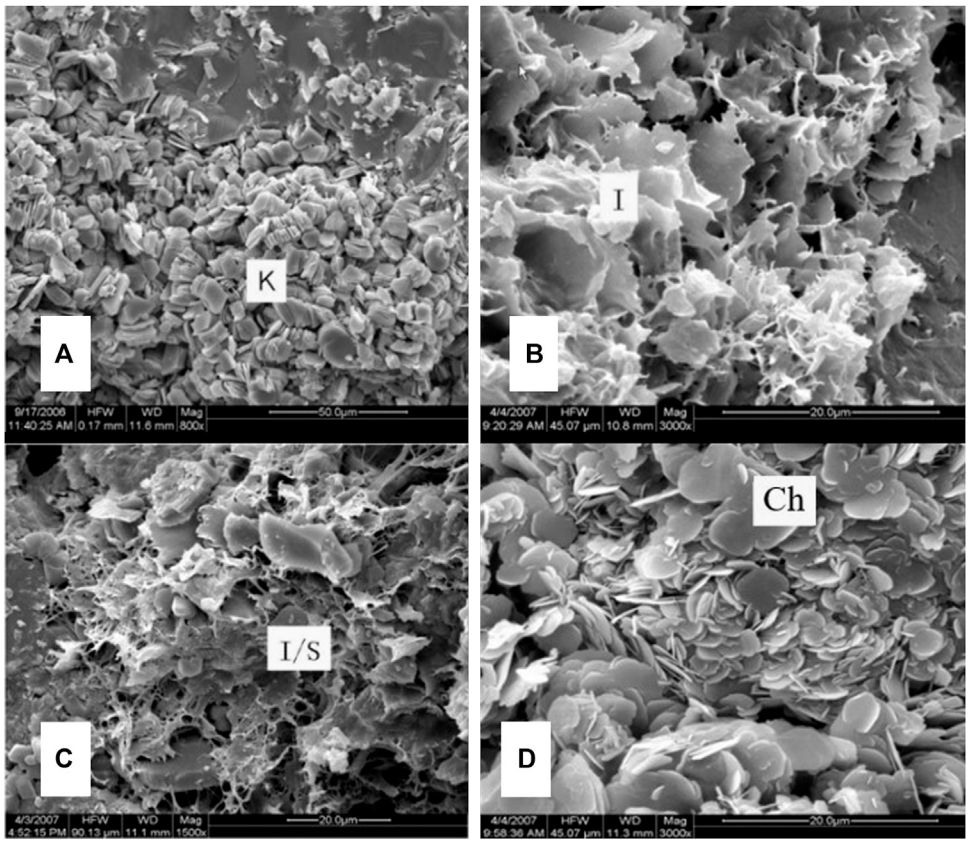

FIGURE 3 | SEM images of clay minerals [**(A)** kaolinite, **(B)** illite, **(C)** illite smectite mixed layer, **(D)** chlorite].

morphologies are book-page-like, worm-like, and accordion-like. Kaolinite is mostly distributed in the intergranular pores in the form of pore filling (**Figure 3A**). Kaolinite is easy to move with fluids under the scouring of fluids because of the loose intracrystalline structure and then block and divide the pores and throats. Therefore, kaolinite is an important velocity-sensitive mineral. Illite is attached to the particle surface or filled in the intergranular pores in the form of leaves or silk hairs (**Figure 3B**). The leaf-like crystallites separate the pores into several fine pores, which increase the tortuosity of flow channels. The hair-like crystallites are easily washed away by water and then block pores and throats, which leads to the decrease of porosity and permeability of reservoirs. The illite smectite mixed layer is an intermediate product of montmorillonite transformed to illite, and its morphologies are burr and curl. It has three typical structures, namely, lamellar structure, honeycomb structure, and flocculent structure (**Figure 3C**). Compared with other clay minerals, the illite smectite mixed layer has very strong water sensitivity. Chlorite is often symbiotic with authigenic quartz, and its morphologies are needle-like, pompon-like, and rose-like. The chlorite is distributed in pores in the form of pore filling and pore backing. Generally, the needle-like chlorite is mostly filled with pore backing on the surface of the particles, while the pompon-like and rose-like chlorites are filled in the pores (**Figure 3D**). Chlorite can be transformed from minerals such as biotite, hornblende, and montmorillonite. However, the authigenic chlorite is generally rich in high-valence iron ions, which easily react with the acid solution (e.g., HCl) in the drilling fluid to cause precipitation and reservoir damage. Therefore, chlorite is an acid-sensitive mineral.

Variation Characteristics of the Content and Composition of Clay Minerals

The 10 selected core samples were extracted and dried at first, and then the X-ray diffraction method was used for the quantitative analysis of whole-rock minerals and clay minerals. The analysis results are presented in **Table 1**. As shown in **Table 1**, the alkali in the ASP system affects the content of the rock-forming minerals and clay mineral rock. The total amount of quartz is reduced after ASP flooding, and the potassium feldspar content is also reduced, while the plagioclase (albite) content increases slightly. Furthermore, the total content of clay minerals decreases after ASP flooding; therein, the relative content of the illite decreases, but the relative content of the chlorite and illite smectite mixed layer increases. However, the variation of kaolinite content in different core samples is quite different. Kaolinite contents in some samples decrease, while they increase in others.

TABLE 1 | Variation of rock mineral composition and content before and after ASP flooding.

Core number	Depth (m)	Mineral composition and relative content (%)				Mixed-layer ratio (%S)		Type and relative content of clay mineral (%)						Total amount of clay minerals (%)	Remark
		Quartz	Potassium feldspar	Anorthose	Calcite	I/S[a]	C/S[b]	S[c]	I[d]	K[e]	C[f]	I/S	C/S		
W1	941.42	50.8	20.9	24.6	—	15	—	—	20	69	4	7	—	3.7	Water flooding
W2	941.44	51.9	21.7	22.8	—	15	—	—	18	71	6	5	—	3.6	Water flooding
W3	941.99	52.5	19.8	23.5	0.3	15	37	—	8	73	5	5	9	3.9	Water flooding
W4	942.01	48.4	26.5	21.6	—	15	—	—	15	76	6	3	—	3.5	Water flooding
W5	942.03	50.2	21.6	22.1	—	15	—	—	10	77	8	5	—	6.1	Water flooding
S1	941.43	38.9	17.8	39.8	—	20	—	—	3	83	8	6	—	3.5	ASP flooding
S2	942.00	37.1	18.2	41.1	—	20	—	—	2	85	6	7	—	3.6	ASP flooding
S3	942.07	36.2	18.6	42.8	—	20	—	—	8	58	20	14	—	2.4	ASP flooding
S4	942.13	34.8	18.9	42.9	—	20	—	—	7	56	21	16	—	3.4	ASP flooding
S5	942.14	44.3	16.9	35.7	—	20	—	—	4	61	18	17	—	3.1	ASP flooding

[a]*Illite smectite mixed mineral.*
[b]*Chlorite smectite mixed mineral.*
[c]*Smectite.*
[d]*Illite.*
[e]*Kaolinite.*
[f]*Chlorite.*

In addition, ASP flooding changes the chemical composition of the rock. The ASP system injected into the reservoir, especially the alkali, on the one hand, will dissolve the rock minerals (e.g., kaolinite and feldspar), thereby causing the elemental components (e.g., silicon and aluminum) in the rock minerals to be transferred from the solid phase to the formation water; on the other hand, the aluminum and silicon ions which are dissolved by the alkali will regenerate the crystalline precipitate of aluminosilicate in other places under certain conditions (Maggio et al., 2010; Wu et al., 2015a; Song et al., 2015).

The feldspar of rock-forming minerals and some kaolinites are mostly eroded by alkali in the ASP flooding system. As a non-expanded clay mineral, kaolinite is one of the most common authigenic clay minerals in sandstone reservoirs, and it is also an indicator mineral for feldspar dissolution (Xing, 1983). The feldspar can generate kaolinite under eluviation, and its chemical reaction is as follows:

$$(K, Na, Ca)[AlSi_3O_8] + H^+ \rightarrow Al_2Si_2O_5(OH)_4 + (K^+, Na^+, Ca^{2+}) + Si^{4+}.$$

The reaction equation for the dissolution of kaolinite by alkali is as follows:

$$Al_4[Si_4O_{10}](OH)_8 + 8OH^- = 4Al(OH)_3\downarrow + 4SiO_3^{2-} + 2H_2O.$$

Kaolinite can be transformed into albite under the action of alkali, and the reaction equation is as follows:

$$Al_2[Si_2O_5](OH)_4 + 2Na^+ + 2OH^- + 4Si(OH)_4 = 2NaAlSi_3O_3 + 11H_2O.$$

It can be concluded that the increase of anorthose content after ASP flooding is due to the formation of albite from kaolinite under the action of alkali. The content of the illite smectite mixed layer is increased, which is the aluminosilicate scale formed by mineral recrystallization (Lu and Guan, 1999). There are two reasons for the increase in kaolinite content. One is the newly formed kaolinite by feldspar under eluviation, and the other is the precipitation and accumulation of kaolinite particles in formation water caused by the adsorption flocculation of the polymer in the ASP system (Liu et al., 2014; Mansa et al., 2017). The increase in chlorite content is an aluminosilicate precipitate formed by mineral recrystallization in an alkaline environment.

INFLUENCE OF VARIATION OF CLAY MINERALS ON RESERVOIR PHYSICAL PROPERTIES

Influence on the Pore Structure of Reservoir

It can be seen from the SEM images of core samples before ASP flooding that the core intergranular pores include the primary intergranular pores and the secondary intergranular pores. The main cements in the core are clay minerals. Among the clay mineral cements, it can be seen from **Figure 4A** that the kaolinite cements in the pores in the form of pore-filling and blocks the pore throats; parts of illite and chlorite are cemented on the surface of the particles in the form of pore-backing to decrease the pore space, and the other part is cemented in the pores in the form of pore-filling and blocks the pore throats (**Figure 4B**).

It can be seen from the SEM images of core samples after ASP flooding that the clay minerals block the pore throat, and the pore structure coefficient and the tortuosity of pore throat increase after ASP flooding. The kaolinite and illite in the clay minerals adhere to the surface of the rock particles and extend into the pore space, thereby causing the shrinkage of the primary intergranular pore throat (**Figure 5A**). In addition, the local pore throat is enlarged due to the dissolution of clay minerals and rock particles by alkali (**Figure 5B**).

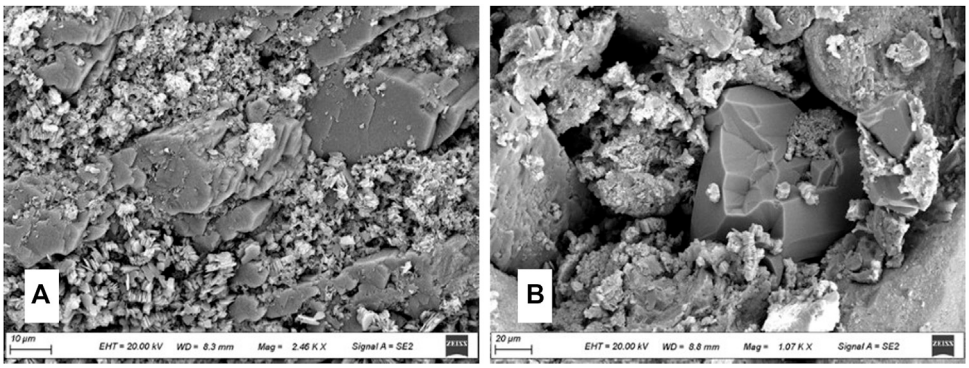

FIGURE 4 | Intergranular pore morphology before ASP flooding (**A**: surface of particles and pore throats, **B**: pore throats).

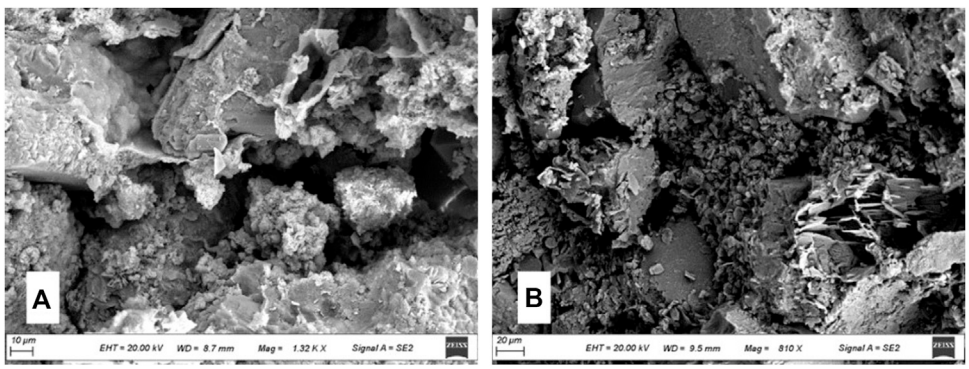

FIGURE 5 | Intergranular pore morphology after ASP flooding (**A**: primary intergranular pore throat, **B**: local pore throat).

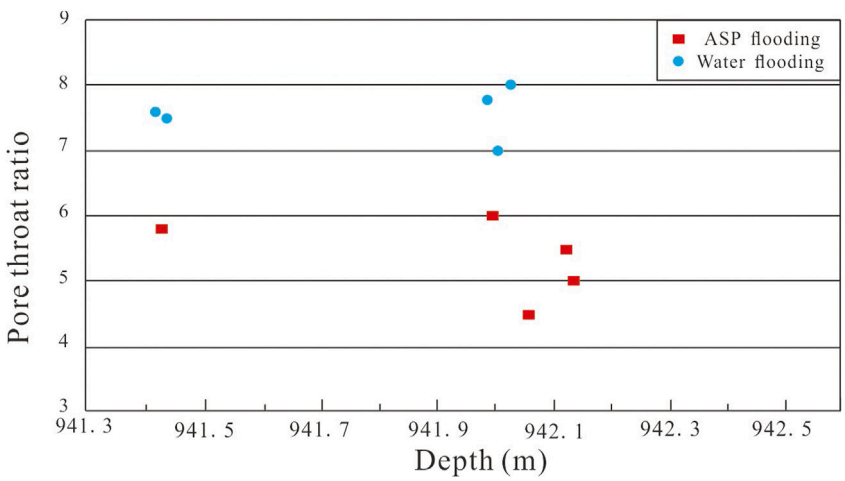

FIGURE 6 | Variation characteristics of pore–throat ratio before and after ASP flooding.

In addition, according to the analysis of the 3D nondestructive core sample pore structure obtained by CT scanning, the reservoir pore–throat ratio (ratio of pore radius and throat radius) and pore throat coordination number (throat number connecting each pore) decreased significantly after ASP flooding (**Figure 6** and **Figure 7**). The reason for this phenomenon is that the alkali component in the ASP system erodes the clay minerals and rock particles (feldspar) in the

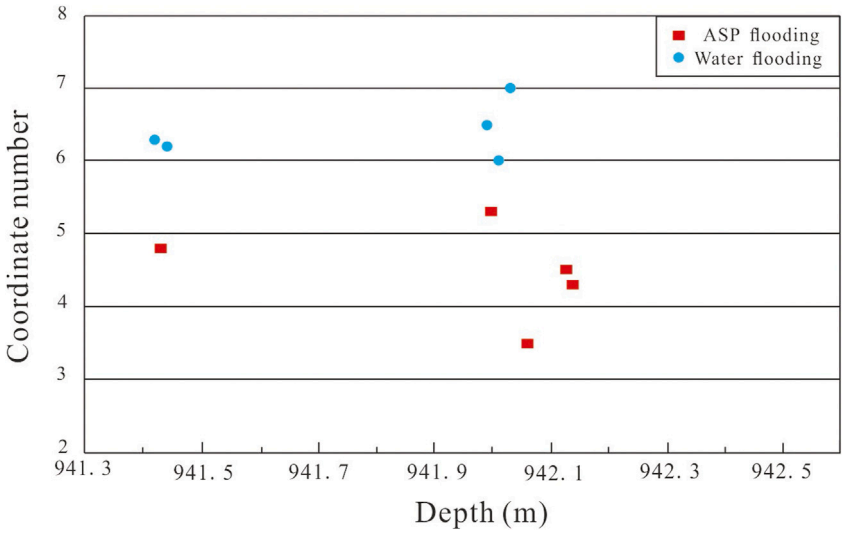

FIGURE 7 | Variation characteristics of pore throat coordinate number before and after ASP flooding.

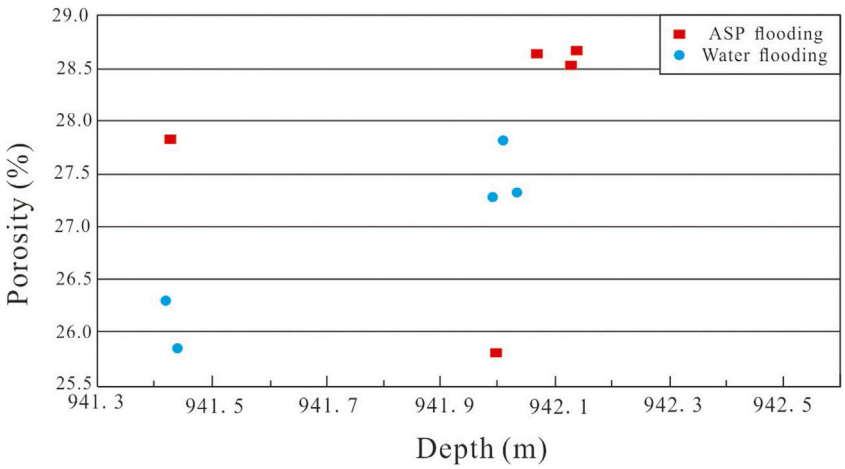

FIGURE 8 | Variation characteristics of porosity before and after ASP flooding.

reservoir during ASP flooding. The clay minerals and rock particles are chemically unstable, which are then dissolved by alkali migrating with the composite system, thereby increasing the diameter of the local pore throat (Loucks et al., 2012). In addition, the fine particles in reservoir fluids are easily adsorbed, trapped, and retained in the narrow throat by the polymer, causing throat blockage and reducing the effective communication in throats.

Influence on Porosity and Permeability of Reservoir

Figure 8 and **Figure 9** show the physical properties of core samples before and after ASP flooding; we can conclude that the changing trends of porosity and permeability are consistent after ASP flooding. The average porosity of the core samples increases, which is 0.97% higher than the value before ASP flooding. Sixty percent of the core porosity increases by more than 28%, and the maximum value is 28.66%. The core permeability after ASP flooding is mainly distributed between 663.19 and 882.88 mD. Compared with that of the cores before ASP flooding, the permeability increases significantly, and the increment is 195.09 mD. The influence of ASP flooding on the physical properties of cores is mainly caused by the dissolution of rock skeleton, clay minerals, and cuttings by alkali components in the ASP system (Olajire, 2014). Part of the pore throats become large because of alkali dissolution and fine particle migration; therefore, the physical properties become better. However, some parts of pore throats become smaller, and the tortuosity of the pore throat increases because of the accumulation and

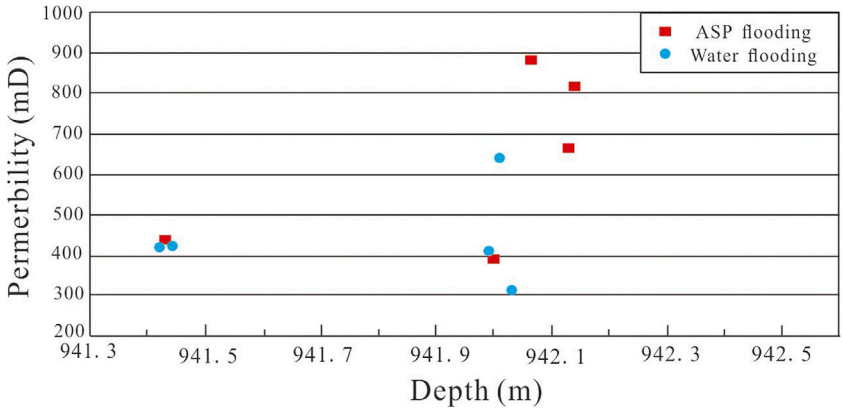

FIGURE 9 | Variation characteristics of permeability before and after ASP flooding.

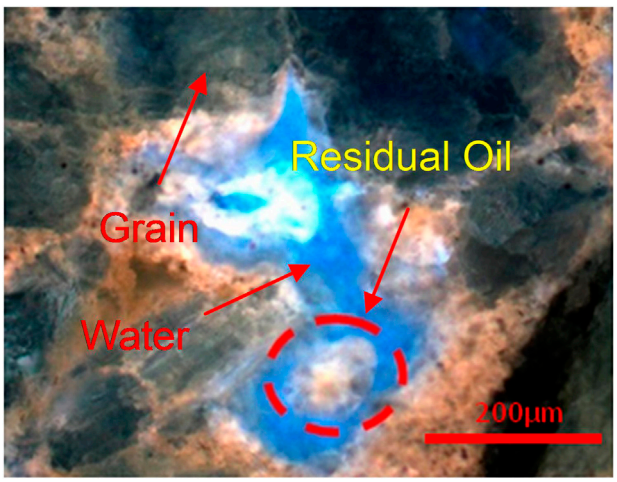

FIGURE 10 | Distribution of petroleum-clay mixed residual oil.

precipitation of fine particles in the pore fluids, thereby leading to a decrease in porosity and permeability. The porosity and permeability of the reservoir are polarized and the heterogeneity is enhanced after ASP flooding.

INFLUENCE OF VARIATION OF CLAY MINERALS ON RESIDUAL OIL

The transformation of clay minerals leads to changes in the pore structure of the reservoir, which affects the formation and distribution of residual oil. It can be seen from the fluorescence images of core samples after ASP flooding in ultra-high-water-cut-stage reservoirs that there are many isolated "petroleum-clay mixed" residual oil in the middle of pores after ASP flooding (**Figure 10**).

At present, the Naner Zone in the north of Daqing placanticline in Songliao Basin has entered the stage of ultra-high water cut development. The kaolinite in the Sa II reservoir is a velocity-sensitive mineral. The kaolinite aggregation has poor adhesion to the skeleton particles, and the binding force between kaolinite wafers is also very weak. The kaolinite lamellar crystal aggregation is mechanically and chemically eroded by the injected ASP flooding solutions, causing the crystal skeleton of aggregation to be destroyed to form fine particles. In addition, the feldspar eluviation also produces new kaolinite. These tiny mineral fragments or newly formed kaolinite are driven by the injection fluid flow to produce particle migration. Then, the kaolinite particles migrating with the fluid are mixed with the microspheres of emulsified crude oil and are adsorbed and accumulated by the polymer in the local intergranular pores (Zhang et al., 2007; Zhang et al., 2010; Ren et al., 2015; Mansa et al., 2017). As a result, the isolated petroleum-clay mixed residual oil is formed and distributed in the intergranular pores and pore throats of the reservoir (**Figure 10**). The laser confocal scanning microscopy technique was used to quantify the proportion of different types of residual oil (Liang et al., 2018). The average content of petroleum-clay mixed residual oil is 4.8% (a percentage of the total volume of the sample), accounting for 44.2% of the total residual oil reserves. Compared with the core samples before the ASP flooding, the proportion of petroleum-clay mixed residual oil content in the total residual oil reserves after ASP flooding increased by 12.9%. The petroleum-clay mixed residual oil associated with clay minerals is the main occurrence state of residual oil after ASP flooding.

CONCLUSION

1) After ASP flooding, the total amount of clay minerals decreases, and the content of illite decreases, while the contents of the illite smectite mixed layer and chlorite increase. The kaolinite content varies greatly. On the one hand, the kaolinite is dissolved by alkali, and its content decreases; on the other hand, the kaolinite particle in pore fluid precipitates and gathers under the adsorption flocculation of the polymer, and its content increases.

Because kaolinite can block the reservoir pore throat, it increases the difficulty of subsequent enhanced oil recovery (EOR).

2) After ASP flooding, the clay minerals block the pore throat, increase the tortuosity of pore fluid flow, and shrink the original intergranular pore throats. In addition, the dissolution of the clay minerals enlarges the local pore throat, decreases the pore–throat ratio and coordination number, and increases the porosity and permeability. Variation of clay minerals after ASP flooding not only enhances the reservoir heterogeneity but also influences the formation and distribution of residual oil.
3) The petroleum-clay mixed residual oil associated with clay minerals is a new type of residual oil. It is formed by the mixed aggregation of clay minerals and oil under the action of polymer in the process of ASP flooding and is mainly distributed in the intergranular pores or the pore throats with high clay mineral content. The clay-petroleum mixed oil is the main occurrence state of residual oil after ASP flooding, and the development of this type of residual oil will greatly improve the oil recovery of ultra-high-water-cut-stage oilfields.

DATA AVAILABILITY STATEMENT

The original contributions presented in the study are included in the article/Supplementary Material; further inquiries can be directed to the corresponding author.

AUTHOR CONTRIBUTIONS

YL was responsible for the main experiment, analysis, and part of the writing work; WL was responsible for the data sorting and revision work; HW was responsible for part of the writing work and revision work. ZL was responsible for the experimental design and part of the writing work.

FUNDING

This study was supported by the National Science and Technology Major Project (Grant No. 2016ZX05054013).

REFERENCES

Chen, S., Han, Y., Fu, C., Zhang, h., Zhu, Y., and Zuo, Z. (2016). Micro and Nano-Size Pores of clay Minerals in Shale Reservoirs: Implication for the Accumulation of Shale Gas. *Sediment. Geology.* 342 (aug.1), 180–190. doi:10.1016/j.sedgeo.2016.06.022

Cheng, J. C., Wu, J. Z., and Hu, J. Q. (2014). Key Theories and Technologies for Enhanced Oil Recovery of Alkaline/surfactant/polymer Flooding. *Acta Petrolei Sinica* 35 (2), 310–318. (in Chinese with English abstract). doi:10.7623/syxb201402011

Cheng, J. C., Xu, D. P., Sui, X. G., and Wang, H. W. (2012). "The First Successful Field Demonstration of Alkaline Surfactant and Polymer Flooding through Thin Layer," in Abu Dhabi International Petroleum Conference and Exhibition, Abu Dhabi, UAE, November 11–14, 2012, SPE. doi:10.2118/161306-ms

Fang, W., Jiang, H., Li, J., Li, W., Li, J., Zhao, L., et al. (2016). A New Experimental Methodology to Investigate Formation Damage in clay-bearing Reservoirs. *J. Pet. Sci. Eng.* 143, 226–234. doi:10.1016/j.petrol.2016.02.023

Gao, Y., Wang, C., Liu, Z., Du, X., and Ibarra, D. E. (2015). Diagenetic and Paleoenvironmental Controls on Late Cretaceous clay Minerals in the Songliao basin, Northeast china. *Clays Clay Miner.* 63 (6), 469–484. doi:10.1346/ccmn.2015.0630605

Houben, M. E., Desbois, G., and Urai, J. L. (2013). Pore Morphology and Distribution in the Shaly Facies of Opalinus Clay (Mont Terri, Switzerland): Insights from Representative 2D BIB-SEM Investigations on Mm to Nm Scale. *Appl. Clay Sci.* 71 (JAN), 82–97. doi:10.1016/j.clay.2012.11.006

Hu, W. S., Lu, B. Q., and Zhang, W. J. (2005). An Approach to Tectonic Evolution and Dynamics of the Songliao Basin. *Chin. J. Geology.* 40, 16–31. Chinese Cite Code: 0563-5020(2005)01-0016-16.

Huang, B., Wang, C., Zhang, W., Fu, C., Liu, H., and Wang, H. (2020). Study on the Stability of Produced Water from Alkali/surfactant/polymer Flooding under the Synergetic Effect of Quartz Sand Particles and Oil Displacement Agents. *Processes* 8 (3), 315. doi:10.3390/pr8030315

Kazempour, M., Manrique, E. J., Alvarado, V., Zhang, J., and Lantz, M. (2013). Role of Active Clays on Alkaline-Surfactant-Polymer Formulation Performance in sandstone Formations. *Fuel* 104 (2013), 593–606. doi:10.1016/j.fuel.2012.04.034

Liang, Y. J., Li, Z. A., Li, J., and Sun, X. D. (2018). "Distribution of Microscopic Remaining Oil after ASP Flooding in Saertu Oilfield in Daqing," in Proceedings of the International Field Exploration and Development Conference 2018, Singapore, October 2019. Springer Series in Geomechanics and Geoengineering, 1653–1662. doi:10.1007/978-981-13-7127-1_158

Liu, Y. K., Cai, L. Z., Qu, G. H., and Wang, F. J. (2013). Research on Microscopic Characteristics of Remaining Oil Distribution after Strong Alkali ASP Flooding by Laser Scanning Confocal Technology. *Sustain. Dev. Nat. Resour.* 616-618, 757–761. doi:10.4028/www.scientific.net/AMR.616-618.757

Liu, G., Jiang, H., and Min, W. (2014). Study on Calculation for Polymer Flooding Incremental Oil. *Pet. Geology. Recovery Efficiency* 21 (2), 32–34+50. (in Chinese with English abstract). doi:10.13673/j.cnki.cn37-1359/te.2014.02.008

Liu, Y. K., Fan, M., Zhang, D., Wang, F. J., Liang, S., and Zhao, X. Y. (2015). Microscopic Characteristics of the Remained Oil after ASP Flooding. *Pet. Geology. Oilfield Dev. Daqing* 34 (2), 117–120. (in Chinese with English abstract). doi:10.3969/j.issn.1000-3754.2015.02.023

Loucks, R. G., Reed, R. M., Ruppel, S. C., and Hammes, U. (2012). Spectrum of Pore Types and Networks in Mudrocks and a Descriptive Classification for Matrix-Related Mudrock Pores. *AAPG Bulletin* 96 (6), 1071–1098. doi:10.1306/08171111061

Lu, G. W., and Guan, J. T. (1999). Influence of Temperature on Wetting Coefficient of Oil-Water-Quartz System. *J. Univ. Pet. , China* 23 (5), 92–94. (in Chinese with English abstract).

Maggio, R. D., Gajo, A., and Wahid, A. S. (2010). Chemo-mechanical Effects in Kaolinite. Part 1: Prepared Samples. *Géotechnique* 61, 449–457. doi:10.1680/geot.8.P.067

Mansa, R., Piegang, G. B. N., and Detellier, C. (2017). Kaolinite Aggregation in Book-like Structures from Non-aqueous media. *clays clay miner* 65 (3), 193–205. doi:10.1346/ccmn.2017.064059

Olajire, A. A. (2014). Review of Asp Eor (Alkaline Surfactant Polymer Enhanced Oil Recovery) Technology in the Petroleum Industry: Prospects and Challenges. *Energy* 77 (dec), 963–982. doi:10.1016/j.energy.2014.09.005

Ren, C. H., Luo, Y., Wang, L. H., Jin, Y. X., Wang, T., Feng, X., et al. (2015). Investigation on Crude Oil Emulsification and Oil Displacement Technology. *Adv. Fine Petrochemicals* 16 (4), 12–15. (in Chinese with English abstract). doi:10.13534/j.cnki.32-1601/te.2015.04.004

Sheng, J. J. (2016). Formation Damage in Chemical Enhanced Oil Recovery Processes. *Asia-pac. J. Chem. Eng.* 11, 826–835. doi:10.1002/apj.2035

Song, K. P., He, J. G., and Yang, J. (2015). Influence of Base ASP Flooding on the Reservoir Pore Structure. *J. China Univ. Pet.* 39 (5), 164–172. (in Chinese with English abstract). doi:10.3969/j.issn.1673-5005.2015.05.023

Song, W. L., Pan, J., and Gao, Y. H. (2011). Effect of clay Content on the Adsorption Loss of Surfactant in Asp Floods Systems. *Amr* 225-226, 158–161. doi:10.4028/www.scientific.net/amr.225-226.158

Sui, J., Zhao, H. Q., and Lv, X. G. (2000). *Study of Large Fluvial-delta Depositional Reservoir of Daqing Oilfield*. Beijing: Petroleum Industry Press. (in Chinese).

Wang, Z. Z., Hu, R. T., Ren, G. H., Li, G. R., Liu, S. Y., Xu, Z. H., et al. (2019). Polyetheramine as an Alternative Alkali for Alkali/surfactant/polymer Flooding. *Colloids Surf. A: Physicochemical Eng. Aspects* 581, 123820. doi:10.1016/j.colsurfa.2019.123820

Wu, C. Y., Hou, J. R., Zhao, F. L., Zhang, F. M., Hao, H. D., and Liu, G. (2015a). Study on the Microscopic Mechanism of Driving Remaining Oil by ASP Compound System after Water Flooding. *Pet. Geology. Recovery Efficiency* 22 (5), 84–88. (in Chinese with English abstract). doi:10.13673/j.cnki.cn37-1359/te.2015.05.012

Wu, X. L., Yin, Y. D., Wu, G. P., Lu, A. H., Hou, Z. W., Ding, H. R., et al. (2015b). Study on the Reaction of Alkali/Surfactant/Polymer and Reservoir Cores in Daqing Oilfield. *Chem. Eng. Oil Gas* 44 (5), 66–72. (in Chinese with English abstract). doi:10.3969/j.issn.1007-3426.2015.05.014

Xing, S. Q. (1983). Evolutional Characteristics of Authigenic Quartz and Feldspar in Sandstones and Their Geological Significance. *Pet. Geology. Oilfield Dev. Daqing* 2 (3), 171–177. (in Chinese with English abstract).

Xing, S. Q., and Jiang, H. Q. (1993). *Characteristics and Diagenesis of continental sandstone Reservoir in Songliao basin*. Haerbin: Heilongjiang Science and Technology Press. (in Chinese).

Xv, Z. J., Wang, X., Wang, Y., and Pan, Y. (2015). Experimental Study on the Mechanism of ASP Flooding. *Contemp. Chem. Industry* 44 (1), 24–26. (in Chinese with English abstract). doi:10.13840/j.cnki.cn21-1457/tq.2015.01.008

Zhang, L. J., Yue, X. A., and Guo, Z. J. (2010). Study on Emulsification of ASP Compound System with Daqing and Dagang Oil. *Pet. Geology. Recovery Efficiency* 17 (3), 74–76. (in Chinese with English abstract).

Zhang, X. J., Ji, W., Kang, Z. J., Sun, D. Y., Wang, J., and Na, R. X. (2009). The Development of the ASP Flooding Recovery Technique. *Hangzhou Chem. Industry* 39 (2), 5–8. (in Chinese).

Zhang, X. P., Hu, Y. H., Huang, H. J., and Deng, M. J. (2007). Aggregation Behavior of Ultrafine Kaolinite in Water. *J. China Univ. Mining Tech.* 36 (4), 514–517. (in Chinese with English abstract).

Zhao, H. Q., Fu, Z. G., Lv, X. G., Tian, D. H., and Wang, G. Y. (2000). Methods for Detailed Description of Large Fluvial-delta Depositional Reservoir. *Acta Petrolei Sinica* 21 (4), 109–113. (in Chinese with English abstract).

Zhao, Y. T., Sun, J., and Shan, X. L. (2017). Clay Minerals in an Oil-Sand deposit and Their Effect on Oil-Bearing Properties. *Pet. Sci. Tech.* 35 (6), 578–585. doi:10.1080/10916466.2016.1266366

Zhu, H., Huang, C., Ju, Y., Bu, H., Li, X., Yang, M., et al. (2021). Multi-scale Multi-Dimensional Characterization of clay-hosted Pore Networks of Shale Using FIBSEM, TEM, and X-ray Micro-tomography: Implications for Methane Storage and Migration. *Appl. Clay Sci.* 213, 106239. doi:10.1016/j.clay.2021.106239

Zhu, H., Ju, Y., Qi, Y., Huang, C., and Zhang, L. (2018). Impact of Tectonism on Pore Type and Pore Structure Evolution in Organic-Rich Shale: Implications for Gas Storage and Migration Pathways in Naturally Deformed Rocks. *Fuel* 228, 272–289. doi:10.1016/j.fuel.2018.04.137

Conflict of Interest: Author WL was employed by Daqing Oilfield Co., Ltd.

The remaining authors declare that the research was conducted in the absence of any commercial or financial relationships that could be construed as a potential conflict of interest.

Publisher's Note: All claims expressed in this article are solely those of the authors and do not necessarily represent those of their affiliated organizations, or those of the publisher, the editors, and the reviewers. Any product that may be evaluated in this article, or claim that may be made by its manufacturer, is not guaranteed or endorsed by the publisher.

frontiers in Earth Science

ORIGINAL RESEARCH
published: 24 December 2021
doi: 10.3389/feart.2021.786667

Evolutions of Oil Generation and Expulsion of Marine-Terrestrial Transitional Shales: Implications From a Pyrolysis Experiment on Water-Saturated Shale Plunger Samples

Qizhang Fan[1,2], Peng Cheng[2,3], Xianming Xiao[1], Haifeng Gai[2,3], Qin Zhou[2,3], Tengfei Li[2,3] and Ping Gao[1]*

[1]School of Energy Resources, China University of Geosciences (Beijing), Beijing, China, [2]State Key Laboratory of Organic Geochemistry, Guangzhou Institute of Geochemistry, Chinese Academy of Sciences, Guangzhou, China, [3]CAS Center for Excellence in Deep Earth Science, Guangzhou, China

OPEN ACCESS

Edited by:
Kai-Jun Zhang,
University of Chinese Academy of Sciences, China

Reviewed by:
Yang Wang,
China University of Mining and Technology, China
Hongxiang Guan,
Ocean University of China, China

***Correspondence:**
Peng Cheng
chengp@gig.ac.cn

Specialty section:
This article was submitted to Geochemistry, a section of the journal Frontiers in Earth Science

Received: 30 September 2021
Accepted: 23 November 2021
Published: 24 December 2021

Citation:
Fan Q, Cheng P, Xiao X, Gai H, Zhou Q, Li T and Gao P (2021) Evolutions of Oil Generation and Expulsion of Marine-Terrestrial Transitional Shales: Implications From a Pyrolysis Experiment on Water-Saturated Shale Plunger Samples. Front. Earth Sci. 9:786667. doi: 10.3389/feart.2021.786667

Shale reservoirs are characterized by self-generation and self-accumulation, and the oil generation and expulsion evolution model of organic-rich shales is one of important factors that obviously influence the enrichment and accumulation of shale oil and gas resources. At present, however, relevant studies on marine-terrestrial transitional shales are inadequate. In this study, a pyrolysis experiment was performed on water-saturated marine-terrestrial transitional shale plunger samples with type II_b kerogen to simulate the evolutions of oil generation and expulsion. The results indicate that marine-terrestrial transitional shales have wider maturity ranges of oil generation and expulsion than marine and lacustrine shales, and the main stages of oil expulsion are later than those of oil generation, with corresponding R_o values of 0.85%–1.15% and 0.70%–0.95%, respectively. Although the oil generation and expulsion process induced a fractionation in compositions between the expelled and retained oils, both the expelled and retained oils of marine-terrestrial transitional shales are dominated by heavy compositions (resins and asphaltenes), which significantly differs from those of marine and lacustrine shales. The kerogen of marine-terrestrial transitional shales initially depolymerized to transitional asphaltenes, which further cracked into hydrocarbons, and the weak swelling effects of the kerogen promoted oil expulsions. The oil generation and expulsion evolutions of these shales are largely determined by their organic sources of terrigenous higher organisms. This study provides a preliminary theoretical basis to reveal the enrichment mechanism of marine-terrestrial transitional shale oil and gas resources.

Keywords: marine-terrestrial transitional shale, pyrolysis experiment, oil generation and expulsion, organic sources, maturity

INTRODUCTION

Organic-rich shales are widely developed in marine, lacustrine, and marine-terrestrial transitional strata in China, and the three types of shales significantly contributed to the oil and gas resources of both conventional and unconventional reservoirs (Zou et al., 2019; Zou et al., 2020). In the Sichuan Basin, for example, giant gas fields in the central Sichuan Basin, including the Anyue, Weiyuan, and Ziyang shale gas plays, were mainly sourced from the Lower Paleozoic marine shales (Zou et al., 2014); several tight sandstone gas reservoirs in the paleo-uplift of the central Sichuan Basin largely came from the Jurassic lacustrine shales (Huang et al., 2019); the Xinchang gas field in the western Sichuan Basin were basically derived from the Upper Triassic marine-terrestrial transitional shales (Chen et al., 2010; Wu et al., 2016). In the last 2 decades, developments of marine shale oil and gas resources in the North America have achieved a great success (Zhou et al., 2019). Marine shale gases and lacustrine shale oils in China also have been commercially developed in the past 10 years (Jin et al., 2019; Zhao et al., 2020). Although marine-terrestrial transitional shales were believed to have a large potential of shale oil and gas resources, few of them have achieved commercial developments until now (Guo et al., 2015; Guo et al., 2021).

Marine-terrestrial transitional source rocks generally have low yields of oil generation, and most of the generated oils remained in source rocks (Liu et al., 2005; Mao et al., 2012). Therefore, these source rocks are commonly believed to have few contributions to normal petroleum reservoirs. However, the oil and gas resources of marine-terrestrial transitional shale reservoirs are largely determined by their oil generation and expulsion model because shale strata generally acted as both source rocks and reservoirs. Although oil generation and expulsion models have been well documented for marine and lacustrine shales in many previous studies (Wei et al., 2012; Han et al., 2015; Tang et al., 2015; Han et al., 2017; Ziegs et al., 2017; Hakimi et al., 2018; Wu et al., 2018), relevant studies on marine-terrestrial transitional shales are still inadequate presently. Marine-terrestrial transitional shales generally have thin single layers and thick cumulative thickness. The sedimentary facies of marine-terrestrial transitional shales vary obviously with burial depth resulting in their organic and inorganic compositions exhibiting obvious heterogeneity, and these shales are obviously richer in terrestrial organic sources than the marine and lacustrine shales (Qin et al., 2016; Su et al., 2016). Because marine-terrestrial transitional shales are quite different from marine and lacustrine shales in both geological and geochemical characteristics, the oil generation and expulsion models deduced from the latter shales failed to be applied on the former shales. At present, oil generation and expulsion characteristics of marine-terrestrial transitional shales are still not fully understood, which limits the development of their oil and gas resources.

In previous studies, dried shale powder samples were commonly used for pyrolysis experiments (Inan and Schenk, 2001; Carr et al., 2009; Liang et al., 2015; Ko et al., 2018). However, this method has several disadvantages to simulate oil generation and expulsion of shale samples. Shale pore structures, especially the microfractures, may be obviously broken during crushing process, which affects the expulsion and storage of generated shale oils. In addition, connate pore waters in source rocks significantly influence oil generation process and the properties of generated oils (Sun et al., 2015). For example, artificially simulated oils generated under water-bearing conditions are more similar with natural oil samples than those generated under anhydrous conditions (Lewan et al., 1979). Differing from the methods in previous studies, in this study, small shale plunger samples that drilled from a lowly mature marine-terrestrial transitional shale core sample were first saturated with water, and then they were used for a pyrolysis experiment to simulate the oil generation and expulsion characteristics. This study intends to provide a preliminary theoretical model to further reveal the enrichment mechanism of marine-terrestrial transitional shale oil and gas resources.

EXPERIMENTS

Pyrolysis Experiments

In this study, water-saturated shale plunger samples were used for the pyrolysis experiment performed in gold tube reactors (Tang et al., 2005; Tian et al., 2012; Gai et al., 2015; Ko et al., 2018). The main experimental procedures are as follows: small shale plunger samples (30 mm in height × 8 mm in diameter) were drilled from the inner part of a big shale core sample in vertical stratification direction. After they were dried in an oven at 105°C for 24 h, the shale plunger samples were saturated with deionized water in a BH-1 pressurized instrument (Cheng et al., 2019). Then, the water-saturate shale plungers were loaded in gold tubes (70 mm length × 9 mm inside diameter), and both sides of the gold tube were filled with quartz sands to collect expelled oils. Next, the gold tubes were separately loaded into pressure vessels in a high-temperature high-pressure pyrolysis oven. The given temperatures of this experiment were 350°C, 375°C, 395°C, 415°C, 435°C, and 460°C, respectively. During the experiment, the pyrolysis instrument was heated at a rate of 20°C/h, and the experimental pressure was maintained approximately 50 MPa (±1 MPa).

TOC and Mineralogical Analysis

Shale samples were powdered to a grain size of less than 180 μm and were eluted by diluted hydrochloric acids to remove the carbonates. After the shale powders were dried in an oven, their TOC contents were analyzed by an Eario El Cube Elemental Analyzer. The analytical errors of the instrument is less than 0.1%. The mineralogical compositions of shales were analyzed by a Bruker D8 Advance x-ray diffractometer. The measurements were performed on shale grains less than 75 μm at 40 kV and 30 mA with Cu Kα radiation. The relative content of minerals was semi-quantitatively calculated based on their

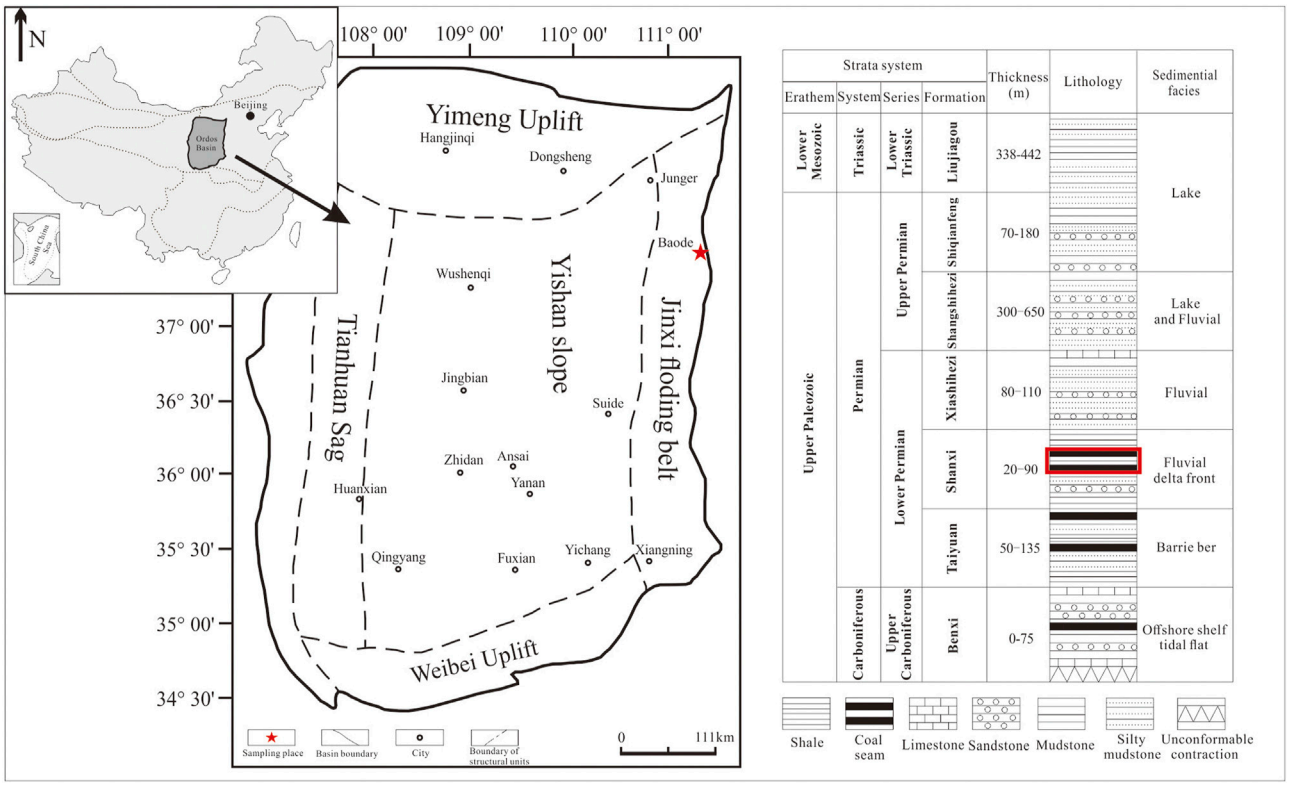

FIGURE 1 | Schematic maps showing the location and stratum of the studied shale sample (modified after Cao et al., 2019 and Su et al., 2005).

TABLE 1 | Geological and geochemical data of the shale sample used for pyrolysis experiment in this study.

Sample	Region	Stratum	Lithology	TOC (%)	R_o (%)	Rock-eval			Mineral compositions (%)						
						T_{max} (°C)	HI (mg/g TOC)	OI (mg/g TOC)	Quart	Clay	Pyrite	Siderite	Feldspar	Anatase	Dolomite
BLG14	Ordos Basin	Lower Permian Shanxi Formation	Black shale	15.65	0.68	434	292	2	33.6	47.5	13.6	1.5	1.3	1.6	0.9

peak areas and was corrected with Lorentz-Polarization method (Chalmers and Bustin, 2008).

Measurement of Vitrinite Reflectance (R_o)

The R_o values of shale samples were measured by a 3Y-DMR microphotometer equipped with a Leica microscope. The light source of this instrument is a high-pressure mercury vapor lamp with an excitation filter of 420–490 nm, and an oil immersion objective 50/1.0 is used for the measurement. Before the measurements, the instrument was calibrated by a standard yttrium aluminum garnet sample (YAG-08–57). A total of 50 individual vitrinite particles was measured for each shale sample, and the average value of these measured R_o values was used in this study.

Collection and Pretreatment of Liquid Hydrocarbons

After the pyrolysis experiment, shale plunger samples and quartz in the gold tube were separated. The shale plunger samples were crushed to powders less than 80 mesh, and then they were extracted with dichloromethane to obtain the retained oils. The collected quartz and gold tube were extracted together with dichloromethane to obtain the expelled oils. Both the retained and expelled oils were weighted by a Sartorius electronic balance with an analytical precision of 0.01 mg. The sum of the expelled and retained oils was the total generated oils. The gross compositions of these oil samples were further separated into four fractions, including saturates, aromatics,

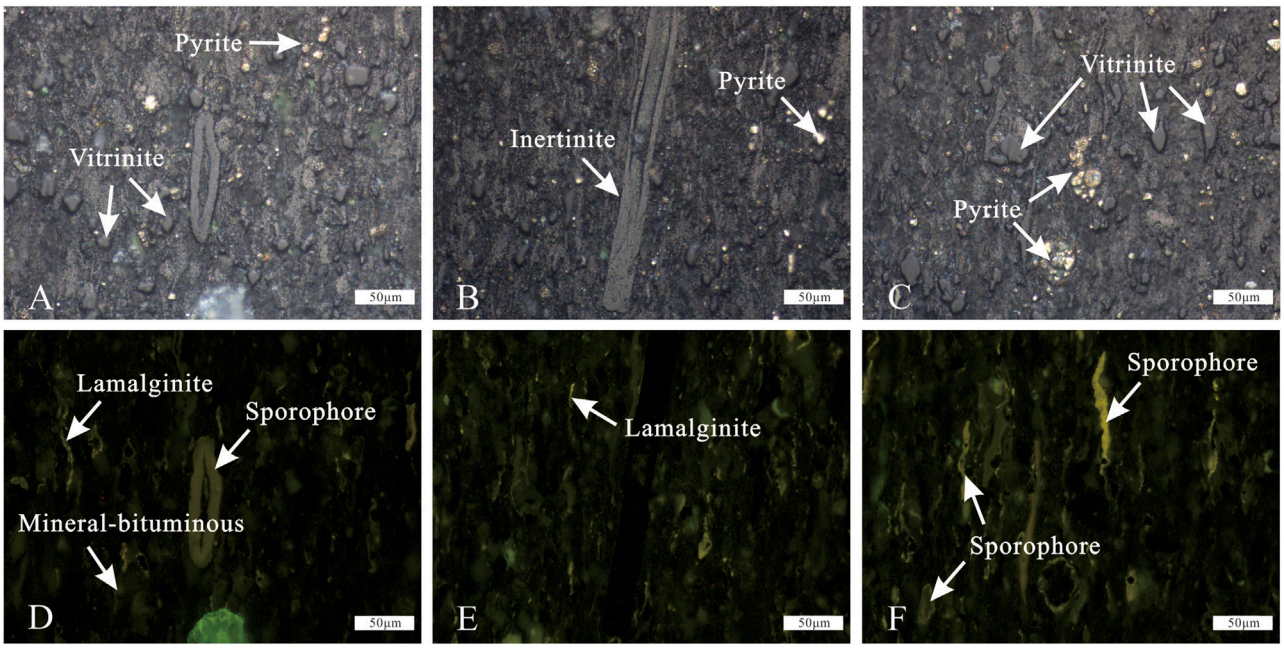

FIGURE 2 | Photomicrographs showing different macerals and organic sources of the studied marine-terrestrial transitional shale sample. **(A, D)** The exinite (sporophore), lamalginite, and mineral-bituminous under reflected light and fluorescence, respectively; **(B, E)** the inertinite, lamalginite, and its debris under reflected light and fluorescence, respectively; **(C, F)** the vitrinite and exinite (sporophore) under reflected light and fluorescence, respectively.

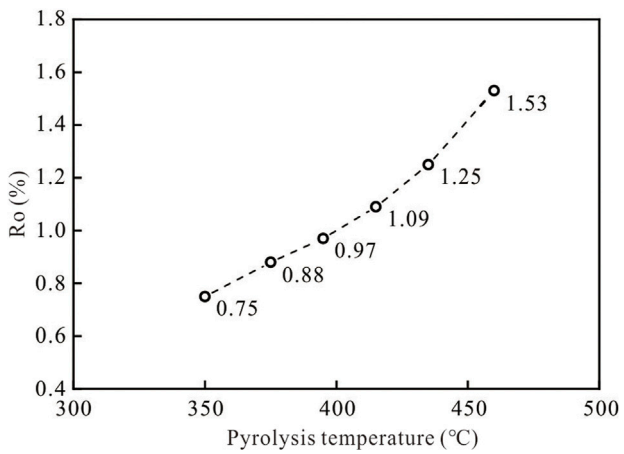

FIGURE 3 | Correlations of the R_o values with the experimental temperatures in this study.

resins, and asphaltenes, by a liquid chromatography on silica columns (Tang et al., 2005).

RESULTS AND DISCUSSION

Geological and Geochemical Characteristics of the Studied Shale

The shale sample used for the pyrolysis experiment was collected from the marine-terrestrial transitional strata of the Lower Permian Shanxi Formation in the northeast of the Ordos Basin (**Figure 1**). It has a low maturity with a R_o value of 0.68% and a high TOC content of 15.65%. The kerogen type of the shale belongs to type II_b based on the van Krevelen diagram (van Krevelen, 1961), and its HI and OI values are 292 mg/g TOC and 2 mg/g TOC, respectively. The minerals of this shale mainly include clays and quartz, with contents of 47.5% and 33.6%, respectively (**Table 1**).

Organic petrology analysis shows that this shale sample has various macerals. It contains plenty of vitrinite and inertinite that

TABLE 2 | Yields of the expelled oil, retained oil, and total oil for the studied marine-terrestrial transitional shale sample at different maturity stages.

Sample number	R_o (%)	Retained oil		Expelled oil		Total oil		Percentage of retained oil (%)[a]	Percentage of expelled oil (%)[b]
		(mg/g rock)	(mg/g TOC)	(mg/g rock)	(mg/g TOC)	(mg/g rock)	(mg/g TOC)		
BLG14–1	0.75	6.92	44.22	1.07	6.84	8.00	51.12	86.57	13.43
BLG14–2	0.88	11.30	72.20	2.84	18.15	14.14	90.35	79.89	20.11
BLG14–3	0.97	13.72	87.67	5.05	32.27	18.77	119.94	73.12	26.88
BLG14–4	1.09	13.67	87.35	6.86	43.83	20.53	131.18	66.60	33.40
BLG14–5	1.25	10.47	66.90	9.49	60.64	19.95	127.48	52.46	47.55
BLG14–6	1.53	5.36	34.25	7.79	49.78	13.15	84.03	40.78	59.22

[a]*Percentage of retained oil (P_{RO}): ratio of the retained oil yield to the total oil yield.*
[b]*Percentage of expelled oil (P_{EO}): ratio of the expelled oil yield to the total oil yield.*

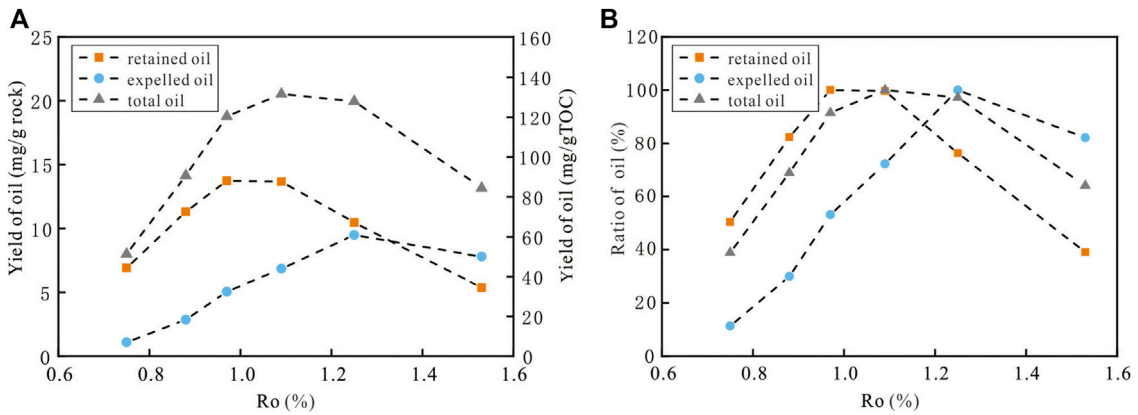

FIGURE 4 | Evolutions of total oil, expelled oil, and retained oil yield **(A)** and their relative yields **(B)** for the studied shale sample at different maturity stages.

exhibit gray color under reflected light (**Figure 2A–C**), and it also contains abundant exinite (sporophore) and lamalginite, which exhibit dark and bright yellow colors, respectively, under fluorescence excitation (**Figure 2D–F**). These characteristics indicate that the organic matter of this shale came from both terrigenous higher organisms and aquatic alga, and the contribution of the former sources was greater than that of latter sources.

Evolutions of Oil Generation and Expulsion

In this study, the R_o values of the artificially maturated shale samples correspond well with experimental temperatures, and they exhibit a significant positive relationship (**Figure 3**). With the experimental temperature increasing from 350°C to 460°C, the R_o value increases from 0.75% to 1.53% (**Table 2**). The maturity range of artificially maturated shales covers from the early oil generation stages to the wet gas stages.

The yields of the expelled oils (Y_{EO}), retained oils (Y_{RO}), and total generated oils (Y_{TO}) are listed in **Table 2**, and the Y_{EO}, Y_{RO}, and Y_{TO} exhibit different evolutions with the increasing maturity (**Figure 4A**). The Y_{EO} increases from 1.07 mg/g rock to the maximum yield of 9.49 mg/g rock with the R_o increasing from 0.75% to 1.25%. However, when the R_o > 1.25%, the Y_{EO} gradually decreases to 7.79 mg/g rock as the R_o increases to 1.53% (**Table 3** and **Figure 4A**). The Y_{RO} increases from 6.92 mg/g rock to the maximum yield of 13.72 mg/g rock with the R_o increasing from 0.75% to 0.97%. However, when the R_o > 0.97%, the Y_{RO} gradually decreases to 5.36 mg/g rock as the R_o increases to 1.53% (**Table 3** and **Figure 4A**). The Y_{TO} increases from 8.00 mg/g rock to the maximum yield of 20.53 mg/g rock with the R_o increasing from 0.75% to 1.09%, which indicates that the generation rates of oils are greater than their pyrolysis rates at this stage. However, when the R_o > 1.09%, the Y_{TO} gradually decreases to 13.15 mg/g rock as the R_o increases to 1.53%, which indicates that the generation rates of oils are smaller than their pyrolysis rates at this stage (**Table 2** and **Figure 4A**). The main oil generation and expulsion stages are generally defined in the range of 30%–80% of the maximum oil yield (Sun et al., 2019). According to this definition, the main stages of oil generation and expulsion are 0.85%–1.15% and 0.70%–0.95%, respectively, for the studied marine-terrestrial transitional shale sample. The main stages of oil expulsion are later than those of oil generation (**Figure 4B**).

Previous pyrolysis experiments performed on lacustrine shales with type I or type II kerogen indicate that these shales begin to generate oils when the R_o > 0.70%, and the oil generation windows are in the R_o range of 0.75%–0.90% (Sun et al., 2019). The differences in oil generation stages of various shales are largely determined by their organic sources. For example, the oil generation thresholds of terrestrial organic

TABLE 3 | Gross compositions of the expelled and retained oils at different maturity stages.

Sample number	R_o (%)	Expelled oil (%)				Retained oil (%)			
		Saturates	Aromatics	Resins	Asphaltenes	Saturates	Aromatics	Resins	Asphaltenes
BLG14-1	0.75	7.27	18.18	5.45	69.09	1.93	8.82	11.30	77.96
BLG14-2	0.88	6.33	25.32	13.90	54.43	2.45	7.34	20.00	70.17
BLG14-3	0.97	9.79	20.28	20.30	49.65	3.87	9.61	22.40	64.11
BLG14-4	1.09	15.85	16.67	30.10	37.40	7.17	11.03	22.00	59.85
BLG14-5	1.25	18.75	17.75	31.80	31.75	14.30	16.93	27.80	40.94
BLG14-6	1.53	19.59	26.32	32.20	21.93	20.17	17.85	35.50	26.50

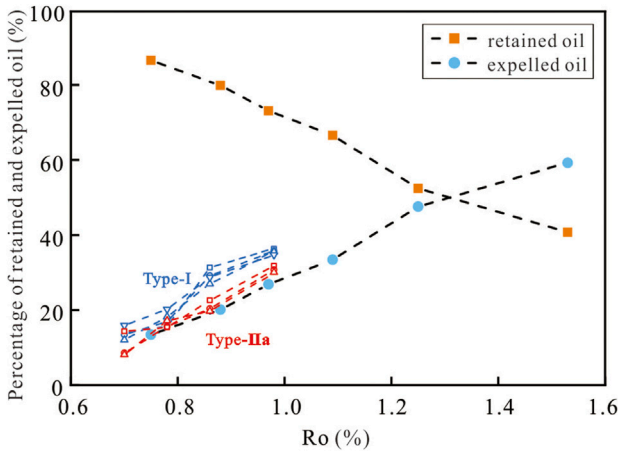

FIGURE 5 | Relative percentages of the expelled (P_{EO}) and retained oils (P_{RO}) in total generated oils at different maturity stages for the studied marine-terrestrial transitional shale. The data of type I and II_b lacustrine shales are cited from Sun et al. (2021).

matters, such as vitrinite and exinite, are generally at relative low maturity stages with R_o values of 0.50%–0.55%, and the main oil generation stages covered a wide maturity range with R_o values of 0.55%–1.00% (Li et al., 2002; Shuai et al., 2009). However, the oil generation threshold of aquatic alginates is generally at a higher maturity stage with the R_o value of 0.70%, and its main oil generation stage generally covers a shorter maturity range with R_o values of 0.70%–0.90%. In contrast to lacustrine shales, the studied marine-terrestrial transitional shale is richer in terrestrial organic matter, which results in an earlier oil generation threshold and a wider oil generation window.

The relative percentages of expelled (P_{EO}) and retained oils (P_{RO}) in total generated oils obviously vary at different maturity stages (**Figure 5**). With the R_o increasing from 0.75 to 0.97%, the P_{EO} successively increases from 14% to 34%, while the P_{RO} progressively decreases from 86% to 67%. When the R_o values <1.25%, the P_{RO} is higher than the P_{RO}; however, the P_{RO} is lower than the P_{RO} when the R_o values >1.25% (**Figure 5**). Heavy liquid hydrocarbons in the retained oils progressively cracked into light liquid hydrocarbons and promoted oil expulsions during the high maturity stages (Li et al., 2017). Shao et al. (2020) also reported that the peak P_{EO} value of Barnett lacustrine shales occurred in the late wet gas stage with the R_o value of 1.75%. For the Shahejie Formation lacustrine shales in the Bohaiwan Basin (Sun et al., 2021), the shales with type I and II_a kerogen generally have higher P_{EO} values than the shales with type II_b and III kerogen (**Figure 5**). Under similar maturity conditions, the studied marine-terrestrial transitional shale has lower P_{EO} values than the lacustrine shales; however, its P_{EO} values significantly increase at high maturity stages, which indicates that oil expulsions are enhanced at high maturity stages for the studied shale.

The evolution model of oil generation and expulsion of the studied marine-terrestrial transitional shale is different from that of lacustrine shales reported by previous studies. Compared with the lacustrine shales, the marine-terrestrial transitional shales have earlier oil generation thresholds and wider oil generation windows. In addition, the P_{EO} values are similar for the two types of shales, while the P_{EO} values of marine-terrestrial transitional shales are significantly enhanced at high maturity stages. However, it should be pointed out that further studies need to be performed on more marine-terrestrial transitional shale samples to verify the applications of this oil generation and expulsion model under geological conditions.

Changes in Gross Compositions of the Expelled and Retained Oils

The changes in gross compositions of the expelled and retained oils can be approximately divided into three stages. At the early stage with R_o < 0.97%, the gross compositions slightly changed with the maturity for both expelled and retained oils (**Figure 6**), which indicates that the fractionation effect caused by oil generation and expulsion is weak at this stage. At the middle stage with the R_o ranging from 0.97% to 1.25%, the light compositions (saturates and aromatics) obviously enriched while the heavy compositions (resins and asphaltenes) significantly decreased for both expelled and retained oils (**Figure 6**), because the kerogen generated more light compositions at this maturity stage. The percentages of the light compositions in expelled oils are significantly higher than those in retained oils (**Figure 6**), because the light compositions have low viscosity and tend to migrate (Pepper and Corvi, 1995). Therefore, a significant fractionation occurred between the expelled and retained oils at this maturity stage. At the late stage with R_o > 1.25%, only a small number of light compositions were generated from kerogen; meanwhile, part of the retained and expelled oils cracked into gaseous

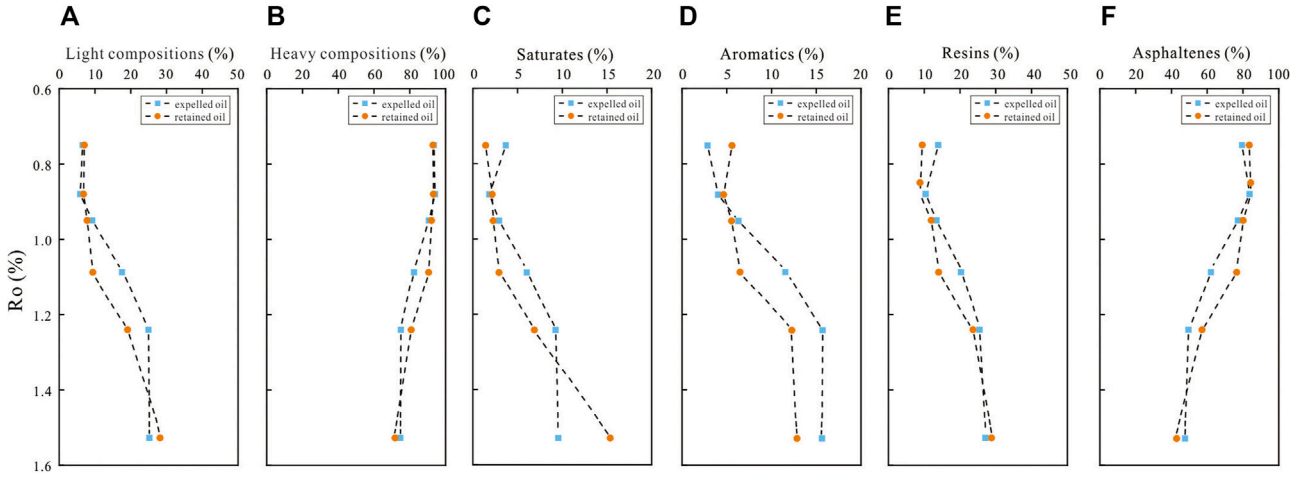

FIGURE 6 | Changes in the gross compositions of the expelled and retained oils with increasing maturity for the studied marine-terrestrial transitional shale sample.

hydrocarbons. Therefore, with the increasing maturity, the differences in gross compositions between the two types of oils gradually decrease.

It is noteworthy that heavy compositions, especially the asphaltenes, are dominated in both retained and expelled oils during the oil generation and expulsion processes. At the maturity stages with the R_o range from 0.75% to 0.97%, the percentages of asphaltene in the expelled and retained oils account for 50%–69% and 63%–77%, respectively. At the high maturity stage with R_o of 1.53%, the percentages of asphaltene in the two types of oils account for 54% and 62%, respectively (**Table 3**). The gross compositions of expelled and retained oils significantly differ from those of lacustrine shales. At the stages with R_o values of 0.71%–1.41%, the light compositions account for 50%–69% and 63%–77% for the Eocene Shahejie lacustrine shales in the Bohaiwan Basin, respectively; moreover, with the increasing maturity, the resin content decreases while the asphaltene content increases for the lacustrine shales (Sun et al., 2021). Asphaltenes are dominated in the retained and expelled oils of marine-terrestrial transitional shales because of their abundant terrestrial organic sources.

Mechanisms of Oil Generation and Expulsion

Ungerer et al. (1990) proposed that hydrocarbon generations from kerogen pyrolysis were mainly through two approaches, i.e., the depolymerization and functional group desorption. The former refers to the idea that kerogen initially cracks to intermediate products (resin and asphaltene), and then these intermediate products are further decomposed to oils and gases. The latter refers to the notion that functional groups initially bonded in kerogen skeletons can be directly liberated from the kerogen and form hydrocarbons. In this study, the Y_{TO} exhibits obvious positive correlations with the resin yield (Y_R) and its percentage during the main oil generation and expulsion stages (**Figures 7A,B**). The Y_{TO} is positively correlated with the asphaltenes yield (Y_A) and its percentage when the R_o < 1.09%, while it shows no obvious correlations with the Y_A and its percentage when R_o > 1.09% (**Figures 7C,D**). Combined with the gross compositions and their evolutions of the expelled and retained oils (**Figure 6**), this study indicates that the organic matter of this studied marine-terrestrial transitional shale first depolymerized to asphaltenes at the early stages of oil generation, and then the transitional asphaltenes were further cracked into hydrocarbons at the late stages of oil generation, while the organic matter of lacustrine shales generates hydrocarbons mainly *via* transitional resins (Sun et al., 2021). Therefore, shales with different sedimentary facies are diverse in oil generation mechanism.

The oil generation and expulsion of shales are mainly controlled by their geochemical properties, including TOC content, kerogen type, maturity, and mineral compositions (Pepper and Corvi, 1995; Chen et al., 2014; Liang et al., 2015), and by their geological conditions, including geological temperature and pressure, water-bearing characteristic, strata thickness, and its boundary condition (Lewan 1997; Chen and Cha, 2005). Previous studies indicated that the pore systems of shales were fully adsorbed and filled by generated oils before oil expulsions, and kerogen swelling effects were the controlling factor on the oil retention in shale reservoirs (Li et al., 2016; Han et al., 2017; Ziegs et al., 2017; Shao et al., 2018). This study further shows that the marine-terrestrial transitional shale exhibits obvious oil expulsion under experimental conditions. Under similar maturity and kerogen-type conditions, marine-terrestrial transitional shales have similar P_{EO} values with lacustrine shales. The high P_{EO} values of the studied marine-terrestrial transitional shale can be illustrated by the following factors.

The kerogen swelling effect is closely related to kerogen types, and it decreases in the order of type I, type II_a, and type II_b kerogen. For example, the swelling amounts of type I, II_a, and II_b

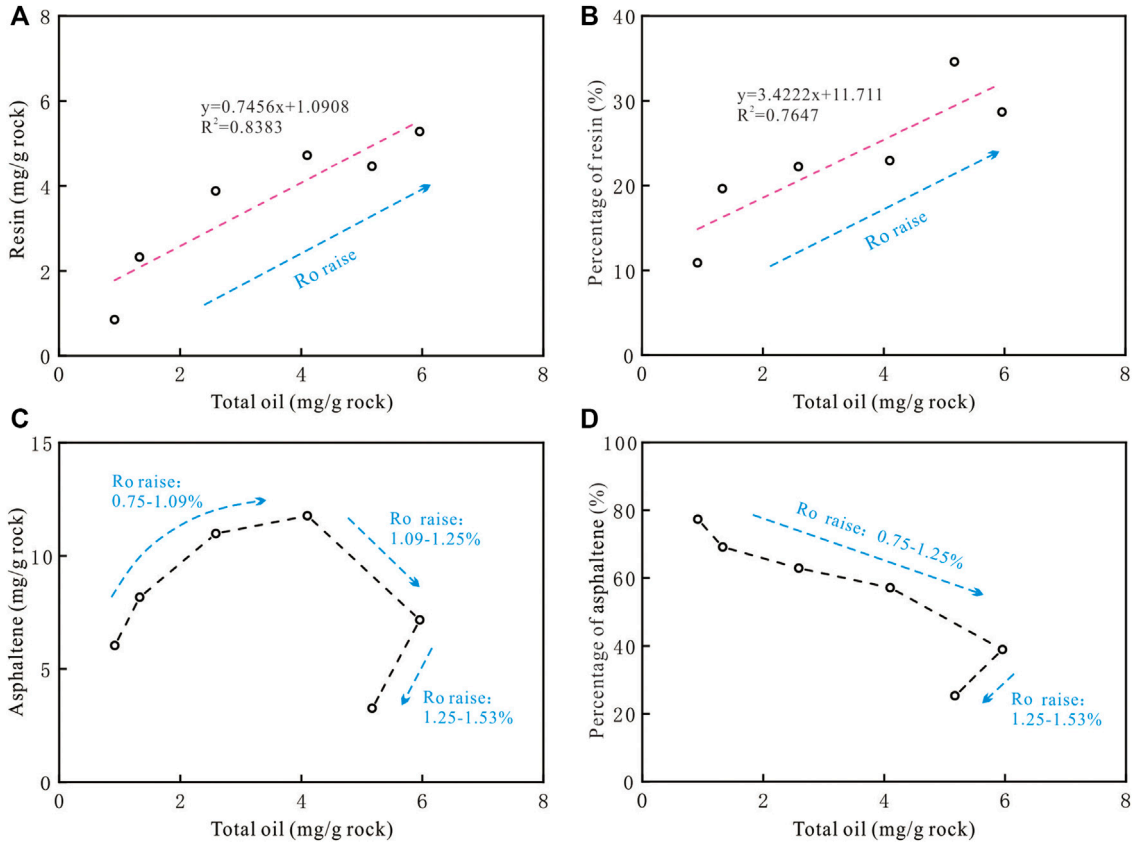

FIGURE 7 | Correlations of the total oil yield (Y_{TO}) with the resin (Y_R) and asphaltene yields (Y_A) as well as their percentages in total oils at different maturity stages.

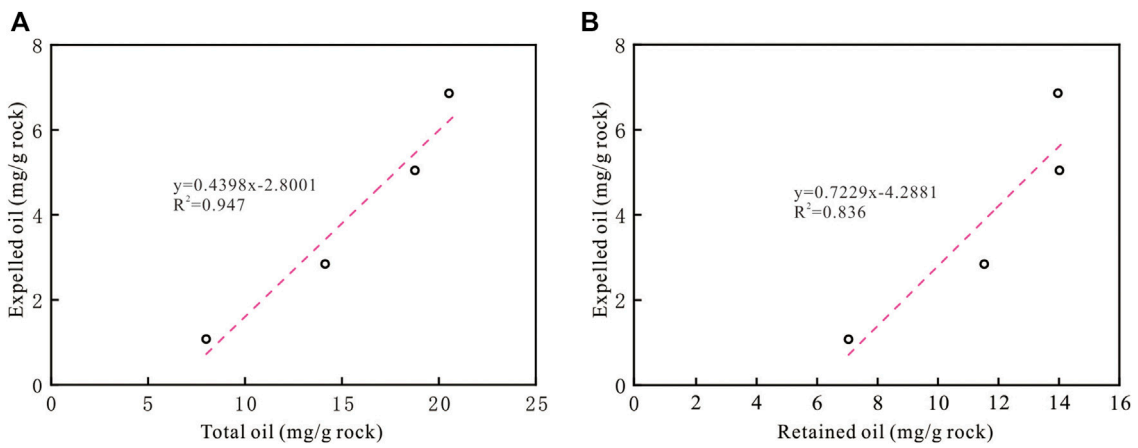

FIGURE 8 | Correlations of the expelled oil contents with the total generated oil contents **(A)** and the retained oil contents **(B)** for the studied shale sample during the main oil generation and expulsion stages with the R_o value of 0.75%–1.09%.

kerogen, with a low maturity of 0.5%, are 142 mg/g TOC, 119 mg/g TOC, and 95 mg/g TOC, respectively (Tian et al., 2014). According to the intercept of the linear correlation equations in **Figure 8**, this study further estimated that the oil expulsion threshold of the studied marine-terrestrial transitional shale corresponded to the Y_{TO} value of 6.4 mg/g rock and the Y_{RO} value of 5.9 mg/g rock. The maximum Y_{RO} value of this shale is 88 mg/g TOC (**Figure 4**) and is much lower than the maximum Y_{RO} values of the type I and type II_a lacustrine shales, with values of 300–350 mg/g TOC and 150–200 mg/g TOC, respectively (Sun

et al., 2021). Although some retained oils are stored in inorganic-hosted nanopores of minerals, most of the retained oils are associated with the kerogen swelling effect (Li et al., 2016; Zhao et al., 2019). The studied marine-terrestrial transitional shale with type II_b kerogen has a low capacity of retaining oils resulting from its weak kerogen swelling effect, which may be the main mechanism for its high oil expulsion efficiency.

Under geological conditions, shale reservoirs generally contain some pore waters that significantly influence the accumulation and enrichment of shale oil and gas resources (Lewan 1997; Burnham 1998; Carr et al., 2009; Lewan and Roy, 2011; Cheng et al., 2018). The pore waters not only take up the pore spaces available for oil storage, but also occupy pore surfaces and change the interfaces between hydrocarbons and pore walls, which significantly prompts oil migrations and expulsions (Korb et al., 2014; Ma et al., 2015; Cheng et al., 2017; Zolfaghari et al., 2017). Moreover, pore waters may also cause an overpressure in shale pore systems, and thus enhance the oil expulsion efficiency (Zhang et al., 2011; Huang et al., 2017). In addition, since the oil expulsion efficiency is positively correlated with the TOC content (Zhang et al., 2006; Sun et al., 2021), the high TOC content of the studied shale sample may also raise its oil expulsion efficiency.

At present, the oil generation and expulsion model of marine-terrestrial transitional shale remains unclear. The results of this study show that oil expulsions of marine-terrestrial transitional shales with high TOC contents may occur under geological conditions, and the oil expulsion efficiency and the geochemical properties of expelled and retained oils are largely determined by the organic sources and maturities of shales. The new understanding on the oil generation and expulsion model in this study may have a certain theoretical significance for the exploration and development of marine-terrestrial transitional shale resources. However, the oil generation and expulsion model of marine-terrestrial transitional shales with type III kerogen needs to be investigated in further studies.

CONCLUSION

In this study, a pyrolysis experiment was performed on water-saturated marine-terrestrial transitional shale plunger samples, to simulate the evolutions of oil generation and expulsion. The main conclusions are as follows:

1) In contrast to marine and lacustrine shales, marine-terrestrial transitional shales have wider maturity ranges of oil generation and expulsion, and the main stages of oil expulsion are later than those of oil generation, with corresponding R_o values of 0.85%–1.15% and 0.70%–0.95%, respectively.
2) The expelled and retained oils of marine-terrestrial transitional shales exhibit obvious fractionations in compositions during the oil generation and expulsion process. However, the two types of oils are dominated by heavy compositions, which significantly differs from the generated oils from marine and lacustrine shales.
3) The oil generation and expulsion evolutions of marine-terrestrial transitional shales are largely determined by their organic sources of terrigenous higher organisms. The kerogen of these shales initially depolymerized to transitional asphaltenes, which further cracked into hydrocarbons, and the weak swelling effects of the kerogen promoted oil expulsions.

DATA AVAILABILITY STATEMENT

The original contributions presented in the study are included in the article/Supplementary Material, Further inquiries can be directed to the corresponding authors.

AUTHOR CONTRIBUTIONS

QF: Conceptualization, Methodology, Data curation, Writing - Original Draft. PC: Conceptualization, Methodology, Review and Editing. XX: Supervision, Review and Editing. HG: Methodology and Review. QZ: Investigation and Editing. TL: Review and Editing. PG: Review and Editing. All authors listed have made a substantial, direct, and intellectual contribution to the work and approved it for publication.

FUNDING

This study was supported by the National Natural Science Foundation of China (U1810201, 41402116, and 42173031), the Natural Science Foundation of Guangdong Province (2021A1515011381), and the Independent Project of the SKLOG (2020–2). The experimental data in this study were measured in the Experimental Platform of Organic Geochemistry, the Public Technical Service Center of Guangzhou Institute of Geochemistry, CAS.

ACKNOWLEDGMENTS

We are indebted to Prof. Zhang Kaijun and Huang Qiangtai as well as two reviewers for their insightful comments and suggestions that have greatly improved the manuscript.

REFERENCES

Burnham, A. K. (1998). Comment on "Experiments on the Role of Water in Petroleum Formation" by M.D. Lewan. *Geochim. Cosmochim. Acta* 62 (12), 2207–2210.

Cao, Y., Han, H., Liu, H.-w., Jia, J.-c., Zhang, W., Liu, P.-w., et al. (2019). Influence of Solvents on Pore Structure and Methane Adsorption Capacity of Lacustrine Shales: An Example from a Chang 7 Shale Sample in the Ordos Basin, China. *J. Pet. Sci. Eng.* 178, 419–428. doi:10.1016/j.petrol.2019.03.052

Carr, A. D., Snape, C. E., Meredith, W., Uguna, C., Scotchman, I. C., and Davis, R. C. (2009). The Effect of Water Pressure on Hydrocarbon Generation Reactions:

Some Inferences from Laboratory Experiments. *Pet. Geosci.* 15 (1), 17–26. doi:10.1144/1354-079309-797

Chalmers, G. R. L., and Bustin, R. M. (2008). Lower Cretaceous Gas Shales in Northeastern British Columbia, Part I: Geological Controls on Methane Sorption Capacity. *Bull. Can. Pet. Geology.* 56 (1), 1–21. doi:10.2113/gscpgbull.56.1.1

Chen, Z. H., and Cha, M. (2005). Geochemical Characteristics of Source Rocks in Dongying Depression. *Geochimica* 34 (01), 79–87. doi:10.19700/j.0379-1726.2005.01.010

Chen, D., Huang, X. H., Li, L. T., Deng, K., Zheng, J. H., and Hong, Q. (2010). Characteristics and History of Hydrocarbon Expulsion of the Upper Tertiary Source Rocks in the Western Sichuan Depression. *Nat. Gas Industry* 30 (05), 41–45. doi:10.3787/j.issn.1000-0976.2010.05.010

Chen, J. P., Sun, Y. G., Zhong, N. N., Huang, Z. K., Deng, C. P., Xie, L. J., et al. (2014). The Efficiency and Model of Petroleum Expulsion from the Lacustrine Source Rocks within Geological Frame. *Acta Geol. Sin.* 88 (11), 2005–2032. doi:10.1111/1755-6724.12373_3

Cheng, P., Tian, H., Xiao, X., Gai, H., Li, T., and Wang, X. (2017). Water Distribution in Overmature Organic-Rich Shales: Implications from Water Adsorption Experiments. *Energy Fuels* 31, 13120–13132. doi:10.1021/acs.energyfuels.7b01531

Cheng, P., Xiao, X., Tian, H., and Wang, X. (2018). Water Content and Equilibrium Saturation and Their Influencing Factors of the Lower Paleozoic Overmature Organic-Rich Shales in the Upper Yangtze Region of Southern China. *Energy Fuels* 32, 11452–11466. doi:10.1021/acs.energyfuels.8b03011

Cheng, P., Xiao, X., Wang, X., Sun, J., and Wei, Q. (2019). Evolution of Water Content in Organic-Rich Shales with Increasing Maturity and its Controlling Factors: Implications from a Pyrolysis experiment on a Water-Saturated Shale Core Sample. *Mar. Pet. Geol.* 109, 291–303. doi:10.1016/j.marpetgeo.2019.06.023

Gai, H., Xiao, X., Cheng, P., Tian, H., and Fu, J. (2015). Gas Generation of Shale Organic Matter with Different Contents of Residual Oil Based on a Pyrolysis experiment. *Org. Geochem.* 78, 69–78. doi:10.1016/j.orggeochem.2014.11.001

Guo, S. B., Fu, J. J., Gao, D., and Li, H. Y. (2015). Research Status and Prospects for marine-continental Shale Gases in China. *Pet. Geol. Exp.* 37 (05), 535–540. doi:10.11781/sysydz201505535

Guo, S. B., Wang, Z. L., and Xiao, M. (2021). Exploration prospect of Shale Gas with Permian Transitional Facies of Some Key Areas in China. *Pet. Geol. Exp.* 43 (03), 377–385. doi:10.11781/sysydz202103377

Hakimi, M. H., Alaug, A. S., Ahmed, A. F., Yahya, M. M. A., El Nady, M. M., and Ismail, I. M. (2018). Simulating the Timing of Petroleum Generation and Expulsion from Deltaic Source Rocks: Implications for Late Cretaceous Petroleum System in the Offshore Jiza-Qamar Basin, Eastern Yemen. *J. Pet. Sci. Eng.* 170, 620–642. doi:10.1016/j.petrol.2018.06.076

Han, Y., Mahlstedt, N., and Horsfield, B. (2015). The Barnett Shale: Compositional Fractionation Associated with Intraformational Petroleum Migration, Retention, and Expulsion. *Bulletin* 99 (12), 2173–2202. doi:10.1306/06231514113

Han, Y., Horsfield, B., Wirth, R., Mahlstedt, N., and Bernard, S. (2017). Oil Retention and Porosity Evolution in Organic-Rich Shales. *Bulletin* 101 (6), 807–827. doi:10.1306/09221616069

Huang, H., Chen, S., Lu, J., Ma, J., and He, J. (2017). The Influence of Water on the thermal Simulation experiment of Hydrocarbon Generation and Expulsion. *Pet. Sci. Technol.* 35 (8), 783–788. doi:10.1080/10916466.2016.1277239

Huang, D., Yang, G., Yang, Z., Yang, T. Q., Bai, R., and Li, Y. C. (2019). New Understanding and Development Potential of Tight Oil Exploration and Development in Sichuan Basion. *Nat. Gas Geosci.* 30 (08), 1212–1221. doi:10.11764/j.issn.1672-1926.2019.07.005

Inan, S., and Schenk, H. J. (2001). Evaluation of Petroleum Generation and Expulsion from a Source Rock by Open and Restricted System Pyrolysis Experiments. Part I. Extrapolation of Experimentally–Derived Kinetic Parameters to Natural Systems. *J. Anal. Appl. Pyrolysis* 58, 213–228. doi:10.1016/S0165–2370(00)00188–1

Jin, Z. J., Bai, Z. R., Gao, B., and Li, M. W. (2019). Has China Ushered in the Shale Oil and Gas Revolution? *Oil Gas Geol.* 40 (03), 451–458. doi:10.11743/ogg20190301

Ko, L. T., Ruppel, S. C., Loucks, R. G., Hackley, P. C., Zhang, T., and Shao, D. (2018). Pore-types and Pore-Network Evolution in Upper Devonian-Lower Mississippian Woodford and Mississippian Barnett Mudstones: Insights from Laboratory thermal Maturation and Organic Petrology. *Int. J. Coal Geol.* 190, 3–28. doi:10.1016/j.coal.2017.10.001

Korb, J.-P., Nicot, B., Louis-Joseph, A., Bubici, S., and Ferrante, G. (2014). Dynamics and Wettability of Oil and Water in Oil Shales. *J. Phys. Chem. C* 118 (40), 23212–23218. doi:10.1021/jp508659e

Lewan, M. D., and Roy, S. (2011). Role of Water in Hydrocarbon Generation from Type-I Kerogen in Mahogany Oil Shale of the Green River Formation. *Org. Geochem.* 42 (1), 31–41. doi:10.1016/j.orggeochem.2010.10.004

Lewan, M. D., Winters, J. C., and McDonald, J. H. (1979). Generation of Oil-Like Pyrolyzates from Organic-Rich Shales. *Science* 203 (4383), 897–899. doi:10.1126/science.203.4383.897

Lewan, M. D. (1997). Experiments on the Role of Water in Petroleum Formation. *Geochim. Cosmochim. Acta* 61 (17), 3691–3723. doi:10.1016/S0016–7037(97)00176–210.1016/s0016-7037(97)00176-2

Li, X. Q., Xiong, B., Ma, A. L., Wang, F. Y., and Zhong, N. N. (2002). Advance of Organic Petrology in Oil and Gas Exploration. *J. Jianghan Pet. Inst.* 24 (01), 15–19. doi:10.3969/j.issn.1000-9752.2002.01.005

Li, Z., Zou, Y.-R., Xu, X.-Y., Sun, J.-N., Li, M., and Peng, P. A. (2016). Adsorption of Mudstone Source Rock for Shale Oil - Experiments, Model and a Case Study. *Org. Geochem.* 92, 55–62. doi:10.1016/j.orggeochem.2015.12.009

Li, Z. M., Rui, X. Q., Xu, E. S., Yang, Z. H., and Ma, Z. L. (2017). Simulation of Hydrocarbon Generation and Expulsion for Brown Coal with Transitional Organic Matter Type II_2-III under Near Geological Conditions. *J. China Coal Soc.* 42 (01), 249–256. doi:10.13225/j.cnki.jccs.2016.0566

Liang, M., Wang, Z., Zheng, J., Li, X., Wang, X., Gao, Z., et al. (2015). Hydrous Pyrolysis of Different Kerogen Types of Source Rock at High Temperature-Bulk Results and Biomarkers. *J. Pet. Sci. Eng.* 125, 209–217. doi:10.1016/j.petrol.2014.11.021

Liu, D. H., Fu, J. M., Xiao, X. M., Chen, D. Y., and Geng, A. S. (2005). Origin and Appraisal of Coal Derived Gas and Oil. *Pet. Exploration Dev.* 32 (04), 137–141. doi:10.3321/j.issn:1000-0747.2005.04.023

Ma, Z. L., Zheng, L. J., Zhao, Z. X., and Ge, Y. (2015). Effect of Fluid Medium in Source Rock Porosity on Oil Primary Migration. *Pet. Geology. Exp.* 37 (01), 97–101. doi:10.7603/s40972-015-0016-4

Mao, R., Mi, J. K., and Zhang, S. C. (2012). Study on the Hydrocarbon Generation Characyeristics of Different Coaly Source Rocks by Gold–Tube Pyrolysis Experiments. *Nat. Gas Geosci.* 23 (06), 1127–1134. doi:10.11764/j.issn.1672-1926.2012.06.021

Pepper, A. S., and Corvi, P. J. (1995). Simple Kinetic Models of Petroleum Formation. Part III: Modelling an Open System. *Mar. Pet. Geol.* 12 (4), 417–452. doi:10.1016/0264-8172(95)96904-5

Qin, Y., Shen, J., and Shen, Y. L. (2016). Joint Mining Compatibility of Superposed Gas-Bearing Systems: A General Geological Problem Extraction of Three Natural Gases and Deep CBM in Coal Series. *J. China Coal Soc.* 41 (01), 14–23. doi:10.13225/j.cnki.jccs.2015.9032

Shao, X., Pang, X., Li, H., Hu, T., Xu, T., Xu, Y., et al. (2018). Pore Network Characteristics of Lacustrine Shales in the Dongpu Depression, Bohai Bay Basin, China, with Implications for Oil Retention. *Mar. Pet. Geol.* 96, 457–473. doi:10.1016/j.marpetgeo.2018.06.015

Shao, D., Zhang, T., Ko, L. T., Li, Y., Yan, J., Zhang, L., et al. (2020). Experimental Investigation of Oil Generation, Retention, and Expulsion within Type II Kerogen-Dominated marine Shales: Insights from Gold-Tube Nonhydrous Pyrolysis of Barnett and Woodford Shales Using Miniature Core Plugs. *Int. J. Coal Geology.* 217, 103337. ARTN 103337. doi:10.1016/j.coal.2019.103337

Shuai, Y. H., Zhang, S. C., and Chen, J. P. (2009). Comparison of the Oil Potential of Coal and Coaly Mudstone. *Geochimica* 38 (6), 583–590. doi:10.19700/j.0379-1726.2009.06.008

Su, X., Lin, X., Zhao, M., Song, Y., and Liu, S. (2005). The Upper Paleozoic Coalbed Methane System in the Qinshui basin, China. *Bulletin* 89 (1), 81–100. doi:10.1306/07300403125

Su, Y. F., Zhang, Q. H., Qu, X. R., and Wei, Z. C. (2016). Geological Evaluation of marine-continental Transitional-Facies Shale Gas and Optimal Selection of Favorable Areas, Shanxi Province. *Nat. Gas Explor. Dev.* 39 (03), 1–5. doi:10.3969/j.issn.1673-3177.2016.03.001

Sun, L. N., Zhang, M. F., Wu, C. J., Xiong, D. M., and Su, L. (2015). The Effect of Water Medium on the Products of Different Pyrolysis System. *Nat. Gas Geosci.* 26 (03), 524–532. doi:10.1007/s12209-015-2667-6

Sun, J., Xiao, X., Cheng, P., and Tian, H. (2019). Formation and Evolution of Nanopores in Shales and its Impact on Retained Oil during Oil Generation and Expulsion Based on Pyrolysis Experiments. *J. Pet. Sci. Eng.* 176, 509–520. doi:10.1016/j.petrol.2019.01.071

Sun, J., Xiao, X., Cheng, P., Wang, M., and Tian, H. (2021). The Relationship between Oil Generation, Expulsion and Retention of Lacustrine Shales: Based on Pyrolysis Simulation Experiments. *J. Pet. Sci. Eng.* 196, 107625. ARTN 107625. doi:10.1016/j.petrol.2020.107625

Tang, Y., Huang, Y., Ellis, G. S., Wang, Y., Kralert, P. G., Gillaizeau, B., et al. (2005). A Kinetic Model for Thermally Induced Hydrogen and Carbon Isotope Fractionation of Individual N-Alkanes in Crude Oil. *Geochim. Cosmochim. Acta* 69 (18), 4505–4520. doi:10.1016/j.gca.2004.12.026

Tang, X., Zhang, J., Jiang, Z., Zhao, X., Liu, K., Zhang, R., et al. (2015). Characteristics of Solid Residue, Expelled and Retained Hydrocarbons of Lacustrine Marlstone Based on Semi-closed System Hydrous Pyrolysis: Implications for Tight Oil Exploration. *Fuel* 162, 186–193. doi:10.1016/j.fuel.2015.09.009

Tian, H., Xiao, X., Wilkins, R. W. T., and Tang, Y. (2012). An Experimental Comparison of Gas Generation from Three Oil Fractions: Implications for the Chemical and Stable Carbon Isotopic Signatures of Oil Cracking Gas. *Org. Geochem.* 46, 96–112. doi:10.1016/j.orggeochem.2012.01.013

Tian, S. S., Xue, H. T., and Lu, S. F. (2014). "Discussion on the Mechanism of Different Types of Kerogen Remaining Oil and Gas," in 2014 Annual Meeting of Chinese Geoscience Union (Beijing: Annual Meeting of Chinese Geoscience Union), 2509–2512.

Ungerer, P., Burrus, J., Doligez, B., Chenet, P. Y., and Bessis, F. (1990). Basin Evaluation by Integrated 2-dimensional Modeling of Heat-Transfer, Fluid-Flow, Hydrocarbon Generation, and Migration. *AAPG Bull.–Am. Assoc. Pet. Geol.* 74 (3), 309–335. doi:10.1306/0c9b22db-1710-11d7-8645000102c1865d

van Krevelen, D. W. (1961). *Coal: Typology-Chemistry-Physics-Constitution*. Amsterdam: Elsevier, 514.

Wei, Z., Zou, Y.-R., Cai, Y., Wang, L., Luo, X., and Peng, P. A. (2012). Kinetics of Oil Group-type Generation and Expulsion: An Integrated Application to Dongying Depression, Bohai Bay Basin, China. *Org. Geochem.* 52, 1–12. doi:10.1016/j.orggeochem.2012.08.006

Wu, X. Q., Wang, P., Liu, Q. Y., Li, H. J., Chen, Y. B., and Zeng, H. H. (2016). The Source of Natural Gas Reservoired in the 5th Member of the Upper Triassic Xujiahe Formation in Xinchang Gasfield. The Western Sichuan Depression and its Implication. *Nat. Gas Geosci.* 27 (08), 1409–1418. doi:10.11764/j.issn.1672-1926.2016.08.1409

Wu, Y., Zhang, Z., Sun, L., Li, Y., Su, L., Li, X., et al. (2018). The Effect of Pressure and Hydrocarbon Expulsion on Hydrocarbon Generation during Pyrolyzing of continental Type-III Kerogen Source Rocks. *J. Pet. Sci. Eng.* 170, 958–966. doi:10.1016/j.petrol.2018.06.067

Zhang, W. Z., Yang, H., and Li, J. F. (2006). Leading Effect of High-Class Source Rock of Chang 7 in Ordos Basin on Enrichment of Low Permeability Oil–Gas Accumulation. *Pet. Explor. Dev.* 33 (03), 289–293. doi:10.3321/j.issn:1000-0747.2006.03.006

Zhang, L. J., He, S., Qian, J. Z., and Ma, Z. L. (2011). Formation Water of Near-Critical Properties and its Effects on the Processes of Hydrocarbon Generation and Expulsion. *Earth Sci.* 36 (01), 83–92. doi:10.3799/dqkx.2011.009

Zhao, W. Z., Hu, S. Y., Hou, L. H., Yang, T., Li, X., and Guo, B. C. (2020). Types and Resource Potential of continental Shale Oil in China and its Boundary with Tight Oil. *Pet. Explor. Dev.* 47 (01), 1–10. doi:10.1016/s1876-3804(20)60001-5

Zhao, X. Z., Zhou, L. H., Pu, X. G., Jin, F. M., and Shi, Z. N. (2019). Favorable Formation Conditions and Enrichment Characteristics of Lacustrine Facies Shale Oil in Faulted lake basin:a Case Study of Member 2 of Kongdian Formation in Cangdong Sag, Bohai Bay Basin. *Acta Petrolei Sin.* 40 (09), 1013–1029. doi:10.7623/syxb201909001

Zhou, Q. F., Jin, Z. J., Yang, G. F., and Dong, N. (2019). Shale Oil Exploration and Production in the U.S. : Status and Outlook. *Oil Gas Geol.* 40 (03), 469–477. doi:10.11743/ogg20190303

Ziegs, V., Horsfield, B., Skeie, J. E., and Rinna, J. (2017). Petroleum Retention in the Mandal Formation, Central Graben, Norway. *Mar. Pet. Geol.* 83, 195–214. doi:10.1016/j.marpetgeo.2017.03.005

Zolfaghari, A., Dehghanpour, H., and Holyk, J. (2017). Water Sorption Behaviour of Gas Shales: I. Role of Clays. *Int. J. Coal Geol.* 179, 130–138. doi:10.1016/j.coal.2017.05.008

Zou, C. N., Du, J. H., Xu, C. C., Wang, Z. C., Zhang, B. M., Wei, G. Q., et al. (2014). Formation, Distribution, Resource Potential and Discovery of the Sinian-Cambrian Giant Gas Field, Sichuan Basin, SW China. *Pet. Explor. Dev.* 41 (03), 278–293. doi:10.1016/s1876-3804(14)60036-7

Zou, C. N., Yang, Z., Huang, S. P., Ma, F., Sun, Q. P., and Li, F. F. (2019). Resource Types, Formation, Distribution and Prospects of Coal–Measure Gas. *Pet. Explor. Dev.* 46 (03), 433–442. doi:10.1016/s1876-3804(19)60026-1

Zou, C. N., Pan, S. Q. i., Jiang, Z. H., Gao, J. L., Yang, Z., and Wu, S. T. (2020). Shale Oil Anf Gas Revolution and its Impact. *Acta Petrolei Sin.* 41 (01), 1–12. doi:10.7623/syxb202001001

Conflict of Interest: The authors declare that the research was conducted in the absence of any commercial or financial relationships that could be construed as a potential conflict of interest.

Publisher's Note: All claims expressed in this article are solely those of the authors and do not necessarily represent those of their affiliated organizations, or those of the publisher, the editors, and the reviewers. Any product that may be evaluated in this article, or claim that may be made by its manufacturer, is not guaranteed or endorsed by the publisher.

frontiers in Earth Science

ORIGINAL RESEARCH
published: 13 January 2022
doi: 10.3389/feart.2021.781782

The Occurrence of Bedding-Parallel Fibrous Calcite Veins in Permian Siliciclastic and Carbonate Rocks in Central Thailand

Piyaphong Chenrai[1,2], *Thitiphan Assawincharoenkij*[1]*, *John Warren*[2], *Sannaporn Sa-nguankaew*[2], *Sriamara Meepring*[1], *Kasira Laitrakull*[3] and *Ian Cartwright*[4]

[1]Applied Mineral and Petrology Special Task Force for Activating Research (AMP STAR), Department of Geology, Faculty of Science, Chulalongkorn University, Bangkok, Thailand, [2]M.Sc. Program in Petroleum Geoscience, Faculty of Science, Chulalongkorn University, Bangkok, Thailand, [3]PTT Exploration and Production, Bangkok, Thailand, [4]School of Earth Atmosphere and Environment, Monash University, Melbourne, VIC, Australia

Bedding-parallel fibrous calcite veins crop out at two Permian carbonate localities in the Phetchabun area, central Thailand, within the Nam Duk and Khao Khwang Formations. Samples are studied to determine their petrographic, geochemical and isotopic character, depositional and diagenetic associations and controls on the formation of fibrous calcite across the region. Biomarker and non-biomarker parameters are used to interpret organic matter sources in the vein-hosting units, the depositional environment and levels of source rock maturation in order to evaluate source rock potential in the two Formations. Carbon and oxygen isotope values of the veins and the host are determined to discuss the source of carbonates and diagenetic conditions. The petroleum assessment from the Khao Khwang and Nam Duk Formations suggests that both Formations are a petroleum potential source rock with type II/III kerogen deposited in an estuarine environment or a shallow marine environment and a slope-to-basin marine environment or an open marine environment, respectively. The bedding-parallel fibrous calcite veins from the Khao Khwang and Nam Duk Formations are divided into two types: 1) beef and, 2) cone-in-cone veins. The carbon and oxygen isotope compositions from the fibrous calcite veins suggest that the calcite veins could be precipitated from a carbon source generated in the microbial methanogenic zone. The results in this study provide a better understanding of the interrelationship between the bedding-parallel fibrous calcite veins and petroleum source rock potential.

Keywords: fibrous calcite vein, stable isotope, petroleum source rock, Permian carbonate platform, petrography

OPEN ACCESS

Edited by:
Kai-Jun Zhang,
University of Chinese Academy of Sciences, China

Reviewed by:
Peng Yang,
Northwest University, China
Yu Qi,
Yanshan University, China

***Correspondence:**
Thitiphan Assawincharoenkij
thitiphan.a@chula.ac.th

Specialty section:
This article was submitted to Geochemistry, a section of the journal Frontiers in Earth Science

Received: *23 September 2021*
Accepted: *27 December 2021*
Published: *13 January 2022*

Citation:
Chenrai P, Assawincharoenkij T, Warren J, Sa-nguankaew S, Meepring S, Laitrakull K and Cartwright I (2022) The Occurrence of Bedding-Parallel Fibrous Calcite Veins in Permian Siliciclastic and Carbonate Rocks in Central Thailand. Front. Earth Sci. 9:781782. doi: 10.3389/feart.2021.781782

1 INTRODUCTION

Bedding-parallel fibrous calcite veins are found in sedimentary rocks from Cambrian to Palaeogene strata in many locations worldwide (Cobbold and Rodrigues, 2007; Cobbold et al., 2013; Heindel et al., 2015; Kershaw and Guo, 2016; Ma et al., 2016; Cabral et al., 2019). Rocks hosting the veins are typically mixed siliciclastic–carbonate rocks, such as calcareous mudstones, argillaceous limestones and lime muds consistently rich in organic matter with low permeabilities (Franks, 1969; Cobbold and Rodrigues, 2007; Rodrigues et al., 2009; Cobbold et al., 2013; Heindel et al., 2015; Meng et al.,

2017; Tribovillard et al., 2018). Such fibrous calcite veins are globally identified across organic-entraining sedimentary basins, and are used in petroleum exploration as monitors of hydrocarbon generation (e.g., Zanella, and Cobbold, 2012; Meng et al., 2017; Luan et al., 2019; Zhang et al., 2021). Despite many studies of these veins, their origin is still debated; many studies infer the veins relate to overpressuring at times of hydrocarbon generation (e.g., Warren et al., 1998; Zhang et al., 2016; Meng et al., 2017; Luan et al., 2019). Other studies suggest the veins precipitate in unconsolidated sediments at shallow depth beneath the seafloor during times of increased concentrations of carbon dioxide in seawater and the atmosphere (Greene et al., 2012; Heindel et al., 2015; Kershaw and Guo, 2016). Times of elevated carbon dioxide concentration are generally associated with mass extinction events, including end-Permian (P-T) boundary and the end-Triassic (T-J) boundary, and are tied to large scale volcanic eruptions (e.g., Greene et al., 2012; Kershaw and Guo, 2016).

The studied fibrous calcite veins are divided into two endmembers; 1) beef and, 2) cone-in-cone veins (Cobbold et al., 2013). Calcite beef vein contains subvertical fibrous calcite crystals perpendicular to bedding in the host rock, with a smooth boundary between the host rock and the vein. Cone-in-cone veins generally consist of conical bundles of calcite fibrous representing a crystal growth character radiating from the bedding plane of the host rock. The mechanism of the calcite vein development is interpreted open-fracture fill into accommodation space created once pore pressure exceeds lithostatic pressure and hydrofracturing occurs (Zanella and Cobbold, 2012; Cobbold et al., 2013). The overpressure process can be driven by sediment degassing, especially in organic-rich rocks with low permeability, or during hydrocarbon generation (Osborne and Swarbrick, 1997; Simms, 2004; Zhang et al., 2016).

Bedding-parallel fibrous calcite veins have been found (this study) within petroleum carbonate source rocks in Thailand. In addition, the carbonate rocks hosted the fibrous calcite veins are believed to be the main petroleum source rock that contributes hydrocarbons to commercial gas fields in the Khorat Plateau located in northeast Thailand (Racey, 2011). These carbonate source rocks are Permian rocks having hydrocarbon peak generation in Late Triassic (Kozar et al., 1992). Thus, the fibrous calcite veins from this study could contribute to the ongoing discussion on the forming mechanism of fibrous calcite veins and their use as potential indicators of hydrocarbon expulsion in sedimentary basins. Carbon and oxygen isotope signatures of calcite veins offer valuable information as to the nature of changing fluid activity and geochemistry in sedimentary basins during diagenesis. Recent publications of isotope studies of fibrous calcite crystals in sedimentary basins have quantified formation mechanisms and the nature of parent waters (e.g., Demeny et al., 2010; Yu et al., 2015; Hooker et al., 2019; Luan et al., 2019).

This paper is the first to document and quantify bedding-parallel fibrous calcite veins in Thailand. It is part of our groups ongoing geochemical and isotopic documentation of Permian carbonate and siliciclastic rocks in Thailand. The aim of this study is to describe characteristics of the calcite fibrous veins and to assess the petroleum source rock potential of the hosting fine-grained Permian carbonates. Results of our study are relevant to petroleum exploration in the region and worldwide.

2 GEOLOGICAL BACKGROUND

Permian carbonates in central Thailand are exposed along the western edge of the Khorat Plateau (**Figure 1**). Permian rocks in this region consist of three major elements: the Khao Khwang Platform, the Pha Nok Khao Platform and the Nam Duk Basin located in the west, the east and middle of the Loei-Phetchabun Fold Belt, respectively (Wieldchowsky and Young, 1985; **Figure 1A**). Geologically, the Permian carbonate rocks are interpreted as a suite of Permian rift basins on the southern margin of the Indochina terrane, controlled by extensional faults (Booth and Sattayarak, 2011; Morley et al., 2013). The Indochina terrane drifted away from the northern margin of Gondwana by the Early-Middle Permian (Yan et al., 2018). Both Permian carbonate platforms, Khao Khwang and Pha Nok Khao, are extensive, distally-steepened ramps, composed of varying proportions of carbonates and lesser siliciclastics. Based on outcrop data, in what is a structurally complex orogenic region, a simplified regional model is made up of a siliciclastic-rich Nam Duk basin lies adjacent to and separates two large carbonate-dominant platforms (Wieldchowsky and Young, 1985; **Figure 1A**). To the south, the Nam Duk Basin also forms outer western boundary of the Indochina terrane. Our study focuses on the carbonates and siliciclastic rocks of the Khao Khwang and Nam Duk Formations that crop out in this area (Udchachon et al., 2014).

The Khao Khwang Formation was deposited in a shallow-marine carbonate platform characterized by mixing of carbonate rocks (massive to medium-to-thick, well-bedded to muddy limestones) mixed with siliciclastic sediments (Nakornsri, 1981; Ridd et al., 2011). The age of the Khao Khwang Formation is late Early Permian (Kungurian) to early Middle Permian (Guadalupian) (Metcalfe and Sone, 2008; Chitnarin et al., 2012). To the east, the somewhat deeper water Nam Duk Formation is dominated by siliciclastic and pelagic rocks of Early to Late Permian age, deposited in a slope-to-basin marine environment (Booth and Sattayarak, 2011; Ueno and Charoentitirat, 2011). The Nam Duk Formation comprises cherts, tuffs, shales, sandstones and calci-turbidites and limestone-dominated mass transport deposits (Helmcke and Kraikhong, 1982; Chonglakmani, 2005; Vattanasak et al., 2020). At the end of the Guadalupian across the Khao Khwang Platform, the limestone sequence is truncated by two major erosional surfaces which were responses to global sea-level lowstands (Udchachon et al., 2014). Tectonic uplift in parts of the Loei-Phetchabun Fold Belt began around the Guadalupian–Lopingian boundary and continued up to the Triassic (e.g., Bunopas, 1983; Chonglakmani and Sattayarak, 1984; Chonglakmani and Helmcke, 2001). Permian strata are now separated from overlying Mesozoic sediments by the Indosinian I unconformity; moreover, most Paleozoic strata in

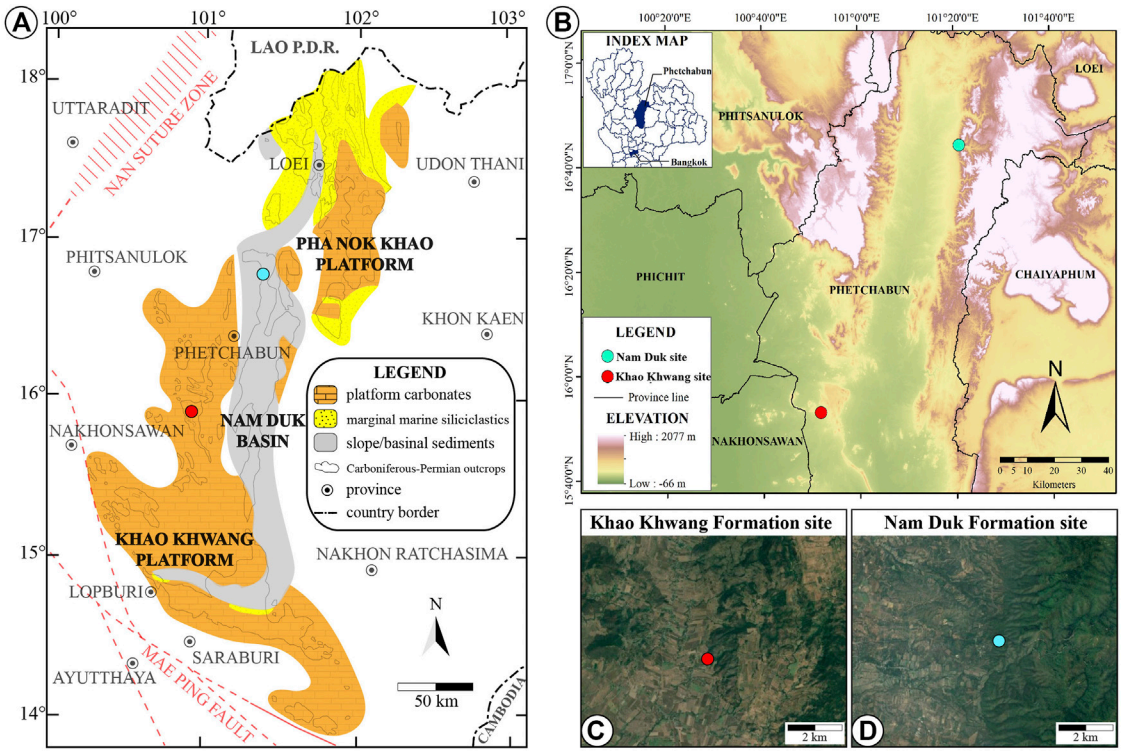

FIGURE 1 | (A) distribution of the Permian rocks, the Khao Khwang and Pha Nok Khao Platforms, separated by the Nam Duk Basin in the Loei-Phetchabun Fold Belt, central Thailand (modified from Ueno and Charoentitirat, 2011); **(B)** sample locations (Nam Duk and Khao Khwang sites) in Phetchabun Province, Thailand; **(C)** sample collection at Khao Khwang Formation; **(D)** sample collection at Nam Duk Formation.

the region were widely deformed during this same Indosinian I event (Ridd et al., 2011).

Potential source rocks in these Formations are both marine shales and micritic limestones and are known to be regionally extensive throughout the various Permian carbonate platforms (Racey, 2011; Chenrai and Fuengfu, 2019). Although Permian source rocks, based on limited well and outcrop data, are interpreted as thermally overmature with peak generation in Late Triassic (Kozar et al., 1992), regionally they are still attractive, with potential for further exploration in central and northern Thailand.

3 MATERIALS AND METHODS

3.1 Field Sampling and Sample Preparation

Field study and rock sampling are performed in two study areas in Phetchabun Province (**Figure 1B**). In total, 12 rock samples were selected for detailed study from a range of samples from the Khao Kwang and Nam Duk Formations. The 12 samples contained fibrous calcite veins suitable for petrography and geochemical analyses. Generally, bedding-parallel fibrous calcite veins documented in this study occur within calcareous mudstones and argillaceous limestones. Samples referred to as "outcrop samples" in this paper are not taken directly from the surface. Instead, samples were collected by digging some 0.10 and 0.30 m into the outcrop to ensure that visibly unweathered material was obtained. Any remaining weathered parts of the samples were removed before proceeding with detailed analysis. Samples were then cleaned with distilled water, acetone, and dichloromethane to eliminating any remaining surface contamination. All washed samples for organic geochemical analysis were crushed into small chips in a hammer and jaw-crusher and then into powder by dish mill grinder. Powder samples were then put into pre-washed glassware for further extractable organic matter and gas chromatography–mass spectrometric determinations. Petrographic samples were cut into rock slabs, and thin sections were made to observe fibrous calcite characteristics. Samples for isotope analysis were extracted from vein regions in rock slabs by using a dental technician's drill in traverses that extracted a sample volume every 5 mm along traverses than ran from the host rock across a vein, or stacked veins, and back into host rock on the other side of the vein.

3.2 Gas Chromatography-Mass Spectrometry

Gas chromatography-mass spectrometry (GC-MS) is an instrumental technique for identifying the molecular mass of organic compounds by their ionized compositions. In this study, GC-MS was performed at the Scientific and Technological Research Equipment Centre Chulalongkorn University to

analyze biomarker and non-biomarker compounds from bitumen extracts. The saturated hydrocarbon fraction from the rock samples was dissolved in n-pentane and analyzed with an Agilent 7000C GC/MS (triple quadrupole) machine, with an ion source temperature of 250°C and ionizing energy of 70 eV. The column used in this study is a 30 m long DB-5 (5% Phenyl Methyl Siloxane) with a 250 µm inner diameter and 0.25 µm film thickness. Starting temperature is 80°C and is held for 3 min. The column temperature is heated from 80°C to 310°C at 4°C/minutes and held for 30 min at 310°C. The total analysis time is 90 min. Chromatograms were acquired in scanning: 35–700 molecular weight and selected-ion-monitored (SIM) for compound identification and integration. The distribution of organic compounds in the bitumen extracts was monitored by fragmentograms of *n*-alkane (m/z 85) and steranes (m/z 217). Details of the analytical procedure used are summarized in Moustafa and Morsi (2012).

3.2.1 Long-Chain Saturated Hydrocarbon (*n*-Alkane) Distribution

Chromatogram distribution of *n*-alkane and isoprenoids from the saturated hydrocarbon extraction displays aliphatic fractions of all analyzed samples. The distribution of *n*-alkanes can be used to indicate organic matter source. Short chain *n*-alkanes (lower than C_{20}) are characteristic of microbial input. In addition, medium chain *n*-alkanes (C_{11}–C_{20}) are considered to indicate algal and/or bacterial origin for the organic materials. Long chain *n*-alkanes (more than C_{20}), high boiling point *n*-alkanes, are commonly attributed to the contribution of terrestrial waxes, especially in the C_{25}–C_{33} range (Peters and Moldowan, 1993). In this study, the Pr/Ph, Pr/n-C_{17} and Ph/n-C_{18} outputs are also used for determining the source of organic matter and conditions in the depositional environment (e.g., Shanmugam, 1985; Wang et al., 2010; Al-Khafaji et al., 2020). Biomarker parameters used in this study are presented as follows:

1) Pristane ($C_{19}H_{40}$) and phytane ($C_{20}H_{42}$) are regular isoprenoid hydrocarbons, which both were derived from the phytol side chain of chlorophyll molecule (Miles, 1989). Pristane and phytane ratio (Pr/Ph) is commonly used for determining redox conditions and organic matter inputs in various depositional environments during sedimentation and diagenesis (Powell, 1988; Chandra et al., 1994; Large and Gize, 1996). High Pr/Ph values (>3.0) indicates oxic conditions often associated with terrigenous organic matter input, while low values (<1.0) typify anoxic conditions, commonly hypersaline or carbonate environments and values between 1.0 and 3.0 suggest intermediate conditions (sub-oxic conditions) (Amane and Hideki, 1997; Peters et al., 2005). In addition, Pr/Ph ratio can be used to indicate lithology from analyzed samples, for instance, marine carbonates (Pr/Ph < 1), marine shales (Pr/Ph 1–3), and non-marine shales/coals (Pr/Ph > 3) (Hughes et al., 1995).
2) The combination of acyclic isoprenoids compared to *n*-alkanes (Pr/n-C_{17} and Ph/n-C_{18}) provides valuable information about organic matter source, biodegradation, maturation and depositional environment. In general, isoprenoids are more resistant to biodegradation than *n*-alkanes, and are used to determine any influence from early microbial degradation (Landais, 1996). Moreover, the Ph/n-C_{17} ratio tends to be less than 0.5 in environments with abundant aerobic bacterial activity, whereas values of more than 1 tend to indicate low levels of aerobic bacterial activity (Lijmbach, 1975).
3) Sterane biomarker measures indicate carbon number distribution of sterols that can be used to interpret organic matter source and depositional environment by plotting regular sterane compositions (C_{27}, C_{28} and C_{29}) in a tertiary diagram (Huang and Meinschein, 1979; Moldowan et al., 1985; Shanmugam 1985). The domination of C_{27} steranes represents a marine-influenced system and marine plankton, C_{28} sterane predominance suggests an organic matter deposited in lacustrine facies, and the influence of C_{29} sterane suggests a terrestrial environment as higher plant input and a swamp deposit environment (Peters and Moldowan, 1993).

3.3 Carbon and Oxygen Stable Isotope Analysis

Stable isotopes of $\delta^{13}C$ and $\delta^{18}O$ of the veins and host rock samples are measured by utilizing techniques outlined in Allègre (2008) after extracting powder samples using a dental technician's drill. The stable isotopes were carried out at Monash University, Australia. The purpose of this study is to better understand fluid carbon sources for the fibrous calcite veins and fluid evolution during different burial stages, tied to calcite precipitation. The carbon sources for the fibrous calcite vein in organic-rich rocks come from inorganic carbon in the host sediment and organic carbon from organic matter (both depositional and catagenic). The inorganic carbon source is expected to have $\delta^{13}C$ values near the seawater $\delta^{13}C$ value through time, whereas the organic carbon source is significantly depleted in the host rock by biological processes (Luan et al., 2019). Therefore, if no external fluids contributed to the host rock, especially within low permeability host rocks, the fibrous calcite vein is expected to have bulk isotopic compositions close to the host rock. All analyses are reported in per mill (‰) relative to the Vienna-PeeDee Belemnite (V-PDB) standard.

4 RESULTS

4.1 Bedding Parallel Fibrous Character

The dominant lithology of samples from the Khao Khwang Formation is argillaceous limestone. In general, the succession in the study area comprises limestone (approximately 1–50 cm) interbedded with calcareous mudstone to argillaceous limestone (approximately 1–10 cm) (**Figures 2A,B**). In contrast, the rock samples from the Nam Duk Formation are calcareous mudstones interbedded with sandstones (**Figures 2C,D**). Bedding-parallel fibrous calcite veins are around 1–7 cm from

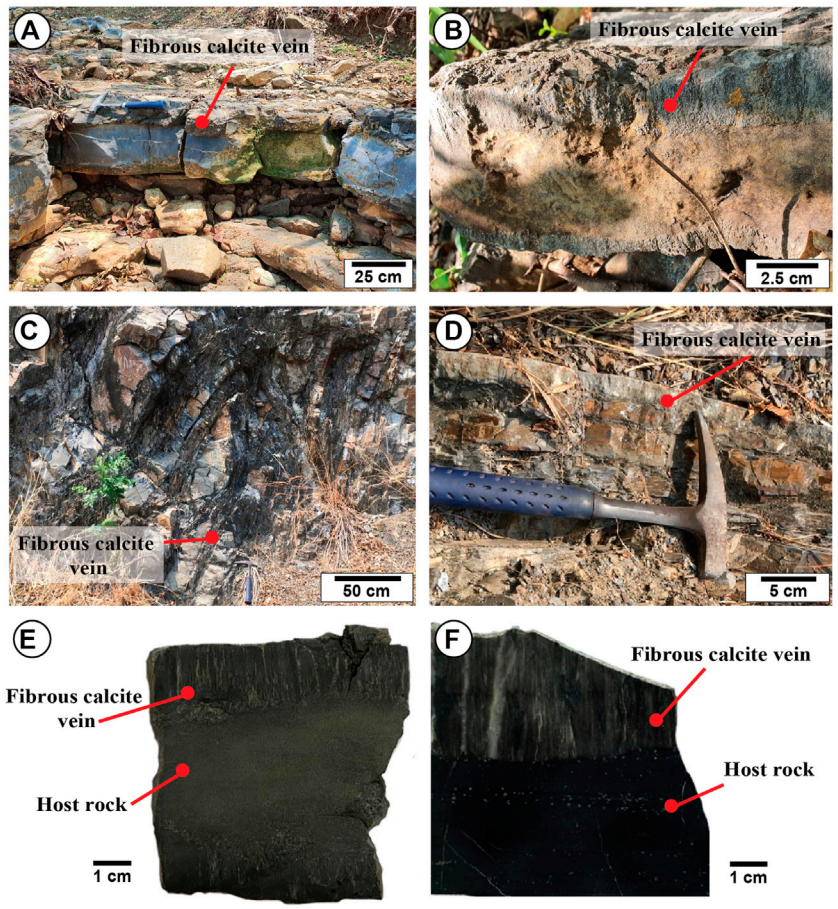

FIGURE 2 | (A),(B) the fibrous calcite veins of the Khao Khwang Formation; **(C),(D)** the fibrous calcite veins of the Nam Duk Formation; **(E),(F)** polished slab of bedding-parallel fibrous calcite veins from the Khao Khwang Formation **(E)** and the Nam Duk Formation **(F)**.

exposed bedding plane surfaces in their host rock outcrops (**Figures 2E,F**) and oriented approximately parallel to the inferred bedding planes in both Khao Khwang and Nam Duk Formations (**Figures 2E,F**).

4.1.1 Khao Khwang Formation

Both types of the fibrous calcite vein (beef and cone-in-cone) are observed in this Formation, but cone-in-cone veins tend to dominate. Most fibrous calcite crystals commonly entrain solid inclusions composed of variable proportions of insoluble mud components, organic matter, and pyrite (**Figure 3A**). In some samples, cone-in-cone veins and granulars grade into beef veins at the base of the cone interval (**Figures 3A,B**). Generally, solid (host-mud) inclusions outline sinusoidal patterns within the fibrous calcite of the cone-in-cone vein intervals (**Figure 3C**). In contrasts, there are few to no solid inclusions in the beef veins (**Figure 3D**). Accompanying pressure solution features are seen in the host rock matrix in Khao Khwang samples, especially stylolites and microstylolite (**Figure 3E**). Framboidal pyrite ranging from 5.7 to 65 μm is common in most recrystallized host rock (**Figure 3F**).

4.1.2 Nam Duk Formation

In contrast to the Khao Khwang samples, fibrous calcites in the Nam Duk Formation are mostly in beef veins, with sharp contacts with the adjacent the host rock surfaces (**Figure 4A**). A median suture line is observed in the Nam Duk vein samples indicating the growth direction of the fibrous calcites (**Figure 4B**). The fibrous calcite crystals have widths around 0.2–1.0 cm, with twinning (**Figure 4C**). Solid inclusions are indistinctive to absent in the samples from this Formation. When present they are mostly small amounts of insoluble clay minerals, organic matter and pyrite. In addition, irregular quartz vein crystals are found in the calcite veins and in the siliciclastic rock matrix of this Formation (**Figure 4C**). Shear deformation is seen in sand grains floating in a clay-dominated matrix (**Figure 4D**). Pyrite is also present within the host rocks in various forms, including euhedral, framboidal, and aggregate framboid morphologies ranging from 0.1 to 0.5 mm.

4.2 Molecular Geochemistry

The quality of TOC and pyrolysis data as published in previous studies, using standard petroleum industry methodologies, is

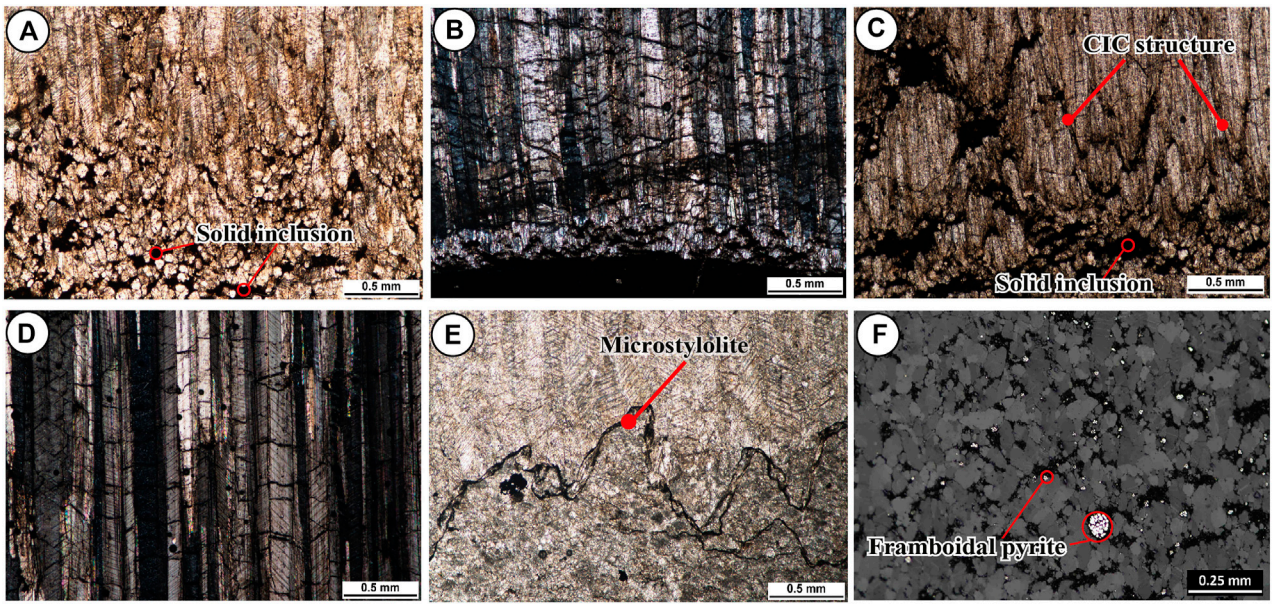

FIGURE 3 | Photomicrographs of the Khao Khwang Formation. **(A)** Solid inclusions in the fibrous calcite vein and a change from equant calcite to fibrous calcite; **(B)** a change from cone-in-cone to beef vein textures; **(C)** beef veins in the Khao Khwang samples; **(D)** cone-in-cone veins are commonly found in the Khao Khwang samples and are characterized by a nested cone geometry; **(E)** microstylolite; and **(F)** framboidal pyrite is common in the host rock matrix.

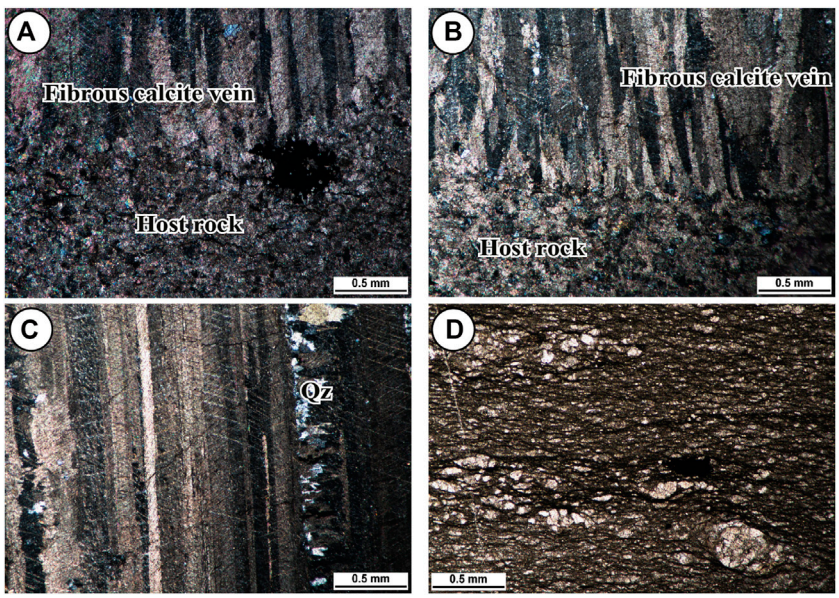

FIGURE 4 | Photomicrographs of the Nam Duk Formation. **(A)** Beef veins typify the Nam Duk samples; **(B)** a change from the host rock to beef vein with a median suture line; **(C)** calcite twining in beef vein associated with quartz crystals; **(D)** sand grains floating in the host rock matrix.

compromised, likely due to strong maturation (e.g., Chenrai and Fuengfu, 2019). Accordingly, in this study, organic matter source and the depositional conditions are determined using alternative tools such as non-biomarker and biomarker parameters. Molecular geochemical results and biomarker ratios from samples measured in this study are summarized in **Table 1**.

4.2.1 *n*-Alkanes Distribution

Gas chromatograms of saturated hydrocarbon fractions from the analyzed samples are shown in **Figure 5** and display a full suite of saturated hydrocarbons including C_8–C_{35} *n*-alkanes, isoprenoids, pristane (Pr) and phytane (Ph). The *n*-alkane distribution from the two Formations suggests that the

TABLE 1 | The molecular geochemical results and biomarker ratios of the Khao Khwang (KK) and Nam Duk (ND) samples. C_{27}, C_{28} and C_{29} are regular sterane compositions converted to a percentage.

Sample	Pr/Ph	Pr/n-C_{17}	Ph/n-C_{18}	C_{27} (%)	C_{28} (%)	C_{29} (%)
KK-1	1.55	0.48	0.34	38.57	25.68	35.75
KK-2	1.29	0.58	0.16	37.95	30.86	31.19
KK-3	0.94	0.57	0.17	37.89	18.68	43.43
KK-4	0.32	0.25	0.31	28.13	27.74	44.13
KK-5	0.38	0.23	0.20	33.03	29.50	37.47
KK-6	0.47	0.21	0.32	30.61	27.15	42.24
ND-1	0.84	0.22	0.13	55.40	17.93	26.67
ND-2	1.20	0.32	0.14	53.29	14.21	32.50
ND-3	1.58	0.38	0.14	51.85	21.95	26.20
ND-4	1.04	0.14	0.14	54.36	18.46	27.18
ND-5	0.96	0.06	0.04	53.68	18.69	27.62
ND-6	1.22	0.15	0.09	48.87	18.80	32.33
KK average	0.83	0.39	0.25	34.36	26.60	39.04
ND average	1.14	0.22	0.12	52.91	18.34	28.75

organic materials are derived from different sources. A predominance of medium to long molecular weight compounds (nC_{20}–nC_{30}) in the Khao Khwang samples suggest a mixed contribution from terrigenous and marine organic matter (**Figure 5A**). Nam Duk samples exhibit a predominance of short molecular weight compounds (nC_{15}–nC_{18}) suggesting marine organism inputs (**Figure 5B**; Tissot et al., 1978). Pr/Ph ratios (less than 3) also confirm that samples from both Formations were deposited in a marine environment (**Table 1**).

4.2.2 Pristane (Pr)/n-C_{17} and Phytane (Ph)/n-C_{18}

A cross-plot diagram between Pr/n-C_{17} and Ph/n-C_{18} shows that the Khao Khwang and Nam Duk samples are dominated by a combination of terrigenous kerogen type III and marine kerogen type II (**Figure 6**). These plots also suggest both Formations were deposited in sub-oxic to oxic condition and that the Nam Duk samples are more mature than the Khao Khwang samples. Pristane and phytane concentrations of both Formations are typically lower

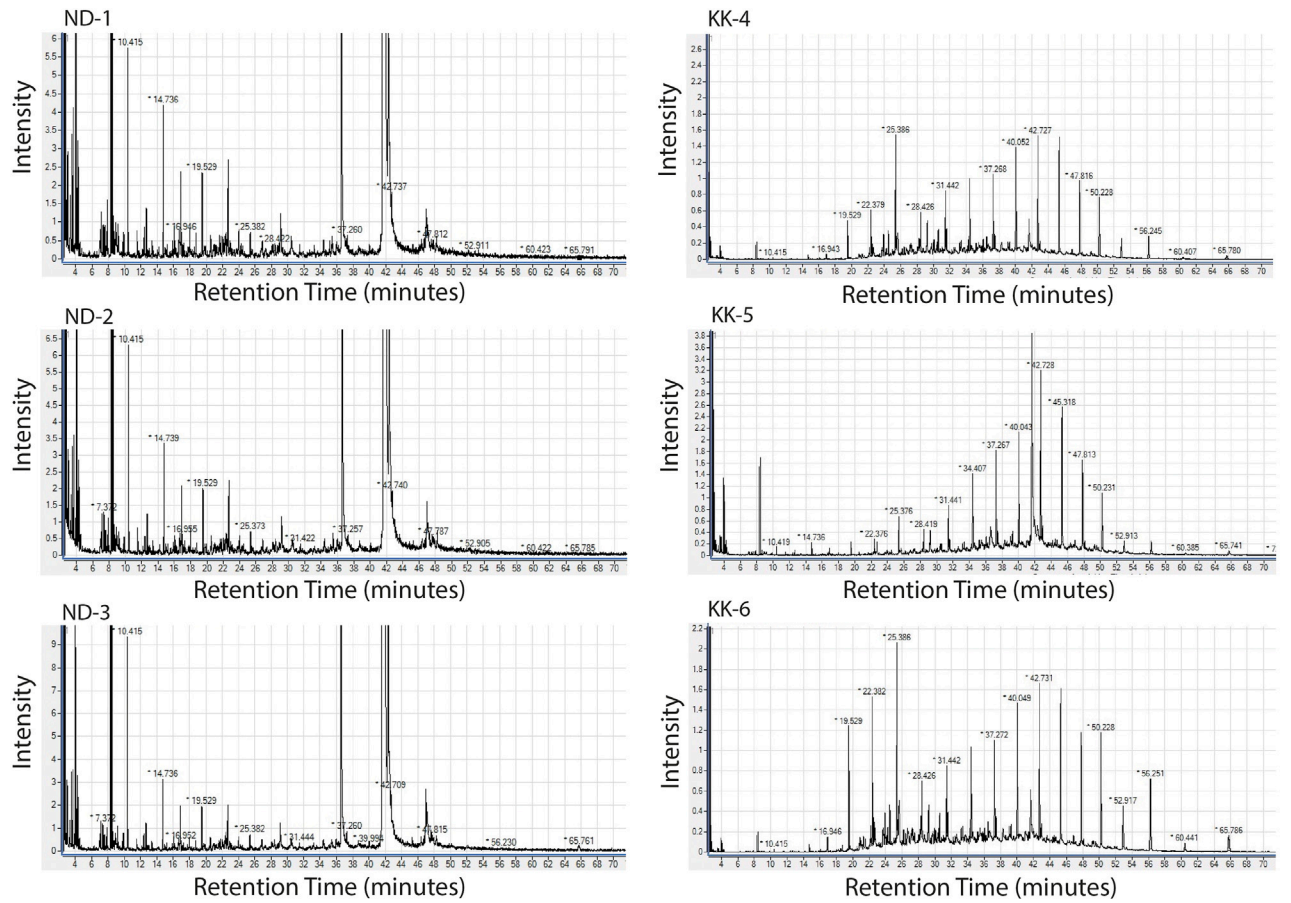

FIGURE 5 | The examples of mass chromatograms showing n-alkane distributions for **(A)** the Khao Khwang Formation (KK-4, KK-5, KK-6) and **(B)** the Nam Duk Formation (ND-1, ND-2, ND-3).

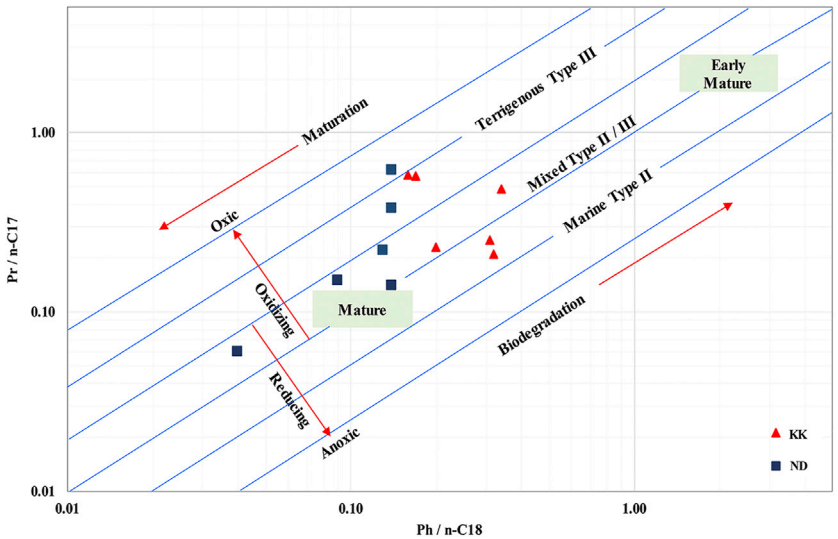

FIGURE 6 | Plot of pristane/n-C_{17} (Pr/n-C_{17}) versus phytane/n-C_{18} (Ph/n-C_{18}) for the Khao Khwang (KK) and Nam Duk (ND) Formations.

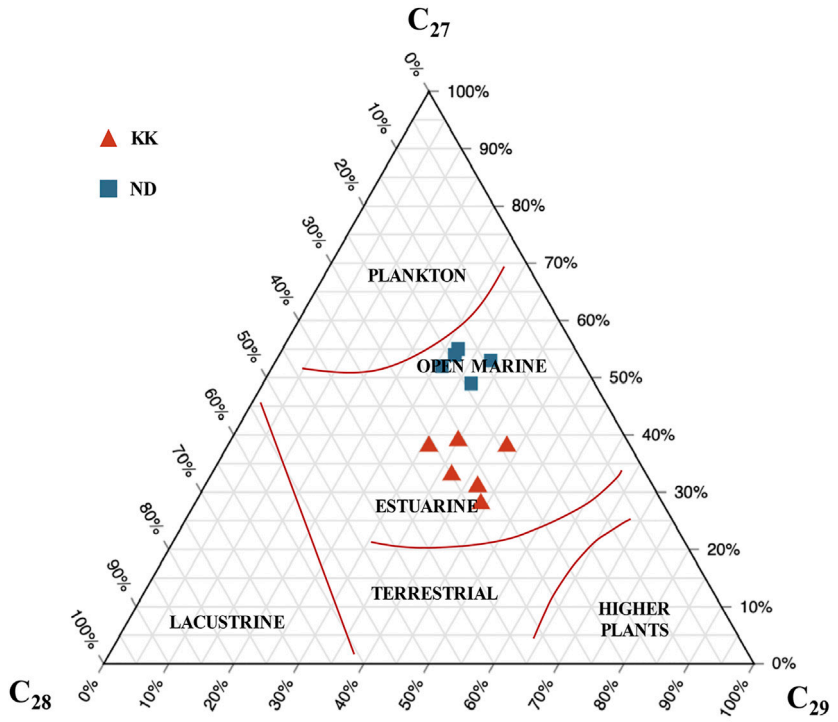

FIGURE 7 | Ternary diagram of relative abundance of C_{27}, C_{28} and C_{29} regular steranes shows organic matter source and depositional environment of the samples from the Khao Khwang (KK) and Nam Duk (ND) Formations.

than n-C_{17} and n-C_{18}, respectively. The Pr/n-C_{17} ratios of the Khao Khwang samples range from 0.2 to 0.6, and from 0.1 to 0.9 for the Nam Duk samples (**Table 1**). Additionally, the Ph/n-C_{18} ratios of the Khao Khwang samples range from 0.2 to 0.3, and from 0.04 to 0.1 for the Nam Duk samples (**Table 1**).

4.2.3 Steranes and Terpanes

The relative abundance of C_{27}, C_{28} and C_{29} steranes from this study was converted to a percentage and plotted in a ternary diagram (**Table 1**; **Figure 7**). The average abundances of C_{27}, C_{28} and C_{29} regular steranes of the Khao Khwang samples are 34.36,

TABLE 2 | The carbon and oxygen isotope compositions of the fibrous calcite vein and host rock matrix of the Khao Khwang (KK-5) and Nam Duk (ND-1) samples.

Sample	δ^{18}O PDB (‰)	δ^{13}C PDB (‰)	Sample	δ^{18}O PDB (‰)	δ^{13}C PDB (‰)
	KK-5			ND-1	
Vein	−10.65	2.87	Vein	−12.42	3.75
Vein	−11.09	2.77	Vein	−11.45	4.15
Vein	−10.36	2.96	Vein	−11.19	4.36
Vein	−10.56	2.97	Vein	−11.91	3.13
Vein	−10.67	2.96	Matrix	−12.53	2.69
Matrix	−10.20	2.69	Matrix	−13.79	2.20
Matrix	−10.38	2.78	Matrix	−13.49	2.45
Matrix	−10.48	2.70	Matrix	−14.03	2.04
Matrix	−11.83	2.20	Matrix	−13.34	2.23
Matrix	−10.06	2.50	Matrix	−14.27	1.67
Vein	−9.98	3.01	Matrix	−13.64	2.12
Vein	−9.96	3.15	Matrix	−14.02	2.16
Vein	−11.14	2.82	Matrix	−13.85	2.26
			Matrix	−14.10	2.14
			Matrix	−14.88	1.95
Avg. total	−10.57	2.80		−13.26	2.62
Avg. vein	−10.55	2.94		−11.74	3.85
Avg. matrix	−10.59	2.57		−13.81	2.17

26.60 and 39.04%; and 52.91, 18.34 and 28.75% for the Nam Duk samples (**Table 1**). The regular steranes suggest that the organic matter came from a marine environment with elevated C_{27} and C_{29}, and were deposited in estuarine (or shallow marine) to open marine settings. This interpretation is also supported by Pr/n-C_{17} and Ph/n-C_{18} ratios (**Figure 6**).

4.3 Carbon and Oxygen Stable Isotopes

The results of stable carbon and oxygen isotope analyses of the samples from both Formations are summarized in **Table 2** and plotted in **Figure 8**. The δ^{18}O values of the fibrous calcite veins and host rock matrices of the Nam Duk samples are more depleted than the Khao Khwang samples. The fibrous calcite veins from the Nam Duk samples also show higher values of δ^{13}C compared to the Khao Khwang samples, indicating overall heavier carbon isotope compositions. The carbon and oxygen isotope compositions of the Khao Khwang and Nam Duk samples are plotted along with the sample profile in **Figure 9** and **Figure 10**, respectively. The carbon and oxygen isotope compositions of the fibrous calcite veins are generally quite similar to those in the host rock matrix, especially within the Khao Khwang samples (**Figures 9**, **10**). The carbon isotope compositions of the fibrous calcite vein are slightly more elevated than in the host rock matrix, presumably reflecting incorporation of organic carbon into vein cement.

4.3.1 Khao Khwang Formation

The δ^{13}C values of the fibrous calcite veins range from +2.77 to +3.15‰ with an average value of +2.94‰. The δ^{13}C values of the host rock matrix ranges from +2.20 to +2.78‰ with an average value of +2.57‰. The δ^{18}O values of the fibrous calcite veins range from −9.96 to −11.09‰ with an average value of −10.55‰ and between −10.06 and −11.83‰ in the matrix with an average value of −10.59‰. Accordingly, the δ^{13}C and δ^{18}O values of the fibrous calcite are slightly different from the matrix.

4.3.2 Nam Duk Formation

The δ^{13}C values of the fibrous calcite vein range from +3.13 to +4.36‰ with an average value of +3.85‰. In the host rock matrix, the δ^{13}C values range from +1.67 to +2.69‰ with an average value of +2.17‰. The δ^{18}O values of the fibrous calcite vein are between −11.19 and −12.42‰ with an average value of −11.74‰ and are between −12.53 and −14.88‰ in the host rock matrix with an average value of −13.26‰. The δ^{18}O values from the host rock matrix are more depleted than from the fibrous

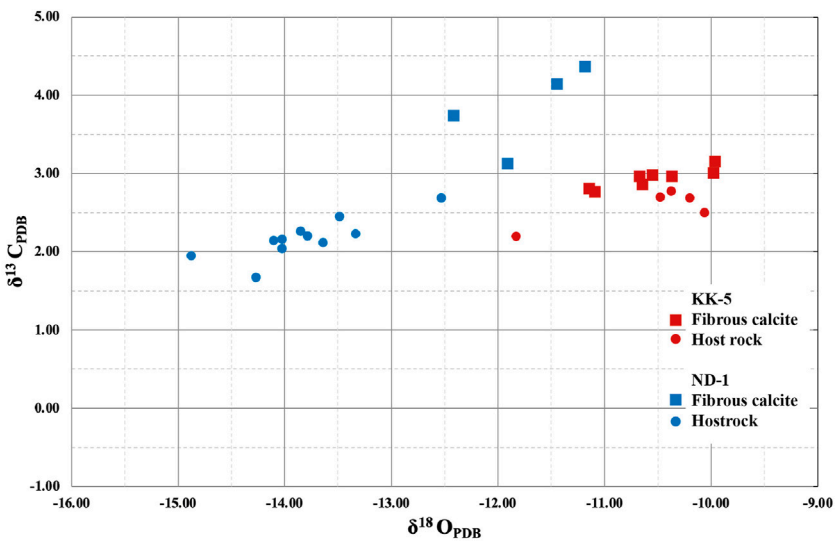

FIGURE 8 | Carbon and oxygen isotope compositions from the fibrous calcite vein and host rock of the Khao Khwang (KK-5) and Nam Duk (ND-1) samples.

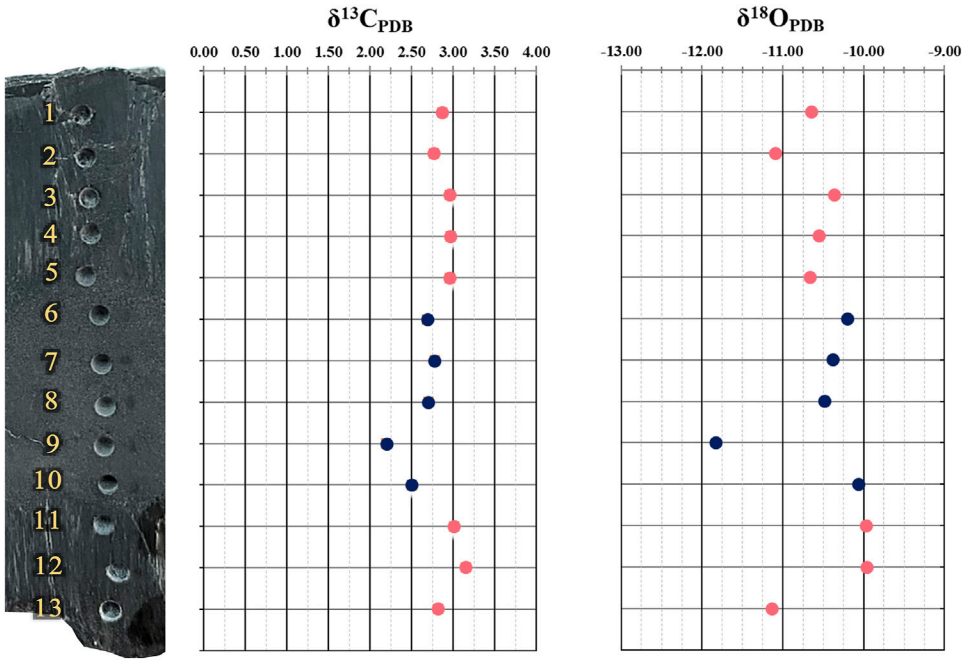

FIGURE 9 | The transection diagram of the Khao Khwang sample (KK-5) shows $\delta^{13}C$ PDB and $\delta^{18}O$ PDB isotopic composition of host rock (black dots) and fibrous calcite veins (red dots) from top to bottom of the samples. The boundary between the fibrous calcite vein and host rock is indicated by yellow dashed lines.

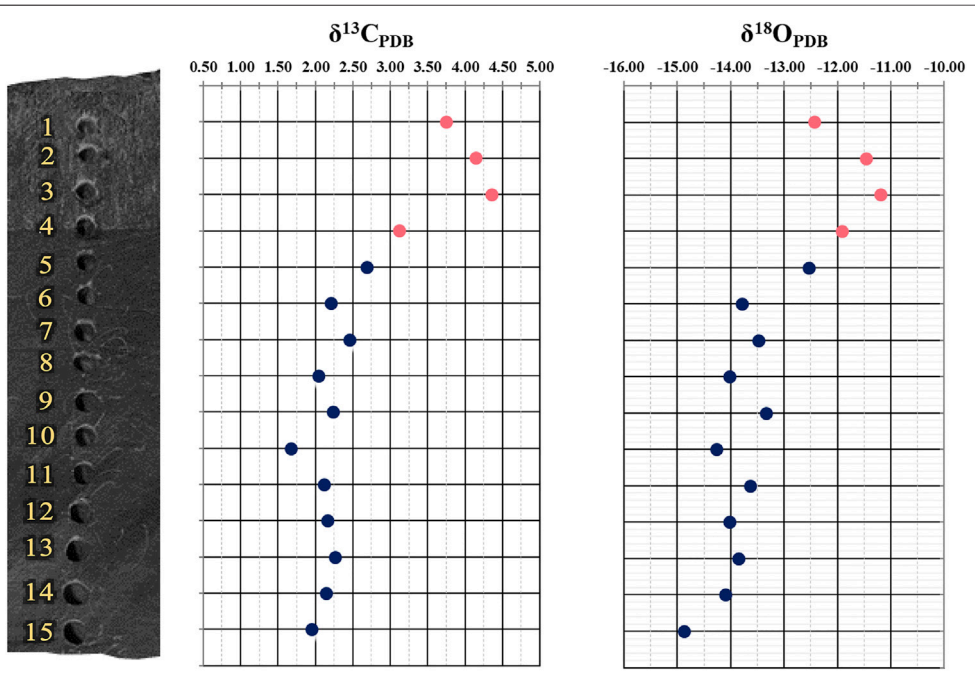

FIGURE 10 | The transection diagram of the Nam Duk sample (ND-1) shows $\delta^{13}C$ PDB and $\delta^{18}O$ PDB isotopic composition of host rock (black dots) and fibrous calcite veins (red dots) from top to bottom of the samples. The boundary between the fibrous calcite vein and host rock is indicated by a yellow dashed line.

calcite veins. The $\delta^{13}C$ values of the fibrous calcite veins are heavier than from the host rock matrix.

5 DISCUSSION

5.1 Paleo-Depositional Environment

Biomarker analysis of soluble organic matter (bitumen) from the rock samples hosting the fibrous calcite veins has contributed to a better understanding of the characteristics of the depositional environments (e.g., Waples and Machihara, 1991; Sivan et al., 2008). In this study, organic facies and depositional environment are interpreted using Pr/Ph ratio, Pr/n-C_{17} and Ph/n-C_{18} cross plots and sterane distributions (e.g., Shanmugam, 1985). Samples from both Formations have similar isoprenoid, *n*-alkane and sterane distributions, and thus are similar in depositional environment, organic matter type and maturity (**Figures 5–7**; **Table 1**). Molecular geochemical data from both Formations suggest that the rock samples are deposited in a marine environment with a mixed source of organic matter from the marine and terrestrial. However, there are slight differences in likely paleo-geography and thermal maturation between the two Formations.

Based on these data, rock samples from the Khao Khwang Formation are believed to have been deposited in a lagoonal/estuarine or shallow marine environment. In contrast, based on *n*-alkane and sterane distributions, the Nam Duk Formation was deposited in a somewhat deeper water slope environment. That is, a higher proportion of land plant material was deposited within the Khao Khwang Formation. These interpretations coincide with results from previous studies on depositional environments for both Formations (e.g., Chitnarin et al., 2008; Chenrai and Fuengfu, 2019). The same settings of the relevant organic facies are confirmed by the bivariate plot trends of the Pr/Ph ratio, the Pr/n-C_{17} and Ph/n-C_{18} cross plot and the tertiary diagram of regular steranes (**Figure 7**).

5.2 Petroleum Potential Source Rock

Total organic carbon (TOC) contents in the Khao Khwang Formation imply fair to excellent source rock potential (Racey, 2011; Chenrai and Fuengfu, 2019). Unfortunately, there is no similar data measure for the Nam Duk Formation. However, the Pr/n-C_{17} and Ph/n-C_{18} cross plot reveals that the samples from both Formations contain a mixed kerogen, between type III and type II, deposited under sub-oxic to oxic conditions. It should be noted that these analyzed data are from outcrop samples that may be somewhat oxidized, tied to exposure to the more oxic conditions near the present-day landsurface. If organic matter was first deposited in anoxic to sub-oxic conditions, the rock samples would be considered potential oil and gas sources for both Formations. Abundant framboidal pyrites having a various size from 5.7 μm to 0.5 mm within the rock samples, especially from the Khao Khwang Formation, also suggest that the samples were deposited under relatively anoxic conditions (Wilkin et al., 1996; Liu et al., 2019). The Nam Duk Formation was likely deposited further from a terrestrial organic matter source than the Khao Khwang Formation, based on *n*-alkane and sterane distributions. This implies fine-grained rocks in the Khao Khwang Formation have a higher petroleum potential than the Nam Duk Formation. Thermal maturation of the Nam Duk Formation is interpreted to be higher than the Khao Khwang Formation, based on the Pr/n-C_{17} and Ph/n-C_{18} cross plot (**Figure 6**). This higher thermal maturation interpretation is supported by the $\delta^{18}O$ values of the Khao Khwang samples being more negative than the Nam Duk samples (**Figure 8**), indicating that the calcites within the Khao Khwang samples were precipitated at somewhat higher temperatures (Al-Aasm et al., 1993).

5.3 Fibrous Calcite Development

Bedding-parallel calcite veins are widely documented, as are interpretations of the formative mechanisms driving aligned fibrous crystal growth within sedimentary strata during burial diagenesis and compaction (Franks, 1969; Cobbold et al., 2013). Nam Duk samples are dominated by beef veins with a smooth continuous boundary between the fibrous calcites and host rock bedding surface. This probably indicates that the beef veins grew at a consistent rate. On the other hand, the Khao Khwang samples mostly fibrous calcite cone-in-cone veins, with abundant inclusions of host-mud. These samples likely grew under more fluctuating conditions, with times of rapid growth indicated by intervals enclosing more mud inclusions. The ability of the calcite to encase mud inclusions likely indicates that the host rock was also semi to unconsolidated at the time of calcite crystal growth. Beef veins without mud inclusions suggest a more brittle or consolidated host rock at the time of fibrous calcite precipitation (e.g., Meng et al., 2017). Hence, beef veins in the Nam Duk Formation likely formed during deeper burial diagenesis and in more compacted situations than cone-in-cone veins in the Khao Khwang Formation. Both the cone-in-cone and beef vein fabrics are a fibrous growth response to saturated conditions in a hydrologic regime derived from local carbonaceous fluids within the host rock. Individual crystal fibers grew vertically and inward during the periodic opening of the vein space.

Stable isotope compositions can be used to refine interpretations of growth style and relative timing of fibrous calcite development. Negative signatures in organic matter can provide evidence of an organic bicarbonate (HCO_3^-) sourced in zones of bacterial sulphate reduction in shallow-burial anaerobic environments (Irwin et al., 1977). The bicarbonate fixed in fibrous calcites precipitated in this zone usually inherit $\delta^{13}C$ signatures from this organic matter; hence a much-depleted carbon isotope composition is expected to occur in calcites formed in this zone ($\delta^{13}C < -25‰$ PDB; Irwin et al., 1977). After sulphate is totally consumed in the bacterial sulphate reduction zone, the microbial methanogenic zone is entered; there Archaeal methanogens can continue to be active until temperatures reach ~75°C (the petroleum generation window; Morad, 2009).

Samples from the two Formations show positive $\delta^{13}C$ values, suggesting that the heavy carbon in the formative bicarbonate was influenced by microbial activity in a methanogenic zone that underlay the bacterial sulphate reduction zone. There the carbon

dioxide (CO_2) generated within the microbial methanogenic zone tends to have heavy carbon isotope compositions ($\delta^{13}C \approx 0–15‰$ PDB) via microbial fermentation (Raiswell, 1987; Wolff et al., 1992). Thus, if the buried organic-rich rocks still have organic matter remaining after passing through the bacterial sulphate reduction zone, they can generate carbon dioxide with $\delta^{13}C$ enriched carbon. This leads to progressive ^{13}C enrichment in bicarbonate fixed as calcite forming within the rocks. Fibrous calcite veins in this zone are expected to be similar to the veins in the two Formations. Overall $\delta^{13}C$ carbon composition will be positive if there is no subsequent external fluid intrusion, as is likely due to the ongoing low permeability of the host rocks (Luan, et al., 2019). Thus, moderate positive $\delta^{13}C$ values from the Khao Khwang and Nam Duk Formations possibly suggest a carbon source from carbon dioxide influenced by microbial methanogenesis.

Oxygen isotope compositions of the fibrous calcite veins from both Formations are more depleted when compared to the range of Permian carbonate rock precipitation in equilibrium with Permian seawater as −4.8‰ PDB (Veizer et al., 1999). The measured negative oxygen isotope signatures (≈−10 to −13‰) are too negative and likely reflect ongoing local rock-buffered rock-fluid interactions, carbonate precipitation and re-equilibration is occurring in modified marine pore waters within adiagenetic systems at somewhat deeper burial depths where the temperature are progressively increasing (Hodgson, 1966; Dickson and Coleman, 1980; Marshall, 1982; Nuriel, et al., 2011; Uysal, et al., 2011; Warren et al., 2014).

6 CONCLUSION

The bedding-parallel fibrous calcite veins from the Khao Khwang and Nam Duk Formations are divided into two types; beef and cone-in-cone veins. Their carbon and oxygen isotope compositions suggest that the calcite veins were precipitated from a carbon source by carbon dioxide generated in the zone of microbial methanogenesis, giving $\delta^{13}C$-enriched carbon isotope compositions. Thus, the fibrous calcite veins of the two Formations exhibit moderate positive $\delta^{13}C$ values at the present day. Their $\delta^{18}O$-depleted isotope compositions indicated that the fibrous calcite veins re-equilibrated in locally-derived warmer fluids (no external carbon source) likely tied to somewhat deeper burial. The fibrous calcite veins are interpreted to be precipitated in the surrounding semi-consolidated sediments, and so calcite crystals are preserved as cone-in-cone veins with abundant host-mud inclusions. Beef veins that typify the Nam Duk Formation are believed to have precipitated in more consolidated fine-grained sediment hosts in the somewhat deeper burial zone compared to the Khao Khwang Formation.

Our petroleum assessment of the Khao Khwang and Nam Duk Formations suggests that both Formation are a petroleum potential source rock with type II/III kerogen. The depositional environment of organic matter in the Khao Khwang Formation was either an estuarine environment or a shallow marine environment. Organic signatures in the Nam Duk Formation suggest a somewhat deeper water slope-to-basin marine setting or an open marine environment. Thus, results in this study provide a better understanding between the bedding-parallel fibrous calcite veins and petroleum source rock potential in a sedimentary basin using analytical approaches that could also be applied for petroleum exploration in a frontier area.

DATA AVAILABILITY STATEMENT

The original contributions presented in the study are included in the article/supplementary material, further inquiries can be directed to the corresponding author.

AUTHOR CONTRIBUTIONS

PC and TA: Conceptualization, field collection, methodology, formal analysis, investigation, writing manuscript; JW: review and editing manuscript; SS: field collection, laboratory investigation, preparing manuscript; SM: petrography investigation; IC: isotope analysis.

ACKNOWLEDGMENTS

The authors gratefully acknowledge the financial support from the Ratchadaphisek Somphot Endowment Fund under Outstanding Research Performance Program, Chulalongkorn University (Sci-Super VII_64_002). Reviewers are thanked for their useful and constructive comments.

REFERENCES

Al-Aasm, I. S., Muir, I., and Morad, S. (1993). Diagenetic Conditions of Fibrous Calcite Vein Formation Black Shales: Petrographic, Chemical and Isotopic Evidence. *Bull. B. Can. Petrol. Geol.* 41, 46–56. doi:10.35767/gscpgbull.41.1.046

Al-Khafaji, A. J., Hakimi, M. H., Mohialdeen, I. M. J., Idan, R. M., Afifyf, W. E., and Lashin, A. (2020). Geochemical Characteristics of Crude Oils and basin Modelling of the Probable Source Rocks in the Southern Mesopotamian Basin, South Iraq. *J. Petrol. Sci. Eng.* 196, 107641. doi:10.1016/j.petrol.2020.107641

Allegre, C. J., and Sutcliffe, C. (2008). *Isotope Geology*. Cambridge: Cambridge University Press. doi:10.1017/CBO9780511809323

Amane, W., and Hideki, N. (1997). Geochemical Characteristics of Terrigenous and marine Sourced Oils in Hokkaido, Japan. *Org. Geochem.* 28, 27–41. doi:10.1016/s0146-6380(97)00102-2

Booth, J., and Sattayarak, N. (2011). "Subsurface Carboniferous-Cretaceous Geology of NE Thailand," in *The Geology of Thailand*. Editors M. F. Ridd, A. J. Barber, and M. J. Crow (London: The Geological Society), 185–222.

Bunopas, S. (1983). "Palaeozoic Succession in Thailand," in Proceedings of the Workshop on Stratigraphic Correlation of Thailand and Malaysia 1983 Conference, Haad Yai, Thailand, 39–76.

Cabral, F. A. A., Silveira, A. C., Ramos, G. M. S., Miranda, T. S., Barbosa, J. A., and Neumann, V. H. M. L. (2019). Microfacies and Diagenetic Evolution of the Limestones of the Upper Part of the Crato Formation, Araripe Basin,

Northeastern Brazil. *Braz. J. Geol.* 49 (1), e20180097. doi:10.1590/2317-4889201920180097

Chandra, K., Mishra, C. S., Samanta, U., Gupta, A., and Mehrotra, K. L. (1994). Correlation of Different Maturity Parameters in the Ahmedabad-Mehsana Block of the Cambay basin. *Org. Geochem.* 21 (3–4), 313–321. doi:10.1016/0146-6380(94)90193-7

Chenrai, P., and Fuengfu, S. (2019). Organic Geochemistry of the Lower Permian Tak Fa Formation in Phetchabun Province, Thailand: Implications for its Paleoenvironment and Hydrocarbon Generation Potential. *Acta Geochim.* 39 (3), 291–306. doi:10.1007/s11631-019-00370-w

Chitnarin, A., Crasquin, S., Charoentitirat, T., Tepnarong, P., and Thanee, N. (2012). Ostracods (Crustacea) of the Early-Middle Permian from Central thailand (Indochina Block). Part I. Order Palaeocopida. *Geodiversitas* 34, 801–835. doi:10.5252/g2012n4a5

Chitnarin, A., Crasquin, S., Chonglakmani, C., Broutin, J., Grote, P. J., and Thanee, N. (2008). Middle Permian Ostracods from Tak Fa Limestone, Phetchabun Province, Central Thailand. *Geobios* 41, 341–353. doi:10.1016/j.geobios.2007.09.001

Chonglakmani, C. (2005). *Paleogeography of the Permian System in the Saraburi-Nakhon Ratchasima area (in Thai)*. Thailand: Suranaree University of Technology.

Chonglakmani, C., and Helmcke, D. (2001). Geodynamic Evolution of Loei and Phetchabun Regions - Does the Discovery of Detrital Chromian Spinels from the Nam Duk Formation (Permian, North-Central Thailand) Provide New Constraint? *Gondwana Res.* 4, 437–442. doi:10.1016/s1342-937x(05)70343-9

Chonglakmani, C., and Sattayarak, N. (1984). *Geological Map of Thailand on 1: 250,000 Scale: Sheet Changwat Phetchabun (NE47-16)*. Bangkok, Thailand: Department of Mineral Resources.

Cobbold, P. R., and Rodrigues, N. (2007). Seepage Forces, Important Factors in the Formation of Horizontal Hydraulic Fractures and Bedding-Parallel Fibrous Veins ('beef' and 'Cone-in-Cone'). *Geofluids* 7, 313–322. doi:10.1111/j.1468-8123.2007.00183.x

Cobbold, P. R., Zanella, A., Rodrigues, N., and Løseth, H. (2013). Bedding-parallel Fibrous Veins ('Beef' and 'Cone-in-Cone'): Worldwide Occurrence and Possible Significance in Terms of Fluid Overpressure, Hydrocarbon Generation and Mineralization. *Mar. Pet. Geology.* 43, 1–20. doi:10.1016/j.marpetgeo.2013.01.010

Demény, A., Kele, S., and Siklósy, Z. (2010). Empirical Equations for the Temperature Dependence of Calcite-Water Oxygen Isotope Fractionation from 10 to 70°C. *Rapid Commun. Mass. Spectrom.* 24 (24), 3521–3526. doi:10.1002/rcm.4799

Dickson, J. A. D., and Coleman, M. L. (1980). Changes in Carbon and Oxygen Isotope Composition during limestone Diagenesis. *Sedimentology* 27, 107–118. doi:10.1111/j.1365-3091.1980.tb01161.x

Franks, P. C. (1969). Nature, Origin, and Significance of Cone-in-Cone Structures in the Kiowa Formation (Early Cretaceous), North-Central Kansas. *J. Sediment. Res.* 39, 1483–1454. doi:10.1306/74d71e51-2b21-11d7-8648000102c1865d

Greene, S. E., Bottjer, D. J., Corsetti, F. A., Berelson, W. M., and Zonneveld, J.-P. (2012). A Subseafloor Carbonate Factory across the Triassic-Jurassic Transition. *Geology* 40 (11), 1043–1046. doi:10.1130/g33205.1

Heindel, K., Richoz, S., Birgel, D., Brandner, R., Klügel, A., Krystyn, L., et al. (2015). Biogeochemical Formation of Calyx-Shaped Carbonate crystal Fans in the Subsurface of the Early Triassic Seafloor. *Gondwana Res.* 27 (2), 840–861. doi:10.1016/j.gr.2013.11.004

Helmcke, D., and Kraikhong, C. (1982). On the Geosynclinals and Orogenic Evolution of Central and Northeastern Thailand. *J. Geol. Soc.* 5, 47–52.

Hodgson, W. A. (1966). Carbon and Oxygen Isotope Ratios in Diagenetic Carbonates from marine Sediments. *Geochim. Cosmochim. Acta* 30, 1223–1233. doi:10.1016/0016-7037(66)90121-9

Hooker, J. N., Abu-Mahfouz, I. S., Meng, Q., and Cartwright, J. (2019). Fractures in Mudrocks: Advances in Constraining Timing and Understanding Mechanisms. *J. Struct. Geol.* 125, 166–173. doi:10.1016/j.jsg.2018.04.020

Huang, W.-Y., and Meinschein, W. G. (1979). Sterols as Ecological Indicators. *Geochim. Cosmochim. Acta* 43, 739–745. doi:10.1016/0016-7037(79)90257-6

Hughes, W. B., Holba, A. G., and Dzou, L. I. P. (1995). The Ratios of Dibenzothiophene to Phenanthrene and Pristane to Phytane as Indicators of Depositional Environment and Lithology of Petroleum Source Rocks. *Geochim. Cosmochim. Acta* 59, 3581–3598. doi:10.1016/0016-7037(95)00225-o

Irwin, H., Curtis, C., and Coleman, M. (1977). Isotopic Evidence for Source of Diagenetic Carbonates Formed during Burial of Organic-Rich Sediments. *Nature* 269 (5625), 209–213. doi:10.1038/269209a0

Kershaw, S., and Guo, L. (2016). Beef and Cone-in-Cone Calcite Fibrous Cements Associated with the End-Permian and End-Triassic Mass Extinctions: Reassessment of Processes of Formation. *J. Palaeogeogr.* 5, 28–42. doi:10.1016/j.jop.2015.11.003

Kozar, M. G., Crandall, G. F., and Hall, S. E. (1992). "Integrated Structural and Stratigraphic Study of the Khorat Basin, Rat Buri Limestone (Permian), Thailand," in Proceedings of National Conference on Geological Resources of Thailand, Potential for Future Development, Bangkok: Thailand (Bangkok, Thailand: Department of Mineral Resources), 682–736.

Landais, P. (1996). *Petroleum Geochemistry and Geology*. New York: American Chemical Society, 743.

Large, D. J., and Gize, A. P. (1996). Pristane/phytane Ratios in the Mineralized Kupferschiefer of the Fore-Sudetic Monocline, Southwest Poland. *Ore Geol. Rev.* 11, 89–103. doi:10.1016/0169-1368(95)00017-8

Lijmbach, W. M. (1975). "SP (1) on the Origin of Petroleum," in Proceedings of the 9th World Petroleum Congress, Tokyo, Japan, May 11–16, 1975.

Liu, Z., Chen, D., Zhang, J., Lü, X., Wang, Z., Liao, W., et al. (2019). Pyrite Morphology as an Indicator of Paleoredox Conditions and Shale Gas Content of the Longmaxi and Wufeng Shales in the Middle Yangtze Area, South China. *Minerals* 9 (7), 428. doi:10.3390/min9070428

Luan, G., Dong, C., Azmy, K., Lin, C., Ma, C., Ren, L., et al. (2019). Origin of Bedding-Parallel Fibrous Calcite Veins in Lacustrine Black Shale: a Case Study from Dongying Depression, Bohai Bay Basin. *Mar. Pet. Geol.* 102, 873–885. doi:10.1016/j.marpetgeo.2019.01.010

Ma, C., Dong, C., Luan, G., Lin, C., Liu, X., and Elsworth, D. (2016). Types, Characteristics and Effects of Natural Fluid Pressure Fractures in Shale: A Case Study of the Paleogene Strata in Eastern China. *Pet. Exploration Dev.* 43 (4), 634–643. doi:10.1016/s1876-3804(16)30074-x

Marshall, J. D. (1982). Isotopic Composition of Displacive Fibrous Calcite Veins: Reversals in Pore Water Composition Trends during Burial Diagenesis. *J. Sediment. Res.* 52, 615–630. doi:10.1306/212f7fb3-2b24-11d7-8648000102c1865d

Meng, Q., Hooker, J., and Cartwright, J. (2017). Early Overpressuring in Organic-Rich Shales during Burial: Evidence from Fibrous Calcite Veins in the Lower Jurassic Shales-With-Beef Member in the Wessex Basin, UK. *J. Geol. Soc.* 174, 869–882. doi:10.1144/jgs2016-146

Metcalfe, I., and Sone, M. (2008). Biostratigraphy and Palaeobiogeography of Lower Permian (Lower Kungurian) Conodonts from the Tak Fa Formation (Saraburi Limestone), Thailand. *Palaeogeogr. Palaeoclimatol. Palaeoecol.* 257 (1–2), 139–151. doi:10.1016/j.palaeo.2007.09.014

Miles, J. A. (1989). *Illustrated Glossary of Petroleum Geochemistry*. Oxford: Oxford University.

Moldowan, J. M., Seifert, W. K., and Gallegos, E. J. (1985). Relationship between Petroleum Composition and Depositional Environment of Petroleum Source Rocks. *AAPG Bull.* 69, 1255–1268. doi:10.1306/ad462bc8-16f7-11d7-8645000102c1865d

Morad, S. (2009). "Carbonate Cementation in Sandstones: Distribution Patterns and Geochemical Evolution," in *Carbonate Cementation in Sandstones*. Editors S. Morad (John Wiley & Sons), 1–26. doi:10.1002/9781444304893.ch1

Morley, C. K., Ampaiwan, P., Thanudamrong, S., Kuenphan, N., and Warren, J. (2013). Development of the Khao Khwang Fold and Thrust Belt: Implications for the Geodynamic Setting of Thailand and Cambodia during the Indosinian Orogeny. *J. Asian Earth Sci.* 62, 705–719. doi:10.1016/j.jseaes.2012.11.021

Moustafa, Y. M., and Morsi, R. E. (2012). "Biomarkers," in *Chromatography and its Applications*. Editor S. Dhanarasu (Croatia: Intech), 165–186.

Nakornsri, N. (1981). *Geology and Mineral Resources of Amphoe Ban Mi (ND 47-4)*. Bangkok, Thailand: Department of Mineral Resources.

Nuriel, P., Rosenbaum, G., Uysal, T. I., Zhao, J., Golding, S. D., Weinberger, R., et al. (2011). Formation of Fault-Related Calcite Precipitates and Their Implications for Dating Fault Activity in the East Anatolian and Dead Sea Fault Zones. *Geol. Soc. Lond. Spec. Publications* 359 (1), 229–248. doi:10.1144/sp359.13

Osborne, M. J., and Swarbrick, R. E. (1997). Mechanism for Generative Overpressure in Sedimentary basin: a Reevalution. *AAPG Bull.* 81, 1023–1041. doi:10.1306/522B49C9-1727-11

Peters, K. E., and Moldowan, J. M. (1993). *The Biomarker Guide: Interpreting Molecular Fossils in Petroleum and Ancient Sediments*. Englewood Cliff: Pentice Hall.

Peters, K. E., Walters, C. C., and Moldowan, J. M. (2005). *The Biomarker Guide*. Cambridge: Cambridge University Press, 471.

Powell, T. G. (1988). Pristane/phytane Ratio as Environmental Indicator. *Nature* 333, 604. doi:10.1038/333604a0

Racey, A. (2011). "Petroleum Geology," in *The Geology of Thailand*. Editors M. F. Ridd, A. J. Barber, and M. J. Crow (London: The Geological Society), 351–392.

Raiswell, R. (1987). Non-steady State Microbiological Diagenesis and the Origin of Concretions and Nodular Limestones. *Geol. Soc. Lond. Spec. Publications* 36 (1), 41–54. doi:10.1144/gsl.sp.1987.036.01.05

Ridd, M. F., Barber, A. J., and Crow, M. J. (2011). *The Geology of Thailand*. London: The Geological Society. doi.org/doi:10.1144/GOTH

Rodrigues, N., Cobbold, P. R., Loseth, H., and Ruffet, G. (2009). Widespread Bedding-Parallel Veins of Fibrous Calcite ('beef') in a Mature Source Rock (Vaca Muerta Fm, Neuquén Basin, Argentina): Evidence for Overpressure and Horizontal Compression. *J. Geol. Soc.* 166, 695–709. doi:10.1144/0016-76492008-111

Shanmugam, G. (1985). Significance of Coniferous Rain Forests and Related Organic Matter in Generating Commercial Quantities of Oil, Gippsland Basin, Australia. *AAPG Bull.* 69, 1241–1254. doi:10.1306/ad462bc3-16f7-11d7-8645000102c1865d

Simms, M. J. (2004). The Wessex Basin (Dorset and Central Somerset). *Geol. Conservation Rev. Ser.* 30, 53–107. doi:10.1016/j.jhg.2004.07.003

Sivan, P., Datta, G. C., and Singh, R. R. (2008). Aromatic Biomarkers as Indicators of Source, Depositional Environment, Maturity and Secondary Migration in the Oils of Cambay Basin, India. *Org. Geochem.* 39, 1620–1630. doi:10.1016/j.orggeochem.2008.06.009

Tissot, B., Deroo, G., and Hood, A. (1978). Geochemical Study of the Uinta Basin: Formation of Petroleum from the Green River Formation. *Geochim. Cosmochim. Acta* 42, 1469–1485. doi:10.1016/0016-7037(78)90018-2

Tribovillard, N., Petit, A., Quijada, M., Riboulleau, A., Sansjofre, P., Thomazo, C., et al. (2018). A Genetic Link Between Synsedimentary Tectonics-Expelled Fluids, Microbial Sulfate Reduction and Cone-in-Cone Structures. *Mar. Pet. Geol.* 93, 437–450. doi:10.1016/j.marpetgeo.2018.03.024

Udchachon, M., Burrett, C., Thassanapak, H., Chonglakmani, C., Campbell, H., and Feng, Q. (2014). Depositional Setting and Paleoenvironment of an Alatoconchid-Bearing Middle Permian Carbonate Ramp Sequence in the Indochina Terrane. *J. Asian Earth Sci.* 87, 37–55. doi:10.1016/j.jseaes.2014.02.012

Ueno, K., and Charoentitirat, T. (2011). "Carboniferous," in *The Geology of Thailand*. Editors M. F. Ridd, A. J. Barber, and M. J. Crow (London: The Geological Society), 71–136.

Uysal, I. T., Feng, Y.-x., Zhao, J.-x., Bolhar, R., Işik, V., Baublys, K. A., et al. (2011). Seismic Cycles Recorded in Late Quaternary Calcite Veins: Geochronological, Geochemical and Microstructural Evidence. *Earth Planet. Sci. Lett.* 303, 84–96. doi:10.1016/j.epsl.2010.12.039

Vattanasak, H., Chonglakmani, C., Feng, Q., and Morley, C. K. (2020). Chert Geochemistry, Depositional Setting, Stratigraphic and Structural Significance for the Permian Nong Pong Formation, Khao Khwang Fold and Thrust Belt, Saraburi, Thailand. *J. Asian Earth Sci.* 191, 104234. doi:10.1016/j.jseaes.2020.104234

Veizer, J., Ala, D., Azmy, K., Bruckschen, P., Buhl, D., Bruhn, F., et al. (1999). 87Sr/86Sr, δ13C and δ18O Evolution of Phanerozoic Seawater. *Chem. Geology.* 161, 59–88. doi:10.1016/s0009-2541(99)00081-9

Wang, Z.-Y., Xin, Y.-Z., Gao, D.-M., Li, F.-M., Morgan, J., and Xing, B.-S. (2010). Microbial Community Characteristics in a Degraded Wetland of the Yellow River Delta. *Pedosphere* 20, 466–478. doi:10.1016/s1002-0160(10)60036-7

Waples, D. W., and Machihara, T. (1991). "Biomarkers for Geologists," in *American Association of Petroleum Geologists Methods in Exploration Series*, 91–99.

Warren, J. K., George, S. C., Hamilton, P. J., and Tingate, P. (1998). Proterozoic Source Rocks: Sedimentology and Organic Characteristics of the Velkerri Formation, Northern Territory, Australia. *AAPG Bull.* 82, 442–463. doi:10.1306/1d9bc435-172d-11d7-8645000102c1865d

Warren, J., Morley, C. K., Charoentitirat, T., Cartwright, I., Ampaiwan, P., Khositchaisri, P., et al. (2014). Structural and Fluid Evolution of Saraburi Group Sedimentary Carbonates, central Thailand: A Tectonically Driven Fluid System. *Mar. Pet. Geol.* 55, 100–121. doi:10.1016/j.marpetgeo.2013.12.019

Wieldchowsky, C. C., and Young, J. D. (1985). "Regional Facies Variation in Permian Rocks of the Phetchabun Fold and Thrust Belt, Thailand," in Proceedings of the on Geology and Mineral Resources Development of North-Eastern Thailand 1985 Conference, Khon Kaen, Thailand (Khon Kaen, Thailand: Khon Kaen University), 41–55.

Wilkin, R. T., Barnes, H. L., and Brantley, S. L. (1996). The Size Distribution of Framboidal Pyrite in Modern Sediments: an Indicator of Redox Conditions. *Geochim. Cosmochim. Acta* 60 (20), 3897–3912. doi:10.1016/0016-7037(96)00209-8

Wolff, G. A., Rukin, N., and Marshall, J. D. (1992). Geochemistry of an Early Diagenetic Concretion from the Birchi Bed. *Org. Geochem.* 19, 431–444. doi:10.1016/0146-6380(92)90010-u

Yan, Y., Huang, B., Zhang, D., Charusiri, P., and Veeravinantanakul, A. (2018). Paleomagnetic Study on the Permian Rocks of the Indochina Block and its Implications for Paleogeographic Configuration and Northward Drifting of Cathaysialand in the Paleo-Tethys. *J. Geophys. Res. Solid Earth* 123 (6), 4523–4538. doi:10.1029/2018jb015511

Yu, H., Zhou, X., Wang, J., Guo, C., Wei, H., and Chen, D. (2015). The Origin of Bedding-Parallel Fibrous Calcite Veins in the Lower Permian Chihsia Formation in Western Hubei Province, South China. *Sci. Bull.* 60 (20), 1778–1786. doi:10.1007/s11434-015-0903-z

Zanella, A., and Cobbold, P. R. (2012). "Beef: Evidence for Fluid Overpressure and Hydraulic Fracturing in Source Rocks During Hydrocarbon Generation and Tectonic Events: Field Studies and Physical Modelling," in Proceeding of the Geofluids VII international conference, Rueil-Malmaison, June, 2012.

Zhang, J., Jiang, Z., Jiang, X., Wang, S., Liang, C., and Wu, M. (2016). Oil Generation Induces Sparry Calcite Formation in Lacustrine Mudrock, Eocene of East China. *Mar. Pet. Geol.* 71, 344–359. doi:10.1016/j.marpetgeo.2016.01.007

Zhang, J., Jiang, Z., Wang, S., Wang, R., Zhang, Y., and Du, W. (20221). Bedding-Parallel Calcite Veins as a Proxy for Shale Reservoir Quality. *Mar. Pet. Geol.* 127, 104975. doi:10.1016/j.marpetgeo.2021.104975

Conflict of Interest: Author KL was employed by the company PTT Exploration and Production.

The remaining authors declare that the research was conducted in the absence of any commercial or financial relationships that could be construed as a potential conflict of interest.

Publisher's Note: All claims expressed in this article are solely those of the authors and do not necessarily represent those of their affiliated organizations, or those of the publisher, the editors and the reviewers. Any product that may be evaluated in this article, or claim that may be made by its manufacturer, is not guaranteed or endorsed by the publisher.

frontiers in Earth Science

ORIGINAL RESEARCH
published: 21 January 2022
doi: 10.3389/feart.2021.770236

Topographic and Climatic Control on Chemical Weathering of Mountainous Riverine Sediments of Hainan Island, South China Sea

Fangjian Xu[1,2], Bangqi Hu[2,3], Jingtao Zhao[3], Xiting Liu[4], Ruyong Cui[3], Xue Ding[3,5], Guifeng Wang[6] and Jianping Huang[7]*

[1]College of Marine Science, Hainan University, Haikou, China, [2]Laboratory for Marine Mineral Resources, Qingdao National Laboratory for Marine Science and Technology, Qingdao, China, [3]Qingdao Institute of Marine Geology, Ministry of Natural Resources, Qingdao, China, [4]College of Marine Geosciences Key Laboratory of Submarine Geosciences and Prospecting Technology, Ocean University of China, Qingdao, China, [5]State Key Laboratory of Loess and Quaternary Geology, Institute of Earth Environment, Chinese Academy of Sciences, Xi'an, China, [6]Marine Geological Institute of Hainan Province, Haikou, China, [7]School of Geoscience, China University of Petroleum, Qingdao, China

Hainan Island, the largest island in the northwestern South China Sea (SCS), is characterized by many tropical mountainous rivers that flow into the SCS. The geochemistry of these riverine sediments and the factors controlling the weathering intensity are still not well understood. In this study, sedimentary geochemistry has been investigated by using 45 riverine sediments collected from 18 major rivers on Hainan Island. The Hainan riverine sediments are only first-cycle rather than polycyclic sediments, and they faithfully reflect the present weathering intensity. The high and steady values of the Chemical Index of Alteration (CIA) indicate that the riverine sediments at different parts of the Hainan Island have overall undergone intensive chemical weathering. The low values of Weathering Index of Parker (WIP) and high α_{Ca}, α_{K}, α_{Sr}, and α_{Ba} values of north Hainan indicate the highest weathering degree, which is mainly influenced by the flat topography. The values of α_{Na}, α_{K}, α_{Sr}, and α_{Ba} of southwest Hainan which are higher than those of east Hainan suggest that the leaching of elements such as Na, K, Sr, and Ba is more extreme (i.e., more intensive weathering). These are mainly caused by the different physical denudation due to different summer precipitation. Overall, the Hainan Island is featured by intensive chemical weathering and is classified as a typical transport-limited weathering regime. Therefore, the geochemistry of the riverine sediments of the Hainan Island is different from that of sediments in tectonically active regions (e.g., Taiwan Island).

Keywords: geochemistry, riverine sediment, weathering, Hainan Island, South China Sea

OPEN ACCESS

Edited by:
Jiangong Wei,
Guangzhou Marine Geological Survey, China

Reviewed by:
Chao Li,
Tongji University, China
Yancheng Zhang,
Sun Yat-sen University, China

****Correspondence:***
Bangqi Hu
bangqihu@gmail.com

Specialty section:
This article was submitted to Geochemistry, a section of the journal Frontiers in Earth Science

Received: *03 September 2021*
Accepted: *28 December 2021*
Published: *21 January 2022*

Citation:
Xu F, Hu B, Zhao J, Liu X, Cui R, Ding X, Wang G and Huang J (2022) Topographic and Climatic Control on Chemical Weathering of Mountainous Riverine Sediments of Hainan Island, South China Sea. Front. Earth Sci. 9:770236. doi: 10.3389/feart.2021.770236

HIGHLIGHTS

The Hainan riverine sediments have undergone high weathering conditions.
The highest chemical weathering intensities of sediments in north Hainan are mainly influenced by the flat topography.
Weathering difference between southwest and east Hainan is caused by different summer rainfall conditions due to the orographic effect of the central mountains.
The weathering processes of the sediments in Hainan are typical transport-limited weathering regimes.

INTRODUCTION

Rivers are the main passages of land-derived sediments into the sea. The mineralogical and geochemical characteristics of sediments are controlled by lithology, topographic settings, weathering, diagenesis, sedimentary sorting, and recycling in catchments, and can be used to better understand the geochemical cycle, land–ocean interaction, and global change (Gaillardet et al., 1997; Yang et al., 2004; Liu et al., 2007; Li and Yang, 2010; Clift et al., 2014; Li G. et al., 2016; Jian et al., 2020; Xu et al., 2021).

Numerous studies have focused mainly on world-class rivers, such as the Amazon (Gaillardet et al., 1997; Bouchez et al., 2011), Mekong (Egashira et al., 1997), Congo (Dupré et al., 1996; Dinis et al., 2020), Yangtze and Yellow (Yang et al., 2004), and Pearl (Liu et al., 2007) rivers, because they play leading roles in delivering the great mass of water and terrestrial materials to the sea. However, subsequent studies have found that small rivers may have distinctive features in comparison to the major river systems in the world (Milliman and Syvitski, 1992; Milliman and Farnsworth, 2011; Yang and Yin, 2018). Thus, the significance of rivers with small drainage basins has been reconsidered. Recently, the characteristics of sediment geochemistry in small rivers, for example, central Japan (Ohta et al., 2005), western Korea (Xu et al., 2009), southeast China (Zhou et al., 2010; Su et al., 2017; Jian et al., 2020), Taiwan Island (Li et al., 2013; Deng et al., 2019), Malaysia, Sumatra, Borneo (Liu et al., 2012), Luzon, and Philippines (Liu et al., 2009), have aroused wide concern.

Hainan Island is the second largest island in China and the highest island in the northern South China Sea (SCS) and is located at the low latitude tropical area with heavy rainfall but low sediment load (~4 Mt/yr, million tons per year, Zhang et al., 2013). Clay mineralogy analysis suggested that the weathering status of Hainan is comparable with that of the Pearl River and is inconsistent with that of rivers in Taiwan (Hu et al., 2014). To our knowledge, the geochemistry of the riverine sediments of Hainan Island and the weathering mechanism have not been constrained systemically, which are characterized by different lithological and topographic settings, and along with the tropical East Asian monsoon climate but with different rainfall. In this study, sediment geochemistry has been investigated on 45 riverine sediments collected from 18 major rivers on the Hainan Island. Our objectives are to 1) reveal the characteristic features of sediment geochemistry, 2) establish a geochemistry database for riverine sediments from Hainan Island, and 3)

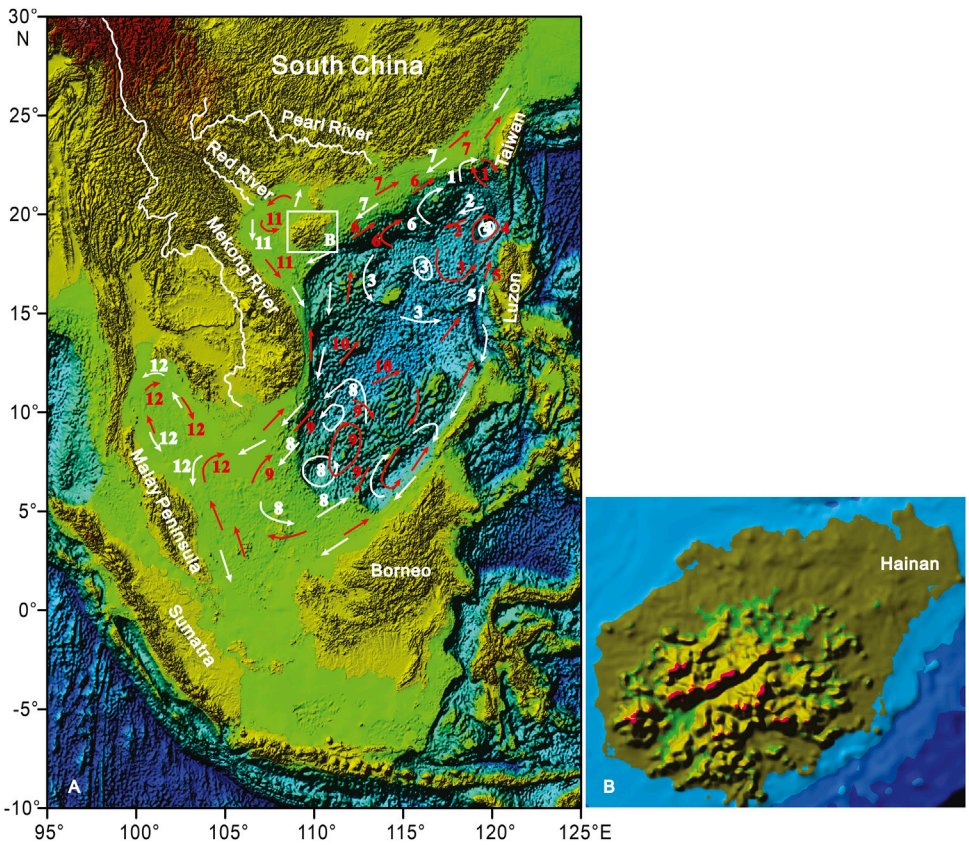

FIGURE 1 | (A) Location map of the Hainan Island and the surface currents in the South China Sea. **(B)** Topographic map of the Hainan Island. Numbers for winter (white) and summer (red) surface currents: 1, loop current; 2, SCS branch of Kuroshio; 3, NW Luzon Cyclonic Gyre; 4, NW Luzon Cyclonic Eddy; 5, NW Luzon Coastal Current; 6, SCS Warm Current; 7, Guangdong Coastal Current; 8, SCS Southern Cyclonic Gyre; 9, SCS Southern Anticyclonic Gyre; 10, SE Vietnam Offshore Current; 11, Gulf of Tonkin Surface Current; 12, Gulf of Thailand Surface Current. Major surface currents after Liu et al. (2016).

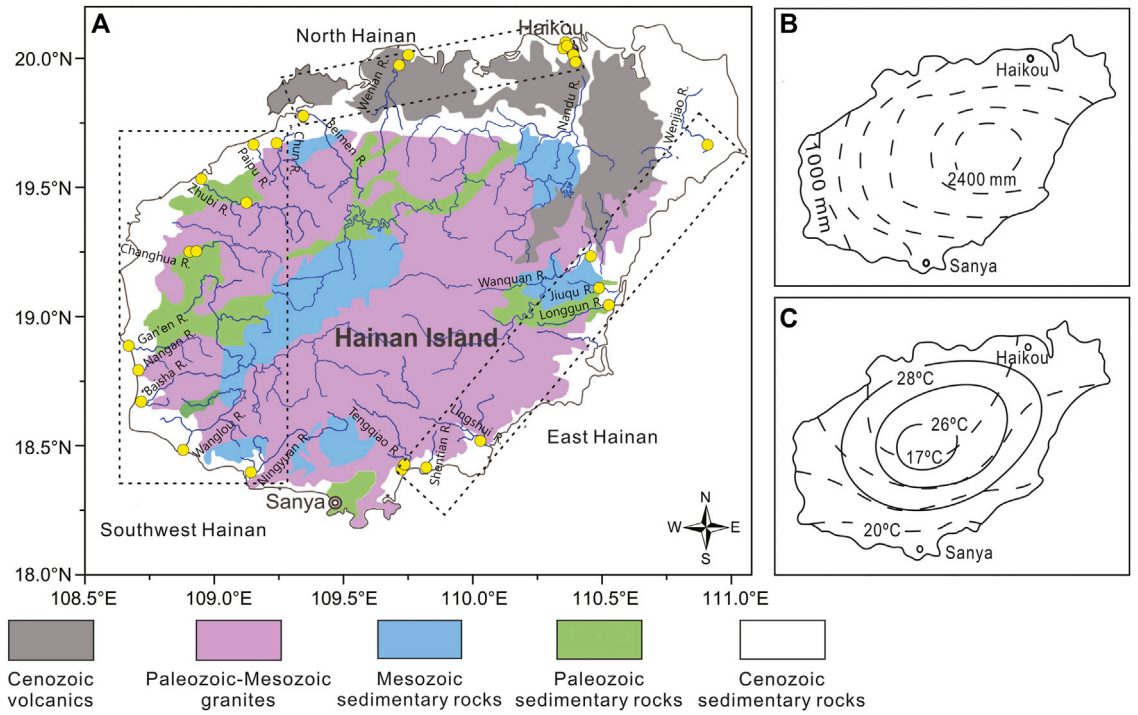

FIGURE 2 | (A) Geological map and the locations of riverine samples on the Hainan Island. Modified from Shi et al. (2011) and Hu et al. (2014). **(B)** Annual rainfall and **(C)** temperature of January (dashed lines) and July (solid lines) of the Hainan Island (modified from http://gzdl.cooco.net.cn/testdetail/91943/). The blue lines indicate the river networks. Note that some of the sampling sites are overlapped on the map.

discuss the factors controlling the chemical weathering intensity of sediments in tropical Hainan.

Regional Setting

Hainan Island is the second largest island (35.4×10^3 km^2, **Figure 1A**) in China. The Hainan Island is tectonically stable (Metcalfe, 2009) and is characterized by central high mountains surrounding low hills, platforms, and plains in coastal regions (**Figure 1B**). The high mountains are located south of the central part of the island, accounting for 25.1% of the island's area. The vast platforms are mainly distributed in the north Hainan (20–50 m above sea level), accounting for about one-third of the total area of the island (http://www.hnszw.org.cn/xiangqing.php?ID=54349, **Figure 1B**). The main rock types are granitic rocks which are mainly exposed in the southwest and east Hainan, and basalts are distributed predominantly in north Hainan. Sedimentary rocks, including slate, sandstone, limestone, and volcanic clastic, are scattered on the island, while Quaternary sediments have existed mainly in the coastal plain regions (**Figure 2A**, Shi et al., 2011).

The Hainan Island is located on the northern edge of the tropics and is dominated by a tropical monsoon climate with dense vegetation cover (Committee of Vegetation Map of China, 2007; Zhang et al., 2013). The annual mean rainfall is ~1,500 mm, with ~80% of it occurring between May and October (http://www.worldweather.org), especially during the tropical cyclone period (Zhang et al., 2013). A large rainfall difference occurred between different parts of Hainan because of the orographic effect of the central mountains. The annual mean rainfall is distributed in a ring pattern, tending to reduce from more than 2,000 mm in the east and central Hainan to less than 1,000 mm in the southwest Hainan (**Figure 2B**). Fluvial drainage systems are well developed in the region. There are more than 100 rivers with a drainage area of over 100 km^2 each. Over the past several decades, the total discharge and the total riverine sediment load from Hainan are ~31×10^9 m^3/yr and ~4 Mt/yr (Zhang et al., 2013), respectively.

The annual mean temperature is 25.4°C, with a maximum between May and October (http://www.worldweather.org). In July, the isotherm showed concentric circles, increasing from the central mountain to the coastal areas. In January, temperatures were lower in north Hainan, increasing from the northern to the southern areas (**Figure 2C**). In general, there is a relatively wet and dry climate in east and southwest Hainan.

MATERIALS AND METHODS

Sampling and Analytical Methods

A total of 45 riverine samples were collected downstream of estuary sites from 18 rivers on the Hainan Island in 2013 (**Figure 2A**). According to the lithology and climate conditions, the 18 studied rivers were grouped into three provinces: north Hainan (3 rivers), east Hainan (6 rivers), and

southwest Hainan (9 rivers). These sediment samples were collected from surface channels or bed deposits. The fine-grained fraction (<63 μm, after eliminating sand) used for geochemical analysis was wet-sieved from the bulk samples to minimize the grain-size effect (Yang et al., 2002; Bouchez et al., 2011; Li et al., 2013; Guo et al., 2018), then oven-dried, and ground to a powder. The major and trace elements were analyzed using an X-ray fluorescence spectrometer (XRF, Axios PW4400) and Perkin Elmer ELAN DRC II ICP-MS, respectively. The analytical accuracy was determined by analyzing certified reference materials (BCR-2, BHVO-2, GBW07315, and GBW07316). The analytical precision, as verified by replicate analysis, was better than 5%. The clay mineral compositions of the sediments have been reported by Hu et al. (2014).

Calculation of Weathering Indexes

The Chemical Index of Alteration (CIA) and the Weathering Index of Parker (WIP) have been widely used as proxies for the chemical weathering intensity in drainage basins. The CIA value is used to quantify the chemical weathering degree experienced by sediments, referring to the progressive loss of mobile elements such as Na, Ca, and K (Nesbitt and Young, 1982). The higher CIA values indicate stronger weathering which could be interpreted as a measure of the conversion extent of feldspars to clays. In contrast, the WIP simply reflects concentrations of Mg, Ca, Na, and K, and thus, it is considerably affected by quartz dilution and used to evaluate weathering in quartz-rich sediments (Garzanti et al., 2013; Garzanti et al., 2014). Using molecular proportions, the CIA and WIP were calculated as follows:

$$CIA = 100 \times \left(\frac{Al_2O_3}{Al_2O_3 + CaO* + Na_2O + K_2O} \right), \quad (1)$$

$$WIP = 100 \times \left(\frac{CaO*}{0.7} + \frac{2Na_2O}{0.35} + \frac{2K_2O}{0.25} + \frac{MgO}{0.9} \right), \quad (2)$$

where CaO* represents CaO associated with the silicate fraction only and is corrected for carbonate and phosphate (apatite). If the mole fraction of CaO ≤ Na_2O, then the value of CaO was used. If CaO > Na_2O, then the mole of CaO* was taken equivalent to Na_2O (McLennan, 1993).

Weathering intensities can be calculated for each single element (Ca, Na, K, Sr, and Ba) mobilized during incongruent weathering of silicates by comparing its concentration to that of an immobile element in samples and the upper continental crust (UCC, i.e., α value, Gaillardet et al., 1999; Garzanti et al., 2013). We calculated the α value with reference to the concentration of an immobile element whose magmatic compatibility is close to that of the mobile element (Gaillardet et al., 1999):

$$\alpha_{Ca} = \frac{[Ti/Ca]_{Sample}}{[Ti/Ca]_{UCC}}, \quad (3)$$

$$\alpha_{Na} = \frac{[Sm/Na]_{Sample}}{[Sm/Na]_{UCC}}, \quad (4)$$

$$\alpha_{K} = \frac{[Th/K]_{Sample}}{[Th/K]_{UCC}}, \quad (5)$$

$$\alpha_{Sr} = \frac{[Nd/Sr]_{Sample}}{[Nd/Sr]_{UCC}}, \quad (6)$$

$$\alpha_{Ba} = \frac{[Th/Ba]_{Sample}}{[Th/Ba]_{UCC}}. \quad (7)$$

The α ratios could also minimize the effects of quartz dilution, grain size, and recycling. According to the definition of the α value, α <1 indicates enrichment and α >1 implies depletion with respect to the UCC.

Major and Trace Elements, and the Chemical Weathering Intensity

The element concentrations are shown in **Table 1**. Most of the Hainan riverine sediments have Sc/Th values smaller than 1, while two samples have values higher than 1 on the north Hainan (**Figure 3A**). The CIA values of all the samples range from 72 to 90 (mean of 81), which indicates moderate to intensive weathering occurred in the Hainan Island. The CIA values exhibit no obvious correlation with Sc/Th ratios (**Figure 3A**). The WIP values of all the samples range from 18 to 52 (mean of 34). The CIA and WIP values of all the samples display an inverse linear relationship (**Figure 3B**), showing a similar trend with the Taiwan rivers (Selvaraj and Chen, 2006), Pearl, Red, and Mekong (Liu et al., 2007), Malay Peninsula, Sumatra, Borneo (Liu et al., 2012), and Luzon rivers (Liu et al., 2009). As shown in **Table 2**, the similar values of the CIA at different parts of the Hainan Island suggest the similar weathering degree of Hainan riverine sediments. However, the lower mean WIP value of north Hainan suggests a higher weathering degree.

The weathering indexes, such as α_{Ca}, α_{Na}, α_{K}, α_{Sr}, and α_{Ba}, are also >1 (**Table 2**). As shown in **Figure 3C**, a high coefficient correlation can be observed between some indexes indicating that these indexes give relatively consistent information on the weathering degree of Hainan riverine sediments. Overall, the α_{Ca}, α_{K}, α_{Sr}, and α_{Ba} values of north Hainan are higher than those of the southwest and east Hainan (**Figure 3C**). This also suggests the higher weathering degree of the north Hainan Island.

DISCUSSION

Topographic Control on the Highest Weathering of North Hainan

The elements Sc and Th are largely water immobile during chemical weathering. Typically, felsic rocks generally have Sc/Th values smaller than 1, and mafic rocks have higher Sc/Th values (Taylor and McLennan, 1985). Most of the Hainan riverine sediments have Sc/Th values smaller than 1, indicating the dominance of the felsic rocks in the catchment (i.e., granitic rocks and Quaternary sediments). Only two samples have Sc/Th values higher than 1 on the north Hainan, indicating the influence of the mafic rocks in the catchment (i.e., basalt rocks). The CIA values exhibit no obvious correlation with Sc/Th ratios (**Figure 3A**), suggesting that the chemical weathering intensities are mostly independent of the lithology of their source areas. This is consistent with the previous studies on

TABLE 1 | Major (unit %) and trace element (unit mg kg^{-1}) concentrations in the Hainan riverine sediments.

	Station	SiO_2	Al_2O_3	Fe_2O_3	MgO	MnO	CaO	Na_2O	K_2O	TiO_2	P_2O_5	Sc	V	Rb	Sr	Zr	Nb	Ba	Hf	Th	Nd	Sm
SW Hainan	NYH-1C	56.0	18.5	6.0	2.20	0.15	0.84	0.26	3.60	0.92	0.19	10.2	74	175	117	343	27.5	446	11.4	26.3	51.2	9.0
	NYH-2C	56.4	21.2	7.5	2.49	0.21	0.84	0.24	3.89	1.01	0.27	12.6	78	205	96	305	25.5	413	9.5	33.4	53.7	9.7
	WLH-1C	53.8	18.3	5.5	2.06	0.17	0.71	0.36	3.50	0.93	0.20	12.0	78	217	105	136	25.9	446	4.5	39.3	55.3	9.8
	WLH-2C	53.4	21.5	3.8	2.11	0.03	0.62	0.37	3.73	1.05	0.10	15.0	89	269	103	114	29.6	424	3.9	53.5	74.7	13.5
	WLH-4C	52.3	19.6	6.0	2.11	0.19	0.80	0.42	3.40	0.94	0.20	12.9	88	233	103	116	25.5	439	3.7	43.6	55.3	10.5
	BSH-2C	58.2	16.2	3.6	1.98	0.06	0.85	0.16	5.30	0.75	0.13	10.1	54	307	103	299	34.4	438	10.5	67.5	71.6	12.8
	NGH-1C	57.5	15.1	4.6	2.07	0.09	1.17	0.19	4.45	0.88	0.17	11.3	64	253	116	293	31.1	454	9.5	84.7	74.3	12.8
	NGH-2C	58.5	15.0	4.0	2.10	0.07	0.89	0.14	4.27	0.90	0.16	9.2	58	227	114	292	28.5	481	9.9	46.9	60.1	10.3
	GEH-2C	60.1	16.2	4.1	2.09	0.11	0.33	0.07	4.16	0.80	0.14	11.2	55	256	51	227	31.5	415	7.2	48.8	67.8	13.8
	CHJ-1C	46.3	18.1	13.3	2.69	0.44	1.31	0.24	2.76	0.75	0.27	12.9	72	178	151	283	23.5	506	9.4	39.5	58.7	11.4
	CHJ-2C	44.6	17.9	13.9	2.64	0.42	1.21	0.23	2.58	0.71	0.27	11.8	69	162	156	246	20.8	588	8.1	28.0	53.3	10.2
	CHJ-3C	43.8	17.9	14.4	2.73	0.49	1.25	0.18	2.53	0.73	0.26	13.2	77	176	153	169	19.9	591	5.2	30.1	58.1	11.7
	CHJ-4C	45.3	18.9	15.6	2.62	0.52	1.65	0.22	2.72	0.82	0.26	13.5	80	184	159	559	25.4	573	16.9	57.7	84.7	16.2
	CHJ-5C	46.2	18.8	15.8	2.64	0.55	1.65	0.22	2.82	0.85	0.26	13.4	82	188	153	528	24.2	550	15.1	42.0	67.9	14.0
	CHJ-6C	43.6	18.5	16.2	2.62	0.67	1.53	0.26	2.71	0.85	0.27	14.0	88	192	137	710	26.5	468	20.4	72.0	91.3	18.2
	ZBJ-1C	51.5	17.8	6.7	2.30	0.26	0.87	0.46	2.50	0.89	0.27	13.8	110	154	64	168	16.5	411	5.0	18.1	38.7	7.4
	ZBJ-2C	51.5	17.7	6.9	2.48	0.26	0.89	0.10	2.75	0.87	0.32	14.2	115	180	77	239	17.8	467	6.8	28.0	45.4	9.1
	ZBJ-3C	54.0	20.3	7.3	2.80	0.25	0.78	0.39	2.96	1.14	0.27	13.5	94	181	102	603	26.0	328	18.0	64.3	61.4	11.6
	ZBJ-4C	50.6	19.2	6.9	2.70	0.24	0.67	0.06	2.77	0.97	0.36	13.1	96	184	102	245	21.3	312	7.2	30.2	41.9	8.1
	PPQ-1C	48.8	21.3	6.6	2.92	0.24	0.62	0.24	3.43	1.03	0.34	10.5	95	178	89	432	27.1	300	11.6	27.7	43.2	8.2
	PPQ-2C	51.8	22.1	7.3	3.15	0.27	0.66	0.42	3.59	1.05	0.38	14.5	97	232	95	229	26.5	303	6.8	34.8	49.9	9.4
	CJ-1C	61.2	12.5	2.9	2.07	0.09	0.92	0.02	3.02	0.59	0.16	7.4	52	142	117	322	14.8	400	9.0	24.5	38.8	7.7
N Hainan	BMJ-1C	66.7	11.1	3.1	1.76	0.05	0.40	0.23	1.98	0.99	0.15	8.2	57	89	62	796	24.8	256	25.5	94.5	137.3	23.1
	BMJ-2C	65.1	12.4	3.0	1.83	0.05	0.41	0.15	2.03	1.08	0.18	10.2	57	88	64	1,438	29.3	256	40.8	116.9	186.2	34.3
	BMJ-3C	63.4	11.8	2.9	1.81	0.04	0.38	0.08	2.26	0.77	0.13	10.2	61	115	65	269	18.9	304	7.8	32.3	39.7	7.5
	WLJ-1C	55.4	17.2	6.2	1.80	0.09	0.46	0.51	1.47	1.61	0.33	11.4	100	73	54	225	26.0	273	6.2	20.1	39.1	6.9
	WLJ-2C	52.5	18.4	7.4	1.73	0.09	0.50	0.48	1.44	1.88	0.38	14.4	120	79	56	303	31.0	279	8.3	31.4	60.4	10.9
	WLJ-3C	49.1	20.0	8.7	1.70	0.10	0.57	0.49	1.34	2.00	0.37	14.4	136	79	52	336	31.8	284	9.1	40.3	71.6	13.2
	WLJ-4C	49.2	17.8	9.8	1.93	0.13	0.43	0.51	1.59	2.02	0.23	16.2	154	94	57	210	29.6	287	5.5	16.7	36.9	7.5
	WLJ-5C	52.3	17.8	7.8	1.74	0.13	0.40	0.47	1.46	1.88	0.31	13.9	123	81	53	202	28.9	264	5.5	18.4	36.8	7.0
	WLJ-6C	31.0	23.3	20.9	1.25	0.17	0.10	1.37	0.14	3.25	0.19	29.0	255	11	9	206	26.9	87	5.4	5.4	16.6	4.2
	NDJ-1C	38.1	22.4	12.6	2.28	0.12	0.91	1.13	1.71	2.21	0.34	21.5	192	101	76	197	31.2	277	5.2	18.5	40.7	7.9
	NDJ-2C	50.0	17.9	8.5	2.82	0.07	0.59	0.78	2.70	1.00	0.25	16.0	132	147	76	173	20.7	377	4.8	22.7	34.1	6.4
	NDJ-3C	44.5	19.2	8.3	2.47	0.04	1.05	1.32	2.22	1.05	0.69	12.9	111	122	106	150	21.7	333	4.0	22.2	41.8	8.0
	NDJ-5C	48.9	20.7	8.2	2.94	0.10	0.58	0.88	2.54	1.17	0.33	15.3	123	141	80	147	23.2	336	4.3	22.4	47.5	8.8
	NDJ-6C	47.0	21.0	9.6	2.01	0.15	0.72	0.62	1.84	2.12	0.29	15.1	145	103	74	195	29.3	347	5.4	19.3	35.9	7.1
E Hainan	WJH-1C	50.2	17.7	5.8	1.33	0.04	0.35	0.74	1.14	2.15	0.24	11.8	112	65	62	274	35.8	191	7.2	21.8	32.0	6.0
	WJH-2C	53.0	15.3	7.6	2.89	0.08	4.14	1.06	1.53	1.25	0.39	9.8	97	63	171	140	21.6	262	3.6	13.4	19.8	4.1
	WQH-8C	56.0	25.0	10.8	2.98	0.18	2.24	0.13	3.89	1.32	0.36	14.5	136	186	144	247	24.0	477	6.5	39.1	63.8	12.2
	JQJ-1C	60.9	15.3	4.8	2.24	0.04	0.35	0.43	1.76	0.74	0.30	8.9	88	71	71	192	12.1	323	5.2	12.6	24.3	4.4
	JQJ-2C	57.0	15.3	5.5	2.13	0.05	0.34	0.27	1.86	0.77	0.36	9.8	99	82	66	178	12.9	345	4.8	11.6	22.9	4.1
	LSH-1C	49.4	22.5	6.0	2.25	0.08	1.10	0.56	3.37	1.04	0.19	12.6	82	193	200	313	28.7	525	9.8	46.2	54.7	9.7
	LSH-2C	50.2	21.5	5.7	2.29	0.08	1.21	0.52	3.55	1.02	0.18	13.0	79	195	214	349	28.2	549	11.3	57.7	55.1	10.0
	STH-1C	47.8	25.6	6.2	1.82	0.07	0.85	0.19	2.67	1.03	0.13	13.4	100	147	158	270	22.8	551	7.6	29.3	45.8	7.8
	TQH-3C	52.0	21.0	6.1	2.25	0.06	0.64	0.44	3.64	0.92	0.18	13.7	78	191	115	174	23.1	460	5.3	38.7	57.1	10.5

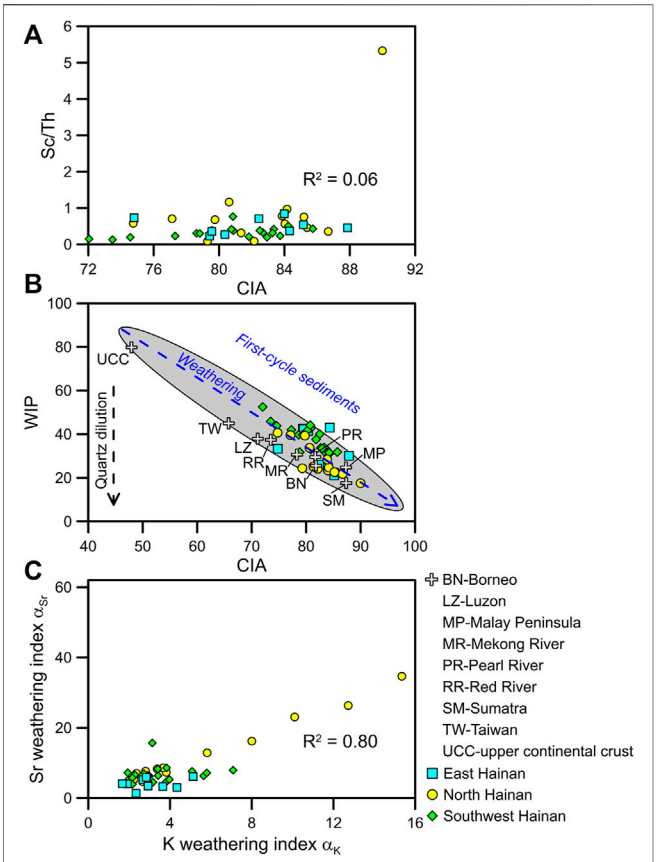

FIGURE 3 | Relationships between **(A)** CIA and Sc/Th, **(B)** CIA and WIP, and **(C)** α_K and α_{Sr} in riverine sediments of the Hainan Island. The CIA and WIP values of the UCC (Rudnick and Gao, 2003), Taiwan rivers (Selvaraj and Chen, 2006), Pearl, Red, and Mekong (Liu et al., 2007), Malay Peninsula, Sumatra, Borneo (Liu et al., 2012), and Luzon rivers (Liu et al., 2009) are also shown for comparison.

silicate weathering in river basins of mainland China (Li and Yang, 2010; Shao et al., 2012; Bi et al., 2015).

The comparison of CIA and WIP indexes could be used to identify the composition changes caused by weathering and recycling. The relationship between CIA and WIP is linear for first-cycle muds as well as for quartz-poor igneous materials (Garzanti et al., 2013; Garzanti et al., 2014; Guo et al., 2018). The inverse linear relationship of the CIA and WIP (**Figure 3B**) indeed suggests that the Hainan sediments only experienced a first sedimentary cycle, and thus faithfully reflects the present weathering intensity. Thus, the significantly low WIP values of sediments in north Hainan indicate strong chemical weathering intensity in the area.

Alkaline and alkaline earth metals tend to be depleted in riverine sediments due to their mobility during water–rock interactions (Stallard, 1988; Canfield, 1997; Garzanti et al., 2013). The α_{Ca}, α_{Na}, α_K, α_{Sr}, and α_{Ba} values are always >1 (**Table 2**), indicating that most alkali and alkaline elements in parent rocks on the Hainan Island can be easily and intensively weathered under warm and humid climate conditions. As shown in **Table 2**, the α_{Ca}, α_K, α_{Sr}, and α_{Ba} values of the north Hainan are much higher than those of the east and southwest Hainan, also indicating higher weathering degree than the latter. As noted above, the vast platforms are mainly distributed in the north Hainan, while the high mountains are located south of the central part of the island. Indeed, the topography could exert an important impact on sediment and its comminution process (Bi et al., 2015; Li C. et al., 2016). Considering that there is no obvious difference in climate conditions between the north and east Hainan (**Figure 2**), the chemical weathering intensities are also independent of the lithology of their source areas. We suggest that the highest chemical weathering intensities of sediments in north Hainan are mainly influenced by the flat topography under a favorable monsoon climate.

TABLE 2 | Proxies for the chemical weathering intensity of the Hainan riverine sediments.

	CIA	WIP	α_{Ca}	α_{Na}	α_K	α_{Sr}	α_{Ba}
Southwest Hainan	80.5	37.9	6.0	52.5	3.4	6.6	5.9
North Hainan	82.5	27.7	16.1	27.9	5.6	12.4	7.5
East Hainan	82	33.8	9.9	17.9	3.1	4.1	4.3

Lower Rainfall Control on Higher Weathering of Southwest Than East Hainan

The CIA and WIP values of sediments on the southwest and east Hainan Island are similar, indicating the similar weathering degree of the riverine sediments. However, the α_{Na}, α_K, α_{Sr}, and α_{Ba} values of southwest Hainan are much higher than those of the east Hainan. These suggest that although the overall weathering degree of the southwest Hainan is comparable with the east Hainan, the leaching of elements such as Na, K, Sr, and Ba is more extreme. This is also supported by the more negative Eu anomalies at the southwest than the east Hainan (0.45 and 0.65, respectively, unpublished data), reflecting stronger feldspar dissolution. The east and southwest Hainan are both located in a tectonically stable area (Metcalfe, 2009). Moreover, the main rock types are the same, that is, granitic rocks (Shi et al., 2011). As noted above, located in the rain shadow because of the orographic effect of the central mountains, the summer rainfall of southwest Hainan is lower than that of east Hainan. In addition, southwest Hainan is rich in light and heat, leading to a large amount of evaporation, while evaporation of the east part is relatively small due to heavy rainfall and the long rain period (Yang et al., 2013). Thus, the physical denudation should be stronger in the east than the southwest Hainan Island. The riverine sediments in southwest Hainan may experience longer residence time and stronger weathering intensity than those in east Hainan. Further studies on the "residence time" (Suresh et al., 2013) or "comminution age" (DePaolo et al., 2006; Li et al., 2015) of sediments from the small mountainous rivers in the southwest and east Hainan are needed to confirm this proposal.

Intensive Weathering of Hainan Compared With the Adjacent Area

The weathering trend can be further examined by ternary diagrams of Al_2O_3-CaO*+Na_2O-K_2O (A-CN-K) (Nesbitt and

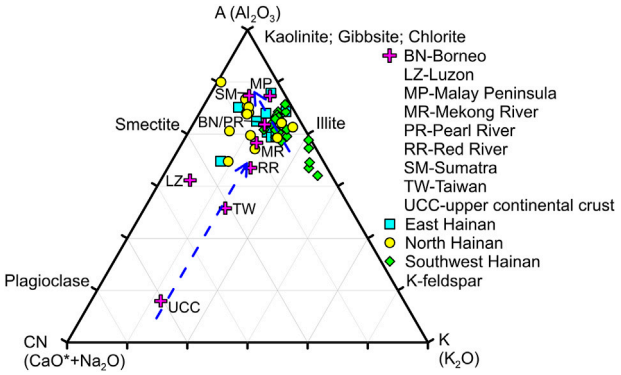

FIGURE 4 | A–CN–K diagram showing the weathering trends of the Hainan riverine sediments. Average data of UCC (Rudnick and Gao, 2003), Luzon (Liu et al., 2009), Taiwan rivers (Selvaraj and Chen, 2006), Red, Mekong, and Pearl (Liu et al., 2007), Borneo (Liu et al., 2012), Sumatra and Malay Peninsula (Liu et al., 2012) rivers are plotted for comparison. Arrows indicate weathering trends exhibited by these sediments.

Young, 1984). Most of the samples of the Hainan Rivers are subparallel to the A–K axis (**Figure 4**). This reflects the strong removal of K-bearing minerals from the parent rocks, indicating the riverine sediments of the Hainan Island have undergone extensive weathering conditions. The chemical weathering intensity of Hainan Island is higher than that of UCC (Rudnick and Gao, 2003), Luzon (Liu et al., 2009), Taiwan rivers (Selvaraj and Chen, 2006), and Red and Mekong (Liu et al., 2007), and comparable with that of Pearl (Liu et al., 2007) and Borneo rivers (Liu et al., 2012), but less than that of Sumatra and Malay Peninsula rivers (Liu et al., 2012).

Clay minerals in riverine sediments originate mainly from the weathering products of parent rocks, and thus can also provide abundant information about weathering types and intensities. The kaolinite formation strongly depends on intensive hydrolysis under warm and humid climates. Illite and chlorite are mainly formed by weak hydrolysis and/or strong physical erosion of bedrock under relatively cold and dry climates (Chamley, 1989). Thus, the kaolinite/(illite + chlorite) ratios could be used to indicate the weathering types (physical erosion vs chemical weathering) of the sediments. The higher kaolinite/(illite + chlorite) values indicate stronger chemical weathering and weaker physical erosion, and *vice versa* (Colin et al., 2010; Wan et al., 2010; Alizai et al., 2012; Hu et al., 2014).

As shown in **Figure 5**, the CIA and kaolinite/(illite + chlorite) show good correlations of the different weathering degrees in the surrounding areas of the SCS. The weathering status of Hainan is comparable with that of the Pearl River in South China, Borneo, and weaker than those of the Malay Peninsula and Sumatra in tropical Southeast Asia. The Malay Peninsula and Sumatra are benefited from stable tectonic settings and tropical climate (Liu et al., 2012), favoring the intensity of chemical weathering with strong hydrolysis. However, the sediments of Taiwan in tropical/subtropical climate, highland part of the Mekong and Red River drainage basins in a subtropical climate, and even North Borneo in a tropical climate are characterized by strong physical erosion and moderate weathering conditions due to the combined effects of tectonic uplift and abundant monsoon rainfall (Liu et al., 2007; Liu et al., 2008; Liu et al., 2012; Sang et al., 2018). The correlations of CIA with kaolinite/(illite + chlorite) support our previous understandings based on the A–CN–K diagram analysis.

For the first and second largest islands in China, the sediment weathering intensities are different on Taiwan and Hainan Island. We can ascribe this to the tectonically active and stable conditions on the two islands (Selvaraj and Chen, 2006; Metcalfe, 2009). The silicate weathering processes of the small rivers in Taiwan Island are typical weathering-limited regimes because of the steep topographic relief and rapid erosion due to plate collision (Bi et al., 2015). The intensive chemical weathering of Hainan suggests that the weathering processes exceed the transportability to remove materials due to the dense vegetation cover (Committee of Vegetation Map of China, 2007) although the heavy rainfall and tropical cyclones can trigger short-term extreme flood events (Zhang et al., 2013). Soils and sediments exposed for long periods could be gradually leached and become strongly depleted in soluble cations (Stallard, 1988; Garzanti et al., 2013). Thus, the weathering processes of the sediments in the Hainan Island are typical transport-limited weathering regimes. This can also be supported by the ~4 Mt/yr riverine sediment load from Hainan (Zhang et al., 2013), which shows a huge difference with Taiwan Island, that is, ~384 Mt/yr (Dadson et al., 2003). Located in a tectonically stable area with

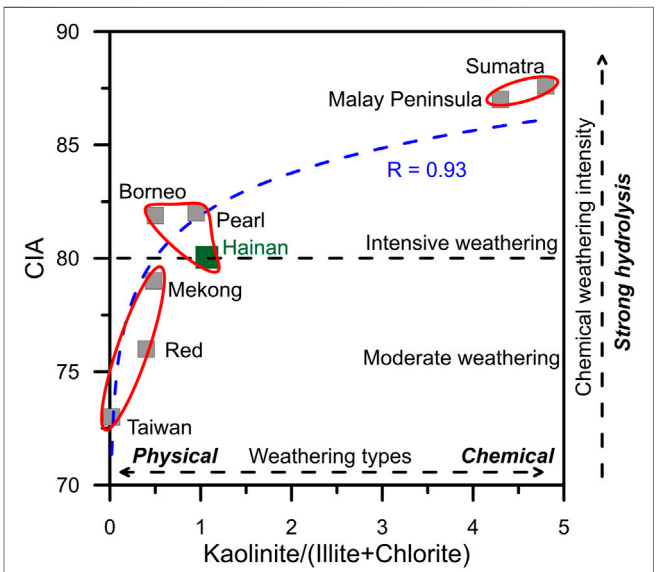

FIGURE 5 | Correlation of CIA with kaolinite/(illite + chlorite) showing the different weathering degrees in the surrounding areas of the SCS. Data of the geochemical elements of Luzon rivers are from the study by Liu et al. (2009), Taiwan rivers from the study by Selvaraj and Chen (2006), the Red, Mekong, and Pearl rivers from the study by Liu et al. (2007), the Malay Peninsula, Sumatra, and Borneo rivers from the study by Liu et al. (2012), and Hainan rivers (this study). Data of the clay minerals of the Luzon rivers are from the study by Liu et al. (2009), the Taiwan rivers from the study by Liu et al. (2008), the Red, Mekong, and Pearl rivers from the study by Liu et al. (2007), the Malay Peninsula, Sumatra, and Borneo rivers from the study by Liu et al. (2012), and Hainan rivers from the study by Hu et al. (2014).

high temperature and rainfall, the Hainan Island could afford sediments with intensive chemical weathering to the sea.

CONCLUSIONS

The concentrations of major and trace elements in the Hainan riverine sediments were analyzed. The high CIA, low WIP, and high weathering indexes (such as α_{Ca}, α_{Na}, α_{K}, α_{Sr}, and α_{Ba} values) indicate an advanced stage of weathering of Hainan sediments. The similar values of the CIA at different parts of the Hainan Island suggest that there is little difference in weathering products although the parent rocks are different. The low WIP and high α_{Ca}, α_{K}, α_{Sr}, and α_{Ba} values of north Hainan indicate the highest weathering degree, which is mainly influenced by the flat topography. The higher α_{Na}, α_{K}, α_{Sr}, and α_{Ba} values of southwest Hainan suggest that although the overall weathering degree of the southwest Hainan is comparable with the east Hainan, the leaching of elements such as Na, K, Sr, and Ba is more extreme. Their main rock types are the same, that is, granitic rocks. The significant difference between the southwest and east Hainan is the low and high summer rainfall. The stronger physical denudation should lead to shorter residence time and lower leaching intensity in the east Hainan than those of the southwest Hainan. Further studies on the "residence time" or "comminution age" of sediments from the small mountainous rivers on the Hainan Island are needed in the future. Compared with the adjacent area, the weathering degree of the Hainan Island is intensive. The weathering status is comparable with that of the Pearl River and Borneo, and relatively weaker than that of the Malay Peninsula and Sumatra due to their stable tectonic settings, and warm and humid climate. The weathering status of Hainan sediments is stronger than those of the Taiwan, Red, and Mekong rivers. Compared to the Taiwan riverine sediments, the weathering processes of the sediments in the Hainan Island are typical transport-limited weathering regimes.

DATA AVAILABILITY STATEMENT

The original contributions presented in the study are included in the article/Supplementary Material, further inquiries can be directed to the corresponding author.

AUTHOR CONTRIBUTIONS

BH contributed to conceptualization; JZ, RC, and XD performed formal analysis; FX, JZ, XL, GW, and JH contributed to original draft preparation; and BH and FX performed review and editing. All authors have read and agreed to the published version of the manuscript.

FUNDING

This study was jointly supported by the National Natural Science Foundation of China (41976192), the Project of the China Geological Survey (DD20191010), the Shandong Provincial Natural Science Foundation of China (ZR2020MD061 and ZR202103010094), the Open Foundation of the State Key Laboratory of Loess and Quaternary Geology (SKLLQG1707 and SKLLQG 1805), the National Key Research and Development Program of China (2018YFC0310001), and the Independent Project of Hainan Key Laboratory of Marine Geological Resources and Environment (2019256 (2020) HNHSKC-01 and ZZ (2020) 2019256-01).

ACKNOWLEDGMENTS

We would like to thank the editor, and two reviewers for their constructive comments and reviews of the earlier versions of this study.

REFERENCES

Alizai, A., Hillier, S., Clift, P. D., Giosan, L., Hurst, A., VanLaningham, S., et al. (2012). Clay mineral Variations in Holocene Terrestrial Sediments from the Indus Basin. *Quaternary Res.* 77, 368–381. doi:10.1016/j.yqres.2012.01.008

Bi, L., Yang, S., Li, C., Guo, Y., Wang, Q., Liu, J. T., et al. (2015). Geochemistry of River-Borne Clays Entering the East China Sea Indicates Two Contrasting Types of Weathering and Sediment Transport Processes. *Geochem. Geophys. Geosyst.* 16, 3034–3052. doi:10.1002/2015GC005867

Bouchez, J., Gaillardet, J., France-Lanord, C., Maurice, L., and Dutra-Maia, P. (2011). Grain Size Control of River Suspended Sediment Geochemistry: Clues from Amazon River Depth Profiles. *Geochem. Geophys. Geosyst.* 12, a–n. doi:10.1029/2010GC003380

Canfield, D. E. (1997). The Geochemistry of River Particulates from the continental USA: Major Elements. *Geochim. Cosmochim. Ac.* 61, 3349–3365. doi:10.1016/s0016-7037(97)00172-5

Chamley, H. (1989). *Clay Sedimentology*. Berlin: Springer-Verlag.

Clift, P. D., Wan, S., and Blusztajn, J. (2014). Reconstructing Chemical Weathering, Physical Erosion and Monsoon Intensity since 25Ma in the Northern South China Sea: A Review of Competing Proxies. *Earth-Sci. Rev.* 130, 86–102. doi:10.1016/j.earscirev.2014.01.002

Colin, C., Siani, G., Sicre, M.-A., and Liu, Z. (2010). Impact of the East Asian Monsoon Rainfall Changes on the Erosion of the Mekong River basin over the Past 25,000yr. *Mar. Geol.* 271, 84–92. doi:10.1016/j.margeo.2010.01.013

Committee of Vegetation Map of China (2007). *Vegetation Map of the People's Republic of China*. Beijing: Geological Publishing House.

Dadson, S. J., Hovius, N., Chen, H., Dade, W. B., Hsieh, M.-L., Willett, S. D., et al. (2003). Links between Erosion, Runoff Variability and Seismicity in the Taiwan Orogen. *Nature* 426, 648–651. doi:10.1038/nature02150

Deng, K., Yang, S., Bi, L., Chang, Y.-P., Su, N., Frings, P., et al. (2019). Small Dynamic Mountainous Rivers in Taiwan Exhibit Large Sedimentary Geochemical and Provenance Heterogeneity over Multi-Spatial Scales. *Earth Planet. Sci. Lett.* 505, 96–109. doi:10.1016/j.epsl.2018.10.012

DePaolo, D. J., Maher, K., Christensen, J. N., and McManus, J. (2006). Sediment Transport Time Measured with U-Series Isotopes: Results from ODP North Atlantic Drift Site 984. *Earth Planet. Sci. Lett.* 248, 394–410. doi:10.1016/j.epsl.2006.06.004

Dinis, P. A., Garzanti, E., Hahn, A., Vermeesch, P., and Cabral-Pinto, M. (2020). Weathering Indices as Climate Proxies. A Step Forward Based on Congo and SW African River Muds. *Earth-Sci. Rev.* 201, 103039. doi:10.1016/j.earscirev.2019.103039

Dupré, B., Gaillardet, J., Rousseau, D., and Allègre, C. J. (1996). Major and Trace Elements of River-Borne Material: The Congo Basin. *Geochim. Cosmochim. Ac.* 60, 1301–1321. doi:10.1016/0016-7037(96)00043-9

Egashira, K., Fujii, K., Yamasaki, S., and Virakornphanich, P. (1997). Rare Earth Element and clay Minerals of Paddy Soils from the central Region of the Mekong River, Laos. *Geoderma* 78, 237–249. doi:10.1016/S0016-7061(97)00031-1

Gaillardet, J., Dupré, B., and Allègre, C. J. (1999). Geochemistry of Large River Suspended Sediments: Silicate Weathering or Recycling Tracer. *Geochim. Cosmochim. Ac.* 63, 4037–4051. doi:10.1016/S0016-7037(99)00307-5

Gaillardet, J., Dupre, B., Allegre, C. J., and Négrel, P. (1997). Chemical and Physical Denudation in the Amazon River Basin. *Chem. Geol.* 142, 141–173. doi:10.1016/S0009-2541(97)00074-0

Garzanti, E., Padoan, M., Setti, M., Najman, Y., Peruta, L., and Villa, I. M. (2013). Weathering Geochemistry and Sr-Nd Fingerprints of Equatorial Upper Nile and Congo Muds. *Geochem. Geophys. Geosyst.* 14, 292–316. doi:10.1002/ggge.20060

Garzanti, E., Vermeesch, P., Padoan, M., Resentini, A., Vezzoli, G., and Andò, S. (2014). Provenance of Passive-Margin Sand (Southern Africa). *J. Geol.* 122, 17–42. doi:10.1086/674803

Guo, Y., Yang, S., Su, N., Li, C., Yin, P., and Wang, Z. (2018). Revisiting the Effects of Hydrodynamic Sorting and Sedimentary Recycling on Chemical Weathering Indices. *Geochim. Cosmochim. Ac.* 227, 48–63. doi:10.1016/j.gca.2018.02.015

Hu, B., Li, J., Cui, R., Wei, H., Zhao, J., Li, G., et al. (2014). Clay Mineralogy of the Riverine Sediments of Hainan Island, South China Sea: Implications for Weathering and Provenance. *J. Asian Earth Sci.* 96, 84–92. doi:10.1016/j.jseaes.2014.08.036

Jian, X., Yang, S., Hong, D., Liang, H., Zhang, S., Fu, H., et al. (2020). Seasonal Geochemical Heterogeneity of Sediments from a Subtropical Mountainous River in SE China. *Mar. Geol.* 422, 106120. doi:10.1016/j.margeo.2020.106120

Li, C.-S., Shi, X.-F., Kao, S.-J., Liu, Y.-G., Lyu, H.-H., Zou, J.-J., et al. (2013). Rare Earth Elements in fine-grained Sediments of Major Rivers from the High-Standing Island of Taiwan. *J. Asian Earth Sci.* 69, 39–47. doi:10.1016/j.jseaes.2013.03.001

Li, C., and Yang, S. (2010). Is Chemical index of Alteration (CIA) a Reliable Proxy for Chemical Weathering in Global Drainage Basins. *Am. J. Sci.* 310, 111–127. doi:10.2475/02.2010.03

Li, C., Yang, S., Lian, E., Bi, L., and Zhang, Z. (2015). A Review of Comminution Age Method and its Potential Application in the East China Sea to Constrain the Time Scale of Sediment Source-To-Sink Process. *J. Ocean Univ. China* 14, 399–406. doi:10.1007/s11802-015-2769-8

Li, C., Yang, S., Zhao, J.-x., Dosseto, A., Bi, L., and Clark, T. R. (2016a). The Time Scale of River Sediment Source-To-Sink Processes in East Asia. *Chem. Geol.* 446, 138–146. doi:10.1016/j.chemgeo.2016.06.012

Li, G., Yan, W., and Zhong, L. (2016b). Element Geochemistry of Offshore Sediments in the Northwestern South China Sea and the Dispersal of Pearl River Sediments. *Prog. Oceanogr.* 141, 17–29. doi:10.1016/j.pocean.2015.11.005

Liu, Z., Colin, C., Huang, W., Le, K. P., Tong, S., Chen, Z., et al. (2007). Climatic and Tectonic Controls on Weathering in south China and Indochina Peninsula: Clay Mineralogical and Geochemical Investigations from the Pearl, Red, and Mekong Drainage Basins. *Geochem. Geophys. Geosyst.* 8, a–n. doi:10.1029/2006GC001490

Liu, Z., Tuo, S., Colin, C., Liu, J. T., Huang, C.-Y., Selvaraj, K., et al. (2008). Detrital fine-grained Sediment Contribution from Taiwan to the Northern South China Sea and its Relation to Regional Ocean Circulation. *Mar. Geol.* 255, 149–155. doi:10.1016/j.margeo.2008.08.003

Liu, Z., Wang, H., Hantoro, W. S., Sathiamurthy, E., Colin, C., Zhao, Y., et al. (2012). Climatic and Tectonic Controls on Chemical Weathering in Tropical Southeast Asia (Malay Peninsula, Borneo, and Sumatra). *Chem. Geol.* 291, 1–12. doi:10.1016/j.chemgeo.2011.11.015

Liu, Z., Zhao, Y., Colin, C., Siringan, F. P., and Wu, Q. (2009). Chemical Weathering in Luzon, Philippines from clay Mineralogy and Major-Element Geochemistry of River Sediments. *Appl. Geochem.* 24, 2195–2205. doi:10.1016/j.apgeochem.2009.09.025

Liu, Z., Zhao, Y., Colin, C., Stattegger, K., Wiesner, M. G., Huh, C.-A., et al. (2016). Source-to-sink Transport Processes of Fluvial Sediments in the South China Sea. *Earth-Sci. Rev.* 153, 238–273. doi:10.1016/j.earscirev.2015.08.005

McLennan, S. M. (1993). Weathering and Global Denudation. *J. Geol.* 101, 295–303. doi:10.1086/648222

Metcalfe, I. (2009). Late Palaeozoic and Mesozoic Tectonic and Palaeogeographical Evolution of SE Asia. *Geol. Soc. London. Spec. Publ.* 315, 7–23. doi:10.1144/SP315.2

Milliman, J. D., and Farnsworth, K. L. (2011). *River Discharge to the Coastal Ocean – A Global Synthesis*. New York: Cambridge University Press.

Milliman, J. D., and Syvitski, J. P. M. (1992). Geomorphic/tectonic Control of Sediment Discharge to the Ocean: the Importance of Small Mountainous Rivers. *J. Geol.* 100, 525–544. doi:10.1086/629606

Nesbitt, H. W., and Young, G. M. (1982). Early Proterozoic Climates and Plate Motions Inferred from Major Element Chemistry of Lutites. *Nature* 299, 715–717. doi:10.1038/299715a0

Nesbitt, H. W., and Young, G. M. (1984). Prediction of Some Weathering Trends of Plutonic and Volcanic Rocks Based on Thermodynamic and Kinetic Considerations. *Geochim. Cosmochim. Ac.* 48, 1523–1534. doi:10.1016/0016-7037(84)90408-3

Ohta, A., Imai, N., Terashima, S., and Tachibana, Y. (2005). Application of Multi-Element Statistical Analysis for Regional Geochemical Mapping in Central Japan. *Appl. Geochem.* 20, 1017–1037. doi:10.1016/j.apgeochem.2004.12.005

Rudnick, R. L., and Gao, S. (2003). "Composition of the continental Crust," in *Treatise on Geochemistry*. Editors D. H. Heinrich and K. T. Karl (Oxford (Pergamon), 1–64. doi:10.1016/b0-08-043751-6/03016-4

Sang, P. N., Liu, Z., Zhao, Y., Zhao, X., Pha, P. D., and Long, H. V. (2018). Chemical Weathering in central Vietnam from clay Mineralogy and Major-Element Geochemistry of Sedimentary Rocks and River Sediments. *Heliyon* 4, e00710. doi:10.1016/j.heliyon.2018.e00710

Selvaraj, K., and Chen, C. T. A. (2006). Moderate Chemical Weathering of Subtropical Taiwan: Constraints from Solid-Phase Geochemistry of Sediments and Sedimentary Rocks. *J. Geol.* 114, 101–116. doi:10.1086/498102

Shao, J., Yang, S., and Li, C. (2012). Chemical Indices (CIA and WIP) as Proxies for Integrated Chemical Weathering in China: Inferences from Analysis of Fluvial Sediments. *Sediment. Geol.* 265-266, 110–120. doi:10.1016/j.sedgeo.2012.03.020

Shi, X., Kohn, B., Spencer, S., Guo, X., Li, Y., Yang, X., et al. (2011). Cenozoic Denudation History of Southern Hainan Island, South China Sea: Constraints from Low Temperature Thermochronology. *Tectonophysics* 504, 100–115. doi:10.1016/j.tecto.2011.03.007

Stallard, R. F. (1988). "Weathering and Erosion in the Humid Tropics," in *Physical and Chemical Weathering in Geochemical Cycles*. Editors A. Lerman and M. Meybeck (Dordrecht, Kluwer), 225–246. doi:10.1007/978-94-009-3071-1_11

Su, N., Yang, S., Guo, Y., Yue, W., Wang, X., Yin, P., et al. (2017). Revisit of Rare Earth Element Fractionation during Chemical Weathering and River Sediment Transport. *Geochem. Geophys. Geosyst.* 18, 935–955. doi:10.1002/2016GC006659

Suresh, P. O., Dosseto, A., Hesse, P. P., and Handley, H. K. (2013). Soil Formation Rates Determined from Uranium-Series Isotope Disequilibria in Soil Profiles from the southeastern Australian highlands. *Earth Planet. Sci. Lett.* 379, 26–37. doi:10.1016/j.epsl.2013.08.004

Taylor, S. R., and McLennan, S. M. (1985). *The Continental Crust: Its Composition and Evolution*. Oxford: Blackwell Scientific Publications.

Wan, S., Li, A., Clift, P. D., Wu, S., Xu, K., and Li, T. (2010). Increased Contribution of Terrigenous Supply from Taiwan to the Northern South China Sea since 3Ma. *Mar. Geol.* 278, 115–121. doi:10.1016/j.margeo.2010.09.008

Xu, F., Hu, B., Zhao, J., Liu, X., Xu, K., Xiong, Z., et al. (2021). Provenance and Weathering of Sediments in the Deep basin of the Northern South China Sea during the Last 38 Kyr. *Mar. Geol.* 440, 106602. doi:10.1016/j.margeo.2021.106602

Xu, Z., Lim, D., Choi, J., Yang, S., and Jung, H. (2009). Rare Earth Elements in Bottom Sediments of Major Rivers Around the Yellow Sea: Implications for Sediment Provenance. *Geo-Mar. Lett.* 29, 291–300. doi:10.1007/s00367-009-0142-x

Yang, S., Jung, H.-S., and Li, C. (2004). Two Unique Weathering Regimes in the Changjiang and Huanghe Drainage Basins: Geochemical Evidence from River Sediments. *Sediment. Geol.* 164, 19–34. doi:10.1016/j.sedgeo.2003.08.001

Yang, S., and Yin, P. (2018). Sediment Source-To-Sink Processes of Small Mountainous Rivers under the Impacts of Natural Environmental Changes and Human Activities. *Mar. Geol. Quat. Geol.* 38, 1–10. (in Chinese with English abstract).

Yang, S. Y., Jung, H. S., Choi, M. S., and Li, C. X. (2002). The Rare Earth Element Compositions of the Changjiang (Yangtze) and Huanghe (Yellow) River Sediments. *Earth Planet. Sci. Lett.* 201, 407–419. doi:10.1016/S0012-821X(02)00715-X

Yang, Z. H., Jia, J. J., Wang, X. K., and Gao, J. H. (2013). Characteristics and Variations of Water and Sediment Fluxes into the Sea of the Top three rivers of Hainan in Recent 50 Years. *Mar. Sci. Bull.* 32, 92–99. (in Chinese with English abstract).

Zhang, J., Wang, D. R., Jennerjahn, T., and Dsikowitzky, L. (2013). Land-sea Interactions at the East Coast of Hainan Island, South China Sea: A Synthesis. *Cont. Shelf Res.* 57, 132–142. doi:10.1016/j.csr.2013.01.004

Zhou, X., Li, A., Jiang, F., and Meng, Q. (2010). A Preliminary Study on Fingerprinting Approach in marine Sediment Dynamics with the Rare Earth Elements. *Acta Oceanol. Sin.* 29, 62–77. doi:10.1007/s13131-010-0051-x

Conflict of Interest: The authors declare that the research was conducted in the absence of any commercial or financial relationships that could be construed as a potential conflict of interest.

Publisher's Note: All claims expressed in this article are solely those of the authors and do not necessarily represent those of their affiliated organizations, or those of the publisher, the editors, and the reviewers. Any product that may be evaluated in this article, or claim that may be made by its manufacturer, is not guaranteed or endorsed by the publisher.

frontiers in Earth Science

ORIGINAL RESEARCH
published: 07 February 2022
doi: 10.3389/feart.2021.778377

Zircon U-Pb Dating for Paragneiss in the Xinxian Area in the Dabie–Sulu Orogenic Belt and Its Geochemical Characteristics

Zhu Shaogong[1], *Liang Yingjie*[2,3], *Zhang Yuquan*[2]* *and Li Zian*[4]*

[1]The 2nd Oil Production Plant of Daqing Oilfield Limited Company, Daqing, China, [2]Key Lab of Mineral and Mineralization, Chinese Academy of Sciences, Guangzhou Institute of Geochemistry, Guangzhou, China, [3]Guangzhou Institute of Geochemistry, Chinese Academy of Sciences (GIGCAS), Beijing, China, [4]School of Marine Sciences, Sun Yat-sen University, Guangzhou, China

In order to understand the subduction of the Yangtze block and its collision with the North China Craton, we performed the elements analysis and zircon U-Pb dating on paragneiss from Xinxian area, which located along the west edge of the Dabie-Sulu ultrahigh-pressure (UHP) metamorphic belt. The major elements analysis showed SiO_2, Al_2O_3, and K_2O were enriched and the rare-earth element (REE) analysis showed the paragneiss had a high content of REEs, especially light rare Earth elements (LREEs). The elements analysis suggest that the protolith of paragneiss may be formed by terrestrial materials. As reflected by cathode luminescence (CL), zircon in rocks was metomorphic and had a core-edge microstructure. The edge of zircon was dated by LA-ICP-MS at 233 ± 24 Ma, which suggests that the paragneiss was formed later than the Triassic. The inherited zircon had a large age range of 456–1,727 Ma, mainly in the range of 705–811 Ma. The wide range of ages suggests that the protolith of paragneiss was sedimentary rocks formed no earlier than the Paleozoic. And the paragneiss from Xinxian area were generated in the Dabie-Sulu ocean basin or abortive ocean basin in the Paleozoic era.

Keywords: zircon U-Pb age, dabie-sulu UHP metamorphic belt, paragneisses, xinxian, protolith of paragneiss

OPEN ACCESS

Edited by:
Lu Lu,
China University of Mining and Technology, China

Reviewed by:
Huichuan Liu,
China University of Petroleum, China
Jian-Jun Fan,
Jilin University, China

***Correspondence:**
Zhang Yuquan
zhangyuquangig@163.com
Li Zian
lizian88@126.com

Specialty section:
This article was submitted to Geochemistry, a section of the journal Frontiers in Earth Science

Received: *16 September 2021*
Accepted: *07 December 2021*
Published: *07 February 2022*

Citation:
Shaogong Z, Yingjie L, Yuquan Z and Zian L (2022) Zircon U-Pb Dating for Paragneiss in the Xinxian Area in the Dabie–Sulu Orogenic Belt and Its Geochemical Characteristics. Front. Earth Sci. 9:778377. doi: 10.3389/feart.2021.778377

INTRODUCTION

As one of the largest UHP metamorphic belts in the world, the Dabie-Sulu belt, located between the northern margin of the Yangtze Craton and the southern margin of the North China Craton, has received much attention. It has been widely investigated since the discovery of coesite and microgranular diamond in its eclogite (Okay et al., 1989; Wang et al., 1989; Shutong et al., 1992; Shu-tong et al., 2003). Many geochronological researches have shown that the Dabie-Sulu UHP metamorphic belt was formed by the subduction of the Yangtze block and its collision with the North China Craton during the Triassic (Liu et al., 2003; Shu-tian and You, 2005). The tectonic evolution of the subduction-collision was recorded by the rock assemblies in this metamorphic belt.

The metamorphic belt is mainly composed of eclogite, gneiss and jadeitite quartzite, among which gneiss is the dominant rock and accounts for a larger proportion than any other rock (Dao-gong et al., 2000; Wang et al., 2000; Zheng et al., 2000; Liu et al., 2004). Some geochronological and geochemical studies showed that the protolith of gneiss was related to the Neoproterozoic rift magmatism on the northern edge of the Yangtze block (Zheng et al., 2003; Zheng et al., 2006). Besides, other studies found that the protolith also contained Paleoproterozoic and Archean

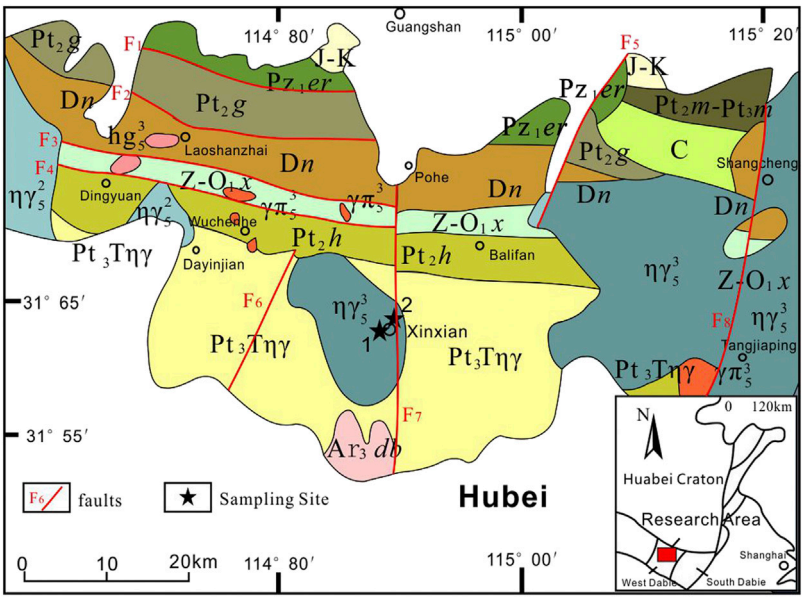

FIGURE 1 | Geological map of the Xinxian area in the Dabie orogenic belt (modified after Kun-guang et al., 2009; Dong-xing et al., 2011). J-K, Jurassic–Cretaceous volcanic rocks and volcano-sedimentary rocks; Kc, Lower Cretaceous Chenpeng Formation; D*n*, Devonian Nanwan Formation; Pz_1er, Lower Paleozoic Erlangping Group; $Z\text{-}O_1$, Sinian–Lower Ordovician Xiaojiamiao Formation-Complex; Pt_2h, Middle Proterozoic Huwan Formation-Complex; Pt_2g, Middle Proterozoic Guishan Formation-Complex; Ar_3db, Neoarchean Dabie Formation-Complex; $\eta\gamma_5^3$, Late Yanshanian monzonitic granite; $\gamma\pi_5^3$, Yanshanian granite porphyry; hg_5^3, Yanshanian quartz diorite; $Pt_3T\ \eta\gamma$, Neoproterozoic Tianpu Sequence granite paragneiss.

metamorphic rocks and some Neoproterozoic and Paleozoic granites (Chen et al., 2013). Geochronological and geochemical analysis of gneiss is helpful for the determination of the characteristics of the protolith and understanding of the magmatic activities of the Yangtze Plate during different ages. Meanwhile, it also helps to understand the subduction of the Yangtze block and its collision with the North China Craton.

Although several geochronological and isotopic studies on metamorphic rocks in the Dabie-Sulu UHP metamorphic belt were carried out in the 1990s, most of them only focused on the northern Dabie area in the east of the metamorphic belt (Wu et al., 2001). The researches of the Xinxian area at the western edge of the metamorphic were largely limited to eclogite and gneiss (Wang et al., 1993; Xue-xie et al., 1993), while paragneiss was less studied (Yang et al., 2009; Yang et al., 2009). Based on these previous studies, we investigated the paragneiss and ages of zircon in paragneiss and further discussed the protolith of paragneiss.

REGIONAL GEOLOGY

The paragneiss in the Xinxian area is distributed in the west edge of the Dabie-Sulu UHP metamorphic belt and is classified into the quartz andesite gneiss assemblage as shown on the 1:500,000 geological map of the Dabieshan orogenic belt (**Figure 1**): The assemblage refers to mica plagioclase gneiss with lenticles of marble, jadeitite, and eclogite (YG_1) and mica plagioclase gneiss with lenticles of eclogite (YG_2) (Shu-tong et al., 2005). Outcropping strata in the Xinxian area mainly include the Lower Paleozoic Erlangping Group (Pz_1er), Middle Proterozoic Huwan Formation (Pt_2h), Middle Proterozoic Guishan Formation-Complex (Pt_2g), Sinian to Ordovician Xiaojiamiao Formation ($Z\text{-}O_1x$), Devonian Nanwan Formation (D*n*), Lower Cretaceous Chenpeng Formation (Kc), and Quaternary (Q).

The paragneiss in the Xinxian area was earlier classified into the Archean Dabie Group (Ar_3db) and Neoproterozoic Tianpu Sequence granite paragneiss ($Pt_3T\ \eta\gamma$). It is dominated by the Dabie gneissic complex composed of metamorphic supracrustal rocks and metamorphic plutonic rocks. Metamorphic supracrustal rocks consisted of biotite monzonite paragneiss, plagioclase hornblende paragneiss, dolomite quartz schist and magnetite quartzite, among others. Metamorphic plutonic rocks were composed of monzonite granite gneiss, muscovite diorite paragneiss and biotite plagioclase paragneiss (Liu et al., 2004). The Archean Dabie Group (Ar_3db) is distributed in the Tongbai-Dabieshan subzone of the Qinling Stratigraphic Zone and is the oldest strata of the Qinling Fold System. It mainly outcrops in the mountainous area at the junction of the three provinces of Henan, Hubei, and Anhui, and its main body is located in the territories of Hubei and Anhui provinces. This group was composed of quartz schist, biotite schist, dolomite plagioclase paragneiss, dolomite monzonite paragneiss, biotite plagioclase paragneiss, hornblende diorite paragneiss and banded migmatite, etc. It is in unconformable contact with the underlying Archean Dabie Group.

Paragneiss samples were collected for subsequent analysis from the Xinxian Qianhe quarry and the north of Xinxian county (the No. 1 and 2 sampling points marked by black stars in **Figure 1**). Samples QH-1, QH1A, and QH-2 were

TABLE 1 | Analytical results of major (%) and trace elements (μg/g) for the Xinxian paragneisses.

Samples	QH-1	QH-2	QH-3	XX4-1	XX4-2	Samples	QH-1	QH-2	QH-3	XX4-1	XX4-2	Samples	QH-1	QH-2	QH-3	XX4-1	XX4-2
SiO_2	76.42	76.10	76.41	75.93	68.29	As	8.22	8.56	8.86	0.00	0.00	Ba	162.00	167.00	181.00	864.90	1176.60
TiO_2	0.09	0.09	0.10	0.18	0.56	Li	1.30	1.15	1.65	0.00	0.00	Hf	9.80	8.76	8.73	7.16	4.90
Al_2O_3	11.65	11.58	11.91	12.58	16.06	Be	4.17	3.79	4.90	0.00	0.00	Ta	1.68	1.61	1.81	1.05	0.77
Fe_2O_3	1.56	1.56	1.49	1.59	3.02	Sc	3.94	4.37	4.17	4.26	6.55	W	0.48	1.06	0.35	0.00	0.00
MnO	0.03	0.03	0.04	0.06	0.07	V	1.35	0.72	2.18	6.42	30.27	Tl	0.40	0.40	0.45	0.00	0.00
MgO	0.00	0.00	0.00	0.15	1.07	Cr	12.30	18.70	6.98	307.50	213.10	Pb	17.40	17.00	20.60	16.74	11.29
CaO	0.13	0.17	0.26	0.14	0.53	Co	0.91	0.82	0.62	2.81	4.28	Bi	0.07	0.05	0.08	0.00	0.00
Na_2O	4.09	3.90	4.07	3.70	4.43	Ni	5.92	7.84	3.22	20.96	14.73	Th	10.20	11.30	11.70	9.22	8.40
K_2O	4.26	4.48	4.43	4.93	3.71	Cu	6.89	5.19	2.68	33.10	24.35	U	2.16	2.05	2.45	1.83	1.67
P_2O_5	0.01	0.01	0.01	0.01	0.09	Zn	55.10	42.70	68.60	30.44	52.59	La	35.20	43.20	43.40	20.29	53.53
LOI	0.45	0.44	0.38	0.23	1.68	Ga	16.90	17.20	18.30	18.20	21.40	Ce	70.70	87.10	84.60	45.50	99.66
Total	98.69	98.35	99.09	99.50	99.51	Ge	1.25	1.40	1.52	2.09	1.65	Pr	8.07	9.75	9.87	6.14	11.64
$Na_2O + K_2O$	8.35	8.38	8.50	8.63	8.14	As	8.22	8.56	8.86	0.00	0.00	Nd	29.00	34.90	34.90	23.71	43.14
Na_2O/K_2O	0.96	0.87	0.92	0.75	1.19	Rb	97.80	101.00	117.00	147.00	116.00	Sm	6.32	7.50	7.84	5.39	7.41
Li	1.30	1.15	1.65	0.00	0.00	Sr	18.80	19.50	10.40	50.24	116.60	Eu	0.25	0.27	0.28	0.91	1.69
Be	4.17	3.79	4.90	0.00	0.00	Y	42.18	54.10	59.07	38.54	43.26	Gd	5.69	6.61	6.66	5.03	6.83
Sc	3.94	4.37	4.17	4.26	6.55	Zr	230.00	212.00	216.00	210.10	178.10	Tb	1.20	1.39	1.45	0.92	1.10
V	1.35	0.72	2.18	6.42	30.27	Nb	18.90	19.60	22.30	14.70	11.38	Dy	7.69	9.04	9.30	5.61	6.28
Cr	12.30	18.70	6.98	307.50	213.10	Mo	6.39	3.86	2.66	0.00	0.00	Ho	1.75	2.13	2.22	1.21	1.29
Co	0.91	0.82	0.62	2.81	4.28	Ag	0.46	0.41	0.48	0.00	0.00	Er	4.99	6.24	6.53	3.52	3.50
Ni	5.92	7.84	3.22	20.96	14.73	Cd	0.18	0.17	0.19	0.00	0.00	Tm	0.78	1.01	1.05	0.54	0.50
Cu	6.89	5.19	2.68	33.10	24.35	In	0.06	0.06	0.07	0.00	0.00	Yb	5.19	6.79	7.29	3.64	3.28
Zn	55.10	42.70	68.60	30.44	52.59	Sn	2.84	3.25	3.63	0.00	0.00	Lu	0.72	0.96	1.04	0.56	0.52
Ga	16.90	17.20	18.30	18.20	21.40	Sb	0.63	0.65	1.77	0.00	0.00	TREE	177.55	216.89	216.43	122.97	240.37
Ge	1.25	1.40	1.52	2.09	1.65	Cs	0.45	0.45	0.96	1.04	2.64	LREE/HREE	5.34	5.35	5.09	4.85	9.32

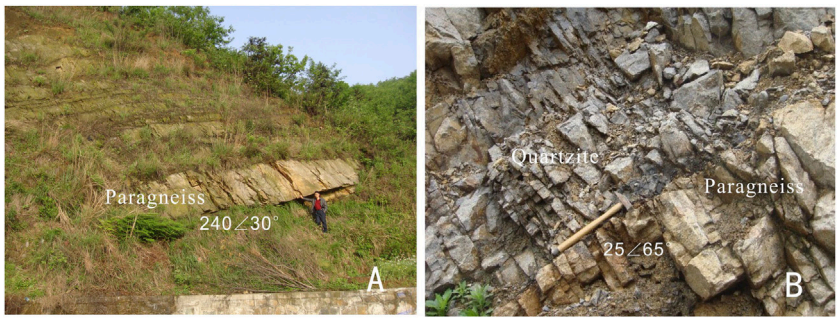

FIGURE 2 | Outcrops of paragneiss in the north of Xinxian county **(A)** and in the Xinxian Qianhe quarry **(B)**.

collected from the quarry (N 31°41.551′, E 114°56.921′) located on the east side of the road to the south of Qianhe village. Samples XX4-1 and XX4-2 were collected from a hill behind the coach station in the north of Xinxian county (N 31°41.329′, E 114°54.262′) **(Figure 2)**. These rocks are off-white and medium to fine-grained and have black and white strips. They are composed of potassium feldspar, plagioclase, quartz, biotite, etc. Samples XX4-1 and XX4-2 were obtained from thick-layered and thin-layered paragneiss, respectively.

ANALYTICAL METHODS

Petrochemical Analysis

Petrochemical tests were conducted on 5 samples from Qianhe and the north of Xinxian county for major and trace elements analyses. Experiments were carried out at the State Key Laboratory of Isotope Geochemistry, Guangzhou Institute of Geochemistry, Chinese Academy of Sciences. Major elements were determined by the Varian Vista-PRO ICP-AES (CCD full-spectrum direct reading ICP-AES), with an analytical error (RSD) of less than 5%. Detailed procedures can be found in (Goto and Tatsumi, 1994). Trace elements were determined by the PE-Elan 6000 ICP-MS in the ultra-purification laboratory of the Guangzhou Institute of Geochemistry, Chinese Academy of Sciences, with a RSD of less than 10%. Detailed procedures can be found in (Liu et al., 1996).

Zircon U-Pb Dating

Zircon samples were processed before U-Pb dating to get rid of mixtures. First, *ca.* 500 g of rock sample was weighed out and crushed into 1 cm^3 grains. Then these grains were put into a 20 cm-size stainless steel bowl and were ground repetitively for 3–5 s each time in an XZW100 vibrating mill until they were broken into 60 mesh. Dust was removed and an aluminum-made batea was used to concentrate heavy minerals. Then through magnetic and electromagnetic processing, magnetic minerals were removed and refined zircon was obtained. Finally, zircon grains with good crystals were hand picked under binocular for dating (Zhang et al., 2004).

LA-ICP-MS zircon U-Pb dating was conducted at the Key Laboratory of Isotope Geochronology and Geochemistry, Guangzhou Institute of Geochemistry, Chinese Academy of Sciences. Zircon grains were fixed by epoxy resin and made into laser ablation sample targets. The sample targets were ground and polished until the central surface of the zircon was exposed. Carbon dust was sprayed on zircon for CL imaging and then was wiped off for LA-ICP-MS U-Pb analysis (single spot laser ablation was used with a diameter of the laser spot of 31 μm and at a firing frequency of 8 Hz). Detailed analytical procedures can be found in (Tu et al., 2011). ^{204}Pb data were used to correct Pb data in zircon. The errors of single data points were within 1σ. The $^{206}Pb/^{238}U$ age was obtained, whose weighted averages were at the 95% confidence level. Experimental results were plotted into concordia diagrams using the software of Isoplot 3.0 (Ludwig, 2012).

EXPERIMENTAL RESULTS

Characteristics of Major Elements

As shown in **Table 1**, results were obtained through the geochemical analysis of major elements. It can be seen that the paragneiss in the Qianhe area has a high content of silicon (SiO_2 = 76.10–76.42%), aluminum (Al_2O_3 = 11.58–11.91%), and alkali elements (Na_2O + K_2O = 8.35–8.50%) but shows a deficiency in titanium (TiO_2 = 0.09–0.10%) and calcium (CaO = 0.13–0.26%). Its potassium content is comparatively high (Na_2O/K_2O = 0.57–0.76) and Aluminous Saturation Index (A/CNK) is in the range of 1.35–1.38, suggesting that the rock is peraluminous.

The paragneiss in the north of Xinxian county is consistent with the one in the Qianhe area in terms of chemical composition, as it is rich in silicon (SiO_2 = 68.29–75.93%), aluminum (Al_2O_3 = 12.58–16.06%) and alkali elements (Na_2O + K_2O = 8.14–8.63%) but poor in titanium and calcium (CaO = 0.14–0.53%). By comparison, its content of potassium (Na_2O/K_2O = 0.79–1.19) is lower than that of the paragneiss in the Qianhe area. As the A/CNK is in the range of 1.43–1.85, it is evident that the rock is peraluminous.

Characteristics of Trace and Rare Earth Elements

The results of trace element analysis are shown in **Table 1**. The total amount of REE was high in the Qianhe paragneiss (QH-1,

TABLE 2 | Zircon LA ICP MS U-Pb age data of Qianhe and Chengbei paragneisses in Xinxian.

No.	Sample	Pb	Th	U	Th/U	207Pb/206Pb	207Pb/235U	206Pb/238U	206Pb/238U
1	QH-1-01	40	210	229	0.92	0.0714 ± 37	1.1861 ± 662	0.1195 ± 20	727.7 ± 11.4
2	QH-1-02	51	276	270	1.02	0.0664 ± 24	1.2130 ± 495	0.1311 ± 22	793.9 ± 12.6
3	QH-1-03	99	139	2381	0.06	0.0764 ± 25	0.3534 ± 119	0.0334 ± 4	211.5 ± 2.3
4	QH-1-04	69	145	1536	0.09	0.0732 ± 27	0.3682 ± 147	0.0361 ± 5	228.6 ± 3.0
5	QH-1-05	106	235	1941	0.12	0.0702 ± 21	0.4249 ± 128	0.0436 ± 6	275.0 ± 3.5
6	QH-1-06	50	253	274	0.92	0.0639 ± 25	1.1170 ± 436	0.1261 ± 27	765.9 ± 15.3
7	QH-1-07	59	222	297	0.75	0.1149 ± 57	1.9402 ± 899	0.1222 ± 16	743.4 ± 9.1
8	QH-1-08	28	113	156	0.72	0.0606 ± 23	1.1113 ± 447	0.1324 ± 22	801.6 ± 12.7
9	QH-1-09	103	753	2008	0.37	0.0920 ± 35	0.4554 ± 174	0.0358 ± 6	227.0 ± 3.9
10	QH-1-10	128	324	2348	0.14	0.0814 ± 31	0.4535 ± 206	0.0398 ± 8	251.7 ± 5.1
11	QH1A-01	63	341	357	0.95	0.0628 ± 30	1.1044 ± 530	0.1261 ± 20	765.4 ± 11.3
12	QH1A-02	39	211	221	0.96	0.0665 ± 38	1.1492 ± 657	0.1237 ± 21	752.1 ± 12.0
13	QH1A-03	45	252	252	1	0.0603 ± 39	1.1180 ± 707	0.1328 ± 24	803.8 ± 13.9
14	QH1A-04	60	355	354	1	0.0608 ± 39	1.0201 ± 639	0.1189 ± 20	724.4 ± 11.7
15	QH1A-05	76	481	429	1.12	0.0639 ± 45	1.1445 ± 786	0.1266 ± 24	768.7 ± 13.8
16	QH1A-06	60	314	333	0.94	0.0622 ± 50	1.1760 ± 915	0.1332 ± 28	805.9 ± 15.9
17	QH1A-07	35	173	214	0.81	0.0621 ± 51	1.1070 ± 858	0.1259 ± 30	764.6 ± 17.2
18	QH1A-08	52	315	306	1.03	0.0633 ± 48	1.1247 ± 830	0.1236 ± 27	751.1 ± 15.4
19	QH1A-09	127	271	358	0.76	0.1749 ± 308	6.9620 ± 2.0643	0.1523 ± 190	913.6 ± 106.5
20	QH1A-10	32	42	532	0.08	0.0810 ± 120	0.8841 ± 2528	0.0563 ± 40	352.9 ± 24.6
21	QH1A-11	60	352	312	1.13	0.0646 ± 55	1.2665 ± 1035	0.1337 ± 26	809.1 ± 14.9
22	QH1A-12	49	276	258	1.07	0.0615 ± 61	1.2061 ± 1155	0.1327 ± 31	803.0 ± 17.4
23	QH1A-13	27	118	157	0.75	0.0597 ± 55	1.0881 ± 981	0.1233 ± 28	749.5 ± 16.3
24	QH1A-14	53	309	295	1.05	0.0563 ± 43	1.0710 ± 796	0.1294 ± 27	784.3 ± 15.6
25	QH1A-15	42	227	271	0.84	0.0548 ± 44	0.8942 ± 675	0.1119 ± 24	684.0 ± 14.0
26	QH1A-16	29	141	161	0.87	0.0490 ± 44	0.9469 ± 795	0.1342 ± 31	811.9 ± 17.7
27	QH1A-17	38	193	209	0.92	0.0478 ± 40	0.9223 ± 719	0.1332 ± 27	806.0 ± 15.6
28	QH1A-18	49	241	278	0.87	0.0529 ± 45	0.9714 ± 789	0.1268 ± 32	769.5 ± 18.1
1	XX4-1-1	34.9	329	230	1.43	0.0781 ± 84	1.0141 ± 1135	0.0914 ± 21	564.0 ± 12.6
2	XX4-1-2	12.7	80	77	1.04	0.1279 ± 157	1.5972 ± 1976	0.0861 ± 27	532.7 ± 15.8
3	XX4-1-3	10.8	92	49	1.88	0.0589 ± 79	1.1037 ± 1517	0.1338 ± 43	809.7 ± 24.5
4	XX4-1-4	30	115	570	0.2	0.0541 ± 66	0.3111 ± 369	0.0406 ± 11	256.3 ± 7.1
5	XX4-1-5	12.6	78	35	2.26	0.2597 ± 331	5.8428 ± 9430	0.1471 ± 102	884.5 ± 57.4
6	XX4-1-6	7.3	87	27	3.28	0.0829 ± 114	1.4493 ± 1909	0.1276 ± 56	774.4 ± 32.1
7	XX4-1-7	50.7	1029	366	2.81	0.0595 ± 62	0.6289 ± 605	0.0734 ± 21	456.8 ± 12.9
8	XX4-1-8	36.5	195	227	0.86	0.0444 ± 46	0.7755 ± 755	0.1181 ± 39	719.7 ± 22.7
9	XX4-1-9	38.1	59	52	1.14	0.2620 ± 372	17.1777 ± 2.9396	0.3072 ± 336	1727.1 ± 165.8
10	XX4-1-10	13.5	73	106	0.69	0.0319 ± 47	0.5059 ± 808	0.1063 ± 56	651.4 ± 32.6
11	XX4-1-11	21.8	116	114	1.01	0.0492 ± 59	0.8956 ± 1072	0.1235 ± 41	750.7 ± 23.5
12	XX4-1-12	20.8	593	83	7.15	0,1119 ± 171	1.7061 ± 4296	0.1011 ± 77	620.8 ± 45.2
13	XX4-1-13	18.8	89	106	0.84	0.0536 ± 73	0.9852 ± 1320	0.1278 ± 36	775.1 ± 20.8
14	XX4-1-14	183.5	346	605	0.57	0.1024 ± 130	3.6523 ± 4709	0.2446 ± 77	1410.5 ± 40.0
1	XX4-2-3	12	125	52	2.41	0.0659 ± 87	1.0539 ± 1352	0.1207 ± 39	734.8 ± 22.3
2	XX4-2-4	19.3	173	100	1.72	0.0915 ± 103	1.3240 ± 1624	0.1032 ± 30	633.4 ± 17.7
3	XX4-2-5	16.1	138	90	1.53	0.0639 ± 72	0.9180 ± 982	0.1078 ± 33	660.2 ± 18.9
4	XX4-2-6	21.5	209	130	1.61	0.0496 ± 69	0.6700 ± 907	0.0966 ± 29	594.5 ± 17.3
5	XX4-2-7	14.9	105	75	1.4	0.0830 ± 90	1.4476 ± 1451	0.1289 ± 45	781.6 ± 25.5
6	XX4-2-8	11.7	93	62	1.49	0.0647 ± 86	1.0191 ± 1356	0.1156 ± 36	705.4 ± 20.8
7	XX4-2-9	8.1	72	41	1.74	0.0734 ± 137	1.1542 ± 1995	0.1171 ± 44	713.8 ± 25.5
8	XX4-2-10	16.1	136	74	1.84	0.0845 ± 102	1.3956 ± 1534	0.1208 ± 35	735.1 ± 20.2
9	XX4-2-11	11.9	64	68	0.94	0.0561 ± 121	0.9941 ± 1955	0.1276 ± 59	774.1 ± 33.7
10	XX4-2-12	22.2	224	104	2.16	0.0667 ± 217	1.1527 ± 3379	0.1229 ± 87	747.4 ± 50.1
11	XX4-2-13	10	81	45	1.82	0.0879 ± 395	1.6321 ± 6640	0.1293 ± 12	783.7 ± 73.0
12	XX4-2-14	14.1	73	53	1.39	0.2033 ± 1171	5.3510 ± 2.7974	0.1599 ± 208	956.0 ± 115.8

QH-2, and QH-3), up to 117.55–216.89 μg/g. As shown in the chondrite-normalized REE diagram (**Figure 3**), LREEs were enriched as La/Yb was between 4.27 and 4.86 and the negative Eu anomaly was evident (δEu is 0.12–0.13) (Sun and McDonough, 1989). Besides, its pattern curve was skewed to the right and had an obvious V valley. As shown in the primitive mantle-normalized trace element spider diagram (**Figure 4**), elements such as Rb, K, Th, and U were enriched in the paragneiss in the Qianhe area whereas elements such as Ba, Nb, Sr, and Ti were depleted.

The total amount of REEs was also high in the Xinxian paragneiss (XX4-1, XX4-2), up to 122.97–240.37 μg/g. Its chondrite-normalized REE plot was similar to that of the paragneiss of the Qianhe area; however, the content of heavy

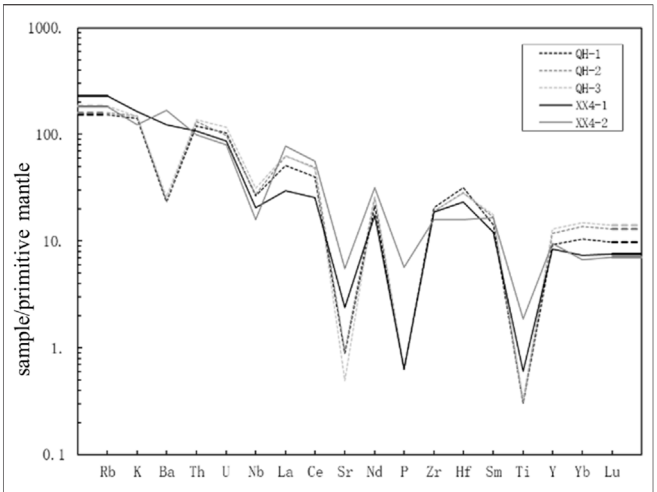

FIGURE 3 | Primitive mantle-normalized trace-elements spider diagram.

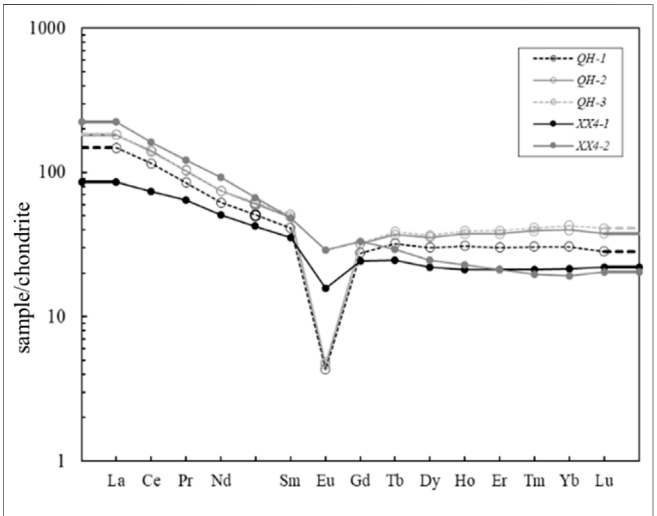

FIGURE 4 | Chondrite-normalized REE plot of paragneiss.

rare Earth elements (HREE) was higher with La/Yb in the range of 4.00–11.71. Besides, the negative Eu anomaly was relatively indistinct with δEu of 0.53–0.73. As shown in the spider diagram (**Figure 4**), elements such as Rb, K, Ba, Th, and U were enriched in the paragneiss in the north of Xinxian county whereas elements such as Nb, Sr, and Ti were depleted.

Results of Zircon Dating

Zircon U-Pb dating was conducted on Samples QH-1 and QH-1-A from the Qianhe area and Samples XX4-1 and XX4-2 from the north of Xixian county. The CL image (**Figure 5**) shows that zircon grains were of similar sizes with a length to width ratio of about 1:2. All zircons contained detrital zircon and most of them had a clear core-edge double structure. Detrital zircon in the core of zircons had oscillatory zoning. For most zircons, the edge was darker than the core **(Table 2)**.

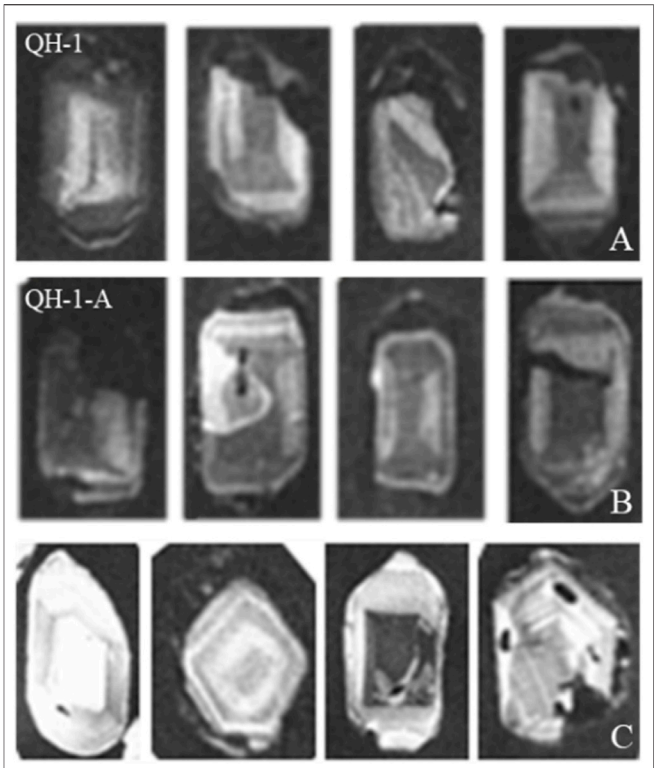

FIGURE 5 | CL images of zircon in paragneiss (**(A)** Qianhe QH-1 sample, **(B)** Qianhe QH-1-A sample, **(C)** XX4-1 thick-layered paragneiss sample and XX4-2 thin-layered paragneiss sample from the north of Xinxian county).

Five points on the detrital zircon of the metamorphic composite zircon sample QH-1 were selected for the determination of Th and U concentrations (**Figure 5A**). The ratio of Th/U suggests that these zircons were formed during the Proterozoic at the ages of 801, 793, 756, 743, and 727 Ma, respectively. Five points on the edge of the metamorphic composite zircon were dated at 251, 228, 226, and 211 Ma, respectively (**Figure 6**).

A total of 17 points on the detrital zircon of the metamorphic composite zircon sample QH-1-A were selected for the determination of Th and U concentrations (**Figure 5B**). Four age ranges were obtained: 913, 811-803, 784-724, and 684 Ma. One point on the edge of the metamorphic zircon was dated at 352 Ma.

A total of 24 points on the detrital zircon of Xinxian metamorphic composite zircon samples were selected for the determination of Th and U concentrations (**Figure 5C**). These points have a wide age range: 456–1,727 Ma. One point on the edge of the metamorphic zircon was dated at 256 Ma.

U-Pb dating results for the edge of the metamorphic zircon and the metamorphic composite zircon were more concentrated, with ages ranging from 211 to 352 Ma and concordant ages of 233 ± 24 Ma. Besides, the Th/U ratios of these seven points are in the range of 0.08–0.37 while three of them are below 0.1, significantly smaller than the Th/U ratio of magmatic zircon (generally greater than 0.4) and closer to that of metamorphic

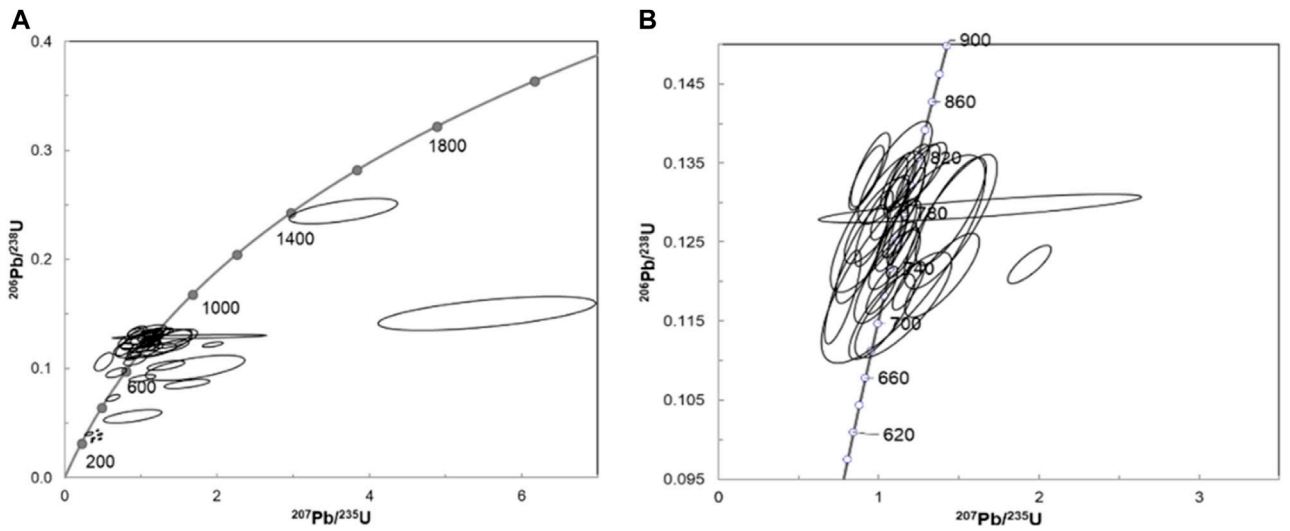

FIGURE 6 | Zircon U-Pb concordia diagram for paragneisses **(A)**; zircon U-Pb concordant ages in the range of 705–811 Ma **(B)**.

zircon (Bryant et al., 2002). As suggested by the U-Pb dating results, the detrital zircons in the samples were mainly formed during the Neoproterozoic (564–884 Ma), with their ages mainly in the range of 705-811 Ma. However, some detrital zircons were formed in the Paleozoic and Middle Proterozoic as shown by dating results.

DISCUSSION

Analysis of Zircon U-Pb Dating Results

Two results were obtained from zircon U-Pb dating. The first one was about the edge of metamorphic zircon, whose age was in the range of 211–352 Ma and concordant age was 233 ± 24 Ma. The other result was about detrital zircon in metamorphic zircon, whose age ranged from 456 to 1,727 Ma, mostly between 705 and 811 Ma.

The edge of the metamorphic zircon in samples was dated to the Triassic, suggesting that paragneiss in Xinxian county experienced high-pressure metamorphism during the Triassic. It was consistent with a large amount of previous research on the metamorphic age of the Dabie-Sulu UHP metamorphic belt which confined the age to the Triassic. Hacker et al. (1998) suggested that the metamorphism of the Dabie-Sulu UHP metamorphic belt reached its peak at 245 Ma through zircon dating for paragneiss. Liu et al. (2006) found through U-Pb dating for the edge of metamorphic zircon with coesite that the metamorphic event of the Dabie-Sulu UHP metamorphic belt took place during 240–225 Ma. Our work suggests that the edge of metamorphic zircon is consistent with the data reported by previous researchers, providing further evidence that paragneiss in Xinxian county experienced ultrahigh-pressure metamorphic events during the Triassic.

The dating results of detrital zircon showed that many samples were dated to the middle of the Neoproterozoic, which accounted for about 72% of the total number of samples. Their age range of 700–800 Ma was consistent with the characteristic zircon age of rocks in the Yangtze block (Rowley et al., 1997; Hacker et al., 1998). Considering no large-scale magmatic activity was recorded in the Middle Neoproterozoic in the North China craton, the protolith of the paragneiss in Xinxian county was hence supposed to originate from the Yangtze block. As the magmatic activity was caused by the breakdown of the Rodinia supercontinent, the protolith of the paragneiss of Xinxian county may contain granite formed in the Middle Neoproterozoic in the Yangtze block. In addition, part of detrital zircon in Sample XX4-2 was dated to the Paleozoic (456–532 Ma), which was consistent with data obtained by previous researches of the paragneiss of the UHP belt (Hacker et al., 1998; Liu et al., 2004). However, such age data were in small amount in previous researches and were considered to be the result of the loss of Pb, or due to the fact that the core and edge of zircon were not separated. Hence, these data were not widely discussed or constraining the age by the fugacity state of the paragneiss and orthogneiss (Fu-lai and Xue, 2007). Additionally, (Yuan et al., 2015) found that the core of metamorphic zircon in paragneiss in Luotian of Hubei province was mostly dated to the Paleozoic. No signs of Pb loss could be found, and the boundary between the margin and core was also clear on CL images. Further, considering parts of zircon were dated to the Paleozoic in our work and they had the Th/U ratio close to the ratio range of zircon of magmatic origin (Dao-gong et al., 2001), part of the protolith of the paragneiss was supposed to form later than 456 Ma. As some detrital zircon in the samples was dated to the Middle Proterozoic, the source material of the protolith could possibly come from the crustal residual of the Middle Proterozoic in the Yangtze block rather than from the Paleozoic sedimentary cover.

Protolith Analysis

With regard to the protolith of the paragneiss of the Dabie-Sulu UHP metamorphic belt, it was considered in previous research to be mainly granite formed by the magma coming from the Rodinia rift in the Neoproterozoic at the north edge of the Yangtze block (Zheng et al., 2003). Based on geochemical analysis of the paragneiss in the Dabie belt and Cretaceous granite, the source materials were likely to come from the north edge of the subducting Yangtze block (Frost and Frost, 2011). Therefore, some researchers proposed that the paragneiss in the Dabie belt and Cretaceous granite were produced at different horizons of the Yangtze block (Shu-guang et al., 1997).

The samples of paragneiss from Xinxian had a high SiO_2 content, up to 68.29–76.42%, and their A/CNK reached 1.35–1.85, indicating they are peraluminous. The alkali content ranged between 8.14 and 8.63%, in which the content of potassium is relatively high as the ratio of Na_2O/K_2O is between 0.57 and 1.19. The content of calcium was low and in the range of 0.13–0.53% (Wong et al., 2009; Frost and Frost, 2011). Light rare Earth elements (LREEs) were enriched in the samples and negative Eu anomaly was distinct. Elements such as Rb, K, Th, and U were enriched whereas elements such as Nb, Sr, and Ti were depleted. This distribution pattern suggests that the protolith was formed by the materials of the continental crust (Chen et al., 2006). Felsic magma generated by partial melting of felsic rock under high pressure can extract Si, K, Na, LILEs, and LREEs (Hermann and Green, 2001), and hence, the magma can become enriched in silicon, alkali, aluminum and LREEs while depleted in calcium and magnesium and iron. As Gu found LILEs and LREEs were depleted in eclogite (Gu et al., 2013), it suggests that the paragneiss in Xinxian county might be partially melted, like the felsic magma formed under high pressure. The continuous process from sub-solidus dehydration to partial melting within the UHP gneissic rocks is also evidenced by experimental and petrological observations in Shuanghe paragneiss (Liu and Wu, 2013). According to the geochemical characteristics of the samples, the protolith is likely to be sedimentary rock that has been partially melted during the subduction and retreat of the Yangtze block (Wallis et al., 2005).

Tectonic Setting of the Shuanghe UHP Metamorphic Protolith

By volume, the gneiss occupies between 70 and 80% of the Dabie-Sulu complex (e.g., Dao-gong et al., 2000; Wang et al., 2000; Hui-fen et al., 2001). Of these, 40–60% comprise foliated, garnet-bearing, A-type granitic rock (Shu-tian and You, 2005). These rocks are associated with jadeite-quartzites and marbles that formed from quartz sandstone and limestone respectively. According to the zircon U-Pb dating results, the protoliths of these rocks are controlled by Paleozoic Dabie - Sulu basin. Distributions of the major-elements of these rocks are high SiO_2, alkali-rich, high Na_2O and low Al_2O_3. The mineral component is more rich in alkaline ferromagnesian. The sedimentary origins of these protoliths appear to be neritic facies, some of which are clastic sediments (quartz sandstone to arkoses) and chemical sediments (limestone). These are characteristic of the continental slope environment. The Dabie-Sulu ocean basin was not a mature ocean; it lacked deep-water sedimentation, such as siliceous deposits and turbidites. It evidently lacked contemporaneous pillow lavas and cumulates of ophiolite rock assemblages which is why we have not found remnants of ophiolitic melanges (Wang and Cong Bo-lin, 1998). As the Dabie-Sulu ocean basin was an aborted oceanic basin, it narrowed, with a resultant increase in salinity. This ultimately led to the oceanic basin sediments becoming increasingly alkaline. This provided the necessary material conditions for the formation of alkaline mafic minerals (sodic pyroxenes and amphiboles) during the Late Triassic metamorphism of these rocks.

CONCLUSION

1) Paragneiss in the Qianhe and Chengbei areas of Xinxian county experienced a metamorphic event during 233 ± 24 Ma, suggesting that the rock was formed later than the Permian.
2) Paragneiss in Xixian county is enriched in silicon, alkali, aluminum and LREEs while depleted in calcium, magnesium and iron. Besides, negative Eu anomalies are evident. It suggests that the protolith may be formed by terrestrial materials.
3) Detrital zircon in paragneiss in the Qianhe area and north of Xinxian county was dated to 456–1727 Ma, mainly in the range of 705–811 Ma. It suggests that the protolith should be formed no earlier than 456 Ma. And they were generated in the Dabie-Sulu ocean basin or abortive ocean basin in the Paleozoic era.

DATA AVAILABILITY STATEMENT

The original contributions presented in the study are included in the article/Supplementary Material, further inquiries can be directed to the corresponding authors.

AUTHOR CONTRIBUTIONS

LY was responsible for most of the experimental analysis and paper writing; ZY was responsible for sampling and experimental processing; LZ was responsible for the experimental design and the paper revision.

ACKNOWLEDGMENTS

Researcher Xianglin Tu, Key Laboratory of Isotope Dating and Geochemistry, Guangzhou Institute of Geochemistry, Chinese Academy of Sciences, and others assisted in U-Pb age determination and provided many valuable comments, and we would like to express our sincere gratitude.

REFERENCES

Bryant, D. L., Ayers, J. C., Gao, S., Miller, C. F., and Zhang, H. (2002). "Geochronologic Constraints on the Location of the Sino-Korean/Yangtze Suture and Evolution of the Northern Dabie Shan," in *AGU Spring Meeting Abstracts* (Boulder: Geological Society of America Bulletin).

Chen, W, Zhao-wen, X, Hong-chao, L, Xiao-nan, Y, Jin-quan, C, Wang, H, et al. (2013). Petrogenesis and Origin of the Xinxian Granitic Batholith in Henan Province and its Implication for the Tectonic Evolution of the Western Dabie Area. *Acta Geologica Sinica* 87 (10), 1510–1524.

Chen, Y., Ye, K., Liu, J.-B., and Sun, M. (2006). Multistage Metamorphism of the Huangtuling Granulite, Northern Dabie Orogen, Eastern China: Implications for the Tectonometamorphic Evolution of Subducted Lower continental Crust. *J. Metamorphic Geology.* 24 (7), 633–654. doi:10.1111/j.1525-1314.2006.00659.x

Dao-gong, C., Isachsen, C., Xia-chen, Z., Zhou, T., Chen, H., and Xia, Q. (2000). The Zircons U-Pb Ages of Qianshan Gneiss in Anhui. *Chin. Sci. Bull.* 45 (02), 214–217. doi:10.1007/BF02886187

Dao-gong, Chen., Bin-xian, Li., Xia, Qun-ke., Wu, Yuan-bao., and Chen, Hao. (2001). An Evaluation of Zircon U-Pb Dating for Metamorphic Rocks and Comments on Zircon Ages of Dabie Orogen. *Acta Geologica Sinica* 17 (01), 129–138. doi:10.2118/69841-PA

Dong-xing, Z., Guo-min, H., and Shi-wei, Z. (2011). Geochemical Characteristics and Metallogeniss of Early Cretaceous Granites in Western Dabie Orogen and Their Association with Mineralization: Evidence from Tangjiaping Granite Porphyry and Xinxian Batholith. *Mineral. Exploration* 2 (05), 568–573.

Frost, C. D., and Frost, B. R. (2011). On Ferroan (A-type) Granitoids: Their Compositional Variability and Modes of Origin. *J. Petrol.* 52 (1), 39–53. doi:10.1093/petrology/egq070

Fu-lai, L., and Xue, H. (2007). Review and prospect of SHRIMP U-Pb Dating on Zircons from Sulu-Dabie UHP Metamorphic Rocks. *Acta Petrologica Sinica* 23 (11), 2737–2756. doi:10.3969/j.issn.1000-0569.2007.11.006

Goto, A. T., and Tatsumi, Y. O. (1994). Quantitative Analysis of Rock Samples by an X-ray Fluorescence Spectrometer (I). *Rigaku J.* 11 (1), 40–59. doi:10.1097/00024382-199401001-00145

Gu, X, Liu, Y, and Deng, L (2013). Geochronology and Petrogenesis of Eclogite from the Luotian Dome, North Dabie Complex Zone (central China), and Their Element and Isotope Behavior during Exhumation. *Chin. Sci. Bull.* 58 (22), 2132–2137. doi:10.1360/972013-589

Hacker, B. R., Ratschbacher, L., Webb, L., Ireland, T., Walker, D., and Shuwen, D. (1998). U/Pb Zircon Ages Constrain the Architecture of the Ultrahigh-Pressure Qinling-Dabie Orogen, China[J]. *Earth Planet. Sci. Lett.* 161 (1–4), 215–230. doi:10.1016/s0012-821x(98)00152-6

Hermann, J., and Green, D. H. (2001). Experimental Constraints on High Pressure Melting in Subducted Crust. *Earth Planet. Sci. Lett.* 188 (1-2), 149–168. doi:10.1016/s0012-821x(01)00321-1

Hui-fen, X., Yang, T., Fu-lai, L., and Liou, J. G. (2001). Multi Age-Time Evolution of Granite Gneisses-Granite in the Southern Sulu HP-UHP Metamorphic Belt. *Acta Geologica Sinica* 75 (03), 371–378.

Kun-guang, Y., Xie, J., Liu, Q., She, Z., and Chang-qian, M. (2009). Deformation Characteristics of Foliated Granite and Dating of Zircon in Western Dabie Margin. *Sci. China,Ser.D.* 39 (04), 464–473. doi:10.1007/s11430-009-0001-7

Liu, F., Liou, J. G., and Xue, H. (2006). Identification of UHP and Non-UHP Orthogneisses in the Sulu UHP Terrane, Eastern China: Evidence from SHRIMP U-Pb Dating of Mineral Inclusion-Bearing Zircons. *Int. Geology. Rev.* 48 (12), 1067–1086. doi:10.2747/0020-6814.48.12.1067

Liu, F., Xu, Z., and Song, B. (2003). Determination of UHP and Retrograde Metamorphic Ages of the Sulu Terrane:Evidence from SHRIMP U-Pb Dating on Zircons of Gneissic Rocks[J]. *Acta. Geologica. Sinica.* 77 (2), 229–237.

Liu, Q., and Wu, Y. (2013). Dehydration Melting of UHP Eclogite and Paragneiss in the Dabie Orogen: Evidence from Laboratory experiment to Natural Observation. *Chin. Sci. Bull.* 58, 4390–4396. doi:10.1007/s11434-013-6075-9

Liu, X. C., Borming, J., Liu, D. Y., Dong, S. W., and Li, S. Z. (2004). SHRIMP U–Pb Zircon Dating of a Metagabbro and Eclogites from Western Dabieshan (Hong'an Block), China, and its Tectonic Implications. *Tectonophysics* 394 (3-4), 171–192. doi:10.1016/j.tecto.2004.08.004

Liu, Y, Liu, H, and Xian-hua, L (1996). Simultaneous and Precise Determination of 40 Trace Elements in Rock Samples Using ICP-MS. *Geochimica* 25 (06), 552–558.

Ludwig, K. R. (2012). *Isoplot 3.75 A Geochronological Toolkit for Microsoft Excel*, 5. Berkeley: Berkeley Geochronology Center Special Publication, 1–77.

Okay, A. I., Shutong, X., and Sengör, A. M. C. (1989). Coesite from the Dabie Shan Eclogites, central China. *ejm* 1 (4), 595–598. doi:10.1127/ejm/1/4/0595

Rowley, D. B., Xue, F., Tucker, R. D., Peng, Z. X., Baker, J., and Davis, A. (1997). Ages of Ultrahigh Pressure Metamorphism and Protolith Orthogneisses from the Eastern Dabie Shan: U/Pb Zircon Geochronology[J]. *Earth Planet. Sci. Lett.* 151 (3-4), 191–203. doi:10.1016/s0012-821x(97)81848-1

Shu-guang, L., Hui-min, L., Yi-zhi, C, Xiao, Y, and De-liang, L (1997). Dabie-Sulu UHP Metamorphic Chronology Body -Ⅱ. Zircon U-Pb Isotope System. *Sci. China,Ser.D.* 27 (03), 200–206.

Shu-tian, S., Zeng-qiu, Z., Zhou, H., and You, Z. (2005). Polyphase Tectonometamorphic Evolution of UHP Metamorphic Rocks in the Dabie-Sulu Region, East-central China. *Acta Petrologica Sinica* 21 (4), 1175–1188. doi:10.3321/j.issn:1000-0569.2005.04.016

Shu-tong, X., Guan-bao, C., Liu, Y., Wu, W., Shu-tian, S., and Zeng-qiu, Z. (2005). *Geological Map of Dabie Mountain Orogenic belt (1/500000)*. Beijing.

Shu-tong, X., Liu, Y., Guan-bao, C., Compagnoni, R., Rolfo, F., He, M., et al. (2003). Diamond from the Dabie Shan-Sulu Area Metamorphic Rocks[J]. *Chin. Sci. Bull.* 48 (10), 1069–1075. doi:10.1126/science.256.5053.80

Shutong, X., Wen, S., Yican, L., Laili, J., Shouyuan, J., Okay, A. I., et al. (1992). Diamond from the Dabie Shan Metamorphic Rocks and its Implication for Tectonic Setting. *Science* 256 (5053), 80–82. doi:10.1126/science.256.5053.80

Sun, S.-s., and McDonough, W. F. (1989). Chemical and Isotopic Systematics of Oceanic Basalts: Implications for Mantle Composition and Processes. *Geol. Soc. Lond. Spec. Publications* 42 (1), 313–345. doi:10.1144/gsl.sp.1989.042.01.19

Tu, X-l., Zhang, H., Deng, W-f., Ling, M-x., Liang, H-y., Liu, Y., et al. (2011). Application of Resolution In-Situ Laser Ablation ICP-MS in Trace Element Analyses. *Geochimica.* 40 (1), 83–98. in Chinese with English abstract

Wallis, S., Tsuboi, M., Suzuki, K., Fanning, M., Jiang, L., and Tanaka, T. (2005). Role of Partial Melting in the Evolution of the Sulu (Eastern China) Ultrahigh-Pressure Terrane. *Geol* 33 (2), 129–132. doi:10.1130/g20991.1

Wang, Q., and Cong, B. (1998). Tectonic Framework of the Ultrahigh Pressure Metamorphic Zone from the Dabie Mountains. *Acta Petrologica Sinica* 14 (04), 481–492.

Wang, Q., Xu, J., Wang, J., Zhao, Z., Wang, R., Qiu, J., et al. (2000). The Recognition of Adakite-type Gneisses in the North Dabie Mountain and its Implication to Ultrahigh Pressure Metamorphic Geology. *Chin.Sci.Bull.* 45 (21), 1927–1933. doi:10.1007/bf02909680

Wang, X, Wen-yuan, C, Liu, S, Zhang, L, and Chun-jing, W (1993). Discovery of Coesite-Bearing Eclogites from Southern Henan Province. *Acta Petrologica Sinica* 9 (02), 181–185.

Wang, X., Liou, J. G., and Mao, H. K. (1989). Coesite-bearing Eclogite from the Dabie Mountains in central China. *Geol* 17 (12), 1085–1088. doi:10.1130/0091-7613(1989)017<1085:cbeftd>2.3.co;2

Wong, J., Sun, M., Xing, G., Li, X. H., Zhao, G., Wong, K., et al. (2009). Geochemical and Zircon U–Pb and Hf Isotopic Study of the Baijuhuajian Metaluminous A-type Granite: Extension at 125–100Ma and its Tectonic Significance for South China. *Lithos* 112 (3-4), 289–305. doi:10.1016/j.lithos.2009.03.009

Wu, Y., Dao-gong, C., Xia, Q., and Cheng, H. (2001). SIMS U-Pb Dating of Zircons from Shuanghe Orthogneiss, Dabie Area[J]. *Bull. Mineralogy Petrol. Geochem.* 20 (04), 298–301. Available at: http://espace.library.uq.edu.au/view/UQ:105962

Xue-xie, L., Kang, W., and Pei-cang, X. (1993). Discovery Coesite in Eclogite and Kyante Quartzite from the Dabie Mountains, Henan Province. *J. Jilin University(Earth Sci. Edition)* 23 (03), 256–261.

Yang, S., Wu, Y., Xiao-chi, L., Wang, M., Peng, M., and Wen-fang, J. (2009). U-pb Ages of Detrital Zircon from Meta-Sedimentary Rock from the Huwan Shear Zone, Western Dabie Terrain and Their Geological Significance. *Earth Sci. (Journal China Univ. Geosciences)* 34 (01), 179–188. doi:10.3321/j.issn:1000-2383.2009.01.016

Yuan, Y., Xia, B., Zhang, Y., Lian-ze, X., and He, L. (2015). Geochemical Characteristics and Zircon U-Pb Ages of Gneiss in Luotian Country, Hubei Province. *Acta Geologica Sinica* 89 (01), 49–57.

Zhang, Y., Xia, B., Liang, H., Liu, H., and Lin, Q. (2004). Characteristics of Zircons for Dating from Daping Mylonitized Alkaline Granite in Yunnan

and Their Geologic Implications. *Geol. J. China Universities* 10 (03), 378–384. doi:10.1007/BF02873097

Zheng, X., Cheng-wei, J., Ming-guo, Z., and Shi, Y. (2000). Approach to the Source of the gray Gneisses in North Dabie Terrain: Sm-Nd Isochron Age and Isotope Composition[J]. *Acta Petrologica Sinica* 16 (2), 194–198.

Zheng, Y. F., Fu, B., Gong, B., and Li, L. (2003). Stable Isotope Geochemistry of Ultrahigh Pressure Metamorphic Rocks from the Dabie–Sulu Orogen in China: Implications for Geodynamics and Fluid Regime. *Earth-Science Rev.* 62 (1-2), 105–61. doi:10.1016/s0012-8252(02)00133-2

Zheng, Y. F., Zhao, Z. F., Wu, Y. B., Zhang, S. B., Liu, X., and Wu, F. Y. (2006). Zircon U–Pb Age, Hf and O Isotope Constraints on Protolith Origin of Ultrahigh-Pressure Eclogite and Gneiss in the Dabie Orogen. *Chem. Geology.* 231 (1-2), 135–158. doi:10.1016/j.chemgeo.2006.01.005

Conflict of Interest: Author ZS was employed by the company The 2nd Oil Production Plant of Daqing Oilfield Limited Company.

The remaining authors declare that the research was conducted in the absence of any commercial or financial relationships that could be construed as a potential conflict of interest.

Publisher's Note: All claims expressed in this article are solely those of the authors and do not necessarily represent those of their affiliated organizations, or those of the publisher, the editors, and the reviewers. Any product that may be evaluated in this article, or claim that may be made by its manufacturer, is not guaranteed or endorsed by the publisher.

frontiers in Earth Science

ORIGINAL RESEARCH
published: 28 March 2022
doi: 10.3389/feart.2022.799280

Paleoclimate Records of the Middle Okinawa Trough Since the Middle Holocene: Modulation of the Low-Latitude Climate

Lei Liu[1,2,3,4], *Hongxiang Guan*[1,2,3]*, *Lanfang Xu*[5,6], *Zhilei Sun*[3,4] *and Nengyou Wu*[1,3,4]*

[1]*Frontiers Science Center for Deep Ocean Multispheres and Earth System, Department of Environment Science and Engineering, Ocean University of China, Qingdao, China,* [2]*Key Lab of Submarine Geosciences and Prospecting Techniques, MOE and College of Marine Geosciences, Ocean University of China, Qingdao, China,* [3]*Laboratory for Marine Mineral Resources, Qingdao National Laboratory for Marine Science and Technology, Qingdao, China,* [4]*Key Laboratory of Gas Hydrate, Qingdao Institute of Marine Geology, Ministry of Natural Resources, Qingdao, China,* [5]*Guangzhou Institute of Energy Conversion, Chinese Academy of Sciences, Guangzhou, China,* [6]*University of Chinese Academy of Sciences, Beijing, China*

The ubiquity of glycerol dibiphytanyl glycerol tetraethers (GDGTs) and their temperature sensitivity make them one of the most effective tools for paleoclimate reconstruction. High- and low-latitude climates influence the Okinawa Trough (OT). It receives diverse inputs from the East China Sea, the western Pacific, and the Kuroshio Current, providing good conditions for paleoclimate studies. Here, isoprenoid GDGTs (isoGDGTs), branched GDGTs, and hydroxylated GDGTs (OH-GDGTs) were studied to reconstruct the sea surface temperature (SST) of the central OT for the past 8.2 kyr using the tetraether index of 86 carbon atoms at low latitudes (TEX_{86}^{H}) and the ring index of OH-GDGTs (RI-OH). The GDGT-0/crenarchaeol ratios ranged from 0.39 to 0.98. The branched and isoprenoid tetraether index and the methane index values were lower than 0.1 and 0.5, respectively, indicating that the isoGDGTs were mainly derived from marine *Thaumarchaeota* and that TEX_{86}^{H} could be used to reconstruct the paleotemperatures. The TEX_{86}^{H} SSTs ranged from 21.6 to 27.2°C during 8.2 kyr. The overall range of TEX_{86}^{H} SSTs is close to the $U_{37}^{K'}$ SST of the middle OT and reflects the mean annual SST. In contrast, RI-OH temperatures varied from 17.4 to 26.0°C, showing a lower trend than TEX_{86}^{H} SSTs. The core top RI-OH temperature is 24.1°C, in line with the mean annual seawater temperature at 40 m (24.2°C) in the study area, which likely reflects the subsurface temperature in this case. The small overall warming trend of TEX_{86}^{H} SSTs agrees with the increasing intensity of the Kuroshio Current during the last 8.2 kyr, indicating that the SST evolution is governed by the Kuroshio Current that transports heat from the western tropical Pacific. The decreasing temperature differences between TEX_{86}^{H} and RI-OH and between $U_{37}^{K'}$ and RI-OH showed increased mixing of the upper water column, which was in good accordance with the increasing low-latitude winter insolation decoupling from the East Asian summer monsoon. The cold event that occurred at 7.4–6.6 kyr was magnified (~5°C) at the TEX_{86}^{H} and RI-OH temperatures and possibly caused by tephra's significant input (~7.3 kyr).

Keywords: isoprenoid glycerol dibiphytanyl glycerol tetraethers, hydroxylated glycerol dibiphytanyl glycerol tetraethers, TEX_{86}^{H}, sea surface temperature, okinawa trough

OPEN ACCESS

Edited by:
Jiangong Wei,
Guangzhou Marine Geological Survey, China

Reviewed by:
Xiaowei Zhu,
South China Sea Institute of Oceanology, CAS, China
Zhifeng Wan,
Sun Yat-sen University, China

***Correspondence:**
Hongxiang Guan
guanhongxiang@ouc.edu.cn
Nengyou Wu
wuny@ms.giec.ac.cn

Specialty section:
This article was submitted to Geochemistry, a section of the journal Frontiers in Earth Science

Received: *21 October 2021*
Accepted: *18 February 2022*
Published: *28 March 2022*

Citation:
Liu L, Guan H, Xu L, Sun Z and Wu N (2022) Paleoclimate Records of the Middle Okinawa Trough Since the Middle Holocene: Modulation of the Low-Latitude Climate. Front. Earth Sci. 10:799280. doi: 10.3389/feart.2022.799280

INTRODUCTION

The Okinawa Trough, located in the western North Pacific, was influenced by the East Asian monsoon (ESM). Paleoclimate records indicated that correlations between temperature variation and East Asian summer monsoon (EASM) precipitation have become weak since the middle Holocene (Liew et al., 2006; Peterse et al., 2011; Park et al., 2014). However, such records in marine sediments are sparse (Xu et al., 2018 and references therein). The Okinawa Trough (OT) has been regarded as an ideal location for paleoclimatic, paleohydrogeological, and paleoceanographic studies because it is within the influence of the climate of both the high-latitude North Atlantic and the low-latitude western Pacific Ocean (Sun et al., 2005; Kubota et al., 2010; Ruan et al., 2015; Xu et al., 2018). The seasonal variations in EAM are driven by Northern Hemisphere summer and winter solar insolation, reflecting teleconnection with the high-latitude North Atlantic (An et al., 2001; Wang et al., 2005; Ruan et al., 2015; Huang and Sarnthein, 2021). The Kuroshio Current (KC) originates from the western Pacific warm pool and transports massive amounts of warm and salty water into the OT (Hu et al., 2015; Zheng et al., 2016). Paleoclimate indicators have demonstrated the influences of both the EAM and KC on the OT paleoclimate, such as oxygen isotopes (Kubota et al., 2010), Mg/Ca ratios of planktonic foraminifera (Sun et al., 2005), alkenone unsaturation index ($U^{K'}_{37}$; Ruan et al., 2015), and the tetraether index of 86 carbon atoms (TEX_{86}; Xu et al., 2018). Sea surface temperatures (SSTs) from different locations of the OT tend to reveal different controlling factors on the paleoclimate (Ruan et al., 2015; Zhao et al., 2015; Xu et al., 2018). The cold anomalies recorded in the northern Atlantic, such as the 4 kyr event, have affected the northern and southern OT paleoclimate (Sun et al., 2005; Ruan et al., 2015; Zhao et al., 2015). The $U^{K'}_{37}$ SST of the southern OT has been observed to have decreased since 7.4 kyr BP (Ruan et al., 2015), which was attributed to the reduction in Northern Hemisphere summer solar insolation and the weakening of EASM intensity (Ruan et al., 2015 and references therein). However, in the southern OT, Xu et al. (2018) found that paleotemperatures from $U^{K'}_{37}$/TEX_{86} decoupled from the EASM during the last 13.3 kyr BP. In contrast, the western tropical Pacific and Northern Hemisphere winter solar insolation were demonstrated to be the controlling factors of SSTs. Whether EAM changes in the OT are in phase with temperature changes in the EAM region during the Holocene remains unsolved (Liew et al., 2006; Peterse et al., 2011; Park et al., 2014). Therefore, further investigations are needed to elucidate the OT paleotemperature evolution and the controlling factors.

The TEX_{86} index (**Table 1**) was proposed by Schouten et al. (2002) based on the increasing number of cyclopentane rings in isoprenoid glycerol dibiphytanyl glycerol tetraethers (isoGDGTs) with increasing temperature (Gliozzi et al., 1983; Uda et al., 2001; Sinninghe Damsté et al., 2002). The export depth of the TEX_{86} signal in the water column is still under debate (Schouten et al., 2002, 2013; Ingalls et al., 2006; Rueda et al., 2009; Jia et al., 2012; Zhang and Liu, 2018). Most researchers now regard TEX_{86} as a better reflection of subsurface temperatures (Huguet et al., 2007; Jia et al., 2012). However, some studies have shown that TEX_{86} corresponds well with the annual mean SST (Ingalls et al., 2006; Rueda et al., 2009). Consequently, the use of TEX_{86} for temperature reconstruction in specific areas needs to be evaluated.

Marine Group I (MG-I) *Thaumarchaeota* were proposed to produce isoGDGTs used in the TEX_{86} equation (**Table 1**; **Supplementary Figure S1**; Brochier-Armanet et al., 2008; Spang et al., 2010). To achieve better accuracy, Kim et al. (2010) proposed TEX^{L}_{86} for high latitudes (<15°C) and TEX^{H}_{86} for low latitudes (>15°C) according to studies on global ocean samples (**Table 1**). To further assess the proxy, the Bayesian regression approach, which offers several advantages, was introduced to the TEX_{86}–SST calibration to provide a comprehensive estimation of past changes in SST from TEX_{86} in both modern and ancient environments (Tierney and Tingley, 2014). However, many environmental factors, except for SSTs, are included in the Bayesian regression approach for TEX_{86}–SST calibrations, making it more challenging to apply in geological sites than TEX^{L}_{86}/TEX^{H}_{86} (Kim et al., 2010; Tierney and Tingley, 2014). Since isoprenoid tetraethers produced by marine *Thaumarchaeota* can be mixed with those from *Euryarchaeota* thriving in seawater and *Thaumarchaeota* in soils, indicators such as branched and isoprenoid tetraether index (BIT; Hopmans et al., 2004) and methane index (MI; Zhang et al., 2011) are used to assess isoGDGTs contributed from soil origin and *Euryarchaeota*. For example, an MI less than 0.5 is used to preclude the contribution of methanotrophic archaea (Zhang et al., 2011). In addition to isoGDGTs, hydroxylated GDGTs (OH-GDGTs) are widespread in marine environments (Liu et al., 2012; Fietz et al., 2013; Huguet et al., 2013; Lü et al., 2015). In culture experiments, archaea affiliated with *Thaumarchaeota* Group I.1a have produced OH-GDGTs (Liu et al., 2012; Elling et al., 2014), which were not observed in *Thaumarchaeota* Group I.1b (Sinninghe Damsté et al., 2012b). The ratio of sum OH-GDGTs relative to sum isoGDGTs was related to SSTs and increased with increasing latitude (Huguet et al., 2013). In addition, a positive correlation between the number of cyclopentane rings of OH-GDGTs and SSTs was reported in the surface sediments from the subpolar and polar areas (Fietz et al., 2013). Although the mechanism for OH-GDGTs in response to SST is unclear, the ring index based on OH-GDGTs (RI-OH) is a potential approach for temperature reconstruction (**Table 1**; Lü et al., 2015; Yang et al., 2018).

TABLE 1 | Initial definitions of various proxies are used in this article.

Index	Definitions	authors
TEX_{86}	$(\frac{GDGT-2+GDGT-3+crenarchaeol\ isomer}{GDGT-1+GDGT-2+GDGT-3+crenarchaeol\ isomer})$	Schouten et al. (2002)
TEX^{L}_{86}	$log(\frac{GDGT-2}{GDGT-1+GDGT-2+GDGT-3})$	Kim et al. (2010)
RI − OH	$\frac{[OH-GDGT-1]+2\times[OH-GDGT-2]}{[OH-GDGT-1]+[OH-GDGT-2]}$	Lü et al. (2015)
BIT	$\frac{([GDGT-Ia]+[GDGT-IIa]+[GDGT-IIIa])}{([GDGT-Ia]+[GDGT-IIa]+[GDGT-IIIa]+Crenarchaeol)}$	Hopmans et al. (2004)
MI	$\frac{[GDGT-1]+[GDGT-2]+[GDGT-3]}{[GDGT-1]+[GDGT-2]+[GDGT-3]+[Crenarchaeol]+[crenarchaeol\ isomer]}$	Zhang et al. (2011)
%GDGT − 2	$\frac{GDGT-2}{[GDGT-1]+[GDGT-2]+[GDGT-3]+[crenarchaeol\ isomer]}$	Sinninghe Damsté et al. (2012a)

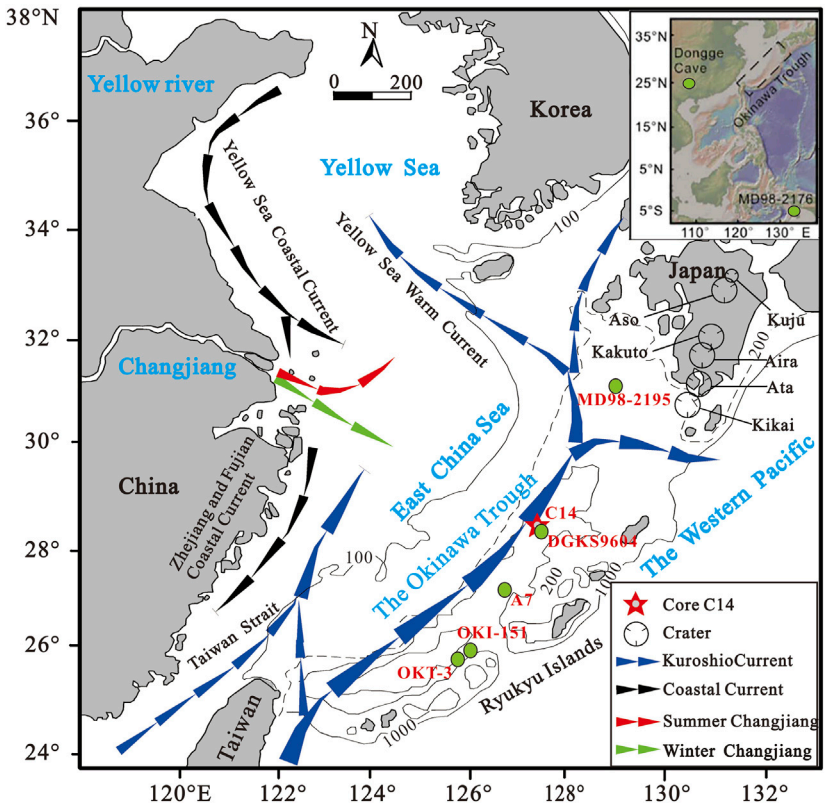

FIGURE 1 | Location of core C14 in the middle Okinawa Trough (OT) and selected paleoenvironmental settings, including Dongge Cave in southern China (Dykoski et al., 2005), core MD98-2176 in the western tropical Pacific (Stott et al., 2004), cores A7 (Sun et al., 2005) and DGKS9604 (Yu et al., 2009) in the middle OT, cores OKT-3 (Zhao et al., 2015) and OKI-151 (Xu et al., 2018) in the southern OT, and core MD98-2195 (Yamamoto et al., 2013) in the northern OT. The map was revised from Dou et al. (2010). The Contour unit is meter. Volcano locations around Japan were modified according to Machida (1999).

TEX_{86}^{H} has been used to reconstruct the paleotemperature records of the southern and northern OT, and a gradual warming trend has been identified since the Holocene (Yamamoto et al., 2013; Zhao et al., 2015; Xu et al., 2018). Generally, shifts in the main axis and changes in the KC strength, variations in EAM, sea-level changes, and freshwater inputs are potential factors for paleoclimate changes in the OT (Jian et al., 2000; Kubota et al., 2010; Zhao et al., 2015). The influence of the EAM on SST variations was identified in the middle and northern OT (Yu et al., 2009; Kubota et al., 2010). However, low-latitude western tropical Pacific dominance via KC variations has been demonstrated in the southern OT (Xu et al., 2018). Therefore, factors controlling the paleotemperature in specific areas of the OT need to be clarified. Here, we used TEX_{86}^{H} temperatures and temperatures calibrated from RI-OH as an approach to reconstruct the paleoclimate and hydrological evolution of the middle OT since the middle Holocene.

OCEANOGRAPHIC SETTING

The OT, a back-arc basin, formed from the subduction of the Philippine Sea Plate beneath the Eurasian Plate at the Ryukyu Trench (**Figure 1**; Sibuet et al., 1998; Guo et al., 2022). The strike direction of the middle OT is approximately NE–SW, E–W to the south, and NNE–SSW to the north (Wu et al., 2014). The EAM and KC have been reported to dominate the modern oceanography of the middle OT (Ruan et al., 2015; Zhao et al., 2015). Two distinct seasons are present due to the seasonal reversals of the EAM, driven by the annual cycle of insolation and its effect on the land-sea thermal contrast (Dykoski et al., 2005; Sun et al., 2005; Wang et al., 2005; Huang and Sarnthein, 2021). In the boreal summer, a warm, wet season caused by the northward migration of the intertropical convergence zone and the maximum monsoonal convective rainfall dominates the OT (Wang et al., 2005; Zheng et al., 2014). In contrast, northeasterly winds lead to a cool, dry season in the boreal winter (Diekmann et al., 2008; Zheng et al., 2014). The KC, originating from the Western Pacific warm pool, flows northeast above the OT and returns to the North Pacific through the Tokara Strait (Yu et al., 2009; Hu et al., 2015), taking warm, saline water into the OT (Hu et al., 2015).

The sea level has been roughly constant for the study area during the last 8.2 kyr BP (Liu et al., 2004). The sediment core C14 is far from the coastline and the shelf of the East China Sea (ECS; **Figure 1**). At present, the mean annual SST is 24.8°C, with

TABLE 2 | Planktonic foraminifera ^{14}C age data.

series	Depth (cmbsf)	Planktonic foraminifera	AMS ^{14}C age (yr BP)	Calibrated age (yr BP)
498910	35–37.5[a]	*G.ruber* + *G.sacculifer*	660±30	616–730
498911	65–67.5	*G.ruber* + *G.sacculifer*	930±30	994–820
498912	155–157.5[a]	*G.ruber* + *G.sacculifer*	1890±30	1858–2045
498913	245–247.5	*G.ruber* + *G.sacculifer*	2800±30	3172–2957
498914	365–367.5[a]	*G.ruber* + *G.sacculifer*	4350±30	4943–5227
498915	455–457.5	*G.ruber* + *G.sacculifer*	5840±30	6831–6646
498916	545–547.5	*G.ruber* + *G.sacculifer*	6500±30	7520–7385
498917	575–577.5[a]	*G.ruber* + *G.sacculifer*	7340±30	8170–8327

[a]*Data from Xu et al. (2020).*

summer and winter seasonal temperatures of approximately 27.8 and 22.1°C, respectively. The maximum SST near the core site is 28.7 °C in August, and the minimum is 21.5°C in February (Locarnini et al., 2013).

METHODS

Materials and Age Model

Sediment core C14 (580 cm in length) was retrieved from the middle OT at a water depth of approximately 1100 m (**Figure 1**; 28°39.587′N, 127°19.194′E). The top part of the core was lost during sampling. To make up the lost part, the upper 10 cm of core C10 (28°38.8′N, 127°21.283′E; water depth of 960 m) was utilized to represent the missing top part. After sampling, the sediment core was segmented, transported to the laboratory, and kept at −20°C until analysis. A tephra layer was found between depths of 532.5 and 442.5 cm.

To obtain AMS ^{14}C dating for the core, eight samples of the planktonic foraminifer *Globigerinoides ruber* (*G. ruber*) and *G. sacculifer* were selected at equal intervals and analyzed by Beta Analytic Inc., United States (**Table 2**). The raw ^{14}C dates were calibrated using the Marine13 dataset (Reimer et al., 2013) and expressed in calibrated years BP (years before AD 1950). We adopted a ΔR value of 30 ± 41 years in the calibration.

Lipid Extraction

37 samples were collected at 15–30 cm intervals from core C14 (36 samples from core C14 and 1 from core C10). They were freeze-dried and homogenized. Twenty to 30 g of powder (dry weight) were Soxhlet-extracted for 72 h with a mixture of dichloromethane and methanol (9:1; v:v) to obtain the total lipid extracts (TLEs). The TLE was separated into neutral (n-hexane) and polar (methanol) fractions with a silica gel column. The polar fractions were filtered through a 0.45 μm polytetrafluoroethylene filter membrane (PTFE) to remove particulate matter and stored at −20°C.

Instrumental Analysis

The dried polar fractions were redissolved in 300 μl *n*-hexane and isopropanol (98.2:1.8, v/v). No internal standard was added. The analysis was performed on an Agilent 1200 series high-performance liquid chromatography–atmospheric pressure chemical ionization-6460 triple, quadruple mass spectrometer (HPLC–APCI-MS^2) following the analytical protocol of Hopmans et al. (2016). Separation was achieved on two HPLC silica columns (BEH HILIC columns, 2.1 × 150 mm, 1.7 μm) in series, maintained at 30°C. The GDGTs were eluted isocratically for 25 min with 18% B, followed by a linear gradient to 35% B in 25 min and then a linear gradient to 100% B in 30 min and kept in for 10 min to clean the column with a constant flow rate of 0.2 ml/min. Finally, the gradient of B was back at 18% for 20 min to re-equilibrate the column. Solvent A was *n*-hexane, and B was *n*-hexane: isopropanol (9:1, v/v). The GDGTs were ionized in an atmospheric pressure chemical ionization chamber and detected using single ion monitoring (SIM) mode. The relative abundance of compounds was determined by integrating the areas of the $(M + H]^+$ (protonated molecular ion) peaks at 1302, 1300, 1298, 1296, and 1292 for isoGDGTs and OH-GDGTs (Liu et al., 2012) and 1050, 1048, 1046, 1036, 1034, 1032, 1022, 1020, and 1018 for branched GDGTs (brGDGTs). The analytical error for duplicate measurements was better than ±0.008. The positive ion APCI settings were set as follows (Hopmans et al., 2016): probe heater temperature, 400°C; sheath gas (N_2) pressure, 50 AU (arbitrary units); auxiliary gas (N_2) pressure, 5 AU; spray current, 5 μ A; capillary temperature, 3500°C; S-lens, 100 V.

TEX_{86}^{H}, RI-OH and BIT

In this study, the SST calibration of the TEX_{86}^{H} proxy (Kim et al., 2010) was used to reconstruct the paleoclimate evolution due to the high temperatures of over 15°C (low latitude) in the OT. Cren' represents the crenarchaeol isomer (see **Supplementary Figure S1** for details).

$$TEX_{86}^{H} = \log\left(\frac{GDGT-2+GDGT-3+Cren'}{GDGT-1+GDGT-2+GDGT-3+Cren'}\right);$$
$$SST = 68.4\times\left(TEX_{86}^{H}\right) + 38.6 \quad (1)$$

The empirical equation of RI-OH (Lü et al., 2015) was used to supplement the SST reconstruction.

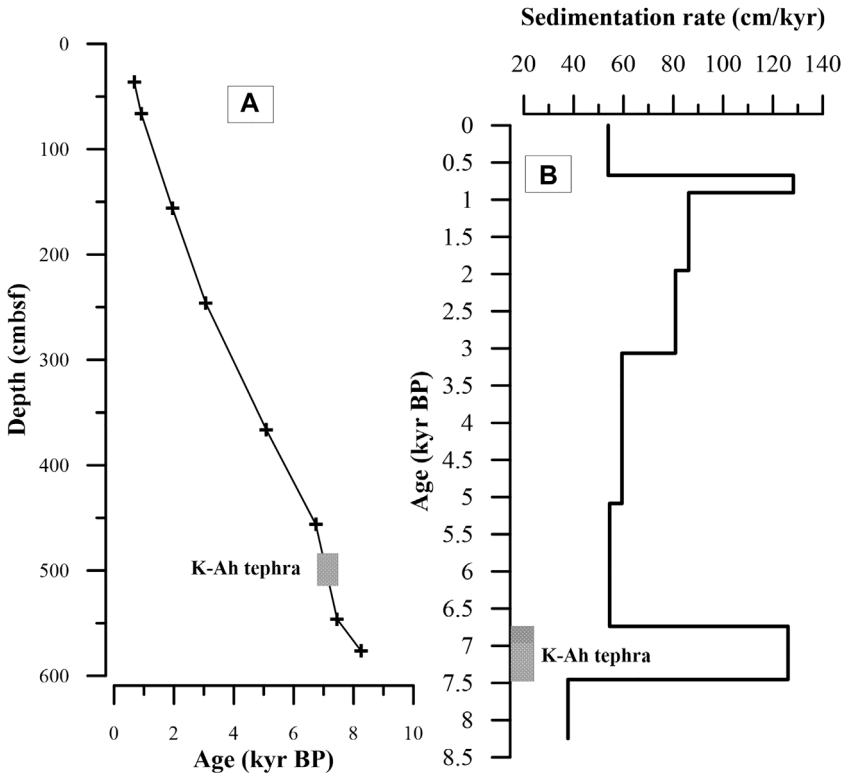

FIGURE 2 | (A) Age-depth model of core C14; **(B)** sedimentation rates of core C14.

$$\begin{aligned} \text{RI}-\text{OH} &= \frac{[\text{OH}-\text{GDGT}-1]+2\times[\text{OH}-\text{GDGT}-2]}{[\text{OH}-\text{GDGT}-1]+[\text{OH}-\text{GDGT}-2]}; \\ \text{SST} &= 35.71\times\text{RI}-\text{OH}-32.86 \end{aligned} \quad (2)$$

Based on the analytical error (±0.008), we calculated the corresponding errors, which are approximately ±0.4°C and ±0.3°C for calibrations 1) and (2), respectively.

As brGDGT regio isomers were detected (**Supplementary Figure S1**; De Jonge et al., 2014), the BIT formula used in this article was modified as follows:

$$\text{BIT} = \frac{\begin{array}{c}\text{GDGT}-\text{Ia}+\text{GDGT}-\text{IIa}+\text{GDGT}-\text{IIa}' \\ +\text{GDGT}-\text{IIIa}+\text{GDGT}-\text{IIIa}'\end{array}}{\begin{array}{c}\text{Crenarcheaol}+\text{GDGT}-\text{Ia}+\text{GDGT}-\text{IIa} \\ +\text{GDGT}-\text{IIa}'+\text{GDGT}-\text{IIIa}+\text{GDGT}-\text{IIIa}'\end{array}} \quad (3)$$

RESULTS

AMS ^{14}C Dating

The AMS ^{14}C dating results are listed in **Table 2**. The time scale was established by linear interpolation and extrapolation. An age model was set for core C14 after calibration, and the mean sedimentation rate of core C14 was ~70 cm/kyr during the last 8.2 kyr BP (**Figures 2A,B**). For the tephra layer at 532.5–442.5 cm (7.4–6.6 kyr BP), an extremely high sedimentation rate of ~126 cm/kyr was identified (**Figure 2B**).

Distribution of GDGTs

The relative contributions of the isoGDGTs, brGDGTs, and OH-GDGTs are listed in **Table 3**. The isoGDGTs dominated all GDGTs, with contributions ranging from 88 to 98%, while brGDGTs accounted for 1.4–10.3%, and OH-GDGTs accounted for less than 6.0% of the total GDGTs. Crenarchaeol was the most abundant component among the isoGDGTs in all of the samples, accounting for 32–50% of all of the isoGDGTs, followed by GDGT-0 (range 16–32%), whereas only small amounts of GDGT-1, -2, -3, and the crenarchaeol isomer were detected in all of the samples.

Past Temperatures Reconstructed by isoGDGT- and OH-GDGT-Based Proxies

For the past 8.2 kyr BP, the $\text{TEX}_{86}^{\text{H}}$ values in core C14 ranged from −0.25 to −0.17, corresponding to temperatures ranging from 21.6 to 27.2°C (**Equation 2**; **Table 4**; **Figure 3C**). The index of RI-OH in core C14 ranged from 1.41 to 1.65, revealing temperatures ranging from 17.4 to 26.0°C (**Equation 3**; **Table 4**; **Figure 3C**). To better understand TEXH86 and RI-OH temperatures, the mean seasonal and annual temperatures and monthly mean water

TABLE 3 | The contribution of specific GDGTs with depth in core C14.

Sample	Depth (cmbsf)	%isoGDGTs							% (b)	% (OH)		
		% [0]	% [1]	% [2]	% [3]	% [4]	%Cren	%cren'		% [OH-0]	% [OH-1]	% [OH-2]
C10_01	7.5	21.45	5.54	5.82	1.26	12.48	47.67	2.78	2.09	0.25	0.27	0.39
C14_01	37.5	21.68	5.10	5.75	1.21	12.22	47.81	3.16	1.96	0.31	0.33	0.47
C14_02	67.5	20.82	5.45	5.54	1.22	12.00	48.40	3.61	1.93	0.24	0.29	0.50
C14_03	83.75	18.28	9.52	9.78	3.10	3.93	46.79	5.66	2.94	-	-	-
C14_04	97.5	20.79	5.14	5.58	1.20	12.78	48.82	3.13	1.71	0.22	0.25	0.38
C14_05	127.5	20.54	5.14	6.13	1.31	12.46	47.98	3.56	1.87	0.23	0.31	0.47
C14_06	143.75	17.33	7.18	8.69	2.48	8.18	44.51	4.20	7.43	-	-	-
C14_07	157.5	20.96	5.29	5.93	1.26	11.62	48.91	3.41	1.80	0.20	0.27	0.35
C14_08	173.75	25.23	9.14	11.31	1.69	5.60	36.62	4.46	3.33	1.15	0.58	0.89
C14_09	187.5	21.57	5.26	6.07	1.24	11.53	48.52	3.11	1.85	0.20	0.23	0.42
C14_10	203.75	16.29	10.37	12.02	3.03	5.76	36.25	4.91	6.71	1.68	1.19	1.79
C14_11	212.5	20.34	5.45	6.14	1.29	11.86	49.36	3.15	1.57	0.21	0.24	0.39
C14_12	217.5	19.74	5.47	5.55	1.31	11.77	50.44	3.26	1.56	0.22	0.26	0.42
C14_13	228.75	29.09	8.98	9.72	2.30	5.86	33.58	4.74	5.73	-	-	-
C14_14	247.5	20.34	5.31	5.54	1.23	12.97	48.41	3.61	1.76	0.19	0.23	0.41
C14_15	263.75	23.73	9.36	9.82	2.80	4.97	35.58	4.34	5.77	1.74	0.75	1.14
C14_16	277.5	21.19	5.13	5.47	1.18	11.98	49.71	2.95	1.50	0.24	0.25	0.40
C14_17	293.75	27.12	9.35	8.92	2.26	6.14	34.96	5.35	5.90	-	-	-
C14_18	307.5	21.13	5.67	5.65	1.30	12.54	48.32	3.04	1.47	0.24	0.26	0.38
C14_19	323.75	21.95	9.35	10.71	2.11	5.16	34.73	5.66	10.33	-	-	-
C14_20	337.5	19.93	5.24	5.61	1.26	12.36	49.93	3.44	1.42	0.18	0.24	0.39
C14_21	353.75	19.68	9.25	10.39	2.93	6.70	35.68	5.49	5.94	1.80	0.84	1.30
C14_22	367.5	19.90	5.12	5.59	1.17	12.51	50.20	3.22	1.47	0.21	0.25	0.36
C14_23	383.75	18.78	12.18	13.76	3.63	6.19	37.11	5.63	2.72	-	-	-
C14_24	397.5	21.86	5.26	5.80	1.20	12.42	48.27	2.91	1.43	0.23	0.25	0.37
C14_25	413.75	24.83	7.63	9.14	2.24	6.38	37.73	3.98	4.58	1.23	0.94	1.32
C14_26	427.5	22.82	5.83	5.80	1.19	11.66	47.11	2.90	1.62	0.32	0.32	0.43
C14_27	443.75	29.44	7.63	7.50	1.92	4.85	38.14	4.21	3.63	1.24	0.73	0.71
C14_28	457.5	28.62	4.67	3.72	0.86	10.68	46.05	1.90	1.93	0.66	0.53	0.38
C14_29	473.75	23.81	8.90	7.59	1.77	6.13	38.92	2.74	5.37	2.50	1.31	0.96
C14_30	487.5	29.24	4.81	3.62	0.91	11.43	44.48	1.74	2.06	0.73	0.57	0.41
C14_31	503.75	26.67	7.06	6.04	1.46	7.27	40.36	2.16	4.53	2.60	1.10	0.75
C14_32	517.5	29.25	5.17	4.02	0.90	11.48	43.30	1.79	2.18	0.88	0.58	0.45
C14_33	533.75	31.63	6.41	6.54	1.48	8.39	32.20	2.37	5.32	2.32	1.66	1.68
C14_34	547.5	20.13	5.60	5.71	1.14	12.45	49.15	3.09	1.79	0.25	0.31	0.38
C14_35	563.75	23.21	8.50	9.94	2.38	5.47	33.10	5.71	8.29	1.27	1.01	1.12
C14_36	577.5	21.56	5.34	5.96	1.10	12.81	47.57	3.12	1.68	0.25	0.25	0.36

(x), GDGT-x; Cren, crenarchaeol; Cren', crenarchaeol isomer; (b), brGDGTs; (OH-x), OH-GDGT-x

temperatures at different depths are summarized in **Figures 3A,B**.

DISCUSSION

Constrains of GDGT Sources

The isoGDGTs used in TEX_{86} are derived from marine *Thaumarchaeota* (Brochier-Armanet et al., 2008; Spang et al., 2010; Schouten et al., 2013). However, GDGTs-1, -2, -3, and the crenarchaeol isomer can also be synthesized by additional archaea (Sinninghe Damsté et al., 2002; Schouten et al., 2008; Pitcher et al., 2011). For example, marine group II (MG-II) *Euryarchaeota* thriving in shallow water can synthesize GDGTs-1, -2, and -3 (Turich et al., 2007; Schouten et al., 2008). IsoGDGTs from soil and brGDGTs produced *in situ* in marine environments may contribute to the GDGT pool (Hopmans et al., 2004; Peterse et al., 2009; Schouten et al., 2013). Such inputs may affect the application of TEX_{86} in paleotemperature reconstruction. Therefore, indicators such as BIT (Hopmans et al., 2004; De Jonge et al., 2014), GDGT-0/crenarchaeol (Blaga et al., 2009), MI (Zhang et al., 2011), GDGT-2/crenarchaeol (Weijers et al., 2011), %GDGT-2 (Sinninghe Damsté et al., 2012a), and GDGT-2/GDGT-3 (Taylor et al., 2013) were introduced to assess the biological precursors of the isoGDGTs (**Table 1**).

In this study, crenarchaeol was the most abundant component among isoGDGTs, with GDGT-0/crenarchaeol ratios ranging from 0.4 to 1.0 (between 0.2 and 2), suggesting that the isoGDGTs were predominantly produced by MG-I *Thaumarchaeota* in core 14 (Schouten et al., 2008, 2013; Spang et al., 2010). IsoGDGTs introduced by soil and rivers were negligible, as indicated by the low BIT values of 0.01–0.10 (<0.10; **Table 4**; Hopmans et al., 2004; Kim et al., 2010; De Jonge et al., 2014). Apart from terrestrial input, methanotrophic *Euryarchaeota* prevailing in cold seeps can contribute to GDGT-1, -2, and -3 and modify the distribution of isoGDGTs (Elvert et al., 2005; Guan et al., 2019). In this study, the ratios of GDGT-2/crenarchaeol varied from 0.1 to 0.4 (<0.4), GDGT-

TABLE 4 | Various indices were used to evaluate the application of TEX_{86} and reconstruct paleotemperatures in core C14.

Sample	Depth (cmbsf)	Age (kyr)	%GDGT-2	GDGT-0/Cren	GDGT-2/Cren	GDGT-2/GDGT-3	MI	BIT	TEX_{86}^{H}		RI-OH	
									Values	SST (°C)	Values	SST (°C)
C10_01	7.5	0.1	38	0.5	0.1	4.6	0.2	0.02	–0.196	25.2	1.596	24.1
C14_01	37.5	0.7	38	0.5	0.1	4.7	0.2	0.02	–0.177	26.5	1.593	24
C14_02	67.5	0.9	35	0.4	0.1	4.6	0.2	0.01	–0.184	26	1.631	25.4
C14_03	83.75	1.1	35	0.4	0.2	3.2	0.3	0.02	–0.18	26.3	-	-
C14_04	97.5	1.2	37	0.4	0.1	4.7	0.2	0.01	–0.182	26.2	1.605	24.5
C14_05	127.5	1.6	38	0.4	0.1	4.7	0.2	0.02	–0.167	27.2	1.599	24.3
C14_06	143.75	1.8	39	0.4	0.2	3.5	0.3	0.1	–0.166	27.2	-	-
C14_07	157.5	2.0	37	0.4	0.1	4.7	0.2	0.01	–0.176	26.6	1.564	23
C14_08	173.75	2.2	43	0.7	0.3	6.7	0.4	0.06	–0.183	26.1	1.605	24.5
C14_09	187.5	2.3	39	0.4	0.1	4.9	0.2	0.01	–0.177	26.5	1.647	26
C14_10	203.75	2.5	40	0.5	0.3	4.0	0.4	0.05	–0.182	26.2	1.601	24.3
C14_11	212.5	2.6	38	0.4	0.1	4.8	0.2	0.01	–0.18	26.3	1.621	25
C14_12	217.5	2.8	36	0.4	0.1	4.3	0.2	0.01	–0.188	25.8	1.615	24.8
C14_13	228.75	2.9	38	0.9	0.3	4.2	0.4	0.06	–0.186	25.8	-	-
C14_14	247.5	3.1	35	0.4	0.1	4.5	0.2	0.01	–0.179	26.3	1.634	25.5
C14_15	263.75	3.4	37	0.7	0.3	3.5	0.4	0.06	–0.191	25.5	1.601	24.3
C14_16	277.5	3.6	37	0.4	0.1	4.6	0.2	0.01	–0.186	25.9	1.611	24.7
C14_17	293.75	3.9	35	0.8	0.3	4.0	0.3	0.07	–0.195	25.3	-	-
C14_18	307.5	4.1	36	0.4	0.1	4.3	0.2	0.01	–0.195	25.2	1.593	24
C14_19	323.75	4.4	39	0.6	0.3	5.1	0.4	0.1	–0.178	26.4	-	-
C14_20	337.5	4.6	36	0.4	0.1	4.5	0.2	0.01	–0.178	26.4	1.622	25.1
C14_21	353.75	4.9	37	0.6	0.3	3.5	0.4	0.06	–0.174	26.7	1.608	24.6
C14_22	367.5	5.1	37	0.4	0.1	4.8	0.2	0.01	–0.18	26.3	1.59	23.9
C14_23	383.75	5.4	39	0.5	0.4	3.8	0.4	0.03	–0.184	26	-	-
C14_24	397.5	5.6	38	0.5	0.1	4.8	0.2	0.01	–0.185	26	1.591	24
C14_25	413.75	5.9	40	0.7	0.2	4.1	0.3	0.04	–0.175	26.6	1.584	23.7
C14_26	427.5	6.2	37	0.5	0.1	4.9	0.2	0.01	–0.201	24.8	1.575	23.4
C14_27	443.75	6.5	35	0.8	0.2	3.9	0.3	0.03	–0.193	25.4	1.496	20.6
C14_28	457.5	6.7	33	0.6	0.1	4.3	0.2	0.02	–0.236	22.5	1.421	17.9
C14_29	473.75	6.9	36	0.6	0.2	4.3	0.3	0.04	–0.239	22.2	1.424	18
C14_30	487.5	7.0	33	0.7	0.1	4.0	0.2	0.02	–0.247	21.7	1.417	17.7
C14_31	503.75	7.1	36	0.7	0.2	4.1	0.3	0.04	–0.238	22.3	1.406	17.4
C14_32	517.5	7.2	34	0.7	0.1	4.5	0.2	0.02	–0.248	21.6	1.436	18.4
C14_33	533.75	7.4	39	1.0	0.2	4.4	0.3	0.04	–0.209	24.3	1.504	20.9
C14_34	547.5	7.5	37	0.4	0.1	5.0	0.2	0.01	–0.194	25.3	1.548	22.4
C14_35	563.75	7.9	38	0.7	0.3	4.2	0.4	0.08	–0.168	27.1	1.526	21.6
C14_36	577.5	8.2	38	0.5	0.1	5.4	0.2	0.01	–0.183	26.1	1.586	23.8

2/GDGT-3 showed a constant trend below 5.0, the MI index ranged between 0.2 and 0.4 (<0.5), and %GDGT-2 fell in the range of 33–39 (<45), indicating that the contributions of methanotrophic archaea and MG-II *Euryarchaeota* were low (**Table 4**; Blaga et al., 2009; Weijers et al., 2011; Zhang et al., 2011; Sinninghe Damsté et al., 2012a; Taylor et al., 2013). Consequently, isoGDGTs predominantly originating from MG-I *Thaumarchaeota* and TEX_{86}^{H} can be used to reconstruct paleotemperatures in core C14.

Implications of TEX_{86}^{H} Temperatures

TEX_{86}^{H} studies revealed relatively variable temperature records in the OT and ECS (Nakanishi et al., 2012; Xu et al., 2018; Yuan et al., 2018). Yamamoto et al. (2013) compared temperatures derived from Mg/Ca, $U_{37}^{K'}$ and TEX_{86}^{H} at site MD98-2195 of the northern OT. Mg/Ca- and $U_{37}^{K'}$-derived temperatures were assigned to summer and spring seawater temperatures, respectively, because they behaved differently to seasonal variations in the sinking fluxes. Still, the core-top values yielded similarities to summer and spring SSTs, respectively (Yamamoto et al., 2013 and references therein). Since GDGTs in sinking particles were well mixed, the lower TEX_{86}^{H} temperature most likely represented the annual subsurface seawater temperature, as assumed by Yamamoto et al. (2013). However, Zhao et al. (2015) showed similarity between modern summer seawater temperature and core-top TEX_{86}^{H} temperature at the southern OT and concluded that both $U_{37}^{K'}$ and TEX_{86}^{H} temperatures represented summer SSTs. Similar observations were made by Xu et al. (2018), and both $U_{37}^{K'}$ and TEX_{86}^{H} temperatures were used to indicate annual SST at the southern OT. Therefore, TEX_{86}^{H} calibrations for specific locations may be closely related to the specific local hydrology. In this study, the core-top TEX_{86}^{H} and RI-OH temperatures at the study site were 25.2 and 24.1°C, respectively. This is in line with the mean annual SST (24.8°C) and mean annual seawater temperature at 40 m below the sea surface (24.2°C) (**Figure 3A**). In addition, the core-top TEX_{86}^{H} temperature agreed well with the SST in June and November and the average temperature from June to November

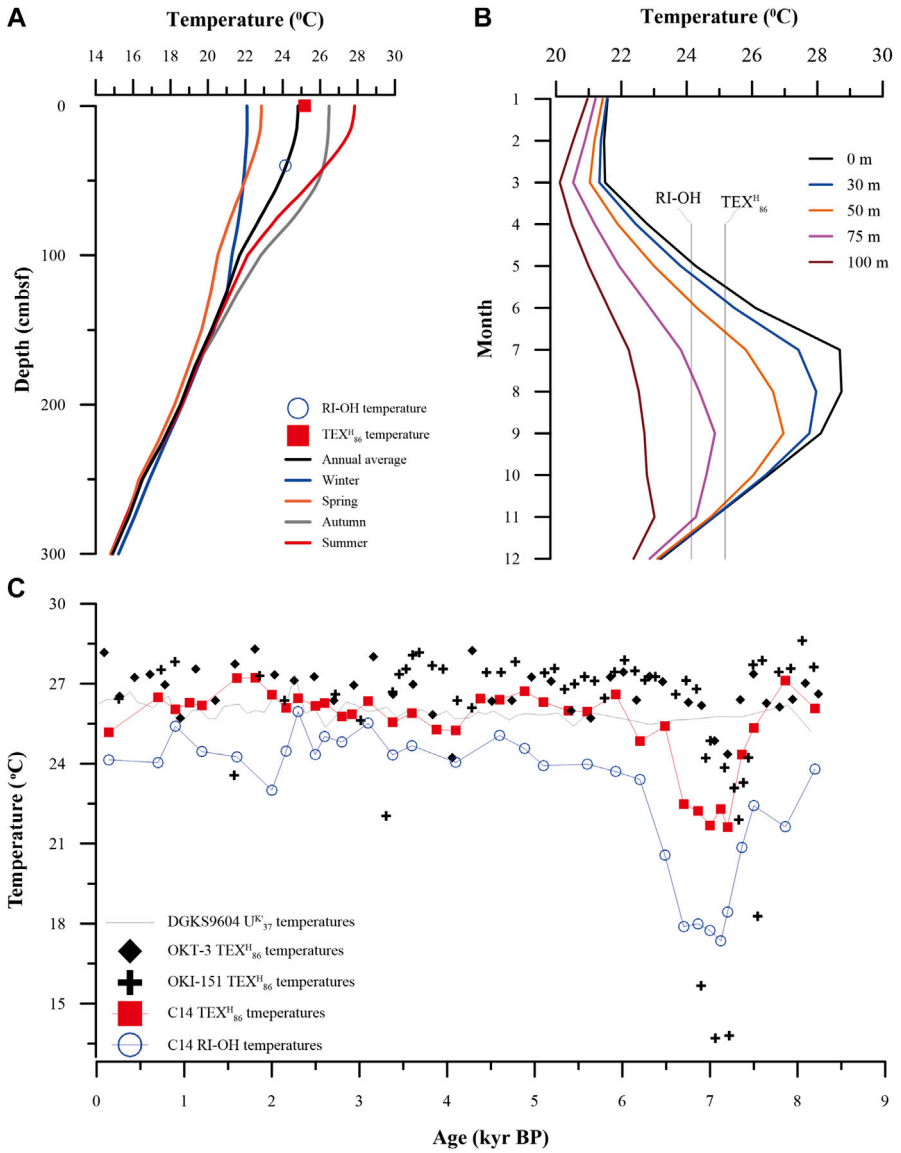

FIGURE 3 | Paleotemperatures derived from core C14 and nearby sites. **(A)** Mean seasonal and annual temperatures at the study site; **(B)** monthly mean water temperatures at different depths at the study site. Data are from Locarnini et al. (2013). **(C)** Comparisons between BIT, TEX_{86}^{H} and RI-OH temperatures from core C14 from the middle OT, TEX_{86}^{H} temperatures from OKT-3 and OKI-151 from the southern OT (Zhao et al., 2015; Xu et al., 2018), and $U_{37}^{K'}$ temperatures from DGKS9604 from the middle OT (Yu et al., 2009).

at depths of 50–7 m (**Figure 3B**). However, TEX_{86}^{H} reflects SST in a specific month, which is unlikely because the GDGTs produced in different seasons have been demonstrated to be suspended and well mixed in the surface water in both the western North Pacific (Yamamoto et al., 2012) and the northern OT (Nakanishi et al., 2012). In this study, the average TEX_{86}^{H} SST (26.1 ± 1°C; except for 7.4–6.6 kyr BP) in core C14 is comparable to the TEX_{86}^{H} SST of the southern OT from 8.2 kyr BP to the present (**Figure 3C**; Zhao et al., 2015; Xu et al., 2018), which is close to the average $U_{37}^{K'}$ SST (26.0 ± 1.3°C; **Figure 3C**) when compared to a nearby site (core DGKS9604; Yu et al., 2009), indicating that the TEX_{86}^{H} temperatures during the last 8.2 kyr BP reflected mean annual SSTs rather than temperatures in a specific short period.

Interestingly, the temperatures derived from RI-OH were generally lower than the TEX_{86}^{H} and $U_{37}^{K'}$ SSTs with a similar changing pattern and trend (**Table 4**; **Figures 3A,C**). To date, the biological precursors of OH-GDGTs remain unclear. To date, OH-GDGTs have been observed in cultures of archaea affiliated with *Thaumarchaeota Group* I.1a (Sinninghe Damsté et al., 2012b; Elling et al., 2014), whereas TEX_{86}-related isoGDGTs are explicitly ascribed to *Thaumarchaeota* Group I.1b (Brochier-Armanet et al., 2008; Spang et al., 2010). The potentially different origins of OH-GDGTs suggest that the RI-OH index may supplement TEX_{86}^{H} in marine environments (Lü et al., 2015). Lü et al. (2015) and Yang et al. (2018) analyzed the surface sediments of the marginal sea in China and revealed a high correlation between RI-OH and the local mean

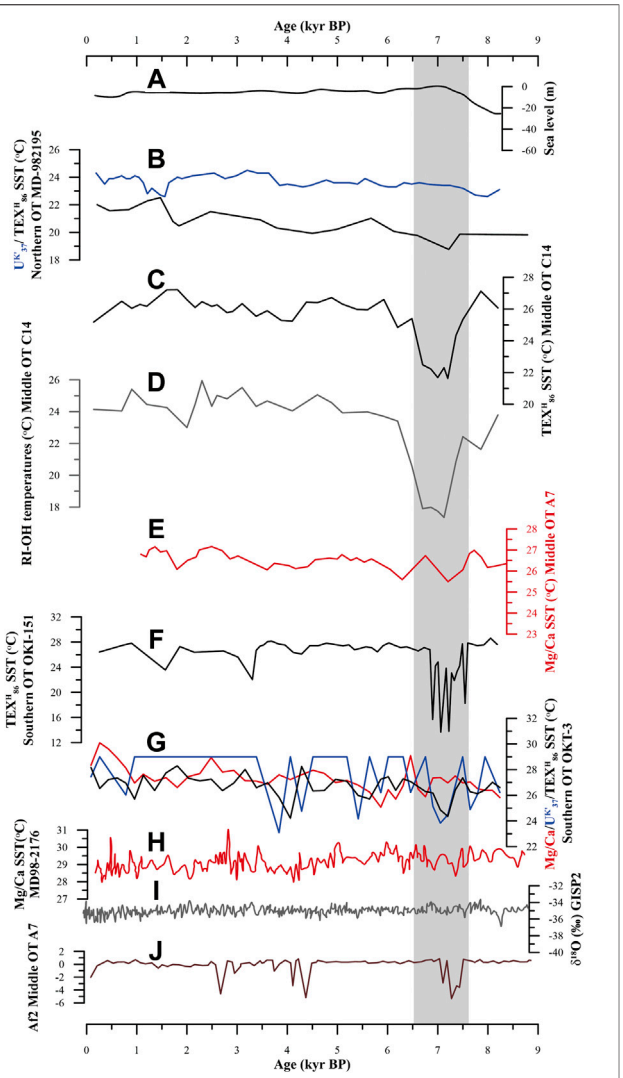

FIGURE 4 | Comparison of paleotemperature variations inferred from core C14 with other paleoclimate data. **(A)** Postglacial sea-level changes in the western Pacific (Liu et al., 2004); **(B)** Temperatures from $U^{K'}_{37}$ (blue) and TEX^{H}_{86} (dark) in core MD98-2195 (Yamamoto et al., 2013); **(C)** TEX^{H}_{86} SST of C14 in this article; **(D)** Temperatures from RI-OH in core C14 in this article; **(E)** Mg/Ca SST of A7 (Sun et al., 2005); **(F)** SST from TEX^{H}_{86} in core OKI-151 (Xu et al., 2018); **(G)** SST from Mg/Ca (red), $U^{K'}_{37}$ (blue) and TEX^{H}_{86} (black) in core OKT-3 (Zhao et al., 2015); **(H)** Mg/Ca SST data from core MD98–2176 in the western tropical Pacific (Stott et al., 2004); **(I)** $\delta^{18}O$ record from the GISP2 ice core (Stuiver and Grootes, 2000); **(J)** the factor representing the western tropical Pacific (Stott et al., 2004); (i) $\delta^{18}O$ record from the GISP2 ice core (Stuiver and Grootes, 2000).

annual SST. Such correlations possibly suggested that OH-GDGTs produced in different seasons have been well mixed in seawater before preservation in sediments (Lü et al., 2015). The core-top RI-OH temperature agreed well with the SSTs in May and December, which most likely reflected subsurface temperatures in the present study (**Figure 3B**).

Cold Events Identified in the Middle Okinawa Trough

In core 14, a warming trend during the last 8.2 kyr BP with an apparent cold event at 7.4–6.6 kyr BP was found using TEX^{H}_{86} and RI-OH proxies. Paleoclimate studies have indicated that the cold anomalies in the North Atlantic may have spread signals of rapid climate changes via the westerlies to the Asian monsoon regions (Dykoski et al., 2005; Sun et al., 2005; Wang et al., 2005). However, studies on the Holocene paleoclimate suggested that the tropical Pacific likely controlled the paleotemperature in East Asia via KC variations rather than the North Atlantic (Lim and Fujiki, 2011; Xu et al., 2018). The KC, the northward branch of the North Pacific subtropical gyre, exerts an influence on the exchange of climatic properties of downstream regions in the Pacific Ocean and is a mediator of the Pacific to the OT (Hu et al., 2015). An intensified trend of the KC since the Holocene has been demonstrated (Sun et al., 2005; Xiang et al., 2007; Diekmann et al., 2008; Yamamoto, 2009). These warm and highly saline waters transported by the KC may have significantly increased the SST of the OT (**Figure 4J**; Zheng et al., 2016). Therefore, the warming of the middle OT may be caused by the enhancement of KC intensities driven by the tropical Pacific during the Holocene. Furthermore, the most remarkable cold event at 7.4–6.6 kyr BP (~7.3 kyr BP) was widely reported in the southern and middle OT (Sun et al., 2005; Zhao et al., 2015; Xu et al., 2018). Since this ~7.3 kyr BP cold event has not been reported in the North Atlantic, factors other than the North Atlantic were likely responsible for the SST decrease in the middle OT (**Figure 4I**; Stuiver and Grootes, 2000). During the 7.4–6.6 kyr BP period, the KC intensity was weakened (Xiang et al., 2007; Hu et al., 2015), potentially contributing to the decreased temperatures of the middle OT (**Figures 4C,J**; Zheng et al., 2016).

However, the ~7.3 kyr BP cold event was magnified in the GDGT-related SST records. In core C14, the TEX^{H}_{86} SST showed a drop of ~5°C at 7.4–6.6 kyr BP (**Figure 4C**). A similar observation has been reported in the southern OT: the TEX^{H}_{86} SST dropped approximately 3–14°C during 7.6–6.9 kyr BP, whereas the Mg/Ca and $U^{K'}_{37}$ SST only showed a drop of 1–3°C during this period (Sun et al., 2005; Kubota et al., 2010; Zhao et al., 2015; Xu et al., 2018). Xu et al. (2018) attributed the 7.6–6.9 kyr BP SST drop to an unknown cold event that occurred during KC intensity weakening. However, the cold event during that period may not be solely responsible for such a large amplitude of decline in TEX^{H}_{86} SST. Global climate change cycles could also have regular influences on the SST of marginal seas (Ho and Laepple, 2015; Ignatov and Gutman, 1999; Debret et al., 2007). Sometimes, the SST of the OT could have suffered from strongly enhanced temperature amplitudes across climate cycles (Debret et al., 2007; Zhao et al., 2014). However, no noticeable long- and short-term climate effect on OT hydrology was reported during the last 7.4–6.6 kyr BP (Bond et al., 1997; Zhao et al., 2014). Factors controlling the abnormal TEX^{H}_{86} SST drop at ~7.3 kyr BP have not been resolved. In core C14, a tephra layer was found from 532.5 to 442.5 cm (K-Ah tephra; 7.4–6.6 kyr BP). A volcanic eruption that occurred at ~7.3 kyr BP has been identified in southwestern Japan (K-Ah tephra; Kitagawa et al., 1995), suggesting that the core C14 site was likely under the scope of the volcanic eruption (**Figure 1**). The K-Ah tephra has been

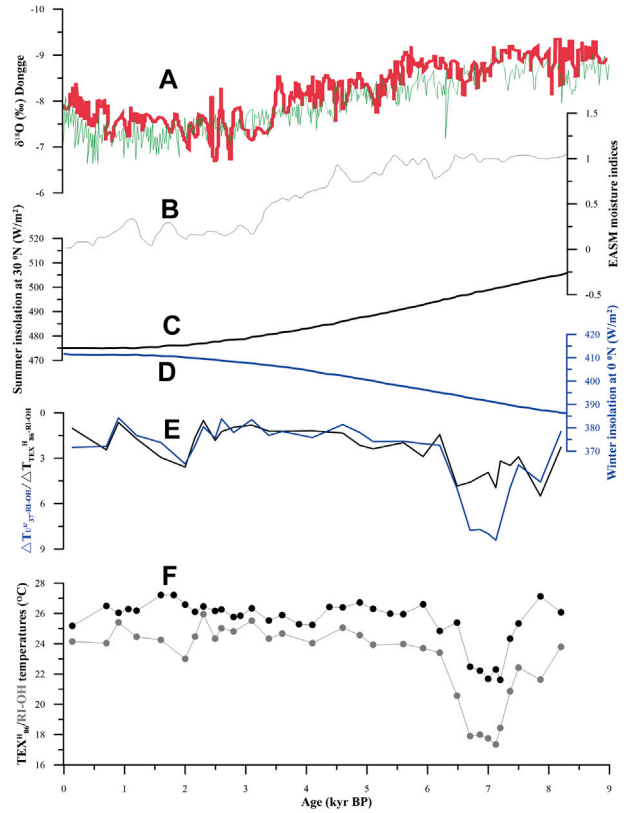

FIGURE 5 | Comparison of sea surface and subsurface temperature differences between TEX_{86}^{H} and RI-OH [$\Delta_{TEX_{86}^{H}-RI-OH}$ (°C)] and between $U_{37}^{K'}$ and RI-OH [$\Delta_{U_{37}^{K'}-RI-OH}$ (°C)] from core C14 ($U_{37}^{K'}$ SST from core DGKS9604 in the study area; Yu et al., 2009) with other paleoclimate data. **(A)** $\delta^{18}O$ records from Dongge Cave stalagmites, China (green: Wang et al., 2005; red: Dykoski et al., 2005); **(B)** the synthesized East Asian summer monsoon (EASM) moisture indices (Wang et al., 2010); **(C)** summer (June) insolation at 30°N (Berger and Loutre, 1991); **(D)** winter (December) insolation at 0°N (Berger and Loutre, 1991); **(E)** $\Delta_{TEX_{86}^{H}-RI-OH}$ (°C) (black) of core C14 and $\Delta_{U_{37}^{K'}-RI-OH}$ (°C) (blue) ($U_{37}^{K'}$ SST from core DGKS9604; Yu et al., 2009); **(F)** temperatures from TEX_{86}^{H} (dark) and RI-OH (gray) in core C14.

widely reported in sediments from the northern to middle OT (Sun et al., 2005; Kubota et al., 2010; Zheng et al., 2016). Modeling studies on Toba volcano in Sumatra have indicated that volcanic eruptions could result in spreading tephra, blocking sunlight, and thus leading to global or regional temperature cooling (Rampino and Self, 1992; Machida, 1999; Oppenheimer, 2002). For core C14, the sedimentation rate during the last 7.4–6.6 kyr BP is exceptionally high (~126 cm/kyr) compared to a nearby site (~20 cm/kyr; DGKS9604; Yu et al., 2009). Therefore, except for the decrease in KC intensity, the cold event and the extremely high sedimentation rate at ~7.3 kyr in core C14 were probably related to volcanic eruptions. The differences between TEX_{86}^{H} SST and SST records from the $U_{37}^{K'}$ and Mg/Ca at ~7.3 kyr BP in the OT may result from distinct sensibilities and responses of specific organisms to climate events (Schouten et al., 2013; Steinke et al., 2008 and references therein). However, the specific and detailed mechanism of the ash impacts on living communities remains unclear and requires further investigation.

Decoupling of the East Asian Summer Monsoon and Paleotemperatures in the Middle OT

The temperature difference between the sea surface and subsurface (ΔT) is sensitive to trace heat and water exchanges, reflecting the depth of the thermocline (DOT) of marginal seas (Jian et al., 2000; Lopes dos Santos et al., 2010; Jia et al., 2012; Yuan et al., 2018). In marginal seas, ΔT has been reported to have a negative relationship with DOT (Jian et al., 2000; Lopes dos Santos et al., 2010; Jia et al., 2012). In the OT, the DOT is mainly controlled by the EAM and KC, which stir the surface of the seawater and cause fluctuations in the DOT. Specifically, the enhancement in the EAM or KC intensities will lead to strengthened mixing of upper water and deepening of the DOT (a reduction in ΔT), and vice versa (Jian et al., 2000; Yamamoto et al., 2013).

In this study, TEX_{86}^{H} and $U_{37}^{K'}$ temperatures (DGKS9604; Yu et al., 2009) were used as SSTs, whereas RI-OH temperatures tentatively served as subsurface temperatures (**Figure 3C**). The temperature differences between TEX_{86}^{H} and RI-OH [$\Delta_{TEX_{86}^{H}-RI-OH}$ (°C)] and between $U_{37}^{K'}$ and RI-OH [$\Delta_{U_{37}^{K'}-RI-OH}$ (°C)] were calculated (**Figure 5E**). From 8.2 kyr BP to the present, a slight overall decrease was found for $\Delta_{TEX_{86}^{H}-RI-OH}$ (°C) and $\Delta_{U_{37}^{K'}-RI-OH}$ (°C), suggesting an increased mixing of the upper water column in the middle OT (**Figure 5E**). Studies on the Holocene EASM intensity showed that the EASM intensity reached a maximum at ~7.0 kyr or ~9.0 kyr (Yang et al., 2019; Liu et al., 2015; Wang et al., 2005; Dykoski et al., 2005). However, the EASM is primarily impacted by summer (June) insolation at 30°N, exhibiting a gradually decreasing trend since 8.2 kyr (**Figure 5C**; Berger and Loutre, 1991). Therefore, the increased mixing of upper water was inconsistent with the EASM intensity, especially over the last 7.0 kyr BP, indicating the decoupling of SSTs in the middle OT with the EASM (**Figures 5A–C**). In the middle Holocene, a decoupling trend between thermal conditions and precipitation has been revealed by pollen sequences from Taiwan (Liew et al., 2006). For land records, decoupling between temperature warming, which was likely caused by the strong influence of low-latitude warm currents, and the EASM intensities were common during the Holocene (Peterse et al., 2011; Park et al., 2014; Wu et al., 2017). The low-latitude warm currents flowing through the OT, such as the KC, may warm and stir the seawater and overstep the influence of high-latitude climates, causing the decoupling of SSTs in the middle OT with the EASM (Zheng et al., 2014, 2016; Xu et al., 2018).

In the present study, the TEX_{86}^{H} SST, revealed a gradual warming trend in the middle OT since 8.2 kyr BP (**Figure 5F**). Modeling of the Holocene climate showed that moderate temperature warming was caused by winter warming that slightly exceeded summer cooling in the tropics (Lorenz et al., 2006). Therefore, the warming trend in the middle OT might be caused by the increased boreal winter insolation at low latitudes (**Figures 5D,F**).

CONCLUSION

Paleotemperatures were reconstructed for the last 8.2 kyr in the middle Okinawa Trough (OT) using TEX_{86}^{H} and RI-OH. IsoGDGTs were mainly derived from marine *Thaumarchaeota,* and TEX_{86}^{H} can be used to reconstruct temperatures of the middle OT, as revealed by GDGT-0/crenarchaeol, BIT, %GDGT-2, and MI. TEX_{86}^{H} temperatures in this study indicated mean annual SSTs close to the $U_{37}^{K'}$ SST of the middle OT. In contrast, RI-OH temperatures were interpreted to represent subsurface temperatures relatively lower than the TEX_{86}^{H} and $U_{37}^{K'}$ SSTs. The cold event at ~7.3 kyr BP and the general warming trend, as revealed by the TEX_{86}^{H} and RI-OH temperatures at 8.2 kyr BP, were attributed to the increasing Kuroshio Current intensity punctuated by a decline at ~7.3 kyr BP. The decreasing temperature differences between TEX_{86}^{H} and RI-OH and between $U_{37}^{K'}$ and RI-OH indicated the decoupling of the SSTs in the middle OT and the East Asian summer monsoon during 8.2 kyr BP. The magnification of the cold phase in TEX_{86}^{H} and the extremely high sedimentation rate at 7.4–6.6 kyr BP were probably partially due to the widespread Kikai-Akahoya tephra (~7.3 kyr).

DATA AVAILABILITY STATEMENT

The original contributions presented in the study are included in the article/**Supplementary Material**, further inquiries can be directed to the corresponding authors.

AUTHOR CONTRIBUTIONS

LL and HG was responsible for writing manuscripts. LX and LL conducted tests. ZS and NW provided the studied samples. HG revised texts, and NW and ZS revised texts and provided comments.

FUNDING

This research was supported by the National Natural Science Foundation of China (91958105 and 91858208) and the Marine S&T Fund of Shandong Province for Pilot National Laboratory for Marine Science and Technology (Qingdao) (No.2021QNLM020002).

ACKNOWLEDGMENTS

The authors are grateful to H. Yang (CUG (Wuhan)] and J. He (GIG, CAS) for technical assistance. We thank F. Xu (CUP, Qingdao) and J. Zhao (QIMG) for offering paleoclimate data, and the help of D. Li (OUC, Qingdao) and X. Lü (CUG (Wuhan)].

SUPPLEMENTARY MATERIAL

The Supplementary Material for this article can be found online at: https://www.frontiersin.org/articles/10.3389/feart.2022.799280/full#supplementary-material

REFERENCES

An, Z., Kutzbach, J. E., Prell, W. L., and Porter, S. C. (2001). Evolution of Asian Monsoons and Phased Uplift of the Himalaya-Tibetan Plateau since Late Miocene Times. *Nature* 411 (6833), 62–66. doi:10.1038/35075035

Berger, A., and Loutre, M. F. (1991). Insolation Values for the Climate of the Last 10 Million Years. *Quat. Sci. Rev.* 10, 297–317. doi:10.1016/0277-3791(91)90033-Q

Blaga, C. I., Reichart, G.-J., Heiri, O., and Sinninghe Damsté, J. S. (2009). Tetraether Membrane Lipid Distributions in Water-Column Particulate Matter and Sediments: a Study of 47 European Lakes along a north-south Transect. *J. Paleolimnol.* 41, 523–540. doi:10.1007/s10933-008-9242-2

Bond, G., Showers, W., Cheseby, M., Lotti, R., Almasi, P., deMenocal, P., et al. (1997). A Pervasive Millennial-Scale Cycle in North Atlantic Holocene and Glacial Climates. *Science* 278, 1257–1266. doi:10.1126/science.278.5341.1257

Brochier-Armanet, C., Boussau, B., Gribaldo, S., and Forterre, P. (2008). Mesophilic Crenarchaeota: Proposal for a Third Archaeal Phylum, the Thaumarchaeota. *Nat. Rev. Microbiol.* 6, 245–252. doi:10.1038/nrmicro1852

De Jonge, C., Hopmans, E. C., Zell, C. I., Kim, J.-H., Schouten, S., and Sinninghe Damsté, J. S. (2014). Occurrence and Abundance of 6-methyl Branched Glycerol Dialkyl Glycerol Tetraethers in Soils: Implications for Palaeoclimate Reconstruction. *Geochimica et Cosmochimica Acta* 141, 97–112. doi:10.1016/j.gca.2014.06.013

Debret, M., Bout-Roumazeilles, V., Grousset, F., Desmet, M., McManus, J. F., Massei, N., et al. (2007). The Origin of the 1500-year Climate Cycles in Holocene North-Atlantic Records. *Clim. Past* 3, 569–575. doi:10.5194/cp-3-569-2007

Diekmann, B., Hofmann, J., Henrich, R., Fütterer, D. K., Röhl, U., and Wei, K.-Y. (2008). Detrital Sediment Supply in the Southern Okinawa Trough and its Relation to Sea-Level and Kuroshio Dynamics during the Late Quaternary. *Mar. Geology.* 255, 83–95. doi:10.1016/j.margeo.2008.08.001

Dykoski, C., Edwards, R., Cheng, H., Yuan, D., Cai, Y., Zhang, M., et al. (2005). A High-Resolution, Absolute-Dated Holocene and Deglacial Asian Monsoon Record from Dongge Cave, China. *Earth Planet. Sci. Lett.* 233, 71–86. doi:10.1016/j.epsl.2005.01.036

Elling, F. J., Könneke, M., Lipp, J. S., Becker, K. W., Gagen, E. J., and Hinrichs, K.-U. (2014). Effects of Growth Phase on the Membrane Lipid Composition of the Thaumarchaeon Nitrosopumilus Maritimus and Their Implications for Archaeal Lipid Distributions in the marine Environment. *Geochimica et Cosmochimica Acta* 141, 579–597. doi:10.1016/j.gca.2014.07.005

Elvert, M., Hopmans, E. C., Treude, T., Boetius, A., and Suess, E. (2005). Spatial Variations of Methanotrophic Consortia at Cold Methane Seeps: Implications from a High-Resolution Molecular and Isotopic Approach. *Geobiology* 3, 195–209. doi:10.1111/j.1472-4669.2005.00051.x

Fietz, S., Huguet, C., Rueda, G., Hambach, B., and Rosell-Melé, A. (2013). Hydroxylated Isoprenoidal GDGTs in the Nordic Seas. *Mar. Chem.* 152, 1–10. doi:10.1016/j.marchem.2013.02.007

Gliozzi, A., Paoli, G., De Rosa, M., and Gambacorta, A. (1983). Effect of Isoprenoid Cyclization on the Transition Temperature of Lipids in Thermophilic Archaebacteria. *Biochim. Biophys. Acta (Bba) - Biomembranes* 735, 234–242. doi:10.1016/0005-2736(83)90298-5

Guan, H., Feng, D., Birgel, D., Peckmann, J., Roberts, H. H., Wu, N., et al. (2019). Lipid Biomarker Patterns Reflect Different Formation Environments of Mussel- and Tubeworm-Dominated Seep Carbonates from the Gulf of Mexico (Atwater Valley and Green Canyon). *Chem. Geology.* 505, 36–47. doi:10.1016/j.chemgeo.2018.12.005

Guo, X., Li, C., Gao, R., Li, S., Xu, X., Lu, Z., et al. (2022). The India-Eurasia Convergence System: Late Oligocene to Early Miocene Passive Roof Thrusting Driven by Deep-rooted Duplex Stacking. *Geosystems and Geoenvironment* 1 (1), 100006. doi:10.1016/j.geogeo.2021.09.005

Ho, S. L., and Laepple, T. (2015). Glacial Cooling as Inferred from marine Temperature Proxies TEX_{86}^{H} and $U_{37}^{K'}$. *Earth Planet. Sci. Lett.* 409, 15–22. doi:10.1016/j.epsl.2014.10.033

Hopmans, E. C., Schouten, S., and Sinninghe Damsté, J. S. (2016). The Effect of Improved Chromatography on GDGT-Based Palaeoproxies. *Org. Geochem.* 93, 1–6. doi:10.1016/j.orggeochem.2015.12.006

Hopmans, E. C., Weijers, J. W. H., Schefuss, E., Herfort, L., Sinninghe Damsté, J. S., and Schouten, S. (2004). A Novel Proxy for Terrestrial Organic Matter in Sediments Based on Branched and Isoprenoid Tetraether Lipids. *Earth Planet. Sci. Lett.* 224, 107–116. doi:10.1016/j.epsl.2004.05.012

Hu, D., Wu, L., Cai, W., Gupta, A. S., Ganachaud, A., Qiu, B., et al. (2015). Pacific Western Boundary Currents and Their Roles in Climate. *Nature* 522, 299–308. doi:10.1038/nature14504

Huang, J., and Sarnthein, M. (2021). One Million Years of Seasonal Seesaw in East Asian Monsoon Winds. *Quat. Sci. Rev.* 274. doi:10.1016/j.quascirev.2021.107277

Huguet, C., Fietz, S., and Rosell-Melé, A. (2013). Global Distribution Patterns of Hydroxy Glycerol Dialkyl Glycerol Tetraethers. *Org. Geochem.* 57, 107–118. doi:10.1016/j.orggeochem.2013.01.010

Huguet, C., Schimmelmann, A., Thunell, R., Lourens, L. J., Sinninghe Damsté, J. S., and Schouten, S. (2007). A Study of the TEX_{86} paleothermometer in the Water Column and Sediments of the Santa Barbara Basin, California. *Paleoceanography* 22, a–n. doi:10.1029/2006PA001310

Ignatov, A., and Gutman, G. (1999). Monthly Mean Diurnal Cycles in Surface Temperatures over Land for Global Climate Studies. *J. Clim.* 12, 1900–1910. doi:10.1175/1520-0442(1999)012<1900:MMDCIS>2.0.CO;2

Ingalls, A. E., Shah, S. R., Hansman, R. L., Aluwihare, L. I., Santos, G. M., Druffel, E. R. M., et al. (2006). Quantifying Archaeal Community Autotrophy in the Mesopelagic Ocean Using Natural Radiocarbon. *Proc. Natl. Acad. Sci.* 103, 6442–6447. doi:10.1073/pnas.0510157103

Jia, G., Zhang, J., Chen, J., Peng, P. a., and Zhang, C. L. (2012). Archaeal Tetraether Lipids Record Subsurface Water Temperature in the South China Sea. *Org. Geochem.* 50, 68–77. doi:10.1016/j.orggeochem.2012.07.002

Jian, Z., Wang, P., Saito, Y., Wang, J., Pflaumann, U., Oba, T., et al. (2000). Holocene Variability of the Kuroshio Current in the Okinawa Trough, Northwestern Pacific Ocean. *Earth Planet. Sci. Lett.* 184, 305–319. doi:10.1016/s0012-821x(00)00321-6

Karner, M. B., DeLong, E. F., and Karl, D. M. (2001). Archaeal Dominance in the Mesopelagic Zone of the Pacific Ocean. *Nature* 409, 507–510. doi:10.1038/35054051

Kim, J.-H., van der Meer, J., Schouten, S., Helmke, P., Willmott, V., Sangiorgi, F., et al. (2010). New Indices and Calibrations Derived from the Distribution of Crenarchaeal Isoprenoid Tetraether Lipids: Implications for Past Sea Surface Temperature Reconstructions. *Geochimica et Cosmochimica Acta* 74, 4639–4654. doi:10.1016/j.gca.2010.05.027

Kitagawa, H., Fukuzawa, H., Nakamura, T., Okamura, M., Takemura, K., Hayashida, A., et al. (1995). AMS 14C Dating of Varved Sediments from Lake Suigetsu, Central Japan and Atmospheric 14C Change during the Late Pleistocene. *Radiocarbon* 37, 371–378. doi:10.1017/S0033822200030848

Kubota, Y., Kimoto, K., Tada, R., Oda, H., Yokoyama, Y., and Matsuzaki, H. (2010). Variations of East Asian Summer Monsoon since the Last Deglaciation Based on Mg/Ca and Oxygen Isotope of Planktic Foraminifera in the Northern East China Sea. *Paleoceanography* 25, a–n. doi:10.1029/2009PA001891

Li, C., Pan, J., and Que, Z. (2011). Variation of the East Asian Monsoon and the Tropospheric Biennial Oscillation. *Chin. Sci. Bull.* 56 (1), 70–75. doi:10.1007/s11434-010-4200-6

Liew, P. M., Lee, C. Y., and Kuo, C. M. (2006). Holocene thermal Optimal and Climate Variability of East Asian Monsoon Inferred from forest Reconstruction of a Subalpine Pollen Sequence, Taiwan. *Earth Planet. Sci. Lett.* 250 (3–4), 596–605. doi:10.1016/j.epsl.2006.08.002

Lim, J., and Fujiki, T. (2011). Vegetation and Climate Variability in East Asia Driven by Low-Latitude Oceanic Forcing during the Middle to Late Holocene. *Quat. Sci. Rev.* 30 (19–20), 2487–2497. doi:10.1016/j.quascirev.2011.05.013

Liu, J., Chen, J., Zhang, X., Li, Y., Rao, Z., and Chen, F. (2015). Holocene East Asian Summer Monsoon Records in Northern China and Their Inconsistency with Chinese Stalagmite $\delta^{18}O$ Records. *Earth-Science Rev.* 148, 194–208. doi:10.1016/j.earscirev.2015.06.004

Liu, J. P., Milliman, J. D., Gao, S., and Cheng, P. (2004). Holocene Development of the Yellow River's Subaqueous delta, North Yellow Sea. *Mar. Geology.* 209, 45–67. doi:10.1016/j.margeo.2004.06.009

Liu, X.-L., Summons, R. E., and Hinrichs, K.-U. (2012). Extending the Known Range of Glycerol Ether Lipids in the Environment: Structural Assignments Based on Tandem Mass Spectral Fragmentation Patterns. *Rapid Commun. Mass. Spectrom.* 26, 2295–2302. doi:10.1002/rcm.6355

Locarnini, R. A., Mishonov, A. V., Antonov, J. I., Boyer, T. P., Garcia, H. E., Baranova, O. K., et al. (2013). World Ocean Atlas 2013, Volume 1: Temperatures. *NOAA Atlas NESDIS* 73, 1–40.

Lopes dos Santos, R. A., Prange, M., Castañeda, I. S., Schefuss, E., Mulitza, S., Schulz, M., et al. (2010). Glacial-interglacial Variability in Atlantic Meridional Overturning Circulation and Thermocline Adjustments in the Tropical North Atlantic. *Earth Planet. Sci. Lett.* 300, 407–414. doi:10.1016/j.epsl.2010.10.030

Lorenz, S. J., Kim, J.-H., Rimbu, N., Schneider, R. R., and Lohmann, G. (2006). Orbitally Driven Insolation Forcing on Holocene Climate Trends: Evidence from Alkenone Data and Climate Modeling. *Paleoceanography* 21 (PA1002), a–n. doi:10.1029/2005pa001152

Lü, X., Liu, X.-L., Elling, F. J., Yang, H., Xie, S., Song, J., et al. (2015). Hydroxylated Isoprenoid GDGTs in Chinese Coastal Seas and Their Potential as a Paleotemperature Proxy for Mid-to-low Latitude Marginal Seas. *Org. Geochem.* 89-90, 31–43. doi:10.1016/j.orggeochem.2015.10.004

Machida, H. (1999). The Stratigraphy, Chronology and Distribution of Distal Marker-Tephras in and Around Japan. *Glob. Planet Change* 21 (1–3), 71–94. doi:10.1016/s0921-8181(99)00008-9

Nakanishi, T., Yamamoto, M., Irino, T., and Tada, R. (2012). Distribution of Glycerol Dialkyl Glycerol Tetraethers, Alkenones and Polyunsaturated Fatty Acids in Suspended Particulate Organic Matter in the East China Sea. *J. Oceanogr.* 68, 959–970. doi:10.1007/s10872-012-0146-4

Oppenheimer, C. (2002). Limited Global Change Due to the Largest Known Quaternary Eruption, Toba ≈74 Kyr BP? *Quat. Sci. Rev.* 21 (14–15), 1593–1609. doi:10.1016/S0277-3791(01)00154-8

Park, J., Lim, H. S., Lim, J., and Park, Y.-H. (2014). High-resolution Multi-Proxy Evidence for Millennial- and Centennial-Scale Climate Oscillations during the Last Deglaciation in Jeju Island, South Korea. *Quat. Sci. Rev.* 105, 112–125. doi:10.1016/j.quascirev.2014.10.003

Peterse, F., Prins, M. A., Beets, C. J., Troelstra, S. R., Zheng, H., Gu, Z., et al. (2011). Decoupled Warming and Monsoon Precipitation in East Asia over the Last Deglaciation. *Earth Planet. Sci. Lett.* 301 (1–2), 256–264. doi:10.1016/j.epsl.2010.11.010

Peterse, F., Schouten, S., van der Meer, J., van der Meer, M. T. J., and Sinninghe Damsté, J. S. (2009). Distribution of Branched Tetraether Lipids in Geothermally Heated Soils: Implications for the MBT/CBT Temperature Proxy. *Org. Geochem.* 40, 201–205. doi:10.1016/j.orggeochem.2008.10.010

Pitcher, A., Hopmans, E. C., Mosier, A. C., Park, S.-J., Rhee, S.-K., Francis, C. A., et al. (2011). Core and Intact Polar Glycerol Dibiphytanyl Glycerol Tetraether Lipids of Ammonia-Oxidizing Archaea Enriched from Marine and Estuarine Sediments. *Appl. Environ. Microbiol.* 77, 3468–3477. doi:10.1128/aem.02758-10

Rampino, M. R., and Self, S. (1992). Volcanic winter and Accelerated Glaciation Following the Toba Super-eruption. *Nature* 359, 50–52. doi:10.1038/359050a0

Reimer, P. J., Bard, E., Bayliss, A., Beck, J. W., Blackwell, P. G., Ramsey, C. B., et al. (2013). Intcal13 and marine13 Radiocarbon Age Calibration Curves 0-50,000 Years Cal BP. *Radiocarbon* 55, 1869–1887. doi:10.2458/azu_js_rc.55.16947

Ruan, J., Xu, Y., Ding, S., Wang, Y., and Zhang, X. (2015). A High Resolution Record of Sea Surface Temperature in Southern Okinawa Trough for the Past 15,000 Years. *Palaeogeogr. Palaeoclimatol. Palaeoecol.* 426, 209–215. doi:10.1016/j.palaeo.2015.03.007

Rueda, G., Rosell-Melé, A., Escala, M., Gyllencreutz, R., and Backman, J. (2009). Comparison of Instrumental and GDGT-Based Estimates of Sea Surface and Air Temperatures from the Skagerrak. *Org. Geochem.* 40, 287–291. doi:10.1016/j.orggeochem.2008.10.012

Schouten, S., Hopmans, E. C., Baas, M., Boumann, H., Standfest, S., Könneke, M., et al. (2008). Intact Membrane Lipids of " Candidatus Nitrosopumilus Maritimus," a Cultivated Representative of the Cosmopolitan Mesophilic Group I Crenarchaeota. *Appl. Environ. Microbiol.* 74, 2433–2440. doi:10.1128/aem.01709-07

Schouten, S., Hopmans, E. C., Schefuß, E., and Sinninghe Damsté, J. S. (2002). Distributional Variations in marine Crenarchaeotal Membrane Lipids: a New Tool for Reconstructing Ancient Sea Water Temperatures? *Earth Planet. Sci. Lett.* 204, 265–274. doi:10.1016/S0012-821X(02)00979-2

Schouten, S., Hopmans, E. C., and Sinninghe Damsté, J. S. (2013). The Organic Geochemistry of Glycerol Dialkyl Glycerol Tetraether Lipids: A Review. *Org. Geochem.* 54, 19–61. doi:10.1016/j.orggeochem.2012.09.006

Sibuet, J.-C., Deffontaines, B., Hsu, S.-K., Thareau, N., Le Formal, J.-P., Liu, C.-S., et al. (1998). Okinawa Trough Backarc basin: Early Tectonic and Magmatic Evolution. *J. Geophys. Res.* 103, 30245–30267. doi:10.1029/98jb01823

Sinninghe Damsté, J. S., Hopmans, E. C., Schouten, S., van Duin, A. C. T., and Geenevasen, J. A. J. (2002). Crenarchaeol: The Characteristic Core Glycerol Dibiphytanyl Glycerol Tetraether Membrane Lipid of Cosmopolitan Pelagic Crenarchaeota. *J. Lipid Res.* 43, 1641–1651. doi:10.1194/jlr.M200148-JLR200

Sinninghe Damsté, J. S., Ossebaar, J., Schouten, S., and Verschuren, D. (2012a). Distribution of Tetraether Lipids in the 25-ka Sedimentary Record of Lake Challa: Extracting Reliable TEX86 and MBT/CBT Palaeotemperatures from an Equatorial African lake. *Quat. Sci. Rev.* 50, 43–54. doi:10.1016/j.quascirev.2012.07.0010.1016/j.quascirev.2012.07.001

Sinninghe Damsté, J. S., Rijpstra, W. I., Hopmans, E. C., Jung, M. Y., Kim, J. G., Rhee, S. K., et al. (2012b). Intact Polar and Core Glycerol Dibiphytanyl Glycerol Tetraether Lipids of Group I.1a and I.1b Thaumarchaeota in Soil. *Appl. Environ. Microbiol.* 78, 6866–6874. doi:10.1128/AEM.01681-12

Spang, A., Hatzenpichler, R., Brochier-Armanet, C., Rattei, T., Tischler, P., Spieck, E., et al. (2010). Distinct Gene Set in Two Different Lineages of Ammonia-Oxidizing Archaea Supports the Phylum Thaumarchaeota. *Trends Microbiol.* 18, 331–340. doi:10.1016/j.tim.2010.06.003

Steinke, S., Kienast, M., Groeneveld, J., Lin, L.-C., Chen, M.-T., and Rendle-Bühring, R. (2008). Proxy Dependence of the Temporal Pattern of Deglacial Warming in the Tropical South China Sea: toward Resolving Seasonality. *Quat. Sci. Rev.* 27, 688–700. doi:10.1016/j.quascirev.2007.12.003

Stott, L., Cannariato, K., Thunell, R., Haug, G. H., Koutavas, A., and Lund, S. (2004). Decline of Surface Temperature and Salinity in the Western Tropical Pacific Ocean in the Holocene Epoch. *Nature* 431 (7004), 56–59. doi:10.1038/nature02903

Stuiver, M., and Grootes, P. M. (2000). GISP2 Oxygen Isotope Ratios. *Quat. Res.* 53, 277–284. doi:10.1006/qres.2000.2127

Sun, Y., Oppo, D. W., Xiang, R., Liu, W., and Gao, S. (2005). Last Deglaciation in the Okinawa Trough: Subtropical Northwest Pacific Link to Northern Hemisphere and Tropical Climate. *Paleoceanography* 20 (4), a–n. doi:10.1029/2004PA001061

Taylor, K. W. R., Huber, M., Hollis, C. J., Hernandez-Sanchez, M. T., and Pancost, R. D. (2013). Re-evaluating Modern and Palaeogene GDGT Distributions: Implications for SST Reconstructions. *Glob. Planet. Change* 108, 158–174. doi:10.1016/j.gloplacha.2013.06.011

Tierney, J. E., and Tingley, M. P. (20142014). A Bayesian, Spatially-Varying Calibration Model for the TEX86 Proxy. *Geochimica et Cosmochimica Acta* 127, 83–106. doi:10.1016/j.gca.2013.11.026

Turich, C., Freeman, K. H., Bruns, M. A., Conte, M., Jones, A. D., and Wakeham, S. G. (2007). Lipids of marine Archaea: Patterns and Provenance in the Water-Column and Sediments. *Geochimica et Cosmochimica Acta* 71, 3272–3291. doi:10.1016/j.gca.2007.04.013

Uda, I., Sugai, A., Itoh, Y. H., and Itoh, T. (2001). Variation in Molecular Species of Polar Lipids from Thermoplasma Acidophilum Depends on Growth Temperature. *Lipids* 36, 103–105. doi:10.1007/s11745-001-0914-2

Wang, Y., Cheng, H., Edwards, R. L., He, Y., Kong, X., An, Z., et al. (2005). The Holocene Asian Monsoon: Links to Solar Changes and North Atlantic Climate. *Science* 308 (5723), 854–857. doi:10.1126/science.1106296

Wang, Y., Liu, X., and Herzschuh, U. (2012). Asynchronous Evolution of the Indian and East Asian Summer Monsoon Indicated by Holocene Moisture Patterns in Monsoonal central Asia. *Quat. Int.* 279-280 (3–4), 526–153. doi:10.1016/j.quaint.2012.08.1829

Weijers, J. W. H., Lim, K. L. H., Aquilina, A., Sinninghe Damsté, J. S., and Pancost, R. D. (2011). Biogeochemical Controls on Glycerol Dialkyl Glycerol Tetraether Lipid Distributions in Sediments Characterized by Diffusive Methane Flux. *Geochem. Geophys. Geosyst.* 12, a–n. doi:10.1029/2011GC003724

Wu, M.-S., Zong, Y., Mok, K.-M., Cheung, K.-M., Xiong, H., and Huang, G. (2017). Holocene Hydrological and Sea Surface Temperature Changes in the Northern Coast of the South China Sea. *J. Asian Earth Sci.* 135, 268–280. doi:10.1016/j.jseaes.2017.01.004

Wu, Z., Li, J., Jin, X., Shang, J., Li, S., and Jin, X. (2014). Distribution, Features, and Influence Factors of the Submarine Topographic Boundaries of the Okinawa Trough. *Sci. China Earth Sci.* 57, 1885–1896. doi:10.1007/s11430-013-4810-3

Xiang, R., Sun, Y., Li, T., Oppo, D. W., Chen, M., and Zheng, F. (2007). Paleoenvironmental Change in the Middle Okinawa Trough since the Last Deglaciation: Evidence from the Sedimentation Rate and Planktonic Foraminiferal Record. *Palaeogeogr. Palaeoclimatol. Palaeoecol.* 243, 378–393. doi:10.1016/j.palaeo.2006.08.016

Xu, F., Dou, Y., Li, J., Cai, F., Zhao, J., Wen, Z., et al. (2018). Low-latitude Climate Control on Sea-Surface Temperatures Recorded in the Southern Okinawa Trough during the Last 13.3 Kyr. *Palaeogeogr. Palaeoclimatol. Palaeoecol.* 490, 210–217. doi:10.1016/j.palaeo.2017.10.034

Xu, L. F., Guan, H. X., Sun, Z. L., Wang, L. B., Mao, S. Y., Liu, L. H., et al. (2020). The Response Mechanism of Organic Matters and Paleoenvironmental Changes in the central Okinawa Trough during the Last 8.2 Ka. *Geochimica (Chinese)* 6, 653–665.

Yamamoto, M., Kishizaki, M., Oba, T., and Kawahata, H. (2013). Intense winter Cooling of the Surface Water in the Northern Okinawa Trough during the Last Glacial Period. *J. Asian Earth Sci.* 69, 86–92. doi:10.1016/j.jseaes.2012.06.011

Yamamoto, M. (2009). Response of Mid-latitude North Pacific Surface Temperatures to Orbital Forcing and Linkage to the East Asian Summer Monsoon and Tropical Ocean-Atmosphere Interactions. *J. Quat. Sci.* 24, 836–847. doi:10.1002/jqs.1255

Yamamoto, M., Shimamoto, A., Fukuhara, T., Tanaka, Y., and Ishizaka, J. (2012). Glycerol Dialkyl Glycerol Tetraethers and TEX86 index in Sinking Particles in the Western North Pacific. *Org. Geochem.* 53, 52–62. doi:10.1016/j.orggeochem.2012.04.010

Yang, X., Yang, H., Wang, B., Huang, L.-J., Shen, C.-C., Edwards, R. L., et al. (2019). Early-Holocene Monsoon Instability and Climatic Optimum Recorded by Chinese Stalagmites. *The Holocene* 29, 1059–1067. doi:10.1177/0959683619831433

Yang, Y., Gao, C., Dang, X., Ruan, X., Lü, X., Xie, S., et al. (2018). Assessing Hydroxylated Isoprenoid GDGTs as a Paleothermometer for the Tropical South China Sea. *Org. Geochem.* 115, 156–165. doi:10.1016/j.orggeochem.2017.10.014

Yu, H., Liu, Z., Berné, S., Jia, G., Xiong, Y., Dickens, G. R., et al. (2009). Variations in Temperature and Salinity of the Surface Water above the Middle Okinawa Trough during the Past 37kyr. *Palaeogeogr. Palaeoclimatol. Palaeoecol.* 281, 154–164. doi:10.1016/j.palaeo.2009.08.002

Yuan, Z., Xiao, X., Wang, F., Xing, l., Wang, Z., Zhang, H., et al. (2018). Spatiotemporal Temperature Variations in the East China Sea Shelf during the Holocene in Response to Surface Circulation Evolution. *Quat. Int.* 482, 46–55. doi:10.1016/j.quaint.2018.04.025

Zhang, Y. G., and Liu, X. (2018). Export Depth of the TEX 86 Signal. *Paleoceanography and Paleoclimatology* 33, 666–671. doi:10.1029/2018PA003337

Zhang, Y. G., Zhang, C. L., Liu, X.-L., Li, L., Hinrichs, K.-U., and Noakes, J. E. (2011). Methane Index: A Tetraether Archaeal Lipid Biomarker Indicator for Detecting the Instability of marine Gas Hydrates. *Earth Planet. Sci. Lett.* 307, 525–534. doi:10.1016/j.epsl.2011.05.031

Zhao, J., Li, J., Cai, F., Wei, H., Hu, B., Dou, Y., et al. (2015). Sea Surface Temperature Variation during the Last Deglaciation in the Southern Okinawa Trough: Modulation of High Latitude Teleconnections and the Kuroshio Current. *Prog. Oceanography* 138, 238–248. doi:10.1016/j.pocean.2015.06.008

Zhao, M., Ding, L., Xing, L., Qiao, S., and Yang, Z. (2014). Major Mid-late Holocene Cooling in the East China Sea Revealed by an Alkenone Sea Surface Temperature Record. *J. Ocean Univ. China* 13, 935–940. doi:10.1007/s11802-014-2641-2

Zheng, X., Li, A., Kao, S., Gong, X., Frank, M., Kuhn, G., et al. (2016). Synchronicity of Kuroshio Current and Climate System Variability since the Last Glacial Maximum. *Earth Planet. Sci. Lett.* 452, 247–257. doi:10.1016/j.epsl.2016.07.028

Zheng, X., Li, A., Wan, S., Jiang, F., Kao, S. J., and Johnson, C. (2014). ITCZ and ENSO Pacing on East Asian winter Monsoon Variation during the Holocene: Sedimentological Evidence from the Okinawa Trough. *J. Geophys. Res. Oceans* 119, 4410–4429. doi:10.1002/2013JC009603

Conflict of Interest: The authors declare that the research was conducted in the absence of any commercial or financial relationships that could be construed as a potential conflict of interest.

Publisher's Note: All claims expressed in this article are solely those of the authors and do not necessarily represent those of their affiliated organizations, or those of the publisher, the editors and the reviewers. Any product that may be evaluated in this article, or claim that may be made by its manufacturer, is not guaranteed or endorsed by the publisher.

Advantages of publishing in Frontiers

OPEN ACCESS
Articles are free to read for greatest visibility and readership

FAST PUBLICATION
Around 90 days from submission to decision

HIGH QUALITY PEER-REVIEW
Rigorous, collaborative, and constructive peer-review

TRANSPARENT PEER-REVIEW
Editors and reviewers acknowledged by name on published articles

Frontiers
Avenue du Tribunal-Fédéral 34
1005 Lausanne | Switzerland

Visit us: www.frontiersin.org
Contact us: frontiersin.org/about/contact

REPRODUCIBILITY OF RESEARCH
Support open data and methods to enhance research reproducibility

DIGITAL PUBLISHING
Articles designed for optimal readership across devices

FOLLOW US
@frontiersin

IMPACT METRICS
Advanced article metrics track visibility across digital media

EXTENSIVE PROMOTION
Marketing and promotion of impactful research

LOOP RESEARCH NETWORK
Our network increases your article's readership